

**Fabrication and efficacy of
poly (beta-amino esters)-based
nanoparticles to enhance antimicrobial
agents delivery to orthopaedic acquired
infections sites**

A thesis submitted in accordance with the conditions
governing candidates for the degree of

Philosophiae Doctor in Cardiff University

by

Silvia Latanza

December 2020

Cardiff School of Pharmacy and Pharmaceutical Sciences
Cardiff University



Acknowledgments

I would like to take the occasion to express my sincere gratitude to all the people that I had the pleasure to meet along this challenging but great journey.

First of all, my supervisor, Dr. Polina Prokopovich, for offering me great support, encouragement and advice and for choosing me as her student to carry out this project.

Then, I would like to thank Dr. Stefano Perni for contributing to improve my research skills, especially in my first year of PhD, and to my colleagues for the pleasant moments spent together in the lab.

I also want to thank Prof. Andrea Brancale for his constant optimism and his helpful guidance as assigned advisor of this project.

My deepest appreciation is addressed to all the staff of the School of Pharmacy and Pharmaceutical Science for their continuous support and their careful attention to all the students of the school.

In addition, I thank the Life Science Research Network of Wales and Cardiff University for funding this research programme and providing the chance to attend scientific conferences.

Finally, I can't thank my family, friends and my endless love Fabio enough, for always being there for me and for making my life plenty of joy and love.

Thank you all, I will always keep these years in my mind and in my heart.

Dedicated to mum, dad and Fabio.

Summary

Total joint replacement (TJR) is the last choice for the treatment of end-stage joint diseases. One of its adverse complications is prosthetic joint infection (PJI), that is often treated in clinical practice with antibiotic loaded bone cements (ALBC). However, their application is considered controversial and a time-limited solution. Indeed, antibiotics provide a short-term burst release which drops below inhibitory levels leading to a gradual loss of their efficacy and to an increase of bacterial resistance. Therefore, to overcome these problems, the development of novel antimicrobial strategies is required.

This work aims to determine the optimal nanocarrier construct, employing poly (β -amino esters) (PBAEs) as polycations, able to provide prolonged antimicrobial agents release as early-stage alternative strategy of prophylaxis for orthopaedic infections.

For this purpose, six diacrylates have been co-polymerized with three amines to form eighteen poly-beta-amino-esters (PBAE) polymers, characterized by ^1H and ^{13}C NMR spectroscopy, Gel Permeation Chromatography (GPC) and zeta potential. Thirty-six nanocoating systems have been obtained, via Layer by Layer technique (LbL), eighteen including chlorhexidine whereas eighteen tobramycin, and the drug release has been monitored over weeks under different pH conditions.

Zeta potential and thermogravimetric analysis examined the binding among drug, PBAEs and nanoparticles. The chlorhexidine has been released for a period between 45 and 60 days and tobramycin over 30 days showing that lower electrostatic interactions of the polyelectrolytes at pH 7.4 increased the release kinetics, while the opposite occurred at pH 5. These results were consistent to the pH degradation profiles of the eighteen PBAEs: the polymers hydrolysed more slowly at pH 5 than pH 7.4.

LbL is a suitable technique that can control antimicrobial agents release by diffusion of the drug through the layers and the possible delamination of the coating from silica nanoparticles for several days. The choice of the monomers employed in the polymerization is crucial and it greatly influences the physicochemical properties of PBAEs, including molecular weight and charge, as well as, the release of the bioactive compound embedded onto the surface of the nanoparticles. Future applications on bone cement of these coating systems will be pursued.

List of contents

LIST OF CONTENTS	IV
LIST OF ABBREVIATIONS.....	XVI
LIST OF FIGURES	XIX
LIST OF SCHEMES.....	XXVI
LIST OF TABLES.....	XXVII
CHAPTER 1: INTRODUCTION.....	1
1.1 ORTHOPAEDIC INFECTIONS	1
<i>Total Joint Replacement (TJR)</i>	1
<i>Prosthetic Joint Infection (PJI)</i>	2
Epidemiology of the infection	2
Risk factors	3
Clinical manifestations.....	4
Type of infections	4
Causative microorganisms	5
<i>Treatment of Prosthetic Joint Infection (PJI)</i>	6
Debridement with prosthesis retention	6
One-stage arthroplasty exchange	6
Two-stage arthroplasty exchange	7
Arthroplasty resection without re-Implantation	7
Amputation	7
<i>Antimicrobial-loaded bone cements</i>	8
The choice of antibiotics	8
Limitations of antibiotic-loaded bone cements	9
Mechanical properties and antimicrobial resistance	9
CLINICAL NEEDS.....	10
ROLE OF POLYMERIC NANOCARRIERS IN ORTHOPAEDIC INFECTIONS.....	11
1.2 LAYER BY LAYER ASSEMBLY TECHNIQUE	12
<i>Types of biomolecules embedded on LbL biofilms</i>	13
Lipid Vesicles	13
Polypeptides.....	14

Nucleic Acid and DNA	14
Proteins	15
<i>LbL film-deposition process</i>	15
<i>Biomedical applications of the LBL technique</i>	16
Cardiovascular devices	16
Wound healing dressing	18
Bone grafts	21
Drug delivery and influent factors.....	22
pH and ionic-strength stimulated release	23
Hydrolytically Induced Release	24
Other applications of the LbL technique	24
LIMITATIONS OF NO-BIODEGRADABLE CATIONIC POLYMERS	25
1.3 POLY (β -AMINO ESTERS).....	26
<i>Synthesis</i>	26
<i>Structures and properties</i>	27
<i>PBAEs formulations</i>	27
Nanocomposites.....	27
Films.....	28
Fibers	28
Gels	28
Micelles	29
<i>PBAEs applications</i>	29
Gene delivery	29
Ocular genetic diseases	31
Immunotherapy	31
Chemotherapy delivery	32
Small cell lung cancer (SCLC).....	33
Codelivery	33
Antimicrobial delivery.....	34
Protein delivery	34
Antioxidant delivery	35
Scaffolds for tissue repairing.....	35

1.4 AIM OF PROJECT	37
CHAPTER 2: MATERIALS AND METHODS	40
CHEMICALS	40
PROTOCOL FOR AMINO-FUNCTIONALISED SILICA NANOPARTICLES (AFSi-NPs)	40
PROTOCOL FOR POLY- β AMINO-ESTERS (PBAE) SYNTHESIS.....	41
LAYER BY LAYER (LBL) SELF-ASSEMBLY PROTOCOL	42
CHLORHEXIDINE DIACETATE.....	44
CHLORHEXIDINE AND POLY (β AMINO-ESTERS) LOADED SILICA AMINO FUNCTIONALISED NANOPARTICLES	45
<i>Matrix 1: Alg-CHX-Alg-A1</i>	46
<i>Matrix 2: Alg-CHX-Alg-A2</i>	46
<i>Matrix 3: Alg-CHX-Alg-A3</i>	47
<i>Matrix 4: Alg-CHX-Alg-B1</i>	47
<i>Matrix 5: Alg-CHX-Alg-B2</i>	47
<i>Matrix 6: Alg-CHX-Alg-B3</i>	48
<i>Matrix 7: Alg-CHX-Alg-D1</i>	48
<i>Matrix 8: Alg-CHX-Alg-D2</i>	49
<i>Matrix 9: Alg-CHX-Alg-D3</i>	49
<i>Matrix 10: Alg-CHX-Alg-E1</i>	50
<i>Matrix 11: Alg-CHX-Alg-E2</i>	50
<i>Matrix 12: Alg-CHX-Alg-E3</i>	50
<i>Matrix 13: Alg-CHX-Alg-F1</i>	51
<i>Matrix 14: Alg-CHX-Alg-F2</i>	51
<i>Matrix 15: Alg-CHX-Alg-F3</i>	52
<i>Matrix 16: Alg-CHX-Alg-G1</i>	52
<i>Matrix 17: Alg-CHX-Alg-G2</i>	53
<i>Matrix 18: Alg-CHX-Alg-G3</i>	53
TOBRAMYCIN.....	54
TOBRAMYCIN AND POLY (β AMINO-ESTERS) LOADED SILICA AMINO FUNCTIONALISED NANOPARTICLES	54
<i>Matrix 19: Alg-TOB-Alg-A1</i>	54
<i>Matrix 20: Alg-TOB-Alg-A2</i>	55
<i>Matrix 21: Alg-TOB-Alg-A3</i>	55

<i>Matrix 22: Alg-TOB-Alg-B1</i>	56
<i>Matrix 23: Alg-TOB-Alg-B2</i>	56
<i>Matrix 24: Alg-TOB-Alg-B3</i>	57
<i>Matrix 25: Alg-TOB-Alg-D1</i>	57
<i>Matrix 26: Alg-TOB-Alg-D2</i>	57
<i>Matrix 27: Alg-TOB-Alg-D3</i>	58
<i>Matrix 28: Alg-TOB-Alg-E1</i>	58
<i>Matrix 29: Alg-TOB-Alg-E2</i>	59
<i>Matrix 30: Alg-TOB-Alg-E3</i>	59
<i>Matrix 31: Alg-TOB-Alg-F1</i>	60
<i>Matrix 32: Alg-TOB-Alg-F2</i>	60
<i>Matrix 33: Alg-TOB-Alg-F3</i>	61
<i>Matrix 34: Alg-TOB-Alg-G1</i>	61
<i>Matrix 35: Alg-TOB-Alg-G2</i>	61
<i>Matrix 36: Alg-TOB-Alg-G3</i>	62
NANOPARTICLES CHARACTERIZATION	62
SIZE MEASUREMENTS	62
<i>a. Dynamic Light Scattering (DLS)</i>	62
<i>b. Transmission electron microscopy</i>	63
ZETA POTENTIAL MEASUREMENTS	63
THERMOGRAVIMETRIC ANALYSIS (TGA)	64
CHLORHEXIDINE RELEASE QUANTIFICATION	64
TOBRAMYCIN RELEASE QUANTIFICATION	66
PBAES CHARACTERISATION	67
<i>Nuclear Magnetic Resonance (NMR)</i>	67
<i>PBAE molecular weight (MW) and hydrolysis through Gel Permeation Chromatography (GPC) and zeta potential</i>	67
CHAPTER 3: POLY (B-AMINO ESTERS) (PBAE): SYNTHESIS AND CHARACTERISATION	70
INTRODUCTION	70
POLYMER PREPARATION	71
<i>Polymer synthesis</i>	71

<i>Polymer characterisation</i>	72
Nuclear Magnetic Resonance (NMR)	72
Log P determination	72
Molecular weight (MW) determination of PBAEs via Gel Permeation Chromatography (GPC)	73
Poly (β -amino) esters hydrolysis	73
RESULTS.....	75
A1	75
Chemical procedure	75
Chemical identification	75
A2	77
Chemical procedure	77
Chemical identification	77
A3	79
Chemical procedure	79
Chemical identification	79
B1	81
Chemical procedure	81
Chemical identification	81
B2	83
Chemical procedure	83
Chemical identification	83
B3	85
Chemical procedure	85
Chemical identification	85
D1	87
Chemical procedure	87
Chemical identification	87
D2	89
Chemical procedure	89
D3	91
Chemical procedure	91

Chemical identification	91
<i>E1</i>	93
Chemical procedure	93
Chemical identification	93
<i>E2</i>	95
Chemical procedure	95
Chemical identification	95
<i>E3</i>	97
Chemical procedure	97
Chemical identification	97
<i>F1</i>	99
Chemical procedure	99
Chemical identification	99
<i>F2</i>	101
Chemical procedure	101
Chemical identification	101
<i>F3</i>	103
Chemical procedure	103
Chemical identification	103
<i>G1</i>	105
Chemical procedure	105
Chemical identification	105
<i>G2</i>	107
Chemical procedure	107
Chemical identification	107
<i>G3</i>	109
Chemical procedure	109
Chemical identification	109
HYDROLYSIS OF PBAES.....	111
<i>A1</i>	111
<i>A2</i>	112
<i>A3</i>	114

<i>B1</i>	115
<i>B2</i>	117
<i>B3</i>	119
<i>D1</i>	120
<i>D2</i>	122
<i>D3</i>	123
<i>E1</i>	125
<i>E2</i>	127
<i>E3</i>	128
<i>F1</i>	130
<i>F2</i>	131
<i>F3</i>	133
<i>G1</i>	135
<i>G2</i>	137
<i>G3</i>	138
DISCUSSION	142
<i>Polymeric characterisation</i>	143
<i>PBAE hydrolysis studies</i>	144
CONCLUSIONS	150
CHAPTER 4: CHLORHEXIDINE AND PBAE LOADED ON SILICA NANOPARTICLES VIA LAYER BY LAYER (LBL) COATING	152
INTRODUCTION	152
MATERIALS AND METHODS	153
<i>Chemicals</i>	153
<i>Nanoparticles preparation</i>	153
<i>Synthesis of Poly (β amino) esters (PBAEs)</i>	154
<i>Layer by layer self-assembly</i>	154
<i>Nanoparticles surface characterisation</i>	156
<i>Size measurements: TEM and DLS</i>	156
<i>Zeta potential measurements</i>	156
<i>Thermogravimetric analysis (TGA)</i>	157

<i>Chlorhexidine release quantification</i>	157
RESULTS.....	158
NANOPARTICLES SURFACE CHARACTERIZATION	158
<i>Size measurements</i>	158
<i>ζ potential measurements</i>	158
Bilayer: Alg-CHX.....	158
A1.....	159
A2.....	161
A3.....	162
B1.....	164
B2.....	165
B3.....	166
D1.....	167
D2.....	168
D3.....	169
E1.....	170
E2.....	171
E3.....	172
F1.....	173
F2.....	174
F3.....	176
G1.....	177
G2.....	178
G3.....	179
<i>Thermogravimetric analysis (TGA)</i>	181
Bilayer: Alg-CHX.....	181
A1.....	182
A3.....	185
B1.....	187
B2.....	188
B3.....	189
D1.....	190

D2.....	192
D3.....	193
E1.....	195
E2.....	196
E3.....	198
F1.....	199
F2.....	200
F3.....	202
G1.....	204
G2.....	206
G3.....	207
<i>Chlorhexidine release determination</i>	209
Bilayer: Alg-CHX.....	209
A1.....	210
A2.....	211
A3.....	212
B1.....	214
B2.....	215
B3.....	216
D1.....	217
D2.....	219
D3.....	220
E1.....	221
E2.....	222
E3.....	223
F1.....	224
F2.....	225
F3.....	226
G1.....	228
G2.....	229
G3.....	230
DISCUSSION.....	232

Silica amino-functionalization	232
Size measurements	232
Zeta potential.....	233
Thermogravimetric analysis (TGA).....	235
Chlorhexidine mechanism of action	11
Chlorhexidine release profiles.....	237
CONCLUSIONS	240
CHAPTER 5: TOBRAMYCIN AND PBAE LOADED ON SILICA NANOPARTICLES VIA LAYER BY LAYER (LBL) COATING	242
INTRODUCTION	242
MATERIALS AND METHODS	243
Chemicals.....	243
Nanoparticles preparation	243
Synthesis of poly (β -amino) esters (PBAE).....	243
Layer by layer (LbL) self-assembly	244
Nanoparticles surface characterisation	245
Zeta potential measurements.....	245
Thermogravimetric analysis (TGA).....	245
Tobramycin release quantification	246
RESULTS.....	247
NANOPARTICLES SURFACE CHARACTERISATION	247
ζ potential measurements	247
Bilayer: Alg-TOB.....	247
A1.....	248
A2.....	249
A3.....	250
B1.....	251
B2.....	252
B3.....	253
D1.....	255
D2.....	256

D3.....	257
E1.....	258
E2.....	259
E3.....	260
F1.....	261
F2.....	262
F3.....	263
G1.....	265
G2.....	266
G3.....	267
<i>Thermogravimetric analysis (TGA).....</i>	<i>268</i>
Bilayer: Alg-TOB.....	269
A1.....	270
A2.....	271
A3.....	272
B1.....	273
B2.....	275
B3.....	275
D1.....	277
D2.....	278
D3.....	280
E1.....	281
E2.....	282
E3.....	283
F1.....	284
F2.....	286
F3.....	287
G1.....	288
G2.....	289
G3.....	290
<i>Tobramycin release determination.....</i>	<i>292</i>
Bilayer: Alg-TOB.....	292

A1.....	293
A2.....	294
A3.....	295
B1.....	296
B2.....	297
B3.....	298
D1.....	299
D2.....	300
D3.....	301
E1.....	302
E2.....	303
E3.....	304
F1.....	306
F2.....	307
F3.....	308
G1.....	309
G2.....	310
G3.....	311
DISCUSSION	313
<i>Zeta potential measurements</i>	313
<i>Thermogravimetric analysis (TGA)</i>	315
<i>Tobramycin mechanism of action</i>	10
<i>Tobramycin release quantification</i>	317
CONCLUSIONS	321
CHAPTER 6: GENERAL CONCLUSION AND FUTURE PERSPECTIVE	322
REFERENCES	325
APPENDIX	346

List of abbreviations

¹³C NMR: Carbon Nuclear Magnetic Resonance

¹H NMR: Proton Nuclear Magnetic Resonance

AF-SiNPs: Amino-functionalised silica nanoparticles

ALBC: Antibiotic loaded bone cement

Alg: Alginate

Amine 1: Piperazine

Amine 2: 4,4 trimethyldipiperidine

Amine 3: N-N bis [3-(methylamino) propyl] methylamine

APTES: 3-aminopropyl-triethoxysilane

BL: bilayer

CDCl₃: Deuterated chloroform

CHT: Chitosan

CHX: Chlorhexidine

Col I: Collagen type I

Da: Dalton

DAIR: Debridement, Antibiotics Implant Retention

DCM: Dichloromethane

Diacrylate A: 1,4 butanediol diacrylate

Diacrylate B: 1,6 hexanediol diacrylate

Diacrylate D: Neopentyl glycol diacrylate

Diacrylate E: 1,3 butanediol diacrylate

Diacrylate F: Bisphenol A ethoxylate diacrylate

Diacrylate G: Tricyclo [5.2.1.0²⁻⁶] decanodimethanol diacrylate

DLS: Dynamic Light Scattering

DMSO: dimethyl sulfoxide

DOX: doxorubicin

E. coli: *Escherichia coli*

GPC: Gel Permeation Chromatography

GS: Gentamicin sulphate

HPLC: High-Performance Liquid Chromatography

HYA: Hyaluronic acid

kDa: kilodalton
LbL: Layer by Layer
LogP: Partition Coefficient
MHz: Megahertz
MIC: Minimum Inhibitory concentration
mMol: millimole
mV: millivolt
MW: molecular weight
NJR: National Joint Registry
nm: nanometer
NMR: Nuclear Magnetic Resonance
OA: Osteoarthritis
OPA: o-phaldialdehyde reagent
PAH: poly(allylamine)
PBAE: poly(beta-amino) esters
PBS: Phosphate Buffered Saline
PDI: polydispersity index
PEG: polyethylene glycol
PEI: poly(ethylenimine)
PEM: Polyelectrolytes Multilayer
PHP: *trans*-4-hydroxy-L-proline ester
PJI: Prosthetic Joint Infection
pKa: Acid Dissociation Constant
PLGA: poly(L-glutamic acid)
PLL: poly(L-lysine)
PMMA: poly(methyl) methacrylate
pMSN: mesoporous silica nanoparticles
ppm: part per million
QL: Quadruple layer
RID: Refractive Index Detector
rpm: Revolutions per Minute
S. aureus: *Staphylococcus aureus*

SCLC: Small Cell Lung Cancer
SD: standard deviation
TEM: Transmission Electron Microscopy
TEOS: Tetraethyl orthosilicate
TGA: Thermo-gravimetric analysis
THF: Tetrahydrofuran
TJA: Total Joint Arthroplasty
TJR: Total Joint Replacement
TKA: Total Knee Arthroplasty
TMS: Tetramethylsilane
TOB: Tobramycin

List of figures

Figure 2.1: AFSi-NPs synthesis

Figure 2.2: General reaction for PBAE synthesis

Figure 2.3: Single quadruple layer composition

Figure 2.4: Chlorhexidine diacetate chemical structure

Figure 2.5: Tobramycin chemical structure

Figure 2.6: Representative chlorhexidine diacetate calibration curve

Figure 2.7: Representative tobramycin calibration curve

Figure 2.8: PEG calibration curve

Figure 3.1: MLogP values for all PBAEs

Figure 3.2: A1 structure and NMR characterisation

Figure 3.3: A2 structure and NMR characterisation

Figure 3.4: A3 structure and NMR characterisation

Figure 3.5: B1 structure and NMR characterisation

Figure 3.6: B2 structure and NMR characterisation

Figure 3.7: B3 structure and NMR characterisation

Figure 3.8: D1 structure and NMR characterisation

Figure 3.9: D2 structure and NMR characterisation

Figure 3.10: D3 structure and NMR characterisation

Figure 3.11: E1 structure and NMR characterisation

Figure 3.12: E2 structure and NMR characterisation

Figure 3.13: E3 structure and NMR characterisation

Figure 3.14: F1 structure and NMR characterisation

Figure 3.15: F2 structure and NMR characterisation

Figure 3.16: F3 structure and NMR characterisation

Figure 3.17: G1 structure and NMR characterisation

Figure 3.18: G2 structure and NMR characterisation

Figure 3.19: G3 structure and NMR characterisation

Figure 3.20a: Molecular weight (MW) and hydrolysis of A1 in 30 days at both pH5 and pH7

Figure 3.20b: A1 charge hydrolysis at pH5 and pH7.4 for 30 days

Figure 3.21a: Molecular weight (MW) and hydrolysis of A2 in 30 days at both pH5 and pH7

Figure 3.21b: A2 charge hydrolysis at pH5 and pH7.4 for 30 days

Figure 3.22a: Molecular weight (MW) and hydrolysis of A3 in 30 days at both pH5 and pH7

Figure 3.22b: A3 charge hydrolysis at pH5 and pH7.4 for 30 days

Figure 3.23a: Molecular weight (MW) and hydrolysis of B1 in 30 days at both pH5 and pH7

Figure 3.23b: B1 charge hydrolysis at pH5 and pH7.4 for 30 days

Figure 3.24a: Molecular weight (MW) and hydrolysis of B2 in 30 days at both pH5 and pH7

Figure 3.24b: B2 charge hydrolysis at pH5 and pH7.4 for 30 days

Figure 3.25a: Molecular weight (MW) and hydrolysis of B3 in 30 days at both pH5 and pH7

Figure 3.25b: B3 charge hydrolysis at pH5 and pH7.4 for 30 days

Figure 3.26a: Molecular weight (MW) and hydrolysis of D1 in 30 days at both pH5 and pH7

Figure 3.26b: D1 charge hydrolysis at pH5 and pH7.4 for 30 days

Figure 3.27a: Molecular weight (MW) and hydrolysis of D2 in 30 days at both pH5 and pH7

Figure 3.27b: D2 charge hydrolysis at pH5 and pH7.4 for 30 days

Figure 3.28a: Molecular weight (MW) and hydrolysis of D3 in 30 days at both pH5 and pH7

Figure 3.28b: D3 charge hydrolysis at pH5 and pH7.4 for 30 days

Figure 3.29a: Molecular weight (MW) and hydrolysis of E1 in 30 days at both pH5 and pH7

Figure 3.29b: E1 charge hydrolysis at pH5 and pH7.4 for 30 days

Figure 3.30a: Molecular weight (MW) and hydrolysis of E2 in 30 days at both pH5 and pH7

Figure 3.30b: E2 charge hydrolysis at pH5 and pH7.4 for 30 days

Figure 3.31a: Molecular weight (MW) and hydrolysis of E3 in 30 days at both pH5 and pH7

Figure 3.31b: E3 charge hydrolysis at pH5 and pH7.4 for 30 days

Figure 3.32a: Molecular weight (MW) and hydrolysis of F1 in 30 days at both pH5 and pH7

Figure 3.32b: F1 charge hydrolysis at pH5 and pH7.4 for 30 days

Figure 3.33a: Molecular weight (MW) and hydrolysis of F2 in 30 days at both pH5 and pH7

Figure 3.33b: F2 charge hydrolysis at pH5 and pH7.4 for 30 days

Figure 3.34a: Molecular weight (MW) and hydrolysis of F3 in 30 days at both pH5 and pH7

Figure 3.34b: F3 charge hydrolysis at pH5 and pH7.4 for 30 days

Figure 3.35a: Molecular weight (MW) and hydrolysis of G1 in 30 days at both pH5 and pH7

Figure 3.35b: G1 charge hydrolysis at pH5 and pH7.4 for 30 days

Figure 3.36a: Molecular weight (MW) and hydrolysis of G2 in 30 days at both pH5 and pH7

Figure 3.36b: G2 charge hydrolysis at pH5 and pH7.4 for 30 days

Figure 3.37a: Molecular weight (MW) and hydrolysis of G3 in 30 days at both pH5 and pH7

Figure 3.37b: G3 charge hydrolysis at pH5 and pH7.4 for 30 days

Figure 3.38a: Degradation at pH5 of PBAEs synthesised by mixing amine 1, 2 or 3 to the diacrylates A, B, D, E, F or G

Figure 3.38b: Degradation at pH7.4 of PBAEs synthesised by mixing amine 1, 2 or 3 to the diacrylates A, B, D, E, F or G

Figure 4.1: Layer by layer deposition

Figure 4.2: Size measurements for silica amino-functionalized nanoparticles

Figure 4.3: ζ potential measurements for the coating system Si-NH₂NPs-Alg-CHX

Figure 4.4: ζ potential measurements for the coating system Si-NH₂NPs-Alg-CHX-Alg-A1

Figure 4.5: ζ potential measurements for the coating system Si-NH₂NPs-Alg-CHX-Alg-A2

Figure 4.6: ζ potential measurements for the coating system Si-NH₂NPs-Alg-CHX-Alg-A3

Figure 4.7: ζ potential measurements for the coating system Si-NH₂NPs-Alg-CHX-Alg-B1

Figure 4.8: ζ potential measurements for the coating system Si-NH₂NPs-Alg-CHX-Alg-B2

Figure 4.9: ζ potential measurements for the coating system Si-NH₂NPs-Alg-CHX-Alg-B3

Figure 4.10: ζ potential measurements for the coating system Si-NH₂NPs-Alg-CHX-Alg-D1

Figure 4.11: ζ potential measurements for the coating system Si-NH₂NPs-Alg-CHX-Alg-D2

Figure 4.12: ζ potential measurements for the coating system Si-NH₂NPs-Alg-CHX-Alg-D3

Figure 4.13: ζ potential measurements for the coating system Si-NH₂NPs-Alg-CHX-Alg-E1

Figure 4.14: ζ potential measurements for the coating system Si-NH₂NPs-Alg-CHX-Alg-E2

Figure 4.15: ζ potential measurements for the coating system Si-NH₂NPs-Alg-CHX-Alg-E3

Figure 4.16: ζ potential measurements for the coating system Si-NH₂NPs-Alg-CHX-Alg-F1

Figure 4.17: ζ potential measurements for the coating system Si-NH₂NPs-Alg-CHX-Alg-F2

Figure 4.18: ζ potential measurements for the coating system Si-NH₂NPs-Alg-CHX-Alg-F3

Figure 4.19: ζ potential measurements for the coating system Si-NH₂NPs-Alg-CHX-Alg-G1

Figure 4.20: ζ potential measurements for the coating system Si-NH₂NPs-Alg-CHX-Alg-G2

Figure 4.21: ζ potential measurements for the coating system Si-NH₂NPs-Alg-CHX-Alg-G3

Figure 4.22a: Weight loss vs temperature for the bilayer construct Si-NH₂NPs-Alg-CHX

Figure 4.22b: Organic content % for each B layer in the matrix Si-NH₂ NPs-Alg-CHX

Figure 4.23a: Weight loss vs temperature for the construct Si-NH₂NPs-Alg-CHX-Alg-A1

Figure 4.23b: Organic content % for each QL in the matrix Si-NH₂NPs-Alg-CHX-Alg-A1

Figure 4.24a: Weight loss vs temperature for the construct Si-NH₂NPs-Alg-CHX-Alg-A2

Figure 4.24b: Organic content % for each QL in the matrix Si-NH₂NPs-Alg-CHX-Alg-A2
Figure 4.25a: Weight loss vs temperature for the construct Si-NH₂NPs-Alg-CHX-Alg-A3
Figure 4.25b: Organic content % for each QL in the matrix Si-NH₂NPs-Alg-CHX-Alg-A3
Figure 4.26a: Weight loss vs temperature for the construct Si-NH₂NPs-Alg-CHX-Alg-B1
Figure 4.26b: Organic content % for each QL in the matrix Si-NH₂NPs-Alg-CHX-Alg-B1
Figure 4.27a: Weight loss vs temperature for the construct Si-NH₂NPs-Alg-CHX-Alg-B2
Figure 4.27b: Organic content % for each QL in the matrix Si-NH₂NPs-Alg-CHX-Alg-B2
Figure 4.28a: Weight loss vs temperature for the construct Si-NH₂NPs-Alg-CHX-Alg-B3
Figure 4.28b: Organic content % for each QL in the matrix Si-NH₂NPs-Alg-CHX-Alg-B3
Figure 4.29a: Weight loss vs temperature for the construct Si-NH₂NPs-Alg-CHX-Alg-D1
Figure 4.29b: Organic content % for each QL in the matrix Si-NH₂NPs-Alg-CHX-Alg-D1
Figure 4.30a: Weight loss vs temperature for the construct Si-NH₂NPs-Alg-CHX-Alg-D2
Figure 4.30b: Organic content % for each QL in the matrix Si-NH₂NPs-Alg-CHX-Alg-D2
Figure 4.31a: Weight loss vs temperature for the construct Si-NH₂NPs-Alg-CHX-Alg-D3
Figure 4.31b: Organic content % for each QL in the matrix Si-NH₂NPs-Alg-CHX-Alg-D3
Figure 4.32a: Weight loss vs temperature for the construct Si-NH₂NPs-Alg-CHX-Alg-E1
Figure 4.32b: Organic content % for each QL in the matrix Si-NH₂NPs-Alg-CHX-Alg-E1
Figure 4.33a: Weight loss vs temperature for the construct Si-NH₂NPs-Alg-CHX-Alg-E2
Figure 4.33b: Organic content % for each QL in the matrix Si-NH₂NPs-Alg-CHX-Alg-E2
Figure 4.34a: Weight loss vs temperature for the construct Si-NH₂NPs-Alg-CHX-Alg-E3
Figure 4.34b: Organic content % for each QL in the matrix Si-NH₂NPs-Alg-CHX-Alg-E3
Figure 4.35a: Weight loss vs temperature for the construct Si-NH₂NPs-Alg-CHX-Alg-F1
Figure 4.35b: Organic content % for each QL in the matrix Si-NH₂NPs-Alg-CHX-Alg-F1
Figure 4.36a: Weight loss vs temperature for the construct Si-NH₂NPs-Alg-CHX-Alg-F2
Figure 4.36b: Organic content % for each QL in the matrix Si-NH₂NPs-Alg-CHX-Alg-F2
Figure 4.37a: Weight loss vs temperature for the construct Si-NH₂NPs-Alg-CHX-Alg-F3
Figure 4.37b: Organic content % for each QL in the matrix Si-NH₂NPs-Alg-CHX-Alg-F3
Figure 4.38a: Weight loss vs temperature for the construct Si-NH₂NPs-Alg-CHX-Alg-G1
Figure 4.38b: Organic content % for each QL in the matrix Si-NH₂NPs-Alg-CHX-Alg-G1
Figure 4.39a: Weight loss vs temperature for the construct Si-NH₂NPs-Alg-CHX-Alg-G2
Figure 4.39b: Organic content % for each QL in the matrix Si-NH₂NPs-Alg-CHX-Alg-G2
Figure 4.40a: Weight loss vs temperature for the construct Si-NH₂NPs-Alg-CHX-Alg-G3

Figure 4.40b: Organic content % for each QL in the matrix Si-NH₂NPs-Alg-CHX-Alg-G3

Figure 4.41: CHX release profile at pH5 and at pH7.4 for B10 of the construct Alg-CHX

Figure 4.42: CHX release profile at pH5 and at pH7.4 for Q10 of the construct CHX-A1

Figure 4.43: CHX release profile at pH5 and at pH7.4 for Q10 of the construct CHX-A2

Figure 4.44: CHX release profile at pH5 and at pH7.4 for Q10 of the construct CHX-A3

Figure 4.45: CHX release profile at pH5 and at pH7.4 for Q10 of the construct CHX-B1

Figure 4.46: CHX release profile at pH5 and at pH7.4 for Q10 of the construct CHX-B2

Figure 4.47: CHX release profile at pH5 and at pH7.4 for Q10 of the construct CHX-B3

Figure 4.48: CHX release profile at pH5 and at pH7.4 for Q10 of the construct CHX-D1

Figure 4.49: CHX release profile at pH5 and at pH7.4 for Q10 of the construct CHX-D2

Figure 4.50: CHX release profile at pH5 and at pH7.4 for Q10 of the construct CHX-D3

Figure 4.51: CHX release profile at pH5 and at pH7.4 for Q10 of the construct CHX-E1

Figure 4.52: CHX release profile at pH5 and at pH7.4 for Q10 of the construct CHX-E2

Figure 4.53: CHX release profile at pH5 and at pH7.4 for Q10 of the construct CHX-E3

Figure 4.54: CHX release profile at pH5 and at pH7.4 for Q10 of the construct CHX-F1

Figure 4.55: CHX release profile at pH5 and at pH7.4 for Q10 of the construct CHX-F2

Figure 4.56: CHX release profile at pH5 and at pH7.4 for Q10 of the construct CHX-F3

Figure 4.57: CHX release profile at pH5 and at pH7.4 for Q10 of the construct CHX-G1

Figure 4.58: CHX release profile at pH5 and at pH7.4 for Q10 of the construct CHX-G2

Figure 4.59: CHX release profile at pH5 and at pH7.4 for Q10 of the construct CHX-G3

Figure 5.1: ζ potential measurements for the coating system SI-NH₂NPs-Alg-TOB

Figure 5.2: ζ potential measurements for the coating system SI-NH₂NPs-Alg-TOB-Alg-A1

Figure 5.3: ζ potential measurements for the coating system SI-NH₂NPs-Alg-TOB-Alg-A2

Figure 5.4: ζ potential measurements for the coating system SI-NH₂NPs-Alg-TOB-Alg-A3

Figure 5.5: ζ potential measurements for the coating system SI-NH₂NPs-Alg-TOB-Alg-B1

Figure 5.6: ζ potential measurements for the coating system SI-NH₂NPs-Alg-TOB-Alg-B2

Figure 5.7: ζ potential measurements for the coating system SI-NH₂NPs-Alg-TOB-Alg-B3

Figure 5.8: ζ potential measurements for the coating system SI-NH₂NPs-Alg-TOB-Alg-D1

Figure 5.9: ζ potential measurements for the coating system SI-NH₂NPs-Alg-TOB-Alg-D2

Figure 5.10: ζ potential measurements for the coating system SI-NH₂NPs-Alg-TOB-Alg-D3

Figure 5.11: ζ potential measurements for the coating system SI-NH₂NPs-Alg-TOB-Alg-E1

Figure 5.12: ζ potential measurements for the coating system Si-NH₂NPs-Alg-TOB-Alg-E2
Figure 5.13: ζ potential measurements for the coating system Si-NH₂NPs-Alg-TOB-Alg-E3
Figure 5.14: ζ potential measurements for the coating system Si-NH₂NPs-Alg-TOB-Alg-F1
Figure 5.15: ζ potential measurements for the coating system Si-NH₂NPs-Alg-TOB-Alg-F2
Figure 5.16: ζ potential measurements for the coating system Si-NH₂NPs-Alg-TOB-Alg-F3
Figure 5.17: ζ potential measurements for the coating system Si-NH₂NPs-Alg-TOB-Alg-G1
Figure 5.18: ζ potential measurements for the coating system Si-NH₂NPs-Alg-TOB-Alg-G2
Figure 5.19: ζ potential measurements for the coating system Si-NH₂NPs-Alg-TOB-Alg-G3
Figure 5.20a: Weight loss vs temperature for the bilayer construct Si-NH₂NPs-Alg-TOB
Figure 5.20b: Organic content % for each B layer in the matrix Si-NH₂ NPs-Alg-TOB
Figure 5.21a: Weight loss vs temperature for the construct Si-NH₂NPs-Alg-TOB-Alg-A1
Figure 5.21b: Organic content % for each QL in the matrix Si-NH₂NPs-Alg-TOB-Alg-A1
Figure 5.22a: Weight loss vs temperature for the construct Si-NH₂NPs-Alg-TOB-Alg-A2
Figure 5.22b: Organic content % for each QL in the matrix Si-NH₂NPs-Alg-TOB-Alg-A2
Figure 5.23a: Weight loss vs temperature for the construct Si-NH₂NPs-Alg-TOB-Alg-A3
Figure 5.23b: Organic content % for each QL in the matrix Si-NH₂NPs-Alg-TOB-Alg-A3
Figure 5.24a: Weight loss vs temperature for the construct Si-NH₂NPs-Alg-TOB-Alg-B1
Figure 5.24b: Organic content % for each QL in the matrix Si-NH₂NPs-Alg-TOB-Alg-B1
Figure 5.25a: Weight loss vs temperature for the construct Si-NH₂NPs-Alg-TOB-Alg-B2
Figure 5.25b: Organic content % for each QL in the matrix Si-NH₂NPs-Alg-TOB-Alg-B2
Figure 5.26a: Weight loss vs temperature for the construct Si-NH₂NPs-Alg-TOB-Alg-B3
Figure 5.26b: Organic content % for each QL in the matrix Si-NH₂NPs-Alg-TOB-Alg-B3
Figure 5.27a: Weight loss vs temperature for the construct Si-NH₂NPs-Alg-TOB-Alg-D1
Figure 5.27b: Organic content % for each QL in the matrix Si-NH₂NPs-Alg-TOB-Alg-D1
Figure 5.28a: Weight loss vs temperature for the construct Si-NH₂NPs-Alg-TOB-Alg-D2
Figure 5.28b: Organic content % for each QL in the matrix Si-NH₂NPs-Alg-TOB-Alg-D2
Figure 5.29a: Weight loss vs temperature for the construct Si-NH₂NPs-Alg-TOB-Alg-D3
Figure 5.29b: Organic content % for each QL in the matrix Si-NH₂NPs-Alg-TOB-Alg-D3
Figure 5.30a: Weight loss vs temperature for the construct Si-NH₂NPs-Alg-TOB-Alg-E1
Figure 5.30b: Organic content % for each QL in the matrix Si-NH₂NPs-Alg-TOB-Alg-E1
Figure 5.31a: Weight loss vs temperature for the construct Si-NH₂NPs-Alg-TOB-Alg-E2
Figure 5.31b: Organic content % for each QL in the matrix Si-NH₂NPs-Alg-TOB-Alg-E2

Figure 5.32a: Weight loss vs temperature for the construct Si-NH₂NPs-Alg-TOB-Alg-E3
Figure 5.32b: Organic content % for each QL in the matrix Si-NH₂NPs-Alg-TOB-Alg-E3
Figure 5.33a: Weight loss vs temperature for the construct Si-NH₂NPs-Alg-TOB-Alg-F1
Figure 5.33b: Organic content % for each QL in the matrix Si-NH₂NPs-Alg-TOB-Alg-F1
Figure 5.34a: Weight loss vs temperature for the construct Si-NH₂NPs-Alg-TOB-Alg-F2
Figure 5.34b: Organic content % for each QL in the matrix Si-NH₂NPs-Alg-TOB-Alg-F2
Figure 5.35a: Weight loss vs temperature for the construct Si-NH₂NPs-Alg-TOB-Alg-F3
Figure 5.35b: Organic content % for each QL in the matrix Si-NH₂NPs-Alg-TOB-Alg-F3
Figure 5.36a: Weight loss vs temperature for the construct Si-NH₂NPs-Alg-TOB-Alg-G1
Figure 5.36b: Organic content % for each QL in the matrix Si-NH₂NPs-Alg-TOB-Alg-G1
Figure 5.37a: Weight loss vs temperature for the construct Si-NH₂NPs-Alg-TOB-Alg-G2
Figure 5.37b: Organic content % for each QL in the matrix Si-NH₂NPs-Alg-TOB-Alg-G2
Figure 5.38a: Weight loss vs temperature for the construct Si-NH₂NPs-Alg-TOB-Alg-G3
Figure 5.38b: Organic content % for each QL in the matrix Si-NH₂NPs-Alg-TOB-Alg-G3
Figure 5.39: TOB release profile at pH5 and at pH7.4 for B10 of the construct Alg-CHX
Figure 5.40: TOB release profile at pH5 and at pH7.4 for Q10 of the construct CHX-A1
Figure 5.41: TOB release profile at pH5 and at pH7.4 for Q10 of the construct CHX-A2
Figure 5.42: TOB release profile at pH5 and at pH7.4 for Q10 of the construct CHX-A3
Figure 5.43: TOB release profile at pH5 and at pH7.4 for Q10 of the construct CHX-B1
Figure 5.44: TOB release profile at pH5 and at pH7.4 for Q10 of the construct CHX-B2
Figure 5.45: TOB release profile at pH5 and at pH7.4 for Q10 of the construct CHX-B3
Figure 5.46: TOB release profile at pH5 and at pH7.4 for Q10 of the construct CHX-D1
Figure 5.47: TOB release profile at pH5 and at pH7.4 for Q10 of the construct CHX-D2
Figure 5.48: TOB release profile at pH5 and at pH7.4 for Q10 of the construct CHX-D3
Figure 5.49: TOB release profile at pH5 and at pH7.4 for Q10 of the construct CHX-E1
Figure 5.50: TOB release profile at pH5 and at pH7.4 for Q10 of the construct CHX-E2
Figure 5.51: TOB release profile at pH5 and at pH7.4 for Q10 of the construct CHX-E3
Figure 5.52: TOB release profile at pH5 and at pH7.4 for Q10 of the construct CHX-F1
Figure 5.53: TOB release profile at pH5 and at pH7.4 for Q10 of the construct CHX-F2
Figure 5.54: TOB release profile at pH5 and at pH7.4 for Q10 of the construct CHX-F3
Figure 5.55: TOB release profile at pH5 and at pH7.4 for Q10 of the construct CHX-G1
Figure 5.56: TOB release profile at pH5 and at pH7.4 for Q10 of the construct CHX-G2

Figure 5.57: TOB release profile at pH5 and at pH7.4 for Q10 of the construct CHX-G3

List of schemes

Scheme 3.1: PBAEs general mechanism of reaction

Scheme 3.2: Reaction scheme of compound **A1**

Scheme 3.3: Reaction scheme of compound **A2**

Scheme 3.4: Reaction scheme of compound **A3**

Scheme 3.5: Reaction scheme of compound **B1**

Scheme 3.6: Reaction scheme of compound **B2**

Scheme 3.7: Reaction scheme of compound **B3**

Scheme 3.8: Reaction scheme of compound **D1**

Scheme 3.9: Reaction scheme of compound **D2**

Scheme 3.10: Reaction scheme of compound **D3**

Scheme 3.11: Reaction scheme of compound **E1**

Scheme 3.12: Reaction scheme of compound **E2**

Scheme 3.13: Reaction scheme of compound **E3**

Scheme 3.14: Reaction scheme of compound **F1**

Scheme 3.15: Reaction scheme of compound **F2**

Scheme 3.16: Reaction scheme of compound **F3**

Scheme 3.17: Reaction scheme of compound **G1**

Scheme 3.18: Reaction scheme of compound **G2**

Scheme 3.19: Reaction scheme of compound **G3**

List of tables

Table 2.1a: Amines, diacrylates monomers employed for the synthesis of 18 PBAEs

Table 2.1b: PBAEs chemical structures and abbreviations

Table 2.2: LbL matrix of deposited CHX and A1 layers on AFSi-NPs

Table 2.3: LbL matrix of deposited CHX and A2 layers on AFSi-NPs

Table 2.4: LbL matrix of deposited CHX and A3 layers on AFSi-NPs

Table 2.5: LbL matrix of deposited CHX and B1 layers on AFSi-NPs

Table 2.6: LbL matrix of deposited CHX and B2 layers on AFSi-NPs

Table 2.7: LbL matrix of deposited CHX and B3 layers on AFSi-NPs

Table 2.8: LbL matrix of deposited CHX and D1 layers on AFSi-NPs

Table 2.9: LbL matrix of deposited CHX and D2 layers on AFSi-NPs

Table 2.10: LbL matrix of deposited CHX and D3 layers on AFSi-NPs

Table 2.11: LbL matrix of deposited CHX and E1 layers on AFSi-NPs

Table 2.12: LbL matrix of deposited CHX and E2 layers on AFSi-NPs

Table 2.13: LbL matrix of deposited CHX and E3 layers on AFSi-NPs

Table 2.14: LbL matrix of deposited CHX and F1 layers on AFSi-NPs

Table 2.15: LbL matrix of deposited CHX and F2 layers on AFSi-NPs

Table 2.16: LbL matrix of deposited CHX and F3 layers on AFSi-NPs

Table 2.17: LbL matrix of deposited CHX and G1 layers on AFSi-NPs

Table 2.18: LbL matrix of deposited CHX and G2 layers on AFSi-NPs

Table 2.19: LbL matrix of deposited CHX and G3 layers on AFSi-NPs

Table 2.20: LbL matrix of deposited TOB and A1 layers on AFSi-NPs

Table 2.21: LbL matrix of deposited TOB and A2 layers on AFSi-NPs

Table 2.22: LbL matrix of deposited TOB and A3 layers on AFSi-NPs

Table 2.23: LbL matrix of deposited TOB and B1 layers on AFSi-NPs

Table 2.24: LbL matrix of deposited TOB and B2 layers on AFSi-NPs

Table 2.25: LbL matrix of deposited TOB and B3 layers on AFSi-NPs

Table 2.26: LbL matrix of deposited TOB and D1 layers on AFSi-NPs

Table 2.27: LbL matrix of deposited TOB and D2 layers on AFSi-NPs

Table 2.28: LbL matrix of deposited TOB and D3 layers on AFSi-NPs

Table 2.29: LbL matrix of deposited TOB and E1 layers on AFSi-NPs

Table 2.30: LbL matrix of deposited TOB and E2 layers on AFSi-NPs

Table 2.31: LbL matrix of deposited TOB and E3 layers on AFSi-NPs

Table 2.32: LbL matrix of deposited TOB and F1 layers on AFSi-NPs

Table 2.33: LbL matrix of deposited TOB and F2 layers on AFSi-NPs

Table 2.34: LbL matrix of deposited TOB and F3 layers on AFSi-NPs

Table 2.35: LbL matrix of deposited TOB and G1 layers on AFSi-NPs

Table 2.36: LbL matrix of deposited TOB and G2 layers on AFSi-NPs

Table 2.37: LbL matrix of deposited TOB and G3 layers on AFSi-NPs

Table 3.1: Amines and diacrylates employed to PBAE's reaction

Table 3.2: PBAEs molecular weight (MW) determined via GPC and ζ potential

Table 4.1: LbL matrix of deposited alginate and CHX layers on AFSi-NPs

Table 4.2: LbL matrix of deposited CHX and PBAE layers on AFSi-NPs

Table 4.3: Positivity of PBAEs for Q1 of CHX-PBAEs coatings

Table 4.4: Organic content % for CHX-PBAEs for B10 or Q10

Table 4.5: CHX cumulative release at pH5 and pH7.4

Table 5.1: LbL matrix of deposited alginate and TOB layers on AFSi-NPs

Table 5.2: LbL matrix of deposited TOB and PBAE layers on AFSi-NPs

Table 5.3: Positivity of PBAEs for Q1 of TOB-PBAEs coatings

Table 5.4: Organic content % for TOB-PBAEs for B10 or Q10

Table 5.5: TOB cumulative release at pH5 and pH

Chapter 1: Introduction

1.1 Orthopaedic infections

Total Joint Replacement (TJR)

Osteoarthritis (OA) is the most common long-term joint disease which can provoke bone damage and lead to impairment of physical function. The risk of developing OA increases with the age affecting people over 40 years, especially women more than men (Valdes and Stocks, 2018), (Hunter and Bierma-Zeinstra, 2019). Worldwide over 303 million people suffer of OA (James *et al.*, 2018) and 8.75 million people in the UK (Versus Arthritis, 2019). According to the report Global Burden Disease (GBD) of 2017, hip and knee OA are considered the 11th cause of global disability. Indeed, this disorder can affect any joint, but it occurs more often in hands, hips, knees, lower back, neck, elbows and shoulders and it has a significant impact on the life of patient causing pain and disability as well as on society (Swain *et al.*, 2020). Total joint replacement (TJR), is defined as a life-enhancing procedure applied in orthopaedics that aims to offer pain relief, to restore the bone function improving the quality of life of patients (Williams, Garbuz and Masri, 2010), (Kurtz *et al.*, 2007). According to the National Joint Registry (NJR), in the UK a total number of 2,548,896 primary joint replacements was registered in the period between 1 April 2003 and 31 December 2019 and including as follows: 1,191,253 hip surgeries, 1,300,897 knee surgeries, 6,589 ankle surgeries, 45,784 shoulder surgeries and 4,373 elbow surgeries (Registry, 2020). The total number of patients which undergo arthroplasties continues to increase. In the UK, the majority of primary joint replacements are carried out on women (59.9% females and 40.1% males); the median age is 69 years and osteoarthritis (OA) is considered the sole indication for primary surgeries for the 88% of the cases. For instance, considering the number of primary procedures for the year 2018, overall, 96,099 hip, 103,199 knee, 983 ankle, 7,744 shoulder and 782 elbows more surgeries were reported for the year 2019 in the UK. Furthermore, from 1 April 2003 and 31 December 2019, the revision surgeries for hips and knees were 123,891 and 83,042 respectively as well as 803, 5,087 and 1,231 for ankles, shoulders and elbows. Compared to 2018, 7,982 hip, 7,094 knee, 135 ankle, 810 shoulder, 209 elbows more revision surgeries

were reported for the year 2019 (National Joint Registry for England Wales Northern Ireland and the Isle of Man, 2019).

Prosthetic Joint Infection (PJI)

While most of the joint arthroplasties fulfil their important role of pain relief, minority of patients could experience a failure of the TJR and require a further surgery (Wylde *et al.*, 2018). The modes of failure are: aseptic loosening, wear, incorrect position, dislocation, or fracture of the prosthetic material, and materials fatigue. However, infections related to prosthetic joints and their adjacent tissue (PJI), are one of the commonest reason of complications that often involve the removal of the joint, which inevitably require several revision surgeries and in the worst cases, amputation, with a negative impact on the healing time and patient morbidity (Siqueira *et al.*, 2015). Therefore, to achieve an optimal outcome of TJR and patient satisfaction, any risk of complications should be minimized. For example, the success of total hip and knee replacement obtained in last 40 years was the result of the design and application of specific materials, but also it was due to the prevention of infections and the improvement of surgical techniques. Indeed, while prosthetic joint surgery was executed in large scale in the late 1960s, the infection rate registered was between 5-10% for both hip and knee replacement. To reduce the rate of infection, aseptic procedures have been introduced such as: to operate in closed rooms, improvement in the preparation for the surgery, shorter pre-operative hospitalization and the use of antibiotics in the pre-operative phase. Thus, the introduction of these precautions contributed to reduce the infection rate which, for example, in 2016 dropped to 1-3%. While the risk of infection is low for patients who require joint arthroplasty, on the other hand the high demand of arthroplasties may transform this low risk into a considerable burden of infection (Jasper *et al.*, 2016).

Epidemiology of the infection

Prosthetic joint infection (PJI) is reported as failure of the 0.5-2.2% of primary arthroplasties and is the main cause of revision surgery within the five years after the primary operation. Infection is also the major failure of revision surgeries with the incidence rate of 30% which is expected to increase over 40% by 2030 due to the high number of joint replacements performed per year in the UK (over 250,000), (Lenguerrand *et al.*, 2017). Considering 199,298 patients who underwent hip and knee replacement in the UK along the year 2019, over 1,000

operations due to infections were registered only for total knee arthroplasty (TKA) and among these, 85% within the first 30 days and with a median time to infection of 14 days (Registry, 2020). Additionally, USA data showed that there is still the risk of occurring infections over the first year after primary hip and knee arthroplasty. Indeed, a nearly-one quarter of infections after the primary surgery for hip and knee replacements have been diagnosed with a period of 2-10 years after surgery. However, shoulder arthroplasty showed an infection rate between 0.8 and 1.1% similar to the value registered for hip and knee replacements which was 0.5, 0.8 and 1.4% after 1.5-10 years post-surgery. As contrary, the incidence rate for the elbow arthroplasties was high, equal to 3.3%, firstly, because of the rising number of patients affected by rheumatoid arthritis that undergo elbow replacement, then because of limits of the tissue that surrounds the elbow. PJI is also correlated to poor clinical outcomes, prolonged hospital admission and complex revision surgeries which are 2-3 times more expensive than those caused by aseptic failure and has been estimated to be around £100,000 per patient (Lamagni, 2014), (Davidson, Spratt and Liddle, 2019).

Risk factors

Obesity is associated to an increased risk of infections, causing a prolonged operative duration especially for patients with body mass index (BMI) over 35. On the other hand, also for patients with a BMI lower than 25 it was observed a high risk of PJI due to immunosuppression and nutritional deficit (Namba, Inacio and Paxton, 2013). Additionally, glucose levels can increase along the operation affecting the time of surgery and its outcome. Therefore, also diabetes mellitus is considered one of the risk factors rising the incidence of PJI, as well as age and smoking. Moreover, other comorbidities can increase the risk of infections such as: rheumatoid arthritis, prior infection or multiple priory surgeries, and suppressed immune systems (Malinzak *et al.*, 2009). However, it has been found that the incidence of infection post-revision surgery is higher than post-implantation (primary surgery) and possible reasons could be: a non-recognized infection during the revision surgery or prolonged operating time during the revision procedure. In particular, for hip and knee replacement, the prolonged surgery time can be a valid reason for microbial contaminations of the joint an it could dramatically rise the risk of PJI (Friedman *et al.*, 2013).

Clinical manifestations

The clinical manifestations are dependent on several factors such as: the modality of initiation of the infection, the joint involved, the environment around the tissue in which the infection occurs, the host immune response and the virulence of the microorganism that causes the infection (Tsaras *et al.*, 2012). There are also symptoms that can be correlated to PJI and the most significant are pain, erythema, fever or warmth around the joint and swelling of the joint. Several studies reported that 79% of the 100 cases analysed showed pain as one of the commonest clinical manifestation of PJI, followed by the relevance of erythema or joint swelling also discovered in patients that undergo knee arthroplasty (Peel *et al.*, 2012).

Type of infections

One of the classifications for PJI infections is dependent on the time of the infection. For this reason, it is possible to distinguish 3 different typologies: early, delayed and late onset infections. Early onset PJI occurs before than 3 months after the last surgery. These infections start after the operation and can be caused by contamination during the surgery and by virulent microorganisms. Delayed onset infections occur after 3 months of the last surgery but before 12 or 24 months. Their cause is related to microorganisms characterized by less virulence compared to those of the previous typology and for this reason their manifestation is not evident within the first 3 months. Late onset PJI occur after 12 months of the last surgery and they are mostly due to haematogenous infection or an indolent infection started at the time of the surgery (Trebše and Mihelič, 2012), (Porrino *et al.*, 2020). In the 1990 another classification has been developed by Tsukayama, based not only on the time of the infection but also on the mode of occurrence. The first group is represented by positive intraoperative cultures in which during the revision surgery the patient is found to have a positive intraoperative culture. The second category is early postoperative infection which has similar features of the early onset PJI, but it occurs within the first month after the surgery. The third category is late chronic PJI that occurs after 1 month of the surgery whereas the last one is the acute haematogenous infection (Kaltsas, 2004), (GOMES, 2019). There is also another classification considering not only the type of the infection but also the host. Three of the four categories described by Tsukayama are considered: early postoperative, haematogenous and late chronic infections named respectively as type I, II and III. Each grade represented the host status such as: grade A (uncompromised), grade B (compromised) and

grade C (significant compromised). In particular, this classification is widely used for prognostic information and treatment decisions (Mcpherson *et al.*, 2002), (Tande and Patel, 2014).

Causative microorganisms

In orthopaedics, prosthetic joint infections are caused by biofilm formation of communities of microorganisms which, by adhering to the surface of the prosthesis, form a thin film that acts as a barrier against antimicrobial agents (Ayoade, 2020), (Costerton, Stewart and Greenberg, 1999). For instance, PJI occurring within the first few months after the implantation are caused by direct contact with the microorganism along the time of the operation, whereas late infections are often associated to indolent microorganisms or hematogenous seeding of bacteria from a distant site (Kolinsky and Liang, 2018). In particular, early onset infections are caused by virulent microorganisms such as *Staphylococcus aureus* or Gram-negative bacilli. Typically the symptoms are fever, joint pain and wound drainage and at the site of implant there is oedema, erythema and induration (Barrett and Atkins, 2014). Delayed onset infections are associated to the less virulent microorganisms such as Gram-negative staphylococci or Gram-positive *Propionibacterium acnes* which could infect the patient along the implantation and the main symptom is joint pain with or without implant loosening (Zimmerli, 2006). Late onset infections are caused by hematogenous spreading bacteria from distant site and are generally difficult to identify. Clinically, the patient may present symptoms such as chronic pain leading to sepsis and bacteraemia (Tande and Patel, 2014). However, understanding bacteria and their distribution can positively influence the choice of the treatment and the development of preventing strategies. According to National surveillance data for England, the most frequent pathogen that can provoke infections is *Staphylococcus aureus* affected by patients who undergo hip and knee arthroplasty. Indeed, a value of 44% of infections, due to this pathogen, has been registered in the year 2018/19, for patients who required knee and hip implants within 1 year of surgery; 20% of them were methicillin-resistant. Moreover, 31% of infections were characterized by Coagulase-negative staphylococci and the 12% divided between enterococci such as: *Escherichia coli*, *Enterobacter spp*, *Pseudomonas spp* and streptococci (Health Protection Agency, 2018).

Treatment of Prosthetic Joint Infection (PJI)

Successful management of PJI is more often obtained by the combination of surgical intervention and medical therapy. The goals to treat prosthetic joint infection are associated to the restore of the infected joint, the relief from the pain and the eradication of the infection to improve the quality of the life of patients, reducing the chances of morbidity and mortality. There are several surgical strategies applicable for the treatment of PJI such as:

- Debridement with Prosthesis Retention
- One-stage or Direct Arthroplasty exchange
- Two-stage Arthroplasty Exchange
- Resection of the prosthesis without re-implantation
- Amputation

The target of each surgical protocol is the removal of all the infected tissue and in case the implant is retained, the role of the postoperative antimicrobial therapy is to eradicate the remaining infection (Otto-Lambertz *et al.*, 2017), (Tande and Patel, 2014).

Debridement with prosthesis retention

It is a single surgery correlated to a procedure known as DAIR (debridement, antibiotics and implant retention) performed by using open incision followed by irrigation and debridement of infected tissues that surround the prosthesis. For most of the patients the post-operative therapy is intravenous administration of antimicrobials for 2-6 weeks after the surgery (Brandt *et al.*, 1999), (Aboltins *et al.*, 2007).

One-stage arthroplasty exchange

This procedure also named direct exchange refers to open arthrotomy and debridement followed by total removal of the prosthesis and is mainly employed to hip arthroplasty infections. In the same surgery, a new implant is replaced using antimicrobial-loaded poly(methyl)methacrylate (PMMA) in order to fix the arthroplasty in place (Rahman, Kazi and Gollish, 2017), (Klouche *et al.*, 2012). The choice of the antimicrobial depends on the identification of the pathogen which is investigated priory the operation. Although there are many antimicrobial strategies, the most frequent used requires 4-6 weeks of antibiotic via intravenous, followed by a period between 3-12 months of oral antibiotics (Rudelli *et al.*,

2008), (Lamagni, 2014).

Two-stage arthroplasty exchange

This procedure is considered the most effective approach to eradicate infection and preserve joint function and it consists at least of two surgeries. In the first one, infected tissue is debrided, all PMMA components are removed and replaced by an antimicrobial-impregnated PMMA spacer which is implanted in the joint space. After the surgery, firstly, for 4-6 weeks an antimicrobial therapy is executed via intravenous, then, there is a period from 2-6 weeks in which with antibiotic therapy the patient is evaluated in order to understand if the infection is still ongoing. If there is the infection a debridement is again repeated followed by antimicrobial therapy as previously described. This protocol is carried out until the re-implantation cultures are negative. Indeed, when this occurs, a new prosthesis is implanted using antimicrobial-loaded PMMA (Bejon *et al.*, 2010), (Mahmud *et al.*, 2012). Two-stage arthroplasty is a successful procedure for the treatment of PJI specially for hip and knee replacement where the success rate is between 87-100% for hip arthroplasty and it is nearly 90% for knee replacement. On the other hand, elbow arthroplasty is still difficult to treat because of complications like rheumatoid arthritis. In this case, the success rate gained with this procedure is equal to 72% (Osmon *et al.*, 2013), (Biring *et al.*, 2009), (Porrino *et al.*, 2020).

Arthroplasty resection without re-Implantation

Resection without re-implantation is applied as an alternative strategy to avoid amputation when the protocols previously described are not applicable, or when the patients are not suitable candidates for DAIR procedure or one-stage arthroplasty or do not want to undergo multiple surgeries. Additionally, also after resection, antimicrobial treatment is necessary for a period between 4-6 weeks via intravenous administration unless the conditions of the patient require a prolonged therapy (Choi *et al.*, 2014), (Tande and Patel, 2014).

Amputation

Amputation is an option applied to patients for which all the other procedures failed in the treatment of PJI, but fortunately the percentage of cases that require this outcome after joint arthroplasty is extremely low (0.1%). The duration of the antimicrobial therapy depends if all the infected tissue has been removed or not. In case the infection and the amputation site are distant, antimicrobials can be administrated for only 1-2 days after the surgery (Atkinson,

2017), (Tande and Patel, 2014).

Antimicrobial-loaded bone cements

Antibiotic loaded bone cements (ALBC) has been applied as treatment or prevention of orthopaedics over the last three decades and their use is mainly focused on the delivery of high local antibiotics released directly at the site of infection with minimal or no systemic toxicity (Xu *et al.*, 2020), (Regis *et al.*, 2013), (Jiranek, Hanssen and Greenwald, 2006). There are two different types of space fillers used during this procedure: static and articulating spacers. The first type is applied in order to fill the void in the bone after the removal of the prosthesis and it is also called 'non-articulating' spacer. The second type is using to provide more motion and restore the joint structure (Masri *et al.*, 1998), (Miller, Henry and Brause, 2017). Antimicrobials-loaded bone cements have two main functions: firstly, they keep the joint position avoiding muscles contractures, provide mechanical support during the removal of the infected arthroplasty providing at the same time comfort to the patient between the two surgeries. Then, the second function is to increase the systemic therapy between the two surgeries, providing a local antimicrobial therapy (Bistolfi *et al.*, 2011), (Massazza *et al.*, 2015).

The choice of antibiotics

Antibiotic-loaded bone cement is a spacer largely used because of its plasticity and ability to release the drug *in situ* (Webb and Spencer, 2007). However, there are some criteria that need be carefully considered in the choice of the antibiotic before being loaded on bone cements (Farrar, Benson and Milner, 2009). Antibiotics for bone cements corporation should possess: broad antibacterial spectrum involving activity Gram-negative and Gram-positive microorganisms, chemical and thermal stability, low protein binding, high bactericidal activity and potency, solubility in water to promote their release from the bone cement, availability as powder formulation, elution for a long period and low interference with mechanical proprieties of the bone cement (Xu *et al.*, 2014), (Anagnostakos and Kelm, 2009). For example, aminoglycosides are extremely suitable for bone cement applications which satisfy the criteria listed above. This antibiotic class is concentration-dependent and thus, the increase of the drug dose will produce a rise of the antibacterial efficacy, promoting the eradication of bacteria (Krause *et al.*, 2016). In particular, gentamycin and vancomycin are generally incorporated on bone cement due to their antimicrobial activity against respectively

Gram-negative bacteria and Gram-positive bacteria such as *Staphylococcus aureus*. Recent studies report that antibiotic-loaded bone cements reduce significantly the bacteria growth compared to the non-antibiotic cements. Indeed, the employment of aminoglycosides in ALBC have contributed to reduce the incidence of infection in primary arthroplasty, especially in patients that undergo total knee replacement (Wang *et al.*, 2013), (Saleh *et al.*, 2016).

Drawbacks of antibiotic-loaded bone cement application

Although antibiotic-loaded bone cements are strong therapeutics able to eradicate bacteria due to their controlled release ability, the application of these systems in clinical practice present some shortcomings such as: development of antibiotic resistance due to prolonged exposure time, antibiotic effectiveness, loosening of bone cement mechanical properties and costs (Martínez-Moreno *et al.*, 2017), (Hendriks *et al.*, 2004).

Mechanical properties and antimicrobial resistance

Antibiotic elution depends on its physiochemical characteristics and on bone cement composition. For instance, high drug elution is provided by a material which possesses high porosity, which can cause a drop of the material resistance due to the presence of air entrapped in the cement. Therefore, to overcome this issue, a combination among cement brand, antibiotic choice and their mixing procedure needs to be evaluated for each microorganism (e.g. Vancomycin-Palacos LV) (Lewis, 2009), (Pithankuakul *et al.*, 2015).

On the other hand, the surface of antibiotic bone cement can promote the colonization of the bacteria. In particular, antibiotic release from bone cement occurs in few hours with high initial release rate, known as burst release, followed by a slow release, below the minimum inhibitory concentration (MIC), over the next days (Xu *et al.*, 2020) (Lewis, Janna and Bhattaram, 2005). Thus, prolonged exposure to antibiotics at sub-inhibitory levels over longer period of time may lead to the development of resistant bacterial strains. Despite the presence of antibiotic, the surface of bone cement could be a good substrate for the growth of bacteria. However, the adhesion of bacteria on the PMMA surface significantly reduces its affinity to antibiotics. The specific mechanism which explains the lack of effectiveness of antibiotic against a specific bacterial strain is still unknown and its conjugation to orthopaedic biomaterials has not been well studied yet (Farrar, Benson and Milner, 2009), (Perni *et al.*, 2015).

Clinical needs

Among the drawbacks of antibiotic loaded bone cement, there are also other crucial factors. For example, the difficulty of selecting the appropriate antibiotic to load on bone cement due to the wide origin of bacteria that cause prosthetic joint infection as well as high local concentration of antibiotic is reached over short term but lasting only few hours (Prokopovich *et al.*, 2015). This suggests that antibiotic controlled release is highly effective in case of acute infections while in the late infections, the reduction of antibiotics levels increases the possibility of surviving bacteria, which can slowly re-establish biofilm formation followed by bacterial dissemination (Martínez-Moreno *et al.*, 2017). Hence, the development of alternative prophylactic treatments able to control the antibiotic release, by minimising the burst release effect and thus the bacterial resistance, is required.

Tobramycin mechanism of action

Tobramycin is an aminoglycoside which is mainly used as antibiotic to treat severe infections caused by Gram-negative pathogens, and it is effective against *Pseudomonas* strains which are generally resistant to gentamycin (Dhondikubeer *et al.*, 2012). The excellent bactericidal activity of this molecule is the result of chemical binding to the site A on 16S rRNA, which is part of the ribosomal 30S subunit of the bacteria. Therefore, this leads to a misreading of the genetic code, which causes a disruption of the translation and thus, inhibits the ability of the bacteria to carry out the protein synthesis (Kotra, Haddad and Mobashery, 2000). Tobramycin is active against a wide broad spectrum of Gram-negative microorganisms providing, after intramuscular administration, minimum inhibitory concentration (MIC) values such as: 6.25 µg/mL were effective against *Pseudomonas aeruginosa*, *Escherichia coli*, *Enterobacter species*, and *Klebsiella*, whereas it is less effective against *Serratia*, *Proteus* and *Providencia* species which were resistant to more than 25 µg/mL of antibiotic (Kuijpers *et al.*, 2000). However, tobramycin showed also a good activity against *Staphylococcus aureus* strains with MIC ranging between 1.56 and 6.25 µg/mL, but poor activity was observed against *Streptococcus pyogenes*, *S. faecalis* and *D. pneumoniae*, that were instead resistant to more than 12.5 µg/mL of the aminoglycoside (Campoli-Richards and Todd, 1987), (Krause *et al.*, 2016).

Chlorhexidine mechanism of action

Chlorhexidine is an antimicrobial agent with a broad spectrum acting against Gram positive and Gram-negative bacteria, yeasts, dermatophytes and some lipophilic viruses. Its antimicrobial activity is membrane-type focused on the inner cytoplasmic membrane. The presence of the biguanides groups provides its antibacterial action that possesses different effects. For example, at low concentrations the drug exhibits a bacteriostatic action as well as when the concentration becomes higher it shows a bactericidal activity (Jones, 1997), (Faria *et al.*, 2013), (Moureau, Deschneau and Pyrek, 2009). As it is illustrated in the figure 4.60, the antibacterial mode of action of the chlorhexidine is due the positivity of its cationic groups which interact with the bacterial cell surface that is negatively charged and possesses phosphate groups. This step alters the integrity of the membrane and increases the opportunity for the chlorhexidine to bind phospholipids attached to the inner membrane. This mechanism can provoke leakage of low-molecular weight components, as potassium ions, leading to cell lysis (Jones, 1997). The minimum inhibitory concentration (MIC) of chlorhexidine reported in the literature against *Escherichia coli* is 2-8 µg/ml and against *Staphylococcus epidermidis* is ranging between 0.5-2µg/ml (Luo *et al.*, 2016).

Role of polymeric nanocarriers in orthopaedic infections

Over the last 20 years, the development of drug delivery systems based on biodegradable polymers has been widely studied to overcome the limitations of the antibiotics and minimise the burden of orthopaedic infections (Smith *et al.*, 2018), (Karabasz, Bzowska and Szczepanowicz, 2020). Indeed, the use of polymeric nanocarriers presents several advantages such as: improved bioavailability and hydrophilicity of different therapeutics, sustained drug delivery and ability to provide a targeted drug release at the site of infection by reducing the interaction with plasma and cellular proteins (Singh and Lillard, 2009). Typically, nanocarriers correspond to particulate structures with a diameter smaller than 1000 nm where the drug could be entrapped, diffused, absorbed or encapsulated onto nanoconjugate matrix. In this context, polymeric nanoparticles obtained from natural and synthetic polymers are widely employed in biomedical field especially as delivery systems due to their stability and easy surface modification. Additionally, these nanoparticles are used in drug delivery for two main reasons: the small size and the use of biodegradable materials, and their preparation could be tailored to provide controlled drug release by tuning the polymer properties and the

surface chemistry. Among the variety of methods available to prepare polymeric nanocarriers, the Layer by Layer self-assembly is the most common approach applied to form multilayer thin films (Nayanathara, Kermaniyan and Such, 2020), (Chevalier, Gonzalez and Alvarez, 2015).

1.2 Layer by layer assembly technique

The design of thin film coatings has been a critical challenge among scientists since the second half of the 20th century which found application especially in biological and medicinal fields. In particular, two specific techniques such as Langmuir-Blodgett deposition (Blodgett, 1935), (Brunauer and Emmett, 1937) and self-assembled monolayers (SAMs) (Nuzzo and Allara, 1983) are considered the most important processes used to design biocompatible surfaces (Gentile *et al.*, 2015). For instance, Langmuir-Blodgett technique is applied to the deposition of surface active molecules such as phospholipids and fatty acids organised in mono or multilayers thin films (Punkka and Rubner, 1992), whereas Self-Assembled Monolayers (SAMs) are organic surfaces formed by the adsorption of long chain alkanethiols on gold (Ying *et al.*, 2001). The systems obtained by these methods showed an ability to control over the properties of the interface at the molecular scale. Thus, these techniques played a fundamental role on studies of protein adsorption and cell adhesion (Ying *et al.*, 2001), (Mbam *et al.*, 2019). Despite their employment in bio-catalysis, drug delivery and tissue engineering, different drawbacks of both methods influence their application to the biological field (Kern and Schuegraf, 2001), (Henini, 2000), (Matsusaki *et al.*, 2012), (Monolayers and Brushes, 2005). For example, the Langmuir-Blodgett deposition requires long times for the preparation of the biomolecule films, reduced types of biomolecules that can be involved in the system, expensive instrumentation, and among these disadvantages there is the possible instability shown by biomolecules because of weak physical attraction inside the films. On the other hand, the drawbacks of SAMs are limited stability of films under ambient and physiological conditions, small number of substrate types available for this method and low loading of biological components into the films resulting from their monolayer nature (Tkachev *et al.*, 1995). Among these techniques, an alternative and convenient method was introduced by Decher, Hong and co-workers in 1991, called Layer by Layer assembly with the aim of producing structured-controlled thin films for biological applications (Decher and Hong, 1991). This method possesses several benefits such as: a precise control of coating

properties, easy preparation, it is a cheaper process compared to the techniques described above, environmentally friendly, versatile, possibility of obtaining a homogeneous film with controlled thickness, capability of incorporation and controlled release of biomolecules and drugs and robustness of the products used under ambient and physiological conditions (Paula T Hammond, 2012). Furthermore, comparing the systems produced by Langmuir-Blodgett and SAMs techniques, the LbL deposited matrices are more stable films with a higher loading of biological species. Indeed, several types of charged molecules are suitable components for the preparation of the LbL technique such as: biological polysaccharides, inorganic molecular clusters (Liu, Volkmer and Kurth, 2003), dendrimers (Ramalingam *et al.*, 2016), nanoparticles (Ariga *et al.*, 1997), nanotubes (Komatsu *et al.*, 2011), nucleic acids and DNA (Wurster *et al.*, 2013), (Qi *et al.*, 2011), (San Juan *et al.*, 2020), organic dyes (Khan *et al.*, 2016), proteins (Cai *et al.*, 2005), porphyrins (Wu, Zhao and Zhang, 2017) and viruses (Lvov *et al.*, 1994). In the average, the wide variability of substrates available and the versatility of assembly methods substantially rise the importance of this technique (Tang, Zhang, *et al.*, 2006).

Types of biomolecules embedded on LbL biofilms

The determination of the LbL films is connected to the multiplicity of intermolecular interactions where the most important role is played by the cooperative effect of multipoint attractions.

Lipid Vesicles

The first category of biomolecules is represented by lipid vesicles that are composed by amphiphilic organic molecules with low-molecular weight. Including these types of vectors into multilayers through strong electrostatic interactions can cause the breach and then the fusion of the spherical structures of the vesicles (Tang, Jing and Wang, 2000). To avoid this problem, for example, Katagiri *et al.* developed a three-dimensional packed vesicular assembly by using the Cerasome, which is an organic-inorganic hybrid vesicle possessing liposomal membrane and ceramic surface. The stability of the vesicle was improved via modification of its surface occurring by self-condensation of triethoxysilyl groups in water. The success of this method was confirmed by the atomic force microscopy (AFM) that proved the presence of intact vesicles particles in the multilayers (Katagiri *et al.*, 2002). Additionally, Michael *et al.*, provided homogeneity to the surface of the vesicles by polycation absorption

carried out prior to the multilayer deposition. Images obtained by AFM, clearly proved that no disruption of the vesicles occurred along the formation of the lipid bilayer (Michel *et al.*, 2004). Therefore, the success of these methods promoted the use of lipid vesicles as biomolecular reactors or as reservoirs for drug delivery (Michel *et al.*, 2005), (Tang, Wang, Podsiadlo and Nicholas A. Kotov, 2006).

Polypeptides

The secondary structure of polypeptides applied to design multilayer films via LbL was studied by Müller *et al.*, that observed a change of PLL (poly-L-lysine) transition from random to α -helix if dissolved salt solution as sodium perchlorate (NaClO_4). Despite that, when PLL was alternatively coated with poly (maleic acid co- α methylstyrene) (PMA-MS) on silicon substrate, ATR-FTR measurements evidenced that the α -helix state of PLL remained intact and independent from the number of deposited layers (Müller, 2001), (Tsuji, 2019). Additionally, Boulmedais *et al.*, analysed the interactions between PLGA (poly-L-glutamic acid) and PAH (poly-allylamine) multilayer films. While the thickness of the films was exponentially growing once a new layer was embedded onto the system, PLGA underwent to random/ α -helix transition during the self-assembly deposition with PAH. No further change in this structural transition was observed along the film build up process, where the multilayer was alternatively interacting with PLGA and PAH solutions (Boulmedais *et al.*, 2003). These studies suggested that the secondary structures of polypeptides immobilized in LbL films are the same than those present in the polyelectrolyte solution, providing homogeneity in the structure of the multilayer system which was independent from its whole thickness. (Tang, Wang, Podsiadlo and Nicholas A. Kotov, 2006).

Nucleic Acid and DNA

The DNA-containing films show a good activity and strong binding abilities with different DNA-intercalated molecules, involving antitumor drugs. They have been fabricated by Sukhorukov *et al.* with an alternative assembly of anionic DNA strands and cationic polyelectrolytes such as PEI or PLL and following study of DNA conformations in the film with IR, UV-vis and circular dichroism (CD) spectroscopy. The results show that DNA keep its double-helical structure in all the films and that water molecules bind with DNA phosphate groups, penetrating easily

into all types of films (Sukhorukov *et al.*, 1996), (Tang, Wang, Podsiadlo and Nicholas A Kotov, 2006).

Proteins

LbL self-assembly could be applied to coat bioactive proteins into thin films, enhancing their functions and addressing their application as optical and electrochemical biosensors (Takahashi, Sato and Anzai, 2012), as bioactive agents for drug delivery (Saurer *et al.*, 2010), as complexes against environmental stress of food products (Azarikia *et al.*, 2017) or for biotechnology and biomedical applications (Vander Straeten *et al.*, 2017), (Tang Z., *et al.*, 2006). For example, Onda *et al.* designed a multilayer film by alternatively coating the anionic enzyme glucose oxidase (GOD) with polycations such as poly (dimethyldiallyl-ammonium chloride) (PDDA) or poly (ethylenimine) (PEI) (Onda, Ariga and Kunitake, 1999). In this case the immobilisation of GOD into multilayers did not influence its native enzymatic activity which was reduced only for the 20% of GOD before the LbL deposition. Furthermore, for GOD-films no enzymatic denaturation was detected and the enzymatic activity lasted 14 weeks if the system was stored in buffer at 4°C. Finally, it was observed that when the enzyme was embedded into films, there was an improvement of its stability plus an higher tolerance if dissolved in alkaline media (Caseli *et al.*, 2006), (Zhang *et al.*, 2019).

LbL film-deposition process

In the last 20 years many researchers have focused their attention on the production of new generation of scaffolds, composed by 'nanofeatures' which, interacting and influencing cellular behaviour, arise the interest of engineered tissues. Many surface modification processes can be counted into nanotechnologies and among the last developments the surface functionalization at the 'nanoscale' is considered a suitable strategy to obtain appropriate biological responses (Gentile *et al.*, 2015). Among the nanotechnology techniques available in the literature such as Langmuir-Bodgett (Brunauer and Emmett, 1937) and SAMs (Nuzzo and Allara, 1983) depositions, Layer by Layer (LbL) self-assembly is still an attractive method used to design functional coatings. It is a process based on an alternative exposure of charged substrate to solutions positively or negatively charged of polyelectrolytes. After each layer deposition, there is a washing step, mainly carried out with

distilled water in order to reduce the risk of contaminations and to remove excess of polyelectrolytes (Gröger, Lutz and Brunner, 2008).

Modifying some experimental parameters such as polyelectrolyte concentration, pH or ionic strength it is possible to change the properties of the scaffolds like roughness, thickness and porosity. At first glance, only electrostatic interactions between opposite polyelectrolytes determined the rise of the LbL multilayer. Then, other types of interactions were studied: covalent and hydrogen bonding, hydrophobic and coordination bonding and charge transfer (Feng *et al.*, 2007), (Shimazaki *et al.*, 1997), (Xu, Zhu and Sukhishvili, 2011). Because of the nanoscale domain control and all the advantages of the LbL, this method is an attractive process that lead to the fabrication of highly complex, tailor-made coating compositions. One of the benefits of the LbL is related to its performance in water solution at room temperature. This allows the maintenance of the activity of sensitive substrates such as proteins, nucleic acids and other functional biomolecules. Then, this technique promotes the coating of any shape structures with a widely dimensional range, from 10 nm diameter gold nanoparticles, (Gentile *et al.*, 2015), (Schneider and Decher, 2004), (Schneider and Decher, 2008), to large-scale macroscopic 3D objects and surfaces with complex nanometre patterns. LbL can be employed to obtain a high biocompatibility (Ai *et al.*, 2003), (Zheng *et al.*, 2004), in vivo and in vitro: a nanostructure could be exploited to improve the surface topography and load many biomolecules or organic and inorganic nanomaterials. Furthermore, the possibility to coat drugs in separate sets of layers has been pursued in order to promote a strategy for a sequential controlled delivery (Paula Hammond, 2012).

Biomedical applications of the LBL technique

The layer by layer technique has been employed for numerous fields, but in this section applications, such as cardiovascular devices (Amano *et al.*, 2016), (Ren and Ji, 2015), wound healing dressing (Fahmy, Aly and Abou-Okeil, 2018), (Jeckson *et al.*, 2020), bone grafts (Li *et al.*, 2012), (Xing *et al.*, 2017), (Ronca *et al.*, 2016) and nanocarriers for the drug delivery (Pérez-Anes *et al.*, 2015), (Wang, Hao and Cai, 2019), (Wohl and Engbersen, 2012) are going to be accurately described.

Cardiovascular devices

The LbL technique is suitable to substrates of any size and shape and it has been widely used to coat biomolecules into cardiovascular devices and to retain their activity. For example, recently Lin *et al.* took advantage of Layer by Layer technique by designing a multi-layered construct obtained by the combination of heparin (HE), an anticoagulant, and collagen (Col) on stainless steel stents. with the aim of improving the antithrombogenicity and the cytocompatibility of the stent surface. After the deposition, it was observed that the HE/Col multilayer was stable in PBS and that the self-assembly method provided a homogeneous system. Furthermore, *in vitro* studies reported a higher endothelial cell response (ECR) for the modified stents plus a synergic effect of antithrombogenicity and fast endothelialisation promoted by respectively the heparin and the cell compatibility of the collagen. Additionally, it was noticed that the presence of both polyelectrolytes onto the interface multilayer facilitated processes such as the endothelial cell adhesion, spreading and proliferation. Therefore, He/Col multilayers stents via LbL deposition could represent a valid method to improve thromboresistance and fast endothelialisation which are the crucial factors of the stainless steel stents implantation (Lin *et al.*, 2010). On the other hand, in the studies of Chen *et al.*, heparin and collagen were also employed via LbL to modify titanium cardiovascular devices to improve their anticoagulant proprieties. In this case, before the self-assembly deposition, the surface of the metal was, firstly, treated with sodium hydroxide (NaOH) solution. It was observed this modification provided a more porous surface of the titanium due the to the presence of a higher number of hydroxyl groups and to a higher hydrophilicity than the untreated titanium. Then, the surface was modified by coating the positive poly-L-lisine (PLL) as precursor layer, followed by alternative deposition of heparin and collagen through electrostatic interactions. SEM images and FTIR spectra proved that the choice of treating the material surface with NaOH and PLL increased the stability and the thickness of the first layer and it was crucial for the success of the multilayer formation. Moreover, the multilayer system formed by LbL provided a lower platelet adhesion and thus, improved the anticoagulation properties of the titanium (Jaganathan *et al.*, 2014), (Hong *et al.*, 1999), (Chen *et al.*, 2009), (Stathopoulos *et al.*, 2011). Furthermore, LbL technique is also applied to the incorporation of specific agents, for example sirolimus, into the multilayer to treat arterial diseases (Huang and Yang, 2008). For instance, Chen *et al.*, alternatively coated collagen and the strong immune suppressor agent sirolimus in multilayers on metallic stent to treat coronary arterial stenosis. The results of this study showed that the number of drug /collagen

layers influenced the duration of the drug release, which lasted over 28 days, promoting the inhibition of smooth muscle cells growth and therefore avoiding restenosis (Chen *et al.*, 2005) (Huang and Yang, 2008). The combination of different polyelectrolytes coated via LbL has been considered as valid option to improve the properties of catheters and dialysis instruments which are in direct contact with blood flow (Gorbet and Sefton, 2004). For example, Polyethersulphone (PES) is an example of material that is commonly used because of its high ability of membranes ultrafiltration and Sperling *et al.* designed a LbL coating to enhance its wettability and thus its interaction to the proteins of plasma. In particular, PES material modification was based on alternative LbL coating of albumin protein, heparin and endurin, which is the high active fraction of heparin. It was demonstrated that the presence of multilayer systems contributed to reduce the platelet adhesion as well as the combination of both albumin and endurin in the films, decreased the formation of the thrombin-antithrombin complex. (Sperling *et al.*, 2005).

Wound healing dressing

The ideal scaffold employed as dressing for wound repair and designed to protect the injured tissue and promote the healing process, needs to fulfil specific characteristics such as: to protect the wound from bacterial penetration, to provide hydrophilic surface, to be non-toxic and to promote the adhesion and the cells proliferation (Metcalfe and Ferguson, 2007). To reach this target, the surface of these biomaterials could be functionalized in several ways: using a controlled release of bioacides, acting with microbe-repelling, with antiadhesive or antibacterial polymers or peptides (Wang *et al.*, 2006), (Murata *et al.*, 2007), (Li *et al.*, 2006). For example, silver and gold nanoparticles are valid candidates due to their antimicrobial properties as well as silver and Ag ions are commonly used as bioacidal materials for polyelectrolytes multilayer deposition. These metallic materials are bioacide agents acting against a broad spectrum of bacteria, fungi and viruses (Marambio-Jones and Hoek, 2010). In this field, LbL self-assembly could be employed as nanoreactor method, where Ag ions are loaded onto the polyelectrolytes multilayer (PEM) and simultaneously reduced to form Ag nanoparticles (Rahimi *et al.*, 2020), (Podsiadlo *et al.*, 2005). For instance, Zan *et al.* proved that the ion exchange/ reduction approach could be exploited to incorporate Ag nanoparticles into a multilayer system without pH variation. In particular, initially, a multilayer coating, composed by poly (diallyldimethylammonium chloride) (PDDA) and polystyrene

sulfonate (PSS), was dipped into silver nitrate (AgNO_3) to load Ag ions into the film. Then, after a treatment with sodium borohydride (NaBH_4), the excess of silver in ionic form was reduced to form Ag nanoparticles. The antimicrobial activity of multilayers possessing Ag ions and Ag nanoparticles was evaluated against *Escherichia coli*, and exhibited different effects: the system with Ag ionic form provided high activity in the short term whereas the Ag nanoparticles showed a low initial effect but extended to long periods of time (Zan and Su, 2010). On the hand, also gold nanoparticles (GNPs) have been widely used in biological field due to their antimicrobial activities (Zou *et al.*, 2020), (Yang *et al.*, 2017), (Lu *et al.*, 2018). For example, Zhou *et al.*, designed a multilayer construct where GNPs as polyanion and lysozyme (Lys) as polycation were alternatively coated via LbL on cellulose mats. The antibacterial activity against *Staphylococcus aureus* and *Escherichia coli* was investigated for uncoated and coated cellulose mats. It was observed that the multilayer system showed a higher antibacterial efficiency depending on the number of layers coated onto the cellulose mats whereas the uncoated mats hardly showed an inhibitory effect (Zhou *et al.*, 2014). Furthermore, LbL self-assembly is employed to embed releasable antibiotics into multilayers to prevent bacterial colonisation in wounds (Agarwal *et al.*, 2012). For instance, chlorhexidine (CHX) is an example of antiseptic that is incorporated into polyelectrolytes multilayers (PEM). It is an antimicrobial agent which is active against Gram-positive/Gram-negative bacteria and possesses bactericidal effect and a positive charge at physiological pH, whose binding to the negative groups of the bacteria cell walls, alters the bacterial osmotic equilibrium (Lim and Kam, 2008), (Wu *et al.*, 2008). For example, Aubert-Viard *et al.*, developed a wound dressing able to provide a prolonged chlorhexidine release from textile nonwoven poly(ethylene terephthalate) (PET). After surface modification of PET, where the first layer was composed by chitosan (CHT) crosslinked to genipin (GPN); the antimicrobial agent CHX, the anionic methyl-beta cyclodextrin polymer (PDC) and the cationic CHT were alternatively coated via LbL to form the multilayer system. It was observed that the number of layers forming the film could control the CHX release whose antimicrobial activity persisted for 45 days on *E. coli* and *S. aureus* strains (Aubert-Viard *et al.*, 2019). On the other hand, gentamicin is an antibiotic used to treat wound infections and generally chosen as agent to be incorporated into multilayers. It belongs to the category of aminoglycosides and it is mainly active against Gram-negative bacteria but also against Gram-positive bacteria such as *S. aureus* (Kotra, Haddad and Mobashery, 2000). For instance, Chaung *et al.* designed a hydrolytically biodegradable

thin film built via LbL deposition including poly(β -amino) ester (PBAE), hyaluronic acid (HYA) and gentamicin. It was demonstrated that the antibiotic released the multilayers via drug diffusion through the layers, hydrolytic degradation and film disruption. Additionally, *in vitro* studies multilayer system showed efficacy against *S. aureus*, which was comparable to the positive effect exhibited by the direct gentamicin administration (Chuang, Smith and Hammond, 2008). However, LbL technique could be applied as method for surface functionalisation of biomaterials by employing antibacterial polymers or peptides. For instance, polyethyleneimine (PEI) is an example of synthetic polyelectrolyte with antibacterial property. He and Chan evaluated the antimicrobial properties of this polymer by developing a stable PEI multilayer, formed by LbL, and incorporating Ag nanoparticles which were reduced to silver ions after treatment with sodium borohydride (NaBH_4). In particular, the antimicrobial properties of PEI were investigated in presence or absence of embedded Ag nanoparticles. Generally, the multilayer PEI itself has efficient activity against *S. aureus* and *E. coli* upon contact formation, but the presence of Ag nanoparticles into the system increased the efficiency over the 99%, promoting the inhibition of bacteria growth (He and Chan, 2010). On the other hand, chitosan (CHT) is among natural polycationic polymer that is widely used in biomedical application as antimicrobial agent. It is a biocompatible polysaccharide whose amino groups are positively charged below pH 6. Its antimicrobial activity is the result of the interaction between its positively charged molecules and the negatively charged cell membranes causing a change in the cell permeability. This mechanism is active in both conditions when the polymer is in solution or immobilised into multilayers (Yu, Lin and Yang, 2007), (Rabea *et al.*, 2003). Therefore, CHT is employed in biomedical applications via LbL as biomolecule to modify the surface of the materials. For example, Bahrami *et al.*, designed a polyurethane (PU) film where collagen and chitosan were layered through LbL self-assembly. AFM and confocal microscopy confirmed the success of this method of surface modification as well as *in vitro* studies proved that the presence of the 2 biomolecules in the system promoted the growth rate and the proliferation of the fibroblast cells when the film was composed by 3 layers. Thus, the antimicrobial activity of the multilayer was increased than the untreated PU (Bahrami *et al.*, 2020).

Bone grafts

The LbL technique is also applied to enhance the bioactive properties of biodegradable polymers such as poly(L-lactic) acid (PLLA) and poly(lactic-co-glycolic) (PLGA), whose biomedical application is limited due to their hydrophobicity and weak bioactivity (Gentile *et al.*, 2014). To overcome this problem, coating the substrate surface by employing extracellular matrix (ECM) components, such as collagen and hyaluronic acid (HYA), could be an alternative approach to mimic the organic component of the natural bone and to improve the biological properties of the scaffold (Li *et al.*, 2012), (Zhang *et al.*, 2005). For example, Zhao *et al.*, designed a multilayer system by alternatively depositing type I collagen (Col I) and HYA on the surface of PLLA priory modified by covalent bonding to poly(ethylene)imine (PEI). *In vitro* studies on osteoblasts demonstrated that PLLA films enhanced the cell proliferation and the viability compared to the unmodified PLLA. In particular, it was observed that the cell-substrate interaction occurred when Col I was coated as outermost layer in the PLLA film (Zhao *et al.*, 2014). Furthermore, the LbL technique is also applied to increase the bioactivity of metals such as Mg and Mg alloys which are promising candidates for orthopaedic applications. Indeed, these metals are biocompatible materials which rise the rate of bone formation and possess interesting properties such as low density and greater fracture toughness (Kirkland, 2012). Additionally, Mg is an osseo-conductive, non-toxic and biodegradable agent, whereas the Mg alloys (MgA) is highly reactive and its degradation releases a considerable amount of hydrogen that is not acceptable by the human body tissue and can provoke an adverse reactions such as an inflammatory or immunology response (Xin, Hu and Chu, 2011). For example, Peng *et al.*, modified the surface of MgA to obtain higher biological activity, biocompatibility and corrosion resistance. The LbL self-assembly was chosen as strategy to coat a polyanionic gelatin-conjugated hydroxyapatite nanoparticles, and the polycation lysozyme and PEI as transition layer. Comparing the multilayer system to the MgA surface priory its modification, it was observed that the functionalised MgA provided an improvement in the antibacterial activity against *S. aureus* (86% killed) and *E. coli* (92% killed), better hydrophilicity, and increased corrosion resistance than the untreated MgA (Peng *et al.*, 2019). The LbL is used to modify the surface of orthopaedic devices and as coating technique to satisfy the controlled delivery of therapeutic agents to heal bone infections (Egashira, Goodman and Yang, 2014). For instance, Min *et al.*, developed a multilayer system formed by coating via LbL the antibiotic gentamicin sulphate (GS) and the osteoinductive

growth factor BMP-2 separated by a laponite interlayer barrier. In this case a duplex mechanism is involved: the prevention of infections in the implant site by GS release and the stimulation of osseointegration on the implant surface promoted by the growth factor BMP-2 (Min, Braatz and Hammond, 2014).

Drug delivery

In the last 20 years, the requirement of new advanced drug formulations has been mainly related to the capability of the delivery systems to encapsulate drug onto systems that can provide sustained release profiles (Tang, Wang, Podsiadlo and Nicholas A. Kotov, 2006). Drug encapsulation used in biomedical applications presents some advantages such as reduction of the administered drug and reduced side effects, as well as the employment of nanoparticles as therapeutic carriers provides benefits such as controlled drug release, targeted delivery and the ability to by-pass the cellular surface multi-drug resistance mechanism (Park *et al.*, 2018), (Caruso, 1998). In particular, the application of the LbL technique in the controlled release possesses benefits such as: the ability to determine the concentrations of entrapped biomolecules easily only changing the number of polymer layers and the ability of controlling the order and the location of the system with a nano-scale precision. Furthermore, the drug release from multilayer systems formed via LbL could be regulated by the physicochemical properties of the film components: biodegradability, charge density and molecular weight (Choi and Hong, 2014). For example, Hong *et al.*, coated the anionic ovalbumin (Ova) into two different systems including respectively the polycations poly-L-lysine (PLL) and a poly (β -amino) ester (Poly 1) through LbL self-assembly. The systems were developed at pH 6.0 and the release of Ova was evaluated under physiological conditions in PBS. Different release profiles were obtained due to the difference in the charge density between PLL and the poly (β -amino) ester. Indeed, Poly1 provided a burst release caused by its hydrolytic degradation at pH7.4, which was in contrast to the slow protein release observed from the Ova-PLL multilayer. Therefore, the design of LbL system including both PLL and Poly 1 could be an alternative approach for controlling the release of the antigen protein ovalbumin (Ova) (Hong *et al.*, 2011), (Keeney *et al.*, 2015). Additionally, Shukla *et al.*, exploited the versatility of the LbL technique to incorporate the antimicrobial peptide ponicin (G1) into 3 different multilayer systems, where G1 and a poly (β -amino) ester (Poly 2) were embedded as polycations and chondroitin sulfate, alginic acid and dextran sulfate as

polyanions. It was observed that the modulation in the molecular weight of the film components influenced the release of the antimicrobial agent G1. For instance, alginic acid (MW 85 kDa) and chondroitin sulfate (MW 120-190 kDa) diffused more into the film layers moving G1 to the upper layer and causing a burst release. As contrary, no diffusion effect occurred in the dextran sulfate due to its higher molecular weight, 500 kDa, proving a slow but longer (over 12 hours) ponicin (G1) release (Shukla *et al.*, 2010), (W. Feng *et al.*, 2014), (Sosnik, 2014).

pH and ionic-strength stimulated release

The pH modulation could be generally applied as stimulus to trigger the delamination or the dissolution of the multilayer thin films containing biomolecules (Wohl and Engbersen, 2012). This process can mainly occur by increasing the porosity of the film or due to a reduction of the electrostatic interactions between acid/basic groups employed in the film (Burke and Barrett, 2003). Generally, the pH environment in which the multilayer is formed highly affects the interaction among layers. However, pH changes could lead to weak electrostatic interactions among polyelectrolytes causing the disruption of the multilayer system (Keeney *et al.*, 2015). For example, Men *et al.*, developed a multi-layered pH sensitive liposome-PBAE hybrid NPs including the chemotherapy agent doxorubicin (DOX). The protonation of the tertiary amine of PBAE at low pH, increased the DOX release from the film layers, reaching the cell nucleus and promoting the tumour cells death (Men *et al.*, 2020). On the other hand, the change of pH could influence the biomolecules release by inducing porosity in multilayers. For instance, Mendelsohn *et al.* prepared a system where poly(acrylic acid) (PAA) was deposited at pH 3.5 and poly(allylamine hydrochloride) (PAH) at pH 7.5 via LbL. Once the multilayer was coated, it was observed that exposure of the assembled film to acid aqueous solutions with pH ranging between 2.0 and 2.5, promoted the formation of micropores in the multilayer. In particular, the protonation of the carboxyl groups of the PAA occurring at low pH caused a loss of the weak electrostatic interaction between PAA and PHA, leading to a disorganised film, (Detzel, Larkin and Rajagopalan, 2011), (Mendelsohn *et al.*, 2003), (Mendelsohn *et al.*, 2000).

Furthermore, controlled release of biomolecules could be regulated by changing the ionic strength of a solution in order to control the electrostatic interactions between

polyelectrolytes and proteins and therefore to improve the stability of film components. For example, Sukhishvili *et al.* proved that the presence of a hydrogen-bonding polymer into solutions with a high concentrated salt reduces the instability of the film due to the ions which decrease the intensity of electrostatic repulsion between a certain number of ionized groups included into the assembled system (Tang, Wang, Podsiadlo and Nicholas A Kotov, 2006), (Sukhishvili and Granick, 2000).

Hydrolytically Induced Release

The hydrolysis of polyelectrolyte layers and crosslinkers is considered an alternative mechanism of degradation to changes of pH and ionic strength for LbL coatings. In particular, polyanions and biomolecules are alternatively layered between hydrolysable polycations. Once the self-assembly is completed, exposure to an aqueous solution promotes the hydrolysis of the polycation, the degradation of the coating and thus, the release of the biomolecule (Serhan *et al.*, 2019). For example, 1,4 butanediol diacrylate (Poly 1) is a hydrolytic PBAE which is commonly coated as polycation with polyanions such as poly(styrene sulfonate) (PSS), poly(acryl acid) PAA and DNA plasmids. Indeed, the ester groups of the backbone of Poly 1 hydrolyse after being treated with buffer solutions and hence facilitating the biomolecule release (De Villiers *et al.*, 2011), (Wood *et al.*, 2005). Furthermore, another method that lead to the dissolution, erosion or disintegration of polyelectrolytes multilayer systems is the development of the pro-drug approach. This process supports the controlled release of many therapeutics in the target site by the biomolecule bonded to a biocompatible polymer via hydrolysable bond. For example, Thierry *et al.* investigated the delivery of the paclitaxel, a hydrophobic drug and an efficient agent against breast and ovarian cancers by coating, via LbL, the hyaluronan ester prodrug of the chemotherapeutic agent paclitaxel, as polyanion, and chitosan, as polycation, to form a multi-layered construct. The drug release from paclitaxel multilayer occurred via hydrolysis of the ester linkage causing rapid death of tumour cells (Multilayers *et al.*, 2005), (Tang, Wang, Podsiadlo and Nicholas A Kotov, 2006).

Other applications of the LbL technique

Further applications have been evaluated for the LbL and one of these is the regeneration of other tissue such as cartilage, ligaments and nerves. For instance, the application of the glycosaminoglycan chondroitin sulphate to the realization of scaffolds, has different

advantages such as stimulation of the secretion of proteoglycan and type II collagen and promotion of bioactivity of seeded chondrocytes. An example of used artificial graft is PET (poly-ethylene terephthalate) which is a hydrophobic material and it has weak biological properties. In this case, the LbL was applied to improve its biocompatibility, by depositing biocompatible and natural polymers on its surface (Gong *et al.*, 2007).

Moreover, neural prosthetic devices (NPDs) are designed for the diagnosis and the treatment of traumas or neurological conditions, where electrodes are used to interact with neural tissue and to reach the targeted site. The main disadvantage of these devices occurs after the implantation of the electrodes, where a possible formation of a barrier between the device and the tissue could reduce its durability and the efficacy. Therefore, it was essential to improve the electrochemical surface area of the electrodes by developing via LbL conductive nanomaterials (Schwartz, 2004). Moreover, the LbL is also employed to layer biodegradable polymers onto autologous nerve grafts for the treatment of neural gaps. The self-assembly technique is a way to improve neurite outgrowth and axon regeneration by increasing the neurotrophic factors, which are biomolecules supporting the growth, the survival and differentiation of developing and mature neurons (Lee and Wu, 2014). For example, Lee *et al.* suggested that the use of natural polymers as polyelectrolytes can support cell adhesion and proliferation of nerve guides. In particular, with a study, it was observed that the neurite outgrowth and neuron percentage and synaptic functions increased depending on the number of layers of the construct formed via LbL (Lee and Wu, 2014), (Gentile *et al.*, 2015).

Limitations of no-biodegradable cationic polymers

Beyond the success of LbL self-assembly technique, also the choice of the polyelectrolytes plays an important role in the design of the thin layers. For instance, cationic polymers are generally employed to interact with polyanions promoting the formation of multilayer. For example, poly(lysine) (PLL) and poly(ethylene imine) (PEI) are examples of polymers containing amino groups in their backbone (Samal *et al.*, 2012). These polycations are mainly applied in gene delivery as non-viral vectors due to their ability to interact and protect negatively charged strains of DNA (Thomas, Tajmir-Riahi and Pillai, 2019). However, although these molecules showed high transfection efficiency, their no-degradability can cause significant cytotoxic effects. This problem remains a considerable issue for therapeutic applications *in vivo*. Therefore, new polymers possessing hydrolysable moieties were

designed as polymer-based biomaterials applicable for targeted and on demand drug delivery, tissue engineering and disease prevention (Monnery *et al.*, 2017).

1.3 Poly (β -Amino Esters)

Poly (β -Amino Esters) (known as PBAEs) are the results of the conjugation between an acrylate and an amine by Michael addition without the formation of by-products. These blocks of copolymers are attractive compounds possessing inherent biocompatibility, responsiveness, biodegradability and versatility due to their structural diversity as result of the combination of different monomers. This library of polymers can be applied for several applications such as antimicrobials, anticancer drugs, tissue repairing and proteins delivery. In particular, the ester bonds in their backbone are hydrolytically degradable providing excellent biodegradability and a reduced toxicity to these molecules. Besides, the presence of tertiary amine moieties increases their electrostatic interaction with negative charged compounds offering a wide choice to form nanocomposites. Moreover, the amino groups show pH-responsive and charge reversible properties considering their ability to undergo phase transition upon the change of surrounding pH. For this reason, PBAEs are valid candidates for programmable and controlled release (Perni and Prokopovich, 2017a), (Fields *et al.*, 2012)

Synthesis

In 1970 Ferruti *et al* synthesised linear poly (amido amines) as result of conjugation between bifunctional amines to bisacrylamides whereas in 2000 Linn and Langer focused on poly(ester amines) approach naming these molecules PBAEs. This synthetic route was attractive for different reasons: firstly, the possibility to form multiple analogues from commercially available starting materials and then the presence amines and readily degradable linkages in the polymers. As previously mentioned, PBAEs are obtained via one-pot atom-economic Michael addition of amines to acrylates and the polymerization normally occurs at high temperatures (50°C-90°C) within 20-72 h in apolar halogenated (dichloromethane and chloroform) or polar dimethyl sulfoxide (DMSO) solvents (Lynn and Langer, 2000), (Cordeiro *et al.*, 2019).

Structures and properties

The structure of PBAEs mainly depends on the number (N) of reaction sites of both amines and acrylates employed as starting materials. Thus, three types of crude products can be obtained: linear, branched and cross-linked. The first case happens when primary and secondary amines ($N_{\text{AMINE}}=2$) react with two acrylates sites ($N_{\text{ACRYLATE}}=2$) and it is the commonest used. Branched polymers are the results of two sites of amines ($N_{\text{AMINE}}=2$) conjugated to three of acrylates ($N_{\text{ACRYLATE}}=3$) or the opposite ($N_{\text{AMINE}}=3/ N_{\text{ACRYLATE}}=2$) while cross linked PBAEs are obtained by ($N_{\text{ACRYLATE}}=4/ N_{\text{AMINE}}=2$) or vice versa ($N_{\text{AMINE}}=4/ N_{\text{ACRYLATE}}=2$) (Zeng *et al.*, 2019), (Liu *et al.*, 2017).

Mechanical and physiochemical properties of PBAEs depend as well as the structures of the molecules on the monomers chosen for the polymerization. Among them, molecular weights can be influenced providing polymers with a range between 2 and 120 kDa, as well as the polydispersity index (PDI), higher than 1.3 if compared to other polymerizations and marginally altered by the reaction time. As described before, PBAEs possess tertiary amino groups on their backbone; thus, these molecules show outstanding pH-sensitive properties in values of pH between 3.5 and 7.2. The pKaH is highly influenced by the hydrophobicity of the polymers whose increase will, as consequence, decrease the pKaH value. The process will be reversed when the tertiary amino groups are protonated, positively charged and hydrophilic. Besides, PBAEs are quite stable under acidic conditions and will hydrolytically degraded under physiological conditions as result of hydrolysis of the ester bonds and the formation of small molecules such as bis(beta-amino-acids) or diol products (Liu *et al.*, 2019), (Anderson *et al.*, 2005).

PBAEs formulations

Over the few last decades, PBAEs are widely employed in versatile formulations due to their excellent physiochemical and mechanical properties.

Nanocomposites

Conventionally, cationic PBAEs can interact with anionic molecules by electrostatic interactions such as genes or proteins to form nanocomposites. There is no chemical modification occurring along the interaction between the opposite charges of the polymers chain and the anionic therapeutics. On one hand, this technique is suitable for high

throughput screening of several polymers to evaluate their delivery efficacy; on the other, there are few disadvantages, such as short life (1-7 h) of the nanoparticles in aqueous solutions, lack of shells stability and of stability in high ionic strength environment (Samal *et al.*, 2012).

Films

As previously described, the layer by layer technique is usually applied for the formations of films where alternatively opposite charged polyions are embedded onto substratum surfaces. This method of coating shows several pros, for example, easy scale up production and control of drug release rate, plus the ability to load different drugs and to work at room temperature. The drug release mainly occurs by degradation of film multilayers avoiding the diffusion related burst release. However, also in this case there are some cons. In particular, the poor stability in aqueous buffers and the use of non-degradable polyelectrolytes require a higher mechanical strength of films (Bishop *et al.*, 2016).

Fibers

Recently polymeric fibers were developed for drug delivery or to reproduce the topology of the extracellular matrix and the applied technique usually is the electrospinning. These formulations are the results of polymerisable PBAEs macromers that, after being electrospun with the aid of a photoinitiator, were obtained by cross-linking under light irradiation. The PBAEs fibers can be designed with specific properties due to the large library of reactive PBAEs macromers available. Nevertheless, there are some aspects that could be considered as limitations that need more investigations to enhance and extend the applications of the polymer fibers (Großhaus *et al.*, 2020).

Gels

PBAEs gels can be divided into bulk hydrogels and nanogels depending on their morphology and application. These formulations are obtained by chemical conjugation, sol-gel transition of block polymers or synthesis using monomers with multiple sites of reaction. Gels impressively expanded the applications of PBAEs from drug delivery to tissue engineering considering their high compatibility to versatile therapeutics such as hydrophilic/hydrophobic drugs and proteins and their tuneable shapes (K. Yang *et al.*, 2018). However, the excess of organic solvents employed during the synthesis of gels plus the possibility of partial

degradability of these matrices in the human bodies can lead to potential accumulated toxicity and tissue inflammation as severe side effects (Altuncu *et al.*, 2019).

Micelles

The core shell of polymeric micelles is composed by block of copolymers. In particular, hydrophobic PBAEs blocks are used to form amphiphilic copolymers with PEG block via hydrophobic interactions. The matrices are good candidates for the encapsulation of therapeutics with hydrophobic nature especially for improving their solubility, pharmacokinetics and stability. Thus, the versatility of blocks of copolymers provides the formation of PBAEs micelles that can be directed to different applications. Despite these advantages, the poor stability of these formulations could be an undesirable shortcoming that can considerably influence their applications (Nayanathara, Kermaniyan and Such, 2020).

PBAEs applications

PBAEs based micro or nanocarriers are widely employed for drug delivery. Considering that, a typical drug delivery system should fulfil specific requirements, such as, improvement of the drug solubility, provide a prolonged drug release in the body, protection from enzymatic degradation, target selecting preventing tissue degeneration and damage and release the drug under triggers local lesions, nowadays the versatility of PBAEs allows the design of several formulations which can overcome barriers in drug delivery. As reported below, PBAEs are also interestingly used for tissue engineering, gene delivery and immunotherapy applications (Singh and Lillard, 2009), (Liu *et al.*, 2019).

Gene delivery

Gene therapies have always been promising treatments from genetic disorders, cancer and infections, but there are still few barriers to be defeated in gene delivery. For its applications, cationic linear and branched polymers have been designed as well as synthetic nonviral systems like polymeric nanoparticles and liposomes. For instance, polylysine (PLL) and polyethylenimine (PEI) interact with gene molecules and thanks to their 'proton-sponge' effect can provoke the non-specific internalization escaping from endosomes. Nevertheless, the main issue regarding these polymers is related to the cytotoxicity as result of cellular apoptosis and necrosis. Hence, it is extremely necessary the design of polymers that need to be biodegradable, showing low toxicity and providing enzymatic degradation or hydrolysis

after administration. Indeed, PBAEs possessing these characteristics could be potential nonviral candidates for gene delivery (Bishop *et al.*, 2013),

Generally, PBAEs can bind and condense with DNA forming nanoparticles smaller than 150 nm. This increases the cell uptake and significantly improves the gene transfection efficacy. Conventionally, the gene delivery to cell was promoted by PBAEs ending with amino groups rather than with the diacrylate. Indeed, the addition of end-capping amino groups rose the positive charge of these polymers, the affinity of binding negative gene chains and improved the cell uptake and transfection efficacy (Thomas, Tajmir-Riahi and Pillai, 2019).

In clinical translation, the key factor is the stability of the therapeutics and even though PBAEs showed a fast degradation at physiological environment, their combination with DNA increased their stability reducing the degradation of these polymers. The sucrose-protected lyophilized nanoparticles can also stabilise the encapsulated DNA allowing the storage and clinical translation for more than 3 years. For example, Guerrero-Cázares *et al.*, discovered that PBAEs-DNA nanoparticles present higher selectivity to tumour cells in a murine model than in the healthy tissue cells. Pfeifer *et al.*, embedding mannose at the terminations of PBAEs, the uptake of the vector was enhanced by their specific interactions with mannose receptors on macrophages or dendritic cells. In particular, they found out that the gene delivery was higher with polymers having low molecular weights and presence of mannose (Cordeiro *et al.*, 2019). Mastorakos *et al.*, developed a DNA delivery system where PBAE was conjugated to PEG forming core-shell structure with a dense PEG shell. This nanocomposite was able to pass through the human mucus gel layer of the lungs reaching over 4 months of continuous gene transmission after a single administration in a murine model (Mastorakos *et al.*, 2016). Borrós *et al.*, worked on a new family of oligopeptide ending with PBAEs for gene delivery applications. The oligopeptide provided a better interaction between PBAEs and DNA improving the gene transfection efficacy. As example, the arginine-rich oligopeptide shows high positive charge and mixed to anionic agents allowed the development of different formulations. Both high transfection efficacy and low toxicity typical of oligopeptide and PBAEs together overcame limits belonging to natural vectors such as: immunogenicity, poor stability, and issues in manufacturing (Segovia *et al.*, 2014).

Ocular genetic diseases

Among the challenging examples already described for gene delivery, PBAEs could be also applied for the development of nanoparticles as valid treatment for genetic disease of retina. In particular, Sunshine J.C *et al.*, designed a PBAE-based nanoparticle for gene delivery applicable on transfection of retinal pigment epithelial cells (RPE). Firstly, they synthesised a combinatorial library of PBAEs, followed by evaluation of their toxicity and transfection efficiency for a specific cell line (ARPE-19). However, among the polymers developed, a lead PBAE was identified, characterised and compared to commercially available products. After the *in vitro* screening, the transfection efficacy was also investigated *in vivo* by administration via subcutaneous injection of the matrix to mouse RPE. This successful step suggested that PBAE-based nanoparticles can be employed for gene delivery to heal debilitating eye diseases (Sunshine *et al.*, 2012).

Immunotherapy

Biomaterials applied for immunotherapy are generally designed with the aim of protecting encapsulated vaccine cargoes or controlling the drugs release via physical and chemical properties. As result of this approach, immune stimulation could be generated by, for example, Toll-like receptors (TLR) whose presence was detected on dendritic cells (DCs) which play an important role in innate and adaptive immunity. Polymers such as, polystyrene or PLGA, are able to activate DCs promoting pro-inflammatory secretion and T-cell proliferation *in vitro*.

Currently, the increase of intrinsic immunogenic activity executed by these biomaterials is still not clear and for this reason it is essential to investigate which polymers properties can generate these responses. Andorko *et al.*, firstly, proved that the class of PBAEs show intrinsic immunogenic properties whose effects depend on the extent of polymers degradation, then extended their study considering a small library of PBAEs showing different starting molecular weight (MW). PBAEs were synthesised using different diacrylate monomers having an increasing number of carbons in their backbone. Considering the DNA vaccine formulation strategies, particles and fragments were designed via electrostatic interactions followed by evaluation of their degradation. Therefore, it was discovered that properties such as, MW, size, charge and concentration, are linked to the degree of polymers degradation and any variation of these parameters can influence intrinsic immunogenicity. Despite of starting

MWs, the immunogenicity achieved the maximum when the MW dropped within a range between 1500-3000 Da providing an important information for the design of future polymer carries (Andorko and Jewell, 2017).

Chemotherapy delivery

PBAEs are employed in delivering anticancer drugs due to their biocompatibility and pH-responsiveness. Therefore, the discovery of these polymers allows to overwhelm typical disadvantages of the common used anticancer drugs like camptothecin (CPT) such as poor water solubility and pharmacodynamics properties. The application of polymeric nanoparticles aims to increase the drug solubility, to improve the drug release under the triggers in tumor-specific pH, to extend the drug circulation in blood vessels and to target tumor sites (Cordeiro *et al.*, 2019).

Generally, the anticancer drugs are loaded via hydrophobic interactions onto PBAEs polymeric micelles. Normally the pKaH of PBAEs is 6.5 corresponding to the pH value of tumor sites but once these matrices are below their pKaH value, the PBAEs are protonated, becoming positive and promoting via electrostatic interactions the conjugation between nanoparticles surface and tumor cells and their cell internalization. PBAEs become hydrophilic especially under acidosis conditions in the endosomes; in this case the drug release is faster, and it improves the killing efficacy. Moreover, the addition of responsive moieties into PBAEs can have several advantages such as the increase of drug loading efficacy on nanoparticles surface, the drug release rate can be accelerated and an improvement in the stability of polymeric nanoparticles. As one example, polylactic acid (PLA) is widely employed in the design of modified PBAEs nanoparticles (C. Yang *et al.*, 2018).

Another way to destroy tumorous cell is by photodynamic therapy. This technique requires tissue oxygen, light source and photosensitizers to create toxic singlet oxygen (1O_2) and for example, protoporphyrin IX (PpIX) and verteporfin are largely used as photosensitizers. However, these agents present an important limitation like water solubility lack. Therefore, Koo *et al.*, produced a block of PEG-PBAE to enhance PpIX cancer applications. Indeed, in a murine model they noticed that these micelles were increasing the solubility of the drug, the permeability and the release effect. In particular, a fluorescent signal was produced as result of conjugation between the micelles and the tumor sites evidencing images of the tumor and facilitation both its diagnosis and eradication. In addition, Kim *et al.*, designed a triblock

copolymer PEG-PBAE-PEG encapsulating verteporfin to increase its cellular uptake and killing efficacy against lung and breast cancer cells (Kim *et al.*, 2018).

PBAEs based materials are also valid autophagy modulators applied as potential cancer treatments. Autophagy is essential in guaranteeing the cellular metabolism via recycling of cellular components, but its process needs to be controlled in order to reduce cancer cells proliferation. Indeed, Lin *et al.*, synthesised a compound, gold (I) phosphine, able to moderate the release of reactive oxygen species, followed by its incorporation on PBAE micelles through hydrophobic interactions (Lin *et al.*, 2016). This research group discovered the synergism performed by drug loaded-PBAEs micelles and Au compounds in regulating and decreasing autophagy inside the cells. This strategy needs further investigations, but it could be a potential alternative to current cancer treatments (Liu *et al.*, 2019).

Small cell lung cancer (SCLC)

Furthermore, PBAEs are also employed as treatment of small cell lung cancer (SCLC), mainly caused by genetic mutations or inactivation of tumor suppressor genes such as TP53 or RB. It is an aggressive disease which represents 15% of lung cases with the highest fatality rate among all cancers (Kamat *et al.*, 2013). Therefore, new therapeutic approaches are required aiming at long-term survival in this disease. Kamat D.C. *et al.*, synthesised a library of PBAEs with further application of these polymers as potential gene-delivery vectors developing non-viral nanoparticles. These matrices could deliver therapeutic genes showing high efficiency to SCLC cells.

Codelivery

A single drug or gene delivery sometimes cannot provide a good treatment effect due to drug resistance. For this reason, the delivery of more therapeutics is becoming a more interesting challenge among researchers. The employment of PBAEs in drug delivery systems including two therapeutics is currently the methodology mostly used. For instance, Zhang *et al.*, loaded doxorubicin (Dox) and curcumin into PBAEs developing a system showing a synergist effect. Notably, PBAEs allow the interactions between both hydrophobic anticancer drug and oligonucleotides thanks to their hydrophobic domains and positive charge. Codelivery systems showed a better killing efficacy against tumor cells compared to the one performed by a single drug or gene (Zhang *et al.*, 2017).

Antimicrobial delivery

Among their several applications, PBAEs are also employed for antimicrobial delivery to overcome infectious diseases killing bacteria in their biofilm mode of growth. Another goal is also the improvement of drug loading efficacy achieved by the application of several techniques. For example, the layer by layer (LbL) is a coating protocol used by different groups of research to embed opposite charge molecules and hydrophilic antibiotics such as vancomycin and gentamycin belonging to the class of aminoglycosides drugs. For instance, Kim *et al.*, coated via LbL a drug delivery system including PBAEs, gentamycin and diclofenac. This matrix inhibited, for more than two weeks, the bacterial attachment and formation of biofilms to epithelial and osteoprogenitor cells (Kim *et al.*, 2009).

Recently, the use of micelles is becoming more interesting to combat the biological barriers in delivering antimicrobials into bacterial films. Despite of the biofilm bacteria are very difficult to eradicate, micelles able to be quite stable at physiological pH were synthesised as alternative strategy. Thus, these matrices can circulate for longer in the body increasing the chance to react to biofilms. As consequence, once interacted with the biofilms the PBAEs become positive charged rising the electrostatic interaction between the micelles and the polymeric matrix or the bacterial cell membranes (Cordeiro *et al.*, 2019).

Finally, the hydrogels are currently considered promising platform for antimicrobial delivery. Besides, they can prevent bacterial infections thanks to the humid environment ideal for the tissue regeneration. The amines of vancomycin once introduced on PBAE hydrogels can provide a system which can provide longer drug release (K. Yang *et al.*, 2018).

Protein delivery

Protein therapeutics are widely used as disease treatments and are different compared to other drugs due to their deactivation nature depending on surrounding pH, heating or enzymatic degradation. For this reason, it is essential the application of PBAEs to design platforms, like hydrogels or layer by layer coatings, that can enhance the stability of these molecules. For example, Huynh *et al.*, produced a PBAEs based hydrogels to deliver insulin via subcutaneous injection. This delivery system included pentablocked PBAE-PCL-PEG-PCL-PBAE polymers providing a sol-gel transition quite responsive to temperature and pH changes. The loading of the insulin occurred via electrostatic interactions between its negative charged moieties and the amino groups of PBAEs. As result of the *in vivo* studies, the hydrogels

improved the therapeutic efficacy by maintaining the glucose concentration in the blood at normal level for over a week in a rat diabetic model (Huynh *et al.*, 2008).

Hammond *et al.*, developed multilayers coatings via layer by layer deposition for protein therapeutics such as growth factors or antigens. Thanks to their studies they observed that this strategy provides different advantages such as the successful penetration of proteins into skin, the encapsulation and the release of multiple agents and an increase in the stability of proteins against dehydrated conditions during the storage (Shah *et al.*, 2012).

Antioxidant delivery

Generally, antioxidant agents, like polyphenols derivatives compounds, are applied to antioxidant delivery with the aim of reducing the reactive oxygen species formation and thus, the oxidative stress in tissues. To reach this goal, for example, quercetin and curcumin are employed for the synthesis of poly (antioxidant beta-amino esters) (Gupta *et al.*, 2015), (Wattamwar *et al.*, 2012). Afterwards, cross linked hydrogels were designed due to the different acrylate reaction sites on polyphenol monomers. This method increased the solubility and the stability of the antioxidant whose release profile was slow and controlled. Furthermore, using a similar polymerization mechanism, nanogels were produced for cell applications providing a reduction of oxidative stress after stabilization via PEGylation (Jordan, Hilt and Dziubla, 2019).

Scaffolds for tissue repairing

For tissue engineering, a scaffold is a material which promotes cell adhesion and contributes to the formation of new tissue. Theoretically, this matrix should degrade allowing replacement of new tissue in approximately 3-5 months after its implantation minimizing the toxicity by degradation of products and providing support over the time needed for a fracture to heal. Ideally, materials designed for tissue engineering require specific criteria such as degradation, biocompatibility, cytotoxicity, cell attachment and mechanical properties. Thus, a material needs to be degradable, so that it can be replaced by cells and tissue over time. Moreover, it has to be bioactive, integrating with tissues, and biocompatible, avoiding any inflammatory or immune response after its implantation in the body. Furthermore, cell attachment is important for matrix deposition via anchorage dependent cells as well as mechanical properties for increasing the stability of the material (Filipović *et al.*, 2018).

However, traditional polymers synthesis for these applications were considered time consuming due to multiple steps of reactions and purifications steps required. For this reason, also in this case, PBAEs represent a promising approach gained by combinatorial synthesis via single step reactions (Cordeiro *et al.*, 2019). For instance, Brey *et al.*, designed a new biomaterial showing potential characteristics for bone regeneration. In particular, they pursued a screening of a library of PBAEs resulting from a combination between diacrylates and primary amines, to determine an osteoconductive material for mineralized tissue regeneration. Among all the candidates, the optimal one was, firstly, processed into 3-dimensional scaffolds and then implanted into rat cranial defects or via intramuscular implants. Based on that, the biomaterial needs to degrade, not too quickly to provide support and prevent cell adhesion, but also not too slowly to interfere with the growth and the replacement of the natural tissue, this research group noticed that among the 120 PBAEs library synthesised, only 10 macromers met these mass loss criteria. These polymers were characterised by linear or rapid initial release followed by small plateau region. The diversity in the polymers degradation was mainly due to the various hydrophobicity of the monomers resulting in different hydrolysis or water uptake. After cell cultured studies the optimal osteoconductive material showed improved viability profiles and minimal inflammation after subcutaneous implantation followed by successful scaffolds tissue infiltration (Brey, Erickson and Burdick, 2008).

1.4 Aim of project

Total joint replacement is a life-enhancing procedure used to alleviate pain and to improve the mobility of patients affected by osteoarthritis. However, one of its tremendous complications is the development of prosthetic joint infection, which, despite its incidence rate is between 0.5% and 3%, in some rare cases it can lead to death. Therefore, preventing the risk of infection while the arthroplasty surgery is performed, is still an interesting challenge among researchers (Martínez-Moreno *et al.*, 2017), (Prokopovich *et al.*, 2015). The employment of antibiotic loaded bone cement (ALBC) is an approach which allows the achievement of high concentration of antibiotic at the site of infection with no systemic toxicity. However, the use of these systems in clinical practice could be controversial due to the increasing bacterial resistance to antibiotics. In addition, the release profile of these molecules provides a burst release of few hours followed by a slow release below the minimum inhibitory concentration (MIC) within a few days, which is not a long-term solution for the treatment of early and delayed onset infections (1-3 months after the surgery) (Anagnostakos and Kelm, 2009), (Al Thaher *et al.*, 2018a). Hence, to overcome these problems, novel antimicrobial strategies able to improve the performance of ALBC and thus, the quality of life of patients, are required.

In this context, the aims of this PhD project are to develop silica nanocarriers releasing antimicrobial agents using Layer-by-Layer (LbL) technique employing poly (β -amino esters) (PBAEs) as polycations and to establish the optimal nanocarrier construct to provide sustained drug release for future applications on PMMA bone cement. We hypothesize that the choice of the monomers employed in the polymerization of PBAEs is crucial and it greatly influences the physicochemical properties of PBAEs, including molecular weight (MW) and charge, as well as, the release of the bioactive compounds embedded onto the surface of the nanoparticles. Additionally, we hypothesize that LbL self-assembly combined with nanotechnology can provide a sustained release of antimicrobial agents from silica nanoparticles at inhibitory concentrations for a long period of time (1-3 months). This could be considered an early stage approach for a potential long-term prophylaxis from post-surgical orthopaedic infections.

To achieve these goals the objectives were defined as follows:

i. Poly(β -amino esters) synthesis and characterisation

PBAEs are a class of co-polymer polyelectrolytes that exhibit high bio-compatibility, low cost and bio-degradability. PBAEs properties such as charge, molecular weight (MW) influence their hydrolysis and depend on the polymer backbone (Perni and Prokopovich, 2017a). Therefore, in this project a variety of PBAEs have been synthesised using different monomers and have been employed as polycations in the LbL coating of silica nanoparticles. Prior to the coating, PBAEs chemical structures have been identified via Nuclear Magnetic Resonance (NMR) and the polymer hydrolysis was investigated by Gel Permeation Chromatography (GPC) and ZetaSizer through molecular weight (MW) and charge determination.

ii. Silica nanocarriers preparation

In this project, silica nanoparticles were chosen as nanocarrier due to their biocompatibility, high loading capability, easy synthesis and scale up with reasonable costs (Liu *et al.*, 2015). Furthermore, these nanoconjugates include a high surface area containing silanol groups which could be functionalised to increase drug loading and control the kinetics of release depending on the physiochemical properties of the loaded agents (Tamanna, Bulitta and Yu, 2015), (Perni, Martini-Gilching and Prokopovich, 2018). Before proceeding with the LbL, the surface of silica nanoparticles was functionalised by adding amino groups which facilitate the deposition of antimicrobial agents and cationic or anionic polyelectrolytes along the LbL self-assembly technique.

iii. Antimicrobial drug delivery systems development by Layer by Layer deposition

The antimicrobial agents, tobramycin and chlorhexidine were loaded alone onto silica nanocarriers. Tobramycin has been employed as model antibiotic and is among the aminoglycosides used to treat PJI in total joint arthroplasty due to its antimicrobial activity against Gram-negative bacteria and particularly against species of *Pseudomonas* (Slane, Gietman and Squire, 2018), (Dienstag and Neu, 1972). On the other hand, chlorhexidine has been applied as model antimicrobial agent. It is a broad spectrum antiseptic widely used in dental field and effective against Gram-positive and Gram-negative bacteria (Lim and Kam, 2008), (George, Klika and Higuera, 2017). All the PBAEs synthesised and characterised in this

project were employed as polycations in the drug delivery systems. Therefore, tobramycin and chlorhexidine LbL-loaded silica nanoparticles were developed via electrostatic interactions by using a PBAE as polycation and alginate as polyanion. Each nanoconstruct was composed by repetitive quadruple layers of the sequence alginate-tobramycin-alginate-PBAE or alginate-chlorhexidine-alginate-PBAE designed with the aim of providing longer release efficacy. All the nanoconjugates were characterised using Thermal Gravimetric Analysis (TGA) and zeta potential measurements as well as tobramycin and chlorhexidine release profiles were evaluated under different pH conditions and compared the hydrolysis and the chemical structures of the PBAEs.

Chapter 2: Materials and methods

Chemicals

Triton X-100, n-hexanol, Tetraethyl orthosilicate (TEOS), 3 aminopropyl-triethoxysilane (APTS), sodium acetate trihydrate, chlorhexidine diacetate salt hydrate, tobramycin, alginic acid sodium salt from brown algae (medium viscosity), isopropanol, o-phthalaldehyde reagent (OPA), 1,4 butanediol diacrylate (compound A), 1,3 butanediol diacrylate (compound E), neopentyl glycol diacrylate (compound D), 1,6 hexanediol diacrylate (compound B), bisphenol A ethoxylate diacrylate (compound F), tricyclo [5.2.1.0²⁻⁶] decanodimethanol diacrylate (compound G), piperazine (amine 1), 4,4 trimethyldipiperidine (amine 2), N-N bis [3-(methylamino) propyl] methylamine (amine 3), polyethylene glycol standards for Gel Permeation Chromatography (GPC) with molecular weights (MW) as followed: 500 Da, 1000 Da, 2000 Da, 3000 Da, 4000 Da, 6000 Da, 12000 Da, 23500 Da, 36000 Da, 56000 Da have been all purchased from Sigma Aldrich. Cyclohexane and deuterated chloroform (CDCl₃) for NMR from Acros Organics; ammonium hydroxide (29.6%), ethanol absolute 99.8%, acetic acid glacial, dichlorometane (DCM), diethylether and acetonitrile HPLC grade from Fisher Chemicals and PBS (Phosphate Buffered Saline) tablets from Oxford-England (UK).

All the molecules of this thesis were drawn with Perkin Elmer Informatics ChemDraw Professional version 16.0.1.4 (61) (2017).

Protocol for amino-functionalised silica nanoparticles (AFSi-NPs)

500 mg of amino-functionalised silica nanoparticles (AFSi-NPs) were synthesised via one-pot reaction where Triton X-100 (35.4 g) was added to 150 mL of cyclohexane, 32 mL of n-hexanol, 9.6 mL of deionised water and left vigorously stirring at room temperature for 10 minutes. Only after the solution appeared transparent, firstly ammonium hydroxide (29.6%) (1200 µL) and after 20 minutes tetraethyl orthosilicate (TEOS) (2 mL) were both added to the reverse micro-emulsion that was then allowed to stir overnight at room temperature. The following step of the reaction was the amino-functionalization of the silica nanoparticles by adding 3-(amino propyl) triethoxysilane (APTS) (100 µL) to the micro-emulsion kept stirring for one more overnight. As last step of the synthesis, the AFS-NPs were recovered by adding ethanol (99.9%) (200 mL) to break the micro-emulsion followed by centrifugation at 14000 rpm for 10 minutes at 20°C using the Beckman Coulter Optima LE-80K Ultracentrifuge and up to 5 washing steps with deionised water (figure 2.1).

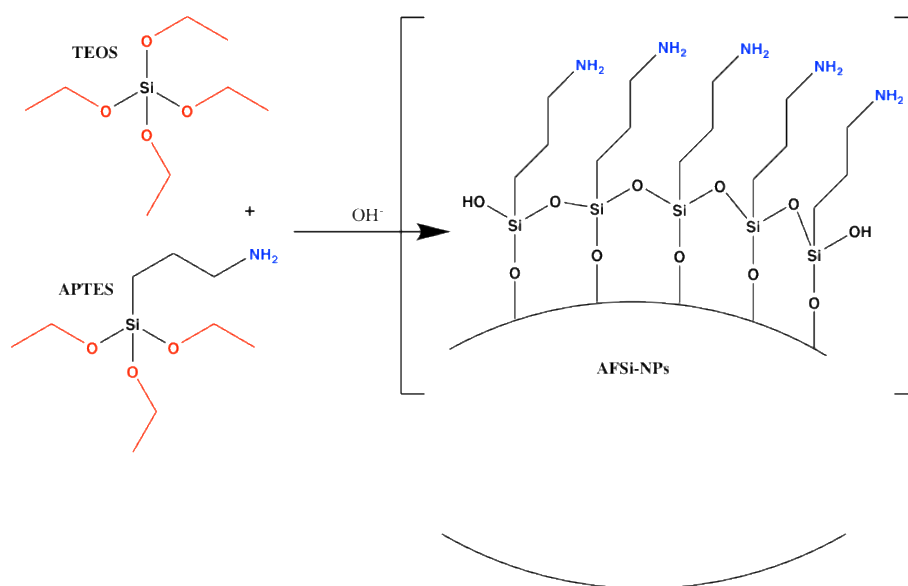


Figure 2.1: Amino-functionalised silica nanoparticles (AFSi-NPs) synthesis

Finally, the nanoparticles were spread into a plate and left drying under fume-hood at room temperature overnight (Stober, 1968), (Al Thaher *et al.*, 2018). Percentage yield was calculated as follows:

%yield = (actual yield/theoretical yield) x 100. E.g.: (90 mg final product/ 100 mg theoretical yield) x 100 = 90% correspondent to the efficiency of the reaction.

Protocol for poly- β amino-esters (PBAE) synthesis

In this thesis, a general strategy for the synthesis of 18 poly(β -amino-esters) was adapted (Lynn and Langer, 2000). These polymers contained tertiary amines in their backbones after conjugation of bis (secondary amine) (1.1 eq) monomers to diacrylates esters (1.0 eq) in dicloromethane (DCM) solution stirring in oil bath at 50°C (figure 2.2). After 48 hours, the polymers were recovered by precipitation in DCM using 30 mL diethyl ether up to 3 times removing the excess of starting materials via centrifugation at 3500 rpm for 5 minutes and *in vacuo*. The crude products were left drying for an overnight.

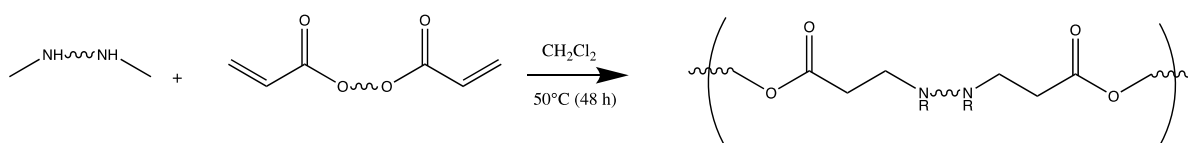


Figure 2.2: General reaction for PBAE synthesis

In this project, 3 secondary amines were added to 6 diacrylates producing, via Michael addition stepwise polymerization, a combinatorial library of 18 linear biodegradable polymers used as versatile biomaterials for future orthopaedical application. In the table 2.1a represented below, there is the list of amines and acrylates monomers and their quantity (mg) chosen for the reactions, plus the yield of reaction.

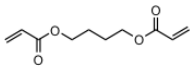
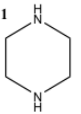
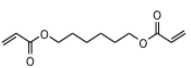
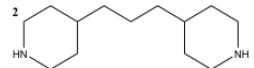
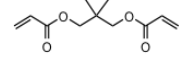
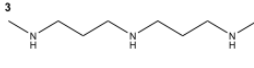
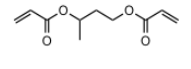
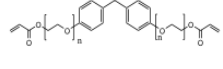

Diacrylates (a)	Amines (b)	mg (a)	mg (b)	solvent	yield (%)
A 	1 	792.88	379.016	DCM	99%
B 	2 	905.08	925.584	DCM	99%
D 	3 	848.96	762.52	DCM	99%
E 		792.88		DCM	99%
F 		2040		DCM	99%
G 		1217		DCM	99%

Table 2.1a: Amines, diacrylates monomers and the quantity used for the synthesis of 18 PBAEs

In the next chapters these polymers will be named: A1, A2, A3, B1, B2, B3, D1, D2, D3, E1, E2, E3, F1, F2, F3, G1, G2, G3 where the letter corresponds to the diacrylate monomer whereas the number to the secondary amine. These polyelectrolytes are dissolvable, biodegradable, biocompatible, low cost and possess a weak positive charge.

Layer by Layer (LbL) self-assembly Protocol

Layer by layer technique was applied to form thin multilayer films by alternatively coating sodium alginate, PBAE and the antiseptic drug chlorhexidine or the aminoglycoside tobramycin via electrostatic interactions onto the surface of the amino-functionalised silica nanoparticles. In particular, the negative charged sodium alginate was loaded as first layer onto the nanocarriers previously functionalised with amino groups as described before. Then,

the chlorhexidine possessing a strong positive charge was added as second layer, followed by the alginate again as third layer and finally the positive charge of the poly (β -amino ester) to complete the first quadruple layer.

The alginate solution (2mg/mL) needed to be prepared the day before to proceed with layer by layer technique due to longer time required to be dissolved in the buffer, whereas the chlorhexidine (10mg/mL) and PBAE solution (2mg/mL), in the same day to avoid issues regarding the biodegradability of the compounds. Fresh acetate buffer solution pH5 was used during the washing steps and for the preparation of all the solution mentioned before. Sodium acetate buffer pH5 was prepared as follows: 70% sodium acetate 0.1 M was added to 30% acetic acid 0.1M. More specifically, 13.6 g of sodium acetate trihydrate were added to 1L bottle and made up to volume with deionised water to provide sodium acetate 0.1 M; as well as 5.81 mL of acetic acid glacial were added to 1L flask and made up to volume with deionised water forming acetic acid 0.1M.

500 mg of dried amino functionalised silica nanoparticles were placed in a 50ml tube test; 20 mL of the polyanion alginate solution were added under stirring for at least 10 minutes. Then, after the centrifugation of the solution for 2 minutes at 5000 rpm at 20°C by using Heraeus megafuge 40R centrifuge provided by Thermo Fisher Scientific UK, the supernatant was removed and replaced with 20 mL of sodium acetate buffer pH5, whose preparation is reported above, for a washing step followed by centrifugation for 2 minutes at 20°C and 4000 rpm. After that, 10 mL of drug solution, whose concentration was 10mg/mL in sodium acetate buffer pH5 (chlorhexidine or tobramycin), were added to the precipitate nanoparticles and stirring for 10 minutes to re-suspend the particles. Once the supernatant was removed by centrifugation (2 minutes, 5000 rpm, at 20°C) one further washing step with acetate buffer was carried out. Subsequently, 20 mL of alginate solution were layered again for 10 minutes followed by centrifugation and washing step with buffer. Afterwards, 20 mL of the polycation PBAE solution were added to gain the fourth layer and after centrifugation and washing step the first quadruple layer was completed (figure 2.3).

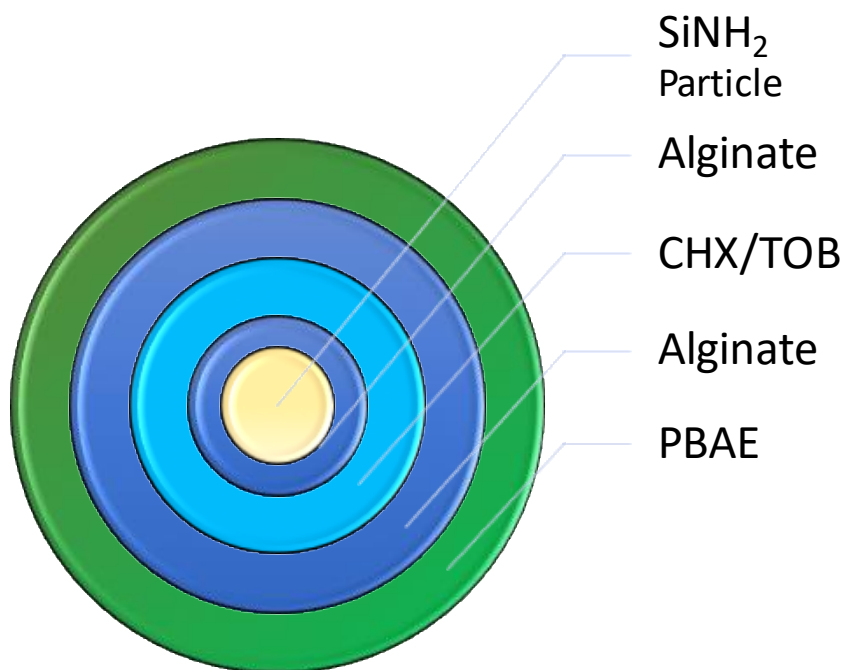


Figure 2.3: single quadruple layer composition

This procedure was carried out up to 10 quadruple layers, embedding in total 40 layers onto the surface of the AFSi-NPS. This number of layers was chosen to minimise the risk of nanoparticles agglomeration observed when more layers were coated onto the nanocarriers. In this project, chlorhexidine and tobramycin were encapsulated onto silica nanoparticles surface via LbL technique including 18 different PBAEs employed as polycations. Therefore, 18 matrices for each drug, such as 18 TOB-PBAEs and 18 CHX-PBAEs, were prepared changing only the PBAE in each multilayer system.

Chlorhexidine

Chlorhexidine is a symmetric molecule composed by 2 chlorophenyl rings, bis-guanide groups connected by a central hexamethylene bridge (figure 2.4). The dicationic nature of this compound makes it extremely interactive with anions and for the presence of the bis guanide family it is considered as a cationic broad-spectrum antimicrobial agent. Indeed, this molecule is a topic antiseptic/disinfectant used for dental application and surgery scrubs and stable between pH 5-8 (Jones, 1997), (Luo *et al.*, 2016). This small molecule is partially soluble in water with logP correspondent to -0.34 (XlogP3) (Daina, Michielin and Zoete, 2017) and its preparation for LbL required 1h as dissolving time in buffer in a sonicated water bath.

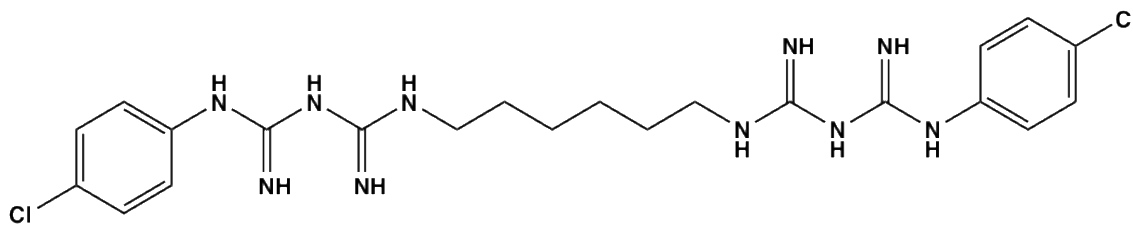


Figure 2.4: Chlorhexidine chemical structure

Chlorhexidine and poly (β amino-esters) loaded silica amino functionalised nanoparticles

The antimicrobial agent, chlorhexidine, was loaded in 18 different matrices and the difference among them was represented by the PBAE, summarised in the table 2.1b below, loaded as polycation.

PBAEs chemical structures	
A1	E1
A2	E2
A3	E3
B1	F1
B2	F2
B3	F3
D1	G1
D2	G2
D3	G3

Table 2.1b: PBAEs chemical structures and abbreviations

Thus, here all the coating delivery systems including chlorhexidine onto amino-functionalised (AFSi-NPs) nanoparticles are listed as matrices 1-18 as follows:

Matrix 1: Alg-CHX-Alg-A1

Quadruple layer no.	Abbreviation	Layers on the surface of AFSi-NPs
1	Q1	AFSi-NPs-alginate- <i>chlorhexidine</i> -alginate- A1
2	Q2	AFSi-NPs-Q1-alginate- <i>chlorhexidine</i> -alginate- A1
3	Q3	AFSi-NPs-Q2-alginate- <i>chlorhexidine</i> -alginate- A1
4	Q4	AFSi-NPs-Q3-alginate- <i>chlorhexidine</i> -alginate- A1
5	Q5	AFSi-NPs-Q4-alginate- <i>chlorhexidine</i> -alginate- A1
6	Q6	AFSi-NPs-Q5-alginate- <i>chlorhexidine</i> -alginate- A1
7	Q7	AFSi-NPs-Q6-alginate- <i>chlorhexidine</i> -alginate- A1
8	Q8	AFSi-NPs-Q7-alginate- <i>chlorhexidine</i> -alginate- A1
9	Q9	AFSi-NPs-Q8-alginate- <i>chlorhexidine</i> -alginate- A1
10	Q10	AFSi-NPs-Q9-alginate- <i>chlorhexidine</i> -alginate- A1

Table 2.2: LbL matrix of deposited CHX and A1 layers on AFSi-NPs

Matrix 2: Alg-CHX-Alg-A2

Quadruple layer no.	Abbreviation	Layers on the surface of AFSi-NPs
1	Q1	AFSi-NPs-alginate- <i>chlorhexidine</i> -alginate- A2
2	Q2	AFSi-NPs-Q1-alginate- <i>chlorhexidine</i> -alginate- A2
3	Q3	AFSi-NPs-Q2-alginate- <i>chlorhexidine</i> -alginate- A2
4	Q4	AFSi-NPs-Q3-alginate- <i>chlorhexidine</i> -alginate- A2
5	Q5	AFSi-NPs-Q4-alginate- <i>chlorhexidine</i> -alginate- A2
6	Q6	AFSi-NPs-Q5-alginate- <i>chlorhexidine</i> -alginate- A2
7	Q7	AFSi-NPs-Q6-alginate- <i>chlorhexidine</i> -alginate- A2
8	Q8	AFSi-NPs-Q7-alginate- <i>chlorhexidine</i> -alginate- A2
9	Q9	AFSi-NPs-Q8-alginate- <i>chlorhexidine</i> -alginate- A2
10	Q10	AFSi-NPs-Q9-alginate- <i>chlorhexidine</i> -alginate- A2

Table 2.3: LbL matrix of deposited CHX and A2 layers on AFSi-NPs

Matrix 3: Alg-CHX-Alg-A3

Quadruple layer no.	Abbreviation	Layers on the surface of AFSi-NPs
1	Q1	AFSi-NPs-alginate- <i>chlorhexidine</i> -alginate- A3
2	Q2	AFSi-NPs-Q1-alginate- <i>chlorhexidine</i> -alginate- A3
3	Q3	AFSi-NPs-Q2-alginate- <i>chlorhexidine</i> -alginate- A3
4	Q4	AFSi-NPs-Q3-alginate- <i>chlorhexidine</i> -alginate- A3
5	Q5	AFSi-NPs-Q4-alginate- <i>chlorhexidine</i> -alginate- A3
6	Q6	AFSi-NPs-Q5-alginate- <i>chlorhexidine</i> -alginate- A3
7	Q7	AFSi-NPs-Q6-alginate- <i>chlorhexidine</i> -alginate- A3
8	Q8	AFSi-NPs-Q7-alginate- <i>chlorhexidine</i> -alginate- A3
9	Q9	AFSi-NPs-Q8-alginate- <i>chlorhexidine</i> -alginate- A3
10	Q10	AFSi-NPs-Q9-alginate- <i>chlorhexidine</i> -alginate- A3

Table 2.4: LbL matrix of deposited CHX and A3 layers on AFSi-NPs**Matrix 4: Alg-CHX-Alg-B1**

Quadruple layer no.	Abbreviation	Layers on the surface of AFSi-NPs
1	Q1	AFSi-NPs-alginate- <i>chlorhexidine</i> -alginate- B1
2	Q2	AFSi-NPs-Q1-alginate- <i>chlorhexidine</i> -alginate- B1
3	Q3	AFSi-NPs-Q2-alginate- <i>chlorhexidine</i> -alginate- B1
4	Q4	AFSi-NPs-Q3-alginate- <i>chlorhexidine</i> -alginate- B1
5	Q5	AFSi-NPs-Q4-alginate- <i>chlorhexidine</i> -alginate- B1
6	Q6	AFSi-NPs-Q5-alginate- <i>chlorhexidine</i> -alginate- B1
7	Q7	AFSi-NPs-Q6-alginate- <i>chlorhexidine</i> -alginate- B1
8	Q8	AFSi-NPs-Q7-alginate- <i>chlorhexidine</i> -alginate- B1
9	Q9	AFSi-NPs-Q8-alginate- <i>chlorhexidine</i> -alginate- B1
10	Q10	AFSi-NPs-Q9-alginate- <i>chlorhexidine</i> -alginate- B1

Table 2.5: LbL matrix of deposited CHX and B1 layers on AFSi-NPs**Matrix 5: Alg-CHX-Alg-B2**

Quadruple layer no.	Abbreviation	Layers on the surface of AFSi-NPs
1	Q1	AFSi-NPs-alginate- <i>chlorhexidine</i> -alginate- B2

2	Q2	AFSi-NPs-Q1-alginate- chlorhexidine -alginate- B2
3	Q3	AFSi-NPs-Q2-alginate- chlorhexidine -alginate- B2
4	Q4	AFSi-NPs-Q3-alginate- chlorhexidine -alginate- B2
5	Q5	AFSi-NPs-Q4-alginate- chlorhexidine -alginate- B2
6	Q6	AFSi-NPs-Q5-alginate- chlorhexidine -alginate- B2
7	Q7	AFSi-NPs-Q6-alginate- chlorhexidine -alginate- B2
8	Q8	AFSi-NPs-Q7-alginate- chlorhexidine -alginate- B2
9	Q9	AFSi-NPs-Q8-alginate- chlorhexidine -alginate- B2
10	Q10	AFSi-NPs-Q9-alginate- chlorhexidine -alginate- B2

Table 2.6: LbL matrix of deposited CHX and B2 layers on AFSi-NPs

Matrix 6: Alg-CHX-Alg-B3

Quadruple layer no.	Abbreviation	Layers on the surface of AFSi-NPs
1	Q1	AFSi-NPs-alginate- chlorhexidine -alginate- B3
2	Q2	AFSi-NPs-Q1-alginate- chlorhexidine -alginate- B3
3	Q3	AFSi-NPs-Q2-alginate- chlorhexidine -alginate- B3
4	Q4	AFSi-NPs-Q3-alginate- chlorhexidine -alginate- B3
5	Q5	AFSi-NPs-Q4-alginate- chlorhexidine -alginate- B3
6	Q6	AFSi-NPs-Q5-alginate- chlorhexidine -alginate- B3
7	Q7	AFSi-NPs-Q6-alginate- chlorhexidine -alginate- B3
8	Q8	AFSi-NPs-Q7-alginate- chlorhexidine -alginate- B3
9	Q9	AFSi-NPs-Q8-alginate- chlorhexidine -alginate- B3
10	Q10	AFSi-NPs-Q9-alginate- chlorhexidine -alginate- B3

Table 2.7: LbL matrix of deposited CHX and B3 layers on AFSi-NPs

Matrix 7: Alg-CHX-Alg-D1

Quadruple layer no.	Abbreviation	Layers on the surface of AFSi-NPs
1	Q1	AFSi-NPs-alginate- chlorhexidine -alginate- D1
2	Q2	AFSi-NPs-Q1-alginate- chlorhexidine -alginate- D1
3	Q3	AFSi-NPs-Q2-alginate- chlorhexidine -alginate- D1
4	Q4	AFSi-NPs-Q3-alginate- chlorhexidine -alginate- D1
5	Q5	AFSi-NPs-Q4-alginate- chlorhexidine -alginate- D1

6	Q6	AFSi-NPs-Q5-alginate- chlorhexidine -alginate- D1
7	Q7	AFSi-NPs-Q6-alginate- chlorhexidine -alginate- D1
8	Q8	AFSi-NPs-Q7-alginate- chlorhexidine -alginate- D1
9	Q9	AFSi-NPs-Q8-alginate- chlorhexidine -alginate- D1
10	Q10	AFSi-NPs-Q9-alginate- chlorhexidine -alginate- D1

Table 2.8: LbL matrix of deposited CHX and D1 layers on AFSi-NPs

Matrix 8: Alg-CHX-Alg-D2

Quadruple layer no.	Abbreviation	Layers on the surface of AFSi-NPs
1	Q1	AFSi-NPs-alginate- chlorhexidine -alginate- D2
2	Q2	AFSi-NPs-Q1-alginate- chlorhexidine -alginate- D2
3	Q3	AFSi-NPs-Q2-alginate- chlorhexidine -alginate- D2
4	Q4	AFSi-NPs-Q3-alginate- chlorhexidine -alginate- D2
5	Q5	AFSi-NPs-Q4-alginate- chlorhexidine -alginate- D2
6	Q6	AFSi-NPs-Q5-alginate- chlorhexidine -alginate- D2
7	Q7	AFSi-NPs-Q6-alginate- chlorhexidine -alginate- D2
8	Q8	AFSi-NPs-Q7-alginate- chlorhexidine -alginate- D2
9	Q9	AFSi-NPs-Q8-alginate- chlorhexidine -alginate- D2
10	Q10	AFSi-NPs-Q9-alginate- chlorhexidine -alginate- D2

Table 2.9: LbL matrix of deposited CHX and D2 layers on AFSi-NPs

Matrix 9: Alg-CHX-Alg-D3

Quadruple layer no.	Abbreviation	Layers on the surface of AFSi-NPs
1	Q1	AFSi-NPs-alginate- chlorhexidine -alginate- D3
2	Q2	AFSi-NPs-Q1-alginate- chlorhexidine -alginate- D3
3	Q3	AFSi-NPs-Q2-alginate- chlorhexidine -alginate- D3
4	Q4	AFSi-NPs-Q3-alginate- chlorhexidine -alginate- D3
5	Q5	AFSi-NPs-Q4-alginate- chlorhexidine -alginate- D3
6	Q6	AFSi-NPs-Q5-alginate- chlorhexidine -alginate- D3
7	Q7	AFSi-NPs-Q6-alginate- chlorhexidine -alginate- D3
8	Q8	AFSi-NPs-Q7-alginate- chlorhexidine -alginate- D3
9	Q9	AFSi-NPs-Q8-alginate- chlorhexidine -alginate- D3

10	Q10	AFSi-NPs-Q9-alginate- chlorhexidine -alginate- D3
-----------	-----	---

Table 2.10: LbL matrix of deposited CHX and D3 layers on AFSi-NPs

Matrix 10: Alg-CHX-Alg-E1

Quadruple layer no.	Abbreviation	Layers on the surface of AFSi-NPs
1	Q1	AFSi-NPs-alginate- chlorhexidine -alginate- E1
2	Q2	AFSi-NPs-Q1-alginate- chlorhexidine -alginate- E1
3	Q3	AFSi-NPs-Q2-alginate- chlorhexidine -alginate- E1
4	Q4	AFSi-NPs-Q3-alginate- chlorhexidine -alginate- E1
5	Q5	AFSi-NPs-Q4-alginate- chlorhexidine -alginate- E1
6	Q6	AFSi-NPs-Q5-alginate- chlorhexidine -alginate- E1
7	Q7	AFSi-NPs-Q6-alginate- chlorhexidine -alginate- E1
8	Q8	AFSi-NPs-Q7-alginate- chlorhexidine -alginate- E1
9	Q9	AFSi-NPs-Q8-alginate- chlorhexidine -alginate- E1
10	Q10	AFSi-NPs-Q9-alginate- chlorhexidine -alginate- E1

Table 2.11: LbL matrix of deposited CHX and E1 layers on AFSi-NPs

Matrix 11: Alg-CHX-Alg-E2

Quadruple layer no.	Abbreviation	Layers on the surface of AFSi-NPs
1	Q1	AFSi-NPs-alginate- chlorhexidine -alginate- E2
2	Q2	AFSi-NPs-Q1-alginate- chlorhexidine -alginate- E2
3	Q3	AFSi-NPs-Q2-alginate- chlorhexidine -alginate- E2
4	Q4	AFSi-NPs-Q3-alginate- chlorhexidine -alginate- E2
5	Q5	AFSi-NPs-Q4-alginate- chlorhexidine -alginate- E2
6	Q6	AFSi-NPs-Q5-alginate- chlorhexidine -alginate- E2
7	Q7	AFSi-NPs-Q6-alginate- chlorhexidine -alginate- E2
8	Q8	AFSi-NPs-Q7-alginate- chlorhexidine -alginate- E2
9	Q9	AFSi-NPs-Q8-alginate- chlorhexidine -alginate- E2
10	Q10	AFSi-NPs-Q9-alginate- chlorhexidine -alginate- E2

Table 2.12: LbL matrix of deposited CHX and E2 layers on AFSi-NPs

Matrix 12: Alg-CHX-Alg-E3

Quadruple layer no.	Abbreviation	Layers on the surface of AFSi-NPs
1	Q1	AFSi-NPs-alginate- <i>chlorhexidine</i> -alginate-E3
2	Q2	AFSi-NPs-Q1-alginate- <i>chlorhexidine</i> -alginate-E3
3	Q3	AFSi-NPs-Q2-alginate- <i>chlorhexidine</i> -alginate-E3
4	Q4	AFSi-NPs-Q3-alginate- <i>chlorhexidine</i> -alginate-E3
5	Q5	AFSi-NPs-Q4-alginate- <i>chlorhexidine</i> -alginate-E3
6	Q6	AFSi-NPs-Q5-alginate- <i>chlorhexidine</i> -alginate-E3
7	Q7	AFSi-NPs-Q6-alginate- <i>chlorhexidine</i> -alginate-E3
8	Q8	AFSi-NPs-Q7-alginate- <i>chlorhexidine</i> -alginate-E3
9	Q9	AFSi-NPs-Q8-alginate- <i>chlorhexidine</i> -alginate-E3
10	Q10	AFSi-NPs-Q9-alginate- <i>chlorhexidine</i> -alginate-E3

Table 2.13: LbL matrix of deposited CHX and E3 layers on AFSi-NPs

Matrix 13: Alg-CHX-Alg-F1

Quadruple layer no.	Abbreviation	Layers on the surface of AFSi-NPs
1	Q1	AFSi-NPs-alginate- <i>chlorhexidine</i> -alginate-F1
2	Q2	AFSi-NPs-Q1-alginate- <i>chlorhexidine</i> -alginate-F1
3	Q3	AFSi-NPs-Q2-alginate- <i>chlorhexidine</i> -alginate-F1
4	Q4	AFSi-NPs-Q3-alginate- <i>chlorhexidine</i> -alginate-F1
5	Q5	AFSi-NPs-Q4-alginate- <i>chlorhexidine</i> -alginate-F1
6	Q6	AFSi-NPs-Q5-alginate- <i>chlorhexidine</i> -alginate-F1
7	Q7	AFSi-NPs-Q6-alginate- <i>chlorhexidine</i> -alginate-F1
8	Q8	AFSi-NPs-Q7-alginate- <i>chlorhexidine</i> -alginate-F1
9	Q9	AFSi-NPs-Q8-alginate- <i>chlorhexidine</i> -alginate-F1
10	Q10	AFSi-NPs-Q9-alginate- <i>chlorhexidine</i> -alginate-F1

Table 2.14: LbL matrix of deposited CHX and F1 layers on AFSi-NPs

Matrix 14: Alg-CHX-Alg-F2

Quadruple layer no.	Abbreviation	Layers on the surface of AFSi-NPs
1	Q1	AFSi-NPs-alginate- <i>chlorhexidine</i> -alginate-F2
2	Q2	AFSi-NPs-Q1-alginate- <i>chlorhexidine</i> -alginate-F2
3	Q3	AFSi-NPs-Q2-alginate- <i>chlorhexidine</i> -alginate-F2

4	Q4	AFSi-NPs-Q3-alginate- chlorhexidine -alginate- F2
5	Q5	AFSi-NPs-Q4-alginate- chlorhexidine -alginate- F2
6	Q6	AFSi-NPs-Q5-alginate- chlorhexidine -alginate- F2
7	Q7	AFSi-NPs-Q6-alginate- chlorhexidine -alginate- F2
8	Q8	AFSi-NPs-Q7-alginate- chlorhexidine -alginate- F2
9	Q9	AFSi-NPs-Q8-alginate- chlorhexidine -alginate- F2
10	Q10	AFSi-NPs-Q9-alginate- chlorhexidine -alginate- F2

Table 2.15: LbL matrix of deposited CHX and F2 layers on AFSi-NPs

Matrix 15: Alg-CHX-Alg-F3

Quadruple layer no.	Abbreviation	Layers on the surface of AFSi-NPs
1	Q1	AFSi-NPs-alginate- chlorhexidine -alginate- F3
2	Q2	AFSi-NPs-Q1-alginate- chlorhexidine -alginate- F3
3	Q3	AFSi-NPs-Q2-alginate- chlorhexidine -alginate- F3
4	Q4	AFSi-NPs-Q3-alginate- chlorhexidine -alginate- F3
5	Q5	AFSi-NPs-Q4-alginate- chlorhexidine -alginate- F3
6	Q6	AFSi-NPs-Q5-alginate- chlorhexidine -alginate- F3
7	Q7	AFSi-NPs-Q6-alginate- chlorhexidine -alginate- F3
8	Q8	AFSi-NPs-Q7-alginate- chlorhexidine -alginate- F3
9	Q9	AFSi-NPs-Q8-alginate- chlorhexidine -alginate- F3
10	Q10	AFSi-NPs-Q9-alginate- chlorhexidine -alginate- F3

Table 2.16: LbL matrix of deposited CHX and F3 layers on AFSi-NPs

Matrix 16: Alg-CHX-Alg-G1

Quadruple layer no.	Abbreviation	Layers on the surface of AFSi-NPs
1	Q1	AFSi-NPs-alginate- chlorhexidine -alginate- G1
2	Q2	AFSi-NPs-Q1-alginate- chlorhexidine -alginate- G1
3	Q3	AFSi-NPs-Q2-alginate- chlorhexidine -alginate- G1
4	Q4	AFSi-NPs-Q3-alginate- chlorhexidine -alginate- G1
5	Q5	AFSi-NPs-Q4-alginate- chlorhexidine -alginate- G1
6	Q6	AFSi-NPs-Q5-alginate- chlorhexidine -alginate- G1
7	Q7	AFSi-NPs-Q6-alginate- chlorhexidine -alginate- G1

8	Q8	AFSi-NPs-Q7-alginate- chlorhexidine -alginate- G1
9	Q9	AFSi-NPs-Q8-alginate- chlorhexidine -alginate- G1
10	Q10	AFSi-NPs-Q9-alginate- chlorhexidine -alginate- G1

Table 2.17 LbL matrix of deposited CHX and G1 layers on AFSi-NPs

Matrix 17: Alg-CHX-Alg-G2

Quadruple layer no.	Abbreviation	Layers on the surface of AFSi-NPs
1	Q1	AFSi-NPs-alginate- chlorhexidine -alginate- G2
2	Q2	AFSi-NPs-Q1-alginate- chlorhexidine -alginate- G2
3	Q3	AFSi-NPs-Q2-alginate- chlorhexidine -alginate- G2
4	Q4	AFSi-NPs-Q3-alginate- chlorhexidine -alginate- G2
5	Q5	AFSi-NPs-Q4-alginate- chlorhexidine -alginate- G2
6	Q6	AFSi-NPs-Q5-alginate- chlorhexidine -alginate- G2
7	Q7	AFSi-NPs-Q6-alginate- chlorhexidine -alginate- G2
8	Q8	AFSi-NPs-Q7-alginate- chlorhexidine -alginate- G2
9	Q9	AFSi-NPs-Q8-alginate- chlorhexidine -alginate- G2
10	Q10	AFSi-NPs-Q9-alginate- chlorhexidine -alginate- G2

Table 2.18: LbL matrix of deposited CHX and G2 layers on AFSi-NPs

Matrix 18: Alg-CHX-Alg-G3

Quadruple layer no.	Abbreviation	Layers on the surface of AFSi-NPs
1	Q1	AFSi-NPs-alginate- chlorhexidine -alginate- G3
2	Q2	AFSi-NPs-Q1-alginate- chlorhexidine -alginate- G3
3	Q3	AFSi-NPs-Q2-alginate- chlorhexidine -alginate- G3
4	Q4	AFSi-NPs-Q3-alginate- chlorhexidine -alginate- G3
5	Q5	AFSi-NPs-Q4-alginate- chlorhexidine -alginate- G3
6	Q6	AFSi-NPs-Q5-alginate- chlorhexidine -alginate- G3
7	Q7	AFSi-NPs-Q6-alginate- chlorhexidine -alginate- G3
8	Q8	AFSi-NPs-Q7-alginate- chlorhexidine -alginate- G3
9	Q9	AFSi-NPs-Q8-alginate- chlorhexidine -alginate- G3
10	Q10	AFSi-NPs-Q9-alginate- chlorhexidine -alginate- G3

Table 2.19: LbL matrix of deposited CHX and G3 layers on AFSi-NPs

Tobramycin

Tobramycin (figure 2.5) is a natural aminoglycoside made up of 5 amino groups (-NH₂) conjugated to a derivate of sugars known as glycoside. It is a water-soluble small molecule with log P_{o/w} equal to -6.19 (XlogP3) (Daina, Michielin and Zoete, 2017) which theoretically confirmed the hydrophilic nature of this compound. This antibiotic derives from *Streptomyces tenebrarius* and it shows an effective bacteriostatic activity against Gram negative bacteria, especially *Pseudomonias* species (Bodey and Stewart, 1972), (Hill *et al.*, 2019).

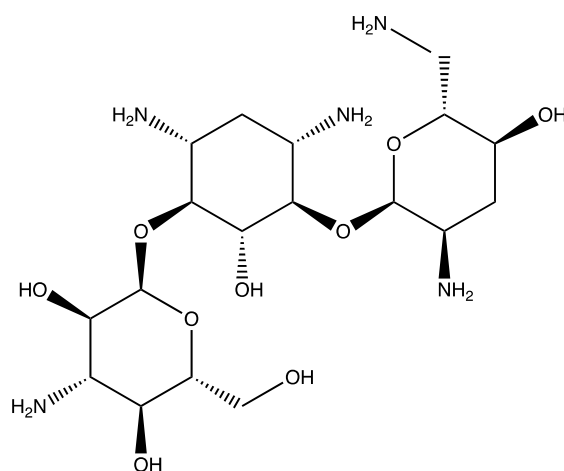


Figure 2.5: Tobramycin chemical structure

Tobramycin and poly (β amino-esters) loaded silica amino functionalised nanoparticles

The antibiotic tobramycin was loaded in 18 different matrices as well as the chlorhexidine diacetate and the difference among them, as mentioned before, was represented by the PBAE loaded as polycation. Thus, here all the nanoconstructs including tobramycin onto amino-functionalised (AFSi-NPs) are listed as matrices 19-36 as follows:

Matrix 19: Alg-TOB-Alg-A1

Quadruple layer no.	Abbreviation	Layers on the surface of AFSi-NPs
1	Q1	AFSi-NPs-alginate- tobramycin -alginate- A1
2	Q2	AFSi-NPs-Q1-alginate- tobramycin -alginate- A1
3	Q3	AFSi-NPs-Q2-alginate- tobramycin -alginate- A1
4	Q4	AFSi-NPs-Q3-alginate- tobramycin -alginate- A1

5	Q5	AFSi-NPs-Q4-alginate- tobramycin -alginate- A1
6	Q6	AFSi-NPs-Q5-alginate- tobramycin -alginate- A1
7	Q7	AFSi-NPs-Q6-alginate- tobramycin -alginate- A1
8	Q8	AFSi-NPs-Q7-alginate- tobramycin -alginate- A1
9	Q9	AFSi-NPs-Q8-alginate- tobramycin -alginate- A1
10	Q10	AFSi-NPs-Q9-alginate- tobramycin -alginate- A1

Table 2.20: LbL matrix of deposited TOB and A1 layers on AFSi-NPs

Matrix 20: Alg-TOB-Alg-A2

Quadruple layer no.	Abbreviation	Layers on the surface of AFSi-NPs
1	Q1	AFSi-NPs-alginate- tobramycin -alginate- A2
2	Q2	AFSi-NPs-Q1-alginate- tobramycin -alginate- A2
3	Q3	AFSi-NPs-Q2-alginate- tobramycin -alginate- A2
4	Q4	AFSi-NPs-Q3-alginate- tobramycin -alginate- A2
5	Q5	AFSi-NPs-Q4-alginate- tobramycin -alginate- A2
6	Q6	AFSi-NPs-Q5-alginate- tobramycin -alginate- A2
7	Q7	AFSi-NPs-Q6-alginate- tobramycin -alginate- A2
8	Q8	AFSi-NPs-Q7-alginate- tobramycin -alginate- A2
9	Q9	AFSi-NPs-Q8-alginate- tobramycin -alginate- A2
10	Q10	AFSi-NPs-Q9-alginate- tobramycin -alginate- A2

Table 2.21: LbL matrix of deposited TOB and A2 layers on AFSi-NPs

Matrix 21: Alg-TOB-Alg-A3

Quadruple layer no.	Abbreviation	Layers on the surface of AFSi-NPs
1	Q1	AFSi-NPs-alginate- tobramycin -alginate- A3
2	Q2	AFSi-NPs-Q1-alginate- tobramycin -alginate- A3
3	Q3	AFSi-NPs-Q2-alginate- tobramycin -alginate- A3
4	Q4	AFSi-NPs-Q3-alginate- tobramycin -alginate- A3
5	Q5	AFSi-NPs-Q4-alginate- tobramycin -alginate- A3
6	Q6	AFSi-NPs-Q5-alginate- tobramycin -alginate- A3
7	Q7	AFSi-NPs-Q6-alginate- tobramycin -alginate- A3
8	Q8	AFSi-NPs-Q7-alginate- tobramycin -alginate- A3

9	Q9	AFSi-NPs-Q8-alginate- tobramycin -alginate- A3
10	Q10	AFSi-NPs-Q9-alginate- tobramycin -alginate- A3

Table 2.22: LbL matrix of deposited TOB and A3 layers on AFSi-NPs

Matrix 22: Alg-TOB-Alg-B1

Quadruple layer no.	Abbreviation	Layers on the surface of AFSi-NPs
1	Q1	AFSi-NPs-alginate- tobramycin -alginate- B1
2	Q2	AFSi-NPs-Q1-alginate- tobramycin -alginate- B1
3	Q3	AFSi-NPs-Q2-alginate- tobramycin -alginate- B1
4	Q4	AFSi-NPs-Q3-alginate- tobramycin -alginate- B1
5	Q5	AFSi-NPs-Q4-alginate- tobramycin -alginate- B1
6	Q6	AFSi-NPs-Q5-alginate- tobramycin -alginate- B1
7	Q7	AFSi-NPs-Q6-alginate- tobramycin -alginate- B1
8	Q8	AFSi-NPs-Q7-alginate- tobramycin -alginate- B1
9	Q9	AFSi-NPs-Q8-alginate- tobramycin -alginate- B1
10	Q10	AFSi-NPs-Q9-alginate- tobramycin -alginate- B1

Table 2.23: LbL matrix of deposited TOB and B1 layers on AFSi-NPs

Matrix 23: Alg-TOB-Alg-B2

Quadruple layer no.	Abbreviation	Layers on the surface of AFSi-NPs
1	Q1	AFSi-NPs-alginate- tobramycin -alginate- B2
2	Q2	AFSi-NPs-Q1-alginate- tobramycin -alginate- B2
3	Q3	AFSi-NPs-Q2-alginate- tobramycin -alginate- B2
4	Q4	AFSi-NPs-Q3-alginate- tobramycin -alginate- B2
5	Q5	AFSi-NPs-Q4-alginate- tobramycin -alginate- B2
6	Q6	AFSi-NPs-Q5-alginate- tobramycin -alginate- B2
7	Q7	AFSi-NPs-Q6-alginate- tobramycin -alginate- B2
8	Q8	AFSi-NPs-Q7-alginate- tobramycin -alginate- B2
9	Q9	AFSi-NPs-Q8-alginate- tobramycin -alginate- B2
10	Q10	AFSi-NPs-Q9-alginate- tobramycin -alginate- B2

Table 2.24: LbL matrix of deposited TOB and B2 layers on AFSi-NPs

Matrix 24: Alg-TOB-Alg-B3

Quadruple layer no.	Abbreviation	Layers on the surface of AFSi-NPs
1	Q1	AFSi-NPs-alginate- tobramycin -alginate- B3
2	Q2	AFSi-NPs-Q1-alginate- tobramycin -alginate- B3
3	Q3	AFSi-NPs-Q2-alginate- tobramycin -alginate- B3
4	Q4	AFSi-NPs-Q3-alginate- tobramycin -alginate- B3
5	Q5	AFSi-NPs-Q4-alginate- tobramycin -alginate- B3
6	Q6	AFSi-NPs-Q5-alginate- tobramycin -alginate- B3
7	Q7	AFSi-NPs-Q6-alginate- tobramycin -alginate- B3
8	Q8	AFSi-NPs-Q7-alginate- tobramycin -alginate- B3
9	Q9	AFSi-NPs-Q8-alginate- tobramycin -alginate- B3
10	Q10	AFSi-NPs-Q9-alginate- tobramycin -alginate- B3

Table 2.25: LbL matrix of deposited TOB and B3 layers on AFSi-NPs

Matrix 25: Alg-TOB-Alg-D1

Quadruple layer no.	Abbreviation	Layers on the surface of AFSi-NPs
1	Q1	AFSi-NPs-alginate- tobramycin -alginate- D1
2	Q2	AFSi-NPs-Q1-alginate- tobramycin -alginate- D1
3	Q3	AFSi-NPs-Q2-alginate- tobramycin -alginate- D1
4	Q4	AFSi-NPs-Q3-alginate- tobramycin -alginate- D1
5	Q5	AFSi-NPs-Q4-alginate- tobramycin -alginate- D1
6	Q6	AFSi-NPs-Q5-alginate- tobramycin -alginate- D1
7	Q7	AFSi-NPs-Q6-alginate- tobramycin -alginate- D1
8	Q8	AFSi-NPs-Q7-alginate- tobramycin -alginate- D1
9	Q9	AFSi-NPs-Q8-alginate- tobramycin -alginate- D1
10	Q10	AFSi-NPs-Q9-alginate- tobramycin -alginate- D1

Table 2.26: LbL matrix of deposited TOB and D1 layers on AFS-NPs

Matrix 26: Alg-TOB-Alg-D2

Quadruple layer no.	Abbreviation	Layers on the surface of AFSi-NPs
1	Q1	AFSi-NPs-alginate- tobramycin -alginate- D2
2	Q2	AFSi-NPs-Q1-alginate- tobramycin -alginate- D2

3	Q3	AFSi-NPs-Q2-alginate- tobramycin -alginate- D2
4	Q4	AFSi-NPs-Q3-alginate- tobramycin -alginate- D2
5	Q5	AFSi-NPs-Q4-alginate- tobramycin -alginate- D2
6	Q6	AFSi-NPs-Q5-alginate- tobramycin -alginate- D2
7	Q7	AFSi-NPs-Q6-alginate- tobramycin -alginate- D2
8	Q8	AFSi-NPs-Q7-alginate- tobramycin -alginate- D2
9	Q9	AFSi-NPs-Q8-alginate- tobramycin -alginate- D2
10	Q10	AFSi-NPs-Q9-alginate- tobramycin -alginate- D2

Table 2.27: LbL matrix of deposited TOB and D2 layers on AFSi-NPs

Matrix 27: Alg-TOB-Alg-D3

Quadruple layer no.	Abbreviation	Layers on the surface of AFSi-NPs
1	Q1	AFSi-NPs-alginate- tobramycin -alginate- D3
2	Q2	AFSi-NPs-Q1-alginate- tobramycin -alginate- D3
3	Q3	AFSi-NPs-Q2-alginate- tobramycin -alginate- D3
4	Q4	AFSi-NPs-Q3-alginate- tobramycin -alginate- D3
5	Q5	AFSi-NPs-Q4-alginate- tobramycin -alginate- D3
6	Q6	AFSi-NPs-Q5-alginate- tobramycin -alginate- D3
7	Q7	AFSi-NPs-Q6-alginate- tobramycin -alginate- D3
8	Q8	AFSi-NPs-Q7-alginate- tobramycin -alginate- D3
9	Q9	AFSi-NPs-Q8-alginate- tobramycin -alginate- D3
10	Q10	AFSi-NPs-Q9-alginate- tobramycin -alginate- D3

Table 2.28: LbL matrix of deposited TOB and D3 layers on AFSi-NPs

Matrix 28: Alg-TOB-Alg-E1

Quadruple layer no.	Abbreviation	Layers on the surface of AFSi-NPs
1	Q1	AFSi-NPs-alginate- tobramycin -alginate- E1
2	Q2	AFSi-NPs-Q1-alginate- tobramycin -alginate- E1
3	Q3	AFSi-NPs-Q2-alginate- tobramycin -alginate- E1
4	Q4	AFSi-NPs-Q3-alginate- tobramycin -alginate- E1
5	Q5	AFSi-NPs-Q4-alginate- tobramycin -alginate- E1

6	Q6	AFSi-NPs-Q5-alginate- tobramycin -alginate- E1
7	Q7	AFSi-NPs-Q6-alginate- tobramycin -alginate- E1
8	Q8	AFSi-NPs-Q7-alginate- tobramycin -alginate- E1
9	Q9	AFSi-NPs-Q8-alginate- tobramycin -alginate- E1
10	Q10	AFSi-NPs-Q9-alginate- tobramycin -alginate- E1

Table 2.29: LbL matrix of deposited TOB and E1 layers on AFSi-NPs

Matrix 29: Alg-TOB-Alg-E2

Quadruple layer no.	Abbreviation	Layers on the surface of AFSi-NPs
1	Q1	AFSi-NPs-alginate- tobramycin -alginate- E2
2	Q2	AFSi-NPs-Q1-alginate- tobramycin -alginate- E2
3	Q3	AFSi-NPs-Q2-alginate- tobramycin -alginate- E2
4	Q4	AFSi-NPs-Q3-alginate- tobramycin -alginate- E2
5	Q5	AFSi-NPs-Q4-alginate- tobramycin -alginate- E2
6	Q6	AFSi-NPs-Q5-alginate- tobramycin -alginate- E2
7	Q7	AFSi-NPs-Q6-alginate- tobramycin -alginate- E2
8	Q8	AFSi-NPs-Q7-alginate- tobramycin -alginate- E2
9	Q9	AFSi-NPs-Q8-alginate- tobramycin -alginate- E2
10	Q10	AFSi-NPs-Q9-alginate- tobramycin -alginate- E2

Table 2.30: LbL matrix of deposited TOB and E2 layers on AFSi-NPs

Matrix 30: Alg-TOB-Alg-E3

Quadruple layer no.	Abbreviation	Layers on the surface of AFSi-NPs
1	Q1	AFSi-NPs-alginate- tobramycin -alginate- E3
2	Q2	AFSi-NPs-Q1-alginate- tobramycin -alginate- E3
3	Q3	AFSi-NPs-Q2-alginate- tobramycin -alginate- E3
4	Q4	AFSi-NPs-Q3-alginate- tobramycin -alginate- E3
5	Q5	AFSi-NPs-Q4-alginate- tobramycin -alginate- E3
6	Q6	AFSi-NPs-Q5-alginate- tobramycin -alginate- E3
7	Q7	AFSi-NPs-Q6-alginate- tobramycin -alginate- E3
8	Q8	AFSi-NPs-Q7-alginate- tobramycin -alginate- E3
9	Q9	AFSi-NPs-Q8-alginate- tobramycin -alginate- E3

10	Q10	AFSi-NPs-Q9-alginate- tobramycin -alginate- E3
-----------	-----	--

Table 2.31: LbL matrix of deposited TOB and E3 layers on AFSi-NPs

Matrix 31: Alg-TOB-Alg-F1

Quadruple layer no.	Abbreviation	Layers on the surface of AFSi-NPs
1	Q1	AFSi-NPs-alginate- tobramycin -alginate- F1
2	Q2	AFSi-NPs-Q1-alginate- tobramycin -alginate- F1
3	Q3	AFSi-NPs-Q2-alginate- tobramycin -alginate- F1
4	Q4	AFSi-NPs-Q3-alginate- tobramycin -alginate- F1
5	Q5	AFSi-NPs-Q4-alginate- tobramycin -alginate- F1
6	Q6	AFSi-NPs-Q5-alginate- tobramycin -alginate- F1
7	Q7	AFSi-NPs-Q6-alginate- tobramycin -alginate- F1
8	Q8	AFSi-NPs-Q7-alginate- tobramycin -alginate- F1
9	Q9	AFSi-NPs-Q8-alginate- tobramycin -alginate- F1
10	Q10	AFSi-NPs-Q9-alginate- tobramycin -alginate- F1

Table 2.32: LbL matrix of deposited TOB and F1 layers on AFSi-NPs

Matrix 32: Alg-TOB-Alg-F2

Quadruple layer no.	Abbreviation	Layers on the surface of AFSi-NPs
1	Q1	AFSi-NPs-alginate- tobramycin -alginate- F2
2	Q2	AFSi-NPs-Q1-alginate- tobramycin -alginate- F2
3	Q3	AFSi-NPs-Q2-alginate- tobramycin -alginate- F2
4	Q4	AFSi-NPs-Q3-alginate- tobramycin -alginate- F2
5	Q5	AFSi-NPs-Q4-alginate- tobramycin -alginate- F2
6	Q6	AFSi-NPs-Q5-alginate- tobramycin -alginate- F2
7	Q7	AFSi-NPs-Q6-alginate- tobramycin -alginate- F2
8	Q8	AFSi-NPs-Q7-alginate- tobramycin -alginate- F2
9	Q9	AFSi-NPs-Q8-alginate- tobramycin -alginate- F2
10	Q10	AFSi-NPs-Q9-alginate- tobramycin -alginate- F2

Table 2.33: LbL matrix of deposited TOB and F2 layers on AFSi-NPs

Matrix 33: Alg-TOB-Alg-F3

Quadruple layer no.	Abbreviation	Layers on the surface of AFSi-NPs
1	Q1	AFSi-NPs-alginate- tobramycin -alginate- F3
2	Q2	AFSi-NPs-Q1-alginate- tobramycin -alginate- F3
3	Q3	AFSi-NPs-Q2-alginate- tobramycin -alginate- F3
4	Q4	AFSi-NPs-Q3-alginate- tobramycin -alginate- F3
5	Q5	AFSi-NPs-Q4-alginate- tobramycin -alginate- F3
6	Q6	AFSi-NPs-Q5-alginate- tobramycin -alginate- F3
7	Q7	AFSi-NPs-Q6-alginate- tobramycin -alginate- F3
8	Q8	AFSi-NPs-Q7-alginate- tobramycin -alginate- F3
9	Q9	AFSi-NPs-Q8-alginate- tobramycin -alginate- F3
10	Q10	AFSi-NPs-Q9-alginate- tobramycin -alginate- F3

Table 2.34: LbL matrix of deposited TOB and F3 layers on AFSi-NPs**Matrix 34: Alg-TOB-Alg-G1**

Quadruple layer no.	Abbreviation	Layers on the surface of AFSi-NPs
1	Q1	AFSi-NPs-alginate- tobramycin -alginate- G1
2	Q2	AFSi-NPs-Q1-alginate- tobramycin -alginate- G1
3	Q3	AFSi-NPs-Q2-alginate- tobramycin -alginate- G1
4	Q4	AFSi-NPs-Q3-alginate- tobramycin -alginate- G1
5	Q5	AFSi-NPs-Q4-alginate- tobramycin -alginate- G1
6	Q6	AFSi-NPs-Q5-alginate- tobramycin -alginate- G1
7	Q7	AFSi-NPs-Q6-alginate- tobramycin -alginate- G1
8	Q8	AFSi-NPs-Q7-alginate- tobramycin -alginate- G1
9	Q9	AFSi-NPs-Q8-alginate- tobramycin -alginate- G1
10	Q10	AFSi-NPs-Q9-alginate- tobramycin -alginate- G1

Table 2.35 LbL matrix of deposited TOB and G1 layers on AFSi-NPs**Matrix 35: Alg-TOB-Alg-G2**

Quadruple layer no.	Abbreviation	Layers on the surface of AFSi-NPs
1	Q1	AFSi-NPs-alginate- tobramycin -alginate- G2

2	Q2	AFSi-NPs-Q1-alginate- tobramycin -alginate- G2
3	Q3	AFSi-NPs-Q2-alginate- tobramycin -alginate- G2
4	Q4	AFSi-NPs-Q3-alginate- tobramycin -alginate- G2
5	Q5	AFSi-NPs-Q4-alginate- tobramycin -alginate- G2
6	Q6	AFSi-NPs-Q5-alginate- tobramycin -alginate- G2
7	Q7	AFSi-NPs-Q6-alginate- tobramycin -alginate- G2
8	Q8	AFSi-NPs-Q7-alginate- tobramycin -alginate- G2
9	Q9	AFSi-NPs-Q8-alginate- tobramycin -alginate- G2
10	Q10	AFSi-NPs-Q9-alginate- tobramycin -alginate- G2

Table 2.36: LbL matrix of deposited TOB and G2 layers on AFSi-NPs

Matrix 36: Alg-TOB-Alg-G3

Quadruple layer no.	Abbreviation	Layers on the surface of AFSi-NPs
1	Q1	AFSi-NPs-alginate- tobramycin -alginate- G3
2	Q2	AFSi-NPs-Q1-alginate- tobramycin -alginate- G3
3	Q3	AFSi-NPs-Q2-alginate- tobramycin -alginate- G3
4	Q4	AFSi-NPs-Q3-alginate- tobramycin -alginate- G3
5	Q5	AFSi-NPs-Q4-alginate- tobramycin -alginate- G3
6	Q6	AFSi-NPs-Q5-alginate- tobramycin -alginate- G3
7	Q7	AFSi-NPs-Q6-alginate- tobramycin -alginate- G3
8	Q8	AFSi-NPs-Q7-alginate- tobramycin -alginate- G3
9	Q9	AFSi-NPs-Q8-alginate- tobramycin -alginate- G3
10	Q10	AFSi-NPs-Q9-alginate- tobramycin -alginate- G3

Table 2.37: LbL matrix of deposited TOB and G3 layers on AFSi-NPs

Nanoparticles characterization

Size measurements

a. Dynamic Light Scattering (DLS)

The size was measured for the silica nanoparticles after the amino-functionalization using the ZetaSizer Nanoseries ZS of Malvern. DLS allows the determination of the size particle by measuring the changes in the intensity of the light scattered from a solution or a suspension.

In particular. DLS refers to Brownian motion that is related to the size of the particle by illumination of the particles with a laser and analysing fluctuations in the scattering light. The correlation between the size of a particle and its speed due to the Brownian motion is represented by the Stokes-Einstein equation, considering that small particles move quickly instead large ones move slowly. It is as followed: $D_h = k_B T / 3\pi\eta D_T$ where D_h is the hydrodynamic diameter, k_B the constant of Boltzmann, T is the thermodynamic temperature, η is the dynamic viscosity and D_T the translational diffusion coefficient (Sun *et al.*, 2016). For the analysis 1 mg of silica nanoparticles after the amino-functionalization was dispersed in 1 mL of sodium acetate buffer pH5 and measured by ZetaSizer using a cuvette cell. The experiment was carried out to provide in total 3 replicates per measurement.

b. Transmission electron microscopy

Transmission electron microscopy (TEM) and scanning transmission electron microscopy (STEM) were performed on a JEOL JEM-2100 operating at 200 kV. Energy dispersive X-ray analysis (EDX) was done using an Oxford Instruments X-MaxN 80 detector and the data analysed using the Aztec software. 2 μ g of sample was prepared by dispersion in ethanol by sonication and 4 μ L of solution were deposited on 300 mesh copper grids coated with holey carbon film. The experiment was carried out in the school of Optometry in Cardiff and the magnification of the images was 100,000 X.

Zeta potential measurements

For all the sequences, the charge of every constituent of each quadruple layer was analysed by the ZetaSizer Nanoseries ZS of Malvern. It is a high-performance equipment that allows the measurement of the size, electrophoretic mobility of proteins, zeta potential of nanoparticles and colloids and the measurement of protein mobility and micro-rheology of protein and polymer solutions. The measurement of the zeta potential is made by a Laser Doppler Micro-electrophoresis. An electric field is applied to dispersed particles or a solution of molecules, whose movement occurs with a velocity that is related to their zeta potential. The velocity is measured by a patented laser interferometric technique, M3 PALS (Phase Analysis Light Scattering). This provides the calculation of electrophoretic mobility and from this the zeta potential and its distribution (Limited, 2011). Each measurement was performed with the following protocol: 1 mg of dried nanoparticles, after new layer coated onto the

nanocarrier surface via LbL deposition, was suspended in 1 mL of sodium acetate pH5 buffer and added to a disposable folded capillary cell DTS1070. The parameters applied for the experiment were as follows: viscosity 1.0500, RI 1.300, dielectric constant 82.0 and temperature 25°C, correspondent to the sodium acetate buffer pH5 used as dispersant. The Smoluchowski model was employed for calculations considering the equation $\zeta = 4\pi\mu\eta/\epsilon$ where ζ is zeta potential, μ is electrophoretic mobility, η is viscosity and ϵ represents the dielectric constant of fluids (HUNTER, 1981). For each measurement, between 10 and 100 runs were performed and 3 replicates per sample. The data interpretation was provided by plotting the result expressed as mV as function of number of layers embedded onto the nanocarrier surface.

Thermogravimetric Analysis (TGA)

For all the developed nanotechnology systems, the Thermogravimetric Analysis was carried out on 2 replicates of 10 mg for each following sample: Q1, Q3, Q5, Q7 and Q10. TGA is a thermal analysis that measures changes in physical and chemical properties of materials as a function of increasing temperature with constant heating rate, or as a function of time with constant temperature and/or constant mass loss. In this case, TGA provides the determination of the loss of drying for each sample. The TGA instrument weights continuously a sample increasing the temperature up to 2000°C (Ng *et al.*, 2018a). For this project, the instrument used was Perkin-Elmer TGA 4000 Thermogravimetric analyser. The method of the analysis included air and each sample was heated from 20°C to 800°C with an increase of 30°C every minute. The risen temperature influenced the sample mass causing an increase of weight loss. Results were plotted evidencing the sample weight loss as function of temperature changes.

Chlorhexidine release quantification

All the sequences were prepared with the aim of evaluating the chlorhexidine release profile. The tenth quadruple layer (Q10), where it was expecting to have the highest released concentration of the antimicrobial agent, was the only quadruple layer considered in the drug profile. For an accurate analysis 3 replicates of each 10 mg of silica coated sample were suspended in 1 ml of two different media: pH5 and pH7.4 in order to have a comparison between pathological and physiological environment (Ribeiro *et al.*, 2012). Then, the samples

were kept in the incubator at 37°C and every 24 hours 1 ml of the supernatant was withdrawn and replaced with fresh buffer from both media.

The drug release was detected by the High-Performance Liquid Chromatography (HPLC) 1100 Series of Agilent Technologies. The column used for the analysis was μ Bondapak C18 silica-based, reverse phase, 125 Å, 10 μ m, 3.9 * 150 mm. The samples were analysed with chlorhexidine isocratic method having 12 minutes as retention time, flow rate of 1 ml/min, mobile phase composed by sodium acetate buffer pH4 45% and acetonitrile 55%. The buffer was made with the following procedure: acetic acid 82% and sodium acetate 18%. Injection volume was 20 μ L and the retention time for chlorhexidine was 6.0 min detected via UV detector at 239 nm.

Before starting the analysis, a calibration curve was built up for the chlorhexidine diacetate. Firstly, a stock solution (1 mg/mL) was prepared, followed by 7 standard solutions gained via serial dilutions with concentration ranging between 0.5mg/mL- 0.125 mg/mL. Standards were diluted with sodium acetate buffer pH5 and the analysis was performed on 3 independent samples for each dilution. Results were plotted on an Excel sheet and an equation has been gained equal to: $y=17915x - 42.742$ and $R^2=0.97608$. (figure 2.6).

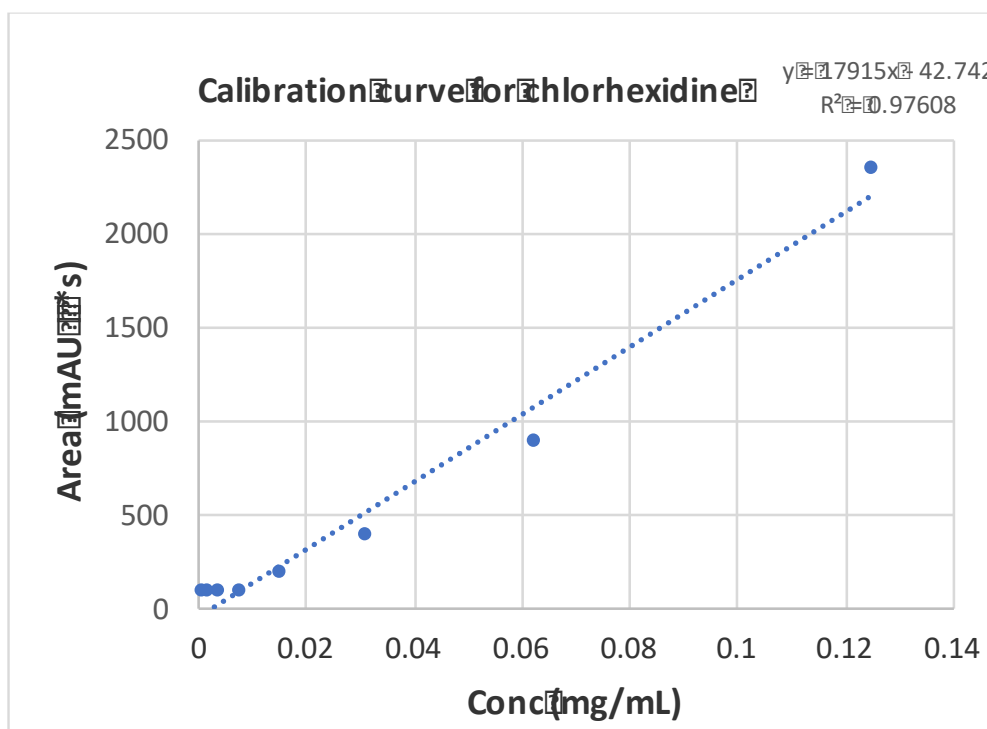


Figure 2.6: Chlorhexidine diacetate calibration curve, *Mean \pm SD (N=1, n=3)

Tobramycin release quantification

The release profile for tobramycin was evaluated applying the same protocol of chlorhexidine diacetate release described in the previous paragraph. However, the drug quantification was detected by fluoroscopy with the aid of a fluoroscan (FLUOROstar Optima, BMG labtech). The amount of tobramycin released from AFS-coated-NPs in both buffers pH5 and pH7.4 required this time the use of the o-phthaldialdehyde (OPA) reagent (Perni and Prokopovich, 2014), that reacting with the amino moieties of the antibiotic, produced a fluorescent conjugate.

The experiment was performed on black 96 well-plates as follows: the total volume of each well corresponded to 280 μL involving firstly 70 μL of PBS, then 70 μL of tobramycin released sample in sodium acetate buffer pH5, 70 μL isopropanol and 70 μL of OPA reagent added protecting it from light. This procedure was repeated for 3 replicates for both media, pH5 and pH7.4. The first 3 columns of each 96 well-plate were kept for eight tobramycin calibrations solutions. After the addition of 70 μL of PBS, from 140 μL of sample added on 3 wells of the first row, 70 μL were transferred on the following 3 wells of the second row by serial dilutions up to the end of the 3 calibration solution columns.

Once prepared, the plate was read using λ excitation=340 nm and λ emission=455 nm as parameters (Interchim Fluoroprobes). The results were plotted on Excel as fluorescence vs concentration ($\mu\text{g}/\text{mL}$) providing a linear trend line for the calibration of tobramycin. The figure 2.7 shows one example of calibration curve obtained among all the analysis.

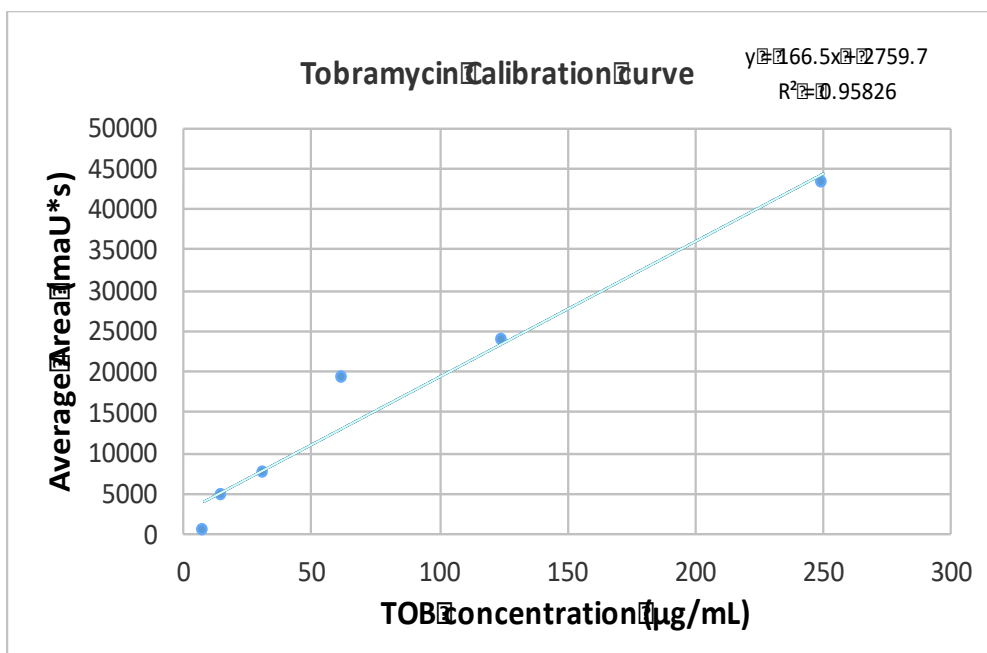


Figure 2.7: Representative tobramycin calibration curve, *Mean \pm SD (N=1, n=3)

PBAEs characterisation

Nuclear Magnetic Resonance (NMR)

All the PBAEs synthesised in this project were characterised by ^1H NMR and ^{13}C NMR. The resonance solvent applied for all the experiments was deuterated chloroform (CDCl_3) purchased by Thermo Scientific Fisher (UK). ^1H NMR spectra were measured on Bruker Avance Ultra Shield spectrometer (500 MHz) at room temperature. Data were recorded as follows: chemical shift in δ ppm (parts per million) from internal standard tetramethylsilane (TMS), multiplicity (s= singlet, d= doublet, t= triplet, m= multiplet), coupling constant (Hz), integration and assignment. ^{13}C NMR spectra were measured on Bruker Avance Ultra Shield spectrometer (125 MHz) at ambient temperature. Chemical shifts were recorded in ppm from the solvent resonance employed as internal standard (e.g. $\text{CDCl}_3 = 77.00$ ppm in ^{13}C NMR spectra, $\text{CDCl}_3 = 7.24$ ppm in ^1H NMR spectra).

PBAE molecular weight (MW) and hydrolysis through Gel Permeation Chromatography (GPC) and zeta potential

GPC is a form of liquid chromatography usually used to purify or analyse mixture of proteins and takes advantages of high resolution made possible by smaller-diameter stationary phases. The molecular weight (MW) and hydrolysis studies were pursued for all the PBAEs

synthesised for this project. In a 50-ml test tube each polymer (10 mg/mL) was dissolved in both buffers pH5 and pH7.4. After solubilisation in buffers, 20 μ L were injected into liquid chromatography LC-20 Ai with refractive index detector RID-20A and GPC post-run as data analysis tool provided by Shimadzu Corporation (UK) to detect the molecular weight (MW). Each independent experiment had 2 replicates per day and per medium. Afterwards, the solutions were both incubated at 37°C, and every 24h 1 mL was collected analysed on GPC up to 30 days.

A calibration curve was built up in order to correlate MW and retention volumes. Thus, 10 PEG standards with known MW (Da) such as: 200, 500, 1000, 2000, 3000, 4000, 6000, 23000, 23500, 36000, were prepared and injected on GPC and correspondent respectively to the points from 10 (lowest MW) to 1 (highest MW) in the figure below. All the samples were run with isocratic method having 25 minutes as retention time, 1.0 mL/min as flow rate, 100% sodium acetate buffer as mobile phase and analytical mode for the RI detector. The column used was Superdex 75 bed dimensions 10/300, bed volume approximately 24 mL column efficiency > 30000m, pH stability between 3 to 12 for regular use and pressure over column maximum 18 bar. The results were processed using Shimadzu software for GPC post-run proving a linear trend line for the calibration curve (figure 2.8).

==== Shimadzu LabSolutions GPC Calibration Curve

<Calibration Curve>

Detector Name : Detector A
Ch# : Channel 1
Method File : C:\LabSolutions\Data\Project1\Silvia\Poly Test + Cal.lcm
Curve Fit Type : Linear
Function : $f(x) = -0.2119725 * x + 6.146507$
R²=0.9869979 Dispersion=0.08106466

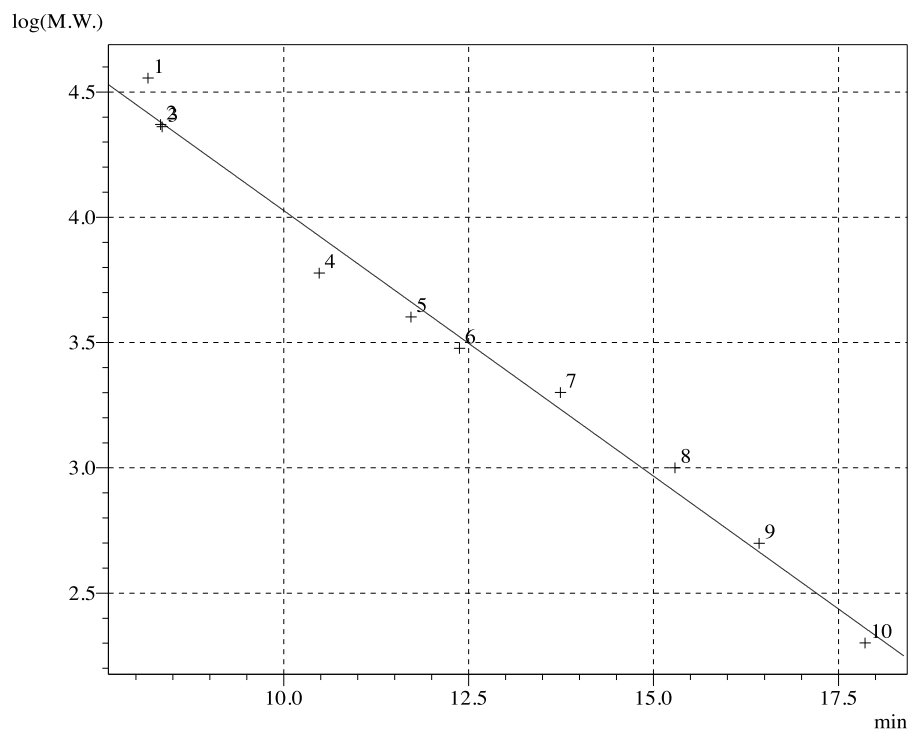


Figure 2.8: PEG calibration curve, *Mean \pm SD (N=1, n=2)

Statistical analysis

All data were expressed as means \pm standard deviation (SD) from at least three independent values. To assess the statistical significance of results between groups, one-way analysis of variance (ANOVA) was performed. Experimental results were considered statistically significant at 95 % confidence level (p-value <0.05). All analyses were run using the Microsoft Excel 2018.

Chapter 3: Poly (β -amino esters) (PBAE): synthesis and characterisation

Introduction

Poly (β -amino esters), known as PBAEs, are cationic polymers obtained by conjugation between acrylates and primary or secondary amines via Michael addition (Perni and Prokopovich, 2017), (Devalapally *et al.*, 2007). In the past few decades these molecules were employed as DNA drug delivery systems showing better biocompatibility and biodegradability compared to the other polymers such as PLL or PEI (Green *et al.*, 2009) (Lehmann-horn *et al.*, 2014). Biodegradability and biocompatibility are the main properties belonging to these compounds (Est-Witte *et al.*, 2020), (Qu *et al.*, 2020), (Eltoukhy *et al.*, 2013), (Green, Langer and Anderson, 2008), (Lynn and Langer, 2000). In particular, the amino-moieties of PBAEs electrostatically interact with DNA plasmid at physiological pH and their degradation leads to small non-toxic by-products such as bis-(β -amino) acids and diol products (Liu *et al.*, 2019) (Zugates *et al.*, 2006), (Green *et al.*, 2006). PBAEs are the result of one-pot reaction; thus, several analogues can be synthesised from commercially starting materials (Cordeiro *et al.*, 2019).

In this chapter, 18 PBAEs were synthesised via Michael addition by conjugating 3 amines to 6 different diacrylates.

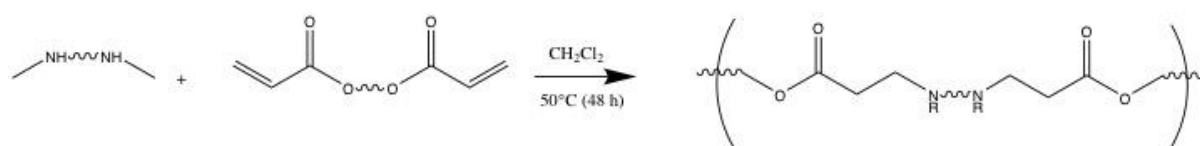
The structure and the molecular weight MW (1300-3100Da) of the 18 crude products were identified by ^1H NMR, ^{13}C NMR and Gel Permeation Chromatography (GPC) whereas the hydrolysis at pH5 and pH7.4 was evaluated via GPC and ζ potential measurements (+10 mV/+36 mV) over a period of 30 days.

The polymeric degradation showed that PBAEs slowly degrade under acid conditions (pH5) and rapidly in the physiological environment (pH7.4) (Akyol *et al.*, 2018), (Eltoukhy *et al.*, 2012), (Lynn and Langer, 2000). However, the work presented in this chapter highlights that the choice of the monomers employed in the polymerization is crucial and it greatly influences the physicochemical properties of PBAEs, especially molecular weight M.W. and charge for their application as vectors for drug delivery systems.

Polymer preparation

Polymer synthesis

Amino-terminated poly (β -amino esters) were obtained by one-pot reaction between amines and diacrylates. Piperazine, 4,4'-trimethyldipiperidine and N,N-Bis[3-(methylamino)propyl]methylamine, were employed as secondary amines monomers and correspondent to amines 1, 2 and 3 in the table 3.1, whereas 1,4 butanediol diacrylate (A), 1-6 hexanediol diacrylate (B), neo-pentyl glycol diacrylate (D), 1-3 butanediol diacrylate (E), bisphenol A ethoxylate diacrylate (F) and tri-cyclodecane dimethanol diacrylate (G) used as diacrylates monomers. The polymerization was carried out by mixing 4.4 mmol of amine to 4 mmol of diacrylate (1.1:1 ratio) in dichloromethane at 50°C in oil bath and left under stirring for 48 hours. The products were recovered by precipitation in diethyl ether and centrifugation at 3500 rpm at 20°C for 5 minutes. This step was repeated up to 3 times to remove any excess of starting materials and the precipitates were concentrated under reduced pressure. The aspect of the final products depended on the choice of the amine: Piperazine or N,N-Bis[3-(methylamino)propyl]methylamine applied as monomers provided clear viscous liquid polymers, whereas 4,4'-trimethyldipiperidine led to white solids poly ((β -amino esters). Scheme 3.1 represents the general scheme of reaction applied to all the polymers synthesised in this project while all the starting materials and the conditions adopted for the PBAEs reaction are illustrated in Table 3.1.



Scheme 3.1: PBAEs general mechanism of reaction

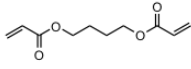
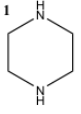
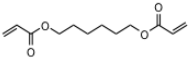
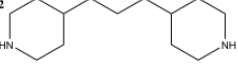
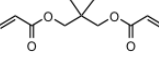
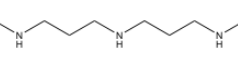
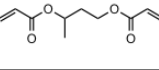
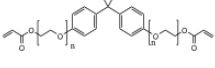

Diacrylates (a)	Amines (b)	mg (a)	mg (b)	solvent	yield (%)
A 	1 	792.88	379.016	DCM	99%
B 	2 	905.08	925.584	DCM	99%
D 	3 	848.96	762.52	DCM	99%
E 		792.88		DCM	99%
F 		2040		DCM	99%
G 		1217		DCM	99%

Table 3.1: Amines and diacrylates employed to PBAE's reaction.

Polymer characterisation

Nuclear Magnetic Resonance (NMR)

All the chemical structures of the PBAEs were characterised by ^1N HMR and ^{13}C NMR. 10 mg of each polymer were dissolved in 1 mL of deuterated chloroform (CDCl_3) and between 0.6-0.7 mL of this sample were withdrawn to perform the analysis. The characterisation occurred by using a Bruker Avance Ultra Shield spectrometer at room temperature at 500 MHz for ^1H NMR and at 125 MHz for ^{13}C NMR. Mestrenova-MestreLab Research-, version 14-1.0-24037 and released on 2019-08-27, was applied as chemistry software for PBAEs spectra interpretation.

Log P determination

Log P, known as partition coefficient, was evaluated by SwissADME software developed by SIB-Swiss Institute of Bioinformatics-version 2019 for all the synthesised polymers and listed on figure 3.1 as MLog P, considering the sum of lipophilic and hydrophilic atoms included in each molecular structure (Mooriguchi *et al.*).

PBAE	MLogP
A1	-0.19
A2	4.23
A3	0.59
B1	0.54
B2	4.8
B3	1.22
D1	0.18
D2	4.52
D3	1.63
E1	-0.19
E2	4.23
E3	0.59
F1	2.06
F2	5.62
F3	2.34
G1	2.55
G2	6.45
G3	2.46

Figure 3.1: MLogP values for all PBAEs.

Molecular weight (MW) determination of PBAEs via Gel Permeation Chromatography (GPC)

For all PBAEs, the molecular weight (MW) was defined by using liquid chromatography LC-20Ai with refractive index (RI) detector RID-20A. As stationary phase, Superdex 75 column, bed dimensions 10/300 and pH stability between 3 to 12, was adopted for the analysis and the conditions chosen for the experiments were as followed: 25 mins retention time, 1.0mL/min as flow rate and 100% acetate buffer pH5 as mobile phase gained by addition of 70% sodium acetate 0.1M to 30% acetic acid 0.1M. Each polymer was dissolved priory every analysis in two separate media, sodium acetate buffer pH5 and phosphate buffer pH7.4 in a concentration of 2mg/mL. 20 μ L was the injected volume for all PBAEs prepared and each independent sample reading had 2 replicates per medium. Data were analysed via GPC post-run software provided by Shimadzu Corporation (UK).

Poly (β -amino) esters hydrolysis

The degradation of PBAEs occurs via hydrolysis and for all the polymers synthesised along this project it was evaluated via chromatography and dynamic light scattering.

In a 50-ml test tube each polymer (2mg/mL) was dissolved in both buffers pH5 and pH7.4. As previously mentioned, the analysis pursued on GPC allowing the MW determination was

considered as day 0 for both media. Afterwards, the solutions were both incubated at 37°C, and every 24h 1 mL was collected and analysed on GPC up to 30 days.

The same conditions were adopted for dynamic light scattering. The charge of PBAEs was measured by ZetaSizer Nanoseries ZS of Malvern on day 0 as starting point for both media and carried out every 24 h over a period of 1 month. Each independent sample reading was pursued adding 1 mL of PBAE/buffers solution to a disposable folded capillary cell DTS1070 and 3 replicates were analysed for each polymer. The dispersant for each PBAE was sodium acetate buffer pH5; the method was Viscosity 1.0500, RI 1.300, Dielectric constant 82.0 and Temperature 25°C and the Smoluchowski model was employed as converter of electrophoretic mobility into zeta potential and its distribution (Perni and Prokopovich, 2017b), (HUNTER, 1981).

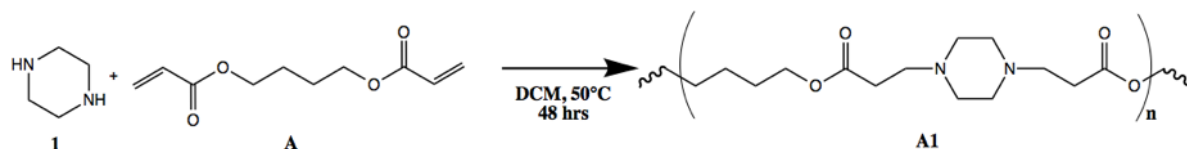
Results

All the reactions were carried out in 100% dichloromethane (DCM) and the efficiency of each reaction was calculated as follows: actual yield/ theoretical yield * 100 (Isac-García *et al.*, 2016). The stoichiometric ratio chosen was diacrylate/amine 1:1.1 due to higher cytocompatibility than PBAEs ending capping with the diacrylate. (Lynn and Langer, 2000).

A1

Chemical procedure

Compound **A1** was prepared according to the general PBAEs synthesis procedure previously described (scheme 3.1). Piperazine (**1**) (4.4 mMol, 379.016 mg) and 1,4 butanediol diacrylate (**A**) (4.0 mMol, 782.88 mg) were reacted to give compound **A1** (scheme 3.2) after precipitation in diethyl ether. Yield 99%.



Scheme 3.2: Reaction scheme of compound **A1**

Chemical identification

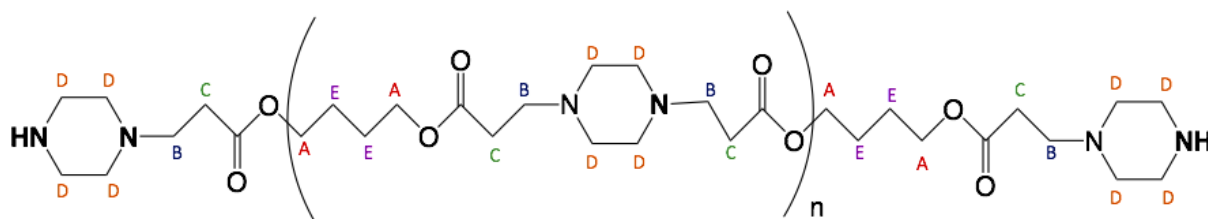


Figure 3.2: A1 structure and NMR characterisation

Monomers ratio: 1.1 (amine): 1.0 (diacrylate)

Solvent stability: DCM and CDCl₃

MLog P: -0.19

MW (GPC): (1395-1502), n=3

Zeta potential: +14.3mV (± 0.95) at pH5, +14.6mV (± 0.51) at pH7.4

Appearance: Yellowish viscous oil

^1H NMR (500 MHz, CDCl_3) δ (ppm): 4.34 – 3.82 (m, 16H) (A), 3.89 – 2.85 (m, 16H) (B), 2.90 – 2.56 (m, 16H) (C), 2.58 – 2.15 (m, 40H) (D), 2.02 – 1.30 (m, 16H) (E).

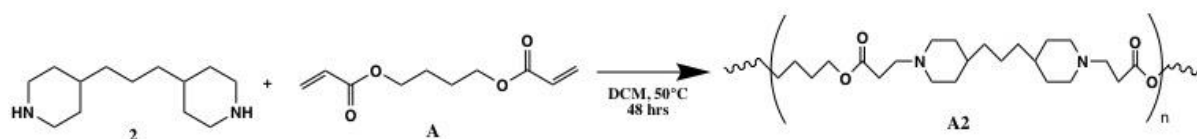
^{13}C NMR (126 MHz, CDCl_3) δ (ppm): 171.95 (C=O), 63.57 (O- CH_2), 53.2 (NH_2 - CH_2), 52.5 (NH_2 - CH_2), 32.9 (- CH_2 -C=O), 25.31 (- CH_2 - CH_2).

The molecular structure of A1 can be divided into 5 main groups (A-E in the figure above) representative of 5 different types of proton peaks (^1H NMR spectrum 1a in appendix section). The protons (-H) of the group A belong to the methylene groups (- CH_2) near the oxygen with chemical shifts ranging between 4.34-3.82 ppm. In the case of A1, among the 16H of the group A, 12H are included in the repeat units (3) whereas 4H are part of the end group of the homopolymer. Additionally, protons of the group B (16H) are representative of the - CH_2 bonded to the nitrogen with chemical shifts between 3.89 and 2.85 ppm, and those of the group C (16H) are part of - CH_2 affected by the nearness of the carbonyl group with values shifted to 2.90-2.56 ppm. Furthermore, protons of the group D belong to the methylene groups of the piperazine, especially 24H in the repeat units and 16H of the end groups of the molecule. Finally, protons of the group E correspond to the 16H of the - CH_2 of the aliphatic chain of the diacrylate monomer. Besides, considering the ^{13}C NMR (1b-appendix), the carbon of the carbonyl group was found at 171.95 ppm, whereas those bonded to the heteroatoms N and O provided chemical shifts ranging between 63.5 and 52.5 ppm. To conclude, the carbon near the carbonyl group was at 32.9 ppm and those of the aliphatic chain were at 25.31 ppm.

A2

Chemical procedure

Compound **A2** (scheme 3.3) was synthesised by adding the secondary amine 4,4 trimethylenepiperidine (**2**) (4.4 mMol, 925.58 mg) to 1,4 butanediol diacrylate (**A**) (4.0 mMol, 782.88 mg) in DCM at 50°C. After 48 hours, the crude product was obtained through precipitation in diethyl ether. Yield 99%.



Scheme 3.3: Reaction scheme of compound **A2**

Chemical identification

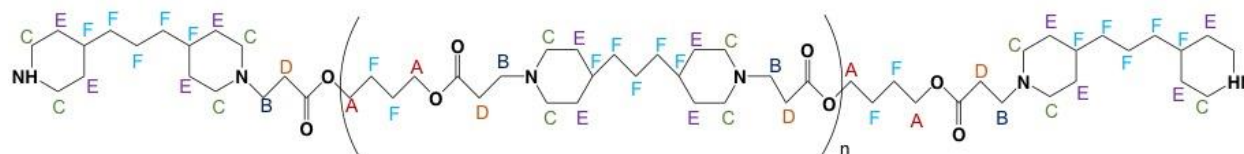


Figure 3.3: **A2** structure and NMR characterisation

Monomers ratio: 1.1 (amine): 1.0 (diacrylate)

Solvent stability: DCM and CDCl₃

MLog P: 4.23

MW (GPC): (1860-1876), **n=3**

Zeta potential: +20.35 mV (± 0.94) at pH5, +20.57 mV (± 1.26) at pH7.4

Appearance: White solid

¹H NMR (500 MHz, CDCl₃) δ (ppm): 4.01 (m, 16H) (A), 2.79 (t, *J* = 14.9 Hz, 16H) (B), 2.53 (m, 40H) (C), 1.81 (m, 16H) (D), 1.58 (m, 40H) (E), 1.16 (m, 56H) (F).

¹³C NMR (126 MHz, CDCl₃) δ (ppm): 172.50 (C=O), 64.07 (O-CH₂), 53.16 (NH₂-CH₂), 36.31 (NH₂-CH₂-Pip), 34.95 (NH₂-CH₂-Pip), 31.80 (-CH-C=O), 25.31 (Pip-CH₂-CH₂-Pip), 23.63 (CH₂-CH₂).

The molecular structure of **A2** is composed by 6 parts (2a-appendix). Protons of the group A, as observed for **A1**, correspond to the -CH₂ near to the oxygen and also in this case there are

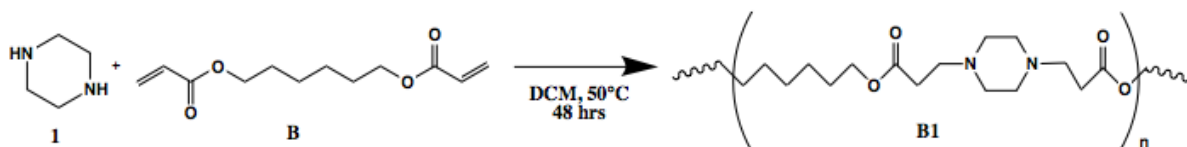
in total 16H, especially 12H belonging to the 3 repeat units and 4H included in the methylene groups of the final part of the molecule. Protons of the group B represent the -CH₂ affected by the nearness of the nitrogen, whereas protons of the groups C and E are characteristics of the -CH₂ of the piperidine. In particular, the 40H of the group C are representative of the methylene groups near the nitrogen of the piperidine, instead those of the group E (40H) near the aliphatic chain between the two piperidine. Finally, protons of the group D correspond to the -CH₂ groups near to the carbonyl group, and those of the group F are correlated to the hydrocarbon -CH of the piperidine and to the methylene groups of the aliphatic chains of both piperidine and diacrylate monomers. Analysing the ¹³CNMR (2b-appendix), similarly to A1, the carbon of the carbonyl group was at 172.50 ppm and those bonded to heteroatoms such as nitrogen and oxygen ranged between 64.07-53.16 ppm. For A2, the signals at 36.31 ppm and at 34.95 ppm were equal to the carbons of the methylene groups of the piperidine, whereas the carbon of the -CH near to the carbonyl group was at 31.80 ppm. Finally, the carbons of the aliphatic chains of the piperidine and diacrylate were respectively found at 25.31 ppm and 23.63 ppm.

The molecular structure of A3 is constituent of 6 groups as well as A2 (3a-appendix). The chemical shifts at 4.12-4.07 ppm correspond to the protons of the group A representative of the -CH₂ near the oxygen, and group B involves the protons of the methylene groups bonded to the nitrogen (16H) plus those of the 2 methyl groups of the nitrogen ending the polymer (6H). Moreover, the signals of the group C belong to the protons of the -CH₂ next to the carbonyl group, whereas those of the group D are part of the methylene groups of the aliphatic chain of the amine monomer. Finally, the protons of the group E and F respectively correspond to the -CH₂ of the aliphatic groups of the diacrylate A and to the methyl groups bonded to the nitrogen of the amine 3. On the other hand, from the ¹³CNMR (3b-appendix), the signal at 172.7 ppm is equal to the carbon of the carbonyl group, and for the carbons bonded to the nitrogen and the oxygen the signal ranged between 64.36-53.96 ppm. In addition, the carbon of the methyl group bonded to the nitrogen ending the homopolymer was at 61.96 ppm, whereas those of the internal methyl groups correlated to the nitrogen were between 25.25 and 23.22 ppm. In the end, the carbons belonging to the methylene groups of the aliphatic chain of the amine provided a chemical shift of 53.96 ppm, whereas those of the diacrylate shifted to 29.30 ppm.

B1

Chemical procedure

Compound **B1** was prepared by mixing Piperazine (1) (4.4 mMol, 379.016 mg) and 1,6 hexanediol diacrylate (B) (4.0 mMol, 905.08 mg) followed by precipitation in diethyl ether (scheme 3.5). Yield 99%.



Scheme 3.5: Reaction scheme of compound **B1**

Chemical identification

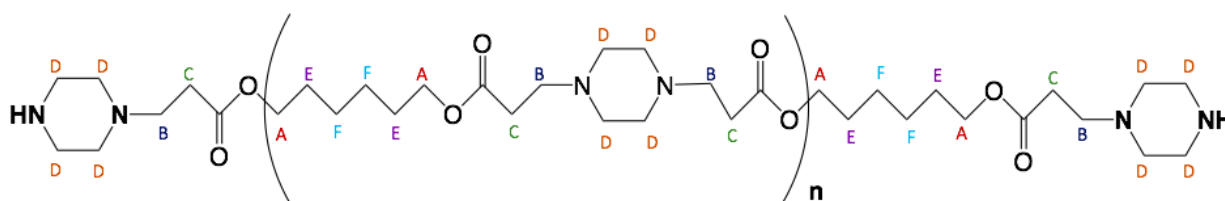


Figure 3.5: **B1** structure and NMR characterisation

Monomers ratio: 1.1 (amine): 1.0 (diacrylate)

Solvent stability: DCM and CDCl₃

MLog P: 0.51

MW (GPC): (1883-2148), **n=4**

Zeta potential: +19.53mV (± 0.55) at pH5, +17.97mV (± 2.01) at pH7.4

Appearance: Yellowish viscous oil

¹H NMR (500 MHz, CDCl₃) δ (ppm): 4.04 (s, 20H) (A), 3.97 – 2.75 (m, 20H) (B), 2.66 (dd, *J* = 19.7, 12.6 Hz, 20H) (C), 2.55 – 2.42 (m, 48H) (D), 1.68 – 1.56 (m, 20H) (E), 1.41 – 1.29 (m, 20H) (F).

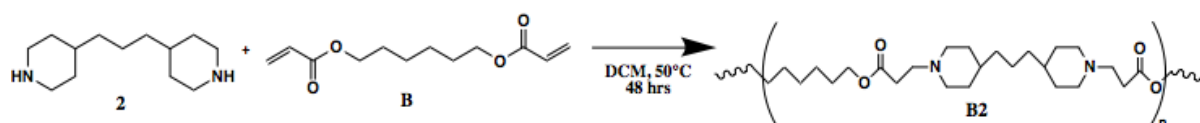
¹³C NMR (126 MHz, CDCl₃) δ (ppm): 171.88 (C=O), 63.62 (O-CH₂), 52.03 (NH₂-CH₂), 32.10 (-CH₂-C=O), 28.60 (O-CH₂-CH₂-CH₂-O) 25.50 (R-CH₂-CH₂-R).

Considering the proton NMR for the PBAE B1 (4a-appendix), the molecular structure of polymer is quite similar to A1, with the difference of 2 more methylene groups in the aliphatic chain of the diacrylate monomer. Therefore, in this case there are 6 groups of protons instead of 5. Protons of the group A correspond to 20H as part of the $-CH_2$ near the oxygen: 16H belonging to the 4 repeat units and 4H to the $-CH_2$ of the end group of the molecule. Furthermore, protons of the groups B, C and D represent respectively protons of the methylene groups bonded to the nitrogen (B), to the carbonyl group (C), and those included in the ring of the piperazine (D). Finally, groups E and F constitute the protons of the $-CH_2$ of the backbone of the diacrylate: in particular, those of the group E are bonded to the methylene groups near to the oxygen, whereas protons of the group F are part of internal $-CH_2$ of the aliphatic chain of the diacrylate with a shifted signal providing a chemical shift between 1.41 and 1.29 ppm. Additionally, also the signals of the carbons obtained by the ^{13}C NMR (4b-appendix) confirmed the similarities observed between the structures of A1 and B1. For instance, the carbon of the carbonyl group was found at 171.88 ppm, those bonded to the heteroatoms N and O ranged between 63-52 ppm, and the carbon of the methylene groups near the carbonyl was at 32.10 ppm. Finally, also the carbons bonded to the protons of the groups E and F showed different chemical shifts which were respectively equal to 28.60 ppm and 25.50 ppm.

B2

Chemical procedure

The secondary amine 4,4 trimethylenepiperidine (2) (4.4 mMol, 925.58 mg) was conjugated to 1,6 hexanediol diacrylate (B) (4.0 mMol, 905.08 mg) to give compound **B2** (scheme 3.6) using DCM as solvent of the reaction in oil bath at 50°C for 48 hours. This poly (β -amino) ester was the result of precipitation of the mixture of reaction in diethyl ether. Yield 99%.



Scheme 3.6: Reaction scheme of compound **B2**

Chemical identification

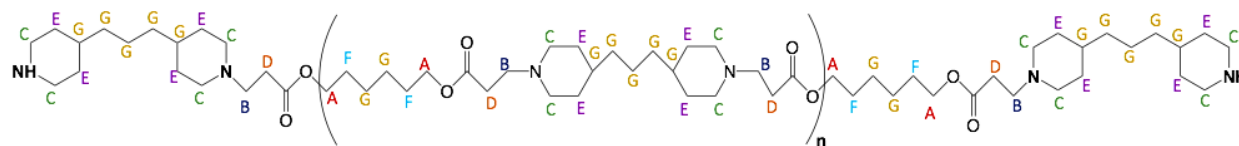


Figure 3.6: **B2** structure and NMR characterisation

Monomers ratio: 1.1 (amine): 1.0 (diacrylate)

Solvent stability: DCM and CDCl₃

MLog P: 4.8

MW (GPC): (2558-2579), **n=4**

Zeta potential: +19.07 mV (\pm 1.7) at pH5, +19.17 mV (\pm 0.51) at pH7.4

Appearance: White solid

¹H NMR (500 MHz, CDCl₃) δ (ppm): 3.98 (s, 20H) (A), 2.80 (m, 20H) (B), 2.65 – 2.33 (m, 48H) (C), 1.99 – 1.78 (m, 20H) (D), 1.52 (d, J = 35.3 Hz, 48H) (E), 1.27 (d, J = 26.4 Hz, 20H) (F), 1.15 (m, 68H) (G).

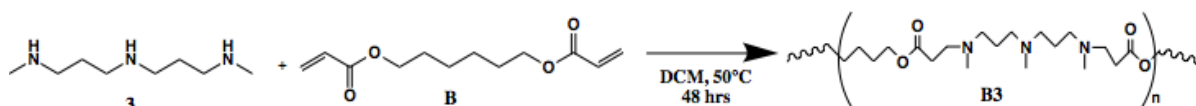
¹³C NMR (126 MHz, CDCl₃) δ (ppm): 172.63 (C=O), 64.76 (O-CH₂), 53.77 (NH₂-CH₂), 36.64 (NH₂-CH₂-Pip), 35.54 (NH₂-CH₂-Pip), 32.23 (-CH-C=O), 28.5 (Pip-CH₂-CH₂-Pip), 25.56 (-R-CH₂-CH₂-CH₂-CH₂-R) 23.63 (Pip-CH₂-CH₂-CH-CH₂-CH₂-Pip), (R-CH₂-CH₂-R).

The molecular structure of B2 (5a-appendix) is similar to the one of A2 showing 2 further methylene groups typical of the structure of the diacrylate B. Thus, also in this case, one additional group of protons was detected presenting overall 7 different groups of protons. Therefore, protons of the group A are representative of the $-CH_2$ near the oxygen and as observed for B1 the repeat units are 4 (16H) plus 4H belonging to the $-CH_2$ of the end group of the homopolymer. Protons of the group B correspond to the methylene groups near the nitrogen; those of the groups C and E to the $-CH_2$ of the piperidine, whereas protons of the D represent the $-CH_2$ the carbonyl groups. Finally, protons of the group F are part of the $-CH_2$ near the methylene group bonded to the oxygen but belonging to the aliphatic chain of the diacrylate, and the group G includes protons of the $-CH$ and $-CH_2$ of the hydrophobic chain of the amine plus the internal $-CH_2$ of the aliphatic chain of the diacrylate. The ^{13}C NMR (5b-appendix) allowed the identification of the carbons bonded to the protons evaluated by 1H NMR: the signals were similar to those of A2 except for the carbons of the methylene groups of the diacrylate which showed chemical shifts equal to 25.56 ppm for the carbons bonded to the protons of the group F and 23.63 ppm for those correlated to the group G.

B3

Chemical procedure

Compound **B3** (scheme 3.7) was synthesised by addition of the amine N,N-Bis[3-(methylamino)propyl]methylamine (**3**) (4.4 mMol, 762.52 mg) to 1,6 hexanediol diacrylate (**B**) (4.0 mMol 905.08 mg) in DCM at 50°C. After 48 hours, the mixture of reaction was treated with diethyl ether allowing the precipitation of the crude product in DCM. Yield 99%.



Scheme 3.7: Reaction scheme of compound **B3**

Chemical identification

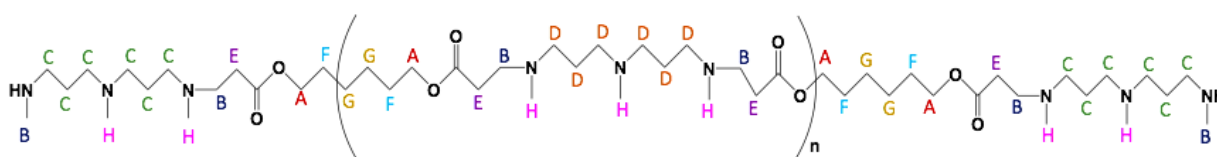


Figure 3.7: **B3** structure and NMR characterisation

Monomers ratio: 1.1 (amine): 1.0 (diacrylate)

Solvent stability: DCM and CDCl₃

MLog P: 1.22

MW (GPC): (2260-2317), n=4

Zeta potential: +15.1 mV (± 0.85) at pH5, +14.53 mV (± 0.51) at pH7.4

Appearance: Yellowish viscous oil

¹H NMR (500 MHz, CDCl₃) δ (ppm): 4.06 (s, 20H) (A), 2.79 – 2.60 (m, 26H) (B), 2.58 – 2.34 (m, 24H) (C), 2.34 – 2.09 (m, 48H) (D), 2.05 – 1.90 (m, 20H) (E), 1.74 (d, J = 61.1 Hz, 20H) (F), 1.63 – 1.44 (m, 20H) (G), 1.34 (s, 48H) (H).

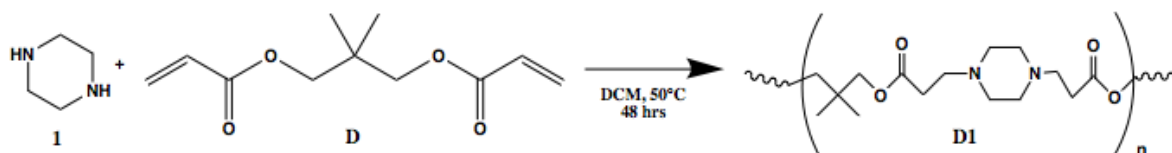
¹³C NMR (126 MHz, CDCl₃) δ (ppm): 172.56 (C=O), 64.30 (O-CH₂), 62.01 (NH-CH₃), 52.43 (NH₂-CH₂), 41.66 (R-CH₂-CR₂-CH₂-O), 32.49(-CH-C=O), 29.79 (R-CH₂-CH₂-NH), 26.29 (CH₃-NR₂), 22.37 (CH₃-NR₂).

The molecular structure of B3 presents 2 more methylene groups typical of the aliphatic chain of the diacrylate B. For instance, considering the proton NMR (6a-appendix), there are 8 groups of protons for this polymer and especially those of the group G belong to the internal -CH₂ of the hydrophobic chain of the diacrylate monomer. This was confirmed by the ¹³CNMR (6b-appendix) showing a chemical shift of 29.79 ppm correspondent to the carbons bonded to the protons of the group G. For the other groups (A-H) similarities were observed between the PBAE A3 and B3.

D1

Chemical procedure

Compound **D1** was gained by polymerisation between Piperazine (**1**) (4.4 mMol, 379.016 mg) and neo-pentyl glycol diacrylate (**D**) (4.0 mMol, 848.96 mg) at 50°C in DCM for 48 hours (scheme 3.8), followed by precipitation in diethyl ether. Yield 99%.



Scheme 3.8: Reaction scheme of compound **D1**

Chemical identification

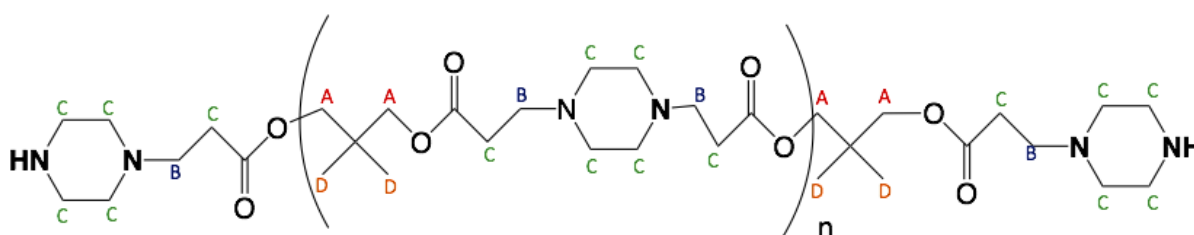


Figure 3.8: **D1** structure and NMR characterisation

Monomers ratio: 1.1 (amine): 1.0 (diacrylate)

Solvent stability: DCM and CDCl₃

MLog P: 0.18

MW (GPC): (1420-1440), n=3

Zeta potential: +16.21mV (± 1.67) at pH5, +15.46mV (± 0.76) at pH7.4

Appearance: Yellowish viscous oil

¹H NMR (500 MHz, CDCl₃) δ (ppm): 3.86 (s, 16H) (A), 2.77 – 2.58 (m, 16H) (B), 2.57 – 2.33 (m, 60H) (C), 0.89 (s, 24H) (D).

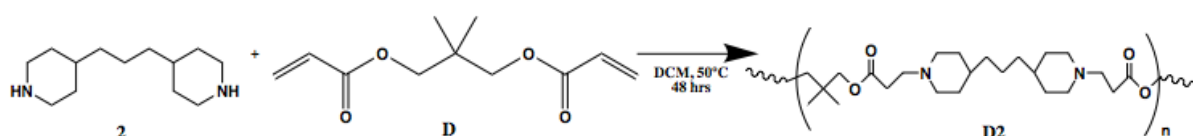
¹³C NMR (126 MHz, CDCl₃) δ (ppm): 171.69 (C=O), 68.96 (O-CH₂), 52.93 (NH₂-CH₂), 34.90 (CH₃-C-CH₃), 32.01 (-CH₂-C=O), 21.64 (-CH₃-CR₃).

The molecular structure of D1 can be divided into only 4 groups considering the proton NMR reported in the spectrum 7a in the appendix section. Protons of the group A are representative of the methylene groups bonded to the oxygen showing a chemical shift of 3.86 ppm. In particular, 12H belong to the 3 repeat units but 4H are part of the end group of the polymer. Moreover, protons of the group B include the -CH₂ near to the nitrogen whereas those of the group C involve respectively the methylene groups of the piperazine and those bonded to the carbonyl groups. Finally, in this molecule there is a quaternary carbon bonded to 2 methyl groups (-CH₃) whose protons belong to the group D: 18H included in the 3 repeat units and 6H in the end group of the PBAE. In the ¹³CNMR (7b-appendix), the carbon correspondent to the carbonyl group was found at 171.69 ppm, whereas those near to the heteroatoms were between 63-52 ppm. Finally, the chemical shift for the quaternary carbon was at 34.90 ppm, instead those at 32.01 ppm and at 21.64 ppm were respectively correspondent to the carbon near the carbonyl group and to the methyl groups of the aliphatic chain of the diacrylate D.

D2

Chemical procedure

Compound **D2** (scheme 3.9) was synthesised by adding the secondary amine 4,4-trimethylenepiperidine (**2**) (4.4 mMol, 925.58 mg) to neo pentyl diacrylate (**D**) (4.0 mMol, 848.96 mg) in DCM at 50°C. After 48 hours, the crude product was obtained through precipitation in diethyl ether. Yield 99%.



Scheme 3.9: Reaction scheme of compound **D2**

Chemical identification

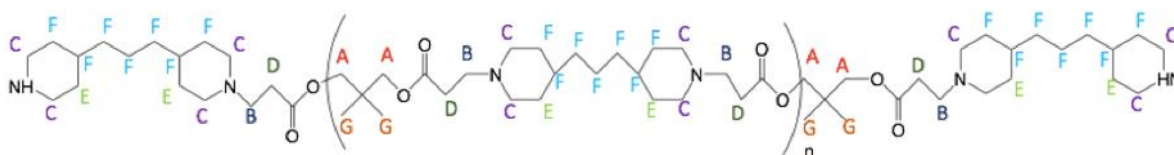


Figure 3.9: **D2** structure and NMR characterisation

Monomers ratio: 1.1 (amine): 1.0 (diacrylate)

Solvent stability: DCM and CDCl₃

MLog P: 4.52

MW (GPC): (1820-1905), n=3

Zeta potential: +19.23 mV (± 1.15) at pH5, +18.27 mV (± 1.21) at pH7.4

Appearance: White solid

¹H NMR (500 MHz, CDCl₃) δ (ppm): 3.86 (s, 16H) (A), 2.88 (d, J = 10.4 Hz, 16H) (B), 2.61 (m, 40H) (C), 1.96 (t, J = 9.6 Hz, 16H) (D), 1.65 (m, 20H) (E), 1.21 (m, 60H) (F), 0.93 (s, 24H) (G).

¹³C NMR (126 MHz, CDCl₃) δ (ppm): 171.48 (C=O), 68.96 (O-CH₂), 53.50 (NH₂-CH₂), 36.44 (NH₂-CH₂-Pip), 34.84 (CH₃-C-CH₃), 32.04 (-CH-C=O), 23.60 (Pip-CH₂-CH₂-Pip), 21.70 (-CH₃-CR₃).

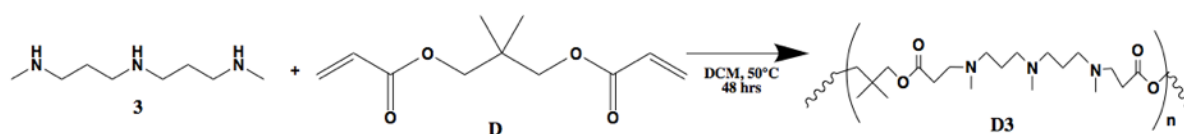
Considering the ¹HNMR for D2 (8a-appendix), the molecule is constituent by 7 different

groups of protons. For example, the group A comprehends the protons of the methylene groups near to the oxygen, and those of the group B are part of the $-CH_2$ near the nitrogen. Furthermore, the protons of the group C are representative of the $-CH_2$ of the piperidine near to the nitrogen, whereas those near to the $-CH$ conjugating the aliphatic chain of the amine to the ring of the piperidine belong to the group E. The protons of the group D correspond to the methylene groups near to the carbonyl groups, and the protons of the group F involves the hydrophobic chain of the amine monomer. Finally, protons correlated to the methyl groups of the diacrylate D are part of the group G. This was confirmed by the ^{13}C NMR, where the carbon of the carbonyl group was at 171.48 ppm and those bonded to the heteroatoms ranged between 68.96 ppm and 53.50 ppm. Then, the carbons of the methylene groups of the piperidine were at 36.44 ppm, whereas those of the aliphatic chain of the amine were found at 23.60 ppm. Finally, the quaternary carbon was equal to 34.84 ppm and the carbons of the methyl group correspondent to 21.70 ppm.

D3

Chemical procedure

Compound **D3** (scheme 3.10) was gained by polymerisation between the amine N,N-Bis[3-(methylamino)propyl]methylamine (**3**) (4.4 mMol, 762.52 mg) and neo pentyl diacrylate (**D**) (4.0 mMol, 848.96 mg) in DCM at 50°C. Precipitation in diethyl ether allowed the purification of the crude product. Yield 99%.



Scheme 3.10: Reaction scheme of compound **D3**

Chemical identification

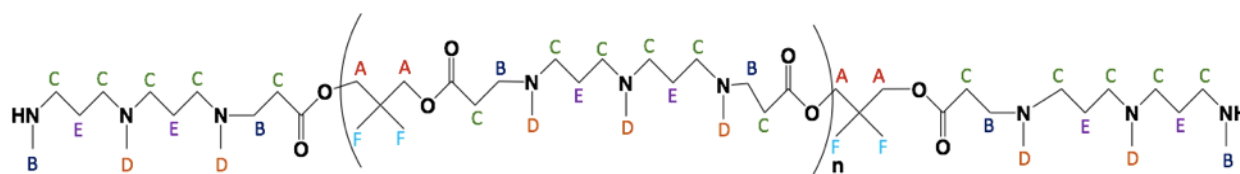


Figure 3.10: **D3** structure and NMR characterisation

Monomers ratio: 1.1 (amine): 1.0 (diacrylate)

Solvent stability: DCM and CDCl₃

MLog P: 1.63

MW (GPC): (1513-1517), $n=3$

Zeta potential: +22.99 mV (± 0.85) at pH5, +22.53 mV (± 0.51) at pH7.4

Appearance: Yellowish viscous oil

¹H NMR (500 MHz, CDCl₃) δ (ppm): 3.87 (s, 16H) (A), 2.73 – 2.62 (m, 22H) (B), 2.53 – 2.42 (m, 56H) (C), 2.24 – 2.16 (m, 39H) (D), 0.96 – 0.90 (m, 20H) (E), 0.88 (s, 24H) (F).

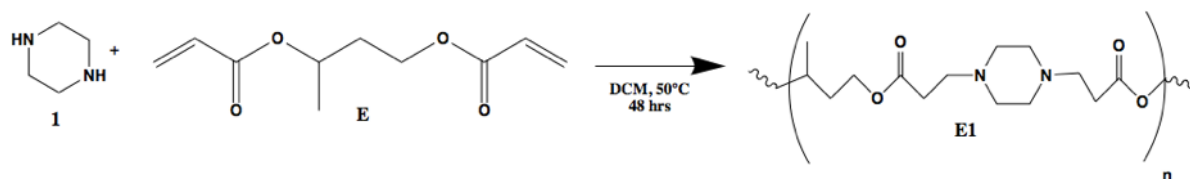
¹³C NMR (126 MHz, CDCl₃) δ (ppm): 172.7 (C=O), 69.06 (O-CH₂), 67.34 (NH-CH₃), 54.59 (NH₂-CH₂), 41.77 (R-CH₂-CR₂-CH₂-O), 34.90 (-CH₂-C=O), 32.68 (R-CH₂-CH₂-NH), 22.19 (CH₃-NR₂), 21.29 (CH₃-NR₂).

The molecular structure of D3 is composed by 6 parts considering the ^1H NMR (9a-appendix) as well as observed for the PBAEs A3. Groups A and B correspond to the protons of the methylene groups near oxygen and nitrogen plus to the methyl groups bonded to the external nitrogen at the end of the molecule, and groups C and E to those of the $-\text{CH}_2$ belonging to the aliphatic chain of the amine monomer and near the carbonyl groups. Additionally, the group D includes protons of the methyl groups bonded to nitrogen of the amine, whereas group F represent protons of the $-\text{CH}_3$ which a part of the hydrophobic chain of the diacrylate D. On the other hand, considering the ^{13}C NMR (9b-appendix), similarly to A3, the chemical shift of the carbon of the carbonyl group was found at 172.7 ppm, and those bonded to the nitrogen and oxygen ranged between 69-67 ppm. The carbons of the methyl groups bonded to the external nitrogen of the amine was at 67.34 ppm, whereas those of the methylene groups of the aliphatic chain of the amine ended to 32.68 ppm. Finally, the carbons of the $-\text{CH}_3$ bonded to the internal nitrogen of the amine ranged between 22.19 and 21.29 ppm.

E1

Chemical procedure

Compound **E1** was prepared by mixing Piperazine (**1**) (4.4 mMol, 379.016 mg) and 1,3 butanediol diacrylate (**E**) (4.0 mMol, 782.88 mg) for 48 hours at 50°C in DCM, followed by after precipitation in diethyl ether. Yield 99% (figure 3.11).



Scheme 3.11: Reaction scheme of compound **E1**

Chemical identification

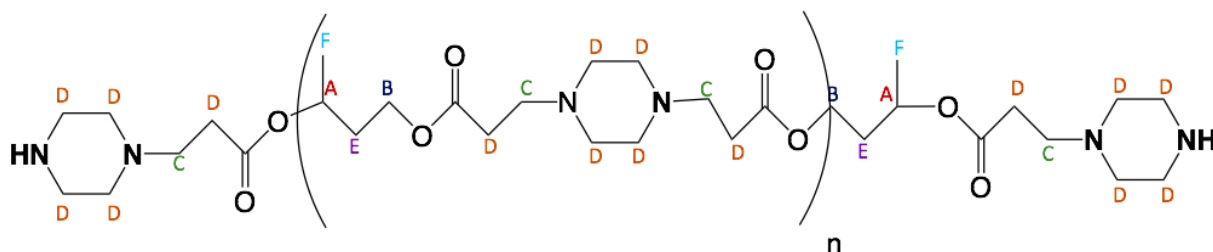


Figure 3.11: **E1** structure and NMR characterisation

Monomers ratio: 1.1 (amine): 1.0 (diacrylate)

Solvent stability: DCM and CDCl₃

MLog P: -0.19

MW (GPC): (1770-1778), *n*=4

Zeta potential: + 20.37mV (± 1.92) at pH5, +20.46mV (± 2.34) at pH7.4

Appearance: Yellowish viscous oil

¹H NMR (500 MHz, CDCl₃) δ (ppm): 4.83 (t, *J* = 22.8 Hz, 5H) (A), 3.95 (s, 10H) (B), 2.51 (m, 20H) (C), 2.32 (m, 68H) (D), 1.63 (m, 10H) (E), 1.08 (s, 15H) (F).

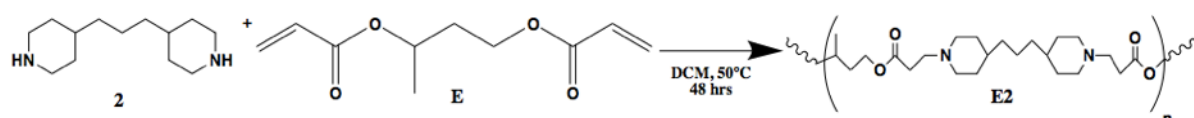
¹³C NMR (126 MHz, CDCl₃) δ (ppm): 171.87 (C=O), 67.86 (O-CH₂), 53.35 (NH₂-CH₂), 52.52 (NH₂-CH₂), 34.70 (-CH₂-C=O), 32.20 (-O-CHR-CH₃), 20.03 (-CH-CH₃).

Analysing the ^1H NMR (10a-appendix), the PBAE E1 is constituent of 6 main areas. In this case, the group A is representative of the carbon-hydrogen bond (-CH) near the oxygen (5H), whereas the group B corresponds to the protons of the methylene groups near the oxygen and the carbonyl group (10H). Moreover, protons of the group C belong to the $-\text{CH}_2$ near the nitrogen and those of the group D are part of the methylene groups of the piperazine. Finally, the groups E and F represent the protons of the short hydrophobic chain and the methyl groups conjugated to the -CH of the diacrylate E. From the ^{13}C NMR (10b-appendix) the carbon of the carbonyl group showed a chemical shift of 171.87 ppm; those of $-\text{CH}_2$ correlated to the heteroatoms were between 67-53 ppm, and the carbons of the methylene groups of the piperazine had a chemical shift of 52.52 ppm. Furthermore, the carbon of the $-\text{CH}_2$ near the carbonyl group was at 34.70 ppm; the signal of the -CH provided a chemical shift of 32.20 ppm, and the carbons of the methyl group and bonded to the -CH were at 20.02 ppm.

E2

Chemical procedure

Compound **E2** (scheme 3.12) was gained by conjugation between the secondary amine 4,4 trimethylenepiperidine (**2**) (4.4 mMol, 925.58 mg) and 1,3 butanediol diacrylate (**A**) (4.0 mMol, 782.88 mg) in DCM at 50°C followed by precipitation in diethyl ether. Yield 99%.



Scheme 3.12: Reaction scheme of compound **E2**

Chemical identification

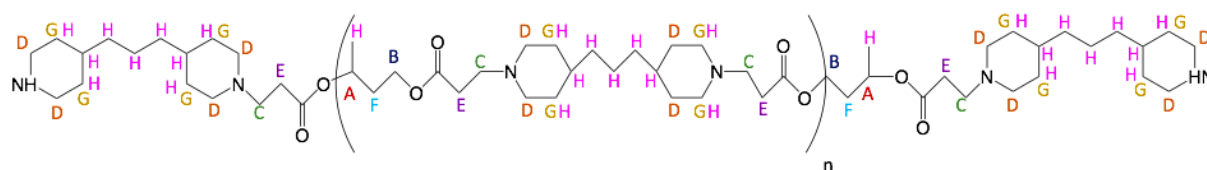


Figure 3.12: **E2** structure and NMR characterisation

Monomers ratio: 1.1 (amine): 1.0 (diacrylate)

Solvent stability: DCM and CDCl₃

MLog P: 4.23

MW (GPC): (2072-2376), n=4

Zeta potential: +12.13 mV (± 0.25) at pH5, +12.17 mV (± 0.41) at pH7.4

Appearance: White solid

¹H NMR (500 MHz, CDCl₃) δ (ppm): 4.89 (m, 5H) (A), 3.96 (m, 10H) (B), 2.75 (d, *J* = 10.2 Hz, 20H) (C), 2.39 (dq, *J* = 14.7, 7.2 Hz, 48H) (D), 1.85 (t, *J* = 9.3 Hz, 20H) (E), 1.71 (m, 10H) (F), 1.47(m, 24H) (G), 1.07 (m, 87H) (H).

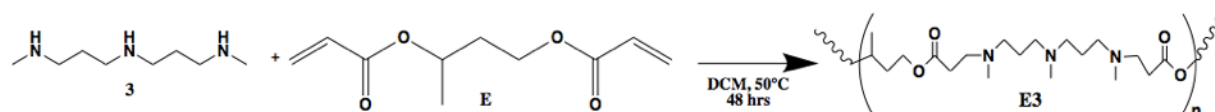
¹³C NMR (126 MHz, CDCl₃) δ (ppm): 172.11 (C=O), 61.08 (O-CH₂), 53.13 (NH₂-CH₂), 36.84 (NH₂-CH₂-Pip), 34.84 (NH₂-CH₂-Pip), 32.20 (-O-CHR-CH₃), 31.53 (-CH₂-C=O), 23.63 (Pip-CH₂-CH₂-Pip), 21.87 (CH₃-R).

The molecular structure of E2 could be divided into 8 groups of protons (11a-appendix). Protons of the group A correspond to the -CH of the diacrylate E; those of the group B are part of the methylene groups near the oxygen whereas protons of the group C belong to the -CH₂ near the nitrogen. The groups D, G and H are representative of the protons of the -CH₂ of the piperidine, the aliphatic chain of the amine and the methyl groups bonded to the -CH of the diacrylate. Finally, the protons of the group E and F are conjugated to the methylene groups near the carbonyl groups and to the -CH₂ of the short chain of the diacrylate E. Considering the ¹³CNMR (11b-appendix), the carbon of the carbonyl group was at 172.11 ppm; those of the heteroatoms at 63-51 ppm and those belonging to the methylene groups of the piperidine ranging between 36-34 ppm. The signal for the -CH of the diacrylate was detected at 32.20 ppm; the carbon of the -CH₂ near the carbonyl group was found at 31.53 ppm, whereas the carbons of both methylene groups of the aliphatic chain of the amine and the methyl groups of the diacrylate were respectively at 23.63 ppm and 21.87 ppm.

E3

Chemical procedure

Compound **E3** (scheme 3.13) was gained by mixing N,N-Bis[3-(methylamino)propyl]methylamine (**3**) (4.4 mMol, 762.52 mg) and 1,3 butanediol diacrylate (**A**) (4.0 mMol, 782.88 mg) in DCM at 50°C. After 48 hours, the polymer was recovered via precipitation in diethyl ether. Yield 99%.



Scheme 3.13: Reaction scheme of compound **E3**

Chemical identification

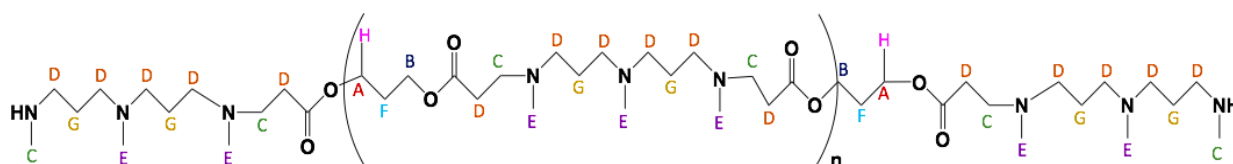


Figure 3.13: **E3** structure and NMR characterisation

Monomers ratio: 1.1 (amine): 1.0 (diacrylate)

Solvent stability: DCM and CDCl₃

MLog P: 0.59

MW (GPC): (1882-1913), **n=4**

Zeta potential: +14.66 mV (± 0.85) at pH5, +12.8 mV (± 0.51) at pH7.4

Appearance: Yellowish viscous oil

¹H NMR (500 MHz, CDCl₃) δ (ppm): 4.91 (m, 5H) (A), 4.08 – 3.95 (m, 10H) (B), 2.66 – 2.54 (m, 26H) (C), 2.51 – 2.24 (m, 68H) (D), 2.14 (s, 48H) (E), 1.92 (s, 10H) (F), 1.63 (s, 24H) (G), 1.10 (s, 15H) (H).

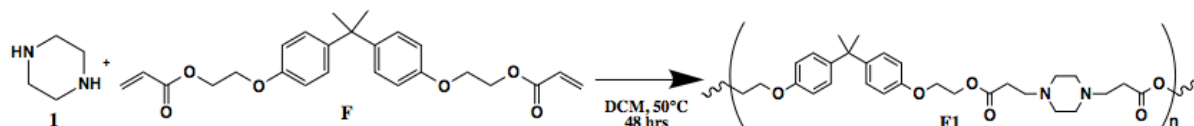
¹³C NMR (126 MHz, CDCl₃) δ (ppm): 172.22 (C=O), 65.75 (O-CH₂), 60.45 (NH-CH₃), 52.65 (NH₂-CH₂), 41.87 (R-CH₂-CR₂-CH₂-O), 34.75 (-CH-C=O), 32.65 (R-CH₂-CH₂-NH), 32.20 (-O-CHR-CH₃), 24.02 (CH₃-NR₂), 20.09 (CH₃-R acrylate).

Considering the ^1H NMR (12a-appendix), the PBAE E3 could be split into 8 groups as observed for E2. Protons of the group A are conjugated to the -CH of the diacrylate; those of the group B and C belong to the methylene groups near respectively oxygen and nitrogen plus the methyl groups bonded to the external nitrogen of the end of the homopolymer. Then, the group D includes the protons of $-\text{CH}_2$ near the carbonyl groups plus those involved in the $-\text{CH}_2$ of the aliphatic chain of the amine as well as protons of the group G. Finally, the groups F and H involves protons of both the $-\text{CH}_2$ of the chain and of the methyl groups bonded to the -CH of the diacrylate E. The identification of E3 via ^1H NMR was confirmed by ^{13}C NMR (12b-appendix). For instance, the carbon of the carbonyl group was at 172.22 ppm; those of the CH_2 near oxygen and nitrogen were between 65-52 ppm, and those of the methyl groups conjugated to the external nitrogen at the end of the molecule was at 60.45 ppm. Moreover, the carbons of the $-\text{CH}_2$ of the piperidine provided a chemical shift of 52.65 ppm, whereas those of the aliphatic chain of the amine were found at 41-32 ppm. Then, the carbon of $-\text{CH}_2$ near the carbonyl group was at 34.75 ppm; the one of -CH was at 32.20 ppm and the carbons of the methyl groups of the diacrylate and the amine ranged between 24-20 ppm.

F1

Chemical procedure

Compound **F1** was synthesised by adding piperazine (1) (4.4 mMol, 379.016 mg) to bisphenol A ethoxylate diacrylate (F) (4.0 mMol, 2040 mg) (scheme 3.14). The polymer was recovered via precipitation in diethyl ether. Yield 99%.



Scheme 3.14: Reaction scheme of compound **F1**

Chemical identification

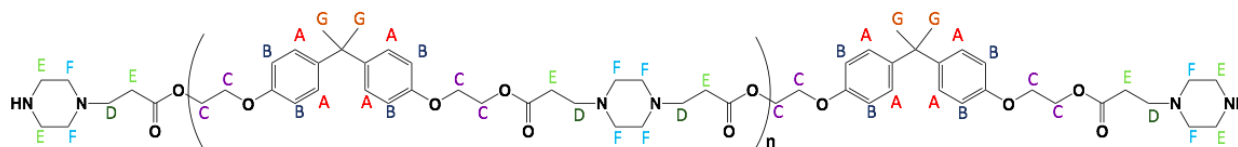


Figure 3.14: **F1** structure and NMR characterisation

Monomers ratio: 1.1 (amine): 1.0 (diacrylate)

Solvent stability: DCM and CDCl₃

MLog P: 2.06

MW (GPC): (2584-2801), n=4

Zeta potential: +29.57mV (± 2.01) at pH5, +29.9mV (± 1.97) at pH7.4

Appearance: Yellowish viscous oil

¹H NMR (500 MHz, CDCl₃) δ (ppm): 7.01 (d, *J* = 7.1 Hz, 20H) (A), 6.70 (d, *J* = 7.6 Hz, 20H) (B), 4.34 – 4.10 (m, 40H) (C), 3.80 – 3.64 (m, 20H) (D), 2.68 – 2.53 (m, 28H) (E), 2.49 – 2.26 (m, 40H) (F), 1.51 (s, 30H) (G).

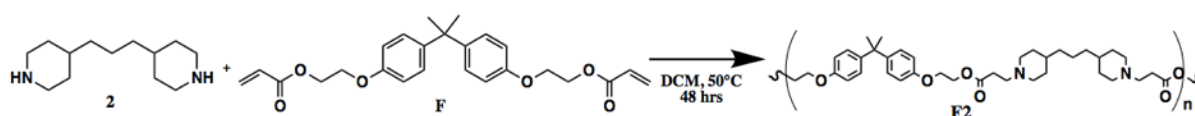
¹³C NMR (126 MHz, CDCl₃) δ (ppm): 172.85 (C=O), 156.42 (O-C-Ar), 143.30 (Ar-C-C-R₃), 127.67 (R₃C-CH-Ar), 113.91 (O-R₂C-CH-Ar), 66.27 (CH₂-O), 63.42 (CH₂-O), 53.46 (CH₂-Pip), 52.25 (CH₂-NH₂), 41.94 (CH₃-C-CH₃), 32.19 (-CH₂-C=O), 31.69 (R₃C-CH₃).

The PBAE F1 is composed by 7 groups of protons (13a-appendix). For example, the group A and B are representative of the protons of the -CH of the aromatic rings of the diacrylate F, whereas the protons of the group C are part of the -CH₂ of the aliphatic chain of the diacrylate near to the oxygen. Furthermore, the groups D and E correspond to the protons of -CH₂ near the nitrogen and those of the external -CH₂ of the piperazine at the end of the molecule plus the protons of the methylene groups near the carbonyl groups. Finally, the rest the -CH₂ of the piperazine are represented by the protons of the group F whereas the group G includes protons of the methyl groups bonded to the quaternary carbon of the diacrylate F. From the ¹³CNMR (13b-appendix), the carbon of the carbonyl group was at 171.85 ppm; the quaternary carbons of the aromatic rings near the oxygen ranged between 156-143 ppm, whereas those of the -CH of the 2 aromatic rings correspondent to 127-113 ppm. Then, carbons of the -CH₂ near the oxygen showed a chemical shift of 66-63 ppm, but those conjugated to the protons of the piperazine were found at 52 ppm. To conclude, the carbons of the -CH₂ near the carbonyl groups were at 32.19 ppm, whereas the quaternary carbon and the carbons of the methyl groups of the diacrylate F were respectively at 41.94 ppm and 31.69 ppm.

F2

Chemical procedure

Compound **F2** (scheme 3.15) was the result of mixing the secondary amine 4,4 trimethylenepiperidine (**2**) (4.4 mMol, 925.58 mg) and bisphenol A ethoxylate diacrylate (**F**) (4.0 mMol, 2040 mg) adopting DCM as solvent of reaction. The synthesis was pursued at 50°C for 48 hours and the crude product was precipitated in diethyl ether. Yield 99%.



Scheme 3.15: Reaction scheme of compound **F2**

Chemical identification

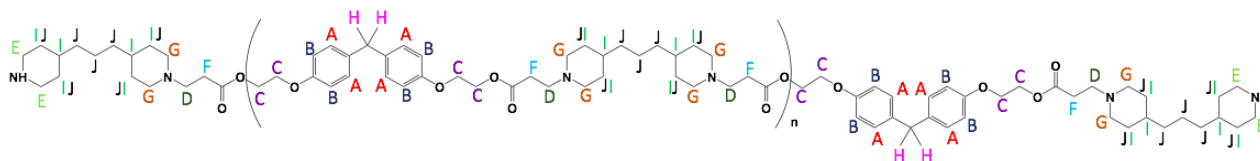


Figure 3.15: **F2** structure and NMR characterisation

Monomers ratio: 1.1 (amine): 1.0 (diacrylate)

Solvent stability: DCM and CDCl₃

MLog P: 5.62

MW (GPC): (2749-2800), **n=3**

Zeta potential: +20.7 mV (± 3.12) at pH5, +21.2 mV (± 0.4) at pH7.4

Appearance: White solid

¹H NMR (500 MHz, CDCl₃) δ (ppm): 7.03 (s, 16H) (A), 6.72 (s, 16H) (B), 4.39 – 3.92 (m, 32H) (C), 3.84 – 3.69 (m, 16H) (D), 3.70 – 3.65 (m, 8H) (E), 2.79 (s, 16H) (F), 2.66 – 2.39 (m, 32H) (G), 1.88 (s, 24H) (H), 1.63 – 1.46 (m, 30H) (I), 1.27 – 1.02 (m, 50H) (J).

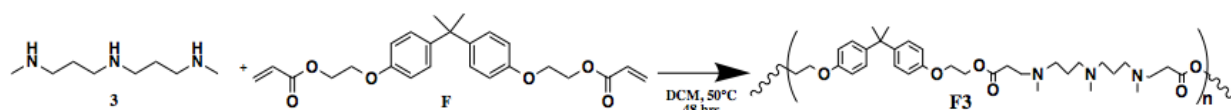
¹³C NMR (126 MHz, CDCl₃) δ (ppm): 172.49 (C=O), 156.41 (O-C-Ar), 143.34 (Ar-C-C-R₃), 127.68 (R₃C-CH-Ar), 113.92 (O-R₂C-CH-Ar), 65.80 (CH₂-O), 63.50 (CH₂-O), 53.54 (CH₂-NH₂), 41.94 (CH₃-C-CH₃), 32.01 (-CH₂-C=O), 36.64 (CH₂-Pip-NH), 32.25 (Alk-CH₂-Piperidine), 31.23 (R₃C-CH₃).

Considering the ^1H NMR (14a-appendix), the PBAE is constituted by 10 groups of protons. As observed for F1, the groups A and B correspond to the protons of aromatic rings of the diacrylate F, and the groups C and D belong to the $-\text{CH}_2$ near the oxygen and the nitrogen. Protons of the group E are representative of the external methylene groups of the piperidine in the end group of the polymer. Then, groups G, I and J comprehend protons of the $-\text{CH}_2$ of the piperidine plus those of the aliphatic chain of the amine. Finally, protons of the group F belong to the $-\text{CH}_2$ near to the carbonyl groups whereas those of the group H are part of the methyl groups of the diacrylate. Analysing the ^{13}C NMR (14b-appendix), the carbon of the carbonyl group was at 172.49 ppm, and the signals of the quaternary carbon of the aromatic rings were at 156-143 ppm. Furthermore, the $-\text{CH}$ of the aromatic rings were between 127 and 113 ppm but the chemical shifts provided by the carbons of the methylene groups near to the oxygen were found at 65-63 ppm. The carbons of the $-\text{CH}_2$ of the piperidine were at 53 ppm; those of the quaternary carbon was at 41.94 ppm and the carbons near to the carbonyl group at 32.01 ppm. Finally, carbons of the $-\text{CH}_2$ of the hydrophobic chain of the amine showed a chemical shift equal to 32.25 ppm, whereas those of the methyl group correspondent to 31.23 ppm.

F3

Chemical procedure

Compound **F3** (scheme 3.16) was the polymer resulting from the synthesis between N,N-Bis[3-(methylamino)propyl]methylamine (**3**) (4.4 mMol, 762.52 mg) and bisphenol A ethoxylate diacrylate (**F**) (4.0 mMol, 2040 mg) in DCM at 50°C. After 48 hours, the crude product was precipitated by using diethyl ether. Yield 99%.



Scheme 3.16: Reaction scheme of compound **F3**

Chemical identification

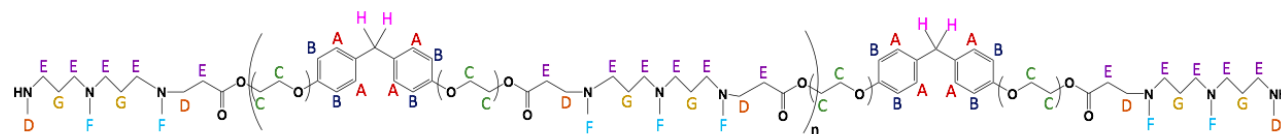


Figure 3.16: **F3** structure and NMR characterisation

Monomers ratio: 1.1 (amine): 1.0 (diacrylate)

Solvent stability: DCM and CDCl₃

MLog P: 2.34

MW (GPC): (3043-3080), **n=4**

Zeta potential: +28.7 mV (± 0.85) at pH5, +24.53 mV (± 0.53) at pH7.4

Appearance: Yellowish viscous oil

¹H NMR (500 MHz, CDCl₃) δ (ppm): 3.98 (m, 40H) (C), 3.85 – 3.76 (m, 26H) (D), 3.72 – 3.54 (m, 68H) (E), 2.76 – 2.52 (m, 48H) (F), 2.21 – 2.12 (m, 24H) (G), 1.57 (s, 30H) (H).

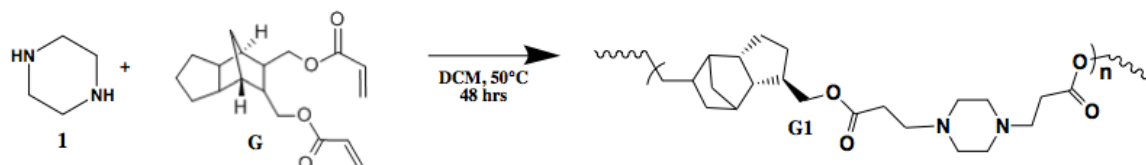
¹³C NMR (126 MHz, CDCl₃) δ (ppm): 172.52 (C=O), 156.37 (O-C-Ar), 143.50 (Ar-C-C-R₃), 127.74 (R₃C-CH₂-Ar), 113.95 (O-R₂C-CH₂-Ar), 67.35 (CH₂-O), 63.61 (CH₂-O), 52.54 (CH₂-NH₂), 41.48 (CH₃-C-CH₃), 31.92 (CH₂-C=O), 54.56 (R-CH₂-CH₂-NH), 41.88 (CH₃-NR₂), 31.34 (CH₃-R acrylate).

The molecular structure of F3 could be divided into 8 group of protons (15a-appendix). Group A and B correspond to the protons of the -CH of the aromatic rings of the diacrylate and those of the group C and D respectively to the -CH₂ near to the oxygen and nitrogen of both diacrylate and amine monomers. In addition, groups E and G represent the protons of the -CH₂ of the aliphatic chain of the amine whereas F and H respectively include protons of methyl groups of both diacrylate and amine. From the ¹³CNMR (15b-appendix) it was observed that the carbon of the carbonyl group was at 172.52 ppm; quaternary carbons of the aromatic rings ranged between 156-143 ppm; carbons of the -CH showed chemical shifts of 127-113 ppm and those of the methylene groups near the oxygen were between 67-63 ppm. Then, the quaternary carbons of the diacrylate correspondent to 41.48 ppm whereas those of the -CH₂ near the carbonyl group were at 31.92 ppm. Finally, the carbons of the methylene groups of the amine were at 54.56 ppm, and the those of the methyl groups of the diacrylate showed a chemical shift at 31.34 ppm.

G1

Chemical procedure

Compound **G1** was synthesised by adding Piperazine (**1**) (4.4 mMol, 379.016 mg) to tri-cyclodecane dimethanol diacrylate (**G**) (4.0 mMol, 1217 mg) in DCM and kept at 50°C for 48 hours. The polymer was recovered via precipitation in diethyl ether (scheme 3.17). Yield 99%.



Scheme 3.17: Reaction scheme of compound **G1**

Chemical identification

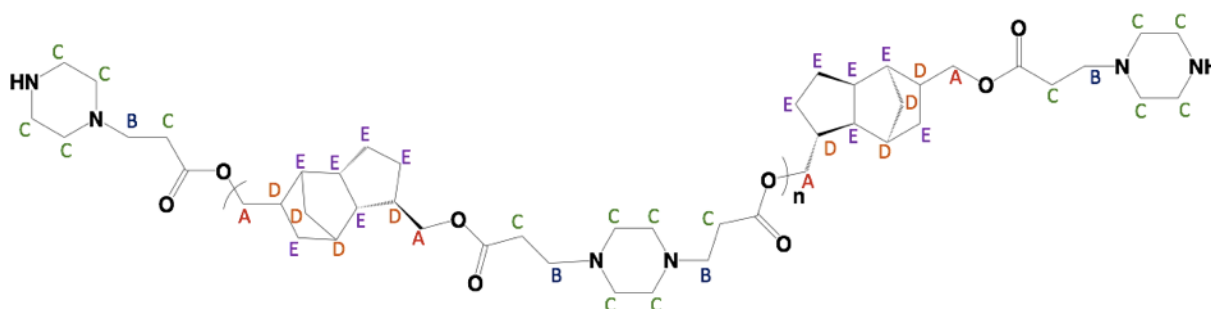


Figure 3.17: **G1** structure and NMR characterisation

Monomers ratio: 1.1 (amine): 1.0 (diacrylate)

Solvent stability: DCM and CDCl₃

MLog P: 2.55

MW (GPC): (1990-2034), $n=4$

Zeta potential: +36.16mV (± 0.46) at pH5, +38.06mV (± 1.43) at pH7.4

Appearance: Yellowish viscous oil

¹H NMR (500 MHz, CDCl₃) δ (ppm): 3.83 – 3.58 (m, 20H) (A), 2.59 – 2.48 (m, 20H) (B), 2.41 – 2.18 (m, 68H) (C), 2.02 – 1.82 (m, 25H) (D), 1.68 – 1.09 (m, 45H) (E).

¹³C NMR (126 MHz, CDCl₃) δ (ppm): 172.19 (C=O), 66.01 (O-CH₂), 53.50 (CH₂-PIP), 52.63 (NH₂-CH₂), 48.82 (CH-CH-cyclo), 44.74 (O-CH₂-CH-cyclo), 40.3 (CH₂-PIP-NH), 38.60 (CH-cyclo), 32.32

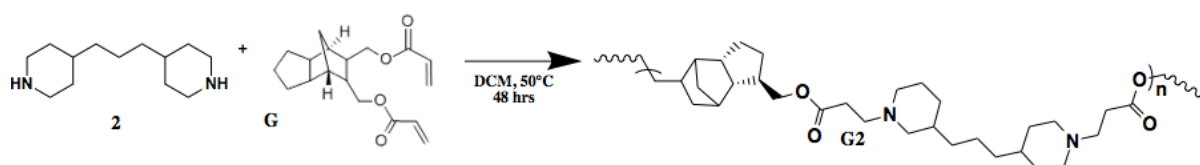
(-CH₂-C=O), 30.80 (CH-cyclo), 27.71 (CH₂-cyclo) 24.44 (CH₂-cyclo).

The PBAE G1 is composed by 5 groups of protons (16a-appendix). Groups A and B respectively correspond to the protons of the methylene groups near to oxygen and nitrogen, and those of the group C represent the protons of -CH₂ of the piperazine and of the -CH₂ near to the carbonyl groups. Then, protons of the -CH of the cyclo groups of the diacrylate G belong to the group D whereas the protons of the methylene groups of the cyclo are included in the group E. Considering the ¹³CNMR (16b-appendix) the carbon of the carbonyl group was found at 172.19 ppm; those bonded to the nitrogen and oxygen ranged between 66-52 ppm and the carbons of the -CH of the cyclo were at 38-30 ppm. Finally, the carbon of the methylene group near to the carbonyl group was at 32.32 ppm and those of the -CH₂ composing the cyclo groups of the diacrylate backbone were between 27-24 ppm.

G2

Chemical procedure

4,4 trimethylenepiperidine (2) (4.4 mMol, 925.58 mg) was conjugated to tri-cyclodecane dimethanol diacrylate (G) (4.0 mMol, 1217 mg) to give compound **G2** (scheme 3.18) adopting DCM as solvent of reaction at 50°C for 48 hours. The product was precipitated by using diethyl ether and dried under vacuum. Yield 99%.



Scheme 3.18: Reaction scheme of compound **G2**

Chemical identification

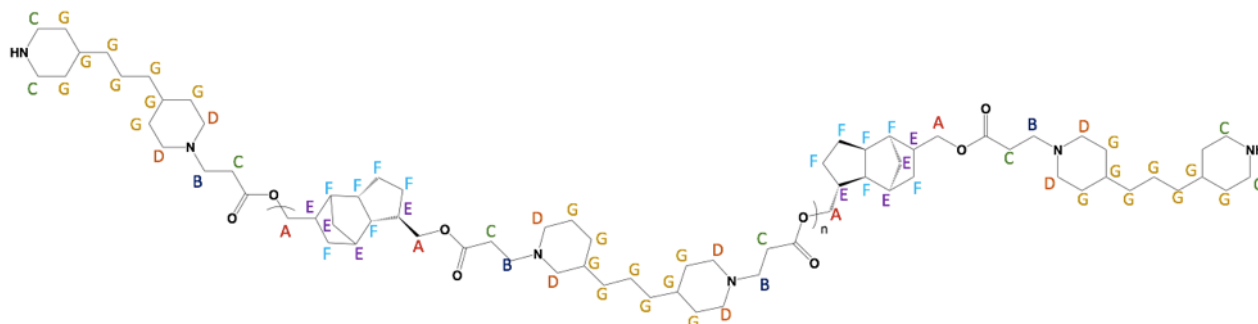


Figure 3.18: **G2** structure and NMR characterisation

Monomers ratio: 1.1 (amine): 1.0 (diacrylate)

Solvent stability: DCM and CDCl₃

MLog P: 6.45

MW (GPC): (2260-2300), n=3

Zeta potential: +27.57 mV (± 0.55) at pH5, +22.17 mV (± 0.5) at pH7.4

Appearance: White solid

¹H NMR (500 MHz, CDCl₃) δ (ppm): 3.80 – 3.57 (m, 16H) (A), 2.73 – 2.59 (m, 16H) (B), 2.54 – 2.39 (m, 24H) (C), 2.40 – 2.25 (m, 32H) (D), 1.85 – 1.72 (m, 20H) (E), 1.53 – 1.39 (m, 36H) (F), 1.13 – 0.88 (m, 80H) (G).

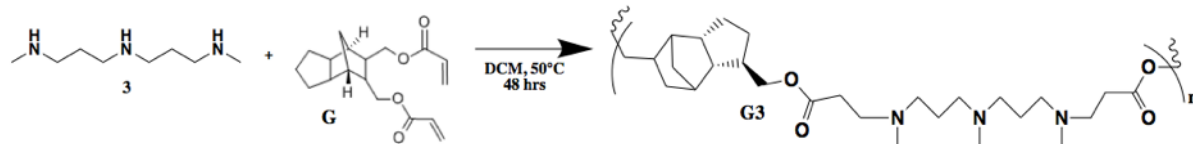
¹³C NMR (126 MHz, CDCl₃) δ (ppm): 172.51 (C=O), 68.01 (O-CH₂), 65.74 (CH₂-Pip), 53.80 (NH₂-CH₂), 49.35 (CH-CH-cyclo), 48.81 (NH₂-CH₂-Pip), 45.43 (O-CH₂-CH-cyclo), 35.46 (CH₂-CH-cyclo), 36.54 (Pip-CH₂-CH₂-Pip), 32.25 (-CH₂-C=O), 31.90 (CH₂-cyclo), 23.81 (CH-cyclo), 24.16 (Pip-CH₂-CH₂-CH-CH₂-CH₂-Pip), 19.3 (Pip-CH₂-CH₂-CH-CH₂-CH₂-Pip).

The molecular structure of G2 is constituent of 7 groups of protons (17a-appendix). Protons of the groups A and B are part of the methylene groups bonded to the oxygen and nitrogen. Moreover, those of the -CH₂ near to the carbonyl groups and protons of the external -CH₂ of the piperidine of the end group of the molecule, belong to the group C. Additionally, the group D correspond to the protons of the -CH₂ of the piperidine near to the nitrogen, whereas group E represents the -CH of the cyclo groups of the diacrylate. Finally, group F and G respectively involve protons of -CH₂ of the cyclo groups and of the -CH₂ included in the ring of the piperidine and in the aliphatic chain of the amine. Considering the ¹³NMR (17b-appendix), the carbon of the carbonyl group was at 172.51 ppm; those conjugated to heteroatoms were between 68 ppm and 53 ppm. The carbons of the cyclo groups of the diacrylate G ranged from 49 ppm to 23 ppm whereas those of the -CH₂ from 35 ppm to 31 ppm. Then, the carbons of the methylene groups near to the carbonyl groups were at 32.25 ppm and those of the -CH₂ of the hydrophobic chain of piperidine ranged between 24.16 ppm to 19.3 ppm.

G3

Chemical procedure

Compound **G3** (scheme 3.19) was gained by mixing N,N-Bis[3-(methylamino)propyl]methylamine (**3**) (4.4 mMol, 762.52 mg) to tri-cyclodecane dimethanol diacrylate (**G**) (4.0 mMol, 1217 mg) in DCM at 50°C. After 48 hours, the crude product was recovered by precipitation in diethyl ether. Yield 99%.



Scheme 3.19: Reaction scheme of compound **G3**

Chemical identification

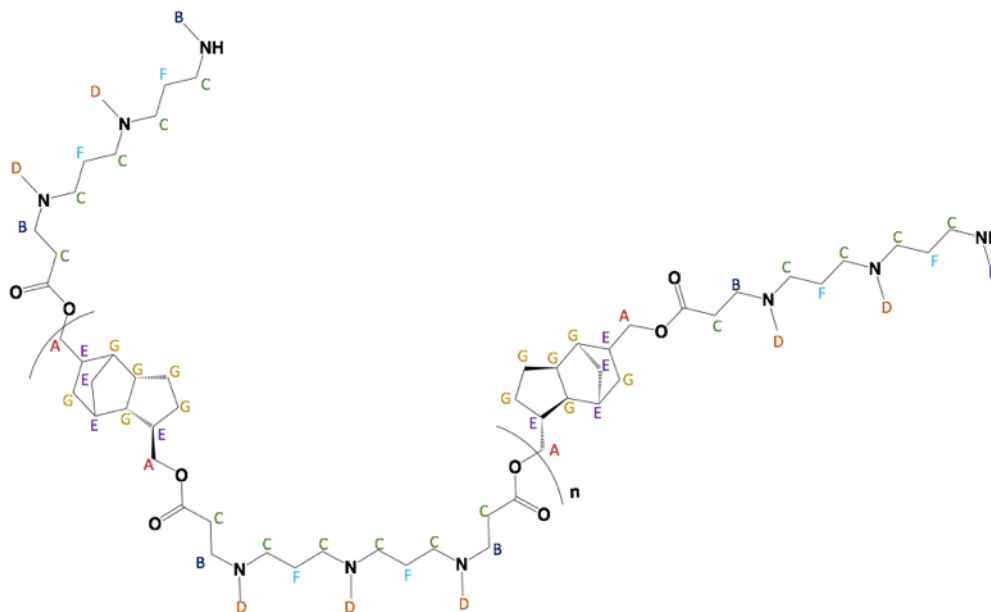


Figure 3.19: **G3** structure and NMR characterisation

Monomers ratio: 1.1 (amine): 1.0 (diacrylate)

Solvent stability: DCM and CDCl₃

MLog P: 2.46

MW (GPC): (2474-2535), **n=4**

Zeta potential: +31.1 mV (± 0.8) at pH5, +29.3 mV (± 0.46) at pH7.4

Appearance: Yellowish viscous oil

^1H NMR (500 MHz, CDCl_3) δ (ppm): 3.90 – 3.75 (m, 20H) (A), 2.72 – 2.60 (m, 26H) (B), 2.53 – 2.32 (m, 68H) (C), 2.20 (s, 45H) (D), 2.05 – 1.91 (m, 25H) (E), 1.85 – 1.74 (m, 24H) (F), 1.69 – 1.29 (m, 45H) (G).

^{13}C NMR (126 MHz, CDCl_3) δ (ppm): 172.68 (C=O), 65.85 (O- CH_2), 54.95 (CH_2 -Pip), 52.52 (NR_2 - CH_2), 48.97 (NR_2 - CH_3), 44.86 (OR- CH_2 - CH -cyclo), 34.21 (NH- CH_3), 38.92 (CH_2 -cyclo), 33.39 (CH -cyclo), 32.23 (- CH_2 -C=O), 30.70 (CH_2 -cyclo), 28.27 (NR_2 - CH_2 - CH_2 -NR- CH_2 - CH_2 -NRH), 20.04 (CH_2 -cyclo).

The PBAE G3 includes 7 groups of protons detected from the ^1H NMR (18a-appendix). The groups A and B are respectively representative of the protons of the methylene groups near to the nitrogen, to the oxygen and of the protons of the methyl groups bonded to the nitrogen ending the molecule. Protons of the $-\text{CH}_2$ of the aliphatic chain of the amine belong to the groups F and C which also involves protons of the $-\text{CH}_2$ near to the carbonyl groups. Then, groups D, E and G correspond to protons of methyl groups bonded to the nitrogen of amine, to the $-\text{CH}$ and the $-\text{CH}_2$ of the cyclo groups included in the backbone of the diacrylate G. Considering the ^{13}C NMR (18b-appendix), the signal belonging to the carbon of the carbonyl group was at 172.68 ppm, whereas those correlated to the $-\text{CH}_2$ near to nitrogen and oxygen ranged between 65-52 ppm. Furthermore, the carbons of the methyl groups bonded to the nitrogen ending the polymer were at 48.97 ppm; those of the $-\text{CH}$ of the cyclo groups were between 44 and 33 ppm, and the carbons conjugated to the protons of the cyclo groups possessed a chemical shift of 38-20 ppm. To conclude, carbons of the $-\text{CH}_2$ near the carbonyl groups were found at 32.23 ppm and those of the $-\text{CH}_2$ of the aliphatic chain of the amine presented a chemical shift equal to 28.27 ppm.

Hydrolysis of PBAEs

All the polymers that has been heretofore described hydrolytically degraded. The hydrolysis was investigated via Gel Permeation Chromatography and light scattering measurements and reproduced in both media, pH5 and pH7.4. In both cases, the analysis was carried out every 24 hours over a period of 30 days keeping the samples in the incubator at 37°C. In this section, all results regarding the degradation of poly-(β)-amino esters will be reported.

A1

The study reported in the figures 3.20a and 3.20b represent the hydrolysis profile of the polymer A1 pursued in two different media, pH5 and pH7.4, considering as parameters the polymer charged by zeta potential, measured in millivolt (mV) and the polymer molecular weight (MW) expressed in Dalton (Da). As it is shown in the figure 20a, MW for A1 was similar for both media (p-value > 0.05), 1457Da at pH5 and 1448Da at pH7.4. The polymer degraded faster at pH7.4 than at pH5: at physiological environment, the hydrolysis significantly occurred within 2 days (p-value < 0.05) and the MW dropped to 144Da; instead under acid conditions the polymer significantly hydrolysed within the first 5 days (p-value < 0.05) reaching 149 Da only after 12 days its dissolution in buffer.

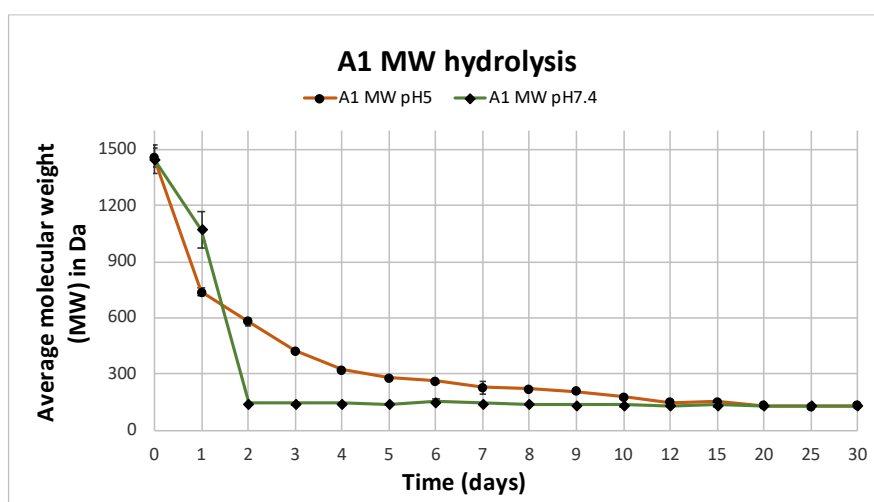


Figure 3.20a: MW and hydrolysis of A1 at pH5 and pH7. Mean \pm SD (N=1, n=2).

In figure 3.20b, the impact of hydrolysis for A1 on charge shows a polymer attitude that was similar (p-value > 0.05) to the MW data reported above. Additionally, also in this case the analysis was carried out for 30 days. Initially, for both media the zeta potential was positive,

14.3 ± 0.95 mV at pH5 and 14.6 ± 0.51 at pH7.4. After 24 hours, at pH7.4 the positive charge of A1 significantly dropped nearly to 0 (p-value < 0.05) and became negative on day 2, -7.07 ± 1.53. From day 3 the negativity slowly increased up to -13.08 ± 2.01 on day 15. The charge of A1 was slightly more stable at pH5: after 24 hours it was still positive, 6.97 ± 1.02, it dropped to negative on the day 2 (p-value < 0.05), -1.65 ± 1.71, reaching -12.43 ± 1.24 on day 20.

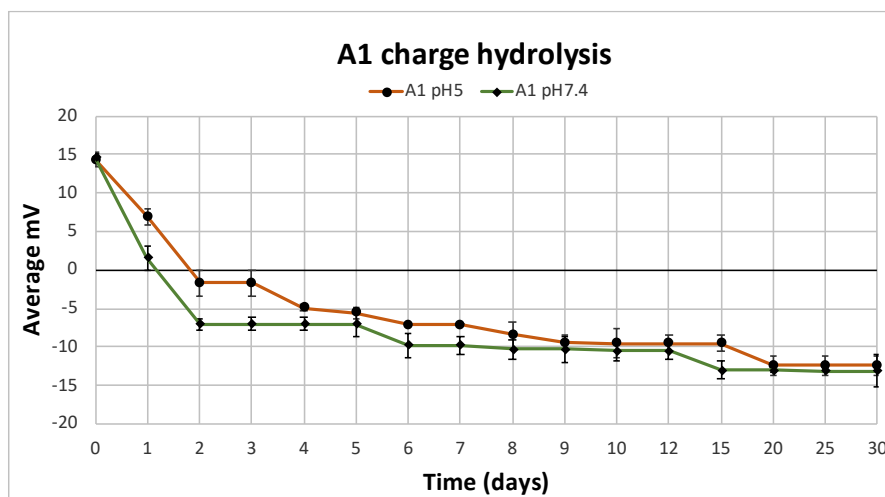


Figure 3.20b: Impact of A1 hydrolysis on charge at pH5 and pH7.4. Mean ± SD (N=1, n=2).

A2

The hydrolysis study was performed also for the polymer A2. The conditions adopted for the experiment were the same chosen for A1. The polymer A2 was dissolved at pH5 and pH7.4 and kept in the incubator at 37°C. Every 24 hours 1 mL from both the solutions was withdrawn and analysed by Gel Permeation Chromatography, storing the rest of samples in the incubator. As it is displayed in the line chart of the figure 3.21a, the molecular weight (MW) detected for the polycation A2 was equal to 1876 Da at pH5 and 1860 Da at pH7.4. At physiological environment, the polymer significantly hydrolysed, after 24 hours showing MW correspondent to 569 Da (p-value < 0.05), then it quickly degraded on day 2 when the M.W. dropped to only 155 Da (p-value < 0.05). Alternatively, the degradation of the polymer at pH5 occurred within 4 days: the molecular weight MW decreased from 1860 Da to 1422 Da on day 1, to 943 Da on day 2, then to 474 Da on day 3 (p-value < 0.05) and only few units of the polymer were left after day 5 showing a value of 176 Da (p-value > 0.05).

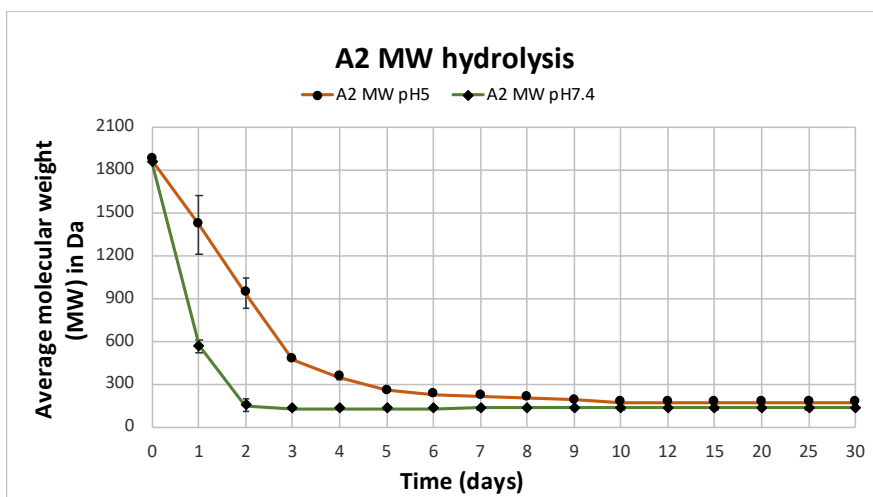


Figure 3.21a: MW and hydrolysis of A2 at pH5 and pH7. Mean \pm SD (N=1, n=2).

Comparing the polymers of the group A until now presented, both A1 and A2 provide quite similar profiles (p-value > 0.05), highlighting higher stability at pH5 than at pH7.4. Furthermore, the hydrolysis study for A2 was performed also by NanoSizer considering as changing parameter the charge measured via zeta potential instead of the molecular weight (MW) mentioned before. In two separate tube tests, 100 mg of A2 were dissolved in 10 mL of sodium acetate buffer pH5 and phosphate buffer pH7.4 respectively. The samples were stored in the incubator at 37°C. Moreover, similarly to the test conditions adopted for GPC, every 24 hours 1 mL from the media solutions was withdrawn and analysed with the NanoSizer. The results are illustrated in the figure 3.21b below.

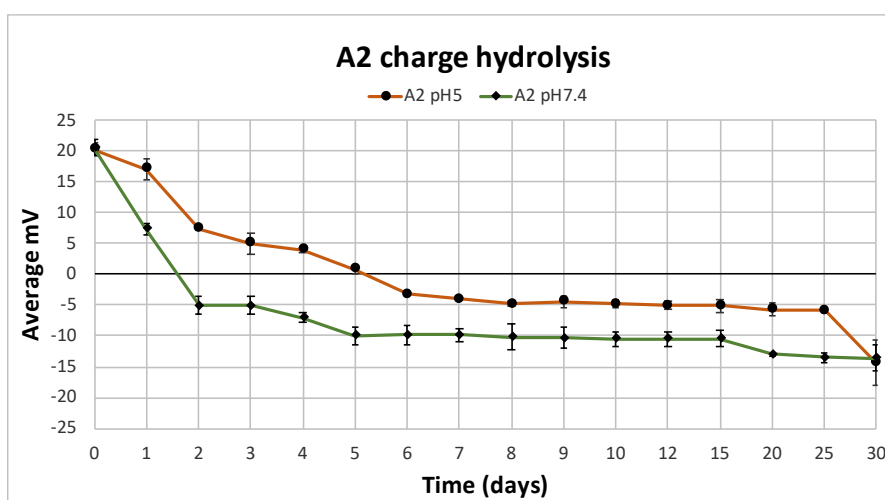


Figure 3.21b: Impact of A2 hydrolysis on charge at pH5 and pH7.4. Mean \pm SD (N=1, n=2).

The experiment was carried out over 30 days. At pH5 the zeta potential was 20.35 ± 0.94 mV on day 0 and it dropped to 0.88 ± 0.65 mV after 5 days (p -value < 0.05). Then, the charge detected was between -3.24 ± 0.26 mV and -5.88 ± 0.44 mV up to day 30 when it decreased to -14.36 ± 3.7 mV. Differently, at pH7.4 starting from 20.57 ± 1.26 mV on day 0, the positivity of polymer reduced straight after 24 hours showing a potential correspondent to 7.36 ± 0.93 mV (p -value < 0.05). On day 2 the potential was reversed, -5.03 ± 1.39 mV (p -value < 0.05), and its negativity constantly increased from day 3 until day 25, -13.53 ± 0.85 mV.

A3

The determination of the molecular weight (MW) followed by the study of the hydrolysis, considering charge and molecular mass of the PBAE, was processed also for the polymer A3. The experiments were run following the same protocols described in advance and the results are reported below in the figures 3.22a and 3.22b.

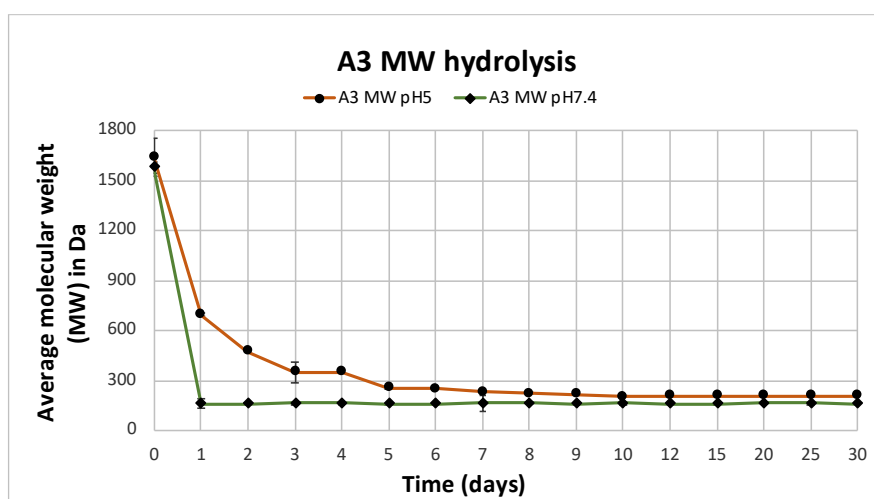


Figure 3.22a: MW and hydrolysis of A3 at pH5 and pH7. Mean \pm SD (N=1, n=2).

The molecular weight (MW) detected for the PBAE A3 at pH5 was 1641 Da on day 0 (figure 3.22a). The polymer mainly hydrolysed within the first 24 hours with the MW value correspondent to 694 Da (p -value < 0.05); the degradation kept slowly occurring until day 5 when only few units of polymer, 258 Da, were left (p -value < 0.05). No significant difference was observed from day 6 to day 30 showing an average of MW units equal to 205 Da (p -value > 0.05). On the other hand, the polymer quickly hydrolysed at pH7.4. Starting from 1580 Da, the MW dropped to 161 Da within only the first 24 hours (p -value < 0.05), showing overall this similar result until day 30 (p -value > 0.05).

The graph of figure 3.22b shows how the charge of A3 changed over 30 days in both media pH5 and pH7.4. The attitude of the polymer is similar to what previously described. Thus, also in this case the polymer degradation promptly occurred under physiological conditions. The charge detected was nearly the same at both media: 9.57 ± 0.51 mV at pH7.4 and 9.8 ± 0.94 mV at pH5.

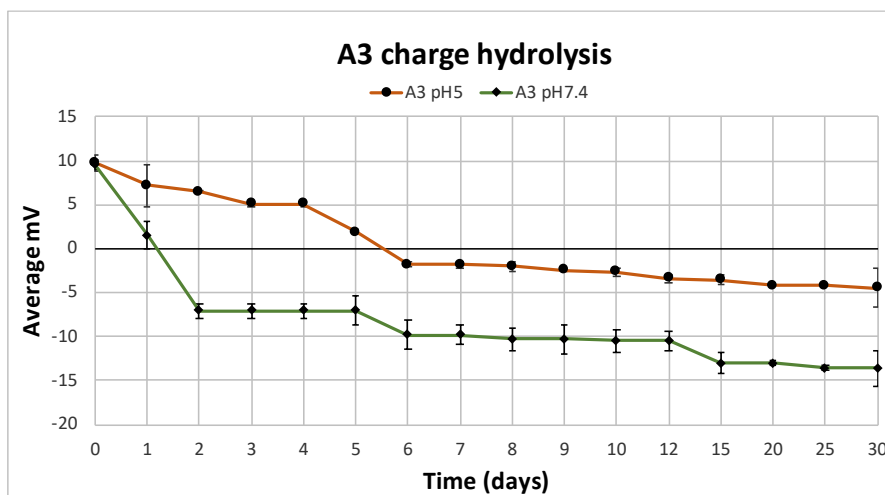


Figure 3.22b: Impact of A3 hydrolysis on charge at pH5 and pH7.4. Mean \pm SD (N=1, n=2).

At pH7.4, it dropped to 1.54 ± 1.53 mV on day 1, it became negative, -7.07 ± 0.79 mV, from day 2 (p -value < 0.05) and then its negativity increased on day 20 reporting a potential of -13 ± 0.25 mV until day 30. Differently, at pH5 the polymer slowly degraded showing similarities with what described above with the MW hydrolysis (p -value > 0.05). Starting from a positive charge, the potential was firstly close to 0 after 5 days, 1.84 ± 0.27 mV, and then definitely reversed from day 6, -1.8 ± 0.23 mV (p -value < 0.05). The negativity gradually continued to rise until day 20 when the zeta potential was finally equal to -4.2 ± 0.14 mV keeping the same value up to day 30 (p -value > 0.05).

B1

The evaluation of the molecular weight followed by the hydrolysis study was performed by GPC and zeta potential also for the PBAEs belonging to the group B, adopting the same conditions chosen for A1, A2 and A3.

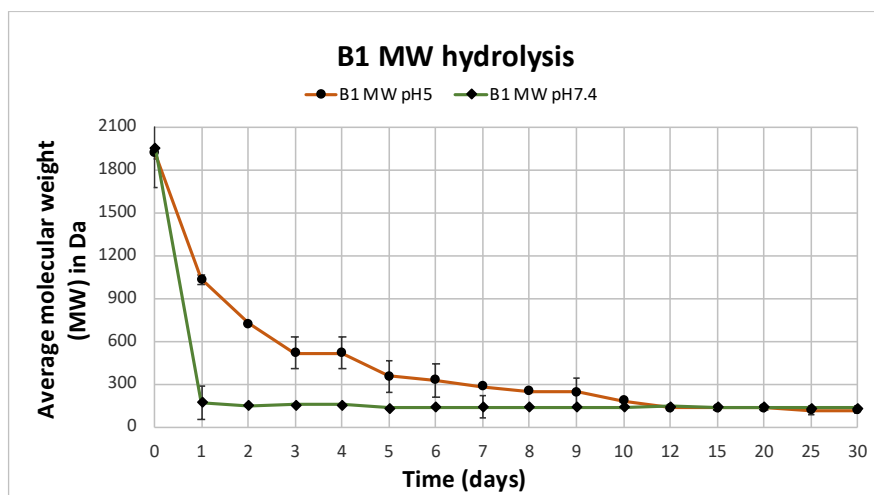


Figure 3.23a: MW and hydrolysis of B1 at pH5 and pH7. Mean \pm SD (N=1, n=2).

The curves shown in the figure 3.23a represent the hydrolysis of the polymer in the two media. Firstly, the molecular weight (MW) detected was equal to 1913 Da at pH5 and 1953 Da at pH7.4 on day 0. Then, a radical decrease in the molecular weight was observed after the first day that the polymer was dissolved in buffer pH7.4 (p-value < 0.05). Indeed, the MW was composed by only few units, 170 Da, until the day 30 (p-value > 0.05). Besides, the rapid hydrolysis at pH7.4, the attitude of B1 was opposite at pH5 highlighting a higher stability and a slower degradation in acidic buffer. In this case, the MW was almost significantly reduced at day 1, 1032 Da (p-value < 0.05), and the hydrolysis gradually continued until day 12 when the value of MW dropped to 132 Da until the day 30 (p-value > 0.05).

In the figure 3.23b it is reported the impact of the hydrolysis for A2 on the charge at both buffers. At pH5 starting from 19.53 ± 0.55 mV, the charge slightly decreased. For instance, it was correspondent to 17.53 ± 0.65 mV at day 1; 15.23 ± 0.85 mV at day 3 and still strongly positive after 7 days, 10.63 ± 0.42 mV (p-value > 0.05). Comparing to the profiles of the group A, it was detected a strong positive charge for over 15 days; only at day 20 it was around 0.98 ± 56 mV and it reversed into negative at day 25, -0.2 ± 0.68 mV showing a significant change from day 0 (p-value < 0.05).

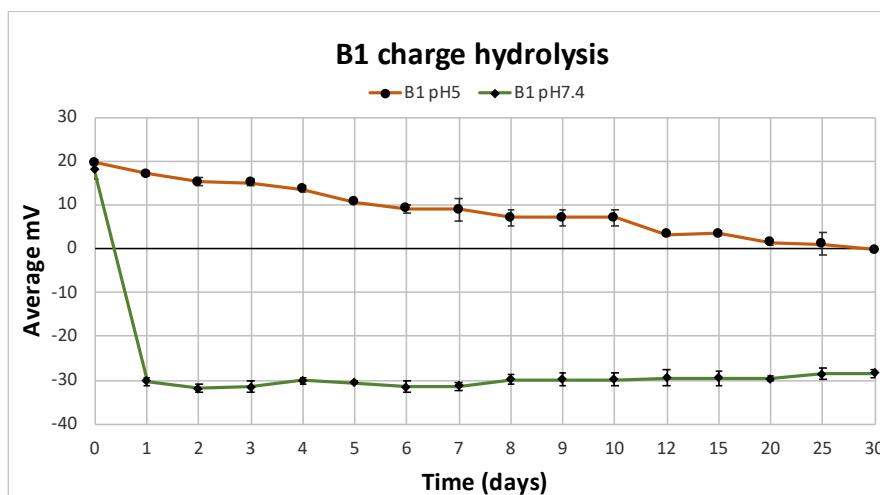


Figure 3.23b: Impact of B1 hydrolysis on charge at pH5 and pH7.4. Mean \pm SD (N=1, n=2).

However, the degradation of B1 at pH7.4 was different to the A1 when dissolved at physiological environment (p-value < 0.05). If the charge was turned into negative on day 2 for A1, in this case instead starting from 17.97 ± 2.01 mV on day 0, it became strongly negative from the day 1, -28.47 ± 1.06 (p-value < 0.05). No significant difference was observed up to the day 30, -30.23 ± 0.98 mV (p-value > 0.05).

B2

The molecular weight (MW) was detected by GPC also for the polymer B2. The figures 3.24a and 3.24b display the PBAE hydrolysis considering both respectively MW and polymer charge measured via zeta potential.

Considering the MW hydrolysis profile, the molecular weight of B2 was 2579 Da at pH5 and 2558 Da at pH7.4. Also, in this case, the polymer was more stable at pH5 rather than at pH7.4. Under acid conditions, B1 slowly hydrolysed and within 15 days. In particular, the MW was 1969 Da on day 1, 985 Da on day 3 (p-value < 0.05) and 565 Da after one week of the polymer dissolution in sodium acetate buffer (p-value < 0.05). Finally, on day 15 only few units of polymer were left, 150 Da with no significant difference up to day 30 (p-value > 0.05). The attitude of B2 was different once dissolved in physiological buffer: it rapidly degraded showing a drastic drop of MW in only 24 hours. Indeed, the value was correspondent to 575 Da on day 1 (p-value < 0.05), 210 Da on day 2 and from day 3 to day 30 130 Da (p-value > 0.05) (figure 3.24a).

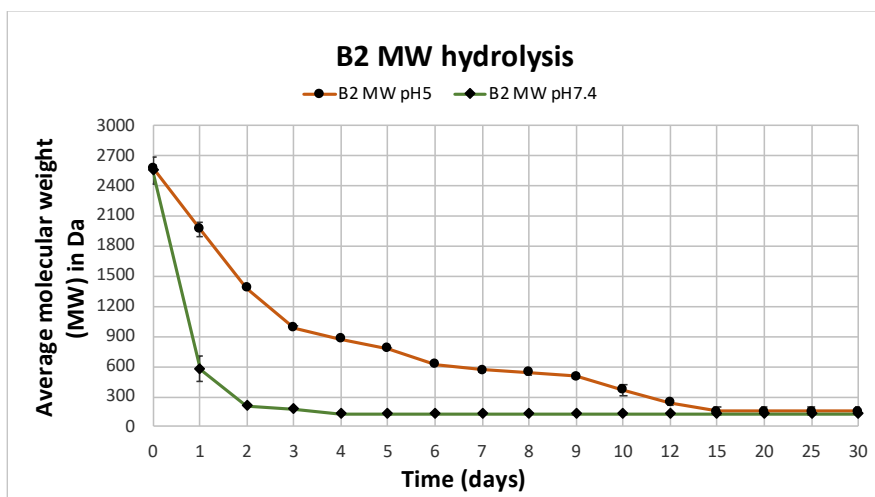


Figure 3.24a: MW and hydrolysis of B2 at pH5 and pH7. Mean \pm SD (N=1, n=2).

The line graph in the figure 3.24b shows the polymer B2 hydrolysed at both media analysing the polymer charge detected via zeta potential instead of the MW. The polycation had an initial positive charge equal to 19.07 ± 1.7 mV at pH5 on day 0. The potential was gradually reduced and reversed into negative within 20 days (p -value < 0.05). Thus, the measured charge was: 18.73 ± 0.66 mV on day 1, 13.14 ± 4.05 mV on day 4 and 6.35 ± 0.7 mV after 7 days. The potential was close to 0 on day 10, 1.9 ± 0.64 mV and it became negative on day 15, -2.47 ± 0.07 mV. Finally, the negativity increased reaching a value of -8.64 ± 1.61 mV on day 25. On the other hand, the positive charge at pH7.4 was easily reversed: initially the value was 19.17 ± 0.57 mV on day 0, then it changed on day 1 (p -value < 0.05), -30.7 ± 1.72 mV keeping a strong negativity from day 2 to day 30, -33.97 ± 1.53 mV (p -value > 0.05).

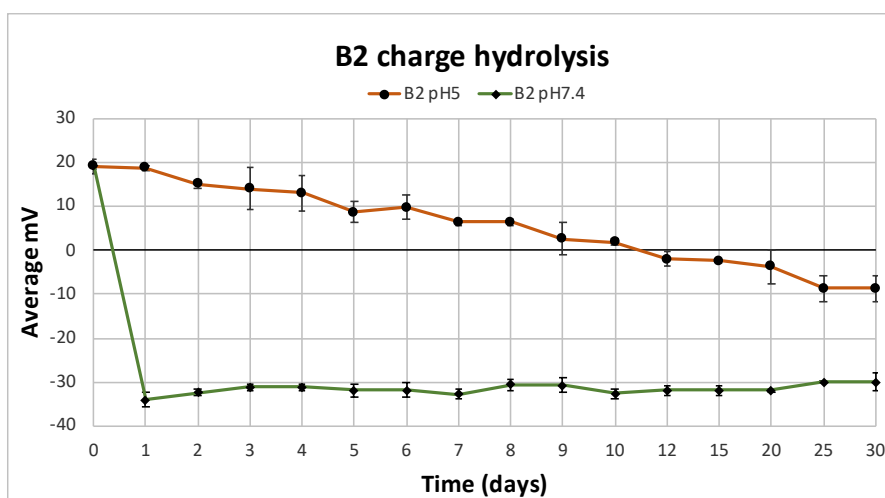


Figure 3.24b: Impact of B2 hydrolysis on charge at pH5 and pH7.4. Mean \pm SD (N=1, n=2).

B3

The studies reported in the figures 3.25a and 3.25b represent the hydrolysis profiles for molecular weight (MW) and charge of the polymer B3 pursued in sodium acetate buffer pH5 and phosphate buffer pH7. As it is shown in the figure 3.25a, the molecular weight of the polycation was initially correspondent to 2317 Da at pH5; it significantly reduced after the first day of dissolution in buffer, 833 Da (p-value < 0.05). The hydrolysis of the polymer steadily progressed from day 2, 492 Da, until day 8 when only few units of B3 were left, 231 Da (p-value < 0.05). No consistent variation of MW was observed from day 8 up to day 30 (p-value > 0.05). Differently, the pathway of B3 degradation at pH7.4 shows a sharp decline of the MW detected on day 0, which fell from 2261 Da to 246 Da in only 24 hours (p-value < 0.05). In the following days, there was no substantial decrease of the value of MW that overall was equal to 154 Da until day 30 (p-value > 0.05).

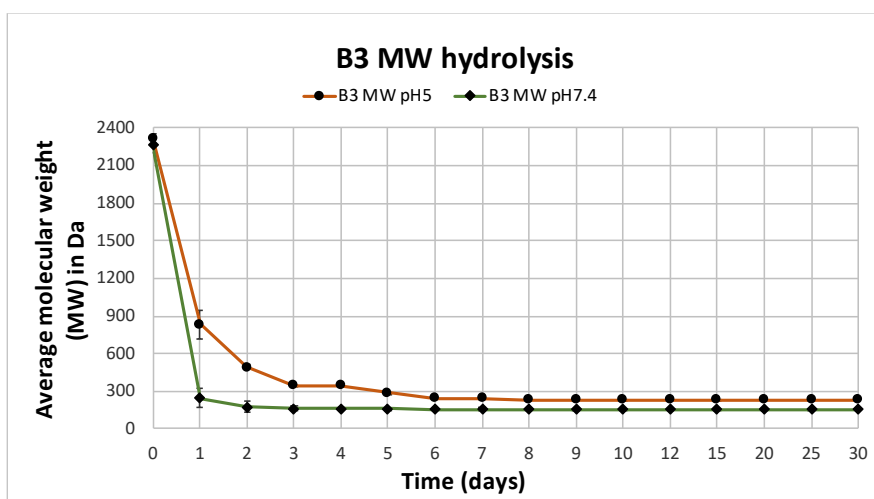


Figure 3.25a: MW and hydrolysis of B3 at pH5 and pH7. Mean \pm SD (N=1, n=2).

The line chart of the figure 3.25b displays the impact of hydrolysis for B3 on charge along a period of 30 days. On day 0 the charge of B3 was positive at both media, 15.1 ± 0.85 mV at pH5 and 14.53 ± 0.51 mV at pH7.4. In the first medium, the polymer hydrolysed within the first 8 days; thus, the positivity of B3 was detected for 8 days and it was around 0, 0.06 ± 0.84 mV, only on day 9 (p-value < 0.05). The charge was then inverted on day 10, when the PBAE showed a weak negativity, -3.22 ± 0.36 mV, which slightly increased on day 25, -9.75 ± 0.56 mV (p-value > 0.05).

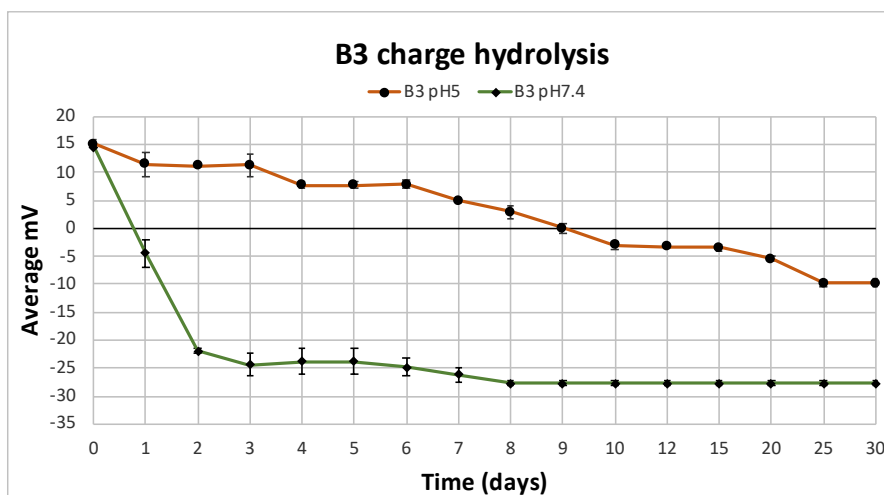


Figure 3.25b: Impact of B3 hydrolysis on charge at pH5 and pH7.4. Mean \pm SD (N=1, n=2).

At pH7.4 the positive charge of the polymer was easily reversed into negative along the first 2 days. Indeed, the potential dropped to -4.48 ± 2.46 mV on day 1 and -21.87 ± 0.46 mV on day 2 (p-value < 0.05). The strong negativity was detected until day 30, -27.73 ± 0.46 mV (p-value > 0.05).

Comparing PBAEs of group B to those of group A, similarities and differences were observed. The hydrolysis of B1, B2 and B3 rapidly occurred at pH7.4 as detected and described for A1, A2 and A3 (p-value > 0.05). However, the degradation under acid conditions for the polymers synthesised by using the diacrylate B, gradually happened compared to those belonging to the group A (p-value < 0.05). Thus, in this case, B1, B2 and B3 appeared to be more stable than A1, A2 and A3.

D1

The hydrolysis study was performed also for the PBAEs gained by conjugation of diacrylate D and amine 1, 2 and 3, by using the same conditions heretofore described. The results of the degradation profiles for D1 are shown in the figures 3.26a and 3.26b.

The molecular weight (MW) detected for D1 was 1440 Da at pH5 and 1421 Da at pH 7.4 on day 0. In acidic buffer, the polymer mainly hydrolysed within the first week. Thus, the MW slowly decreased showing values equal to: 1217 Da on day 1, 987 Da on day 2 which was significantly reduced after 2 days, 439 Da (p-value < 0.05). After day 7 no significant variation of the MW was detected highlighting an average between 200-110 Da until day 30 (p-value > 0.05). At pH7.4 the initial MW of D1 plummeted after one day confirming the rapid hydrolysis of the PBAEs after being dissolved in physiological environment (p-value < 0.05). After the

drop, the value of MW remained almost the same, between 220-240 Da, until day 30 as displayed on the figure below (p -value > 0.05).

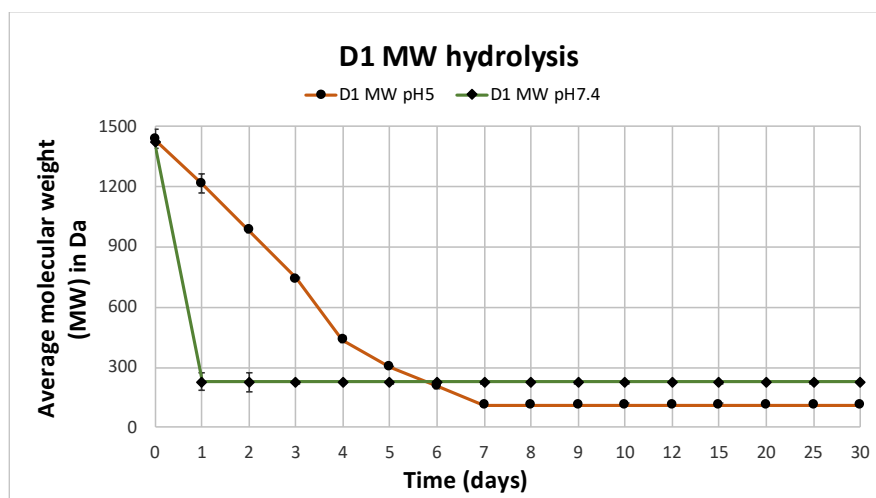


Figure 3.26a: MW and hydrolysis of D1 at pH5 and pH7. Mean \pm SD (N=1, n=2).

The hydrolysis of D1 was also evaluated considering as parameter of analysis the change of its potential (mV) over a period of 30 days allowing a better understanding of the behaviour of this polymer in both media, pH5 and pH7.4.

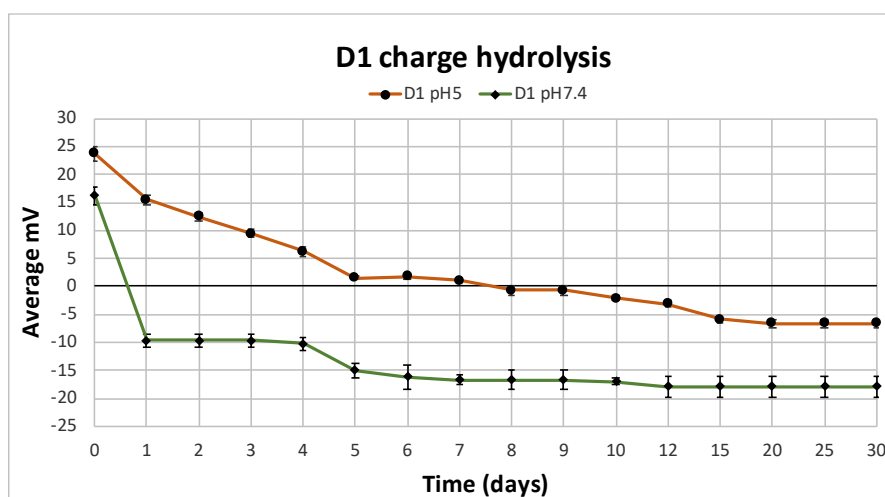


Figure 3.26b: Impact of D1 hydrolysis on charge at pH5 and pH7.4. Mean \pm SD (N=1, n=2).

The positive charge measured via zeta potential was 23.7 ± 1.18 mV at pH5. This analysis evidenced the steady change of the charge under acid conditions. Indeed, the variation of the charge was: 15.46 ± 0.76 mV on day 1, 12.75 ± 0.86 mV on day 3 and 6.25 ± 0.78 mV on day 4. After 8 days, the polymer was still weakly positive and the charge close to 0, 0.704 ± 0.85

mV (p-value < 0.05). Only from day 10 a reversed potential was detected, -2.12 ± 0.38 mV, and the negativity increased reaching -6.6 ± 0.65 mV on day 20 (p-value < 0.05). On the hand, the measured charge of D1 at pH7.4 was in this case lower than what observed at pH5. Starting from 16.21 ± 1.67 mV, it was inverted into negative after the first day, -9.63 ± 1.19 mV (p-value < 0.05). The negativity kept rising in the following days, ending to -17.86 ± 1.85 mV on day 30 (p-value < 0.05).

D2

The determination of the molecular weight and the hydrolysis profiles considering both charge and MW were also determined for the PBAE D2. Protocol for samples preparation and settings for the experiment were exactly the same of the PBAEs heretofore presented.

The MW of the polymer was defined by GPC on day 0, once D2 was completely dissolved in both media, pH5 and pH7.4 (figure 3.27a). Under acid conditions initially the MW detected was 1906 Da and a gradual fall was observed in the following days, for instance, 1430 Da on day 1 and 1251 Da on day 2. Starting from day 3 the polymer hydrolysed more at pH5 showing a reduction of the MW of more than 300 Da. Nevertheless, the hydrolysis was carried out until day 9, when only few units of polymer remain detectable, 189 Da (p-value < 0.05). From day 10 to day 30 no more effective change in the MW were noticed. Differently, at pH7.4 D2 rapidly degraded compared to pH5 (p-value > 0.05). Firstly, the initial MW, 1822 Da, easily dropped to 235 Da on day 1. Then, a further reduction occurred within the second day, 131 Da (p-value < 0.05), without any other variation until day 30 (p-value > 0.05).

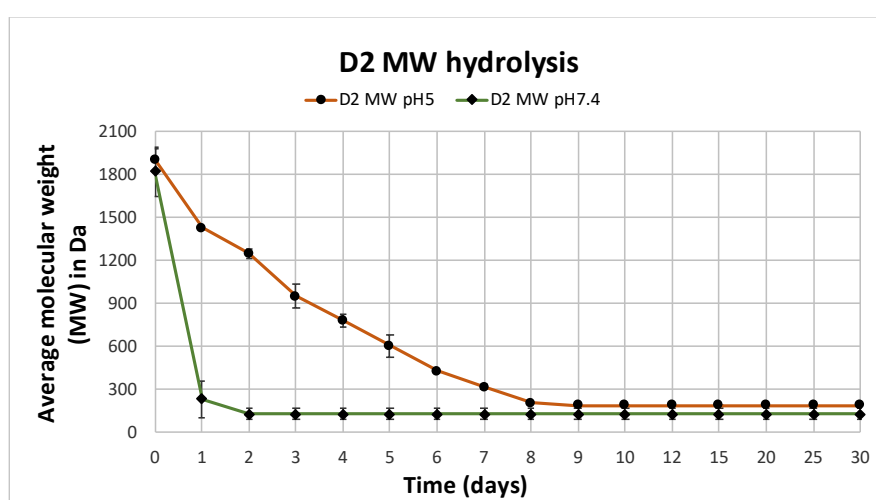


Figure 3.27a: MW and hydrolysis of D2 at pH5 and pH7. Mean \pm SD (N=1, n=2).

Furthermore, to support the hydrolysis via GPC described above, the modulation of the charge for D2 was pursued in both media. The results displayed in the figure 27.b highlight the different attitude of the polymer at pH5 and pH7.4, evidencing a faster hydrolysis at physiological conditions rather than under acidosis. Indeed, in the first case, the potential was initially strongly positive on day 0, 18.27 ± 1.21 mV; then, it was reversed into negative within one day, -8.47 ± 0.8 mV (p-value < 0.05). Furthermore, the negativity doubled increased after 7 more days, -17.87 ± 2.87 mV, reaching a maximum value of -25.87 ± 0.74 mV from day 12 to day 30 (p-value < 0.05).

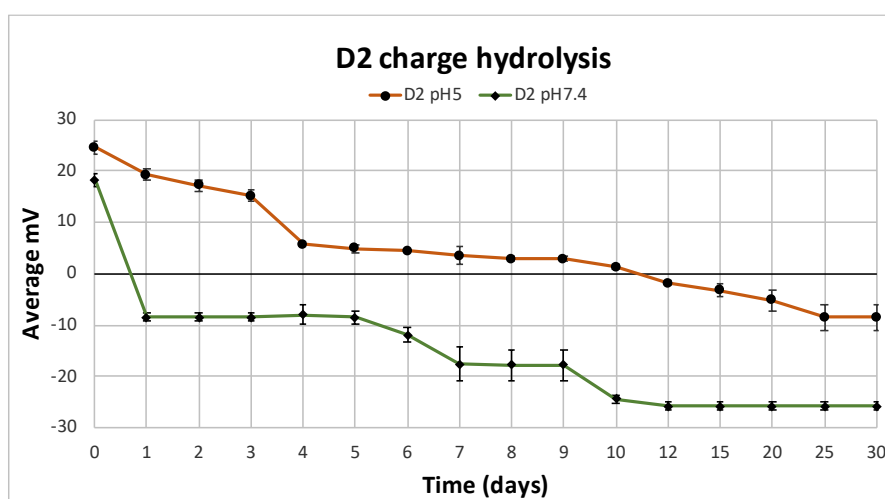


Figure 3.27b: Impact of D2 hydrolysis on charge at pH5 and pH7.4. Mean ± SD (N=1, n=2).

Beside the rapid hydrolysis at pH7.4, the experiment evidenced that D2 was more stable at pH5. The charge was initially 24.63 ± 1.22 mV on day 0; then it slowly decreased within 3 days, 15.22 ± 1.15 mV. Although the potential plummeted on day 4, showing a weak positivity, 5.73 ± 0.4 mV, the polymer was inverted into negative only on day 12, -1.81 ± 0.55 mV. In the end, the negativity steadily increased until day 30 when the measured potential was -8.56 ± 2.51 mV (p-value < 0.05).

D3

To compare the degradation profiles of the polymers belonging to the group D, the hydrolysis was finally performed also for the PBAE D3. As reported in the figure 3.28a, the molecular weight MW was correspondent to 1518 Da at pH5 and 1514 Da at pH7.4 on day 0. In this case,

the polymer showed a better stability at pH5 than at pH7.4. Indeed, after one day being dissolved in acidic buffer, the MW of D3 was significantly reduced to 797 Da (p-value < 0.05). Furthermore, the polymer kept hydrolysing detecting a value of 383 Da on day 2 (p-value < 0.05) and on the average between 230-190 Da from day 3 to day 10. No more variation of MW was observed until day 30 (p-value > 0.05). On the other hand, a sharp fall of the MW, from 1514 Da to 218 Da, was detected after one day of the polymer dissolution in pH7.4 (p-value < 0.05). From day 2 to day 30 no further decrease was noticed, with an average of MW between 165-150 Da (p-value > 0.05).

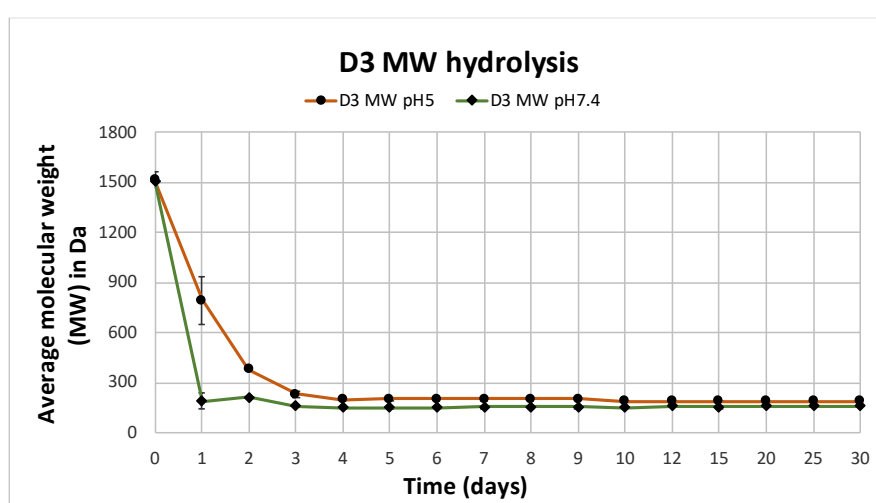


Figure 3.28a: MW and hydrolysis of D3 at pH5 and pH7. Mean \pm SD (N=1, n=2).

The figure 3.28b explained the shift of the potential measured for D3. The experiment allowed to better explain how hydrolysis occurred in both media. At pH5 starting from 22.99 ± 0.85 mV, the positivity of the PBAE dropped within 1 day being half reduced, 13.13 ± 0.5 mV. The major decline was detected on day 2, when the charge was equal to 4.3 ± 0.5 mV. From day 2 the potential of D3 started a gradual reduction: firstly, it was nearly 0 from day 5 to day 8, then it turned into negative from day 9, -1.03 ± 0.36 mV with a regular growth of its negativity until day 30, when the measured charge was equal to -6.0 ± 0.55 mV (p-value < 0.05). At pH7.4, the polymer showed a strong positivity, 22.53 ± 0.51 mV on day 0. In this case, the potential was easily inverted into negative, -4.48 ± 2.46 , on day 1 and the negativity of D3 definitely increased on day 2, -21.87 ± 0.46 mV. A steady rise was observed until day 30, when the measured charge was -27.73 ± 1.2 mV (p-value < 0.05).

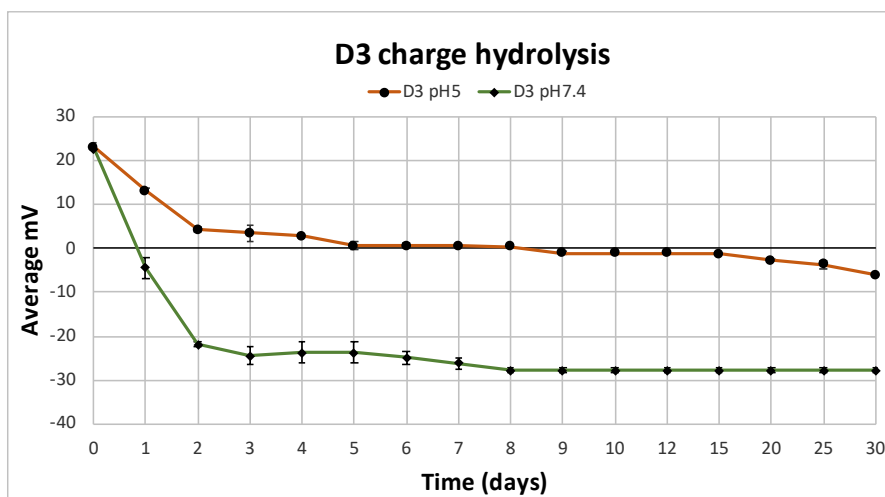


Figure 3.28b: Impact of D3 hydrolysis on charge at pH5 and pH7.4. Mean \pm SD (N=1, n=2).

Overall, the PBAEs possessing D as diacrylate, presented a better stability at pH5 than at pH7.4. Thus, the 3 polymers D1, D2 and D3 similarly hydrolysed as reported for the PBAEs of the groups A and B (p-value > 0.05). However, difference in the degradation timing was observed at pH5: D3 degraded faster than D1 and D2 highlighting the importance of the choice of the amine and its impact on PBAE hydrolysis (p-value < 0.05).

E1

The hydrolysis study was performed also for the polymers synthesised by mixing the diacrylate E and one of the amines 1, 2 and 3 to give respectively E1, E2 and E3.

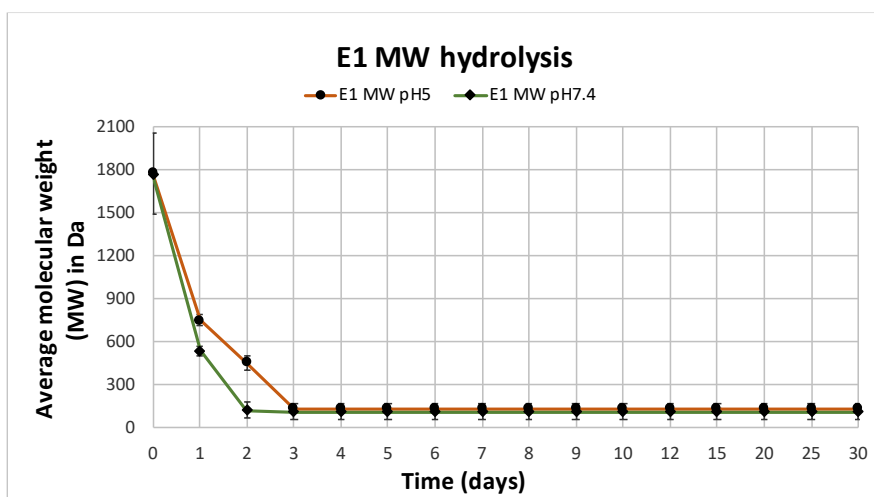


Figure 3.29a: MW and hydrolysis of E1 at pH5 and pH7. Mean \pm SD (N=1, n=2).

The degradation of E1 was evaluated by GPC after the detecting its molecular weight on day 0, 1779 Da at pH5 and 1771 Da at pH7.4, as reported on figure 3.29a above. A consistent reduction of MW was observed at pH5 on day 1, showing a value of 752 Da (p-value < 0.05). Thus, the polymer mainly hydrolysed within 3 days and no significant MW loss was detected from day 3 to day 30 with a range of units between 130-140 Da (p-value > 0.05). The PBAE quickly degraded within few days also at pH7.4. In particular, the MW plummeted from 1779 Da to 539 Da on day 1, to 124 Da on day 2 (p-value < 0.05), with a range of 110-125 Da until day 30 (p-value > 0.05).

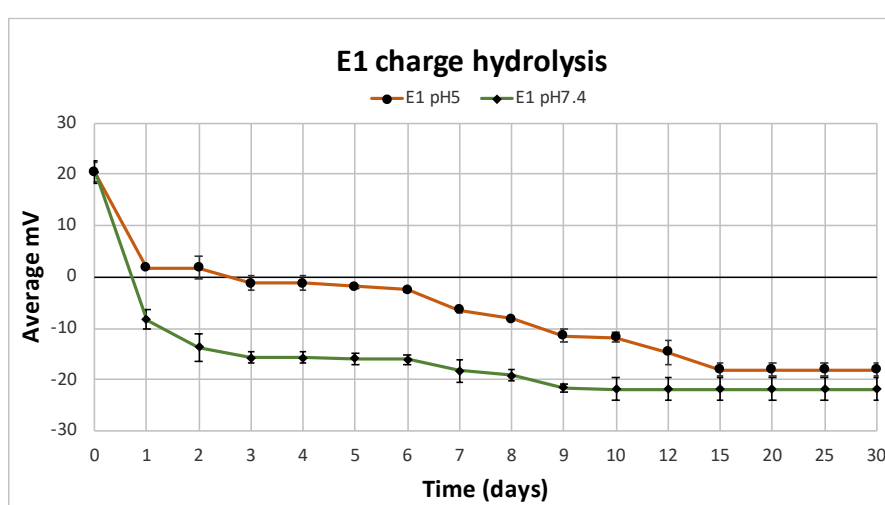


Figure 3.29b: Impact of E1 hydrolysis on charge at pH5 and pH7.4. Mean \pm SD (N=1, n=2).

For the PBAE E1 the hydrolysis was pursued considering also the change of the zeta potential measured at pH5 and at pH7.4 (figure 3.29b). In both cases, on day 0, E1 presented a positive charge correspondent to 20.37 ± 1.92 mV at pH5 and to 20.46 ± 2.34 mV at pH7.4. This experiment confirmed what mentioned before about the reduction of molecular weight M.W. at both media: the hydrolysis occurred within few days and the charge was easily reversed into negative. Under acid conditions, the potential was nearly to 0 until day 3, 1.72 ± 0.10 mV; then it was inverted, and its negativity constantly started increasing reaching -18.11 ± 1.28 mV on day 30 (p-value < 0.05). However, at pH7.4 the charge was turned into negative within one day, -8.32 ± 1.89 mV. According to what observed at pH5, the negativity of the E1 significantly rose until day 30, when the potential measured was equal to -21.89 ± 2.22 mV (p-value < 0.05).

E2

The hydrolysis carried out for E2 is represented by both figures 3.30a and 3.30b. Starting from the modulation of the molecular weight over 30 days, the initial value correspondent to 2376 Da at pH5 and 2073 Da at pH7.4. Compared to the profiles of E1, this polymer slowly hydrolysed in 10 days. A significant drop occurred after day 1, 1426 Da, and day 2, 456 Da (p-value < 0.05). Then E2 gradually degraded and the MW detected was 362 Da on day 7 and 210 Da on day 12 (p-value < 0.05). From day 15 to day 30 only few units of polymer were left with a range between 210 and 180 Da (p-value > 0.05). At pH7.4 the attitude of the PBAE was opposite to the one determined at pH5: the hydrolysis happened within only 2 days. Hence, a substantial reduction of MW was observed from day 0, 2073 Da, to day 1, 241 Da (p-value < 0.05). No significant variation was noticed until day 30 and the value of the MW fluctuated between 140-165 Da (p-value > 0.05).

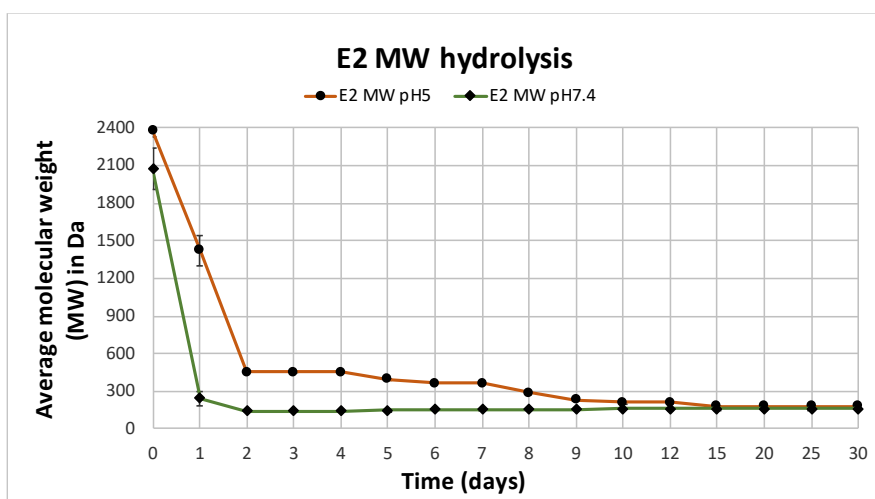


Figure 3.30a: MW and hydrolysis of E2 at pH5 and pH7. Mean \pm SD (N=1, n=2).

The initial positivity of the polymer E2 on day 0 was weaker than the one E1. Thus, the potential was 12.13 ± 0.25 mV at pH5 and 12.17 ± 0.41 at pH7.4. The charge at pH5 was significantly reduced on day 1, 6.83 ± 1.97 mV whereas it was nearly 0 until day 6, 0.10 ± 0.62 mV, and it was inverted into negative only on day 7, -4.2 ± 1.42 mV. Then, the negativity of the polymer slightly rose reaching a value of -6.6 ± 1.23 mV on day 30 (p-value < 0.05).

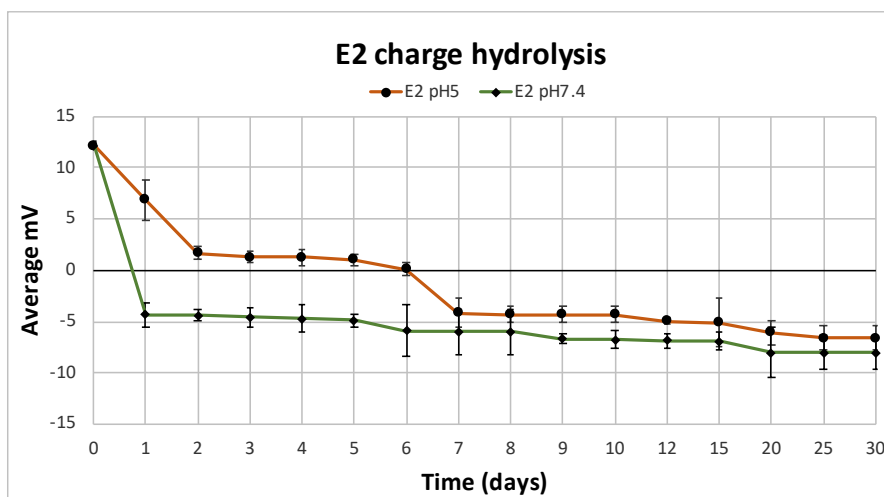


Figure 3.30b: Impact of E2 hydrolysis on charge at pH5 and pH7.4. Mean \pm SD (N=1, n=2).

Under physiological conditions the potential of E2 was reversed within only one day. This explained the faster hydrolysis detected also by GPC considering the MW and described before. Therefore, starting from 12.17 ± 0.41 mV, the polymer became negative on day 1, -4.33 ± 1.22 mV. The negativity of the PBAE kept slowly increasing until day 20 ended to -8.0 ± 1.68 mV (p-value < 0.05).

E3

Among the PBAEs belonging to the group E there was also E3. The hydrolysis studied for this polymer is displayed on both figures 3.31a and 3.31b. Firstly, the molecular weight MW was determined at both media on day 0: 1882 Da at pH5 and 1913 at pH7.4. Under acid conditions, E3 significantly hydrolysed within the first two days. Thus, a consistent degradation was detected on day 1, 551 Da, and on day 2, 220 Da (p-value < 0.05). From day 2, no considerable difference on the value of molecular weight was detected. Therefore, the range was between 200-220 Da (p-value > 0.05). However, under physiological conditions, the hydrolysis quickly occurred, and the molecular weight consistently varied in the first 24 hours. There was a drop of more than 100 units, 188 Da on day 1 (p-value < 0.05), and the modulation of the MW was between 150-170 Da from day 2 to day 30 (p-value > 0.05) (figure 3.31a).

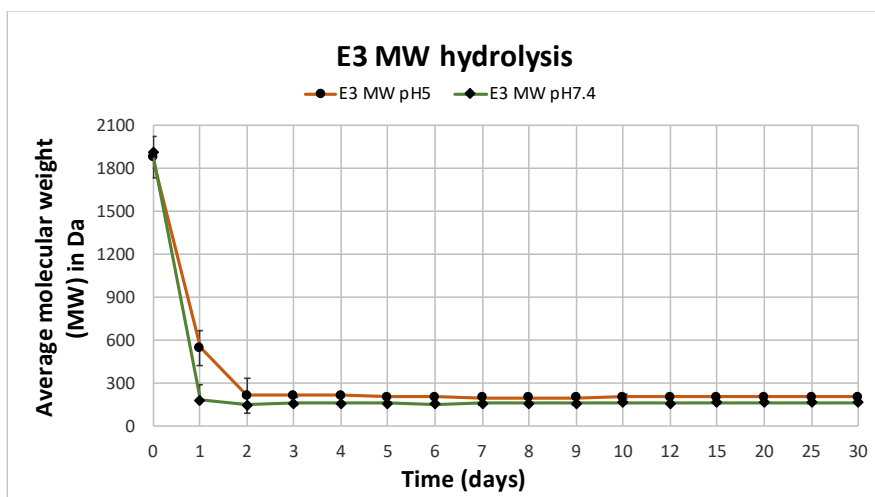


Figure 3.31a: MW and hydrolysis of E3 at pH5 and pH7. Mean \pm SD (N=1, n=2).

To support the hydrolysis performed by GPC, the variation of the charge for E3 was monitored via measurements of its zeta potential (figure 3.31b). The polymer was positive on day 0 showing a similar value to E2: 14.66 ± 0.85 mV at pH5 and 12.8 ± 0.51 mV at pH7.4. In both cases, the potential was inverted in few days. In particular, at pH7.4, it was turned into negative on day 1, reporting a weak negative charge, -1.87 ± 2.46 mV, which considerably increased on day 2, -10.49 ± 0.46 mV. Then the polymer became strongly negative on day 30 reaching a potential equal to -21.98 ± 0.78 mV (p-value < 0.05). At pH5, the potential was reversed in 2 days with a consistent drop of its positivity, firstly, on day 1, 3.91 ± 0.5 mV, then, on day 2 with a charge of -2.27 ± 0.7 mV. The negativity steadily increased from day 3 to day 30 when the measured potential was correspondent to -15.44 ± 1.78 mV (p-value < 0.05).

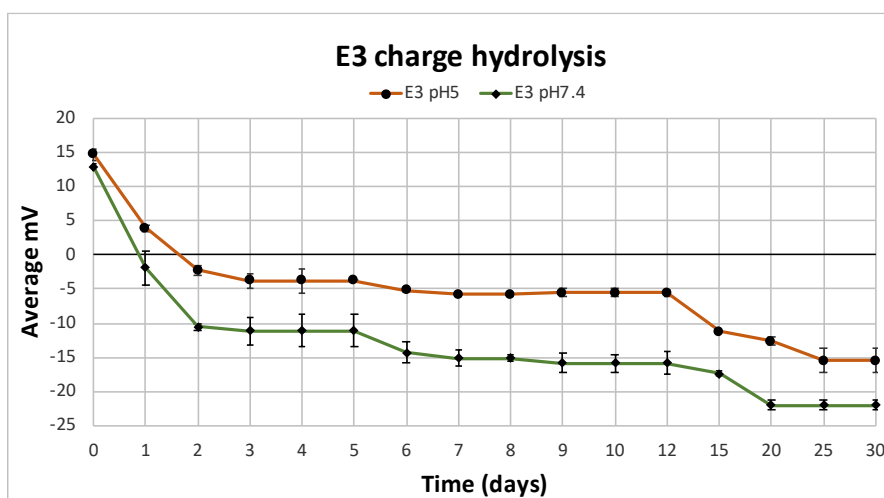


Figure 3.31b: Impact of E3 hydrolysis on charge at pH5 and pH7.4. Mean \pm SD (N=1, n=2).

Comparing the polymers of the group E, E1, E2 and E3 provided profiles quite similar, presenting a weak stability (p -value > 0.05). In both media, the polymers easily hydrolysed considering both parameters potential and molecular weight MW. Hence, among all the PBAEs until now analysed, those possessing E as diacrylate, presented a lower stability due to their fast degradation at both pH5 and pH7.4. No significant difference was observed among the 3 polymers of group E (p -value > 0.05), showing that, in this case, the hydrolysis depended more on the choice of the diacrylate rather than the amines.

F1

The determination of the molecular weight MW and the study of the hydrolysis was carried out also for the polymers of the group F: F1, F2 and F3. For F1 the results are shown in figures 3.32a and 3.32b.

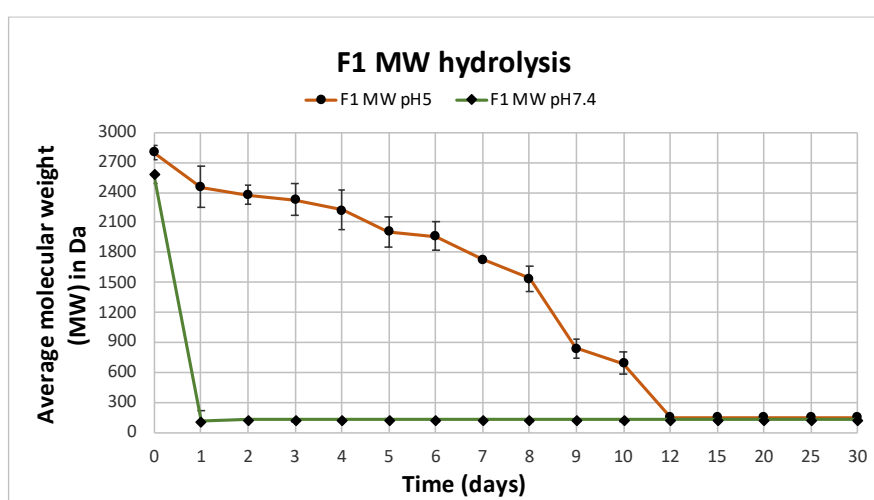


Figure 3.32a: MW and hydrolysis of F1 at pH5 and pH7. Mean \pm SD (N=1, n=2).

The molecular weight MW detected via GPC was 2802 Da at pH5 and 2584 Da at pH7.4. For the hydrolysis of this polymer a substantial difference was observed between the profiles of both media: at pH7.4 F1 quickly hydrolysed in only one day, whereas at pH5 the degradation gradually occurred within 12 days. At physiological environment, from 2584 Da on day 0, there was a considerable drop in the value of MW on day 1, 130 Da (p -value < 0.05). From day 2 until day 30 no difference was observed, and the molecular weight changed between 130-110 Da (p -value > 0.05). However, the polymer slowly degraded after being dissolved in acidic buffer. Furthermore, a moderate decrease of MW was detected: 2456 Da on day 1, 2329 Da on day 3 and 2005 Da on day 5 (p -value < 0.05). The degradation mainly happened

from day 6, 1959 Da, to day 10, 694 Da and the MW kept decreasing until day 12, 155 Da, showing a value that was similarly detected to day 30 (p-value < 0.05).

As reported for the previous PBAEs, also for F1 the hydrolysis was performed considering the modulation of the charge of the polymer and in this case, this experiment highlighted the strong stability of F1 under acidosis. For instance, the initial measured charge was strongly positive on day 0, 29.57 ± 2.01 mV dropped nearly to 0 only on day 25, 0.95 ± 1.83 mV. The positivity of the polymer was detected for the whole period of the analysis and the potential was not reversed into negative along 30 days. In particular, the positivity was mainly reduced after 7 days, 5.35 ± 0.33 mV, and it steady continued decreasing until day 25 (p-value < 0.05).

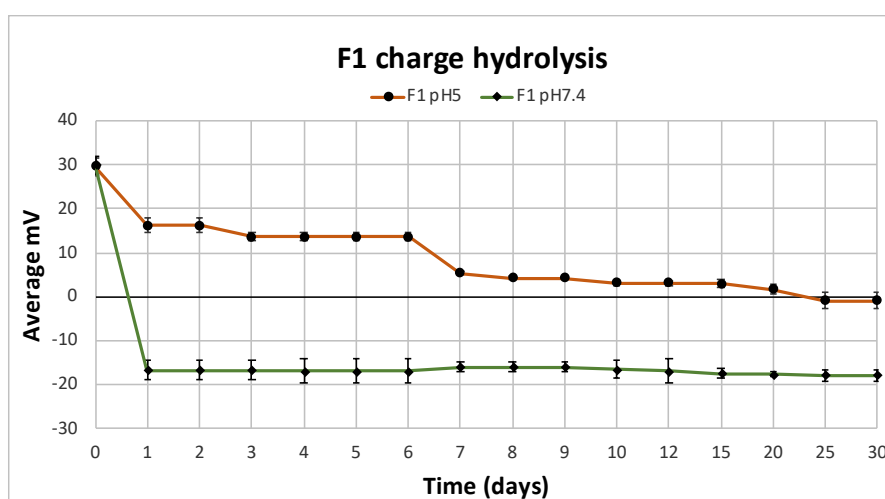


Figure 3.32b: Impact of F1 hydrolysis on charge at pH5 and pH7.4. Mean \pm SD (N=1, n=2).

On the other hand, the attitude of the polymer at pH7.4 was comparable to the other profiles of PBAEs dissolved at the same medium. Indeed, the charge on day 0 was equal to 29.9 ± 1.97 mV and it was promptly turned into negative after the first 24 hours. Thus, the potential on day 1 was strongly negative, -16.77 ± 2.25 mV, and the negativity of the polymer F1 steadily rose reaching -17.93 ± 1.21 mV on day 30 (p-value < 0.05).

F2

The molecular weight MW determination was defined also for F2 and its value corresponded to 2800 Da at pH5 and 2749 Da at pH7.4. Furthermore, the hydrolysis was performed for both charge and MW of this polymer. The figure 3.33a shows how the molecular weight MW

changed along 30 days and the hydrolysis profiles provided once the polymer was dissolved in both media. Indeed, the line graphs highlighted the difference between the two media: at pH5 the polymer slowly hydrolysed whereas at pH7.4 the degradation quickly occurred. Under acid conditions, there was a gradual decline of the MW; the value was 2657 Da on day 1, 2384 Da on day 3, 2055 on day 5 and 1846 Da on day 7. After 2 days it was significantly reduced, 997 Da, and it kept decreasing until day 30 when only few units left, 200 Da (p-value < 0.05). Under physiological conditions, the attitude of F2 was opposite compared to what observed at pH5: starting from 2749 Da on day 0, the MW plummeted to 230 Da on day 1 (p-value < 0.05), with a range between 230-130 Da detected from day 2 to day 30 (p-value > 0.05).

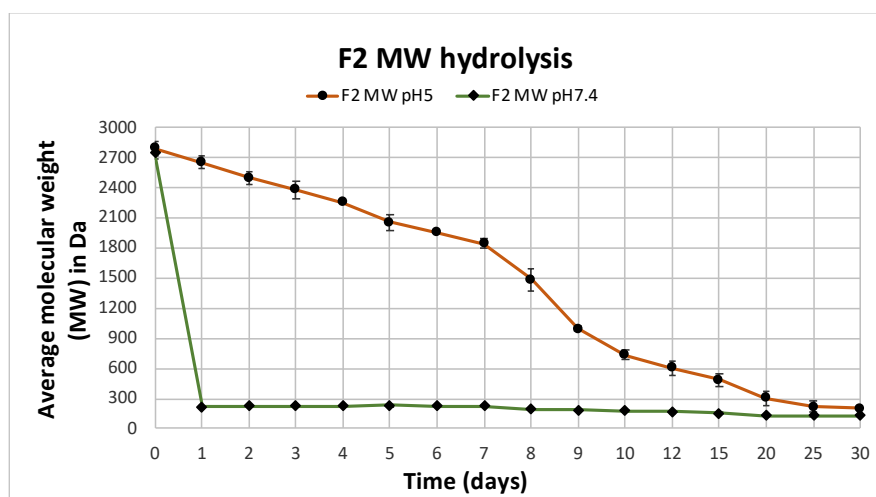


Figure 3.33a: MW and hydrolysis of F2 at pH5 and pH7. Mean \pm SD (N=1, n=2).

Considering the impact of the hydrolysis of A2 on the charge, at pH5 the polymer showed a strong positivity equal to 20.7 ± 3.12 mV; the potential was steadily reduced within the first week of analysis. Indeed, it was 20.53 ± 0.4 mV on day 4 and 19.5 ± 0.65 mV, proving the strong stability of the polymer when dissolved in acidic buffer. A gradual decrease of the positivity was noticed from day 8, 14.8 ± 1.7 mV to day 30 when the polymer was still positive showing a positive charge correspondent to 9.11 ± 1.59 mV (p-value < 0.05). Also, in this case as reported before for F1, the charge of the polymer was positive for the whole period of the experiment, underlining the strong stability heretofore presented by the polymers possessing diacrylate F as starting material. The behaviour of F2 was similar to the other PBAEs once dissolved in pH7.4. Hence, the polymer showed a positive charge of 21.2 ± 0.4 mV, but it was

easily reversed within 24 hours becoming strongly negative -20.76 ± 2.57 mV (p -value < 0.05). The negativity slowly rose from day 2 to day 30 ended up to a potential equal to -22.76 ± 1.32 mV (p -value > 0.05).

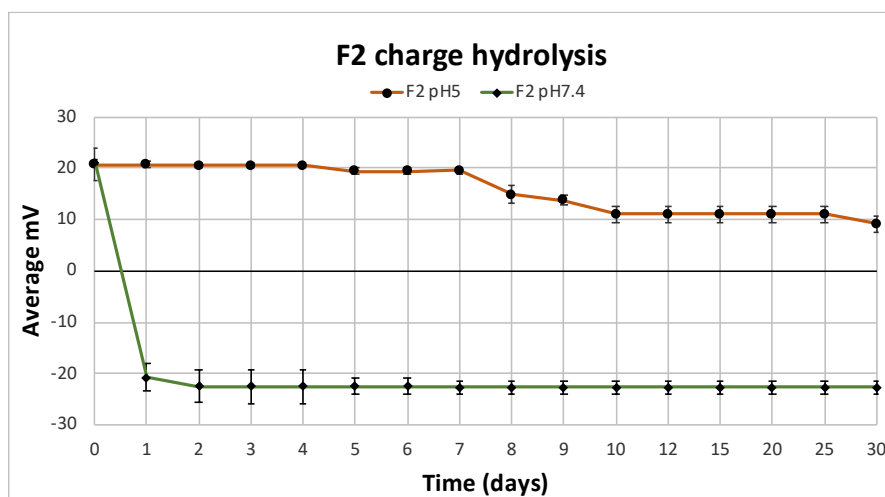


Figure 3.33b: Impact of F2 hydrolysis on charge at pH5 and pH7.4. Mean \pm SD (N=1, n=2).

F3

To conclude the analysis of the polymers of the group F, the hydrolysis was pursued also for the PBAE F3 and the results are shown in both figures 3.34a and 3.34b below.

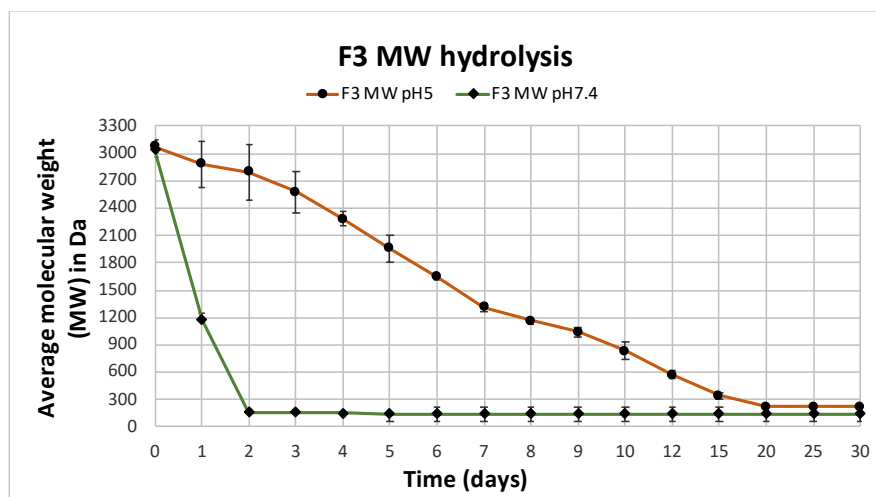


Figure 3.34a: MW and hydrolysis of F3 at pH5 and pH7. Mean \pm SD (N=1, n=2).

The molecular weight MW for F3 was detected via GPC for both media: at pH5 3080 Da and 3043 Da at pH7.4. As described for F1 and F2, also in this case there was a difference between the two profiles. At pH5 the polymer moderately degraded and it was completely hydrolysed

in 20 days. In particular, the MW dropped to 2793 Da on day 2, to 2280 Da on day 4 and it was almost half reduced, 1648 Da, on day 6. The reduction continued and after 10 days of dissolution of the polymer in buffer, the MW was correspondent to 831 Da and the value gradually kept decreasing until day 20, when only 223 Da of polymer remained (p-value < 0.05). No significant variation of MW was observed from day 20 to day 30 with a range of MW between 230-200 Da (p-value > 0.05). However, the hydrolysis of the polymer at pH7.4 occurred within only 2 days. Indeed, on day 1, the detected MW was equal to 1173 Da and it plummeted to 161 Da on day 2 (p-value < 0.05). The modulation of the value for the molecular weight of F2 was between 160-140 regarding rest of the analysis which continued until day 30 (p-value > 0.05).

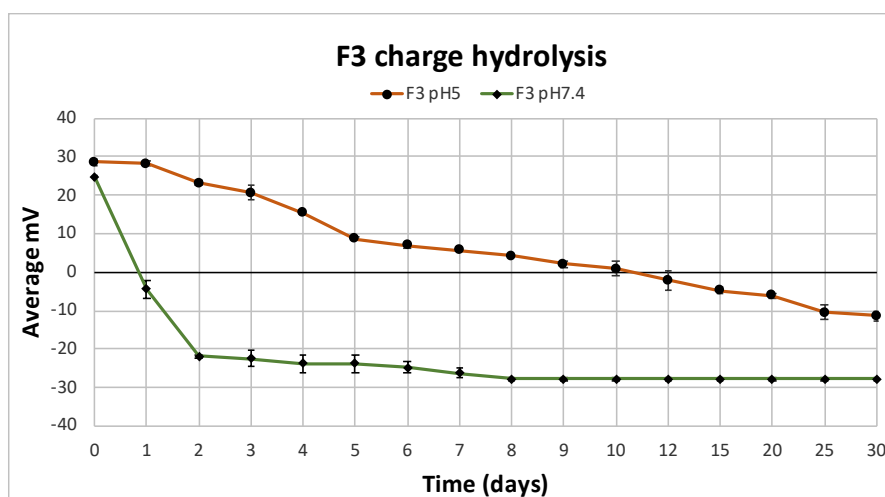


Figure 3.34b: Impact of F3 hydrolysis on charge at pH5 and pH7.4. Mean ± SD (N=1, n=2).

To support the hydrolysis performed for F3 via GPC, the same experiment was carried out considering this time the charge of the polymer measured through zeta potential instead of the molecular weight MW. A strong positive charge was detected on day 0 at both media: 28.7 ± 0.85 mV at pH5 and 24.53 ± 0.76 mV at pH7.4. In an acid environment, the potential of F3 was positive until the first 10 days when it was nearly 0, 0.88 ± 1.85 mV; then, from day 12 it was reversed, -2.06 ± 2.5 mV, with a progress of its negativity which reached -11.35 ± 1.34 mV (p-value < 0.05). However, under physiological conditions, the charge of the polymer was quickly turned into negative in only one day, -4.48 ± 2.46 mV, and in this case a rapid raise of negativity was observed on day 2, with a charge equal to -21.87 ± 0.46 mV. From day 3 to day

30 there a steady increase of the negativity ended to -27.73 ± 0.65 mV after the 30 days of analysis (p -value < 0.05).

To sum up the polymers of the group F presented a strong stability once dissolved at pH5, whereas they rapidly hydrolysed within maximum 2 days at pH7.4. In particular, once dissolved in acidic buffer, F1 and F2 showed a considerable positivity without being reversed into negative for the whole period of analysis. Therefore, this was the main change observed comparing these profiles to the ones of the all PBAEs previously described. On the contrary, comparing F3 to F1 and F2, at pH5, the polymer was stable only for the first 10 days, with a considerable drop of MW and charge afterwards (p -value < 0.05). No significant variation was detected between the profiles of the group F at pH7.4 and the other PBAEs (p -value > 0.05).

G1

The hydrolysis study was carried out also the for the polymers belonging to the group G: G1, G2 and G3 adopting the same protocol used for the analysis of the previous PBAEs. The molecular weight MW detected on day 0 for G1 by GPC was correspondent to 2063 Da at pH5 and 1986 Da at pH7.4. At pH5, there was no reduction in the MW for the first 2 days of the analysis, showing 2045 Da on day 1 and 2022 Da on day. An initial drop was observed from day 3, 1945 Da, to day 6, 1860 Da; then, the MW plummeted to 664 Da on day 7 and kept decreasing until day 15, when only few units left, 220 Da (p -value < 0.05). A low reduction was finally noticed from day 20 to day 30 with a range of value between 220-200 Da (p -value > 0.05) (figure 3.35a).

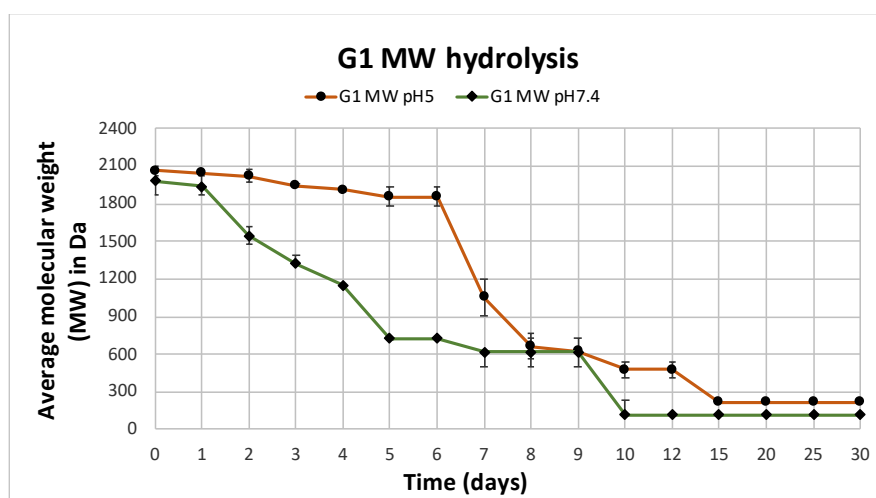


Figure 3.35a: MW and hydrolysis of G1 at pH5 and pH7. Mean \pm SD (N=1, n=2).

On the contrary, at pH7.4 the hydrolysis mainly occurred within 10 days, with a remarkable difference between this profile and those of the other PBAEs, where the hydrolysis lasted only few days. Starting from day 0, with a MW of 1986 Da, firstly, there was a drop from day 2, 1546 Da; then, on day 6 the MW was significantly reduced, 724 Da and it continued going down until day 10 when it reached 119 Da (p-value < 0.05), a value that remained similar until the end of the analysis on day 30 (p-value > 0.05).

Considering the impact of the hydrolysis for G1 on the charge at pH5 the measured potential was equal to 44.33 ± 1.24 mV and 40.77 ± 1.43 mV at pH7.4 as represented by the figure 3.35b. Although the charge of G1 was considerably positive at both media, a difference in both profiles was observed. For instance, at pH5, the potential was still strongly positive after 6 days, showing a value of 33.96 ± 1.0 mV, whereas it started reducing from day 7 firstly, reaching 10.73 ± 0.95 mV on day 10, then, 2.93 ± 0.66 mV on day 20 (p-value < 0.05). No further decrease was notice until day 30 evidencing the strong stability of this polymer without becoming negative as it occurred for most of the PBAEs heretofore analysed (p-value > 0.05).

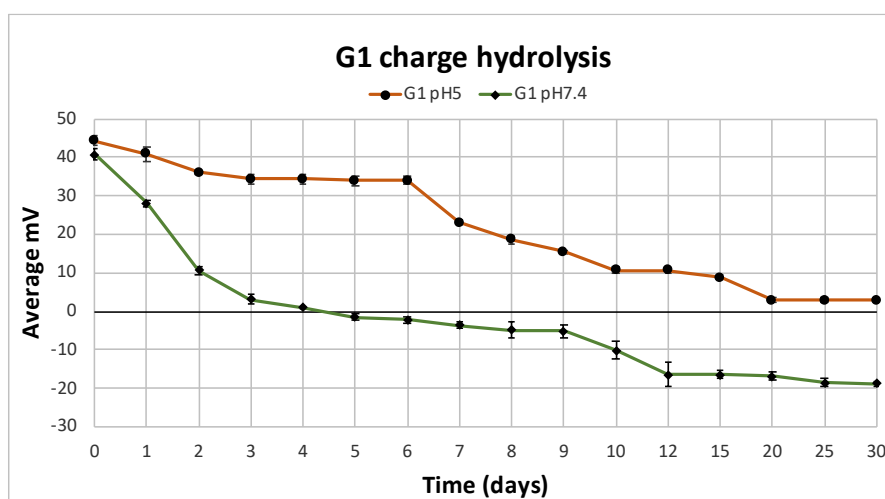


Figure 3.35b: Impact of G1 hydrolysis on charge at pH5 and pH7.4. Mean \pm SD (N=1, n=2).

On the other hand, the strong positivity of G1 at pH7.4 moderately declined on day 1, 28.06 ± 0.94 mV, and dropped to 3.08 ± 1.24 mV on day 3. The potential was then inverted on day 5, -1.46 ± 0.86 mV and the negativity kept increasing reaching -18.73 ± 0.64 mV on day 30. In this case it was observed that at pH7.4 the polymer slowly hydrolysed compared to the

profiles at same pH of the other PBAEs. Indeed, the potential of G1 was reversed into negative within 5 days rather 2 days, whereas the value of MW considerably dropped after 10 days instead of only 24 hours (p-value < 0.05).

G2

Continuing the analysis of group G, the hydrolysis was pursued also for the polymer G2. Firstly, the molecular weight MW was detected by GPC providing a value of 2300 Da at pH5 and 2260 Da at pH7.4 (figure 3.36a). Under acid conditions, the polymer was quite stable; in particular, no significant drop of MW was observed in the first 2 days, showing a value of 2182 Da on day 1 and 2015 Da on day 2 (p-value > 0.05). There was a reduction of more than 1000 Da reported from day 3 to day 7 when the MW was correspondent to 854 Da (p-value > 0.05). Moreover, it continued decreasing ending to 207 Da on day 12 and with a range between 210-190 Da detected from day 15 to day 30 (p-value > 0.05). On the contrary, under physiological conditions, the initial MW detected on day 0 plummeted to 372 Da on day 2 and from that day it steadily kept going down reaching 170 Da on day 8 (p-value < 0.05) and showing a range of value between 160-120 Da from day 9 to day 30 (p-value > 0.05).

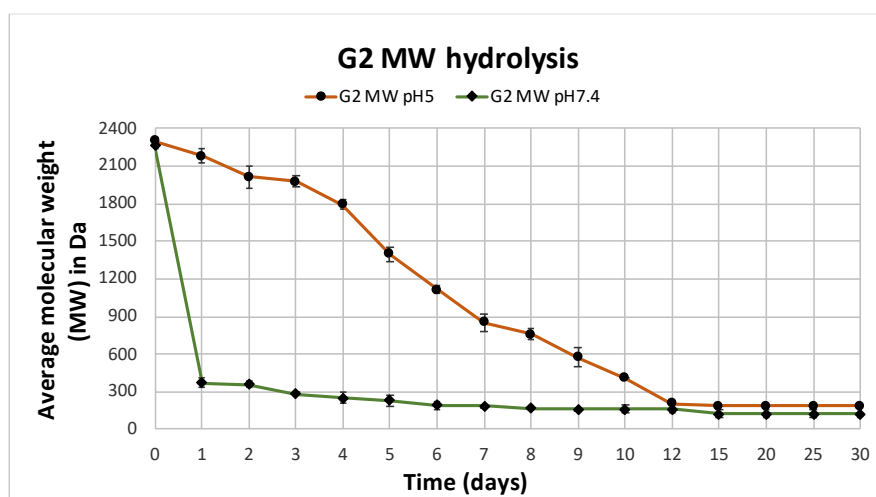


Figure 3.36a: MW and hydrolysis of G2 at pH5 and pH7. Mean \pm SD (N=1, n=2).

To support the results regarding the hydrolysis by degradation of molecular weight MW, the variation of the polymer charge was observed. As represented by the figure 3.36b, the measured charge on day 0 was evaluated for both media: at pH7.4, 22.17 ± 0.51 mV and at pH5 27.57 ± 0.55 mV. In the first case, the potential easily was turned into negative in only 1

day, showing a strong negative charge correspondent to -23.97 ± 1.53 mV (p-value < 0.05). The attitude of the G2 at pH7.4 was quite similar to the profiles of the other PBAEs dissolved in this medium and the negativity slowly rose from day 2 reaching a value of -33.93 ± 0.25 mV on day 30 (p-value < 0.05).

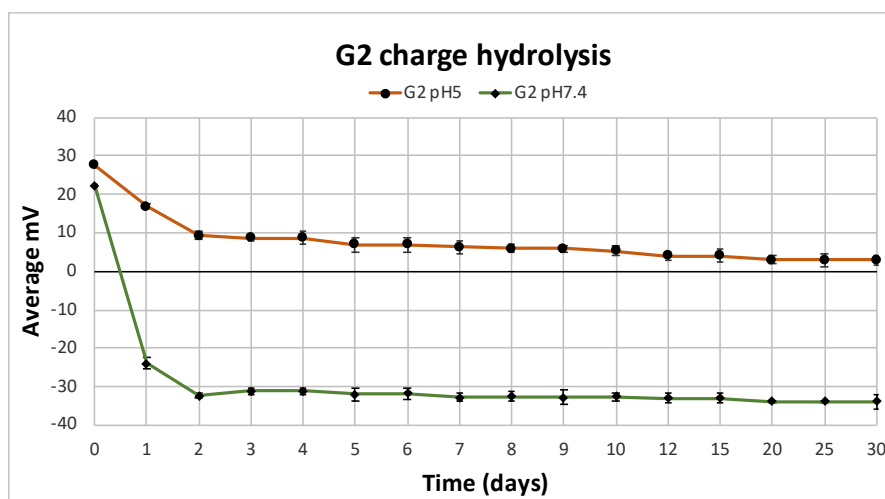


Figure 3.36b: Impact of G2 hydrolysis on charge at pH5 and pH7.4. Mean \pm SD (N=1, n=2).

However, the positivity of the polymer at pH5 was mainly reduced on day 1, 16.83 ± 0.61 mV. From day 2 starting from 9.35 ± 0.89 mV, it steadily decreased and after 7 days the charge was weakly positive, 6.3 ± 1.63 mV (p-value < 0.05). The polymer G2 showed a significant stability when dissolved at pH5 proved by its potential which was still positive after the whole period of the analysis (p-value < 0.05). Hence, the potential of this PBAE as already noticed for G1 was not inverted into negative providing a charge nearly to 0, 2.93 ± 1.12 mV after 30 days (p-value < 0.05).

G3

To conclude the list of the 18 PBAEs synthesised along this project, the determination of the molecular weight MW followed hydrolysis studies were pursued for G3, the last polymer belonging to the group G. Also, in this case, the experiments were realized adopting the same protocol described in advance and the results are reported below in both figures 3.37a and 3.37b.

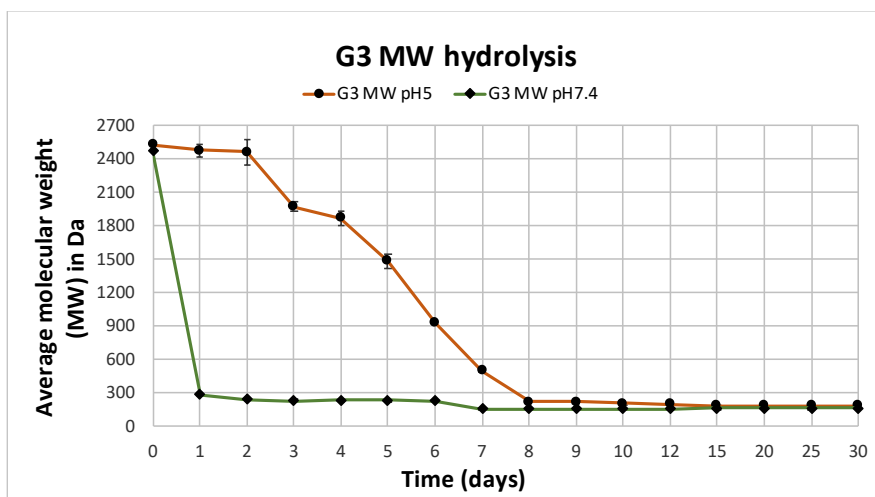


Figure 3.37a: MW and hydrolysis of G3 at pH5 and pH7. Mean \pm SD (N=1, n=2).

As reported above, the molecular weight MW was 2534 Da at pH5 and 2475 Da at pH7.4 on day 0. At pH5, the hydrolysis of the polymer occurred within 8 days, with an initial low decrease of the value of the MW in the first 2 days of analysis, 2482 Da on day 1 and 2465 Da on days 2. However, on day 5 it was detected a reduction of the MW 1100 Da from the value of day 0, 1488 Da, which firstly dropped to 931 Da on day 6, then to 504 Da on day 7 (p-value < 0.05). No further difference was observed from day 8 to day 30 where the MW showed a range between 230-130 Da (p-value > 0.05). On the contrary, the polymer once dissolved at pH7.4 presented a lower stability compared to the profile provided at pH5. For instance, from 2475 Da on day 0, the value of MW plummeted to 292 Da on day 1, as proof of the rapid hydrolysis of G3 at this medium (p-value < 0.05). From day 2 to day 30 the MW was in the average between 290-160 Da (p-value > 0.05). To better explain the hydrolysis via GPC, the degradation of the polymer was studied also considering the charge of G3 and its modulation in a period of 30 days.

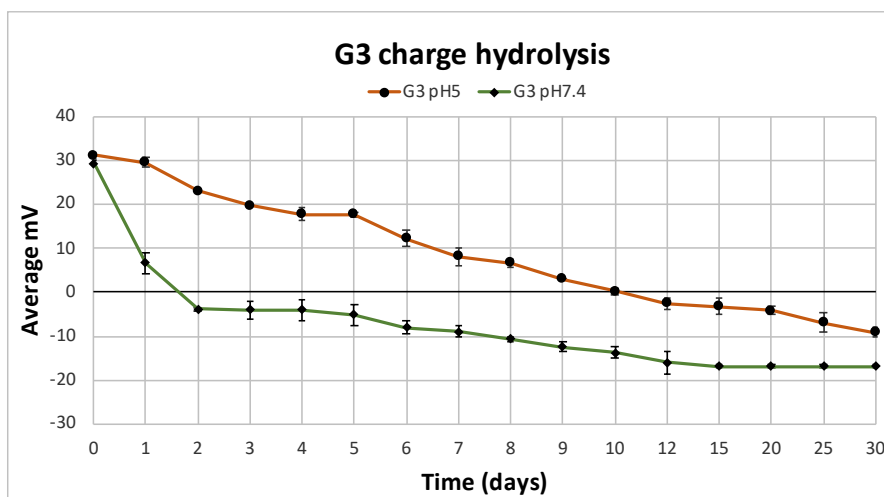


Figure 3.37b: Impact of G3 hydrolysis on charge at pH5 and pH7.4. Mean \pm SD (N=1, n=2).

Firstly, at pH5, the charge was measured on day 0, detecting a strong positivity provided by the polymer, 31.0 ± 0.8 mV; then with measurements carried out every 24 hours it was observed that the charge after 2 days was correspondent to 23.1 ± 0.16 mV dropping to 17.7 ± 0.51 mV on day 5 and to 8.08 ± 0.76 on day 7. The positivity was consistently reduced on day 10, when the charge was nearly to 0, 0.15 ± 0.78 mV and the potential of the polymer was definitely turned into negative from day 12, -2.6 ± 1.21 mV. The negativity continued increasing ending to -9.12 ± 1.12 mV on day 30 (p-value < 0.05). On the other hand, at physiological environment, the charge of G3 was equal to 29.3 ± 0.7 mV and in this case the positivity of the polymer was drastically decreased after the first 24 hours of analysis, 6.68 ± 2.46 mV (p-value < 0.05). The potential was then changed into negative from day 2, -3.9 ± 0.46 mV, reaching -16.78 ± 0.32 on day 15 (p-value < 0.05), a value that was measured also until day 30 (p-value > 0.05).

Comparing the profiles of the PBAEs belonging to the group G, it was observed that G2 and G3 similarly hydrolysed with a difference between the two media: the degradation occurred within few days at pH7 and in at least 10 days at pH5 (p-value > 0.05). On the contrary, G1 provided a slow hydrolysis for both media showing in particular a moderate degradation along 9 days at pH7.4 (p-value < 0.05). Furthermore, similarities were detected among polymers of groups F and G, especially for F1, F2, G1 and G2 (p-value > 0.05). To support this evidence, the hydrolysis carried out considering the charge of the polymers highlighted the gradual hydrolysis at pH5 and the quick degradation at pH7.4 except for G1 (p-value < 0.05).

Overall, considering the all 18 PBAE, the group B, F and G were more stable and among the 3 amines, amine 1 and 2 provided a more gradual hydrolysis when employed as starting material for the PBAEs synthesis.

Discussion

Poly (β -amino) esters (PBAE) are a promising group of polymers originally developed in the 1970, then accurately investigated in the 2000 by Langer and Lynn who mainly focused their research on gene delivery. These molecules are the results of conjugation between diacrylates and primary or secondary amines via one-pot reaction. In fact, with Michael addition there is no formation of side products that would require further purification steps to be eradicated. The presence of tertiary amines on the backbone of PBAEs enhances their buffer capacity for endolysosomal escape as well as they showed low toxicity and higher biocompatibility if compared to other polycations such as poly-L-lysine (PLL) and poly-(ethylenimine) (PEI) (Lynn and Langer, 2000). Moreover, these polymers are biodegradable and pH-responsive as studied by Lee *et al.* that synthesised a library of PBAEs from secondary amines and diacrylates esters observing that the pH sensitivity could be regulated by changing the alkyl group of the diacrylates (Hwang *et al.*, 2007). Besides their application as gene vectors, PBAEs were recently used in biomedical areas as scaffolds for tissue engineering (Safranski *et al.*, 2014) and as delivery systems of active compounds (Keeney *et al.*, 2013).

In this project, a library composed by 18 PBAEs was synthesised by mixing primary and bis(secondary) amines to diacrylates and characterised by ^1H NMR and ^{13}C NMR, molecular weights and surface charge by respectively Gel Permeation Chromatography (GPC) and zeta potential. The reagents were chosen to guarantee chemical diversity including modulation of both hydrophobicity and hydrophilicity (Anderson, Lynn and Langer, 2003). Polymerisation of macromers occurred by a step-growth mechanism leading to linear homopolymer, possessing only one repeated unit, including tertiary amines and ester bonds, and having the molecular weight ranging between 1400-3000 $\text{g}\cdot\text{mol}^{-1}$ and strong positive charge in both media sodium acetate pH5 and phosphate buffer pH7.4. The reaction was carried out adopting dichloromethane (CH_2Cl_2) as organic anhydrous solvent, to moderate the hydrolytic degradation during the synthesis (Cordeiro *et al.*, 2019), and to obtain PBAEs with higher molecular weight than those gained by using tetrahydrofuran (THF) (Lynn and Langer, 2000). Furthermore, depending on the stoichiometric excess of starting materials, PBAEs can be amino or acrylate ended but, for this thesis, the ratio was amine/diacrylate 1.1:1 based on the study pursued by Akinc *et al.* where, among different polymers synthesised by changing the stoichiometric ratios of amines/acrylates, only those amino-terminated provided a more efficient transfection activity (Akinc *et al.*, 2003).

Polymeric characterisation

The synthesis of the 18 PBAEs was verified by NMR spectroscopy dissolving each polymer in deuterated chloroform (CDCl_3) before pursuing the analysis. The success of the reaction was represented by the absence of diacrylate protons on the ^1H NMR of all the crude products. Hence, no peak appeared in the area between 5.8 ppm and 6.4 ppm as reported by Hwang *et al.* (Hwang *et al.*, 2007). A1 and A2 were synthesised as first polymers for this project and their NMR identification was compared to the study pursued by Langer and Lynn. In fact, their PBAEs profiles perfectly matched with those belonging to A1 and A2 and their work was considered a good example for the development of the other PBAEs of our library. In particular, to facilitate the interpretation of the ^1H NMR, the spectrum could be split into 5 parts: the first one corresponds to the protons of CH_2O value for all the PBAEs shifted between 4-4.2 ppm; the second part belongs to the protons of $\text{CH}_2\text{NH}_2\text{R}$ ranging between 3.76-2.8 ppm, then the following peak was representative of the protons of CH_2 bounded to the carbonyl of the ester bond, with a shifted value between 2.90-2.56 ppm. The protons belonging to the piperazine CH_2 were part of a multiplet peak with a chemical shift between 2.5-2.15 ppm and finally the hydrophobic group represented by the alkyl chains on the diacrylate presented was shifted from 2.0 to 1.30 ppm. For A2 the peak area 1.8-1.6 ppm was representative of the protons of the methylene group for the piperidine, whereas the protons of the hydrophobic chain in the amine shifted to 1.5 ppm. Overall the PBAEs possessing piperazine or 4,4 trimethylenpiperidine as amines showed a similar spectrum that was comparable to the polymers synthesised by Lynn and Langer (Lynn and Langer, 2000). For this project six PBAEs were synthesised by conjugating N,N-Bis[3-(methylamino)propyl]methylamine as amine 3 to six different diacrylates. The ^1H NMR was similar to what previously described, except for the peaks belonging the protons of the amine. The multiplet ranging from 2.60 to 2.30 ppm corresponded to the protons of the methylene groups of the amine and the methyl groups bounded to each nitrogen showed a chemical shift between 1.70-1.60 ppm. For all the 18 polymers, the hydrophilic or hydrophobic nature has been theoretically evaluated by calculating LogP (partition coefficient). It was observed that, considering a range of values between -5 and +5, a polymer was more hydrophilic with a LogP that was negative or close to 0, instead it was hydrophobic when LogP was between 0 and +5 or over +5. For instance, looking at the molecular structures of the 18 compounds, PBAEs including amine 1 and 3 and conjugated to diacrylates with short alkyl chain such as A,

D and E showed a LogP close to 0 or negative. On the other hand, PBAEs such as A2 or F2 or possessing F or G as diacrylates had a LogP ranging between 2 and 5 evidencing a more hydrophobic attitude. This was considered a first approach to support and highlight any difference among the polymers in molecular structures and hydrolysis.

PBAE hydrolysis studies

In this project the MW was determined by Gel Permeation Chromatography (GPC) for all the gained final products. Every PBAE was dissolved in two different media, pH5 and pH7.4, to respectively reproduce acidosis and healthy conditions (Kim *et al.*, 2013) and the molecular weight (MW) as well as the charge of PBAEs were measured on day 0. The screening of the PBAEs showed that our library is mainly composed by small molecules with MW ranging between 1400-3000 g·mol⁻¹, polydispersity index (PDI) around 1.0-1.5, according to Akinc *et al.* (Akinc *et al.*, 2003), and charge between +10/+15mV as also reported by Lynn and Langer (Lynn and Langer, 2000). A study of polymeric degradation was carried out for all the 18 PBAEs considering a variable parameter both molecular weight MW and charge over a period of 30 days. It was observed that the polymers degraded via hydrolysis due to the cleavage of the ester bonds in the polymer networks once immersed in buffers. In particular the hydrolysis mainly occurred under physiological conditions due to the formation of small molecules known as diol products (Anderson *et al.*, 2006). In contrast, the hydrolysis slowly occurred at pH5.1, whereas the polymers rapidly degraded if dissolved in buffers with pH values lower than 3.0 and higher than 12.0, anticipating the production of bis-(β-amino acid) secondary products, as demonstrated by Lynn and Langer (Lynn and Langer, 2000). Anderson *et al.* synthesised a library of 120 acrylate terminated PBAEs by mixing primary and bis(secondary) amines to excess of diacrylates. After the synthesis, they studied the degradation of the polymers which consistently occurred under physiological conditions via hydrolysis of the ester bonds to smaller by-products. With this study they evaluated the behaviour of every PBAE considering their variation in the mass loss within a period of 24 hours and after 57 days being dissolved in phosphate buffer pH7.4. In fact, it was observed that those polymers showed a wide range of degradation behaviour with a mass loss of 100% for some networks and a no significant mass loss detected for other PBAEs. In particular, it was observed that the PBAEs providing complete degradation after 24 hours were composed by hydrophilic amines whereas when hydrophobic amines were adopted in the PBAEs synthesis, the mass

loss was definitely lower (Anderson *et al.*, 2006). In this thesis, all the PBAEs hydrolytically degraded once dissolved in both media, pH5 and pH7.4. It was confirmed, as previously described by Anderson *et al.*, that the degradation mainly occurred under physiological conditions and comparing the 3 amines, piperazine (1), 4,4 trimethylenepiperidine (2) and N,N-Bis[3-(methylamino)propyl]methylamine (3), the PBAEs composed by amine 2 degraded more gradually than those gained by mixing amine 3 or amine 1 to diacrylates. This confirmed what noticed with the evaluation of the chemical parameter Log P, the partition-coefficient between to immiscible phases denoting either hydrophilicity or hydrophobicity for the 3 amines with the aid of SwissADME (Daina, Michielin and Zoete, 2017). In fact, it was observed that amine 2 is hydrophobic with a LogP of 2.42, whereas amines 1 and 3 had a better hydrophilicity, with values of LogP respectively correspondent to -0.29 and 0.85 (Daina, Michielin and Zoete, 2017). Furthermore, the chemical versatility provided by the numerous combinations of amines and diacrylates greatly influenced the polymer-degradation. To prove that, firstly, they monitored the hydrolysis of PBAEs by the adopting in the synthesis the same diacrylate, named A, and different amines, named as 1, 6, 7 and 9; then, as contrary, they chose one amine (7) that was mixed to several diacrylates and examined the degradation profiles of the resulting polymers. It was observed that the hydrolysis varied from one or two weeks if PBAEs were composed by more hydrophilic macromers, to three months or more, In case of more hydrophobic starting materials such as diacrylates A and E respectively containing ethylene glycol units or a long aliphatic chain (Anderson *et al.*, 2006), (Anderson, Lynn and Langer, 2003). Considering as example what previously described, also for the 18 PBAEs reported in this chapter the hydrolysis was studied detecting the molecular weight (MW) on day 0 and its modulation after 30 days. Additionally, in our case, the degradation was evaluated comparing the polymer-behaviour under physiological and acidic conditions with the aim of applying our library of PBAEs as networks to facilitate the drug delivery for prophylaxis to treat bone infectious diseases. In the figure 3.38a, the hydrolysis of the all PBAEs at pH5 was represented by three bar graphs where the polymers were split out in three groups of six polycations gained by mixing the six diacrylates to the three different amines. Overall, among the 3 amines, the amine 2 allowed a better control of the polymer degradation if compared to the profiles of the other two amines, 1 and 3, due to its hydrophobicity.

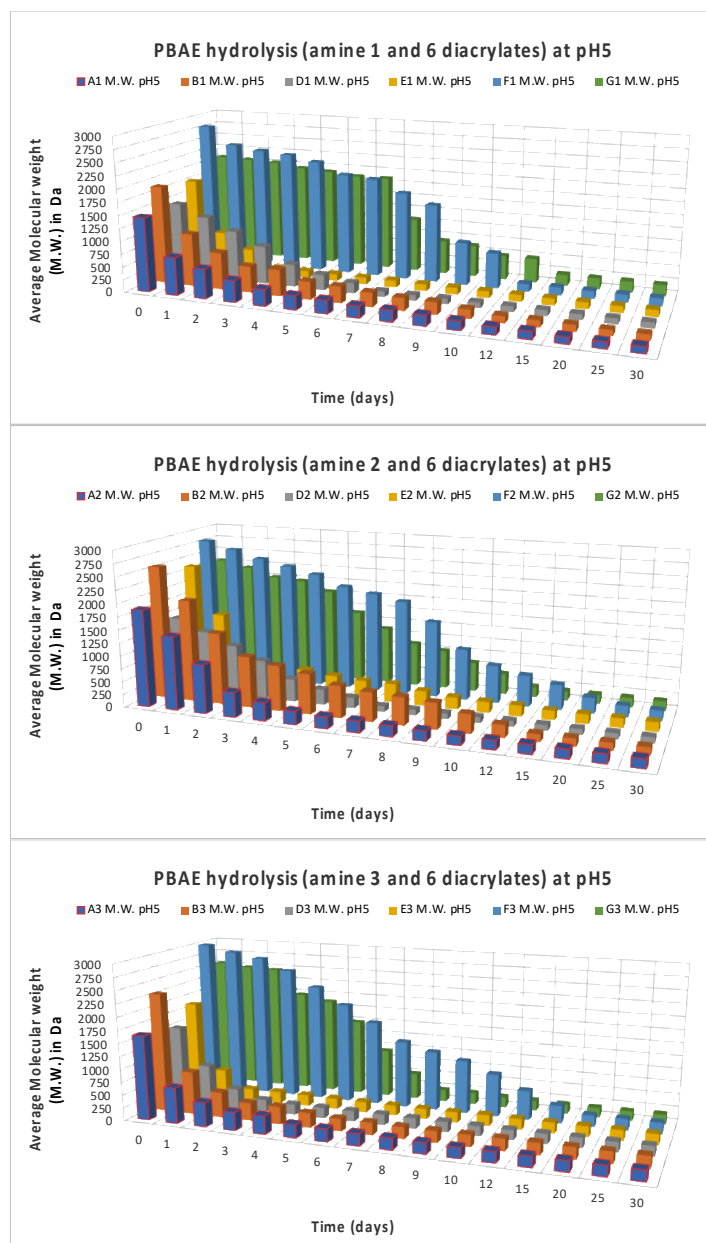


Figure 3.38a: Degradation at pH5 of PBAEs synthesised by mixing amine 1, 2 or 3 to the diacrylates A, B, D, E, F or G.

As contrary, the hydrophilicity of the piperazine (1) and the N,N-Bis[3-(methylamino)propyl]methylamine (3) similarly provided a rapid degradation if added to the diacrylates A, E and D. However, also the choice of the diacrylates influenced the degradation of the polymer. For example, the comparison between B2 and A2 revealed that a longer alkyl chain in the backbone enhanced the stability of the polycations in aqueous phase (Lenarcik and Kierzkowska, 2010), (Hwang *et al.*, 2007). In fact, it was observed that PBAEs composed by diacrylate B, showed better affinity to dissolve in both buffers, pH5 and pH7.4; instead,

those having A, 1,4 butanediol diacrylate, required longer dissolution time when dissolved in PBS (Lynn and Langer, 2000). Thus, this could explain both, the higher pH sensitivity and the gradual hydrolysis, typical of the PBAEs possessing B, 1,6 hexanediol diacrylate, as starting material. However, although their poor solubility in buffers, especially in PBS, for the PBAEs having F (bisphenol A ethoxylate diacrylate) and G (tri-cyclodecane dimethanol diacrylate) as diacrylates, the hydrolysis moderately occurred, independently of the amine adopted in the synthesis.

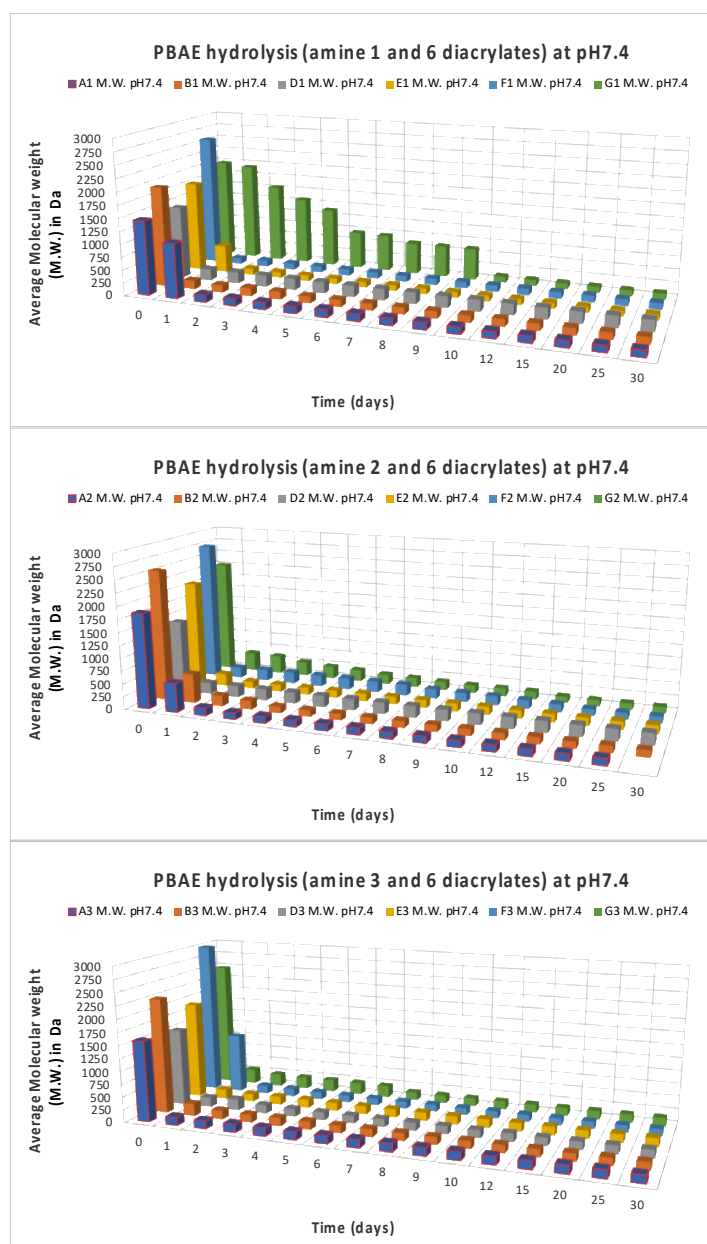


Figure 3.38b: Degradation at pH7.4 of PBAEs synthesised by mixing amine 1, 2 or 3 to the diacrylates A, B, D, E, F or G

As widely discussed, all the PBAEs rapidly degraded under physiological conditions and as it is shown by the figure 3.38b the degradation of the networks mainly occurred within 24 hours or few days, except for G1. In fact, for this polymer the degradation required longer time, almost 10 days, probably due to the hydrophobicity of the diacrylate G and a non-complete dissolution in phosphate buffer which showed, as result, presence of solid particles in the solution along the next days of the analysis. However, the rapid degradation of the PBAEs could be due to the hydrolysis by water and by the secondary amines which act as nucleophilic catalysts. In particular, a higher pH value, as in this case, allows to the free-protonation amines to quickly degrade the polymer. Hence, the hydrolysis by its own amines seems to better explain the degradation occurring within 1 or few days at pH7.4 as studied by Lim *et al.* This group of researchers synthesised a poly (*trans*-4-hydroxy-L-proline ester) (PHP) proving that the degradation of the polymer with pendant carboxylic groups occurred slower than the one of a polyester with amines as pendant group. This was explained by the strong nucleophilicity of the amines which can cause a rapid degradation of the polymer. (L *et al.*, 1999).

PBAE	MW (Da)	ζ potential at pH5	ζ potential at pH7.4
A1	1395-1502	+14.3 \pm 0.95 mV	+14.6 \pm 0.51 mV
A2	1860-1876	+20.35 \pm 0.94 mV	+20.57 \pm 1.26 mV
A3	1580-1640	+9.8 \pm 0.94 mV	+9.57 \pm 0.51 mV
B1	1883-2148	+19.53 \pm 0.55 mV	+17.97 \pm 2.01 mV
B2	2558-2579	+19.07 \pm 1.7 mV	+19.17 \pm 0.51 mV
B3	2260-2317	+15.1 \pm 0.85 mV	+14.53 \pm 0.12 mV
D1	1420-1440	+16.21 \pm 1.67 mV	+15.46 \pm 0.76 mV
D2	1820-1905	+19.23 \pm 1.15 mV	+18.27 \pm 1.21 mV
D3	1513-1517	+22.99 \pm 0.85 mV	+22.53 \pm 0.51 mV
E1	1770-1778	+20.37 \pm 1.92 mV	+20.46 \pm 2.34 mV
E2	2072-2376	+12.13 \pm 0.25 mV	+12.17 \pm 0.41 mV
E3	1882-1913	+14.66 \pm 0.85 mV	+12.8 \pm 0.51 mV
F1	2584-2801	+29.57 \pm 2.01 mV	+29.9 \pm 1.97 mV

F2	2749-2800	+20.7 ± 3.12 mV	+21.2 ± 0.4 mV
F3	3043-3080	+28.7 ± 0.85 mV	+24.53 ± 0.53 mV
G1	1990-2034	+36.16 ± 0.46 mV	+38.06 ± 1.43 mV
G2	2260-2300	+27.57 ± 0.55 mV	+22.17 ± 0.5 mV
G3	2474-2535	+31.1 ± 0.8 mV	+29.3 ± 0.46 mV

Table 3.2: Summary of molecular weight (MW), determined via GPC and ζ potential for the 18 PBAEs

To support the degradation studies performed for the PBAEs presented in this thesis, measurements of ζ potential at both media, pH5 and pH7.4 were carried out and summarized in the table above. All the 18 polymers possessed a positive charge ranging between +10 and +36 mV, and a ζ potential of minimum +10 mV was necessary for PBAEs nanoparticles transfection (Kim, Sunshine and Green, 2014). Moreover, it was found that there was no significant incidence on the polymer positivity by modulating its molecular mass (Sunshine, Peng and Green, 2012). However, in our case it was observed that the variation in the ζ potential was mainly caused by the amine adopted in the synthesis and its attitude to be easily protonated by changes of the pH (Perni and Prokopovich, 2017b). Furthermore, in some cases such as, for B1, B3, D1, D2, E3, F3, G2 and G3, it was detected a lower positive charge at pH7.4, possibly due to a reduced number of protonated nitrogen and showing as result a lower ζ potential (Perni and Prokopovich, 2017b), (Kim, Sunshine and Green, 2014). Nevertheless, the degradation of PBAEs examined by considering ζ potential reinforced the hydrolysis studied analysing the molecular weight (MW) and highlighted either differences and analogies among the synthesised polymers. For example, with a strong positive charge and a moderate hydrolysis, the groups B, F and G could be promising candidates for the early stage of delivering drugs through the cytoplasm via electrostatic interactions for bone tissue regeneration. This will be better discussed in the next chapter, where it is described the application of the 18 PBAEs exploiting their positive charge to prolong the activity of an antimicrobial or an antibiotic to provide prophylaxis to treat infections caused by bone diseases.

Conclusions

Poly(β -amino) esters refer to a class of polymers synthesised via step-growing mechanism by mixing acrylates and primary or secondary amines to form tertiary amines and esters which provided attractive properties to these molecules such as pH-responsiveness and biodegradability. Furthermore, it is known that PBAEs are cationic polymers and that the ester bonds of their backbone hydrolytically degrade which is one the major merit of these networks. In fact, the hydrolysis of PBAEs was found to be interesting due to two main reasons: firstly, the degradation leads to no toxic by-products, then, while these molecules hydrolyse, there is an increase in the transfection efficiency. Hence, PBAEs have several applications, especially for the drug delivery of genes, antimicrobials and anticancer drugs. In this project, 18 degradable linear macromers were synthesised via Michael addition by conjugating 3 amines, piperazine (1), 4,4 trimethylenpiperidine (2) or N,N-Bis[3-(methylamino)propyl]methylamine (3) to 6 different diacrylates monomers, 1,4 butanediol diacrylate (A), 1-6 hexanediol diacrylate (B), neo-pentyl glycol diacrylate (D), 1-3 butanediol diacrylate (E), bisphenol A ethoxylate diacrylate (F) and tri-cyclodecane dimethanol diacrylate (G). To form the 18 amino-terminated PBAEs, the reaction was carried out in dichloromethane (CH_2Cl_2) as molar ratio amine-diacrylates 1.1:1.0 and the combination of those monomers was chosen to provide chemical diversity and for the commercially availability of the reagents. The success of the synthesis lead to a 99% of yield and it was verified by characterisation of the crude products by NMR spectroscopy, ^1H NMR and ^{13}C NMR, Gel Permeation Chromatography (GPC) and ζ potential measurements. The NMR results proved the disappearance of diacrylate protons during the synthesis that were generally visible in the area between 5.8-6.4 ppm, plus the prevalence of methylene protons bonded to the amines. The GPC allowed the evaluation of molecular weight MW ranging between 1300-3100 Da and with polydispersity of 1.0-1.5. We assumed that those polymers were degraded via hydrolysis by cleavage of the ester bonds in the networks when immersed in PBS. Thus, we investigated the degradation of the PBAEs by dissolving them into two different media, sodium acetate buffer pH5 and phosphate buffer pH7.4, to respectively reproduce, endosomal acidosis and physiological conditions. The hydrolysis was determined by monitoring the variation of the molecular weight MW, detected via GPC, over a period of 30 days and our polymers showed a wide range of degradation behaviour. Overall, the hydrolysis at pH 7.4 mainly occurred within 24 hours except for G1, for which it lasted 10 days. As contrary, the reduced availability

of free-protonated nitrogen at pH5 controlled the degradation of the polymers occurring within 10-15 days for PBAEs belonging to groups A, E, D, over 15 days for those of group B and surprisingly over 20 days for the groups F and G. Simultaneously, those results were supported by a parallel study of the charge modulation for the all 18 PBAEs. In the average, it was observed that the charge initially ranging between +10 and +36 mV, was slowly inverted into negative at pH5 whereas rapidly reversed at pH7.4 as well as verified for the degradation by molecular weight MW. We attributed that to the chemical versatility of the monomers: for instance, PBAEs formed by diacrylate with longer alkyl chain presented a lower degradation. Thus, this was the case for B1, B2 and B3, having 2 more methylene groups in the backbone of the diacrylate, which gradually hydrolysed at pH5 if compared to the PBAEs of A, D and E. Additionally, a reduced degradation also occurred when a hydrophobic amine was incorporated into the polymers such as the piperidine (amine 2): hence, we observed a better stability for G2, F2 and B2 and a controlled hydrolysis at pH5 if compared to the degradation behaviour of the other PBAEs. These results led to a better understanding of the role played by the various combinations of amines and diacrylates, in the degradation behaviour of PBAEs which could be controlled and addressed to specific applications. We expect that the differences observed in the hydrolysis of these polymers could find application in tuning encapsulated drug release kinetics to a target profile. For this reason, all the 18 PBAEs described in this chapter were employed for the realisation of controlled release systems to provide prophylaxis as treatment of infections caused by bone diseases.

Chapter 4: Chlorhexidine and PBAE loaded on silica nanoparticles via Layer by layer (LbL) coating

Introduction

The formation of biofilms occurring by colonisation of bacterial species on different surfaces, could represent a serious drawback for implanted materials such as: bone cements for dental and orthopaedical applications, catheters and sutures (Barceló *et al.*, 2016), (Tambunlertchai, Srisang and Nasongkla, 2017), (Harnet *et al.*, 2009), (Perni and Prokopovich, 2020a). Among the strategies adopted to prevent this problem, a good option could be the surface modification by coating with antimicrobial agents via self-assembly technique. Chlorhexidine is a broad-spectrum compound acting against Gram positive and Gram negative, which is widely used to treat dental (Maugeri and Scientifico, 2016), and orthopaedic infections (George, Klika and Higuera, 2017), (MacLean *et al.*, 2019). The structure of the antimicrobial agent includes guanidium groups which, due to their ability to bind bacteria cell membranes, lead to the cell function disruption (Lim and Kam, 2008), (Milestone, Passaretti and Perl, 2008). However, the lack of drug long-term effect can cause repetitive infections and failure of the implant (Smith *et al.*, 2018b), (Luo *et al.*, 2016), (Harnet *et al.*, 2009). Thus, an alternative strategy to provide prophylaxis to treat early and delayed onset infections is required. For instance, the development of drug delivery systems which are able to enhance the release of chlorhexidine could be helpful in reducing the incidence of infections (Perni and Prokopovich, 2020a). The self-assembly technique applied is the layer by layer (LbL) coating, where opposite charged compounds are alternatively loaded on the substrate via electrostatic interactions (Gentile *et al.*, 2015). Therefore, the LbL is considered a successful method to design carriers with high drug content, improving the its solubility and kinetics of release (Jenjob, Phakkeeree and Crespy, 2020), (Schneider and Decher, 2008), (Wood *et al.*, 2005), (Luo *et al.*, 2016), (Gong *et al.*, 2007).

The aim of this chapter is to report the encapsulation of the small molecule chlorhexidine diacetate salt hydrate, via LbL method, onto spherical silica particles, to achieve sustained drug release. To build up multilayers alternatively non-hydrolysable polymer alginate, negatively charged, and hydrolysable poly (β -amino) esters (PBAEs), positively charged, were also embedded onto the nanocarrier surface via electrostatic interactions. More specifically,

18 pH-responsive drug delivery systems were fabricated using 18 different PBAEs whose synthesis and characterisation were described in chapter 3. The drug release rate was dependent on the polymer degradation, which was relying on the structure of the various monomers chosen for the PBAEs synthesis. However, the release of the cargo was also influenced by other factors such as: drug diffusion through the multilayers, the size of the nanocarrier and the pH environment. To prove that the antimicrobial agent release was higher and controlled when PBAEs were embedded onto the drug delivery systems, a bilayer coating was developed, as control system, including only the polymer alginate and the chlorhexidine. In this case, the release was rapid but lasting 25 days, whereas it was longer and controlled, occurring between 2-3 months, when a PBAE was employed in the nanoparticle formulations.

Therefore, in this chapter it was demonstrated that particles possessing PBAEs could be highly efficient carrier coatings. This strategy could represent a promising approach to overcome the disadvantages of the current drug delivery systems such as drug load capability, stability and drug release efficiency.

Materials and methods

Chemicals

All the reagents required for this project are described in the section 2.1 of chapter 2. The buffer solutions were prepared as follows: 100 mL of sodium acetate pH5 were composed by 70% sodium acetate trihydrate (0.1M) and 30% acetic acid (0.1M) instead for 100 mL of the same solution at pH4 the ratio was 82% of acetic acid and 18% sodium acetate trihydrate. Phosphate buffer solution was gained by dissolving 1 tablet of PBS in 100 mL of deionised water.

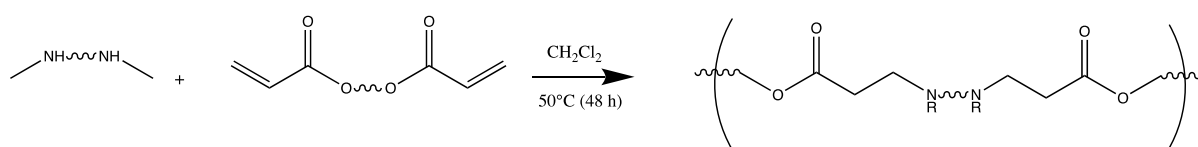
Nanoparticles preparation

For each delivery system, 500 mg of silica nanoparticles (AFSi-NPs) were synthesised and amino-functionalised with the Stöber method, which was accurately described in the section 2.2 of chapter 2. The one-pot synthesis occurred via hydrolysis of tetraethyl orthosilicate

(TEOS) in reverse micro-emulsion followed by amino-functionalisation with 3(amino propyl) triethoxysilane (APTS).

Synthesis of Poly (β amino) esters (PBAEs)

Each polymer was gained by Michael addition of a secondary amine to a diacrylate in a ratio 1.1:1:1, dissolved in DCM in a glass tube and kept stirring for 48 hours in oil bath. Every crude product was recovered by 3 washing steps with diethyl ether followed by centrifugation to remove the excess of starting materials. The list of PBAEs and their monomers are reported in the section 2.3 of the chapter 2.



Scheme 3.2: General PBAE reaction

Layer by layer self-assembly

The fabrication of thin multilayers nanocoating systems was determined by alternative deposition of opposite charged polyelectrolytes and the drug on the surface of AFSi-NPs via electrostatic interactions (figure 4.1).

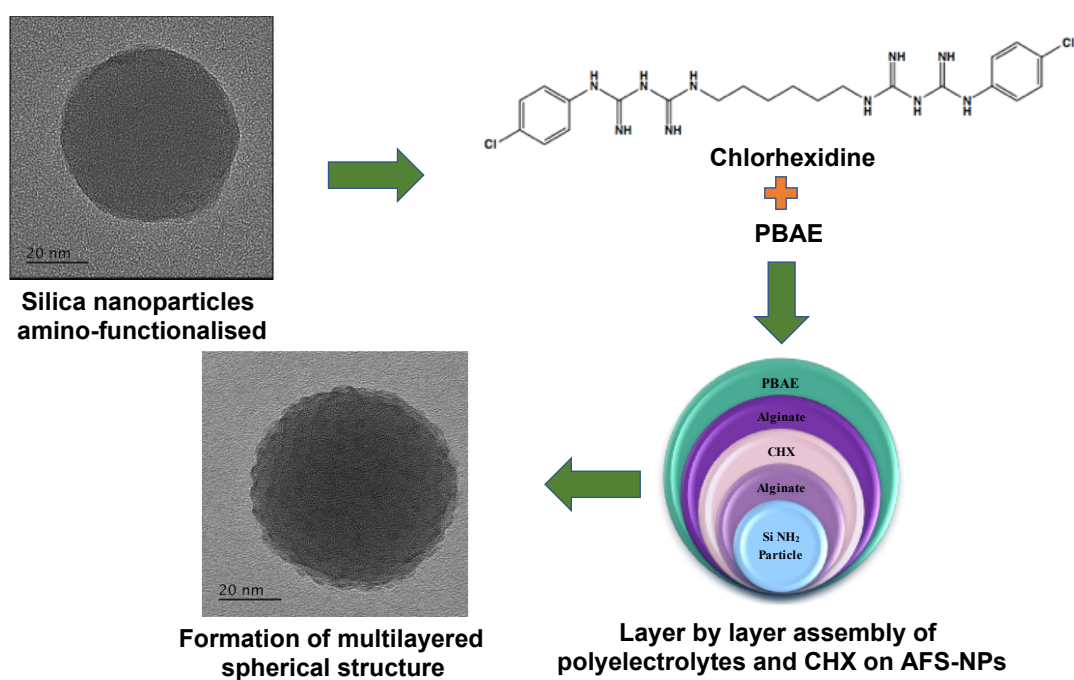


Figure 4.1: Layer by layer deposition

Firstly, only alginate and chlorhexidine were coated producing a drug delivery system of 10 bilayers (table 4.1). The self-assembly was performed in acidic conditions dissolving each polyelectrolyte and the drug in sodium acetate pH5 to reproduce infectious environment. The concentrations used for the LbL were as follows: 2mg/mL of alginate and 10mg/mL of chlorhexidine diacetate.

Bilayer matrix: Alg-CHX

Quadruple layer no.	Abbreviation	Layers on the surface of AFSi-NPs
1	B1	AFSi-NPs-alginate- <i>chlorhexidine</i>
2	B2	AFSi-NPs-B1-alginate- <i>chlorhexidine</i>
3	B3	AFSi-NPs-B2-alginate- <i>chlorhexidine</i>
4	B4	AFSi-NPs-B3-alginate- <i>chlorhexidine</i>
5	B5	AFSi-NPs-B4-alginate- <i>chlorhexidine</i>
6	B6	AFSi-NPs-B5-alginate- <i>chlorhexidine</i>
7	B7	AFSi-NPs-B6-alginate- <i>chlorhexidine</i>
8	B8	AFSi-NPs-B7-alginate- <i>chlorhexidine</i>
9	B9	AFSi-NPs-B8-alginate- <i>chlorhexidine</i>
10	B10	AFSi-NPs-B9-alginate- <i>chlorhexidine</i>

Table 4.1: LbL matrix of deposited alginate and CHX layers on AFSi-NPs

Then, 18 nanocoatings were developed including alginate/chlorhexidine/alginate/PBAE up to ten quadruple layers, embedding a different polymer in each system. In this case, 2mg/mL of PBAE were coated onto AFS-NPs, whereas the concentrations for alginate and antimicrobial agent were the same applied for the bilayer delivery system. A general example of matrix including ten quadruple layers is reproduced by the table 4.2, but the detailed description of all systems designed in this project are reported in the section 2.4.1.1 of the chapter 2.

Quadruple layers matrix: Alg-CHX-Alg-PBAE

Quadruple layer no.	Abbreviation	Layers on the surface of AFSi-NPs
1	Q1	AFSi-NPs-alginate- chlorhexidine -alginate-PBAE
2	Q2	AFSi-NPs-Q1-alginate- chlorhexidine -alginate-PBAE
3	Q3	AFSi-NPs-Q2-alginate- chlorhexidine -alginate-PBAE
4	Q4	AFSi-NPs-Q3-alginate- chlorhexidine -alginate-PBAE
5	Q5	AFSi-NPs-Q4-alginate- chlorhexidine -alginate-PBAE
6	Q6	AFSi-NPs-Q5-alginate- chlorhexidine -alginate-PBAE
7	Q7	AFSi-NPs-Q6-alginate- chlorhexidine -alginate-PBAE
8	Q8	AFSi-NPs-Q7-alginate- chlorhexidine -alginate-PBAE
9	Q9	AFSi-NPs-Q8-alginate- chlorhexidine -alginate-PBAE
10	Q10	AFSi-NPs-Q9-alginate- chlorhexidine -alginate-PBAE

Table 4.2: LbL matrix of deposited CHX and PBAE layers on AFSi-NPs

Nanoparticles surface characterisation

Size measurements: TEM and DLS

The size of the nanoparticles was evaluated before and after the multilayer deposition, via transmission electron microscopy (TEM) on a JEOL JEM-2100 operating at 200 kV. However, the determination of size by dynamic light scattering (DLS) was carried out only for the amino-functionalised nanoparticles due to a partial dissolution of the nanocarrier in the buffer solution after the LbL self-assembly. The parameters required for the measurements are accurately described in the section 2.5.1 of the chapter 2.

Zeta potential measurements

For all the 18 nano-delivery systems and the bilayer nanoconstruct, the zeta potential was measured to detect the modulation of the charge of each polyelectrolyte and the drug once embedded onto the surface of the nanocarrier. The measurements occurred for all the 40 layers, composing the ten quadruple layers, by dissolving the particulate in 1 mL of sodium acetate pH5. Therefore, the electrophoretic mobility for the non-coated and coated nanoparticles was measured via dynamic light scattering (DLS) on Malvern ZetaSizer. The

conditions adopted for the measurements are listed in the section 2.5.2 of chapter 2. All data were expressed as mean \pm standard deviation (SD) for at least 3 measurements.

Thermogravimetric analysis (TGA)

The thermogravimetric analysis was carried out for the nanoparticles of bilayer and quadruple layers coatings by using Perkin-Elmer TGA 4000 instrument with the aim of measuring the weight loss as function of time once more layered were coated onto the nanocarrier surface. For all the matrices, the layers 1, 3, 5, 7 and 10 were object of analysis. Further information about the parameters of the experiment are reported in the section 2.5.3 of chapter 2. All data were expressed as mean \pm standard deviation (SD) for at least 2 measurements per sample.

Chlorhexidine release quantification

The chlorhexidine release was evaluated treating the nanoparticles (10mg) after layer by layer deposition with 1mL sodium acetate buffer pH5 and 1mL PBS in separate eppendorfs to respectively reproduce infectious and physiological environments. Only the last quadruple Q10 or bilayer B10 were object of the analysis due to a higher drug loading. The samples were kept in the incubator at 37°C and every 24 h for each one the medium was withdrawn and replaced with 1mL of fresh buffer. The quantification was determined by measuring the absorbance of the release media via High Performance Liquid Chromatography (HPLC) and the optimised method is described in section 2.5.4 of chapter 2. All data were expressed as mean \pm standard deviation (SD) of 3 replicates per sample.

Results

Nanoparticles surface characterization

Size measurements

The hydrodynamic size of silica nanoparticles amino-functionalized via dynamic light scattering (DLS) was determined through Malvern ZetaSizer by dispersing 1mg of the sample in 1mL of sodium acetate buffer pH5.

The size (nm) distribution measured via DLS and expressed as function of number of particles (percentage) correspondent to 55 ± 7.21 nm with 0.3 as polydispersity index and TEM images reported in the figure 4.1 confirmed the spherical monodisperse shape of the nanocarrier (Al Taher *et al.*, 2018a), (Min, Braatz and Hammond, 2014).

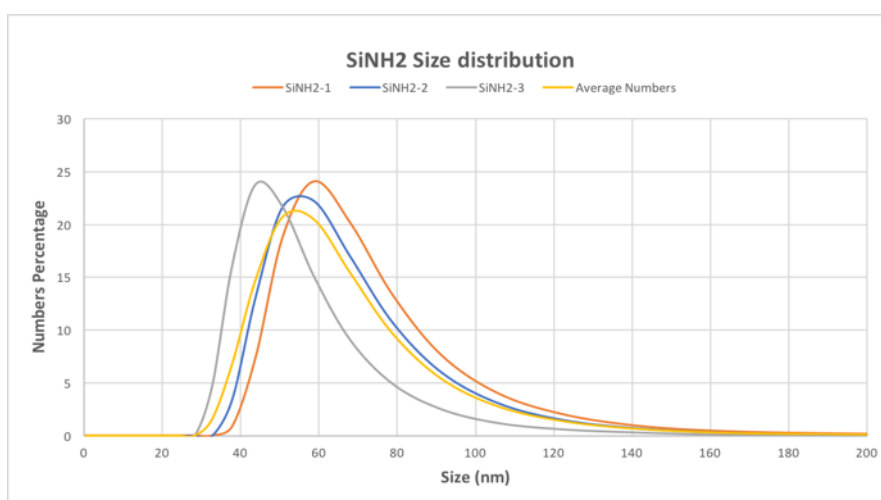


Figure 4.2: Size measurements for silica amino-functionalized nanoparticles. Mean \pm SD (N=1, n=3).

ζ potential measurements

Bilayer: Alg-CHX

First of all, the development of a nano delivery system composed by only sodium alginate and chlorhexidine was formed. The polyelectrolyte and the drug were alternatively coated via LbL as bilayer onto the surface of the nanocarriers for 10 times to form a system including overall 20 layers.

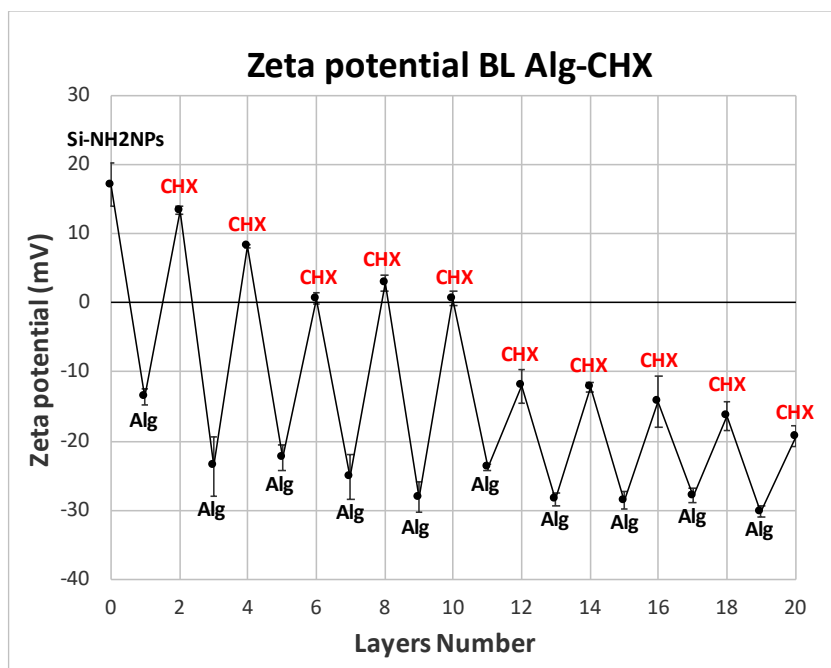


Figure 4.3: ζ potential for the coating system SI-NH₂NPs-Alg-CHX. Mean \pm SD (N=1, n=3).

The potential detected for the nanoparticles alone was positive corresponding to 17.1 ± 3.12 mV and it was reversed once the sodium alginate was layered onto their surface, -13.7 ± 1.15 mV. The charge was inverted again with the coating of the drug showing a positive value of 13.4 ± 0.55 mV as reported in the figure 4.3 below (1-3 layers).

Overall it was observed that the positivity of the CHX was inverted by the strong negativity of the sodium alginate. For instance, the initial positive charge was half decreased on B2, 8.18 ± 0.20 mV, and it was stable on B3, B4 and B5 showing a potential nearby 0, 0.55 ± 0.84 mV. Then, on B6, the charge plummeted to -12.04 ± 2.46 mV and the negativity kept increasing until B10, -19.33 ± 1.53 mV. At first glance, the typical zig-zag pathway proved the success of the multilayer formation by alternatively coating negative and positive polyelectrolytes. However, the potential of the chlorhexidine was positive until B5 and it was switched from B6 by the strong negativity of the alginate. Therefore, the employment in the matrices of the PBAEs was carried in this project with the aim of improving the drug loading efficiency and managing the strong negativity of the alginate.

A1

Zeta potential measurements were conducted for the amino-functionalized silica nanoparticles followed by each layer deposition characterisation for the all 18 delivery

systems developed along this project. The LbL technique has been used to build up to ten quadruple layers (Q1-Q10) for a total of 40 layers and the systems possessing as PBAEs A1, A2 and A3 were our first object of analysis.

Regarding the nanosystem CHX-A1, as it is shown in the figure 4.4, for the first quadruple layers a zig-zag pathway provides alternatively a positive and negative charge typical of the layer by layer technique. Then the profile shifted into the negative area due to the weak positive charge of A1.

The first quadruple layer (1-5 layers) included: silica nanoparticles amino-functionalized, sodium alginate, chlorhexidine, sodium alginate, A1. The value of the silica nanoparticles amino-functionalized was equal to 26.96 ± 0.92 mV. Once the sodium alginate has been layered the charge of the system dropped to a negative value of -26.63 ± 1.19 mV; after the addition of the chlorhexidine the value of the construct became positive, 27 ± 1.1 mV. Then, the subsequent layer with alginate again exhibited a negative charge, -25.4 ± 0.56 mV, which became positive with the layer of the polycation A1 that has weak positive potential equal to 8.8 ± 1.4 mV.

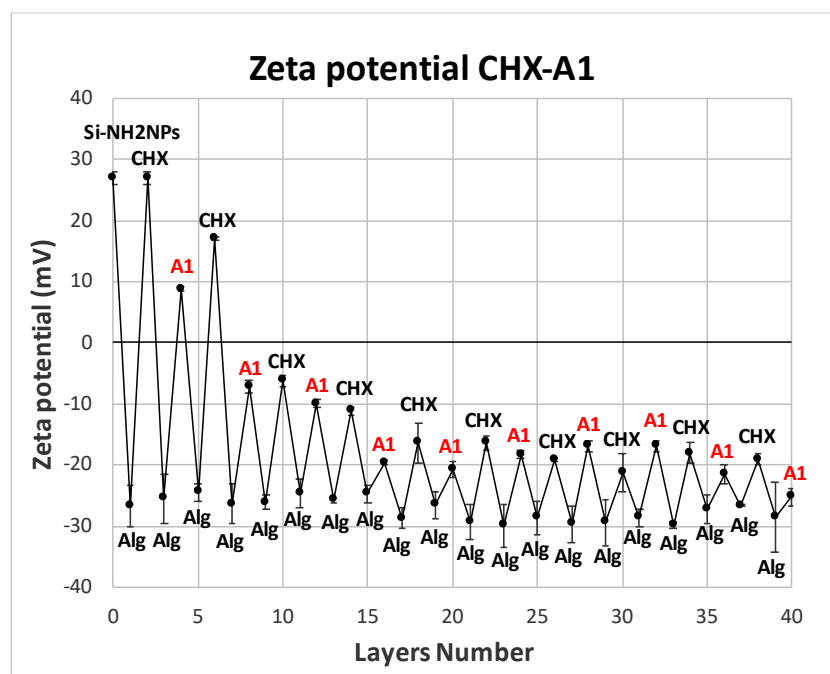


Figure 4.4: ζ potential for the coating system SI-NH₂NPs-Alg-CHX-Alg-A1. Mean \pm SD (N=1, n=3).

The potential of CHX was reduced to 17.1 ± 0.3 mV on Q2 and became negative from Q3, -6.23 ± 0.8 mV, showing a strong negativity once all the 40 layers were embedded onto the system, -19.07 ± 0.6 mV. Differently, the weak positive charge of A1 was easily turned into negative already on Q2, -7.16 ± 0.74 mV, and also in this case it was greatly influenced by the negativity of the sodium alginate. Thus, the potential of the polymer on Q10 was correspondent to -25.2 ± 1.3 mV.

A2

Zeta potential measurements were detected also for the second sequence which included the same drug, chlorhexidine, but a different polycation. In this case, A2 polymer was employed instead of A1.

Compared to A1, the measurements of all the components of this sequence were as following. The silica nanoparticles amino-functionalized showed a potential that was similar to the previous sequence, due to the amino groups added with the Stöber method (26.7 ± 1.06 mV); layering the sodium solution reversed negatively the potential of the Si-NH₂NPs showing a value equal to -21.1 ± 3.4 mV. The chlorhexidine in both the sequences provided in the first quadruple layer (layers 1-5 in the figure 4.5) a strong positive charge, 27 ± 0.99 mV, that was decreased by the addition of the sodium alginate which reduced again the potential to -36.5 ± 4.05 mV. Finally, the coating of the polycation A2, increased the potential, as described for A1 before, showing a value of 10.2 ± 0.36 mV.

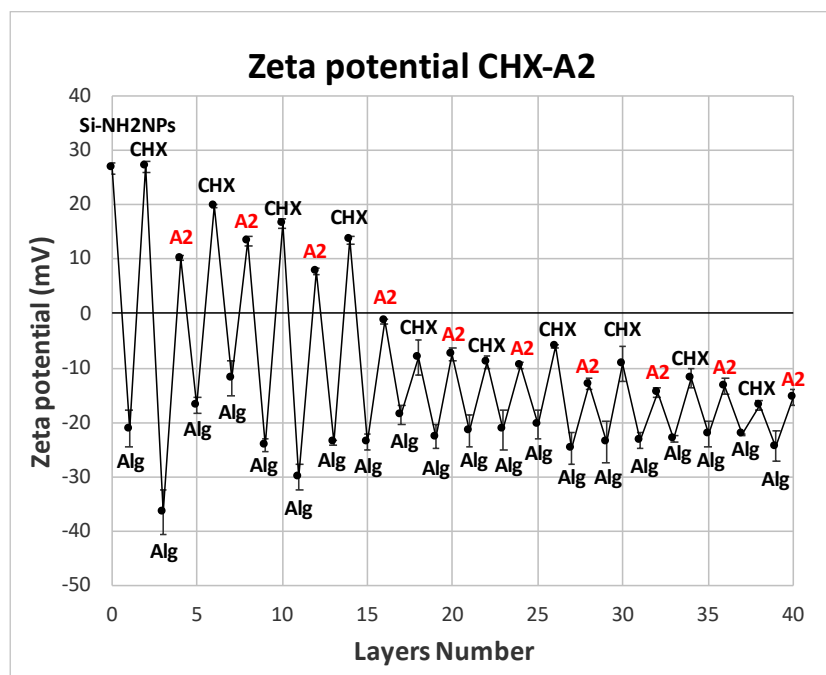


Figure 4.5: ζ potential for the coating system Si-NH₂NPs-Alg-CHX-Alg-A2. Mean \pm SD (N=1, n=3).

It was evident that, the charge of both the polycations A1 and A2 is less strong than the potential provided by the sodium alginate which influenced all the components of the layer by layer due to its strong negativity. For this nanoconstruct it was observed an initial gradual reduction of the positivity detected for the encapsulated drug starting from Q2, 19.8 ± 0.2 mV, to Q4, 13.5 ± 0.64 mV. Then, the potential dropped becoming negative on Q5, -7.99 ± 3.23 mV, presenting a growing negativity ended to -16.96 ± 2.74 mV on Q10. As contrary, firstly, the positivity of A2 slowly decreased to 7.71 ± 0.62 mV on Q3; then, on Q4 the detected charge was slightly negative, -1.41 ± 0.36 mV, followed by an increasing negativity from Q5, -7.52 ± 1.19 mV, and reaching a value of -15.4 ± 1.41 mV on Q10.

A3

A3 was the last polymer of the group A that was adopted for the encapsulation of chlorhexidine on the amino-functionalised silica nanoparticles. Comparing the ζ potential measurements of this construct to those provided by CHX-A1 and CHX-A2 it was observed a higher stability of A3 that contributed to maintain the positivity of the drug until the 5th quadruple layer (figure 4.6).

Starting from 21.63 ± 0.5 mV after amino-functionalisation of the nanoparticles, the potential was inverted into negative, -19.7 ± 2.66 mV with the coating of sodium alginate, then becoming positive again after addition of CHX to the system, 33.43 ± 1.19 . Afterwards, the charge was again reversed by the alginate, -26.97 ± 0.75 mV and to complete the first quadruple layer it went back to positive by the polymer A3, 23.33 ± 3.2 mV.

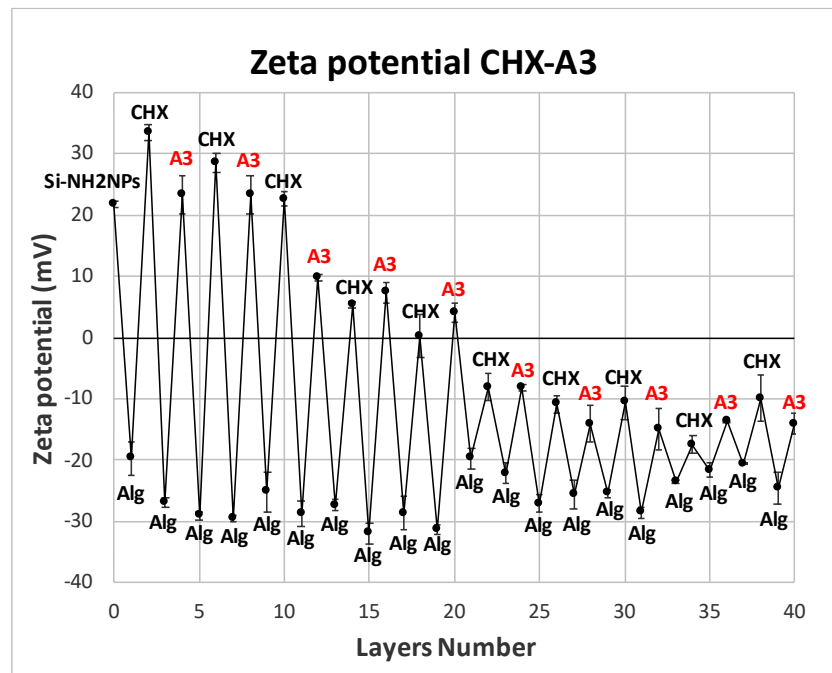


Figure 4.6: ζ potential for the coating system SI-NH₂NPs-Alg-CHX-Alg-A3. Mean \pm SD (N=1, n=3).

Overall, the zig-zag pathway initially presented a wide range of alternative negative and positive charge for the first 5 quadruple layers (Q1-Q5), then it became stable and negative from Q6 to Q10. For instance, considering only CHX and A3, it was observed that the positivity of the antimicrobial agent gradually decreased reaching 5.34 ± 0.51 mV with the 4th quadruple layer (Q4) and 0.23 ± 3.44 mV after Q5 was completed. From Q6 to Q10 its negativity moderately increased ending to -17.45 ± 1.4 mV after 9 quadruple layers were coated on silica nanoparticles. The PBAE A3 provided a good stability to the system and its positivity which was over 20 mV on Q1, dropped to 4.04 ± 1.48 mV on Q5. Its negativity considerably increased from Q6, -8.15 ± 0.6 mV, to Q10 showing a potential of -14.07 ± 1.75 mV.

B1

B1, B2, and B3, were also applied for the coating of the CHX cargo on silica nanoparticles. Initially, for the nanoconstruct CHX-B1, the charge detected for the nanocarriers alone was highly positive, 35.7 ± 1.2 mV, then it turned into negative after the employment of sodium alginate, -27.13 ± 2.45 mV. For Q1, the CHX provided a potential of 33.06 ± 1.65 mV, which was inverted with the addition of sodium alginate, -27.13 ± 0.81 mV, and became again positive by adding B1, 31.6 ± 1.66 mV (figure 4.7).

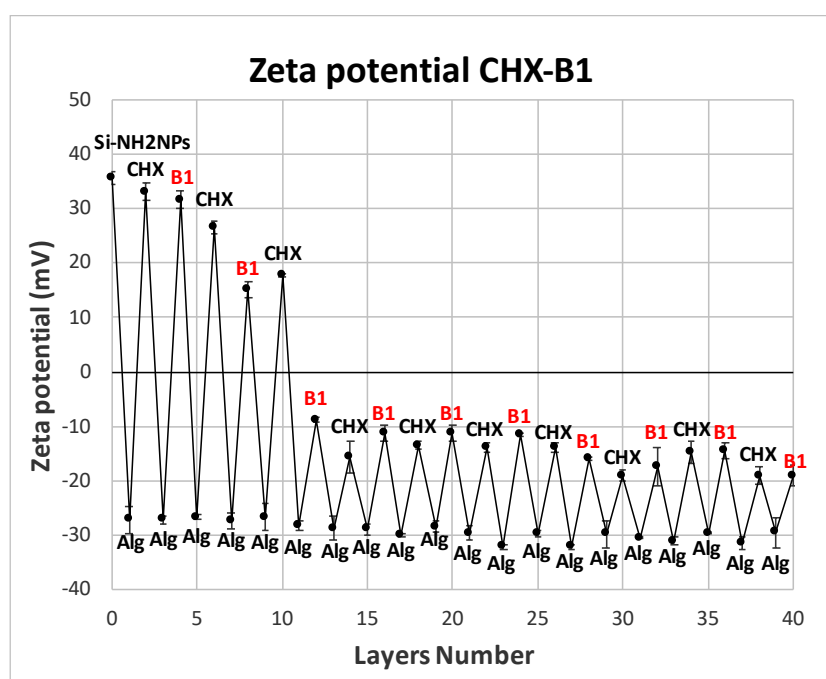


Figure 4.7: ζ potential for the coating system SI-NH₂NPs-Alg-CHX-Alg-B1. Mean \pm SD (N=1, n=3).

The positivity of the CHX gradually reduced on Q2, 26.57 ± 1.24 mV, and Q3 17.7 ± 0.3 mV, where it plummeted into negative from Q4, -8.77 ± 0.5 mV, showing a strong negativity on Q10, -18.99 ± 1.59 mV. On the other hand, the initial strong positivity of B1 on Q1 was half-reduced once the second quadruple layer was completed with a potential equal to 15.0 ± 1.46 mV. In this case the charge of B1 was already reversed on Q3, -8.77 ± 0.5 mV, and the negativity kept increasing reaching -19.1 ± 1.93 mV once all the ten quadruple layers were coated on the silica carriers.

B2

A zig-zag profiles was also developed for the drug delivery system which involved CHX and B2 as PBAE as reported in the figure 4.8. Comparing this profile to the one of the nanoconstruct CHX-B1, it was observed a better distribution of an alternative positive and negative charge from Q1 up to Q9 possibly due to an improved stability of the system provided by the adoption of B2 as PBAE.

For Q1, the potential was initially positive due to the positivity of the added amino groups on the silica nanoparticles, 37.47 ± 0.42 mV and becoming negative once sodium alginate was added on the surface of the nanocarriers, -27.63 ± 0.32 mV. The charge provided by the encapsulated cargo was positive, as observed before, 33.06 ± 0.81 mV; it dropped into negative with the addition for the second time of the sodium alginate, -27.13 ± 1.66 mV, and finally it increased with the coating of B2 onto the system, 29.77 ± 0.55 mV.

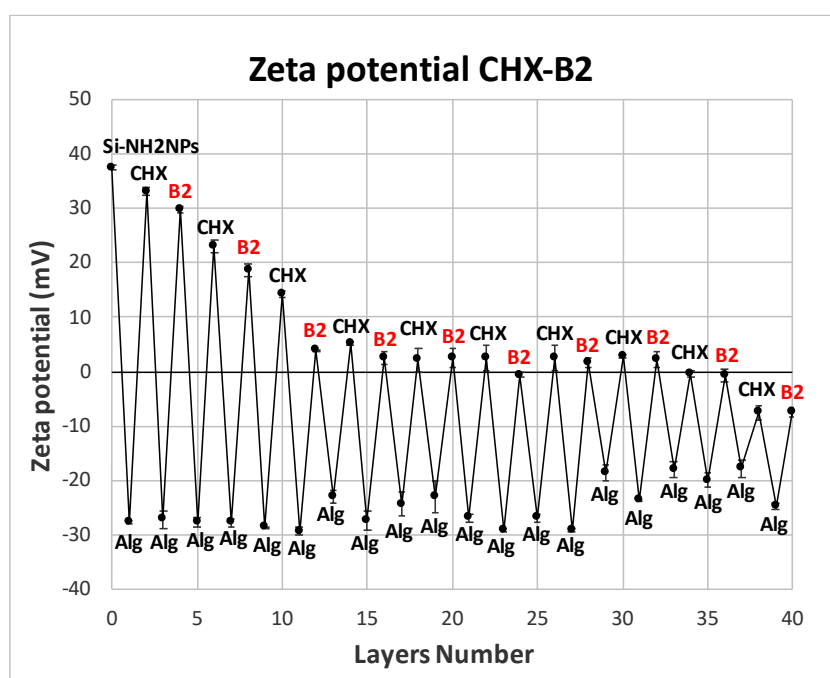


Figure 4.8: ζ potential for the coating system SI-NH₂NPs-Alg-CHX-Alg-B2. Mean \pm SD (N=1, n=3).

In this case, the charge of both CHX and B2 remained positive until Q9 showing a slight decrease of the positivity once each new quadruple layer was employed on the surface of the nanoparticles. For instance, for the CHX the potential was half reduced on Q3, 14.17 ± 0.6 mV, it was around 2.0 mV from Q5 to Q8 and it was reversed only on Q10 reaching $-7.51 \pm$

1.35 mV. As contrary, the initial strong positivity charge of B2, plummeted to 4.01 ± 0.07 mV on Q3, remaining nearby 2.0-0.5 mV from Q4 to Q9 and becoming negative on Q10 showing a potential equal to -7.0 ± 0.86 mV.

B3

To complete the polymers belonging to the group B, also B3 was chosen as polycation for the encapsulation of the chlorhexidine.

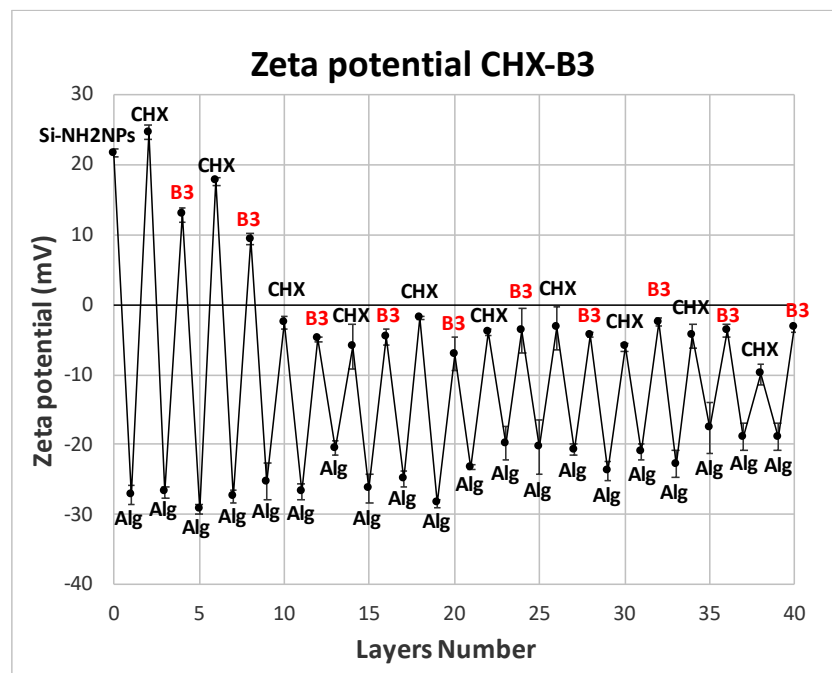


Figure 4.9: ζ potential for the coating system SI-NH₂NPs-Alg-CHX-Alg-B3. Mean \pm SD (N=1, n=3).

Starting from the positive charge of the amino-functionalised silica nanoparticles, 21.63 ± 0.5 mV, the potential was reversed with the sodium alginate, -27.17 ± 1.28 mV, then it was positive with the CHX encapsulation, 24.6 ± 1.04 mV. The sodium alginate inverted the positivity, -26.83 ± 0.72 mV, which rose again with B3, 12.8 ± 0.95 mV. As evidenced in the figure 4.9, the potential of the CHX significantly changed from Q2, 17.6 ± 0.57 mV, to Q3, -2.66 ± 0.92 mV. The negativity slightly increased ending up to -9.96 ± 1.46 mV on Q10. Furthermore, the potential of B2 was modified between Q2 and Q3, showing a positive charge in the first case, 9.34 ± 0.79 , which was turned into negative on Q3, -4.95 ± 0.3 mV and ranging between -3.35 ± 0.61 to -7.09 ± 2.38 mV until Q10.

Overall, between A and B polymers, the profiles provided by the PBAEs of the group B, enhanced the stability of the nanoconstructs in which the polymers were employed, probably due to a more hydrophobic diacrylate adopted as starting material for their synthesis. In particular, among B1, B2 and B3, it was observed that B2 allowed a better zig-zag pathway maintaining its positivity for at least eight quadruple layers. However, although the high positive charge of B1 detected on Q1, the potential of the polymer easily changed with a considerable increase of its negativity after the all 40 layers were embedded onto the system.

D1

Zeta potential measurements were pursued also for the nanoconstructs CHX-D1, CHX-D2, and CHX-D3. At first, the potential of the surface of silica nanoparticles previously amino-functionalized was measured, displaying a positive value equal to 33.3 ± 1.04 mV. Then, in the first quadruple layer (1-5 layers of the figure 4.10), once the sodium alginate was coated onto the nanocarrier surface, the potential dropped to -26.5 ± 2.61 mV.

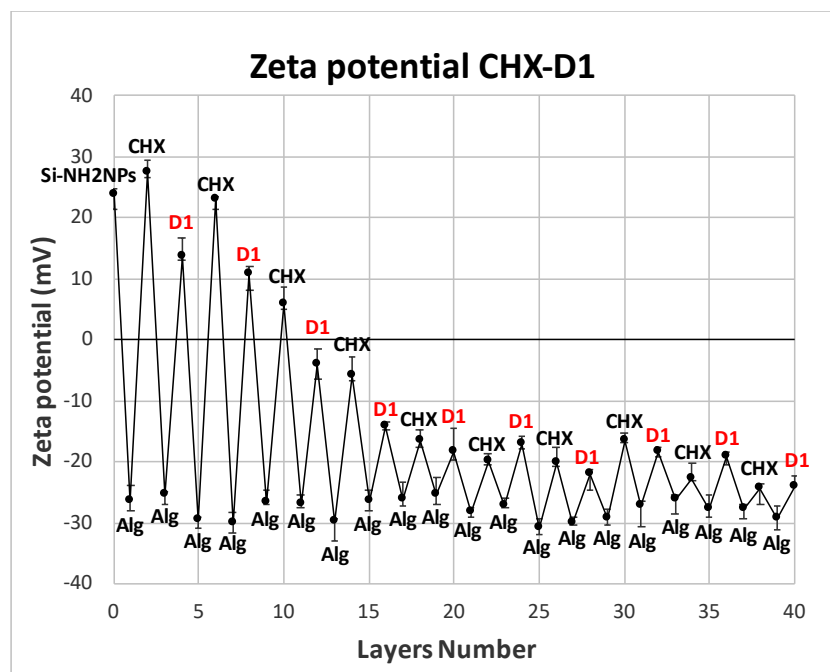


Figure 4.10: ζ potential for the coating system SI-NH₂NPs-Alg-CHX-Alg-D1. Mean \pm SD (N=1, n=3).

After layering the antimicrobial agent, the potential rose up to 27.5 ± 2.02 mV and it decreased again to -30.2 ± 1.46 after the addition of the sodium alginate for the second time.

The polymer D1 was layered in order to complete the first quadruple layer, providing a positive charge, 13.5 ± 3.3 mV, after being coated.

The drug was stable, considering its positivity, for the next two quadruple layers, Q2, showing a charge equal to 22.9 ± 0.52 mV, and Q3, 5.9 ± 2.75 mV, whereas from Q4, the potential plummeted into negative, -5.93 ± 3.22 mV. As previously evaluated, the negativity consistently kept increasing reaching -24.4 ± 0.81 mV on Q10. In the case of the polymer D1, a similar behaviour was observed. For instance, the positive charge was detected for Q2, and it dropped to -4.19 ± 2.61 on Q3 rising up to -24.2 ± 1.84 mV once Q10 was completed.

D2

The measurements were carried out also for the system involving the polycation D2 instead of D1. For the first quadruple layer, as it is shown in 1-5 layers in the figure 4.11, the sodium alginate reversed negatively the potential of the surface of the silica nanoparticles, from 32.7 ± 0.40 mV to -25.9 ± 1.65 m.

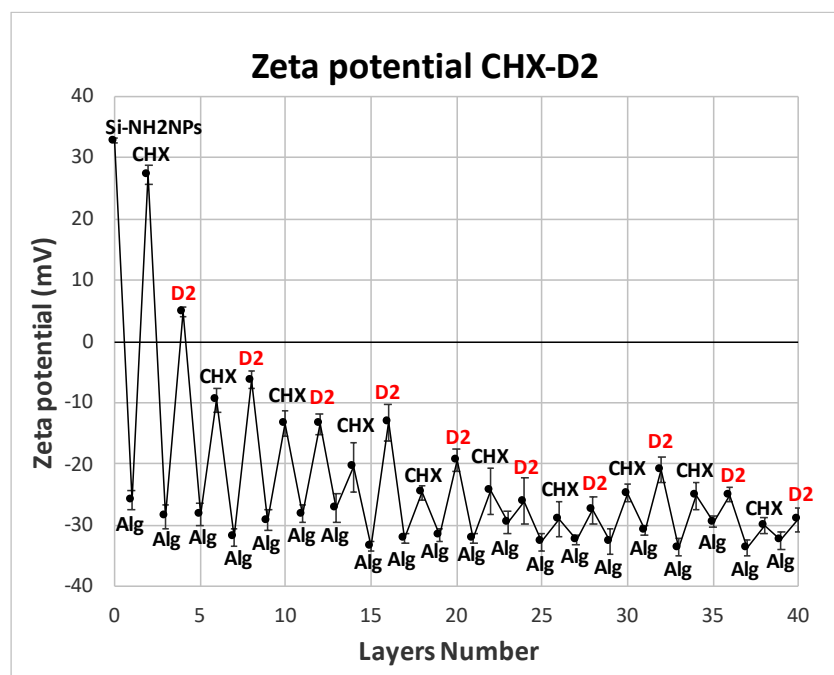


Figure 4.11: ζ potential for the coating system Si-NH₂NPs-Alg-CHX-Alg-D2. Mean \pm SD (N=1, n=3).

The addition of the chlorhexidine inversed the potential into a positive corresponding to 27.3 ± 1.53 mV, then the alginate turned again the charge into negative, -28.5 ± 1.97 mV, followed by the PBAE D2 which reverted the potential to 4.82 ± 0.81 mV.

The zig-zag pathway was representative of the build-up system including CHX and the polycation D2. Considering the potential for the encapsulated drug, it was significantly reduced from Q2, with a value of -9.6 ± 1.9 mV, followed by a constant increase of its negativity which reached -30.0 ± 1.27 mV on Q10. On the other hand, it was observed that the charge of the polymer was lower than the one provided by D1. Indeed, it was easily reversed from Q2, -6.34 ± 1.42 mV, greatly influencing the positivity of the chlorhexidine as described above. The negativity of the polymer was double risen on Q3, -13.4 ± 1.70 mV, becoming stronger once each quadruple layer was added to the system and ending to -29.1 ± 1.97 mV on Q10.

D3

The delivery system possessing D3 as positive network was also object of ζ potential analysis. The first 5 layers were representative of Q1 as followed: the initial positive charge, 21.63 ± 0.5 mV, of the amino-functionalised carriers changed once the sodium alginate was added for the first time, -23.37 ± 1.28 mV; then it went back to positive after the employment of the antimicrobial agent, 24.6 ± 1.04 mV. Furthermore, there was a decrease of the positivity with the addition of sodium alginate for the second time, -26.83 ± 0.72 mV, that rose again by embedding D3 onto the system, 11.33 ± 0.95 mV.

In this case, it was observed a better stability of the system where the positivity of D3 was reduced nearly to 0, without reaching negative values once the all 40 layers were embedded on the nanoparticles surface. In fact, the potential of the PBAE dropped to 7.0 ± 0.79 mV, on Q2 remaining slightly positive until Q10 where the charge was equal to 0.15 ± 0.61 mV. However, the initial strong positivity of the CHX was mainly reduced on Q2, 3.53 ± 0.57 mV, similarly to the value detected on the following quadruple layers, Q3, Q4 and Q5, whereas it plummeted becoming negative from Q6, -2.81 ± 0.52 mV, to Q10, -4.26 ± 1.46 mV (figure 4.12).

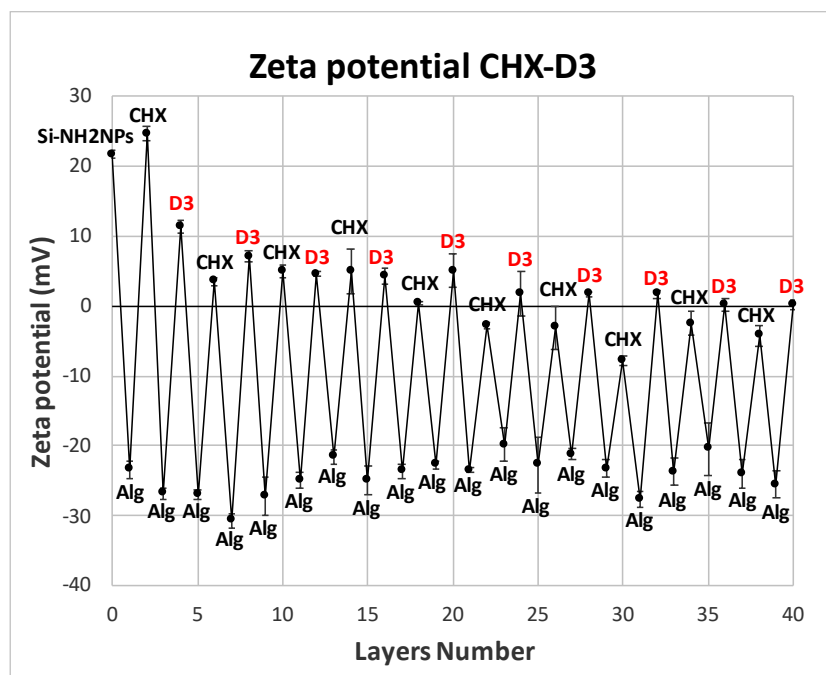


Figure 4.12: ζ potential for the coating system Si-NH₂NPs-Alg-CHX-Alg-D3. Mean \pm SD (N=1, n=3).

Considering the zig-zag pathways provided by the measurements of the systems involving the 3 PBAEs of the group D, it was clear that D3>D1>D2. Hence, D3 enhanced the stability of its nanoconstruct whereas D2 was definitely influenced by the strong negativity of the sodium alginate. As results of that, the profile CHX-D3 provided an improved distribution between positive and negative charge among all the components employed onto the system, but the profile CHX-D2 showed a consistent drop of the positivity of both drug and polymer once each new quadruple layer was added on the surface of the nanoparticles.

E1

The PBAEs of the group E were also chosen as polycation to be coated onto drug delivery system for the encapsulation of the chlorhexidine. Analysing CHX-E1, starting from 23.7 ± 0.65 mV correspondent to the potential of the silica amino-functionalized nanoparticles, the charge dropped to -31.4 ± 1.13 mV once a layer of sodium alginate was coated onto the system. As previously described, the potential value became positive, 11.06 ± 1.19 , due to the chlorhexidine and it was reversed into negative, -32.7 ± 0.38 , once the alginate was embedded for the second time. Finally, the addition of the polycation E1 reduced the negativity of the alginate with a potential of 9.78 ± 1.28 mV, as reported in 1-5 layers in the figure 4.13.

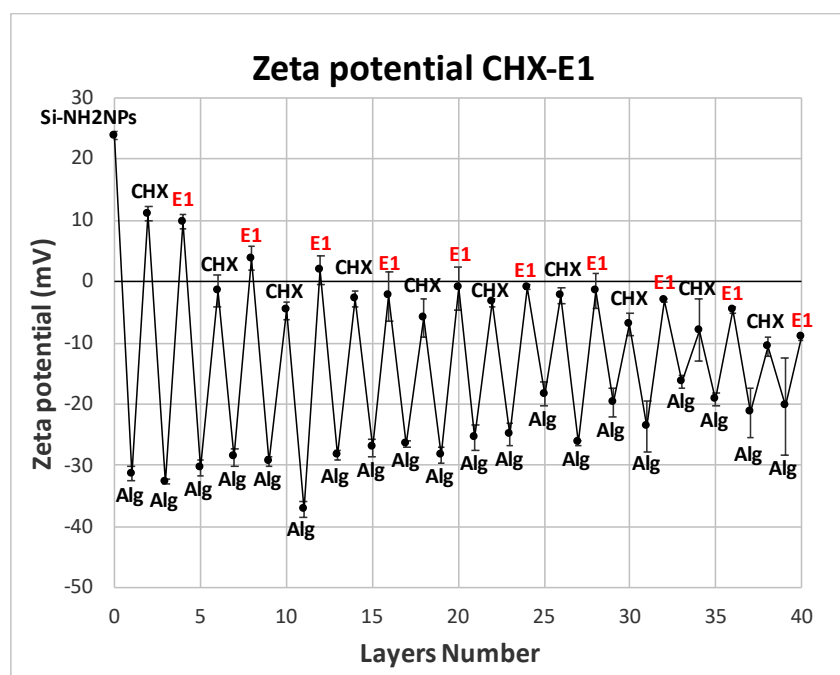


Figure 4.13: ζ potential for the coating system Si-NH₂NPs-Alg-CHX-Alg-E1. Mean \pm SD (N=1, n=3).

Overall, the positivity of both chlorhexidine and E1 was reduced once a new quadruple layer was layered on the silica nanoparticles surface. In particular, the charge of the drug was easily turned into negative already from Q2, -1.63 ± 2.58 mV, and the negativity kept increasing, reaching -9.06 ± 0.57 mV on Q10. In the case of polymer, instead, it remained positive on Q2, 3.73 ± 1.97 mV, and Q3, 1.8 ± 2.36 mV, whereas it dropped to -5.97 ± 3.12 mV on Q5 showing a constant rise of its negativity ended up to -9.06 ± 0.57 mV on Q10.

E2

The results related to the nanotechnology system including E2 produced a pathway comparable to the one of E1 (figure 4.14). As reported for the zeta profile of E1, the potential of the silica nanoparticles was positive, 23.7 ± 0.65 mV, due to the amino groups added with the Stöber method. Then, in the first quadruple layer (1-5 layers), the sodium alginate inverted the potential that became negative, -30.3 ± 2.79 mV, then positive after layering chlorhexidine, 25.03 ± 0.96 mV. Moreover, it changed in negative again due to the alginate that was added for the second time showing a value equal to $-31.8 \pm 1-15$ mV. To complete the first quadruple layer, in this sequence the PBAE E2 was coated instead of E1, reducing the negativity of the sodium alginate to 11.7 ± 0.5 mV.

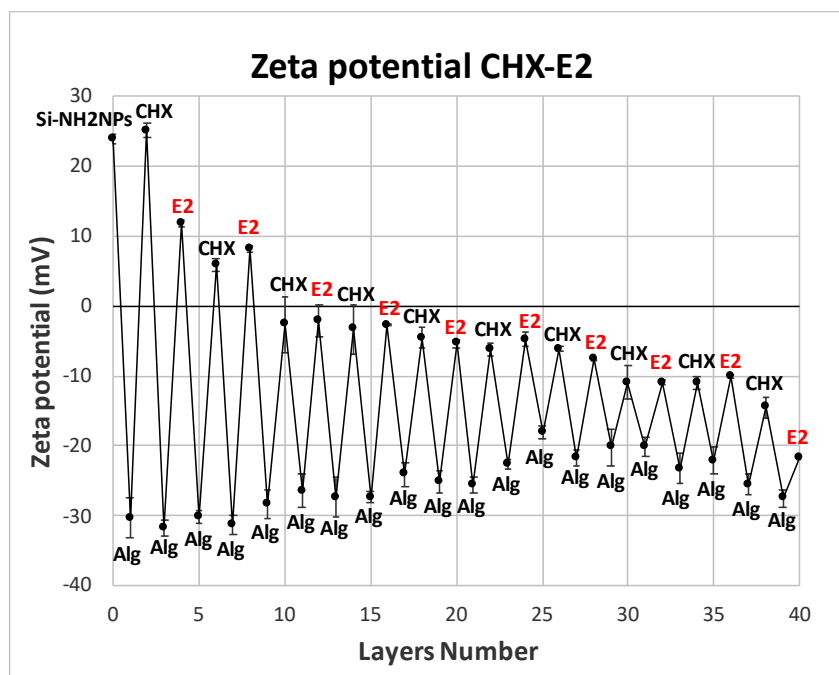


Figure 4.14: ζ potential for the coating system SI-NH₂NPs-Alg-CHX-Alg-E2. Mean \pm SD (N=1, n=3).

Considering the charge stability of the antimicrobial agent, it was observed a reduction of the its positivity from Q2, 5.84 ± 0.88 mV, to Q3, -2.7 ± 3.96 mV. Furthermore, there was a sharp increase of the negativity from Q6, -6.28 ± 0.98 mV, to Q10, -14.5 ± 1.52 mV. As contrary, the polymer was positive on Q2, 8.15 ± 0.46 mV, similarly to what detected for the chlorhexidine, but it was inverted on Q3, -2.16 ± 2.33 mV and it became strongly negative on Q10 showing a potential of -21.67 ± 0.23 mV.

E3

The PBAE E3 was also applied for the improvement of the chlorhexidine delivery from the silica nanocarriers and its profile was compared to those gained by CHX-E1 and CHX-E2. The initial positivity was due to the silica nanoparticles, 21.63 ± 0.5 mV and it changed with the sodium alginate layer, -27.17 ± 1.44 mV. However, as previously reported, the chlorhexidine embedding contributed to reverse into positive the potential, 24.6 ± 1.0 mV, firstly, inverted again with the sodium alginate added for the second time, -26.83 ± 1.25 mV, then returning positive due to the polymer E3, 12.8 ± 0.61 mV, as shown in the layers 1-5 of the figure 4.15.

The positive charge of the chlorhexidine was reduced to 17.6 ± 0.57 mV on Q2 and shifted to -2.66 ± 0.5 mV on Q3. Once a new quadruple layer was embedded onto the carrier surface, a

growing negativity was detected showing a charge equal to -9.96 ± 0.85 on Q10. On the other hand, the reduction of the positivity for E3 was similar to what identified for the cargo: indeed, after a gradual decrease on Q2, 9.34 ± 0.61 mV, the potential of the polymer was greatly influenced by the strong negativity of the sodium alginate, reaching -13.35 ± 4.54 mV on Q10.

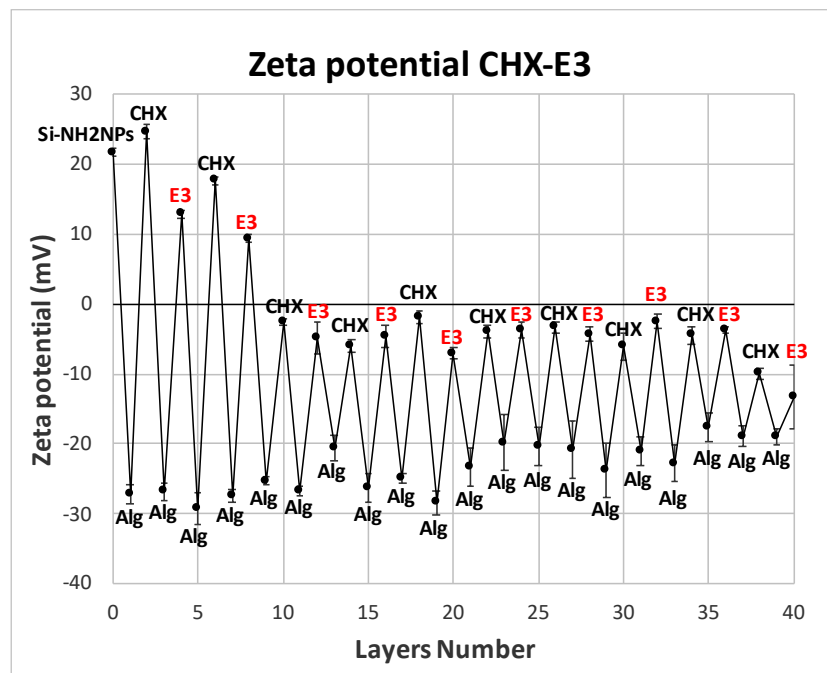


Figure 4.15: ζ potential for the coating system Si-NH₂NPs-Alg-CHX-Alg-E3. Mean \pm SD (N=1, n=3).

Overall, it was observed that the PBAEs of the group E possessed a weak positivity that was easily turned into negative once more sodium alginate was layered onto the system. Thus, the zig-zag profiles of the 3 polycations are representative of the poor stability provided by the polymers to the drug delivery systems. Hence, no significant differences were noticed among CHX-E1, CHX-E2, and CHX-E3: the positivity of each polymer was mainly reduced within the first 2 or 3 quadruple layers coated on the nanoparticles surface and the reason could be related to the short aliphatic and hydrophilic chain typical of 1, 3 butanediol diacrylate (E) adopted for the synthesis of E1, E2 and E3.

F1

The polymers of the group F were applied for the development of CHX-F1, CHX-F2 and CHX-F3 by LbL as heretofore described for the other PBAEs. In the first nanocoating system

polyelectrolytes and the chlorhexidine were layered as followed onto the surface of amino-functionalized silica nanoparticles: sodium alginate, chlorhexidine, sodium alginate, F1. Starting from a strong positive charge, 17.37 ± 0.5 mV, the potential was inverted into negative and corresponding to -29.9 ± 2.19 mV. Subsequently, the chlorhexidine provided a positive charge equal to 29.37 ± 0.85 mV; then the potential was inverted firstly by the layer of the sodium alginate, -28.83 ± 2.75 , then by the addition of the polycation F1, 19.27 ± 0.72 mV (1-5 layers in the figure 4.16).

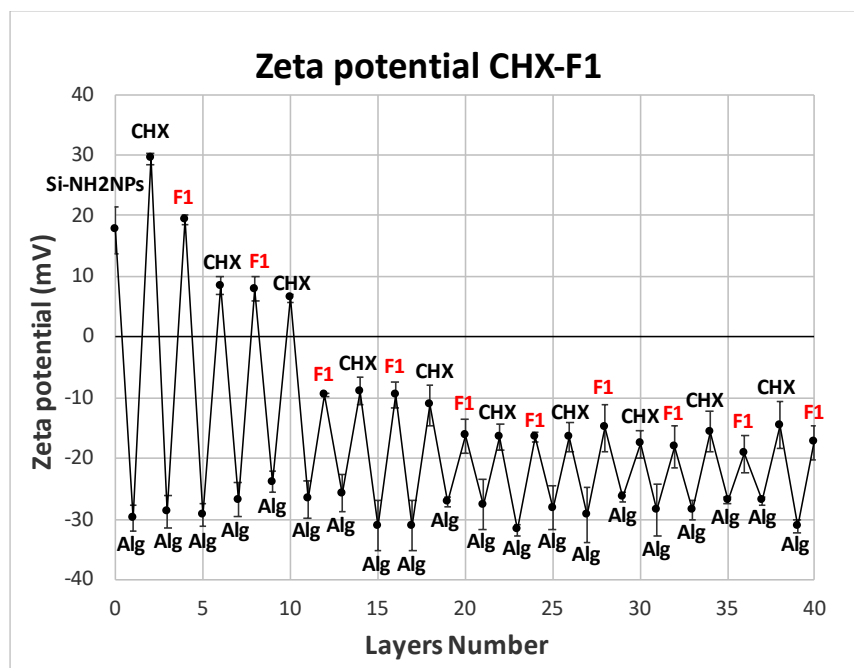


Figure 4.16: ζ potential for the coating system SI-NH₂NPs-Alg-CHX-Alg-F1. Mean \pm SD (N=1, n=3).

In the second quadruple layer both chlorhexidine and F1 remained positive respectively showing, 8.41 ± 1.51 mV and 7.1 ± 2.26 mV. Furthermore, the potential of the encapsulated drug was reverted from Q4, -8.9 ± 2.21 mV and it kept increasing ending to -14.57 ± 3.89 mV on Q10. As contrary, although the polymer presented an initial strong positive charge, its potential was quickly turned into negative, starting from -9.53 ± 0.29 mV to -17.43 ± 2.77 mV once the all 40 layers were coated onto the system.

F2

The nanotechnology system presented in the figure 4.17 involves as followed: silica nanoparticles amino-functionalized, sodium alginate, chlorhexidine, sodium alginate and the

polycation F2. To sum up, in the first quadruple layer (1-5 layers), the initial positive charge equal to 17.07 ± 3.12 mV, was inverted by the sodium alginate to -27.6 ± 0.62 mV, becoming positive again once the chlorhexidine was added onto the system, 25.87 ± 0.87 mV. Moreover, as described before, the layer of the sodium alginate reversed negatively the charge to -26.6 ± 0.55 mV, as well as the polycation F2 converted in positive the potential, 19.13 ± 1.42 mV.

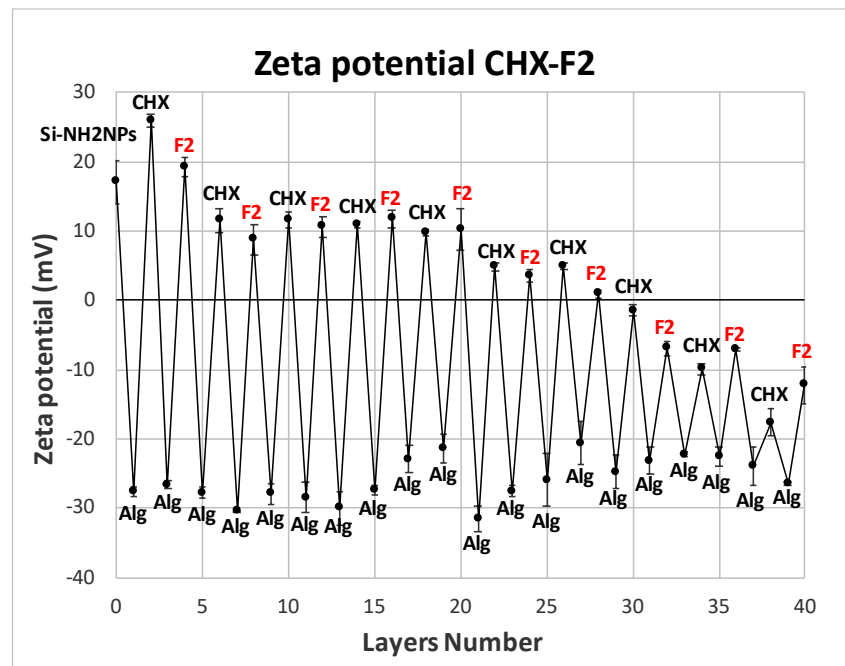


Figure 4.17: ζ potential for the coating system Si-NH₂NPs-Alg-CHX-Alg-F2. Mean \pm SD (N=1, n=3).

The zig-zag pathway shows the improved stability provided by adopting the polymer F2 to this nanoconstruct. For instance, it was observed that the positivity of the encapsulated drug dropped to 11.53 ± 1.77 mV on Q2 and remained stable until Q5; then it was still positive on Q6 and Q7 decreasing to 4.87 ± 0.55 mV. In this case, the potential was reversed only starting from Q8, -1.45 ± 0.84 mV and becoming strongly negative on Q10, -17.63 ± 1.95 mV. In addition, a similar behaviour was observed for F2: the polymer was quite stable due to its strong positivity in sodium acetate buffer pH5. In fact, it slowly degraded showing a potential nearly to 0 on Q7, and it turned into negative on Q8, -6.89 ± 1.02 mV, increasing to -12.23 ± 2.67 mV after all the 40 layers were coated on the nanocarriers.

F3

To complete the polymers belonging to the group F, also F3 was chosen as polycation and employed on the nanoconstruct CHX-F3. The layers 1-5 of the figure 4.18 are representative of the first quadruple layer: a positive charge was initially detected for the nanocarriers after their amino-functionalisation, 17.3 ± 0.5 mV, firstly reversed by the layer of the sodium alginate, -24.83 ± 0.23 mV, then going back to positive with the addition of the drug, 28.0 ± 1.11 mV. Additionally, the charge was again turned into negative with a new layer of sodium alginate, -24.63 ± 1.06 mV and finally becoming positive after the coating of the polymer F3, 25.97 ± 0.76 mV.

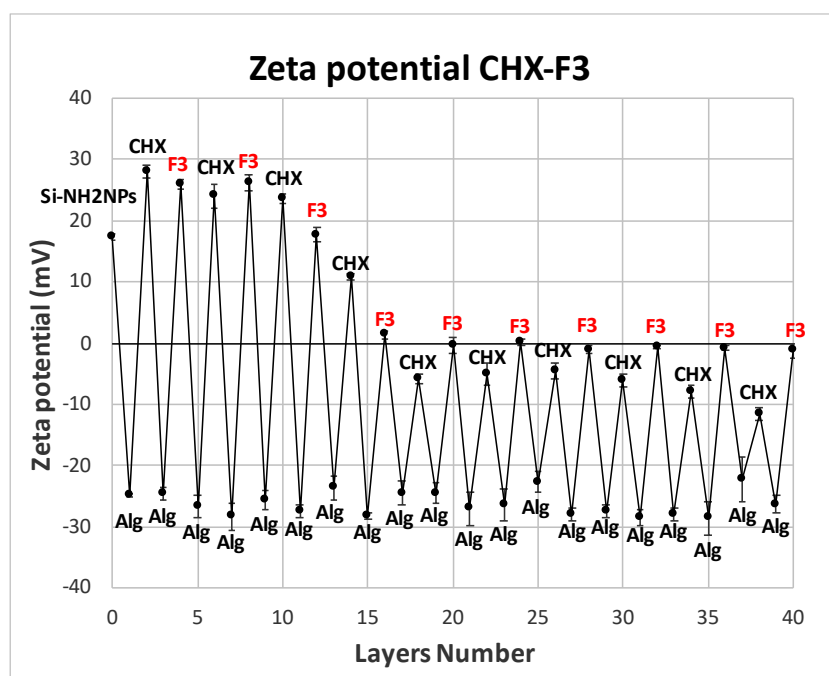


Figure 4.18: ζ potential for the coating system SI-NH₂NPs-Alg-CHX-Alg-F3. Mean \pm SD (N=1, n=3).

Overall, the positivity of the chlorhexidine was preserved for the first 4 quadruple layers, showing a gradual decrease between Q2 and Q3 and dropping to 10.75 ± 0.57 mV on Q4. However, the potential changed from Q5, -5.78 ± 0.79 mV, presenting a considerable increase of the negativity once a new quadruple layer was completed and reaching -11.56 ± 0.98 mV on the final quadruple layer. As contrary, although the strong negativity of the sodium alginate influenced the stability of the system from Q5, it was observed that the positivity of F3 was reduced, ending to 0, but without any change into negative charge. For example, the initial strong positive charge was stable also on Q2, 26.13 ± 1.33 mV, and Q3, 17.7 ± 1.21 mV;

then it dramatically dropped to 1.34 ± 0.75 mV on Q4, remaining nearby 0 until Q10, -1.24 ± 1.13 mV. Regarding to the comparison among the profiles of the PBAEs of the group F, CHX-F2 provided a pathway where the potential is well-distributed between the negative and the positive range, proving that F2 is able to decrease the negativity of the sodium alginate better than the what detected for F3 and F1. The difference in the gained results could find an explanation in the structures of these PBAEs: F2 composed by more hydrophobic starting materials gradually degraded at pH5 and better managing the negativity of the sodium alginate, whereas F1 and F3 showed a lack of this ability probably due to a faster hydrolysis caused by their higher hydrophilicity.

G1

The last 3 nanoconstructs that were developed for this project included as PBAEs G1, G2 and G3. In the case of CHX-G1, the nano-delivery system was composed by as followed: silica nanoparticles amino-functionalized, sodium alginate, the antimicrobial agent chlorhexidine, sodium alginate and the polycation G1.

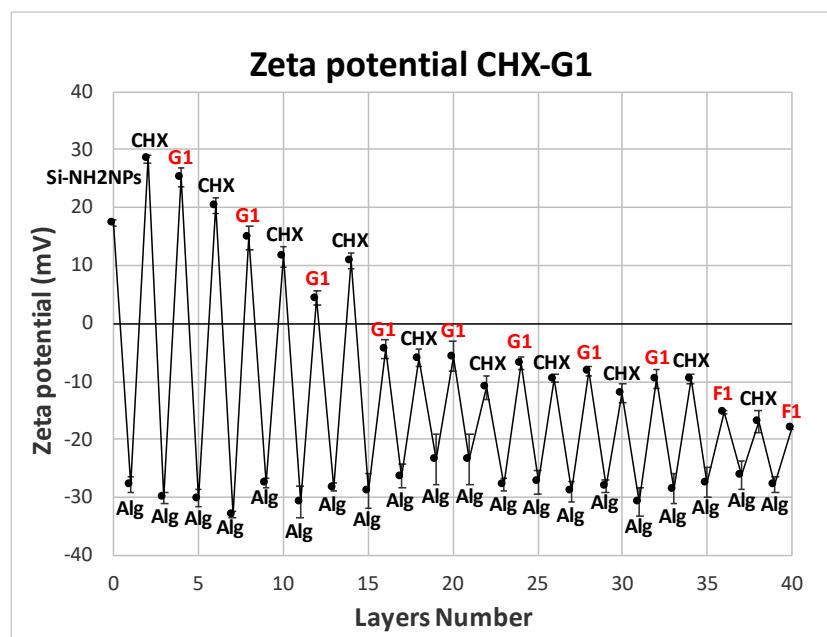


Figure 4.19: ζ potential for the coating system SI-NH₂NPs-Alg-CHX-Alg-G1. Mean \pm SD (N=1, n=3).

The results, reported in the figure 4.19, highlighted the change of the potential after the layer of each component of the sequence. Considering the first quadruple layer (1-5 layers), from a positive charge equal to 17.3 ± 0.5 mV the potential was inverted into a negative value after

the addition of the sodium alginate, -27.8 ± 1.44 mV. The layer of the chlorhexidine converted the potential in positive equal to 28.4 ± 0.75 mV, but it changed again once for the second time the alginate has been coated onto the system, -30.0 ± 0.95 mV. Finally, the first quadruple layer was completed by the addition of the polycation G1, which positively influenced the potential, 25.13 ± 1.65 mV.

Overall, the first 3 quadruple layers are well compensating, then the pathway shifted in the negative area. For instance, the chlorhexidine showed its positivity until Q4 which remained stable around 10.89 ± 1.35 mV; then the charge changed from Q5, -5.92 ± 1.49 mV, with a consistent increase of the negativity ending to -16.97 ± 1.89 mV on Q10. On the other hand, the initial strong positivity of the polymer considerable dropped to 4.43 ± 1.69 mV on Q3 and it was reversed into negative starting from Q4, -4.4 ± 1.18 mV. Furthermore, it was observed a significant rise of the negativity once each quadruple layer was embedded onto the system showing a charge equal to -17.97 ± 0.31 mV on Q10.

G2

The zig-zag profile, represented by the figure 4.20, shows the zeta measurements that were carried out for the nanotechnology system CHX-G2.

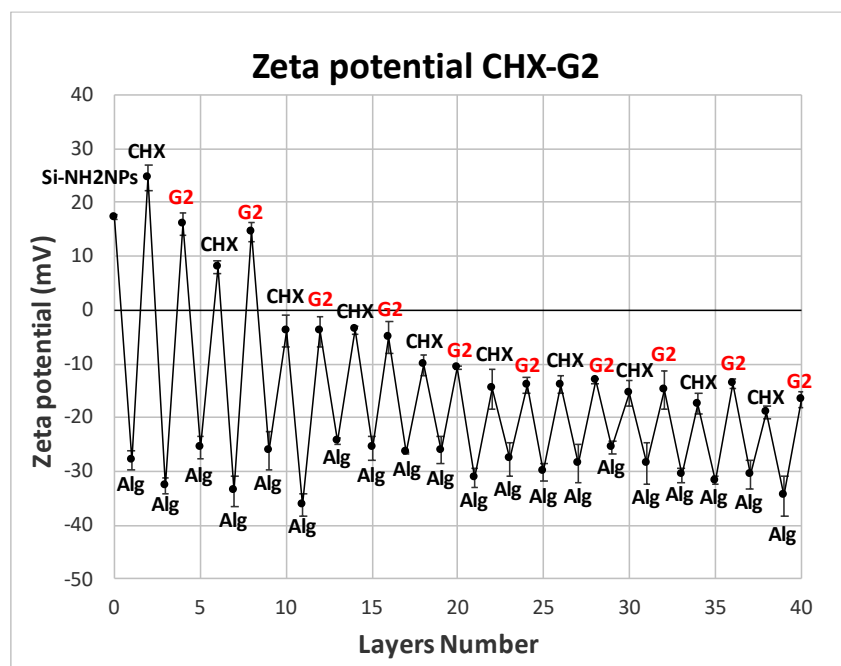


Figure 4.20: ζ potential for the coating system SI-NH₂NPs-Alg-CHX-Alg-G2. Mean \pm SD (N=1, n=3).

The sodium alginate dropped the positive potential of the surface of the silica amino-functionalized nanoparticles, 17.3 ± 0.5 mV, to -27.9 ± 1.69 mV whereas the chlorhexidine once added on the system reversed the potential into a positive 24.6 ± 2.35 mV. The charge was converted again by the sodium alginate showing a value equal to -32.63 ± 2.01 mV and it was turned into positive after the polycation G2 was layered, 16.1 ± 2.02 mV (1-5 layers).

Although G2 showed a strong positivity, the potential of both, drug and polymer, were easily converted. For example, the positive charge representative of the CHX plummeted to 7.97 ± 1.21 on Q2 and it changed into negative starting from Q3, -3.88 ± 2.86 with a consequential increase of negativity ending to -18.98 ± 1.25 mV on Q10. Additionally, the behaviour of the PBAE G2 and its positive charge was inverted as quick as the potential of the drug. For instance, the initial positive charge of G2 was, as first, slightly reduced on Q2, 14.53 ± 1.79 mV. Then, a considerable decline of its positivity was detected on Q3, showing a potential of -4.03 ± 2.7 mV, with a constant increase of the negativity until the final quadruple Q10, where the measured charge was equal to -16.62 ± 1.57 mV.

G3

In the first quadruple layer of the nanoconstruct CHX-G3 (1-5 layers in the figure 4.21), the charge was initially positive, 17.3 ± 3.12 mV, due to the amino-functionalisation of the silica nanoparticles. Firstly, it was reversed once the sodium alginate was layered for the first time onto the system, -27.0 ± 2.68 mV; then the potential became positive with the coating of the encapsulated drug, 25.3 ± 1.48 mV. Additionally, a new layer of sodium alginate changed into negative the charge, -24.8 ± 1.39 mV, which turned back to positive once the polycation G3 was embedded onto the surface of the nanocarriers, 23.4 ± 2.88 mV.

In this case, it was observed a better stability of the delivery system provided by the PBAE G3. In particular, the positivity of the CHX remained stable until Q5, showing a gradual decrease from Q2, 16.8 ± 0.89 mV, to Q5, 7.99 ± 2.93 mV. The potential shifted into negative values on Q6, showing a charge of -8.76 ± 1.88 mV, with a slight rise of the negativity once a new quadruple layer was completed and reaching -9.88 ± 1.25 mV on Q10. As contrary, the initial positivity of G3 was already half-reduced on Q2, 12.4 ± 0.4 mV, with a potential nearby 0 on

Q5, 1.71 ± 0.56 mV. Furthermore, similarly to what detected for the CHX, the charge of the polymer was turned into negative starting from Q6, -4.14 ± 0.36 mV, with no significant variation of the potential until Q10, -4.07 ± 1.57 mV.

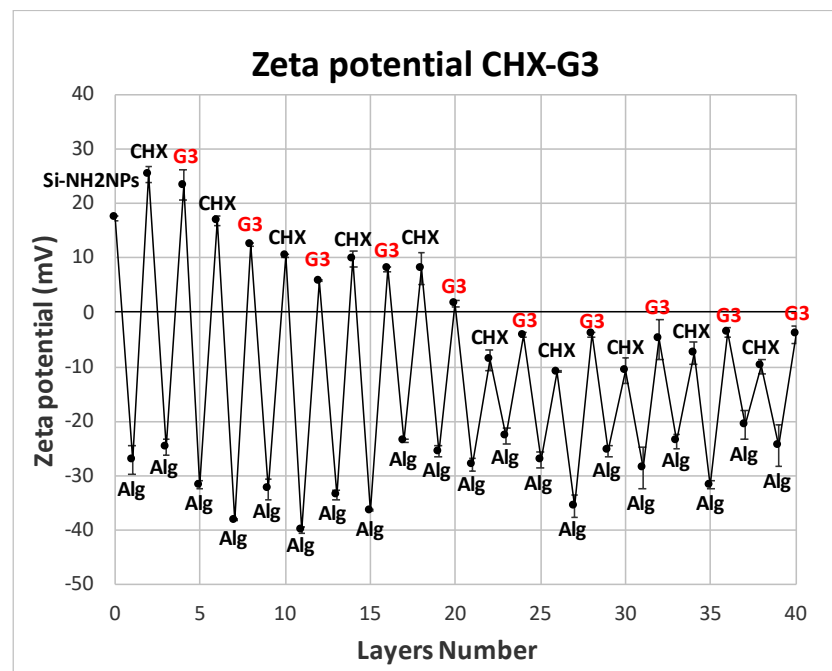


Figure 4.21: ζ potential for the coating system SI-NH₂NPs-Alg-CHX-Alg-G3. Mean \pm SD (N=1, n=3).

To sum up, the PBAEs belonging to the group G showed differences in managing the negativity of the sodium alginate. More specifically, it was noticed that G3 improved the stability of its system allowing an alternative of positivity and negativity for half of the 40 layers embedded onto the surface of the nanoparticles. On the other hand, there was no considerable improvement provided by the coating of G1 and G2 on their systems. In fact, in both cases, although the 2 polymers possessed a strong positive charge after being coated in the first quadruple layer, they quickly degraded. In particular, the positivity of the drug and G1 was kept stable until Q4, whereas only up to Q3 for CHX-G2.

Comparing the zeta potential zig-zag pathways heretofore described for the CHX-PBAEs to the hydrolysis profiles of the PBAEs at pH5 reported in the figure 3.38a of the chapter 3, consistency in the results was observed for G1, F1, B1, A2, B2, F2, A3, D3, F3, and G3 (p-value < 0.05). For instance, polymers such as B1, F1, and G1, including piperazine (amine 1) as amine, showed a positive charge for at least 3 quadruple layers, whereas those such as A3,

D3, F3 and G3, possessing in their molecular structures the amine N-N bis [3-(methylamino) propyl] methylamine (amine 3), maintained their positivity up to Q5 or Q6. Then, the polycations such as for example A2, B2 and F2, possessing the amine 4,4 trimethyldipiperidine (amine 2) in their backbone, slowly hydrolysed at pH5, better controlling the strong negativity of the sodium alginate and providing a positive charge for at least 5-7 quadruple layers.

Thermogravimetric analysis (TGA)

All the nanocoating systems containing all the 18 PBAEs employed for the encapsulation of the antimicrobial agent, chlorhexidine, were analysed by thermogravimetric analysis (TGA) in order to define the weight loss distribution among the layers of polyelectrolytes coated onto the nanoparticles surface. For each drug delivery system, the quadruple layers considered as object of analysis were as followed: Q1, Q3, Q5, Q7 and Q10.

Bilayer: Alg-CHX

First of all, the TGA was pursued for the nanoconstruct including only alternatively sodium alginate and chlorhexidine. Furthermore, as described for ζ potential measurements, these results were compared to those of the coating involving CHX-PBAEs with the aim of evaluating any possible improvement of stability for both drug and nano-delivery systems.

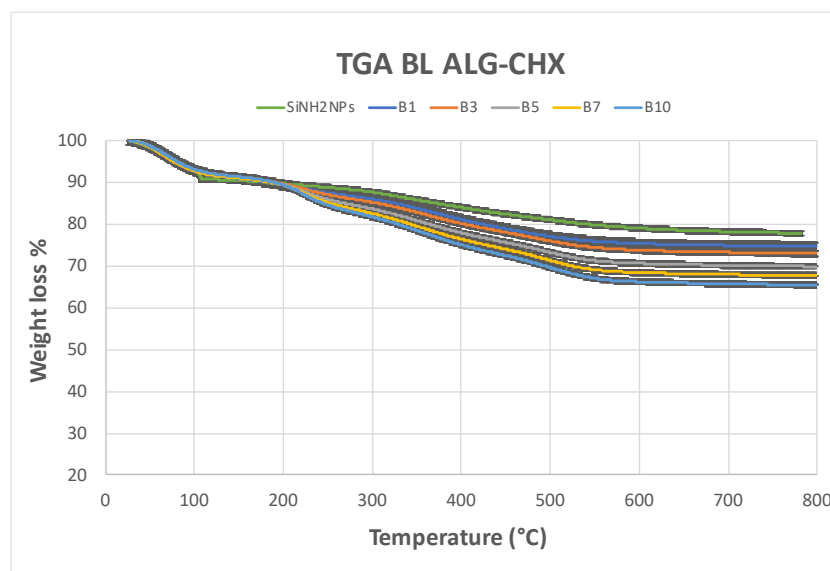


Figure 4.22a: Weight loss vs temperature for Si-NH₂NPs-Alg-CHX. Mean \pm SD (N=1, n=2).

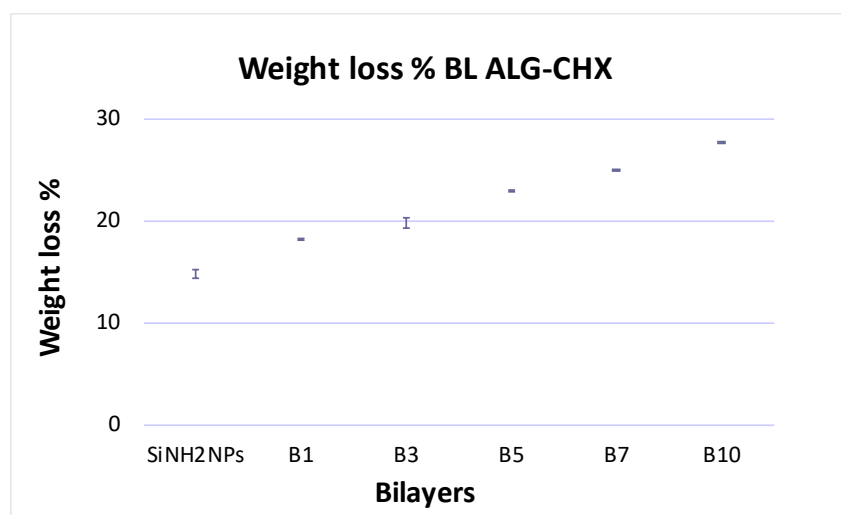


Figure 4.22b: Weight loss % for each B layer in the matrix Si-NH₂ NPs-Alg-CHX. Mean ± SD (N=1, n=2).

In the case of the bilayer nanocoating the layers considered as reference were: the nanocarriers amino-functionalised, B1, B3, B5, B7 and B10 (figure 4.22a). The figure 4.22b shows the distribution of the weight loss percentage among all the bilayers. Starting from the nanocarriers alone, 14.80% ± 0.39, the weight loss slightly increased with no significant differences between B1, 18.20% ± 0.11 and B3, 19.84% ± 0.11. In addition, it rose only of 3% after B5 was completed and of less than 10% once all the 20 layers were coated onto the system with a value of. Thus, as result of that, there was no stable distribution among the layers of polyelectrolyte and encapsulated cargo.

A1

The drug delivery systems composed by CHX and PBAEs belonging to the group A were the first object of thermogravimetric analysis. For the CHX-A1, the quadruple layers considered as reference for the evaluation of the weight loss percentage were: Q1, Q3, Q5, Q7 and Q10 (figure 4.23a).

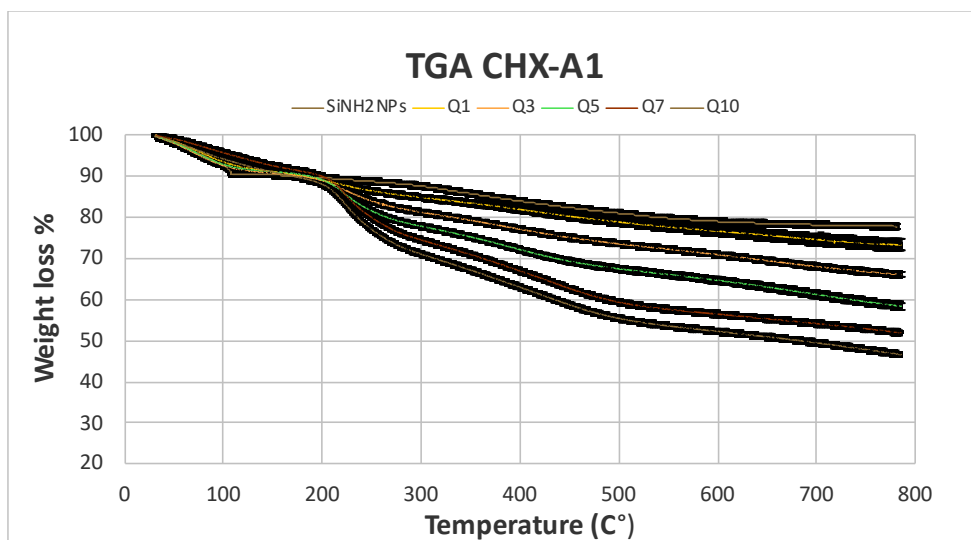


Figure 4.23a: Weight loss vs temperature for Si-NH₂NPs-Alg-CHX-Alg-A1. Mean ± SD (N=1, n=2).

First of all, the samples including the nanoparticles amino-functionalized before starting the LbL were analysed showing a weight loss of $14.79\% \pm 0.39$. Then, for the first 4 layers of Q1 the mass loss was correspondent to $20.22\% \pm 1.08$, followed by a value of $26.55\% \pm 0.49$ for Q3. As it is shown in the figure reported below, the weight loss percentage is increasing once a new quadruple layer is coated onto the surface of the nanocarrier providing values equal to $34.52\% \pm 0.89$ for Q5, $43.80\% \pm 0.69$ for Q7 and $47.63\% \pm 1.49$ for the last quadruple layer Q10 (figure 4.23b).

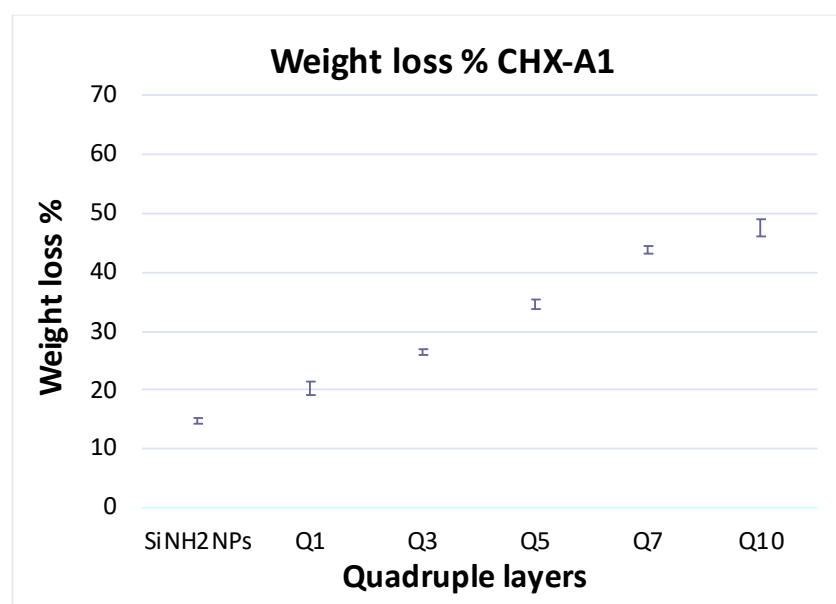


Figure 4.23b: Weight loss % among the QL for the matrix including CHX-A1. Mean ± SD (N=1, n=2).

A2

The results gained for the nanoconstruct CHX-A2 are represented by figure 4.24a and 4.24b which both show the distribution of the weight loss along the 40 layers plus the increasing organic content percentage starting from Q1 to Q10.

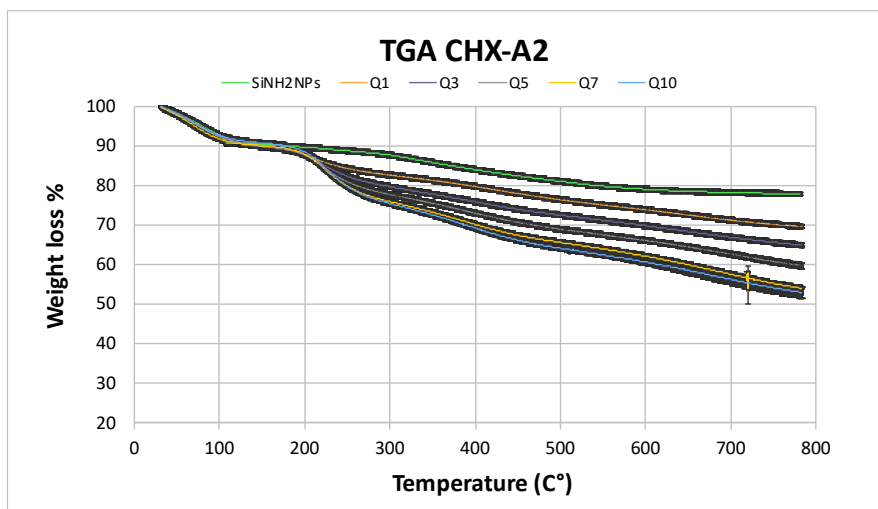


Figure 4.24a: Weight loss vs temperature for the construct Si-NH₂NPs-Alg-CHX-Alg-A2

In A2 layered nanoparticles, starting from a value of $14.79\% \pm 0.39$ correspondent to the silica nanoparticles amino-functionalized, the weight loss percentage reported for the first quadruple layer was correspondent to $22.54\% \pm 0.18$. As expected, the addition of others quadruples layers increased the amount of the weight loss. However, the values in the bar chart below showed that for the sequence with A2 as polycation, the weight loss moderately rose (p -value < 0.05) if compared to the A1 layered nanoparticles.

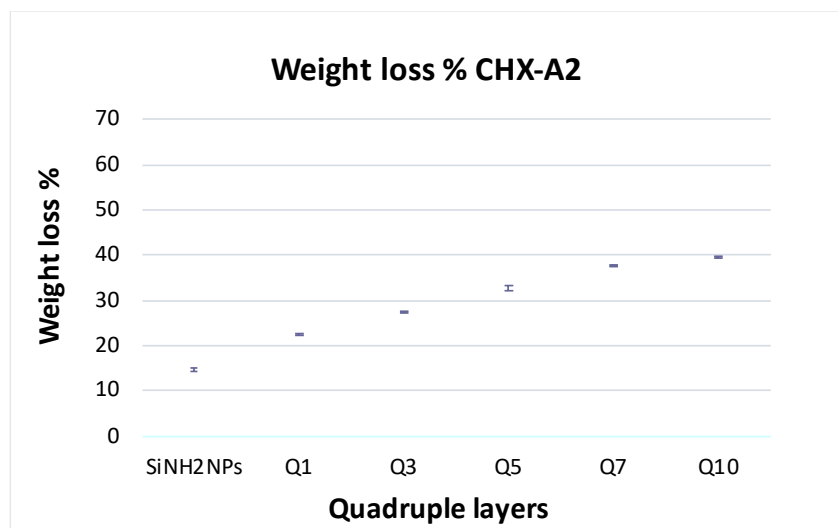


Figure 4.24b: Weight loss % among the QL for the matrix including CHX-A2. Mean \pm SD (N=1, n=2).

In particular, for Q3 there was an increase of 4.91% reaching a value of $27.45\% \pm 0.20$ and for Q5 it was equal to $27.45\% \pm 0.60$. For Q7 it was detected a decrease of 6.14% ($37.66\% \pm 0.20$ for A2 construct) compared to CHX-A1 in which the value was $43.80\% \pm 0.69$. The last quadruple layer Q10 showed for A2 a weight loss percentage of $39.63\% \pm 1.12$ against 47.63 ± 1.49 of A1 with a reduction of 8% in the weight loss reported for the system possessing the PBAEs A2 (p-value < 0.05).

A3

The analysis of the CHX-A3 were representative of the delivery system having as polycation the last PBAE of the group A (figures 4.25a and 4.25b).

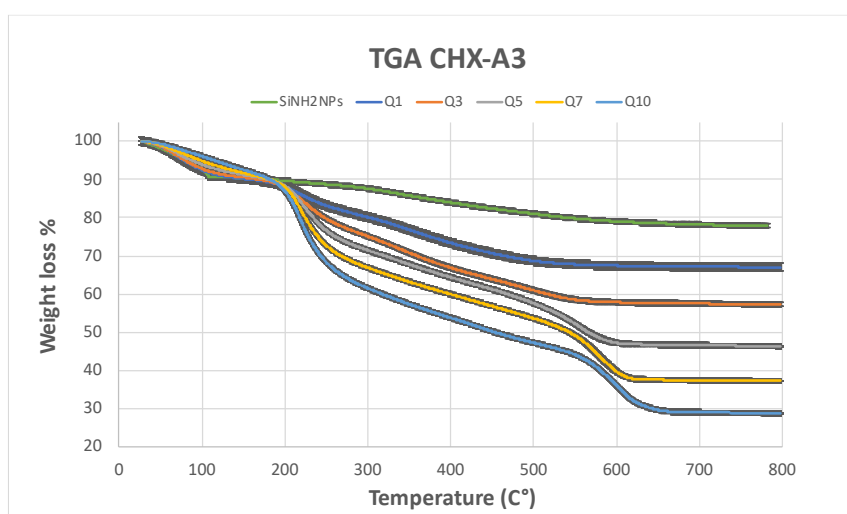


Figure 4.25a: Weight loss vs temperature for the construct Si-NH₂NPs-Alg-CHX-Alg-A3

Starting from the weight loss provided by the nanocarriers alone, $14.80\% \pm 0.39$, there was a significant growth in the organic content up to Q10. For instance, an increment of over 10% was detected for Q1, $25.45\% \pm 0.49$, and for Q3, 35.55 ± 0.56 . Moreover, the value kept rising for Q5, 47.59 ± 0.23 , for Q7, 57.70 ± 0.07 , reaching an organic content percentage equal to 67.31 ± 0.01 on Q10.

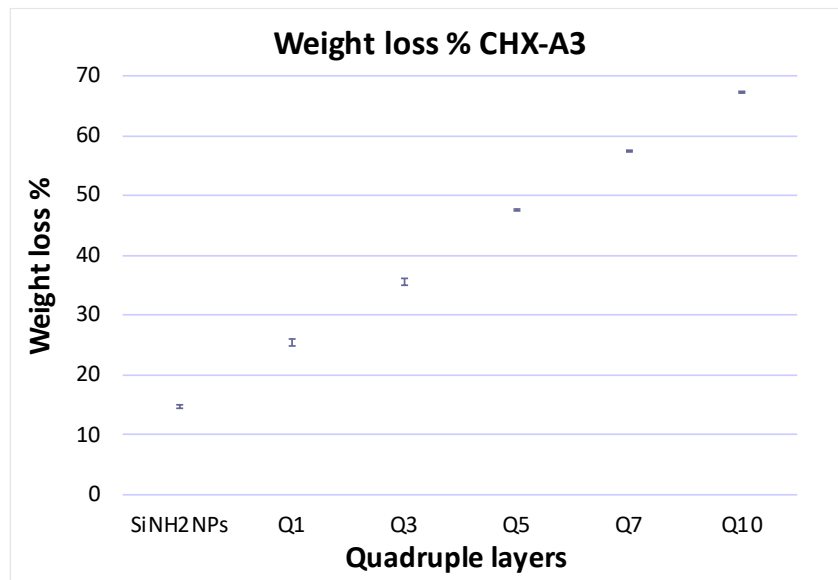


Figure 4.25b: Weight loss % among the QL for the matrix including CHX-A3. Mean \pm SD (N=1, n=2).

Firstly, comparing the systems CHX-PBAE of the group A to the 10 bilayers Alg-CHX, it was observed a significant higher weight loss in coating systems composed by quadruple layers rather than bilayers (p -value < 0.05). Then, differences were also detected among the 3 delivery systems CHX-A1, CHX-A2 and CHX-A3.

To sum up, A3 provided a better distribution of the all 40 layers embedded onto the nanoparticles surface proved by the constant increase of around 10% for the weight loss once each new quadruple layer was coated. Therefore, CHX-A3 showed the highest value for Q10, $67.31\% \pm 0.01$, when compared to Q10 of CHX-A1, $47.63\% \pm 0.39$, and CHX-A2, $39.63\% \pm 1.12$ (p -value < 0.05).

B1

The TGA was performed also for the nanoconstructs where the PBAEs possessing 1,6 hexanediol diacrylate (B) were employed as polycations for the encapsulation of the antimicrobial agent on the silica nanoparticles (figure 4.26a). As already described before, the initial weight loss was provided by the nanocarriers after being amino-functionalised and it was equal to $14.80\% \pm 0.39$. A slight increase was detected once the 4 layers composing the first quadruple layer were coated onto the system, 19.66 ± 0.11 (figure 4.26b), which was quite similar to what gained by Q1 for the coating CHX-A1.

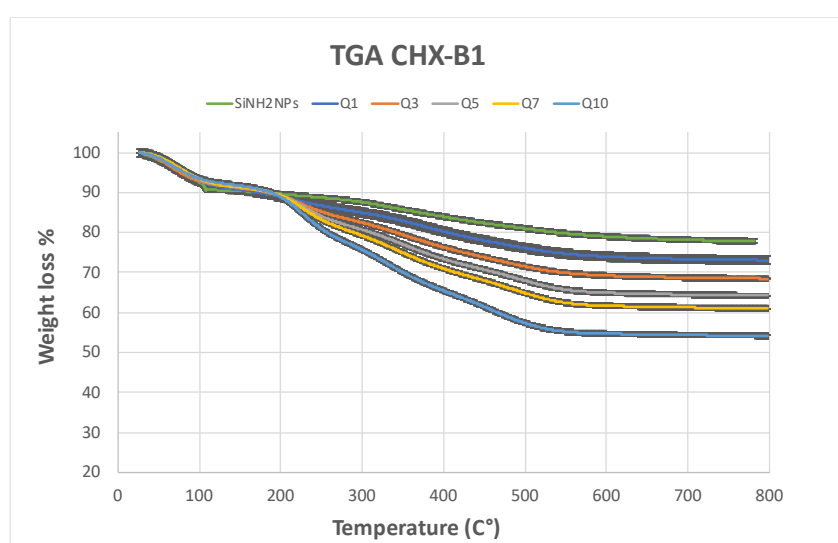


Figure 4.26a: Weight loss vs temperature for the construct Si-NH₂NPs-Alg-CHX-Alg-B1

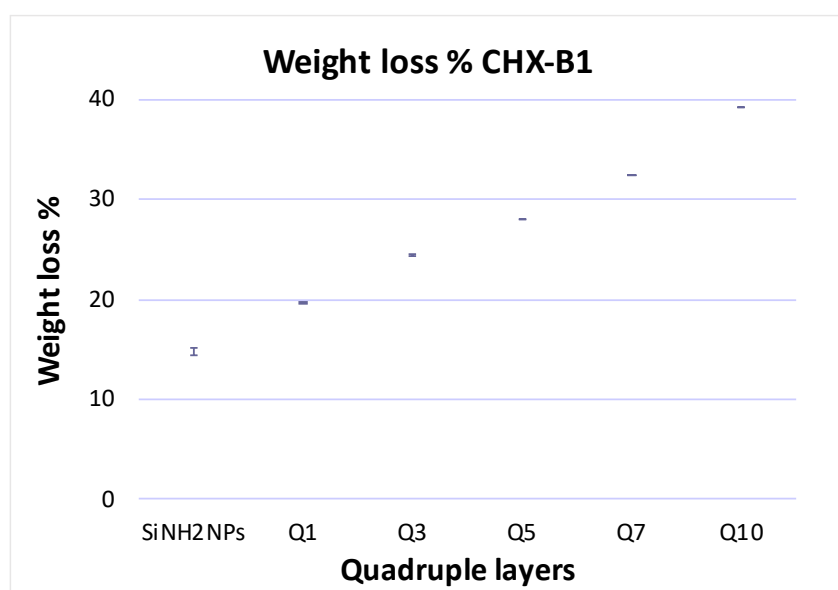


Figure 4.26b: Weight loss % among the QL for the matrix including CHX-B1. Mean \pm SD (N=1, n=2).

The weight loss percentage for Q3 was $24.39\% \pm 0.09$ whereas it was equal to $28.07\% \pm 1.05$ for Q5, and it was significantly reduced if compared to CHX-A1 which instead reached over 30% with Q5 (p -value < 0.05). Additionally, although the weight loss kept rising once a new quadruple layer was coated onto the system, the values detected for Q7 and Q10 for CHX-B1, respectively $32.43\% \pm 1.05$ and $39.27\% \pm 0.7$, were lower than those measured for CHX-A1: $43.80\% \pm 0.69$ for Q7 and $47.63\% \pm 1.49$ for the final quadruple layer (p -value < 0.05).

B2

The variation of the mass due to changes over both time and temperature through thermogravimetric analysis was determined also for the nanoconstruct CHX-B2 and the results are illustrated in both figures 4.27a and 4.27b.

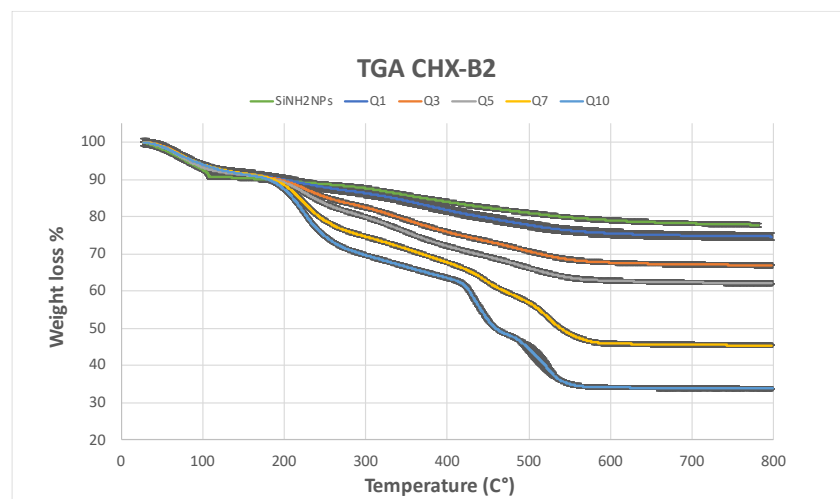


Figure 4.27a: Weight loss vs temperature for the construct Si-NH₂NPs-Alg-CHX-Alg-B2

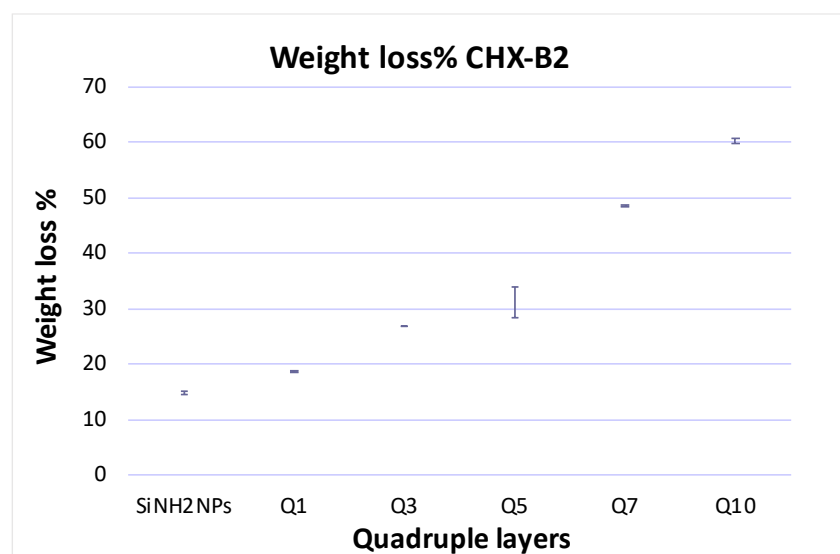


Figure 4.27b: Weight loss % among the QL for the matrix including CHX-B2. Mean \pm SD (N=1, n=2).

Initially the weight loss was correspondent to 14.80 ± 0.39 as already detected for the nanoconstructs previously described; then it was observed a gradual increase of 4% after the coating of the first quadruple layer, 18.89 ± 0.03 , a lower value considering the one measured for Q1 of CHX-A2. The weight loss % kept increasing for Q3 showing a percentage equal to 26.74 ± 1.05 , quite similar for Q3 of the A2 layered nanoparticles as well as for Q5 where the rise was only of the 5%, 31.15 ± 2.91 . Examining the mass loss provided by Q7 and Q10 for both CHX-A2 and CHX-B2, it was noticed that if for the first system there was a difference of only 2% between Q7 and Q10, for CHX-B2 the variation was definitely higher. For instance, the weight loss percentage was equal to 48.60 ± 0.10 for Q7 and 60.20 ± 0.38 for Q10, probably due to a better desorption and distribution of the drug and the polyelectrolytes among all the 10 quadruple layers (p-value < 0.05).

B3

To conclude the PBAEs of the group B employed for the development of the nano-delivery systems possessing the antimicrobial agent as cargo, the TGA was carried out also for the construct CHX-B3 (figures 4.28a and 4.28b).

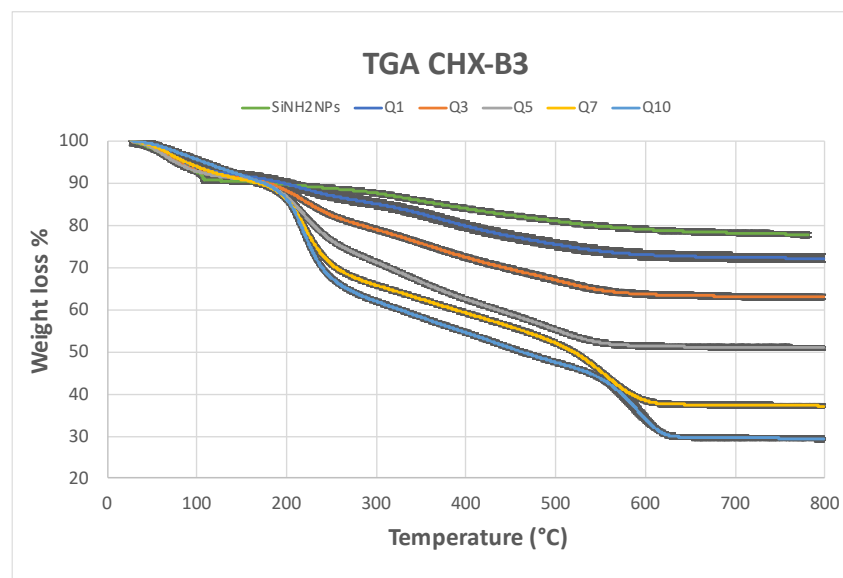


Figure 4.28a: Weight loss vs temperature for the construct Si-NH₂NPs-Alg-CHX-Alg-B3

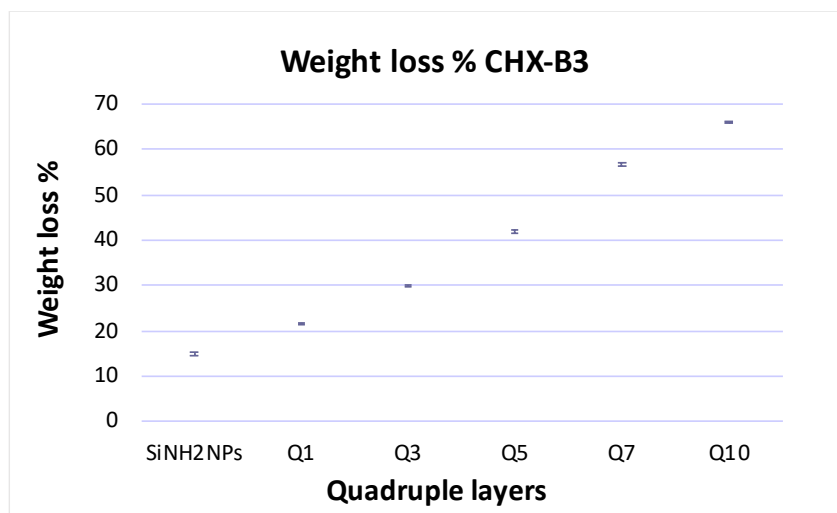


Figure 4.28b: Weight loss % among the QL for the matrix including CHX-B3. Mean \pm SD (N=1, n=2).

Starting from the organic content percentage of the amino-functionalised nanoparticles only, 14.80 ± 0.39 , there was an increase of almost 7% for Q1 showing a value equal to 21.68 ± 0.10 , definitely lower than what detected for Q1 of CHX-A3, 25.45 ± 0.49 . Furthermore, the weight loss increased of the 8% for Q3, 29.95 ± 0.30 , reporting a percentage slightly different if compared to the measurements of Q1 and Q3 of the nanoconstruct CHX-A3. The mass loss kept rising once new quadruple layers were embedded onto the system. For instance, the values for Q5, 41.87 ± 0.40 , Q7, 56.73 ± 0.37 and Q10, 66.19 ± 0.06 , were consistently higher than those reported by the same quadruple layers for CHX-A3 (p-value < 0.05).

Overall, differences in the weight loss percentage were observed between nano-delivery systems composed by PBAEs of the groups A and B: the higher values provided by CHX-B1, CHX-B2 and CHX-B3 indicated a better encapsulation of the drug and an improved desorption among the layers. Additionally, diversities were detected among the systems of the PBAEs synthesised by amines and 1,6 hexanediol diacrylate (B): the larger organic matter detected was for CHX-B3, followed by respectively CHX-B2 and CHX-B1 (p-value < 0.05).

D1

The thermogravimetric analysis was pursued also for the nanotechnology systems involving the polymers of the group D: CHX-D1, CHX-D2 and CHX-D3 and the chart of the figure 4.29a shows the correlation between the weight loss percentage and the temperature starting from the nanoparticles amino-functionalized up to Q10 for CHX-D1.

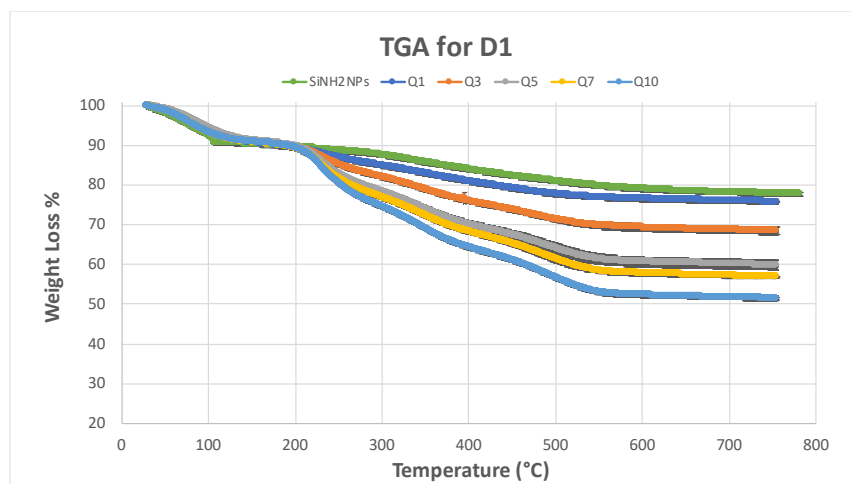


Figure 4.29a: Weight loss vs temperature for the construct Si-NH₂NPs-Alg-CHX-Alg-D1

As it is reported in the bar graph of the figure 4.29b, the weight loss increased when more quadruple layers were embedded onto the surface of the nanoparticles. Indeed, starting from a percentage of 14.79 ± 0.39 after the amino-functionalization of the silica nanoparticles, there was a slight increase for Q1, $18.12\% \pm 0.62$ and $25.81\% \pm 0.85$ for Q3, showing similar values to those of CHX-A1 and CHX-B1. The weight loss % rose up to $34.68\% \pm 0.94$ for the Q5 and $36.41\% \pm 0.08$ for Q7. Finally, the value registered Q10 was equal to $41.94\% \pm 0.37$. In this case, for the final quadruple layer, it was observed that the weight loss percentage was higher than the one provided by CHX-B1, $39.27\% \pm 0.7$ but moderately lower than Q10 for CHX-A1 which corresponded to $47.63\% \pm 1.49$ (p-value < 0.05).



Figure 4.29b: Weight loss % among the QL for the matrix including CHX-D1. Mean ± SD (N=1, n=2).

D2

The results of the nano-delivery system where the polycation D2 was involved for the chlorhexidine encapsulation are reported in both figures 4.30a and 4.30b.

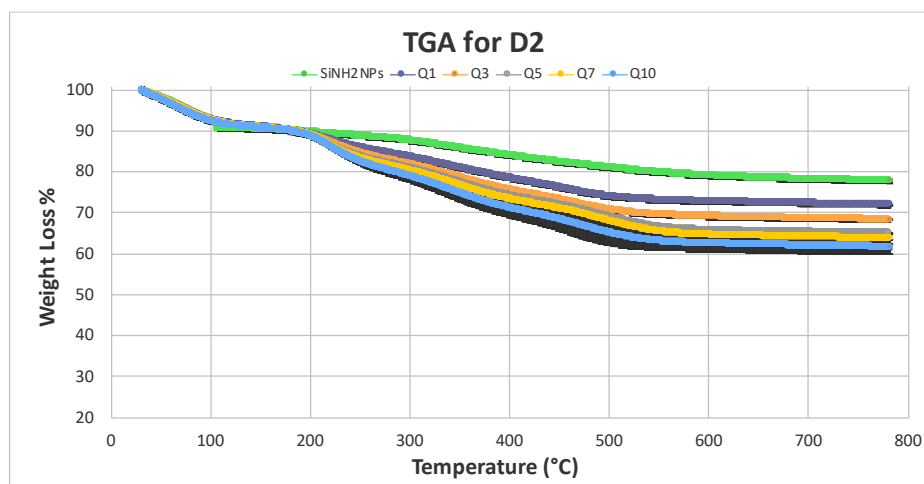


Figure 4.30a: Weight loss vs temperature for the construct Si-NH₂NPs-Alg-CHX-Alg-D2

As reported for the previous TGA experiments, the weight loss percentage for the silica amino-functionalized nanoparticles was equal to 14.79 ± 0.39 and it increased up to $20.91\% \pm 0.05$ in the first quadruple layer (figure 4.30b). This value is slightly higher compared to the percentage of Q1 for the nanoconstruct CHX-B2 but smaller than Q1 detected for CHX-A2 (p -value > 0.05). Moreover, the weight loss % of Q3 for the sequence CHX-D2 was $24.42\% \pm 0.18$, slightly lower than the values of Q3 for both CHX-A2, $27.46\% \pm 0.20$, and CHX-B2, 26.74 ± 1.05 (p -value > 0.05).

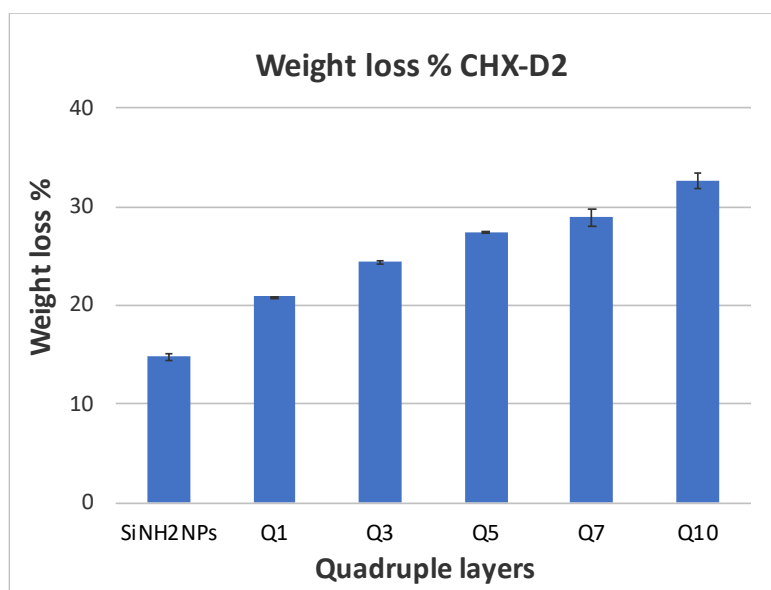


Figure 4.30b: Weight loss % among the QL for the matrix including CHX-D2. Mean \pm SD (N=1, n=2).

The weight loss percentage reported for the other quadruple layers Q5, Q7 and Q10, was equal to 27.49% \pm 0.04, 28.92% \pm 0.85 and 32.58% \pm 0.78, and it was significantly lower considering the measurements of the same quadruple layers for CHX-A2 and CHX-B2 (p-value < 0.05).

D3

To conclude the list of polymers of the group D, the analysis was carried out for the nanoconstruct CHX-D3 considering the modulation of the sample loss over temperature and time changes (figure 4.31a).

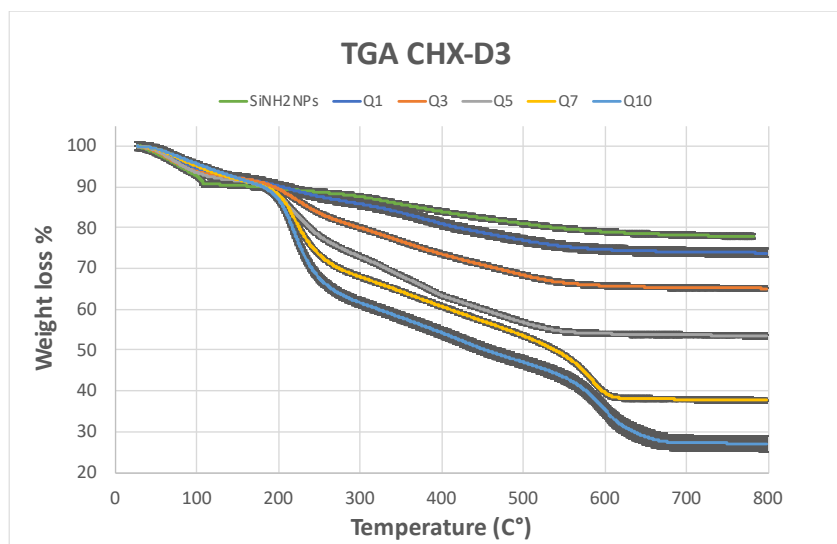


Figure 4.31a: Weight loss vs temperature for the construct Si-NH₂NPs-Alg-CHX-Alg-D3

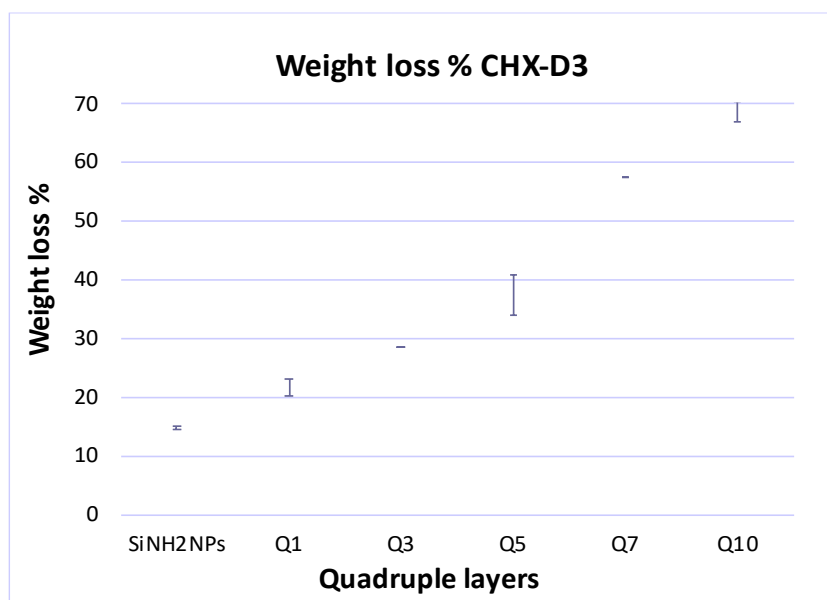


Figure 4.31b: Weight loss % among the QL for the matrix including CHX-D3. Mean \pm SD (N=1, n=2).

Initially the weight loss was equal to $14.80\% \pm 0.39$, then it was doubled after the first 4 layers were coated onto the nanoparticles surface to form Q1, $21.64\% \pm 1.40$, providing a similar value to Q1 of CHX-B3 (p-value > 0.05) and a smaller amount than the one of Q1 for CHX-A3 which correspondent to $25.45\% \pm 0.49$ (p-value > 0.05) (figure 4.31b). Furthermore, for this system, the percentage of weight loss of Q3 for CHX-D3 was the lowest detected, $28.61\% \pm 0.5$, if compared to those of both CHX-A3 and CHX-B3, as well as for Q5, $37.50\% \pm 3.54$, and for Q7, $57.41\% \pm 0.71$ (p-value < 0.05). As contrary, it was observed that the weight loss % measured for Q10 in this system was the greatest gained among the PBAEs possessing amine

3 as starting material and heretofore described. In fact, the value was equal to $68.66\% \pm 1.65$; instead the percentage for CHX-A3 was $67.31\% \pm 0.01$ whereas for CHX-B3 correspondent to $66.19\% \pm 0.06$ (p-value < 0.05).

In conclusion, the results produced by the TGA measurements for the PBAEs belonging to the group D evidenced that the weight loss percentage was dependent on the rise of the temperature along the experiment and the number of layers coated onto the carrier surface via LbL technique. In particular, the highest rate of weight loss gained was observed for CHX-D3, followed by CHX-D1 and CHX-D2.

E1

Thermogravimetric analysis was performed for the sequences CHX-E1, CHX-E2 and CHX-E3. The results regarding the first nanoconstruct are reported in the figures 4.32a and 4.32b, where it is possible to see the distribution of the weight loss among the quadruple layers. First of all, as described before, the first measurement was representative of the silica nanoparticles amino-functionalized which were heated up to 800°C showing a percentage of weight loss equal to $14.79\% \pm 0.39$. Then, it increased after the addition of new quadruple layers onto the system.

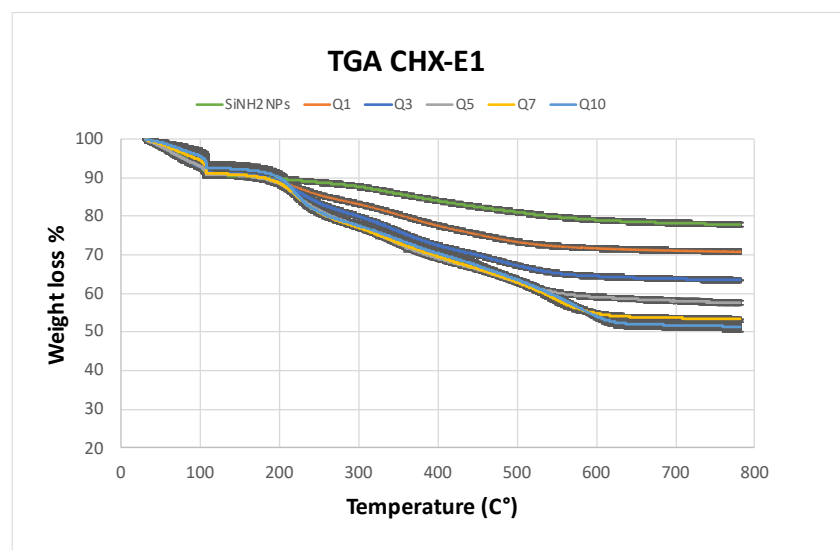


Figure 4.32a: Weight loss vs temperature for the construct Si-NH₂NPs-Alg-CHX-Alg-E1

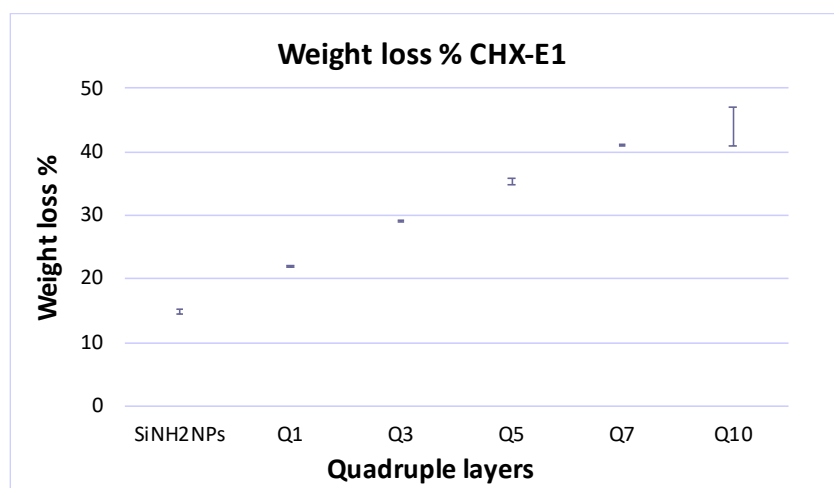


Figure 4.32b: Weight loss % among the QL for the matrix including CHX-E1. Mean \pm SD (N=1, n=2).

The value detected for Q1, $22.06\% \pm 0.10$, was the biggest value obtained among all the nanoconstructs previously described and possessing amine 1 as starting material (p-value < 0.05). The weight loss continued rising up to $29.36\% \pm 0.01$ similarly to what observed for CHX-A1, CHX-B1 and CHX-D1 (p-value > 0.05). The rate of weight loss % related to Q5, Q7 and Q10 were respectively, $35.38\% \pm 0.47$, $41.10\% \pm 0.15$, and $44.05\% \pm 3.04$, showing a profile similar to those of CHX-A1 and CHX-D1 (p-value > 0.05) but with a highest amount of organic content for Q10 if compared to the one of CHX-B1, $39.27\% \pm 0.7$ (p-value < 0.05).

E2

The figures 4.33a and 4.33b illustrate the effect of high temperature and time on the weight loss of the sample CHX-E2 and the increase of the weight loss percentage in the layers Q1, Q3, Q5, Q7 and Q10. In the E2 layered nanoparticles, from a weight loss of $14.79\% \pm 0.39$ as starting point for the nanocarriers alone, it was registered a growth in the values up to Q10.

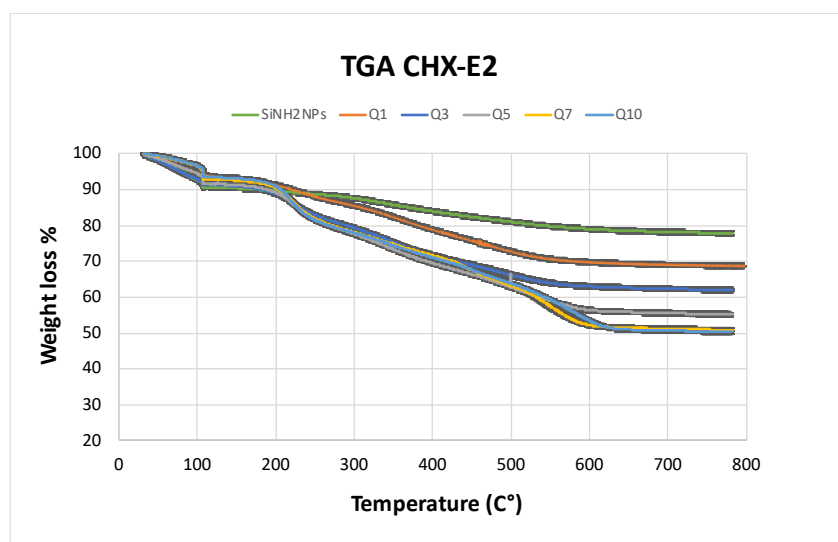


Figure 4.33a: Weight loss vs temperature for the construct Si-NH₂NPs-Alg-CHX-Alg-E2

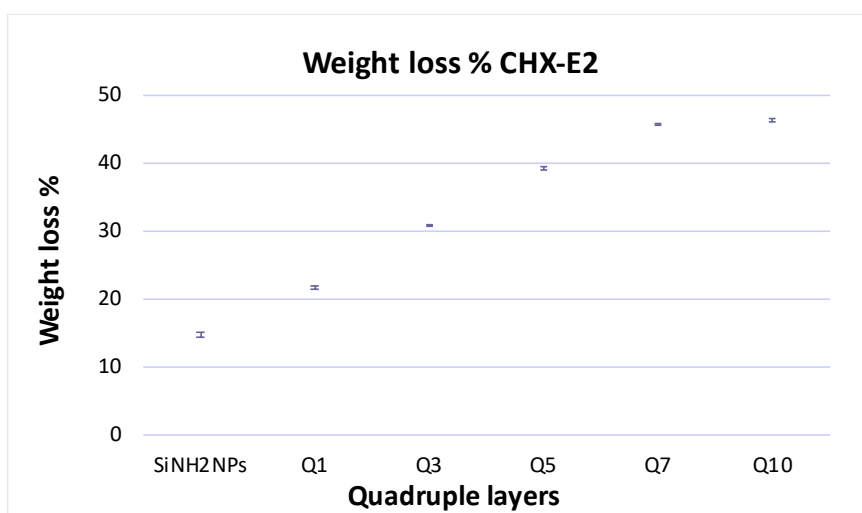


Figure 4.33b: Weight loss % among the QL for the matrix including CHX-E2. Mean \pm SD (N=1, n=2).

The percentage for Q1, in this case $21.75\% \pm 0.36$, was slightly inferior than the one reported for Q1 of CHX-A2, $22.54\% \pm 0.18$ (p -value > 0.05), but bigger than the value of the same quadruple layer provided by CHX-B2, $18.89\% \pm 0.03$, and CHX-D2, $20.91\% \pm 0.05$ (p -value < 0.05). As contrary the weight loss % of Q3 for the nanoconstruct CHX-E2 was the greatest among all the systems having amine 2 as amine and corresponded to $30.94\% \pm 0.02$ (p -value < 0.05). From Q5 to Q10 of CHX-E2, the weight loss percentage was higher than in CHX-A2 and CHX-D2 (p -value < 0.05) but lower than what detected for system CHX-B2 (p -value > 0.05). Thus, the weight loss percentage for Q5, Q7 and Q10 of CHX-E2 was as followed: $39.33\% \pm 0.23$, $45.74\% \pm 0.03$, $46.36\% \pm 0.22$.

E3

To conclude the PBAEs of the group E which were adopted for the development of drug release nano delivery systems, the figures 4.34a and 4.34b report the results regarding the nanoconstruct CHX-E3.

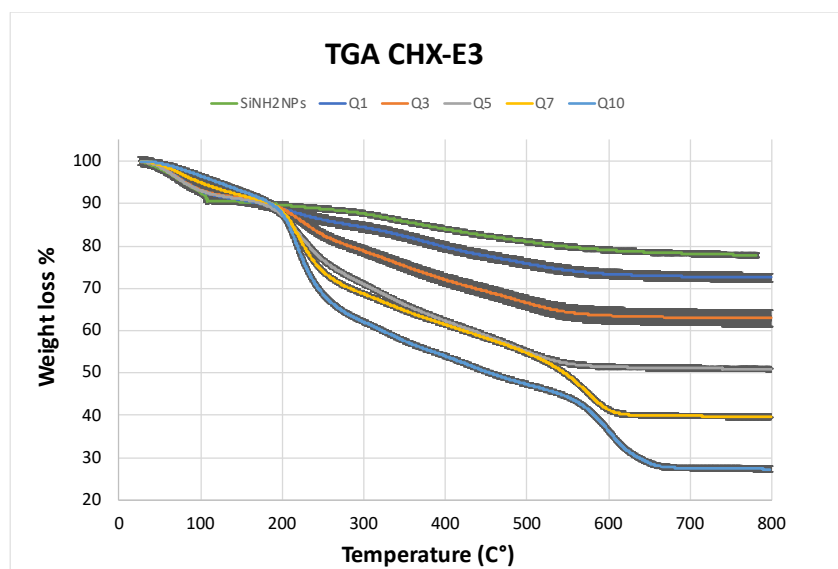


Figure 4.34a: Weight loss vs temperature for the construct Si-NH₂NPs-Alg-CHX-Alg-E3

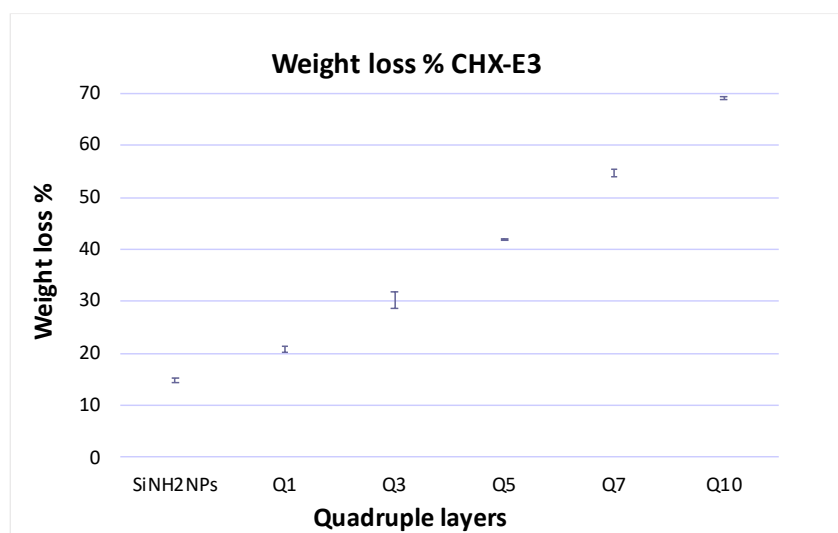


Figure 4.34b: Weight loss % among the QL for the matrix including CHX-E3. Mean \pm SD (N=1, n=2).

In the E3 layered nanoparticles, the weight loss percentage for Q1 was correspondent to $20.94\% \pm 0.59$ which was definitely the lowest value considering the nanoconstructs previously described (p -value < 0.05). Differently, the rate of weight loss % provided by Q3

was equal to $30.26\% \pm 1.61$ that in this case was higher than CHX-D3, $28.61\% \pm 0.5$, and CHX-B3, $29.95\% \pm 0.30$, but reduced examining Q3 for CHX-A3, $35.55\% \pm 0.56$ (p -value < 0.05). The weight loss of the sample CHX-E3 continued rising from Q5 to Q10 showing values of $42.11\% \pm 0.01$ for Q5, $54.78\% \pm 0.72$ for Q7 and $69.19\% \pm 0.25$ for Q10. These results showed similarities to the weight loss percentage detected for Q5 and Q7 of the nanoconstructs until now analysed (p -value > 0.05), whereas the value reported for Q10 of CHX-E3 was the biggest among the systems possessing amine 3 as starting material (p -value < 0.05).

To sum up, among the nanoconstructs including the PBAEs of the group E, it was observed that the weight loss percentage was better distributed in CHX-E3, CHX-E2 and CHX-E1 with a similar weight loss detected for CHX-E1 and CHX-E2 (p -value > 0.05) and a value for Q10 of CHX-E3 which was the highest among the 3 systems (p -value < 0.05).

F1

Additionally, the TGA was performed for the nanotechnology systems in which firstly the chlorhexidine was embedded with the hydrolysable polymer F1, then with polycation F2 and finally with F3. In fact, the figures 4.35a and 4.35b are representative of the results provided by each nanoconstruct.

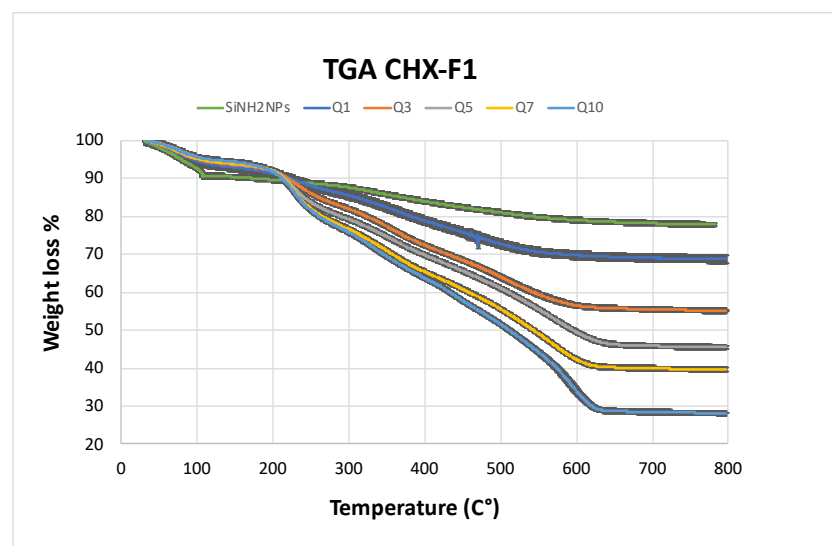


Figure 4.35a: Weight loss vs temperature for the construct Si-NH₂NPs-Alg-CHX-Alg-F1

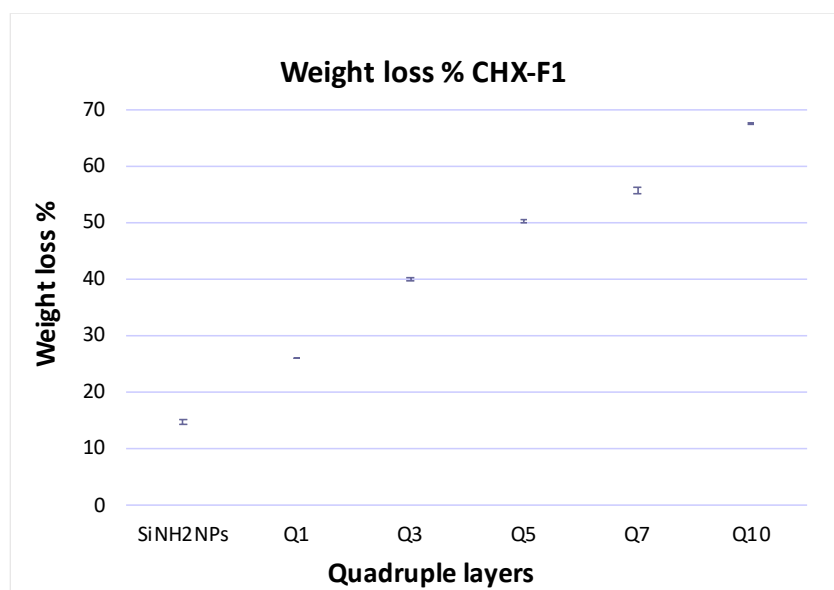


Figure 4.35b: Weight loss % among the QL for the matrix including CHX-F1. Mean \pm SD (N=1, n=2).

For the sequence having CHX-F1, the silica nanoparticles amino-functionalized presented a weight loss equal to $14.79\% \pm 0.39$, followed by an increase up to $25.90\% \pm 0.03$ for Q1 and this value was the greatest gained for Q1 among the all systems previously described. Moreover, similarly to what detected for the previous nano-delivery networks, also for this nanoconstruct the weight loss was rising after a new quadruple layer was coated onto the carrier surface showing values such as: $40.02\% \pm 0.2$ for Q3, $50.11\% \pm 0.26$ for Q5, $55.60\% \pm 0.52$ for Q7 and finally $67.53\% \pm 0.014$ for Q10. In this case, it was noticed a higher weight loss percentage if compared to the sequences previously analysed and having piperazine as chosen amine for the synthesis of the PBAEs (p -value < 0.05).

F2

The experiment of TGA was pursued also for the sequence including CHX-F2 and the results are illustrated by the figures 4.36a and 4.36b below.

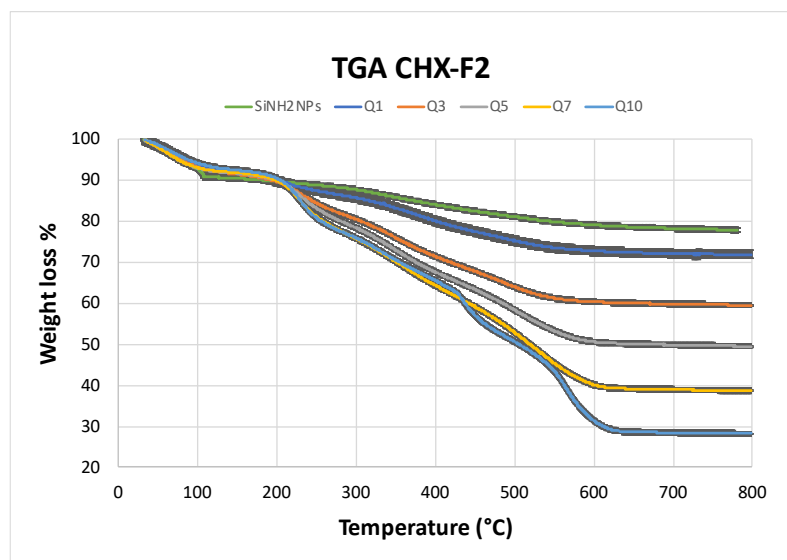


Figure 4.36a: Weight loss vs temperature for the construct Si-NH₂NPs-Alg-CHX-Alg-F2

In the F2 layered nanoparticles, starting from an organic content of $14.79\% \pm 0.39$, the weight loss percentage rose to $21.77\% \pm 0.25$ for the first quadruple layer. This value was definitely similar to the one for Q1 of CHX-E2 (p -value > 0.05) but higher than the percentage of Q1 for CHX-A2, CHX-B2 and CHX-D2 (p -value < 0.05). Additionally, the weight loss % representative of Q3 for the system CHX-F2 and equal to $33.67\% \pm 0.15$, was the greatest value if compared to the percentage provided by Q3 for all the nanoconstructs possessing amine 2 as starting material (p -value < 0.05). Then, similarly to what described for Q1 and Q3, it was observed that also for Q5, Q7 and Q10 in the sequence CHX-F2 the rate of organic matter showed highest values among CHX-A2, CHX-B2, CHX-D2 and CHX-E2 (p -value < 0.05). Therefore, the gained values for the organic matter were as followed: $43.44\% \pm 0.63$ for Q5, $54.29\% \pm 0.21$ for Q7 and $65.85\% \pm 0.52$ for Q10.

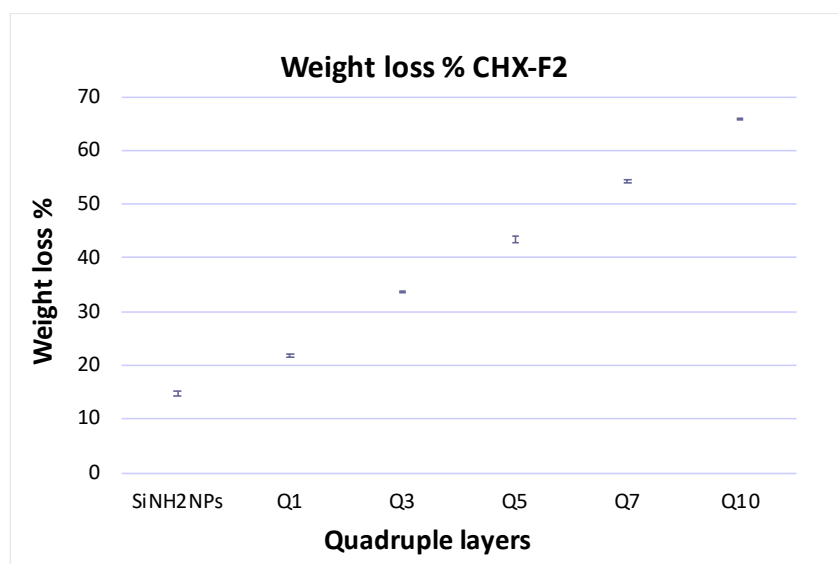


Figure 4.36b: Weight loss % among the QL for the matrix including CHX-F2. Mean \pm SD (N=1, n=2).

For the group F (F1 and F2) the weight loss % is definitely higher compared to the other LbL systems. In particular, the TGA profile for F2 is supported by a zig-zag pathway of zeta potential where F2 seems to be a stronger and more stable polycation than F1.

F3

To complete the polycations of the group F, the TGA was carried out also for the nano-delivery system including F3 as positive network and employed for the encapsulation of the antimicrobial agent on the amino-functionalised silica nanoparticles surface. The change of the weight loss percentage was increasing from the nanoparticles analysed alone to the last quadruple layer Q10 and it is reported by the figures 4.37a and 4.37b.

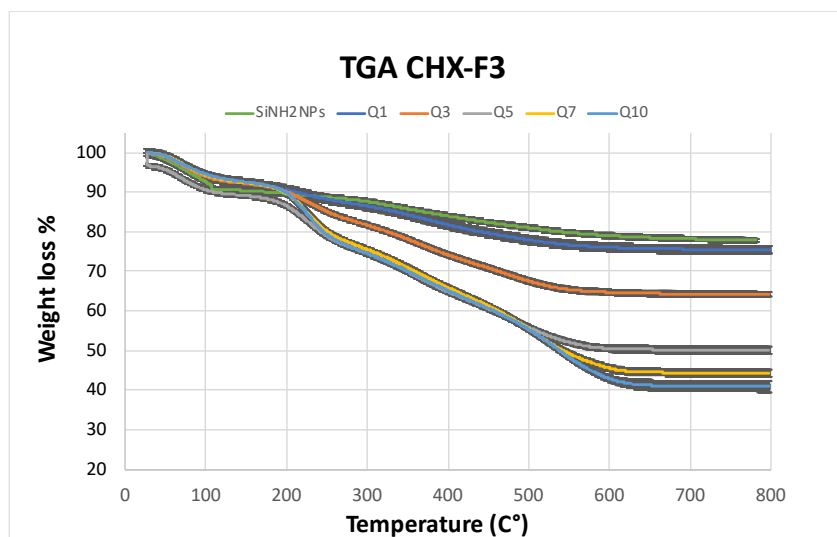


Figure 4.37a: Weight loss vs temperature for the construct Si-NH₂NPs-Alg-CHX-Alg-F3

Starting from the weight loss percentage provided by the nanoparticles alone, $14.80\% \pm 0.39$, there was an increase from Q1 to Q10. For instance, the percentage slightly rose up to $18.65\% \pm 0.44$ for Q1, reporting the lowest detected value among all the nanoconstructs until now analysed and having amine 3 as starting material. As contrary, for Q3 the organic content was equal to $29.79\% \pm 0.44$, a similar rate to what measured for Q3 of CHX-B3, CHX-D3 and CHX-E3 (p -value > 0.05), but definitely lower than Q3 of CHX-A3, $35.5\% \pm 0.56$ (p -value < 0.05). As observed for the previous systems, also in this case the weight loss percentage continued increasing for Q5, Q7 and Q10 showing values correspondent to $37.50\% \pm 3.54$, $57.41\% \pm 0.71$ and $68.66\% \pm 1.65$ and comparable to those of CHX-A3, CHX-B3, CHX-D3 and CHX-E3 (p -value > 0.05).

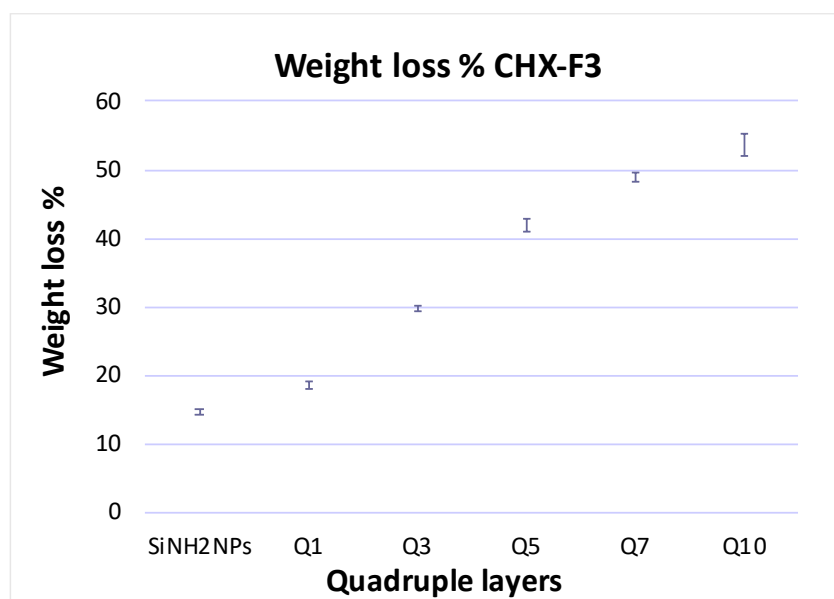


Figure 4.37b: Weight loss % among the QL for the matrix including CHX-F3. Mean \pm SD (N=1, n=2).

Differently to what noticed for the previous nano-delivery systems, examining the results of the constructs including PBAEs of the group F, the highest organic content percentage was provided by CHX-F1, $67.53\% \pm 0.01$, followed by CHX-F2, $65.85\% \pm 0.11$, and CHX-F3, $53.67\% \pm 1.52$. These values illustrated the difference in the distribution of both polymer and drug among the layers highlighting a better stability for the coatings CHX-F1 and CHX-F2 than for CHX-F3 (p-value < 0.05).

G1

To conclude, the TGA was performed also for the sequences possessing respectively G1, G2 and G3. The results regarding the construct CHX-G1 are illustrated in the line graph of the figure 4.38a. Additionally, for this nanotechnology system the thermogravimetric analysis was carried out for five quadruple layers, such as Q1, Q3, Q5, Q7 and Q10, and considered a control for the all 10 quadruple layers. As it was observed in the previous coatings, also in this case the weight loss increased once more quadruple layers were embedded onto the surface of the silica nanoparticles.

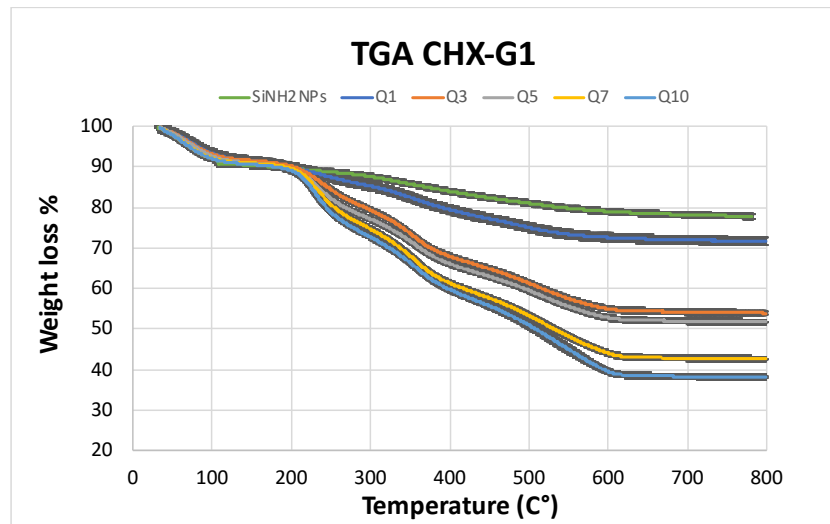


Figure 4.38a: Weight loss vs temperature for the construct Si-NH₂NPs-Alg-CHX-Alg-G1

The weight loss % is displayed in the column graph of the figure 4.38b. Firstly, as reported for the other nanoconstructs, the initial weight loss percentage represented by silica nanoparticles amino-functionalised was equal to $14.79\% \pm 0.39$; then it increased to $21.72\% \pm 0.61$ for Q1, which was similar to CHX-A1, CHX-B1, CHX-D1 and CHX-E1 but lower than CHX-F1, $25.90\% \pm 0.1$ (p -value > 0.05). Finally, the weight loss % was $39.23\% \pm 0.22$, $41.02\% \pm 0.30$, $49.57\% \pm 0.13$ and $53.94\% \pm 0.09$ correspondent respectively to Q3, Q5, Q7 and Q10. It was observed beside CHX-F1 which provided the highest amount, that CHX-G1 showed a rate of weight loss which was greater if compared to CHX-A1, CHX-B1, CHX-D1 and CHX-E1 (p -value < 0.05).

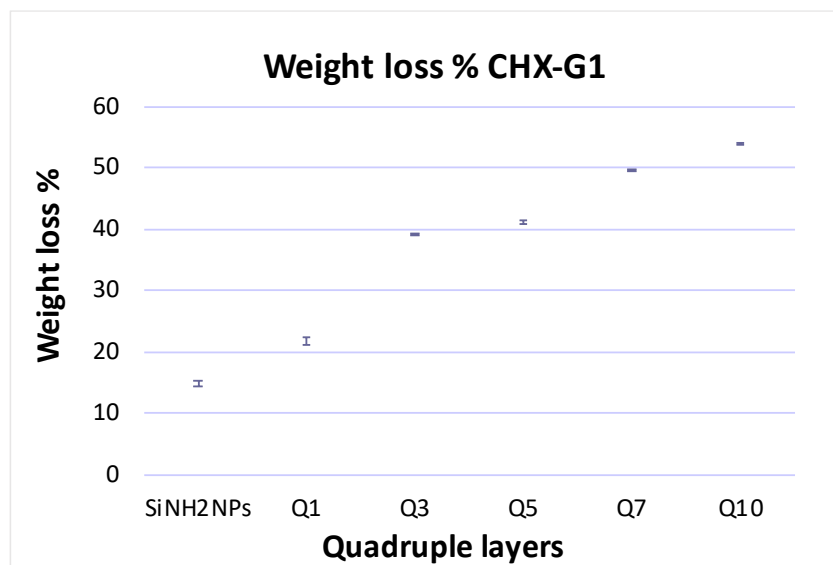


Figure 4.38b: Weight loss % among the QL for the matrix including CHX-G1. Mean \pm SD (N=1, n=2).

G2

The TGA was pursued also for the coating CHX-G2 and the results are reported in the figures 4.39a and 4.39b below.

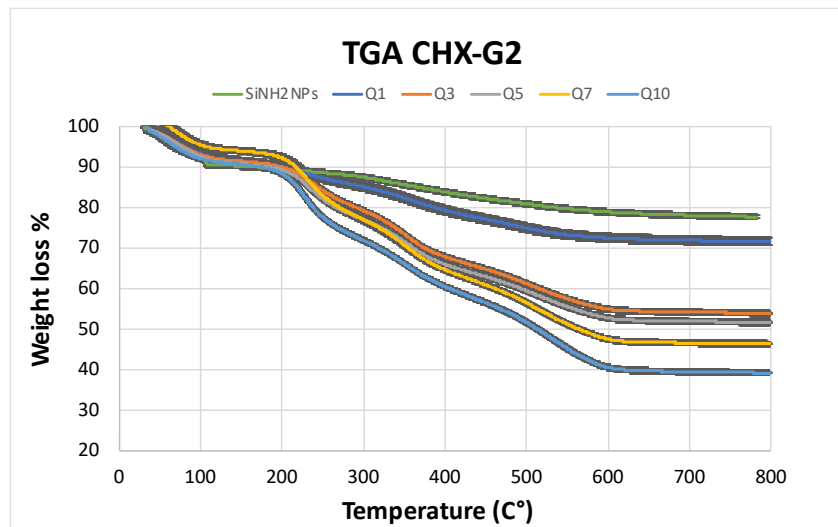


Figure 4.39a: Weight loss vs temperature for the construct Si-NH₂NPs-Alg-CHX-Alg-G2

In the G2 layered nanoparticles, the weight loss % was higher if compared to the sequences having polycations belonging to the groups A, B, D and E, except for the group F for which it was detected the biggest weight loss percentage (p-value < 0.05).

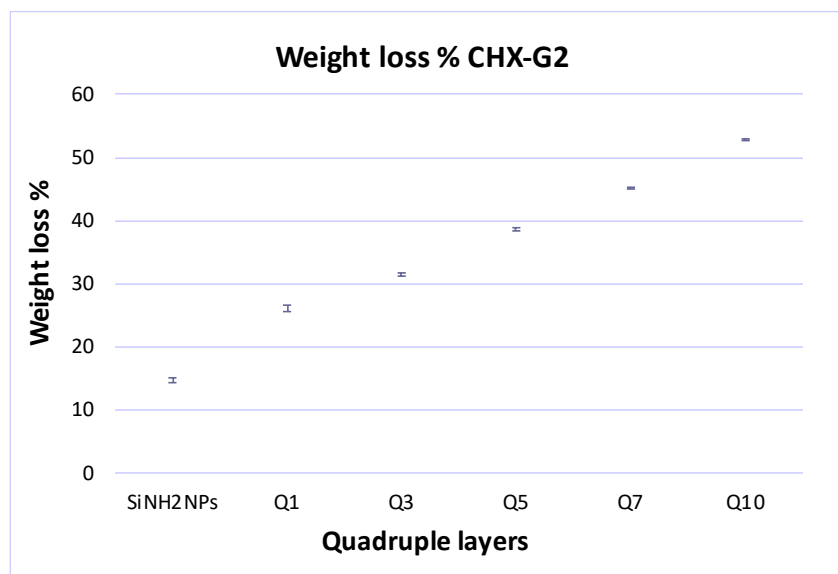


Figure 4.39b: Weight loss % among the QL for the matrix including CHX-G2. Mean \pm SD (N=1, n=2).

As it was already described before, the weight loss for the silica nanoparticles before starting the LbL was correspondent to $14.79\% \pm 0.39$. It rose up to 26.15% in the first quadruple layer as well as it increased again once two more quadruple layers were added onto the system, showing a value for Q3 of $31.47\% \pm 0.05$. Furthermore, it was noticed that the number of quadruple layers and the weight loss % were dependent on high temperature and its sample time exposure. Thus, for the following quadruple layers Q5, Q7 and Q10 the weight loss percentage reported were respectively $38.67\% \pm 0.1$, $45.12\% \pm 0.7$ and $53.03\% \pm 0.42$.

Overall, it was clear that the weight loss % registered for the constructs having the polycations G1 and G2 was higher than what reported for the LbL systems possessing the groups A, B, D and E, but it was lower when compared to the organic decomposition of CHX-F1 and CHX-F2 and quite similar to what detected for CHX-F3 (p-value < 0.05).

G3

The PBAE G3 was the last polymer of the group G and the final polycation among the 18 PBAEs synthesised in this project, to be employed in the coating CHX-G3 with the aim of improving the encapsulation and the release of the antimicrobial agent chlorhexidine. Following the same conditions described before, also in this case the TGA was performed to investigate the change of sample weight loss percentage depending on the increase of temperature, from 0°C to 800°C, over the time of the analysis (figure 4.40a).

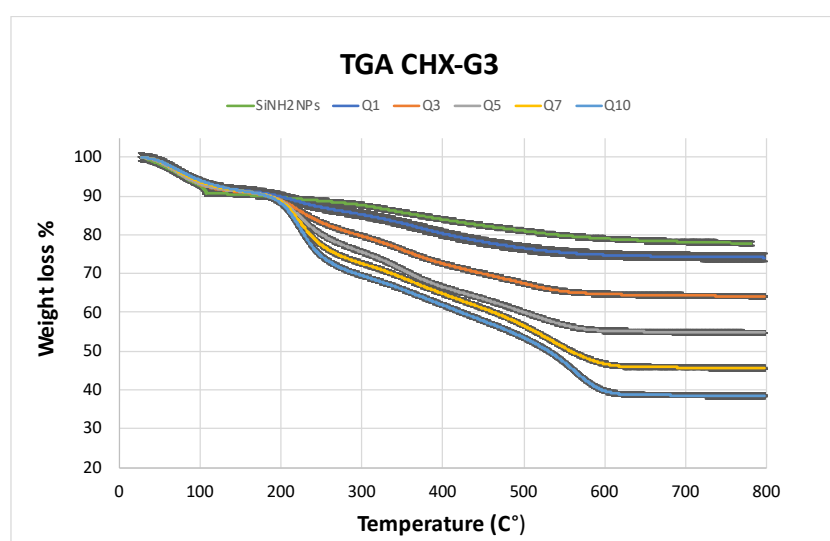


Figure 4.40a: Weight loss vs temperature for the construct Si-NH₂NPs-Alg-CHX-Alg-G3

Initially the weight loss percentage was correspondent only to the amino functionalised silica nanoparticles before starting the LbL process, $14.80\% \pm 0.39$ (figure 4.40b); then, there was a constant increase detected from Q1 to Q10. For instance, after the coating of the first 4 layers onto the carrier surface, the weight loss % rose up to 19.30 ± 0.14 , showing a higher percentage than the one measured for Q1 of CHX-F3 but lower than Q1 of CHX-A3, CHX-B3, CHX-D3 and CHX-E3 (p -value < 0.05). As contrary, the value reported for Q3 of CHX-G3 was equal to 28.92 ± 0.06 , which was similar to Q3 of CHX-D3, 28.61 ± 0.5 , and slightly reduced if compared to the other nanoconstructs (p -value > 0.05). Additionally, the weight loss % of CHX-G3 kept increasing also for Q5, Q7 and Q10 with percentage respectively of 38.36 ± 0.08 , 48.13 ± 0.04 and 55.63 ± 0.52 . The profile of CHX-G3 showed results which were comparable to those of CHX-F3 (p -value > 0.05), but different and decreased considering CHX-A3, CHX-B3, CHX-D3 and CHX-E3 (p -value < 0.05).

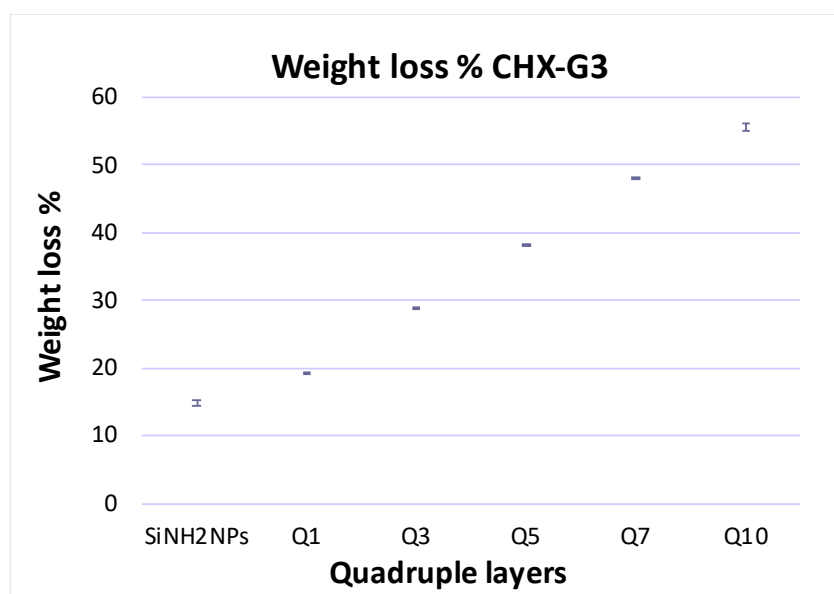


Figure 4.40b: Weight loss % among the QL for the matrix including CHX-G3. Mean \pm SD (N=1, n=2).

Examining the systems possessing the polymers of the group G no difference was observed among their TGA profiles (p -value > 0.05). In fact, the weight loss percentage similarly increased in the 3 nanoconstructs, showing that the highest rate was provided by CHX-G3, 55.63 ± 0.52 , followed by CHX-G1, 53.94 ± 0.09 , and CHX-G2, 53.03 ± 0.42 .

Overall, the thermogravimetric analysis highlighted the success of the encapsulation of the antimicrobial agent in the all 18 CHX-PBAEs nanoconstructs, proved by the weight loss percentage of the last quadruple layer Q10 which was over 40% (Yan et al., 2017). Additionally, comparing the zeta potential profiles of CHX-B1, CHX-F1, CHX-G1, CHX-A2, CHX-B2, CHX-F2, CHX-A3, CHX-D3, CHX-F3, CHX-F3 discussed before, to the TGA results of the same matrices, significantly different were the systems including the PBAEs A3, B2, D3, F1, F2 and F3 (p-value < 0.05). In particular, for the systems including these polymers, the weight loss representative of Q10 was the highest detected among all the nanoconstructs ranging between 60-69%, with a high drug loading and better distribution of drug and PBAEs among all the multilayers.

Chlorhexidine release determination

Once the antimicrobial agent was entrapped into the 18 nanocoating systems, the nanoparticles of the last quadruple layer, Q10, were left drying overnight under fume hood. Chlorhexidine release studies were started by suspending 10 mg of Q10 for each system in two different media: in sodium acetate buffer at pH5 reflecting the joint infection environment and in PBS at pH7.4 representing the physiological environment. The samples were kept in the incubator at 37°C and every 24 hours 1 mL was withdrawn and replace with fresh buffer. The drug release was quantified by HPLC and for both media profiles were built up considering the cumulative release as function of time (days).

Bilayer: Alg-CHX

Following the parameters mentioned before, the first analysis carried out was related to the system composed by 10 bilayers where alternatively sodium alginate and chlorhexidine were coated via electrostatic interactions onto the amino-functionalised silica nanoparticles surface. The release profile is illustrated by the figure 4.41 below.

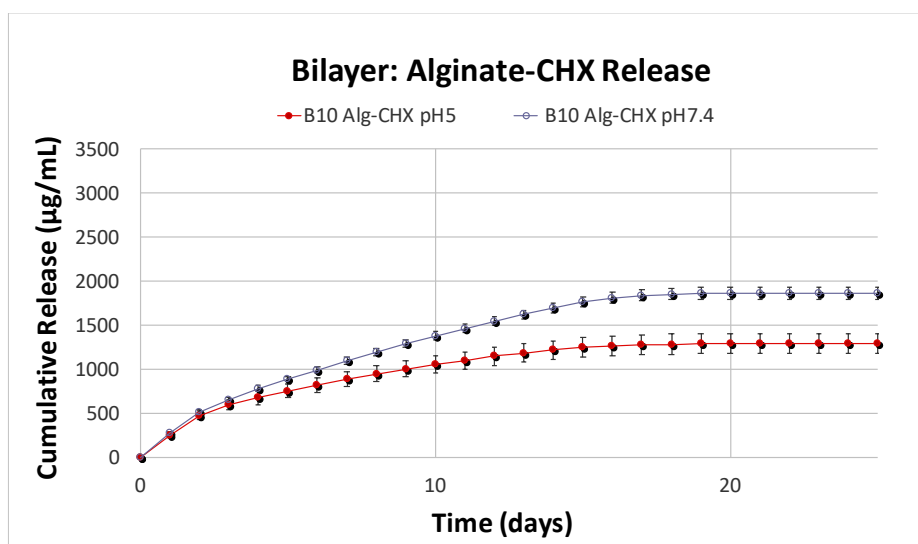


Figure 4.41: CHX release profile at pH5 and at pH7.4 for B10 of the construct Alg-CHX.

For each curve: Mean \pm SD (N=1, n=3).

It was observed that the drug release from the construct alginate-chlorhexidine occurred within 25 days and differences in both media were detected (p-value < 0.05). For instance, the profiles showed a drug release pH dependent: the final cumulative release was correspondent to 1295.83 $\mu\text{g/mL}$ at pH5 whereas it was 1868.21 $\mu\text{g/mL}$ at pH7.4. Additionally, at pH5, the drug was faster released in the first 3 days, reaching an average of 50 $\mu\text{g/mL}$ of daily drug released; on the other hand, at pH7.4, the amount daily released was definitely doubled if compared to pH5 reaching the plateau on day 20 (p-value < 0.05). Thus, under acid conditions the drug was less released due to the stronger electrostatic interactions among the layers, which were more flexible in the physiological environment providing an increased drug release. The profiles of the bilayer Alg-CHX will be considered the control for following drug release pathways provided by the systems where PBAEs were embedded as polycations.

A1

The first system that was object of drug release determination was CHX-A1 and its study was carried out for overall 70 days for both media pH5 and pH7.4. The results reported in the figure 4.42 showed two different profiles highlighting that the drug release was dependent on the pH grade in which the nanoparticles were suspended (p-value < 0.05). For instance, at pH5 the initial daily release was equal to 67.79 $\mu\text{g/mL}$ after the first 24 hours; it was half

reduced on day 2, 31.33 $\mu\text{g}/\text{mL}$ showing an average of daily release between 24-27 $\mu\text{g}/\text{mL}$ from day 3 to day 15. The curve kept rising although there was a reduction of the daily release, 10-20 $\mu\text{g}/\text{mL}$, starting from day 16 to day 46, before reaching the plateau which lasted until day 70 with a cumulative release correspondent to 1125.96 $\mu\text{g}/\text{mL}$.

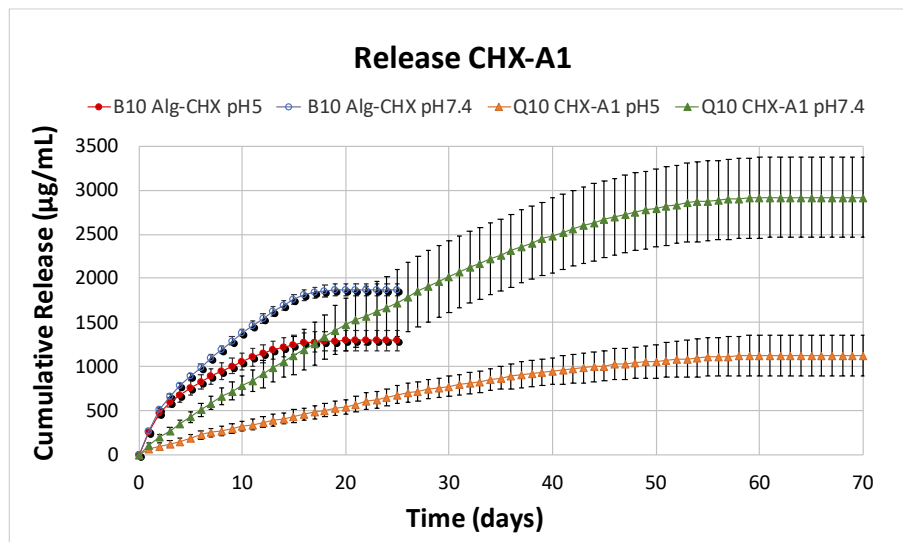


Figure 4.42: CHX release profile at pH5 and at pH7.4 for Q10 of the construct CHX-A1.

For each curve: Mean \pm SD (N=1, n=3).

However, the detected release for pH7.4 was equal to 2916.89 $\mu\text{g}/\text{mL}$ after 70 days. In this case the antimicrobial agent was higher released than at pH5 showing similarities to what measured for B10 of the delivery system composed by alginate and chlorhexidine. The initial daily release for CHX-A1, under physiological conditions, was 105.10 $\mu\text{g}/\text{mL}$ on day 1 and 92.62 $\mu\text{g}/\text{mL}$ on day 2 with an average between 60-76 $\mu\text{g}/\text{mL}$ from day 3 to 20. The amount started decreasing from day 21 to 40, 40-56 $\mu\text{g}/\text{mL}$, and ending to 10-20 $\mu\text{g}/\text{mL}$ until day 54, with a plateau developed from day 55 to 70, with a range of daily release between 9-2 $\mu\text{g}/\text{mL}$.

A2

The drug release was determined also for the system including chlorhexidine and the polycation A2 and the profiles are represented by the figure 4.43 below.

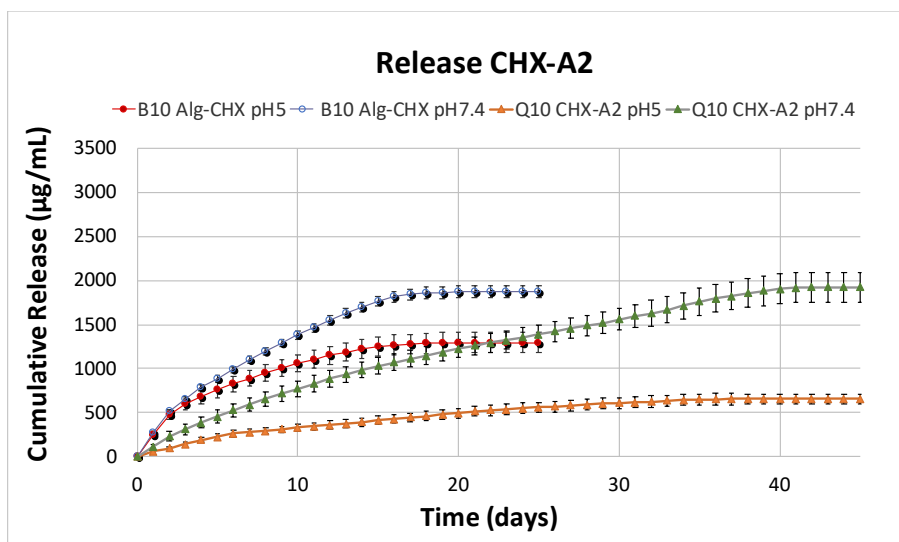


Figure 4.43: CHX release profile at pH5 and at pH7.4 for Q10 of the construct CHX-A2.

For each curve: Mean \pm SD (N=1, n=3).

Comparing the results gained for CHX-A2 to those of CHX-A1 it was noticed that in this case the cargo was significantly slowly released reaching an amount of 656.84 $\mu\text{g}/\text{mL}$ at pH5 and 1920.60 $\mu\text{g}/\text{mL}$ at pH7.4 over a period of 45 days ($p\text{-value} < 0.05$). Under acid conditions, 62.84 $\mu\text{g}/\text{mL}$ of chlorhexidine were released from the construct after the first 24 hours, whereas from day 2 to day 6 the amount was between 48.8-32.9 $\mu\text{g}/\text{mL}$. Then, the daily release dropped with an average of 10.74-21.06 $\mu\text{g}/\text{mL}$ from day 7 to day 30 and reaching the plateau within 15 more days with a release correspondent to 5.04-2.38 $\mu\text{g}/\text{mL}$ from day 31 up to day 45. On the other hand, the rate of drug release detected for the first 2 days at pH7.4 was significantly higher if compared to pH5 ($p\text{-value} < 0.05$), with 116.86-115.60 $\mu\text{g}/\text{mL}$ released per day. For the first 15 days the daily rate was equal to 50.56-78.22 $\mu\text{g}/\text{mL}$, it plummeted to 22.73 $\mu\text{g}/\text{mL}$ until day 39, ending to the plateau with an amount between 16.32-3.40 $\mu\text{g}/\text{mL}$ form day 40 to day 45. Examining both profiles belonging to this nanoconstruct, it was observed that, although the release lasted longer if compared to B10 of Alg-CHX, the rate of daily release was significantly lower for both media that the those provided by the bilayers nanoconstruct ($p\text{-value} < 0.05$).

A3

To conclude the nano-delivery systems constituent by PBAEs synthesised with the diacrylate A, the drug release evaluation was carried out also for the coating CHX-A3. From the results

illustrated in the figure 4.44 it is evident that similarly to what previously described, the drug was faster released at pH7.4 than at pH5, but for this network the release less lasted reaching the plateau after 30 days.

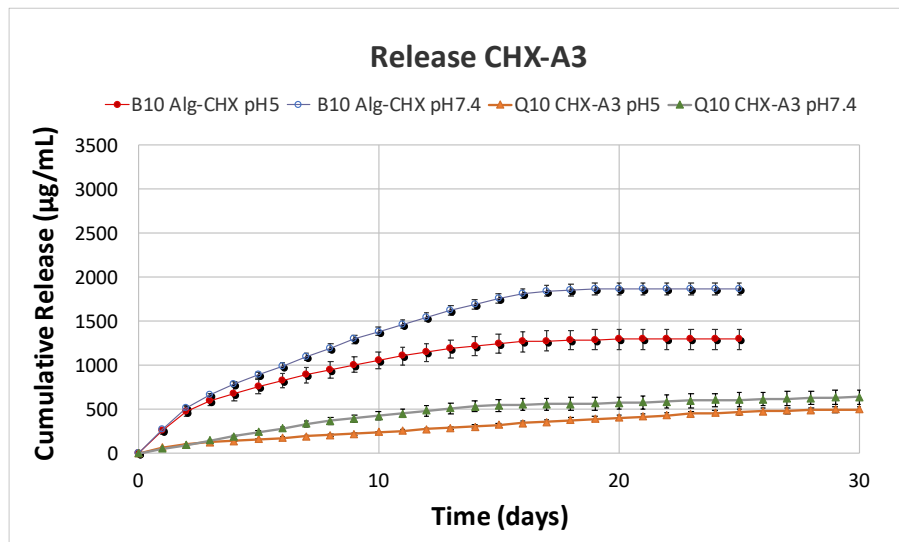


Figure 4.44: CHX release profile at pH5 and at pH7.4 for Q10 of the construct CHX-A3.

For each curve: Mean \pm SD (N=1, n=3).

On day 1 65.95 $\mu\text{g/mL}$ of the antimicrobial agent were released at pH5, following by 35.33 $\mu\text{g/mL}$ on day 2 and 24.69 $\mu\text{g/mL}$ on day 3. From day 4 the rate of daily release was reduced showing a range between 18.85-10.61 $\mu\text{g/mL}$ until day 24, ending to the plateau with a cumulative release of 5.98-2.38 $\mu\text{g/mL}$ measured from day 25 and ending to day 30. As contrary, under physiological environment, the drug was moderately daily released along the first week showing a value of 52.47-40.92 $\mu\text{g/mL}$, which decreased on day 8, 30.28 $\mu\text{g/mL}$, remaining constant until day 13. Furthermore, on day 14 and 15 there was a change of daily amount released which was equal to 18.16-13.16 $\mu\text{g/mL}$, hitting the plateau from day 16 to day 30 showing an average between 9.99-3.76 $\mu\text{g/mL}$ per day.

Considering the nanoconstructs having as polycations the PBAEs of the group A and B10 composed by alginate and chlorhexidine, CHX-A1, CHX-A2 and CHX-A3 provided profiles at both media that were lasting longer but showing a better control of the drug release. However, among the 3 delivery systems, the higher rate of cumulative release was detected for CHX-A1, followed by CHX-A2 and CHX-A3, with a significant initial release of the first 15

days (p-value < 0.05) which was similar for both CHX-A1 and CHX-A2 (p-value > 0.05) but different and lower for CHX-A3 (p-value < 0.05).

B1

The drug release study was performed also for the coatings CHX-B1, CHX-B2 and CHX-B3 possessing the diacrylate B in the backbone of their polycations B1, B2 and B3. For the delivery system CHX-B1, after 70 days the estimated cumulative release was equal to 1116.37 $\mu\text{g}/\text{mL}$ at pH5 and 2187.41 $\mu\text{g}/\text{mL}$ at pH7.4 (figure 4.45).

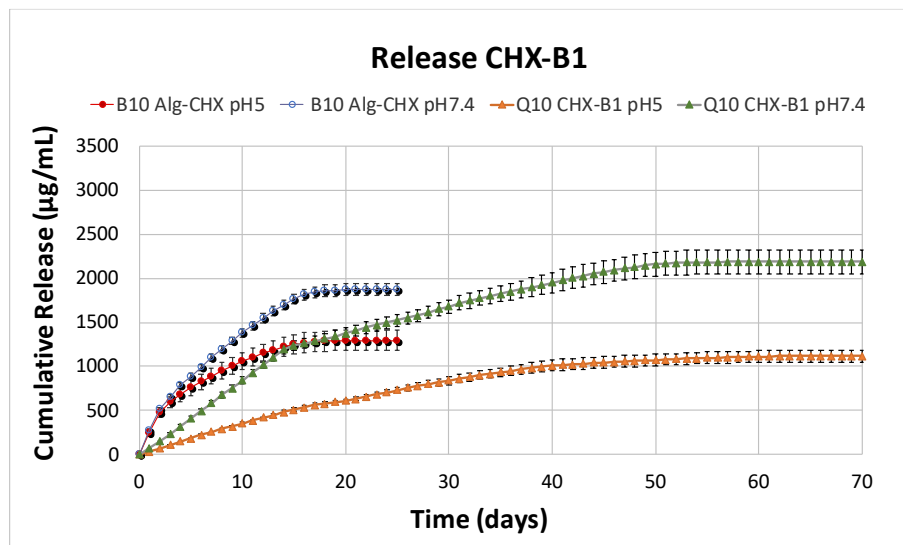


Figure 4.45: CHX release profile at pH5 and at pH7.4 for Q10 of the construct CHX-B1.

For each curve: Mean \pm SD (N=1, n=3).

Under acid conditions, the daily cargo release that was detected from the first day to day 14 was between 43.17-31.19 $\mu\text{g}/\text{mL}$, which considerably decreased showing an average of 27.14-13.05 starting from day 15 up to day 39. The final part of the curve correspondent to the plateau was comprehensive of the days 41-70 where the daily amount of antimicrobial agent released was definitely minimised with a range between 8.25-2.42 $\mu\text{g}/\text{mL}$. As contrary, the drug was higher released at pH7.4 with a daily rate equal to 91.29-74.92 $\mu\text{g}/\text{mL}$ detected for the first 2 weeks after the nanoparticles were treated with the phosphate buffer and incubated at 37°C. Additionally, on day 15 the measured amount was 42.41 $\mu\text{g}/\text{mL}$ whereas a reduction was observed from day 16 to day 46 which was between 36.99-20.18 $\mu\text{g}/\text{mL}$ per day. However, the daily release kept going down reporting values of 19.79-14.23 $\mu\text{g}/\text{mL}$ until

day 50 and reaching the plateau from day 51 to day 70 with a minimal rate of drug released ranging between 7.82-1.48 $\mu\text{g}/\text{mL}$.

B2

The figure 4.46 is representative of the profiles at both media provided by the nanoconstruct CHX-B2. In this case, the drug was released along 70 days with a final cumulative amount of 1648.61 $\mu\text{g}/\text{mL}$ at pH5 and 2592.64 $\mu\text{g}/\text{mL}$ at pH7.4. At pH5 the initial released detected on day 1 was equal to 76.51 $\mu\text{g}/\text{mL}$ followed by a range between 49.43-41.07 $\mu\text{g}/\text{mL}$ released from day 2 to day 14. The measured daily value slowly decreased with a range of 38.40-23.08 $\mu\text{g}/\text{mL}$ until day 40, which was half reduced from day 41 to day 49, 15.26-13.75 $\mu\text{g}/\text{mL}$ and finally dropping to 7.60-1.45 $\mu\text{g}/\text{mL}$ until day 58. On day 59 the daily drug release was minimal and correspondent to 1.43 $\mu\text{g}/\text{mL}$, determining the beginning of the plateau which lasted until day 70.

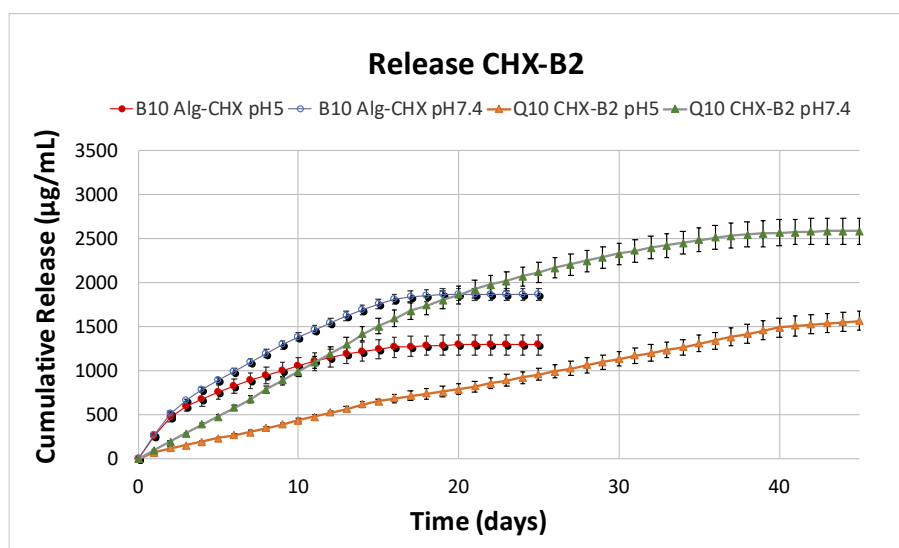


Figure 4.46: CHX release profile at pH5 and at pH7.4 for Q10 of the construct CHX-B2.

For each curve: Mean \pm SD (N=1, n=3).

At pH7.4 the daily drug release varied from 121.14 $\mu\text{g}/\text{mL}$ to 86.63 $\mu\text{g}/\text{mL}$ until day 17 and consistently dropped from day 18 with a range between 62.62-60.92 $\mu\text{g}/\text{mL}$ detected until day 21. On day 22 the rate of drug released was 54.10 $\mu\text{g}/\text{mL}$ but dropped to 49.57-27.12 $\mu\text{g}/\text{mL}$ from day 23 to day 35. Furthermore, the value correspondent to day 36 was 19.81 $\mu\text{g}/\text{mL}$ denoting a reduction of the daily release which continued until day 39, 11.96 $\mu\text{g}/\text{mL}$.

Finally, a further decrease was detected from day 40 to day 44, 6.85-2.10 $\mu\text{g}/\text{mL}$ reaching the plateau starting from day 45 to day 70 a small drug release amount ranging between 1.77 $\mu\text{g}/\text{mL}$ to 1.43 $\mu\text{g}/\text{mL}$.

Comparing the release profile of this nano-delivery system to the one of B10 for Alg-CHX, it was clear that in this case the release lasted longer: a period of 70 days against the 25 days of the bilayers coating. However, it was observed that, although at pH5 the amount of drug released was greater after 25 days for B10 than Q10 of CHX-A1, the latter construct on day 21 at pH7.4 overcame the cumulative release of Alg-CHX showing a value equal to 1925.08 $\mu\text{g}/\text{mL}$.

B3

The figure 4.47 reports the cumulative release profiles at both media for Q10 of CHX-B3. At pH5, the detected daily release on day 1 was 89.18 $\mu\text{g}/\text{mL}$; the amount was half reduced on day 2, 44.55 $\mu\text{g}/\text{mL}$, dropping to 38.18-22.15 $\mu\text{g}/\text{mL}$ from day 3 to day 37. Additionally, the rate of daily release was equal to 14.64 $\mu\text{g}/\text{mL}$ on day 38 and it plummeted to a range between 5.45 $\mu\text{g}/\text{mL}$ to 3.15 $\mu\text{g}/\text{mL}$ from day 39 to day 42. Starting from day 43 it was reached a plateau which lasted up to day 60 and showing a low daily release with an average of 2.77-2.39 $\mu\text{g}/\text{mL}$ and a final cumulative release of 1085.97 $\mu\text{g}/\text{mL}$.

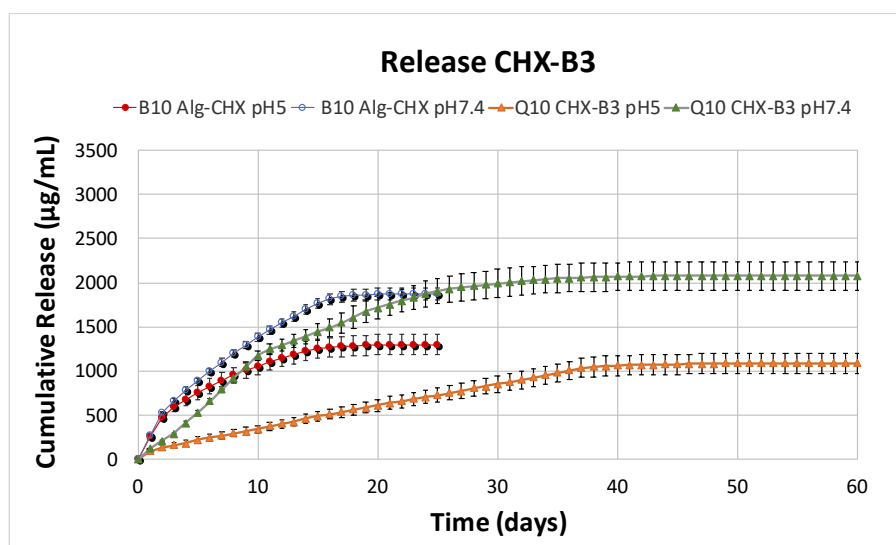


Figure 4.47: CHX release profile at pH5 and at pH7.4 for Q10 of the construct CHX-B3.

For each curve: Mean \pm SD (N=1, n=3).

On the other hand, the cumulative CHX release at pH7.4 was equal to 2077.99 $\mu\text{g}/\text{mL}$ over a period of 60 days. For the first 10 days the daily drug release was ranging between 129.09-82.71 $\mu\text{g}/\text{mL}$; on day 11 it was correspondent to 72.10 $\mu\text{g}/\text{mL}$, whereas it decreased from day 12 to day 23 showing a value ranging between 66.21-32.36 $\mu\text{g}/\text{mL}$. The rate was significantly reduced until day 35 with an amount of 9.57 $\mu\text{g}/\text{mL}$, ending to a plateau from day 41 to day 60 with a small daily release in the average between 3.74 $\mu\text{g}/\text{mL}$ and 2.39 $\mu\text{g}/\text{mL}$. Among the 3 nanoconstructs it was noticed that the antimicrobial agent was highly released when B2 was employed as polycation, followed by B1 and B3 (p-value < 0.05).

The analysis of the results provided by this nanoconstruct allowed to evidence differences between the two media and the cumulative release profile for B10 of Alg-CHX (p-value < 0.05). In particular, it was observed that at pH5 for CHX-B3 the cumulative cargo release was definitely lower than the one of B10 for Alg-CHX (p-value < 0.05), whereas the value detected at pH7.4 after 25 days nearly closed to final cumulative release measured for the same medium of B10 for the system composed by 10 bilayers (p-value > 0.05).

D1

The drug release evaluation was determined also for the nanoconstructs including, as positive polyelectrolytes, PBAEs synthesised with the diacrylate D. For CHX-D1, the chlorhexidine was released from the nanoparticles after LbL for a period of 70 days at both media and the final cumulative release was 1612.70 $\mu\text{g}/\text{mL}$ at pH5 and at pH7.4, 3086.59 $\mu\text{g}/\text{mL}$ (figure 4.48).

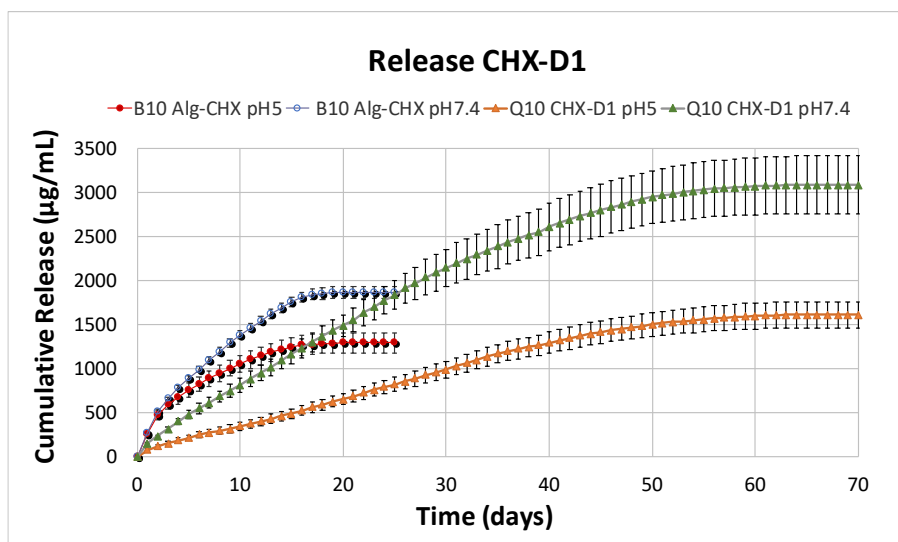


Figure 4.48: CHX release profile at pH5 and at pH7.4 for Q10 of the construct CHX-D1.

For each curve: Mean \pm SD (N=1, n=3).

Examining both profiles, it was evident that as previously described under acid conditions the drug was slowly released due to stronger electrostatic interactions among the polyelectrolytes composing the ten quadruple layers. Thus, starting from an initial daily release detected on day 1 and correspondent to 83.07 $\mu\text{g/mL}$, it was observed that the amount was half reduced on day 2, 41.07 $\mu\text{g/mL}$, whereas it was ranging between 39.8-20.8 $\mu\text{g/mL}$ from day 3 to day 45. Besides, there was a fall of the drug daily release starting from day 46 with a value equal to 17.10 $\mu\text{g/mL}$ which decreased up to 11.28 on day 54. Finally, from day 55 it was reached the plateau with a minimum concentration between 7.8 $\mu\text{g/mL}$ to 2.39 $\mu\text{g/mL}$ ending on day 70. As contrary, the drug release at pH7.4 was definitely higher than at pH5. In fact, the daily drug release was 157.33 $\mu\text{g/mL}$ on day 1, dropping to 83.82-54.41 $\mu\text{g/mL}$ from day 2 to day 31. Additionally, also in this case, a reduction of the amount of drug released was detected: starting from day 32 to day 51 the rate was between 47.73-21.05 $\mu\text{g/mL}$ and from day 52 to 56 the daily release was low, 17.9-10.97 $\mu\text{g/mL}$, ending to a plateau where the value was ranging between 8.48 $\mu\text{g/mL}$ to 2.39 $\mu\text{g/mL}$ especially from day 57 to day 70.

D2

The results regarding the delivery system CHX-D2 are illustrated in the figure 4.49. The antimicrobial agent was released over 90 days followed by a long plateau where the amount of daily release was very low. For instance, at pH5, the total cumulative release was slightly higher than the one previously analysed for CHX-D1, 1683.89 $\mu\text{g}/\text{mL}$. This indicated that, after an initial daily release of 63.93 $\mu\text{g}/\text{mL}$ on day 1 and a range between 43.92-36.73 $\mu\text{g}/\text{mL}$, the rate of drug released was mainly around 20 $\mu\text{g}/\text{mL}$ per day from day 7 to day 47. Thus, the chlorhexidine in this case was less released but for a longer period of time. Moreover, a weak reduction of the daily released was detected from day 48 to day 60 ranging between 15.37-10.02 $\mu\text{g}/\text{mL}$, followed by a long plateau started from day 61 and ending on day 110 with a value of 9.61-2.39 $\mu\text{g}/\text{mL}$.

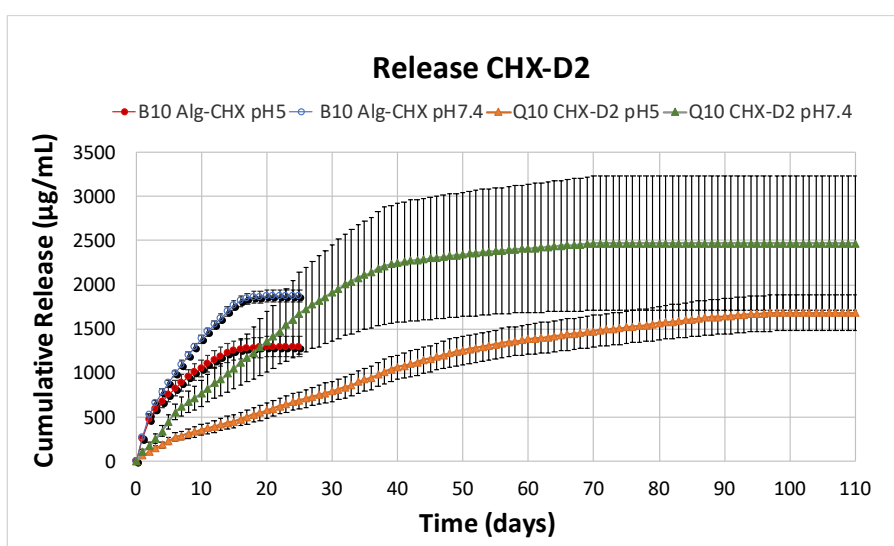


Figure 4.49: CHX release profile at pH5 and at pH7.4 for Q10 of the construct CHX-D2.

For each curve: Mean \pm SD (N=1, n=3).

However, at pH7.4 it was observed that the antimicrobial agent was released for a period of 70 days providing a final cumulative release correspondent to 2470.32 $\mu\text{g}/\text{mL}$. Although the detected value was lower than the amount of CHX-D1, it was clear that the release of the drug was controlled and prolonged with reduced rate per day. For example, initially for the first 6 days the daily amount released was 110.91-82.36 $\mu\text{g}/\text{mL}$ which decreased to 67.43-59.76 $\mu\text{g}/\text{mL}$ from day 7 to day 25. The daily release was then reduced from day 26 to day 37 showing a range between 52.33-30.81 $\mu\text{g}/\text{mL}$, with a drastic drop detected until day 69 where

in the average the value ended to 5.46 $\mu\text{g}/\text{mL}$. Finally, for this system the plateau was detected for longer time: starting from day 70 it lasted until day 110 with a minimum of release of 2.39 $\mu\text{g}/\text{mL}$.

D3

The drug release was determined also for the nanoconstruct having D3 as polycation. At pH5, the daily release was equal to 119.72 $\mu\text{g}/\text{mL}$ on day 1 with a decline of the value within the first week, 87.09-71.13 $\mu\text{g}/\text{mL}$. Additionally, a further decrease was detected from day 8 to day 19, with a range between 42.43 $\mu\text{g}/\text{mL}$ to 29.79 $\mu\text{g}/\text{mL}$; this amount was half reduced up to day 34, 15.40 $\mu\text{g}/\text{mL}$, ending to the plateau where, starting from day 39 to day 50, a small rate between 8.89-3.20 $\mu\text{g}/\text{mL}$ was measured per day (figure 4.50).

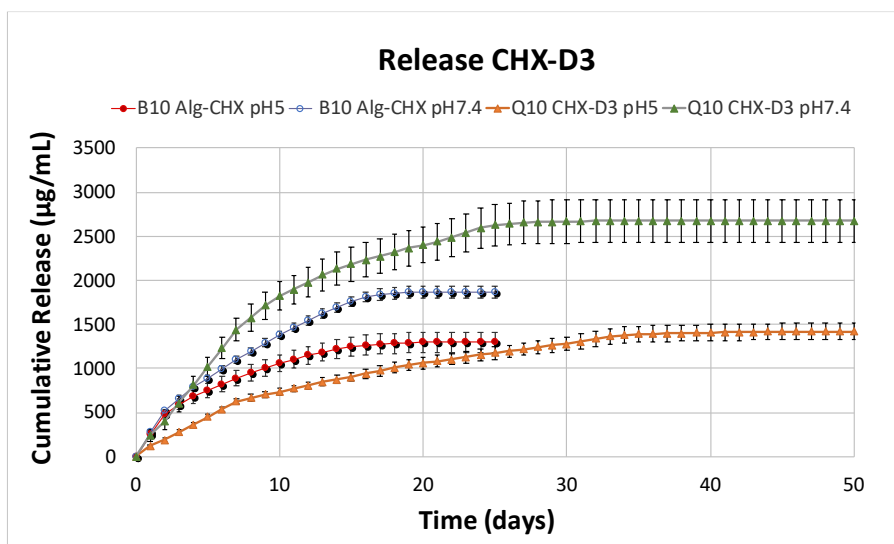


Figure 4.50: CHX release profile at pH5 and at pH7.4 for Q10 of the construct CHX-D3.

For each curve: Mean \pm SD (N=1, n=3).

Under acid conditions, the drug release occurred within 50 days and the cumulative release was correspondent to 1419.86 $\mu\text{g}/\text{mL}$, whereas at physiological environment it was equal to 2676.21 $\mu\text{g}/\text{mL}$. Indeed, at pH7.4, an initial burst release was observed for the first week ranging between 245.03-152.15 $\mu\text{g}/\text{mL}$, followed by a gradual decrease from day 8, 140.37 $\mu\text{g}/\text{mL}$ to day 10, 109.03 $\mu\text{g}/\text{mL}$. As contrary, a drop was detected from day 11, 83.73 $\mu\text{g}/\text{mL}$, a value that was more than half reduced until day 24, 35.02 $\mu\text{g}/\text{mL}$, reaching the plateau from day 27, with a low daily release, 6.84-2.39 $\mu\text{g}/\text{mL}$, until day 50.

Comparing the profiles provided by the drug delivery systems of the group D to the pathway of the bilayer coating Alg-CHX, it was noticed a higher and prolonged release for the cargo-PBAEs nanoparticles. On the other hand, the amount of daily release for CHX-D1, CHX-D2, and CHX-D3 was lower than the rate reached by B10 of Alg-CHX on day 25 which corresponded to its final cumulative release (p -value < 0.05). Finally, among the 3 PBAEs systems, it was observed that the highest rate of cumulative release was provided by CHX-D1, followed by CHX-D3 and CHX-D2 (p -value < 0.05).

E1

The determination of the drug release was performed also for the coatings composed by the CHX and polycations of the group E. Overall, for CHX-E1, the antimicrobial agent was released from the surface of the nanocarrier over a period of 70 days showing a final cumulative release of 1190.26 $\mu\text{g}/\text{mL}$ at pH5 and 1775.34 $\mu\text{g}/\text{mL}$ at pH7.4 (figure 4.51).

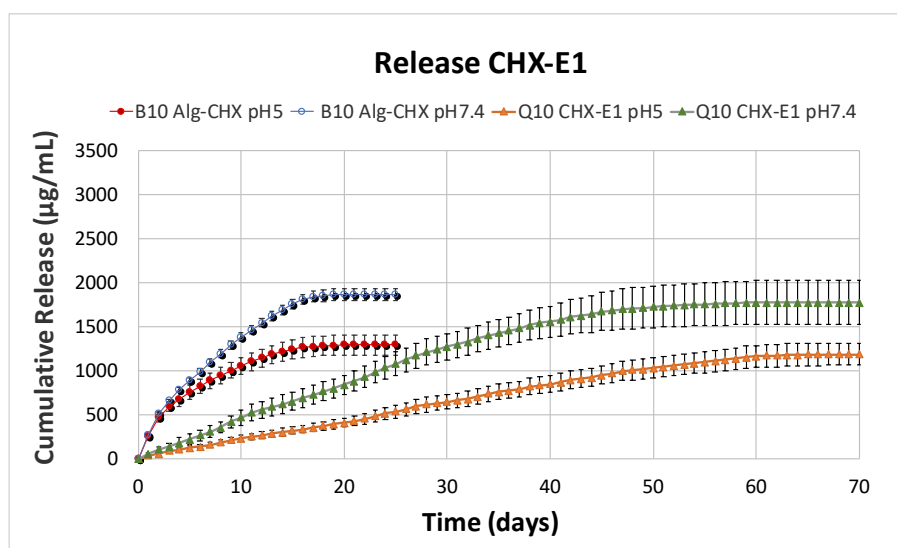


Figure 4.51: CHX release profile at pH5 and at pH7.4 for Q10 of the construct CHX-E1.

For each curve: Mean \pm SD (N=1, n=3).

Under acid conditions, the detected daily release was initially correspondent to 36.79 $\mu\text{g}/\text{mL}$ slowly decreasing from day 2, 32.7 $\mu\text{g}/\text{mL}$, to day 47, 25.08 $\mu\text{g}/\text{mL}$. Starting from day 48, a consistent drop was observed with a value ranging between 15.82-10.8 $\mu\text{g}/\text{mL}$ until day 60. For the last 10 days the amount of drug released was minimum and the curve representative of pH5 reached a plateau showing a range of 6.94-2.39 $\mu\text{g}/\text{mL}$. As contrary, at physiological

environment, the daily drug release for the first few days was significantly higher than at pH5, showing a rate of 59.86 $\mu\text{g}/\text{mL}$ per day (p -value < 0.05). However, from day 2 to day 38, there a further reduction of the value which was between 55.8 $\mu\text{g}/\text{mL}$ and 30.49 $\mu\text{g}/\text{mL}$. The release kept decreasing up to 14.9 $\mu\text{g}/\text{mL}$ on day 47 presenting a long plateau from day 48 to day 70 with a daily release ranging between 8.95-2.39 $\mu\text{g}/\text{mL}$.

E2

For CHX-E2, the drug release was detected for 70 days as well as CHX-E1 with a higher final amount correspondent to 1350.70 $\mu\text{g}/\text{mL}$ at pH5 and 1999.87 $\mu\text{g}/\text{mL}$ at pH7.4 (figure 4.52).

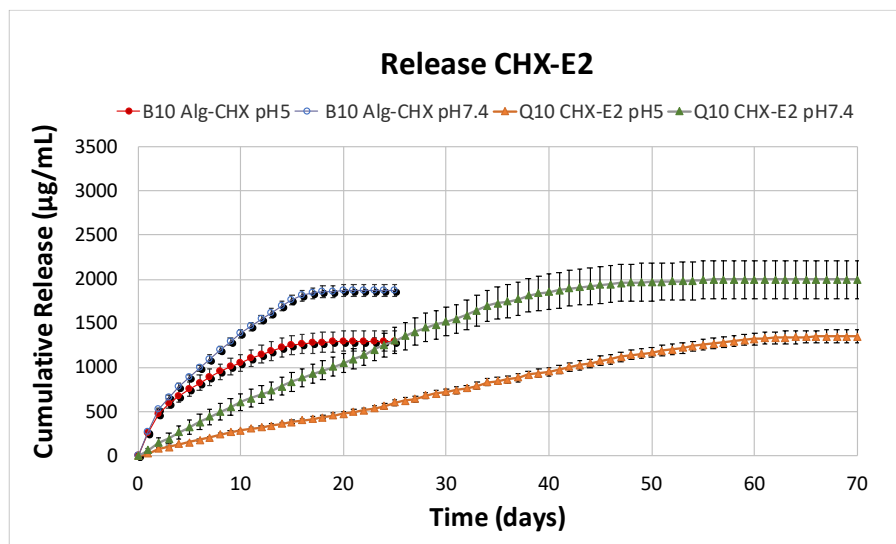


Figure 4.52: CHX release profile at pH5 and at pH7.4 for Q10 of the construct CHX-E2.

For each curve: Mean \pm SD (N=1, n=3).

At pH5, on day 1, the daily drug release was equal to 55.22 $\mu\text{g}/\text{mL}$, which was half reduced on day 2, 33.0 $\mu\text{g}/\text{mL}$ with a further slight decrease until day 8, 27.47 $\mu\text{g}/\text{mL}$. From day 9 to day 28, the amount released was between 24.6-16.53 $\mu\text{g}/\text{mL}$ dropping to 11.50 $\mu\text{g}/\text{mL}$ on day 60. For the following 10 days similarly to what observed at pH5, a tiny drug release was detected, ranging between 6.2-2.39 $\mu\text{g}/\text{mL}$ up to day 70. On the other hand, the daily drug release was 86.30 $\mu\text{g}/\text{mL}$ on day 1 at pH7.4, showing a significant decrease from day 2, 70.22 $\mu\text{g}/\text{mL}$, to day 28, 44.02 $\mu\text{g}/\text{mL}$ (p -value < 0.05). Starting from day 29 there was a decline of the rate registered per day between 41.35-21.26 $\mu\text{g}/\text{mL}$ up to the day 41. Finally, also in this case it was noticed a long plateau as described before for CHX-E1; in particular, for CHX-E2

from day 42 up to day 70 the amount of drug released per day was quite small, ranging between 12.29-2.39 $\mu\text{g}/\text{mL}$ ($p\text{-value} > 0.05$).

E3

The nano delivery system CHX-E3 was the last one having a PBAE synthesised with the diacrylate E and the cumulative release after 50 days was 1417.90 $\mu\text{g}/\text{mL}$ at pH5 and 2417.17 $\mu\text{g}/\text{mL}$ at pH7.4 (figure 4.53). Differently to CHX-E1 and CHX-E2, the employment of E3 allowed a faster drug release lasting less days if compared to the previous two nanoconstructs ($p\text{-value} < 0.05$). In fact, the initial rate released on day 1 was correspondent to 205.73 $\mu\text{g}/\text{mL}$ at pH5, whereas for CHX-E1 and CHX-E2 it was usually around 55-60 $\mu\text{g}/\text{mL}$ ($p\text{-value} < 0.05$). Moreover, for this system there was a considerable fall in the amount of daily release in the first 7 days ended to 86.79 $\mu\text{g}/\text{mL}$, which was half reduced from day 8, 40.94 $\mu\text{g}/\text{mL}$ to day 22, 20.97 $\mu\text{g}/\text{mL}$ ($p\text{-value} < 0.05$). From day 23 to day 33 the release was lower than the beginning showing a range of 20.86-16.27 $\mu\text{g}/\text{mL}$ and reaching the plateau that ended on day 50 with a tiny release of 2.39 $\mu\text{g}/\text{mL}$ ($p\text{-value} > 0.05$). As expected, also the drug was higher released at pH7.4 showing a long plateau of over 20 days similarly to what observed for CHX-E1 and CHX-E2 ($p\text{-value} > 0.05$). In this case, the daily release on day 1 was slightly bigger than at pH5, 266.23 $\mu\text{g}/\text{mL}$, followed by a drastic drop of the amount from day 2, 180.94 $\mu\text{g}/\text{mL}$, to day 8, 109.65 $\mu\text{g}/\text{mL}$ ($p\text{-value} < 0.05$). Additionally, the release slightly decreased from day 7, 93.49 $\mu\text{g}/\text{mL}$, to day 13, 81.08 $\mu\text{g}/\text{mL}$ dropping to 40.39 $\mu\text{g}/\text{mL}$ on day 27. Finally, the last part of curve shows a long plateau typically detected at pH7.4, with a daily drug release, from day 29 to day 50, ranging between 22.45-2.39 $\mu\text{g}/\text{mL}$.

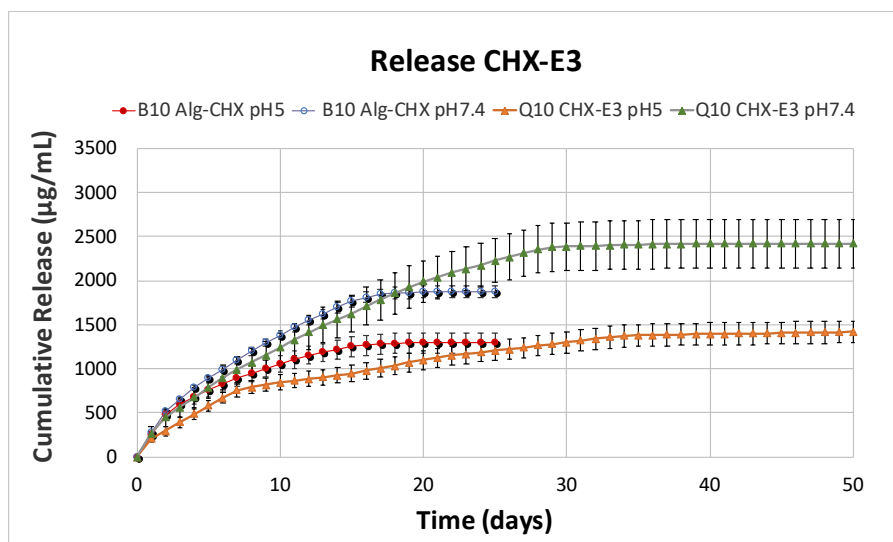


Figure 4.53: CHX release profile at pH5 and at pH7.4 for Q10 of the construct CHX-E3.

For each curve: Mean \pm SD (N=1, n=3).

Overall, CHX-E3 provided for both media the highest and shortest drug release, followed by respectively CHX-E2 and CHX-E1. Comparing these profiles to B10 of Alg-CHX, similarities were observed between CHX-E1 and CHX-E2 and the bilayers nanoconstruct: the antimicrobial agent was released showing in the average the same amount but controlled and prolonged when the PBAEs were embedded on the systems (p-value > 0.05). Differently, at pH5 the release of CHX-E3 was slightly higher than B10 of Alg-CHX, whereas there was already a consistently increase after 25 days at pH7.4 (p-value < 0.05).

F1

The drug release determination was carried out also for the nanoconstructs CHX-F1, CHX-F2 and CHX-F3. For the coating where F1 was chosen as polycation the antimicrobial agent was released over a period of 70 days. For instance, the final cumulative release was 1657.91 $\mu\text{g/mL}$ at pH5 and 2764.73 $\mu\text{g/mL}$ at pH7.4 (figure 4.54). At pH5, it was observed a constant increase of the daily release in the first 10 days: more specifically, starting from day 1, 27.84 $\mu\text{g/mL}$, it rose up to 72.80 $\mu\text{g/mL}$ on day 10. The amount was almost half reduced on day 11, 47.09 $\mu\text{g/mL}$ and it kept decreasing until day 38 showing a rate of 21.15 $\mu\text{g/mL}$. Moreover, the daily release continued slightly going down for the next 20 days ranging between 20.14-10.78 $\mu\text{g/mL}$, followed by a plateau from day 61 to day 70 with a value of 9.09-2.38 $\mu\text{g/mL}$.

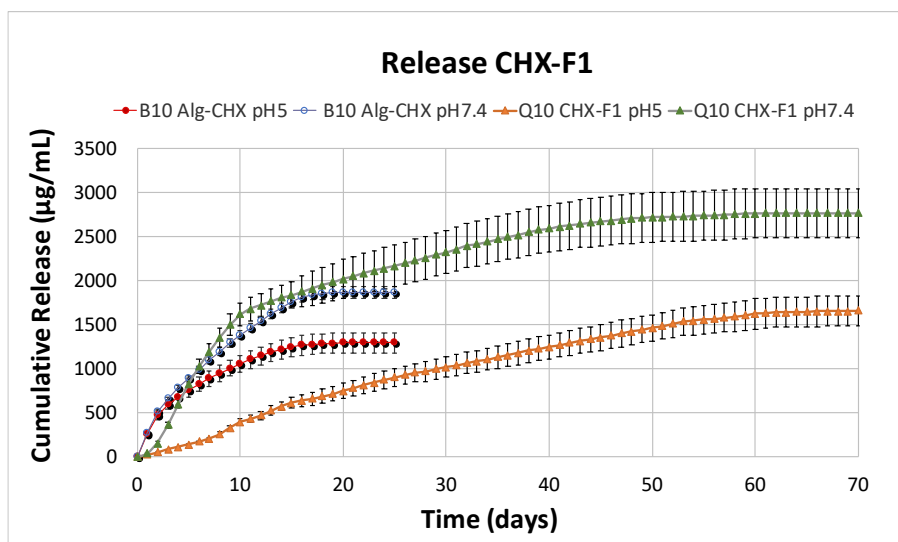


Figure 4.54: CHX release profile at pH5 and at pH7.4 for Q10 of the construct CHX-F1.

For each curve: Mean \pm SD (N=1, n=3).

However, a similar profile was observed at pH7.4: the drug was slowly released for the first 10 days, showing an initial daily release on day 1 equal to 39.88 $\mu\text{g}/\text{mL}$ and ending to 223.74 $\mu\text{g}/\text{mL}$ on day 10. From day 11 the rate of drug release changed dropping to 48.82 $\mu\text{g}/\text{mL}$ and it kept decreasing showing a value of 24.22 $\mu\text{g}/\text{mL}$ on day 38. The amount was then ranging between 18.82-10.32 $\mu\text{g}/\text{mL}$ until day 49 and finally, also in this case, a long plateau was detected from day 50 to day 70 with a minimum daily release correspondent to 5.10-2.39 $\mu\text{g}/\text{mL}$.

F2

For the nanocoating system CHX-F2 the drug release evaluation towards HPLC provided two different profiles for each medium over a period of 70 days, with the total cumulative release correspondent to 1318.69 $\mu\text{g}/\text{mL}$ at pH5 and 3178.49 $\mu\text{g}/\text{mL}$ at pH7.4 (figure 4.55). Under acid conditions, the daily release along the first week was ranging between 55.22-34.05 $\mu\text{g}/\text{mL}$, followed by a decrease from day 8, 33.85 $\mu\text{g}/\text{mL}$, to day 35, 20.92 $\mu\text{g}/\text{mL}$. Then, the amount kept going down showing a value between 20.08-18.79 $\mu\text{g}/\text{mL}$ up to day 52 and from day 53 to day 70 the rate of daily was minimum, 11.32-2.39 $\mu\text{g}/\text{mL}$, as represented by the long plateau belonging to the final part of the profile at pH5. As contrary, if the drug at pH5 was gradually released from the surface of silica amino-functionalised nanoparticles, a burst release for the first week was observed at pH7.4 (p-value < 0.05). For instance, the initial daily

release detected for day 1 and 2 and correspondent to respectively 61.21 $\mu\text{g}/\text{mL}$ and 86.30 $\mu\text{g}/\text{mL}$, was followed by a considerable rise of the daily rate from day 3 to day 7 which was between 421.36-276.21 $\mu\text{g}/\text{mL}$ (p -value < 0.05). Then, the amount plummeted to 64.48 $\mu\text{g}/\text{mL}$ on day 8 and it continued decreasing until day 28, 42.07 $\mu\text{g}/\text{mL}$. Furthermore, the daily drug release was almost half reduced on day 29, 26.01 $\mu\text{g}/\text{mL}$, dropping to 10.32 $\mu\text{g}/\text{mL}$ on day 47. As already noticed for the previous nanoconstructs, a typical long plateau was detected from day 48 to day 70, with a tiny amount of drug released ranging between 8.77-2.39 $\mu\text{g}/\text{mL}$.

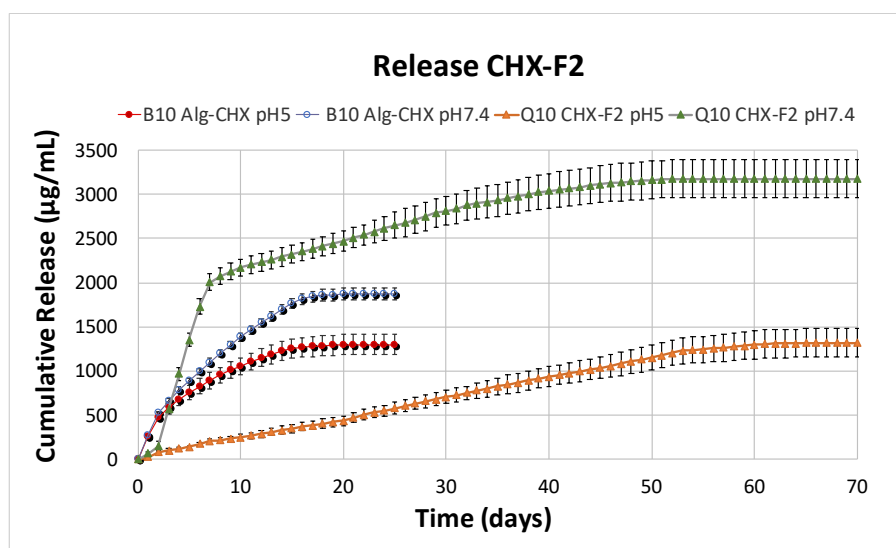


Figure 4.55: CHX release profile at pH5 and at pH7.4 for Q10 of the construct CHX-F2.

For each curve: Mean \pm SD (N=1, n=3).

F3

The nano-delivery system CHX-F3 included the last polymer of the group F which was coated, as F2 and F1, as polycation with the chlorhexidine on the nanocarrier surface with the aim of improving the drug release. Therefore, in this case, the antimicrobial agent was released for the longest period, 90 days, considering all the coatings previously analysed, with the final cumulative release equal to 2131.43 $\mu\text{g}/\text{mL}$ at pH5 and 3131.46 $\mu\text{g}/\text{mL}$ at pH7.4 (figure 4.56).

The detected drug release for day 1 at pH5 was 67.70 $\mu\text{g}/\text{mL}$ followed by a range between 47.50-30.26 $\mu\text{g}/\text{mL}$ per day from day 2 to day 48. The rate of daily drug release dropped to 28.78 $\mu\text{g}/\text{mL}$ on day 49 and it slowly continued decreasing up to day 70, 20.32 $\mu\text{g}/\text{mL}$; the

amount decreased ranging between 19.24-10.66 up to day 79 followed by a plateau lasting 11 days with a small drug release equal to 6.52-2.39 $\mu\text{g}/\text{mL}$. On the other hand, at physiological environment the drug mainly released along the first week showing a range between 170.95-90.98 $\mu\text{g}/\text{mL}$ per day. The amount was then significantly reduced starting from day 8, 55.41 $\mu\text{g}/\text{mL}$, reaching 20.63 on day 58 (p -value < 0.05); then the rate slightly changed from day 59 to day 70, showing a value of 17.34-15.48 $\mu\text{g}/\text{mL}$, followed by a long plateau for further 20 days ending on day 90 and with a low daily release correspondent to 9.02-2.39 $\mu\text{g}/\text{mL}$.

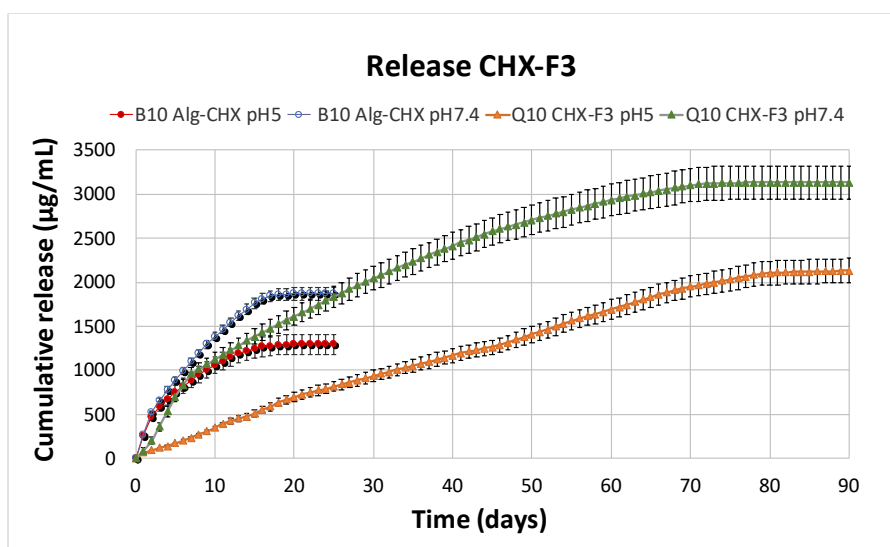


Figure 4.56: CHX release profile at pH5 and at pH7.4 for Q10 of the construct CHX-F3.

For each curve: Mean \pm SD (N=1, n=3).

Considering the 3 coatings, at pH7.4 the highest amount of drug release was reached by CHX-F2 followed by CHX-F3 and CHX-F1 (p -value < 0.05), whereas at pH5 firstly by CHX-F3 then by CHX-F1 and CHX-F2 (p -value < 0.05). However, although there was a difference among the systems regarding the burst release detected at pH7.4 for both CHX-F1 and CHX-F2, the drug release was improved and prolonged when PBAs were entrapped onto the coatings. Thus, comparing the release profiles of B10 for Alg-CHX to those of the chlorhexidine and the polymers of the group F, it was observed that the antimicrobial agent was released for a longer time but after 25 days the amount at both media was lower than what detected for B10 of Alg-CHX (p -value < 0.05).

G1

For the system CHX-G1, it was noticed that the drug was released for 60 days with the total cumulative release equal to 504.24 $\mu\text{g}/\text{mL}$ at pH5 and 636.85 $\mu\text{g}/\text{mL}$ at pH7.4 (figure 4.57). Differently from what described before, in this case, it was observed that the chlorhexidine was less released possibly due to the structure of G1 that showed hydrophobic groups in its backbone. Therefore, the slow hydrolysis of the polymer when dissolved in both media caused a gradual and tiny daily drug release. For instance, under acid conditions, for the first 7 days the drug release per day was between 4.17-5.68 $\mu\text{g}/\text{mL}$, followed by a gradual increase occurring firstly, from day 8, 8.17 $\mu\text{g}/\text{mL}$, to day 11, 10.20 $\mu\text{g}/\text{mL}$ and then from day 12 to day 42 with a range of 11.06-18.47 $\mu\text{g}/\text{mL}$ released per day. Finally, for the next 18 days the rate was minimum composing a long plateau with a range of 8.57-2.39 $\mu\text{g}/\text{mL}$ ending on day 60. As contrary, the drug was moderately released for the first 2 days at pH7.4, showing values such as, 10.12 $\mu\text{g}/\text{mL}$ on day 1 and 14.85 $\mu\text{g}/\text{mL}$ on day 2 with a considerable growth in the daily release starting from day 3, 24.68 $\mu\text{g}/\text{mL}$ up to day 12, 33.09 $\mu\text{g}/\text{mL}$. In addition, there was a slight decline in the daily drug release from day 13, 23.01 $\mu\text{g}/\text{mL}$, to day 24, 12.40 $\mu\text{g}/\text{mL}$, followed by a reduction up to 10.21 on day 39 and a long plateau with a range between 6.78-2.39 $\mu\text{g}/\text{mL}$ up to day 60.

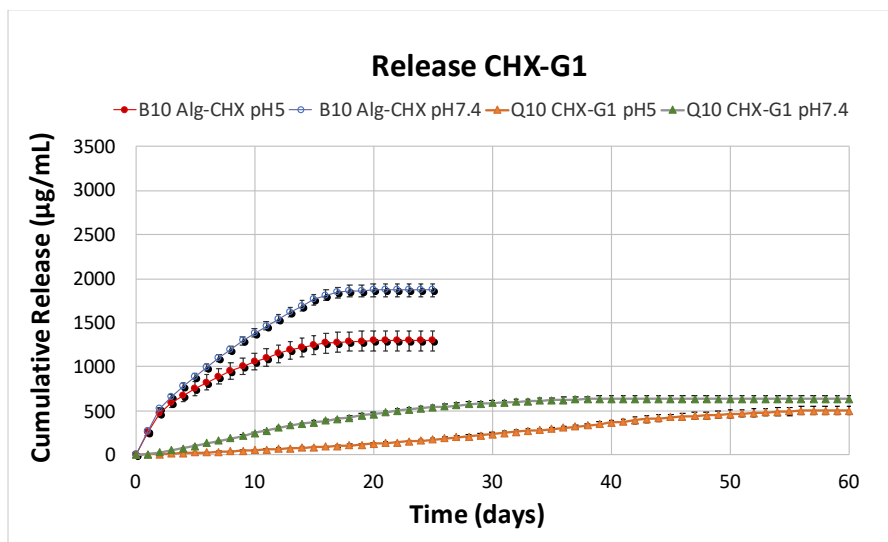


Figure 4.57: CHX release profile at pH5 and at pH7.4 for Q10 of the construct CHX-G1. For each curve: Mean \pm SD (N=1, n=3).

G2

For CHX-G2 the cumulative release after a total of 60 days was equal to 435.62 $\mu\text{g}/\text{mL}$ at pH5 and 564.18 $\mu\text{g}/\text{mL}$ at pH7.4 (figure 4.58).

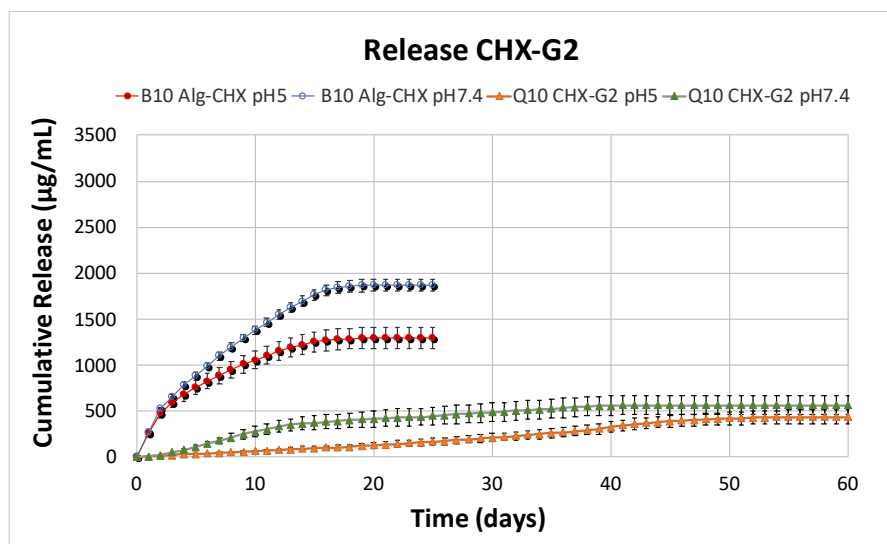


Figure 4.58: CHX release profile at pH5 and at pH7.4 for Q10 of the construct CHX-G2.

For each curve: Mean \pm SD (N=1, n=3).

Under acid conditions, the daily drug release increased firstly, from day 1 to day 12, showing a range between 7.71-10.62 $\mu\text{g}/\text{mL}$, then, from 13 to 41 with a value of 10.63-17.88 $\mu\text{g}/\text{mL}$. The amount plummeted to 9.06 $\mu\text{g}/\text{mL}$ on day 42, and it slowly decreased up to 5.19 $\mu\text{g}/\text{mL}$ on day 54. Finally, the last part of the curve was characterised by a plateau which was detected from day 55 to day 60 showing a tiny rate of daily release equal to 4.72-2.39 $\mu\text{g}/\text{mL}$. At physiological conditions, the drug was gradually released showing a rate of 7.90 $\mu\text{g}/\text{mL}$ on day 1 and 12.64 $\mu\text{g}/\text{mL}$ on day 2, with a moderate increase from day 3 to day 12, with a range of 23.86-33.97 $\mu\text{g}/\text{mL}$. Firstly, starting from day 13 the amount plummeted to 19.33 $\mu\text{g}/\text{mL}$ reaching 10.28 $\mu\text{g}/\text{mL}$ on day 16; then, the reduction kept slowly occurring from day 17 to day 37 with a value between 9.28 $\mu\text{g}/\text{mL}$ and 7.12 $\mu\text{g}/\text{mL}$. As previously noticed for the other nanocoating systems, also for CHX-G2 a long plateau was detected, and, in this case, it lasted from day 38 to day 60 with a minimum daily drug release equal to 6.76-2.39 $\mu\text{g}/\text{mL}$.

G3

The drug release determination was carried out also for the nano- delivery system CHX-G3. The antimicrobial agent in this case was released over 50 days showing overall a cumulative release equal to 815.30 $\mu\text{g/mL}$ at pH5 and 1555.11 $\mu\text{g/mL}$ at pH7.4 (figure 4.59).

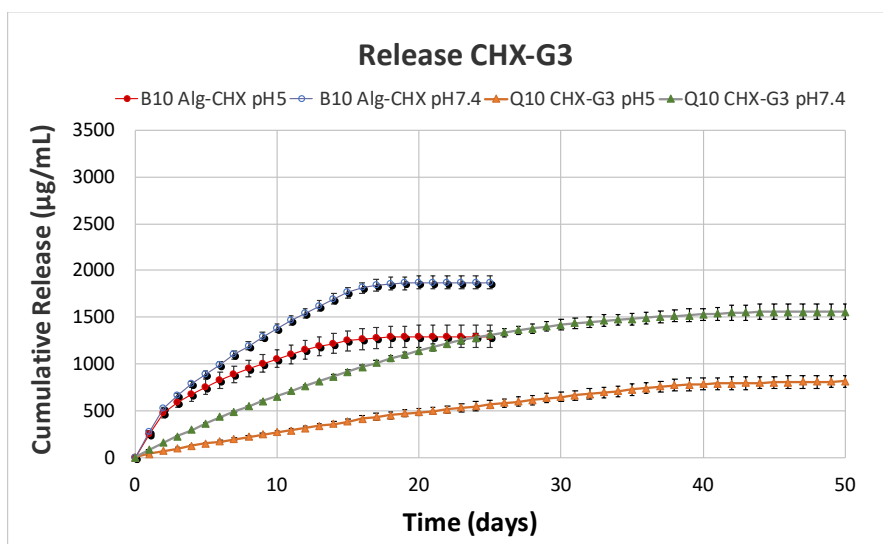


Figure 4.59: CHX release profile at pH5 and at pH7.4 for Q10 of the construct CHX-G3.

For each curve: Mean \pm SD (N=1, n=3).

At pH5, the detected drug release for the first 2 days was correspondent to respectively, 39.37 $\mu\text{g/mL}$ and 32.25 $\mu\text{g/mL}$, followed by a reduction occurring from day 3, 27.63 $\mu\text{g/mL}$, to day 15, 22.81 $\mu\text{g/mL}$. Additionally, the daily drug release kept decreasing showing a range between 19.64-13.92 $\mu\text{g/mL}$ up to day 38, with a long plateau from day 39 today 60, where the amount of release was 8.90-2.39 $\mu\text{g/mL}$ per day. On the other hand, the chlorhexidine was mainly released in the first 19 days: in particular the higher rate of daily release was measured for the first 3 days ranging between 82.03-71.47 $\mu\text{g/mL}$, whereas it gradually went down to 69.01 $\mu\text{g/mL}$ on day 4 and up to 42.96 $\mu\text{g/mL}$ until day 19. Moreover, for the next 15 days there was a further reduction with the daily amount of 10.07 $\mu\text{g/mL}$ on day 34, followed by a long plateau, typically observed at pH7.4, which was lasting up to day 50 and ranging between 8.90-2.39 $\mu\text{g/mL}$.

Overall, it was observed that the antimicrobial agent was less released from the nanoconstructs CHX-G1, CHX-G2, probably due to the hydrophobic groups characterising the

backbones of both polymers G1 and G2 (p-value > 0.05). As contrary, the profiles of CHX-G3 showed a higher rate of drug release caused by a faster hydrolysis of G3 (p-value < 0.05) previously confirmed by the quick variation of its charge and molecular weight (MW). On the other hand, comparing the profiles provided by CHX-G1, CHX-G2 and CHX-G3 to those of B10 for Alg-CHX, it was observed that the drug was entrapped into the systems with the PBAEs of the group G without being completely released as previously noticed for the other nano-coatings. Therefore, as results, the chlorhexidine was too low released when PBAEs were embedded onto the systems whereas the release was higher and faster if the drug was coated only with sodium alginate onto the silica amino-functionalised nanoparticles surface.

Comparing the release of the antimicrobial agent from the CHX-PBAEs nano-delivery systems to the results obtained from TGA and zeta potential profiles, it was observed consistency for the matrices including the PBAEs B2, D3, F1, F2 and F3. For instance, the cargo was highly release from the nanoconstructs possessing the PBAEs of the group F, proving a drug release lasting between 70-90 days and ranging between 1300-2100 $\mu\text{g}/\text{mL}$ at pH5 (p-value < 0.05). Moreover, the drug was released from CHX-B2 system for a period of 70 days and equal to 1648.61 $\mu\text{g}/\text{mL}$, whereas for 50 days with a cumulative release of 1419.86 $\mu\text{g}/\text{mL}$ at pH5 from CHX-D3 (p-value < 0.05). The release profiles of these matrices were supported by the TGA, zeta potential and the PBAE hydrolysis.

Discussion

Silica amino-functionalization

Amorphous SiO₂ nanoparticles possess low toxicity and their surface could be modified to adjust properties such as zeta potential or surface reactivity. Surface functionalization is a technique which allows the improvement of properties of surface nanoparticles by adding alkoxysilanes or amino groups (Kneuer *et al.*, 2000), (Rao *et al.*, 2005). This adjustment could make the SiO₂ vectors suitable for targeting applications in biochemistry, catalysis and drug delivery (Nacken *et al.*, 2003), (Yang *et al.*, 2013), (Greasley *et al.*, 2016). The Stöber method is commonly used to form monodispersed silica spheres with the aim of amino-functionalizing the nanocarriers (Zhang *et al.*, 2013), (Han *et al.*, 2017). This method is based on hydrolysis by tetraethyl orthosilicate (TEOS) in a water-in-oil emulsion plus the addition of amino groups to the silica surfaces by using APTES (3 amino-propyl) triethoxysilane (Stober, 1968), (Masalov *et al.*, 2011), (Wen Li *et al.*, 2020). The water-stable carriers formed with this approach are spherical colloids showing a narrow size distribution and a final size ranging between 10nm to 200 nm (Choi and Chen, 2003), (Wang *et al.*, 2010). Under acidic conditions, SiO₂ nanoparticles provided a negative charged which was turned into positive by the amino-functionalisation with a potential of +20mV (Nacken *et al.*, 2003), (Delcea, Möhwald and Skirtach, 2011). For instance, in this project, the amino-functionalised SiO₂ nanoparticles were synthesised to exploit their ability to electrostatically bind anionic and cationic polyelectrolytes such as the polymer alginate and PBAEs employed to enhance the encapsulation and the release properties of the antimicrobial agent chlorhexidine.

Size measurements

The hydrodynamic size was evaluated by NanoSizer light scattering and as reported in the figure 4.2 the average value corresponds to 54 ± 7.21 nm. This measurement is representative of the silica nanoparticles amino-functionalized and the size is consistent if it is compared with the current preparations of silica nanoparticles amino-functionalized available in the literature. For example, Kardys *et al.*, observed that the Stöber process can provide nanoparticles having a size between 35-335 nm. The adjustment of some parameters of this method, such as the amount of ammonium hydroxide, used as catalyst for hydrolysis, the ethanol, added as reaction medium, and the emulsion timing, can influence the size of the particles (Kardys, Bharali and Mousa, 2013).

Zeta potential

Zeta potential is a simple and easy technique applied for the characterisation of the surface of charged colloids (Honary and Zahir, 2013) and it reflects both the distribution stability state of the nanomaterial and the adsorption of polyelectrolytes and drug on its surface (Sun *et al.*, 2016). Moreover, it allows the analysis of the binding type between the drug and nanoparticles, that is an important characteristic for the rate desorption of the drug in the nanoparticles and for the drug loading efficiency (Honary and Zahir, 2013), (Honary *et al.*, 2009). Therefore, for this project, zeta potential was measured as result of electrostatic interactions among alginate, drug and PBAEs on the surface of the nanocarrier. For all the developed nanocoatings, the charge was determined once a new layer was embedded onto the colloid surface via layer by layer self-assembly adopting sodium acetate buffer pH5 as dispersion medium. The resulting charge of the particles measured by zeta potential is dependent on the balance between protonated and unprotonated groups embedded on the surface, that is influenced by factors as for example the pH of the solution. For instance, the amino groups are protonated at low pH values providing the formation of species -NH_3^+ , becoming neutral when the pH increases. As contrary, this was opposite for carboxylic groups of the alginate, where deprotonation or the protonation of the hydroxyl groups occurs respectively at alkaline and acid environment (W. Feng *et al.*, 2014).

The coating systems described in this thesis, showed that the silica nanoparticles after amino-functionalization had a value equal to $+26.96 \pm 0.92$ mV, due to protonation of amino groups at pH5, that replaced the negative charge typical of the -SiO_4^{4-} groups. After the addition to the system of sodium alginate, as described in the LbL protocol, the potential was inverted again, -19.46 ± 1.55 mV, as result of the electrostatic interaction between the carboxylic group of the polyelectrolyte and the amino groups present on the surface. The deposition of chlorhexidine decreased the availability of carboxyl groups on the surface, reducing afterwards, the number of negative charged groups. Hence, the positivity of the potential increased, $+27.0 \pm 1.0$ mV, due to the presence of different amino groups present in the backbone of the antimicrobial agent, as observed by Fullriede *et al.*, 2016, (Lu *et al.*, 2017).

However, the charge changed becoming again negative, -29.4 ± 0.6 mV, after the sodium alginate was layered on the surface of the nanoparticles, due to the electrostatic binding

between the amino groups and the carboxylic group of the polyelectrolyte. After that, in all the matrices prepared in this project a different PBAE was loaded as 4th layer inverting the charge into positive. The difference in the PBAE positivity, reported in the table below, was mainly dependent on the amino groups of the backbone of the molecular structure of the polymers and on the acid environment in which the LbL self-assembly was carried out.

LbL-assembly coatings	PBAE positive charge on Q1
CHX-A1	+8.8 ± 1.4 mV
CHX-A2	+10.2 ± 0.36 mV
CHX-A3	+23.33 ± 3.2 mV
CHX-B1	+31.6 ± 1.66 mV
CHX-B2	+29.77 ± 0.55 mV
CHX-B3	+12.8 ± 0.95 mV
CHX-D1	+13.5 ± 3.31 mV
CHX-D2	+4.82 ± 0.81 mV
CHX-D3	+11.33 ± 0.95 mV
CHX-E1	+9.78 ± 1.28 mV
CHX-E2	+11.7 ± 0.5 mV
CHX-E3	+12.8 ± 0.61 mV
CHX-F1	+19.27 ± 0.72 mV
CHX-F2	+19.13 ± 1.42 mV
CHX-F3	+25.97 ± 0.76 mV
CHX-G1	+25.13 ± 1.65 mV
CHX-G2	+16.05 ± 2.02 mV
CHX-G3	+23.4 ± 2.88 mV

Table 4.3: Positivity of PBAEs for Q1 of CHX-PBAEs coatings

These values are only representative of the first quadruple layer, but the measurements were performed for all the ten quadruple layers. For instance, as it is shown in the figures 4.4-4.21 in the results section, the produced zig-zag pathway was typical of the multilayers build up

systems as previously studied by (Burke and Barrett, 2003) . The deposition of PBAE onto the nanomaterial surface allowed to understand that the success of the self-assembly was dependent on the polymeric degradation. Therefore, although the polycations of the groups A, B, D, E, F, and G possessed in the average a weak positive charge, the presence of PBAEs into the systems improved the stability of the nanoconstructs. As result of that, it was observed a better ability in managing the strong negativity of the alginate, especially from the profiles provided by CHX-A2, CHX-A3, CHX-B2, CHX-D3 and CHX-F2.

Thermogravimetric analysis (TGA)

Thermogravimetric analysis is normally required for the quantification of the organic and inorganic content of the substrates and it measures the weight loss modulation as function of temperature and time (Ng *et al.*, 2018b). For this project, the temperature was ranging between 20°C and 800°C. As it is illustrated in the figures 4.23-4.40 in the results section, the attitude of the curves for all the coating systems was irrelevant below 100°C showing a low weight loss due to the predominant amount of water adsorbed by the samples as demonstrated by (Donato, Lazzara and Milioto, 2010). Furthermore, when the temperature rose, the weight loss percentage was dependent on the organic ratio coated onto the nanomaterials. Therefore, once the temperature rate went up reaching high values up to 800°C, also the amount of organic content considerably increased as proved by (Redfern and Coats, 1963).

For the silica amino-functionalized nanoparticles the weight loss is the result of the addition of APTES to the surface of the colloids. For all the constructs, a growth of weight loss was observed once one more quadruple layer was coated onto the surface nanoparticles, starting from the first quadruple layer until the last one. In fact, the tenth quadruple layer provided a considerable organic content, confirming the successful drug loading and the polyelectrolytes deposition onto the silica amino-functionalized nanoparticles. Therefore, as reported in the results section, the organic content percentage regarding only Q10 for all the matrices is summarised in the table below.

LbL-assembly coatings	Organic content % for B10/Q10
Alg-CHX	27.67% ± 0.04
CHX-A1	47.63% ± 1.49
CHX-A2	39.63% ± 1.12
CHX-A3	67.31% ± 0.01
CHX-B1	39.27% ± 0.07
CHX-B2	60.20% ± 0.38
CHX-B3	66.19% ± 0.06
CHX-D1	41.94% ± 0.37
CHX-D2	32.58% ± 0.78
CHX-D3	68.66% ± 1.65
CHX-E1	44.05% ± 3.04
CHX-E2	46.36% ± 0.22
CHX-E3	69.19% ± 0.25
CHX-F1	67.53% ± 0.14
CHX-F2	65.85% ± 0.52
CHX-F3	53.67% ± 1.52
CHX-G1	53.94% ± 0.09
CHX-G2	53.03% ± 0.42
CHX-G3	55.63% ± 0.52

Table 4.4: Organic content % for CHX-PBAEs for B10 or Q10

Among all the constructs, the systems having the polycations A3, B2, B3, D3, E3, F1, F2, G1 and G2 appear considerably interesting due to their high organic content percentage. Studies reported the encapsulation of the chlorhexidine in expanded-pore mesoporous silica nanoparticles (pMSN) to synthesize CHX-pMSN. The thermogravimetric analysis evidenced the successful encapsulation of the CHX where the loading efficiency was equal to 44.62% (Yan et al., 2017). For the coating developed in this project, the downward crest occurring around 100°C, might refer to both decomposition of the organic matter and the desorption

of the chlorhexidine. Thus, if the loading amount of drug is high, the encapsulation of the antimicrobial agent could be considered successful and it could be referred especially for the matrices possessing the hydrolysable PBAEs A3, B2, B3, D3, E3, F1, F2, G1 and G2.

Chlorhexidine release profiles

In this research project, the antimicrobial agent was firstly entrapped via LbL on a bilayer system including CHX and alginate only up to 20 layers, then 18 CHX-PBAE nanocoatings were developed with the aim of improving the stability and the release of the cargo. The evaluation of the drug release was performed in two different media, pH7.4 and pH5 representing respectively physiological environment and an acidosis condition typical of the joint infection (Simmen *et al.*, 1993; Kinnari *et al.*, 2010; Ribeiro, Monteiro and Ferraz, 2012). Only Q10 or B10 were object of analysis as layers with the highest amount of CHX released from the nanoparticles surface. However, the pH value can influence the release profile for the chlorhexidine, due to electrostatic interactions that can affect the stability of the construct (Kinnari *et al.*, 2010). For example, the interactions among the layers were weak at pH7.4 but strong at pH5; therefore, in all profiles the drug release was higher at pH 7.4 than at pH5.

LbL-assembly coatings	Cumulative release n° Days (pH5)	Cumulative release n° Days (pH7.4)	*Final cumulative release at pH5	*Final cumulative release at pH7.4
Alg-CHX	25	25	1295.83 µg/mL	1868.21 µg/mL
CHX-A1	70	70	1125.96 µg/mL	2916.89 µg/mL
CHX-A2	45	45	656.84 µg/mL	1920.60 µg/mL
CHX-A3	30	30	501.74 µg/mL	640.16 µg/mL
CHX-B1	70	70	1135.15 µg/mL	2187.41 µg/mL
CHX-B2	70	70	1648.61 µg/mL	2592.64 µg/mL
CHX-B3	60	60	1085.97 µg/mL	2116.16 µg/mL
CHX-D1	70	70	1612.70 µg/mL	3086.59 µg/mL
CHX-D2	110	110	1683.89 µg/mL	2470.32 µg/mL

CHX-D3	50	50	1419.86 µg/mL	2676.21 µg/mL
CHX-E1	70	70	1190.26 µg/mL	1775.34 µg/mL
CHX-E2	70	70	1350.70 µg/mL	1999.87 µg/mL
CHX-E3	50	50	1417.90 µg/mL	2443.42 µg/mL
CHX-F1	70	70	1657.91 µg/mL	2764.73 µg/mL
CHX-F2	70	70	1318.69 µg/mL	3178.49 µg/mL
CHX-F3	90	90	2131.43 µg/mL	3131.46 µg/mL
CHX-G1	60	60	504.24 µg/mL	636.85 µg/mL
CHX-G2	60	60	435.62 µg/mL	564.18 µg/mL
CHX-G3	50	50	815.30 µg/mL	1555.11 µg/mL

***Daily release:** 25-35 µg/mL. **CHX-MIC:** 2-8 µg/mL against *Escherichia coli*, and 0.5-2 µg/mL against *Staphylococcus epidermidis* (Luo *et al.*, 2016). **Table 4.5:** CHX cumulative release at pH5 and pH7.4

This is proved by the table 4.3 above which summarises the quantification the chlorhexidine released by the matrices prepared by LbL self-assembly. Overall, comparing nano-delivery system built up as bilayers to those composed by quadruple layers, it was observed that the presence of PBAEs as polycations into the systems allowed a better protection of the antimicrobial agent and a controlled and longer drug release. Furthermore, the disruption of the systems was mainly dependent on the polymeric degradation, which was influenced by the structure of the monomers adopted as starting materials in the PBAE synthesis. According to the literature, the profiles of the sequences involving A1, A2, A3, D1, D2, D3, E1, E2, and E3 (figures 4.41-4.50) as polycations respect both the surface erosion model for which the cumulative release of the drug unbound rises constantly over time until the plateau is reached and all the deposited layers are eroded causing the diffusion of the drug through the deposited polyelectrolytes layers (Smith *et al.*, 2009). On the other hand, the release curves provided by the polymers belonging to the groups F and G showed an initial burst release in the first week followed by steady decreasing release until it was reached the plateau, where the amount of drug released was too minimal to be detected. This is reported in the figures 4.51-4.59 in the results section. Despite the complexity beyond thin films degradation, the drug release properties were correlated to the solubility of the cargo in buffers, to the hydrolysis of PBAEs and to the weak electrostatic interactions generated by the LbL-assembly. In particular, in the latter case, the Van der Waals forces provide a stable conformation of the

polymers chains which positively influenced the construction of the thin layers (Matsusaki *et al.*, 2012) (Gentile *et al.*, 2015). Therefore, we assume that the different structures of PBAEs, including hydrophilic and hydrophobic monomers, could justify the modulation of both drug load efficiency gained by thermogravimetric analysis and drug release. In addition, the film degradation and the antimicrobial release was mainly observed in first 2 weeks corresponding to the timing of the PBAE hydrolysis. More specifically, the hydrolysable polycations after being completely degraded left the no hydrolysable polymer alginate as base layer, which was stable in both acidic and physiological conditions as widely investigated by Wood *et al.* This group of researchers evaluated the hydrolytic degradation of the LbL thin films including a PBAE and polysaccharide therapeutics, whose disruption and rate of drug released were initially characterised by a swelling period and then followed by linear system degradation. This mechanism was justified by the alternative deposition of no-hydrolysable and hydrolysable polyelectrolytes (Wood *et al.*, 2005). Furthermore, Smith *et al.*, investigated three hydrolysable polycations coated in different systems including flurbiprofen. Poly (3)-cargo provided a release over 10 days whereas poly (2)-cargo showed a release lasting 17 days. This study proved that the release kinetics are independent of the drug but can be influenced by the choice the poly-hydrolysable polymers influencing the stability of the coating (Smith *et al.*, 2009). In our case, we assume that the formulation composed by quadruple layers rather than bilayers better protect the drug, enhancing its physiochemical properties. Additionally, the employment of opposite charged no-hydrolysable and hydrolysable polymers, such as alginate and PBAEs, play a crucial role in the construct conformation. To confirm the data previously discussed, further investigation would be required.

Conclusions

In this chapter, 18 poly (β -amino) esters (PBAEs) were employed as polycations to develop 18 different chlorhexidine (CHX) nanotechnology delivery systems as early stage strategy to provide prophylaxis for orthopaedic infections. The encapsulation of the antimicrobial agent occurred via LbL self-assembly, with alternative deposition of alginate and PBAE onto silica nanoparticles previously amino-functionalized by using the Stöber method. Each matrix was composed by 10 thin quadruple layers and every single quadruple layer involved as follows: sodium alginate, CHX, sodium alginate and PBAE whose synthesis was carried out in the laboratory of Dr. Prokopovich from a wide range of amines and diacrylate monomers commercially available. Conventionally 3 amines were conjugated by Michael addition to 6 diacrylates named as A, B, D, E, F and G to provide: A1, A2, A3, B1, B2, B3, D1, D2, D3, E1, E2, E3 F1, F2, F3 G1, G2 and G3.

The 18 nanocoatings were compared to a unique thin bilayer system including only alginate and CHX embedded via LbL onto the SiO₂-NPs surface up to 10 bilayers. Firstly, the size of the nanocarriers was measured by dynamic light scattering (DLS) and transmission electron microscopy (TEM) priorly and after the LbL deposition. Then, for all the systems, quadruple and bi layers, the characterization of the surface of the nanoparticles was determined by zeta potential measurements and thermogravimetric analysis (TGA). In the first case, the resulting zig-zag pathway proved the success of each layer deposition via electrostatic interactions, whereas TGA allowed to quantify the deposition of hydrolysable (PBAE), no hydrolysable (alginate) polymers and chlorhexidine on the nanoparticles surface by material weight loss as function of time.

CHX release determination was performed by dispersing only Q10 or B10 nanoparticles in two different media, pH5 and pH7.4, representing respectively joint infection and healthy environment. Comparing the 18 nano-delivery systems to the alginate-CHX bilayer, the longer and controlled antimicrobial release provided by CHX-PBAEs coatings explained the importance in protecting the encapsulated drug into the system by employing a combination of hydrolysable and no-hydrolysable polymers. Thus, CHX was released over a period of 25 days from Alg-CHX thin film layer, whereas between 30-110 days from CHX-PBAEs. Furthermore, the drug release was pH-responsive and dependent on polymeric degradation:

in accordance to PBAEs hydrolysis, CHX slowly released at pH5 due to low electrostatic interaction among the layers, instead at pH7.4 reduced ionic strength caused a rapid drug release.

Therefore, due to the results provided, CHX-PBAE thin layers delivery systems could be a promising candidate for the treatment of early and late onset orthopaedic infections.

Chapter 5: Tobramycin and PBAE loaded on silica nanoparticles via Layer by layer (LbL) coating

Introduction

Prosthetic joint infection (PJI) is an undesirable event of total joint arthroplasty (TJA), caused by a broad spectrum of Gram positive and Gram negative bacteria, which could require multiple revision surgeries to successfully eradicate the microorganisms from the infected implant (Tande and Patel, 2014), (Scott and Higham, 2003). To overcome this problem, the formulation of antibiotic loaded nanoparticles, incorporated in bone cement and used for fixation of prosthesis, allowed the targeted and sustained release of the drug over the site of infection enhancing the antibacterial properties (Lee *et al.*, 2015), (Chuang, Smith and Hammond, 2008). Aminoglycosides such as gentamycin, tobramycin and vancomycin are a class of antibiotics which are widely used for the treatment of bacterial infections (Hendriks *et al.*, 2004), (Krause *et al.*, 2016). These agents are concentration-dependent drugs which means that bacteria killing rise by increasing levels of drugs (Hill *et al.*, 2019). In particular, tobramycin is a water-soluble antibiotic which mainly acts against Gram negative bacteria as *Pseudomonas aeruginosa* (Gao *et al.*, 2011). Despite this prompt ability, the current concern regards the rate of drug release which is quite difficult to control (Swearingen *et al.*, 2018), (Smith *et al.*, 2018b). The reason could be related to an initial burst release observed from the systems containing tobramycin providing an initial excess of drug depletion and high local antibiotic concentration which lead to increased toxicity in the host cells. Furthermore, the initial burst release can cause long period of less effective tobramycin concentration which could be below the minimal inhibiting concentration (MIC) simply promoting the antibiotic resistance (Zhou *et al.*, 2018), (Francolini *et al.*, 2017). Therefore, to minimise the incidence of these side effects, it is extremely urgent the development of triggered-release drug delivery systems to exploit the antibiotic properties and improve its kinetics of release (Zhou *et al.*, 2014), (Zhu and Jun Loh, 2015) (Perni and Prokopovich, 2020a).

In this chapter, a facile approach to form pH-responsive layer by layer (LbL) multilayer film systems was developed by coating the positive charged tobramycin onto silica amino-functionalised nanoparticles chosen as nano-vectors. Firstly, the antibiotic was alternatively loaded with only the non-hydrolysable polymer alginate to provide a bilayer system; then the

18 PBAEs detailed described in chapter 3 were employed in the development of 18 different nano-delivery systems where each system was composed by 10 quadruple layers and each quadruple layer included as follows: alginate-TOB-alginate-PBAE. The bilayer and quadruple layer nano-coatings were characterised by zeta potential measurements and thermogravimetric analysis (TGA) and the drug release was quantified by fluorescence detection providing high load drug capacity and controlled drug release over a period of 4 weeks.

This strategy could represent a promising way to control the release of the aminoglycoside tobramycin as early stage prophylaxis for future treatments of early and late onset joint infections.

Materials and methods

Chemicals

All the reagents used for the nanoparticles and nano-delivery systems including the tobramycin and reported in this chapter, are accurately described in the section 2.1 of chapter 2. Buffers pH5 and pH7.4 were prepped as follows: 700 mL of sodium acetate 0.1M (70%) were added to 30mL of acetic acid 0.1M (30%) to produce sodium acetate buffer pH5, whereas 1 tablet of phosphate buffer (PBS) was dissolved in 100 mL deionised water to gain buffer pH7.4.

Nanoparticles preparation

For every nanocoating system, 500 mg of amino-functionalised silica nanoparticles (AFSi-NPs) were employed as nano-vectors and synthesised following the Stöber method (Stober, 1968), whose protocol was specified in the section 2.2 of chapter 2.

Synthesis of poly (β -amino) esters (PBAE)

18 PBAEs were synthesised by Michael conjugation between a diacrylate and a secondary amine in a ratio 1:1.1. The monomers were dissolved in 5mL of dichloromethane (DCM) and kept under stirring in a glass tube in oil bath at 50°C. After 48 h, each polymer was recovered by precipitation in 30 mL of diethyl ether followed by centrifugation for 5 minutes at 3500 rpm to remove the excess of starting materials (Lynn and Langer, 2000). The general scheme

of PBAE reaction, the procedure and the table of monomers adopted for the synthesis are listed in the section 2.3 of chapter 2.

Layer by layer (LbL) self-assembly

Layer by layer technique was applied for the development of multilayer systems composed by quadruple layers or bilayers, where the antibiotic tobramycin was loaded onto the AFSi-NPS surface up to 10 times. Firstly, a bilayer was prepared as represented by the table 5.1 below.

Bilayer matrix: Alg-TOB

Quadruple layer no.	Abbreviation	Layers on the surface of AFSi-NPs
1	B1	AFSi-NPs-alginate- <i>tobramycin</i>
2	B2	AFSi-NPs-B1-alginate- <i>tobramycin</i>
3	B3	AFSi-NPs-B2-alginate- <i>tobramycin</i>
4	B4	AFSi-NPs-B3-alginate- <i>tobramycin</i>
5	B5	AFSi-NPs-B4-alginate- <i>tobramycin</i>
6	B6	AFSi-NPs-B5-alginate- <i>tobramycin</i>
7	B7	AFSi-NPs-B6-alginate- <i>tobramycin</i>
8	B8	AFSi-NPs-B7-alginate- <i>tobramycin</i>
9	B9	AFSi-NPs-B8-alginate- <i>tobramycin</i>
10	B10	AFSi-NPs-B9-alginate- <i>tobramycin</i>

Table 5.1: LbL matrix of deposited alginate and TOB layers on AFSi-NPs

The formation of the multilayer system occurred under acidic condition by using sodium acetate pH5 to reproduce infectious environment (Ribeiro, Monteiro and Ferraz, 2012). Both sodium alginate (2mg/mL) and tobramycin (10mg/mL) were prepared few hours before the beginning of the self-assembly procedure. Then, 18 nano-delivery systems were developed adopting the same conditions for the experiment. In particular, each matrix was composed by 10 quadruple layers and each quadruple layer was including as follows: alginate-TOB-alginate-PBAE (table 5.2). The polymer solution was also freshly prepared (2mg/mL) and the LbL technique is detailed described in the section 2.4 of chapter 2.

Matrix: Alg-TOB-Alg-PBAE

Quadruple layer no.	Abbreviation	Layers on the surface of AFSi-NPs
1	Q1	AFSi-NPs-alginate- tobramycin -alginate-PBAE
2	Q2	AFSi-NPs-Q1-alginate- tobramycin -alginate-PBAE
3	Q3	AFSi-NPs-Q2-alginate- tobramycin -alginate-PBAE
4	Q4	AFSi-NPs-Q3-alginate- tobramycin -alginate-PBAE
5	Q5	AFSi-NPs-Q4-alginate- tobramycin -alginate-PBAE
6	Q6	AFSi-NPs-Q5-alginate- tobramycin -alginate-PBAE
7	Q7	AFSi-NPs-Q6-alginate- tobramycin -alginate-PBAE
8	Q8	AFSi-NPs-Q7-alginate- tobramycin -alginate-PBAE
9	Q9	AFSi-NPs-Q8-alginate- tobramycin -alginate-PBAE
10	Q10	AFSi-NPs-Q9-alginate- tobramycin -alginate-PBAE

Table 5.2: LbL matrix of deposited TOB and PBAE layers on AFSi-NPs

Nanoparticles surface characterisation

Zeta potential measurements

For each layer deposited onto the silica nanoparticles surface the zeta potential was measured by dispersing 1 mg of the nanocarrier after a new layer deposition in 1 mL sodium acetate pH5. For all the layers composing either the 10 quadruple layers or bilayers, the charge of the nanomaterial was measured as result of the electrophoretic mobility under acidic conditions. The detection of the potential occurred via dynamic light scattering (DLS) on Malvern ZetaSizer. The conditions adopted for the measurements are listed in the section 2.5.2 of chapter 2. All data were expressed as mean \pm standard deviation (SD) for at least 3 measurements.

Thermogravimetric analysis (TGA)

For the bilayers B1, B3, B5, B7 and B10 of the system Alg-TOB as well as for the quadruple layers Q1, Q3, Q5, Q7 and Q10 of all the 18 TOB-PBAE matrices, the weight loss percentage was evaluated as function of time by heating the nanoparticles up to 800°C (Ng *et al.*, 2018b). The TGA was carried out by using Perkin-Elmer TGA 4000 instrument and the detailed procedure is reported in the section 2.5.3 of chapter 2. All data were expressed as mean \pm standard deviation (SD) for at least 2 measurements per sample.

Tobramycin release quantification

After the LbL deposition the drug release studies were performed at pH5 and at pH7.4 representing respectively infection and physiological environments (Ribeiro, Monteiro and Ferraz, 2012). The object of analysis was the last quadruple or bilayers B10 or Q10. In particular, 10 mg of each nano construct were suspended in 1 mL of each medium and kept in the incubator at 37°C along all the release period and every 24h the surfactant was withdrawn and replaced with fresh buffers as described in the section 2.5.4 of chapter 2. The release of tobramycin was evaluated by fluoroscopy with the aid of a fluoroscan (FLUOROstar Optima, BMG labtech). The drug release quantification occurred by quantifying the fluorescence of the conjugate formed by adding o-phthaldialdehyde (OPA) reagent to the samples daily withdrawn from the incubator (Perni and Prokopovich, 2014). The test was performed on triplicates per sample dissolved in both media and the description of the applied protocol is detailed in the section 2.5.5 of chapter 2.

Results

Nanoparticles surface characterisation

ζ potential measurements

Bilayer: Alg-TOB

The zeta potential pathway was developed for the bilayer alginate-tobramycin which was composed by overall 20 layers with alternative deposition of the non hydrolysable polymer and the antibiotic onto the surface of the nano-vectors. Starting from the positivity provided by the amino-functionalised nanoparticles, $+17.07 \pm 3.12$ mV, the potential was reversed by deposition of the alginate, -12.57 ± 2.18 mV, and it returned positive once the aminoglycoside was embedded onto the system, $+13.37 \pm 0.55$ mV as illustrated by the figure 5.1 below (layers 1-3).

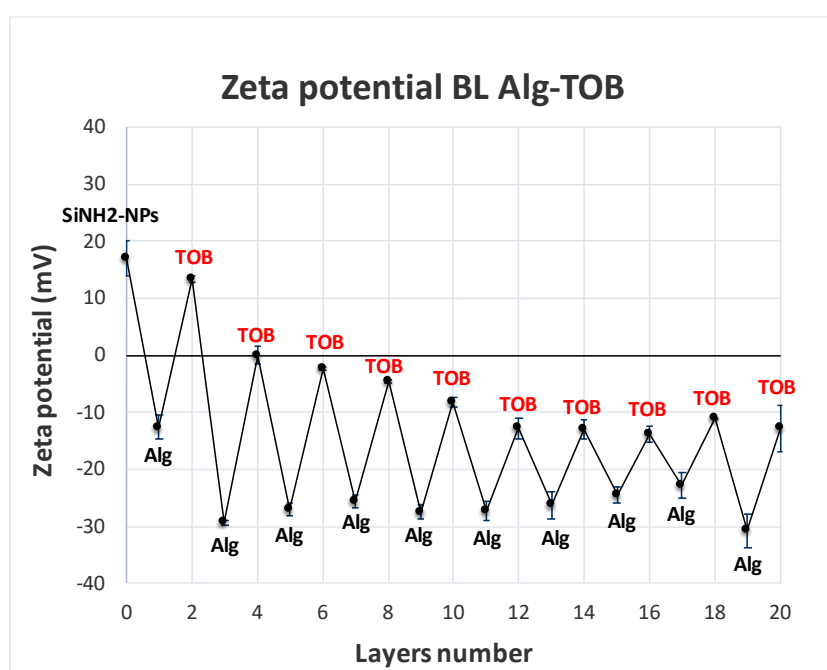


Figure 5.3: ζ potential for the coating system SI-NH₂NPs-Alg-TOB. Mean ± SD (N=1, n=3).

Overall it was observed that the negativity of the sodium alginate reduced the positivity of the drug. For instance, the charge of tobramycin plummeted to 0.01 ± 1.51 mV on B2 showing an increasing negativity from B3, -2.3 ± 0.18 mV, reaching -12.77 ± 2.35 mV on B10. The positivity of the cargo was easily turned into negative: therefore, it is required the development of nano delivery systems enable to enhance the stability of the drug. Thus, in this section all the 18 systems including different PBAE forming with tobramycin and alginate

quadruple layers rather than bilayers will be described and compared to the pathway reported above.

A1

PBAEs, belonging to the group A and possessing 1,4 butanediol diacrylate as diacrylate (A) and piperazine (1), 4-4 trimethyldipiperidine (2) and N,N-Bis[3-(methylamino)propyl]methylamine (3) as amines, were the polycations employed in the nanoconstructs TOB-A1, TOB-A2 and TOB-A3. Each matrix was involving the sequence alginate-TOB-alginate-PBAE to form one quadruple layer which was repeatedly coated onto the silica nanoparticles (AFS-NPs) surface up to 10 times. Thus, in this case, the zeta potential was measured for all the 40 layers.

Starting from a positive potential provided by the amino-functionalised nanoparticles, $+17.07 \pm 3.12$ mV, the charge was easily turned into negative by coating the sodium alginate onto the nanocarrier surface, -18.03 ± 1.68 mV. Additionally, the deposition of the antibiotic showed a considerable positivity equal to $+41.7 \pm 4.31$ mV, which dropped to -13.0 ± 1.01 mV by adding one more of alginate and returning slightly positive after A1 was embedded onto the system, $+2.48 \pm 2.41$ mV as shown by the layers 1-5 reported in the figure 5.2 below.

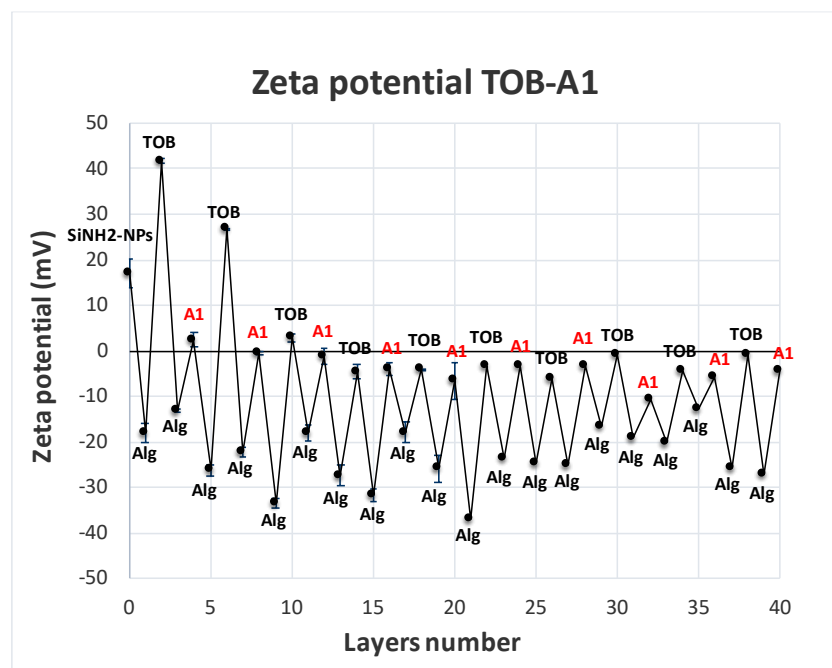


Figure 5.2: ζ potential for the coating system SI-NH₂NPs-Alg-TOB-Alg-A1. Mean \pm SD (N=1, n=3).

The strong positivity of the drug was reduced to $+26.7 \pm 2.96$ mV on Q2 due to the weak positivity detected for the PBAE A1, which instead presented a charge close to 0, -0.5 ± 0.26 mV. The potential of the cargo was then still slightly positive on Q3, $+2.97 \pm 2.07$ mV and it became negative from Q4, -0.75 ± 1.92 mV, reaching a negativity equal to -6.17 ± 1.10 mV on Q7. However, after being inverted, the charge of A1 slightly changed from Q4, -4.03 ± 0.84 mV, up to Q10, -4.37 ± 0.42 mV.

A2

The figure 5.3 is representative of the zig-zag pathway gained by the measurements of zeta potential for each layer deposited onto the nano vectors surface to form the delivery system including tobramycin and the PBAE A2. First of all, the charge was positive for the nanoparticles alone, $+17.07 \pm 3.12$ mV; then, the first quadruple layer was coated as follows: sodium alginate which reversed the potential to -28.63 ± 1.20 mV; the antibiotic providing a positive charge of $+16.9 \pm 1.55$ mV; a second layer of alginate which inverted into negative the potential, -29.6 ± 3.6 mV, and finally the polycation A2 which changed again the potential showing a positivity equal to $+12.9 \pm 1.2$ mV (1-5 layers).

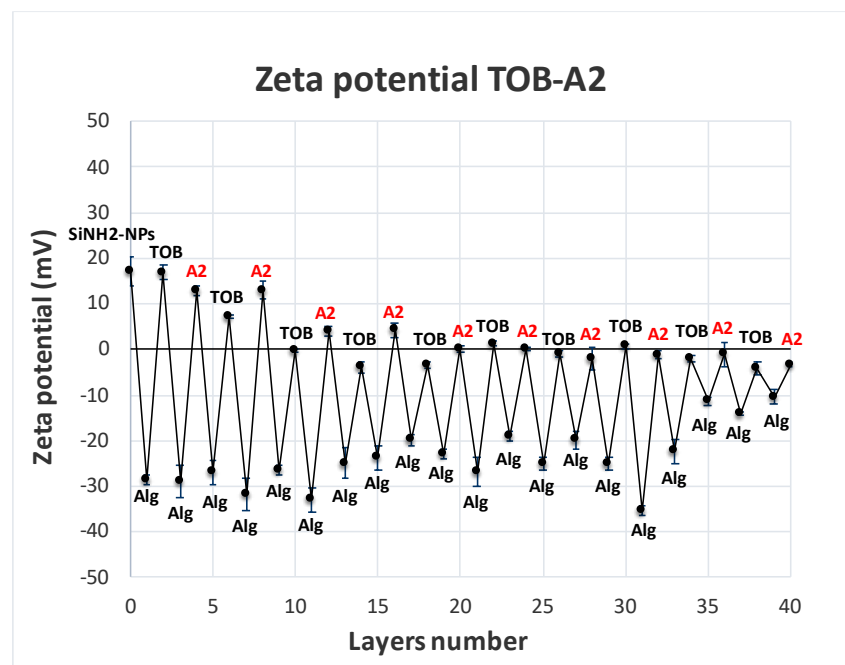


Figure 5.3: ζ potential for the coating system SI-NH₂NPs-Alg-TOB-Alg-A2. Mean \pm SD (N=1, n=3).

The PBAE A2 enhanced the stability of the tobramycin if compared to the profile of TOB-A1. For instance, its positivity was half reduced to $+7.23 \pm 0.38$ mV on Q2 and it remained nearly 0 from Q4 to Q9, reaching -4.2 ± 1.85 mV only on Q10. As contrary, the polymer showed its positivity until Q6. Indeed, for the first two quadruple layers there was no change of its charge which dropped to $+4.1 \pm 1.13$ mV on Q3 and $+0.13 \pm 0.29$ mV on Q6. From Q7 the potential became slightly negative, -1.9 ± 2.51 mV, with no substantial difference in the negativity detected up to Q10, which was correspondent to -3.7 ± 0.47 mV.

A3

A3 was the last polymer, belonging to the group A, employed as polycation into a system including tobramycin. As previously described, the positivity showed by the surface of the nanocarrier before the layer by layer deposition was inverted by adding one layer of sodium alginate, -16.33 ± 1.39 mV and it went back to positive once the antibiotic was embedded into the system, $+25.6 \pm 0.87$ mV. The addition of one more layer of sodium alginate changed the potential into negative, -27.73 ± 0.81 mV which then was reversed again by the deposition of A3, $+15.53 \pm 0.71$ mV.

In this case, the positivity of the drug remained stable until Q4 ending to -6.12 ± 0.55 mV on Q7. For example, on Q2 the potential of tobramycin plummeted to $+6.1 \pm 1.01$ mV, whereas it slowly decreased on Q3 and Q4 where it was equal to $+2.06 \pm 1.65$ mV. However, after being close to 0 on Q5 and Q6, the charge suddenly was turned from Q7 remaining negative up to Q10. The behaviour observed for A3 was similar to what described for the tobramycin. In particular, the positivity showed by the polymer on Q1 was mainly reduced on Q2, $+8.84 \pm 0.27$ mV, and Q3, $+4.31 \pm 1.83$ mV, whereas it slowly decreased on Q4, $+3.47 \pm 1.16$ mV. However, the potential of the polycation was nearby 0 on Q5, followed by an increasing negativity detected from Q6, -3.14 ± 1.24 mV, ending to -5.12 ± 1.18 mV on Q10 (figure 5.4).

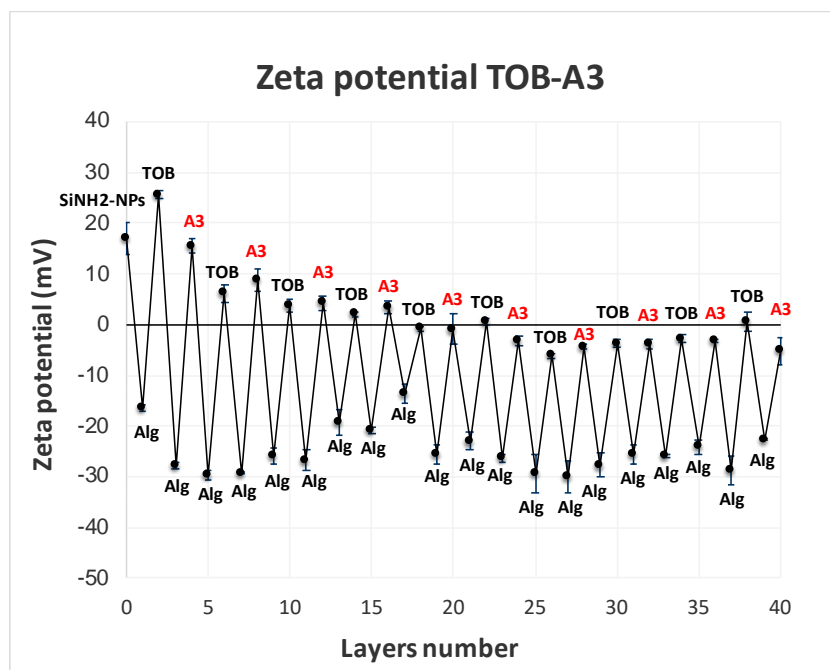


Figure 5.4: ζ potential for the coating system SI-NH₂NPs-Alg-TOB-Alg-A3. Mean \pm SD (N=1, n=3).

Overall, comparing the profiles gained by TOB-A1, TOB-A2 and TOB-A3 to the one of the bilayers nanoconstruct Alg-TOB, it was observed that although the polymers of the group A possessed a weak positive charge, the PBAEs improved the stability of the drug, which in the case of the bilayer showed an increasing negativity already from the third bilayer. On the other hand, among the nano delivery systems formed by quadruple layers, A2 better managed the positivity of the cargo exhibiting its positive charge until Q6. Therefore, the PBAEs which better protected the antibiotic entrapped onto the nanocoatings were, as follows, A2>A3>A1.

B1

B1 was employed as first PBAE of the group B which included B1, B2 and B3. From the positive charge detected for the amino functionalisation of the silica nanoparticles, there was a consistent drop of the positivity due to the alginate coated onto the system, which showed a potential of -30.73 ± 1.24 mV. Furthermore, the addition of tobramycin reversed the charge into positive, $+14.87 \pm 0.85$ mV, which returned negative once the sodium alginate was embedded for the second time, -29.7 ± 0.52 mV. To complete the first quadruple layer, B1 was layered as polycation, proving a further change of the potential which was slightly positive, $+4.41 \pm 0.68$ mV (figure 5.5).

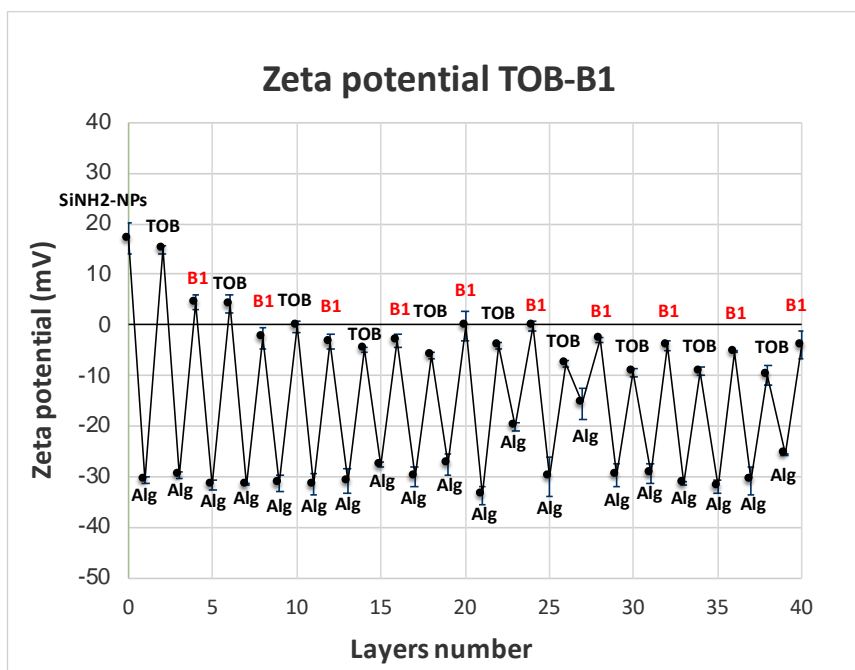


Figure 5.5: ζ potential for the coating system SI-NH₂NPs-Alg-TOB-Alg-B1. Mean \pm SD (N=1, n=3).

As illustrated in the figure above, the initial positive charge of the drug was easily turned into negative, dropping to $+4.11 \pm 0.92$ mV on Q2. Then, after being close to 0 on Q3, 0.38 ± 1.02 mV, the potential was inverted into negative from Q4, -4.84 ± 0.18 mV, reaching -9.8 ± 0.16 mV on Q10. As contrary, the polymer B1 was already a weak polycation from the first quadruple layer. Indeed, it quickly lost its positivity becoming negative on Q2, -2.61 ± 0.18 mV, followed by a slow increase of its negativity ending to -3.96 ± 0.12 mV on Q10.

B2

The zeta potential measurements were also performed for the matrix TOB-B2 as reported in the figure 5.6 below. The first quadruple layer was characterised by alternative positive and negative charge as results of alginate, antibiotic, alginate and B2 employed in this system. Therefore, starting from $+17.07 \pm 3.12$ mV for the AFS-NPs alone, the alginate turned into negative the charge, -13.37 ± 1.20 mV, which returned positive after layering the aminoglycoside onto the nanocarrier surface, $+20.7 \pm 1.01$ mV. Additionally, the potential plummeted into a negative value after the second deposition of the sodium alginate, -26.6 ± 1.97 mV, positively reversing only by coating the PBAE B2, which showed a weak positive charge, $+4.83 \pm 0.17$ mV.

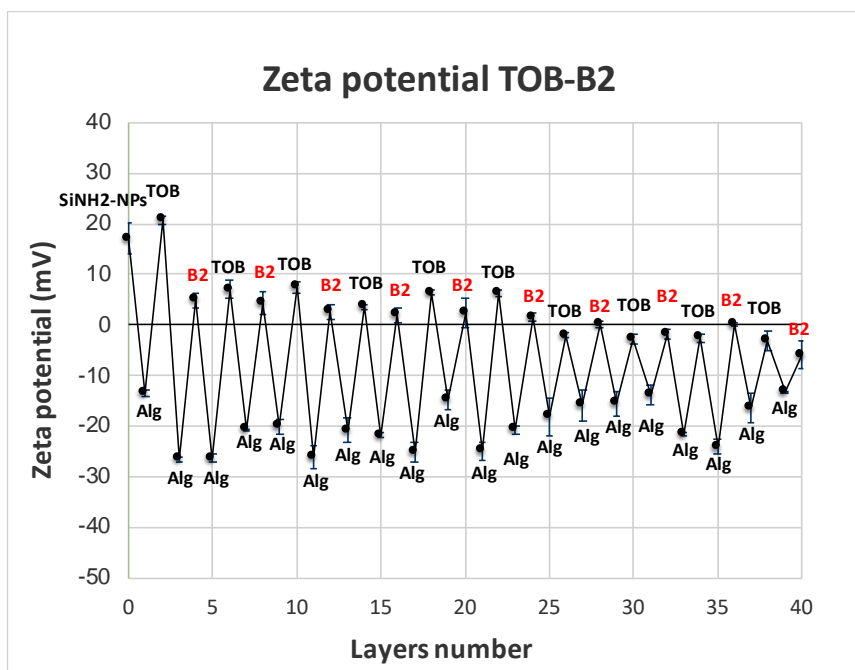


Figure 5.6: ζ potential for the coating system SI-NH₂NPs-Alg-TOB-Alg-B2. Mean \pm SD (N=1, n=3).

Overall, it was observed that although the polymer showed a weak positive charge, it remained positive up to Q7, as well as the cargo which kept being positive until Q6. For example, the potential of tobramycin dropped to $+7.04 \pm 0.25$ mV on Q2, but remaining positive up to Q6, $+6.21 \pm 1.51$ mV. Then, the potential plummeted to -2.01 ± 1.73 mV on Q7 reaching -3.27 ± 0.11 mV on Q10. On the other hand, the positivity of B2 decreased to $+2.6 \pm 0.23$ mV on Q3, staying stable until Q7 where the charge was equal to 0.15 ± 1.17 mV, followed by an increase of the negativity which ended up to -5.91 ± 2.02 mV on Q10.

B3

To complete the polymers belonging to the group B, a zig-zag pathway was finally developed by measuring the nanocoating TOB-B3 along the layer by layer deposition. The initial positive charge detected as result of the amino functionalisation of the silica nanoparticles changed into negative by layering the sodium alginate, -27.8 ± 0.38 mV, and went back to positive after the deposition of the tobramycin, $+14.87 \pm 0.85$ mV. However, the alginate added for the second time and representing the third layer embedded onto the surface of the vectors, turned back to negative the charge showing a value of -28.03 ± 2.10 mV, which changed again once B3 was coated onto the system, $+8.75 \pm 0.33$ mV (figure 5.7).

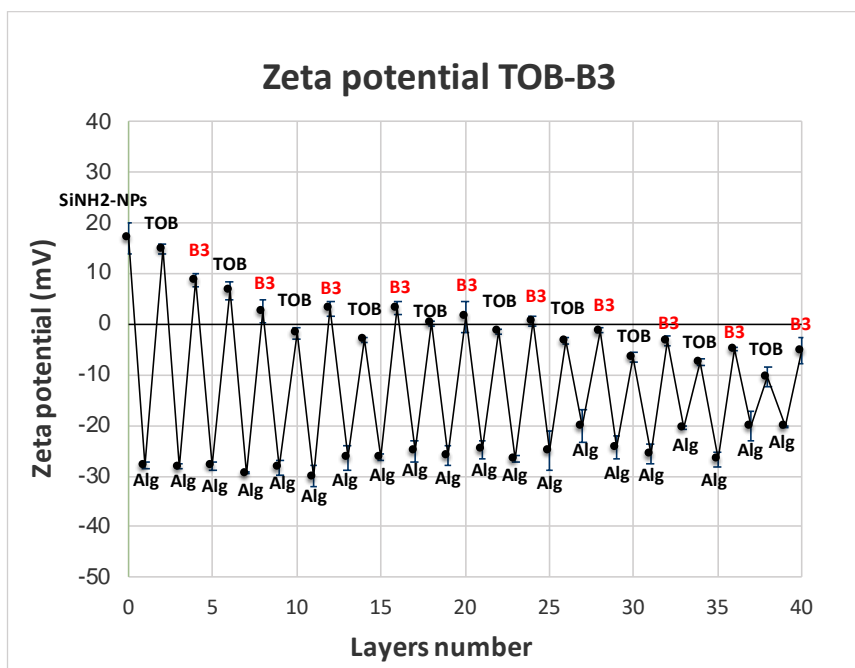


Figure 5.7: ζ potential for the coating system SI-NH₂NPs-Alg-TOB-Alg-B3. Mean \pm SD (N=1, n=3).

In this case, the positivity of the drug was easily inverted on Q3 showing a potential of -1.72 ± 1.23 mV. Furthermore, the negativity steadily increased firstly reaching -3.30 ± 0.74 mV on Q7, then, -10.27 ± 0.96 mV on Q10. The charge of the polymer B3, instead, slightly changed, showing values equal to $+3.32 \pm 1.34$ on Q4 and 0.72 ± 0.92 mV on Q6. As contrary, the potential was inverted starting from Q7, -1.20 ± 0.07 mV followed by a rise of the negativity until Q10 where the charge was correspondent to -5.26 ± 1.57 mV.

Comparing the results of the 3 polymers of the group B, it was observed that although B3 provided the highest initial positive charge, B2 was the more stable among the 3 polycations, showing a better management of the strong negativity of the sodium alginate. As contrary, no substantial difference was observed between the profiles of TOB-B1 and TOB-B3, as well as if these 2 matrices were compared to the bilayers system Alg-TOB. For instance, the potential of the drug was easily reversed into negative already from the second quadruple layer as observed for Alg-TOB. Thus, the employment on the systems of B1 and B3 was no significantly effective as noticed instead for B2.

D1

The zeta potential was pursued also to evaluate the layer by layer deposition of the nano-coatings including the polymers of the group D: TOB-D1, TOB-D2 and TOB-D3. For the first matrix, starting from $+17.07 \pm 3.12$ mV, which was the potential representative of the amino-functionalised nanoparticles before the LbL, there was a reduction of the positivity by employing in the system the alginate, -21.0 ± 2.43 mV. Then, the potential was turned again by adding the tobramycin, $+5.27 \pm 2.37$, to return negative after layering for the second time the alginate, -26.3 ± 0.87 mV. Finally, the first quadruple layer was completed by coating the PBAE D1, which provided a positive charge equal to $+11.8 \pm 3.72$ mV (figure 5.8).

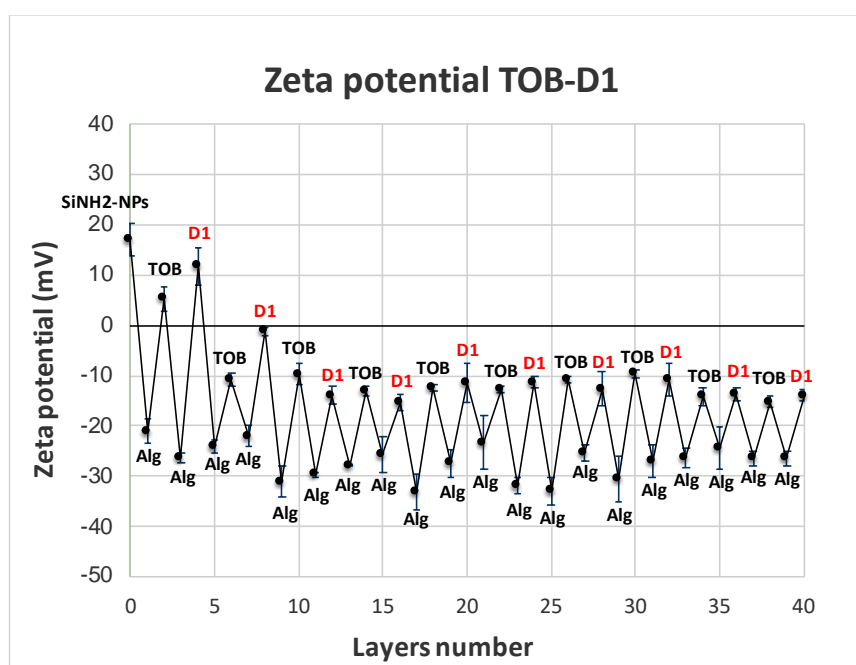


Figure 5.8: ζ potential for the coating system SI-NH₂NPs-Alg-TOB-Alg-D1. Mean \pm SD (N=1, n=3).

The positive charge of the drug was easily turned into negative from Q2, showing a potential of -11.3 ± 0.81 , followed by a steady increase of the negativity that ended up to -15.2 ± 1.79 mV on Q10. In addition, a similar behaviour was observed for the polycation D1, which although presented a positive charge over $+10$ mV, it was incapable of managing the strong negativity of the sodium alginate. For instance, also for D1, there was a drop of its positivity starting from Q2, -9.73 ± 2.17 mV, plus a further rise of the negativity which reached -13.87 ± 1.17 mV on Q10.

D2

The nano delivery system possessing D2 as polycation provided a zig-zag pathway while every polyelectrolyte was embedded onto the nanocarrier surface (figure 5.9). The first quadruple layer was composed by as follows: alginate, tobramycin, alginate and D2 and similarly to what heretofore described each component was alternatively layered. Therefore, the initial positivity of the vectors surface was firstly reversed into negative by the alginate, -26.97 ± 0.71 mV and then changing into positive after the layer of the cargo, $+21.93 \pm 1.27$ mV. In the same way, the 3rd and 4th layers represented by respectively alginate and D2 inverted the potential, which was negative first, -30.93 ± 4.15 mV and finally back to positive, $+15.5 \pm 4.50$ mV.

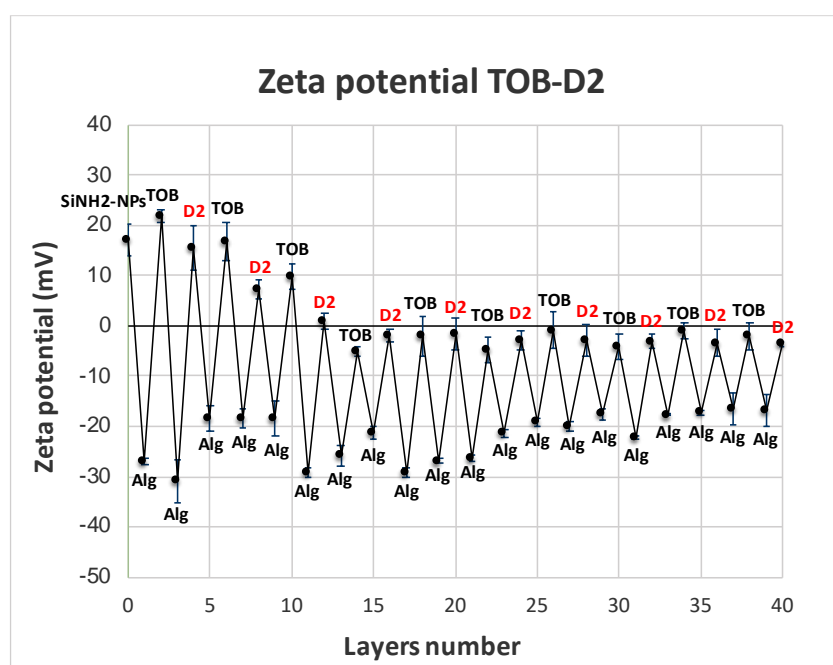


Figure 5.9: ζ potential for the coating system SI-NH₂NPs-Alg-TOB-Alg-D2. Mean \pm SD (N=1, n=3).

Overall, the polycation D2 was able to better control the negativity of the non-hydrolysable polymer if compared to the profile of TOB-D1. In this case, the potential of the drug was positive until Q3, where it dropped to $+9.93 \pm 2.55$ mV, but it became negative on Q5, -2.0 ± 4.04 mV. In particular, for this nanoconstruct, no further increase of negativity was observed for the charge of tobramycin, showing a potential correspondent to -2.07 ± 0.2 mV on Q10. However, the strong positivity of the PBAE, that was detected on Q1, was half reduced on Q2, $+7.2 \pm 1.97$ mV, plummeting to $+1.0 \pm 1.56$ mV on Q3. Additionally, the potential was turned

into negative starting from Q4, -1.9 ± 1.27 mV, and the negativity steadily rose ending to -3.6 ± 0.3 mV on Q10.

D3

To complete the PBAEs of the group D, the zeta potential was performed also for the matrix TOB-D3. Starting from $+17.07 \pm 3.12$ mV, which was the detected charge for the nanoparticles alone, the potential changed to -30.3 ± 1.53 mV once the alginate was added onto the system for the first time. Although the layer of tobramycin turned the charge of the surface of the nanocarrier into positive, $+14.87 \pm 0.85$ mV, there was a further inversion of the potential after depositing the alginate for the second time, which was equal to -31.77 ± 0.31 mV. Finally, the coating of the PBAE D3 formed the first quadruple layer providing a positive charge of $+16.63 \pm 0.87$ mV (figure 5.10).

The polycation D3 properly balanced the strong negativity of the alginate, showing a positive potential up to Q5. In the same way, also the charge of the drug was positive until Q5 and was turned into negative from Q6. For instance, the positivity of the aminoglycoside consistently dropped on Q2, showing a charge correspondent to $+2.03 \pm 0.91$ mV, remaining stable up to Q5, $+1.20 \pm 0.54$ mV. Then, there was a considerable increase of the negativity from Q6, -1.44 ± 1.10 mV, reaching -10.4 ± 0.2 mV on Q10.

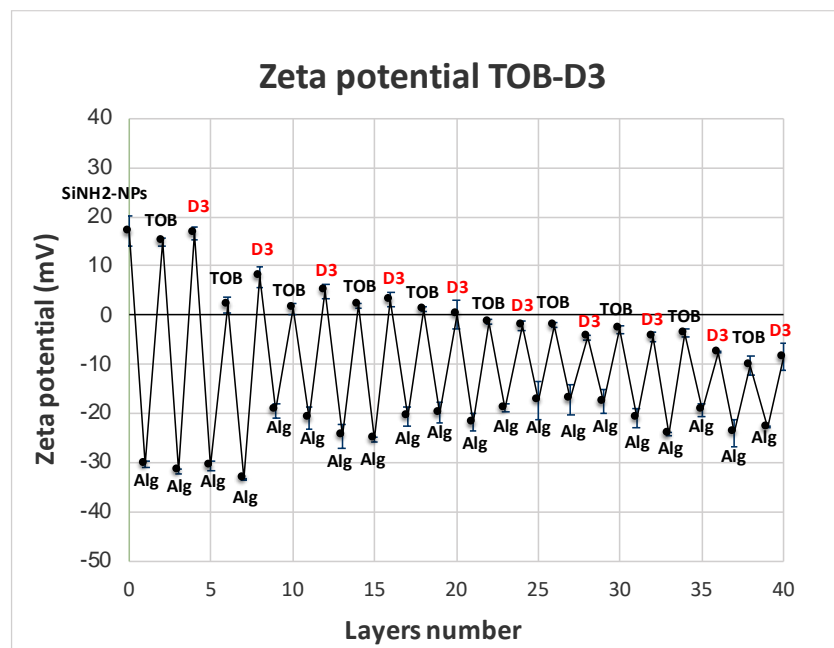


Figure 5.10: ζ potential for the coating system SI-NH₂NPs-Alg-TOB-Alg-D3. Mean \pm SD (N=1, n=3).

On the other hand, the positive charge of D3 mainly changed between Q2 and Q4 showing a potential respectively equal to $+3.14 \pm 2.52$ mV and the potential became negative from Q6, -2.28 ± 1.66 mV, ending to -8.5 ± 0.57 mV on Q10.

Comparing the nano delivery systems of the group D to the bilayers matrix Alg-TOB, it was observed that the presence of PBAEs onto the systems better protected the drug entrapped among the layers coated onto the surface of the nanocarriers. Despite that, among the polycations possessing D as diacrylate in their backbone, it was observed that D2 provided the best stability to the system in which it was embedded, rather than D1 and D3. Thus, depending on the hydrolysis of these polymers and monomers that were employed for their synthesis, $D2 > D3 > D1$ could be the order to classify the PBAEs belonging to the group D.

E1

Regarding TOB-E1, initially, the charge was $+18.93 \pm 1.39$ mV for the surface of the particles, but it dropped to -21.43 ± 0.6 mV by adding the sodium alginate. Then, it was reverted due to the layer of tobramycin, $+10.46 \pm 2.11$ mV, but it returned negative after the coating of the alginate for the second time, -26.47 ± 3.27 mV. Finally, the 4th layer was the PBAE E1 providing a shift into positive charge which was equal to $+13.36 \pm 0.23$ mV (1-5 layers in the figure 5.11).

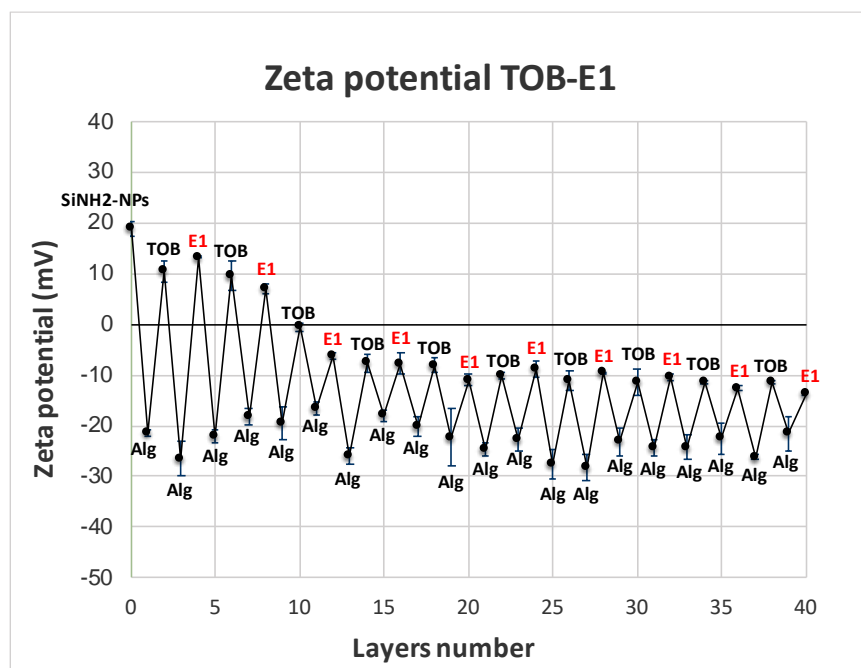


Figure 5.11: ζ potential for the coating system SI-NH₂NPs-Alg-TOB-Alg-E1. Mean \pm SD (N=1, n=3).

The positive charge of the drug was easily reverted showing an initial decrease of the positivity on Q2, $+9.63 \pm 2.89$ mV, which was drastically reduced on Q3, where the potential was close to 0, -0.53 ± 0.74 mV. From Q4, the charge of the cargo was negative, -7.63 ± 1.88 mV, followed by a significant increase of the negativity heading to -11.4 ± 0.4 mV on Q10. As contrary, the positivity of the polycation was quickly turned into negative from Q3, -6.2 ± 0.53 mV, showing a rapid rise of the negativity, once the polymer was embedded in a new quadruple layer onto the particles surface, that led up to -13.6 ± 0.29 mV on Q10.

E2

Zeta potential measurements were carried out also for the nanocoating TOB-E2 and the zig-zag profile is illustrated in the figure 5.12 below. Starting from a strong positivity of the surface resulting from the amino-functionalisation of the nanocarriers, $+17.07 \pm 2.55$ mV, the charge dropped to -23.2 ± 0.14 mV, due to the deposition of the no hydrolysable polymer alginate. Additionally, there were further changes of the potential caused by the other components characterising the first quadruple layer. Thus, as follows: the tobramycin layer provided a positive charge, $+27.33 \pm 1.11$ mV, which was modified by one more layer of alginate, -25.4 ± 0.26 mV, followed by an additional inversion representative of the coating of the polycation E2, $+9.03 \pm 0.34$ mV.

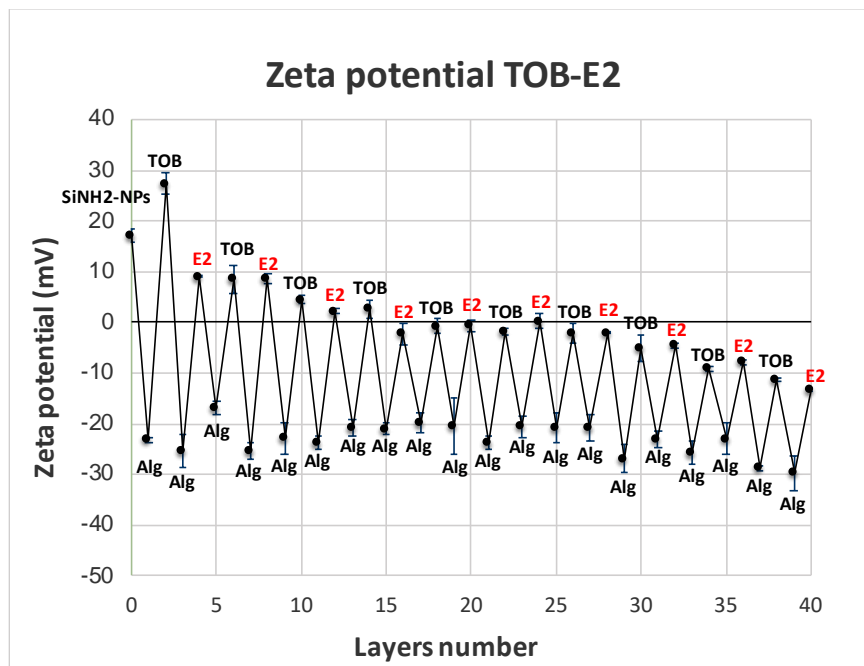


Figure 5.12: ζ potential for the coating system SI-NH₂NPs-Alg-TOB-Alg-E2. Mean \pm SD (N=1, n=3).

In this case, the charge of both drug and polymer was stable until Q6, showing a better ability of E2, rather than of E1, to provide stability to the nanoconstruct. For instance, the positivity of tobramycin was mainly reduced between Q3 and Q4, where the charge was respectively, $+4.5 \pm 0.37$ mV and $+2.63 \pm 0.45$ mV. Furthermore, after being close to 0 on Q5, -0.77 ± 0.12 mV, it became negative with a considerable increase of the negativity from Q6, -1.7 ± 2.22 mV, to Q10, -11.3 ± 0.98 mV. Additionally, the modulation of the charge for the polymer similarly occurred to what previously described for the cargo. Therefore, the positivity of the polymer remained stable for the first 3 quadruple layers whereas it plummeted to -2.14 ± 0.80 on Q7, ending to -13.27 ± 0.12 mV on Q10.

E3

To conclude the PBAEs belonging to the group E, a zig-zag pathway was also developed for the nano delivery system TOB-E3. The initial positivity of nanocarriers alone was reversed by coating the sodium alginate, -18.77 ± 1.02 mV, returning into positive once the tobramycin was added onto the system, $+14.87 \pm 0.85$ mV. Then, the potential became negative again due to the alginate that was layered for the second time onto the surface of the vectors, -18.2 ± 0.46 mV, plus it was finally reverted by coating the PBAE E3, $+6.37 \pm 0.74$ mV (figure 5.13).

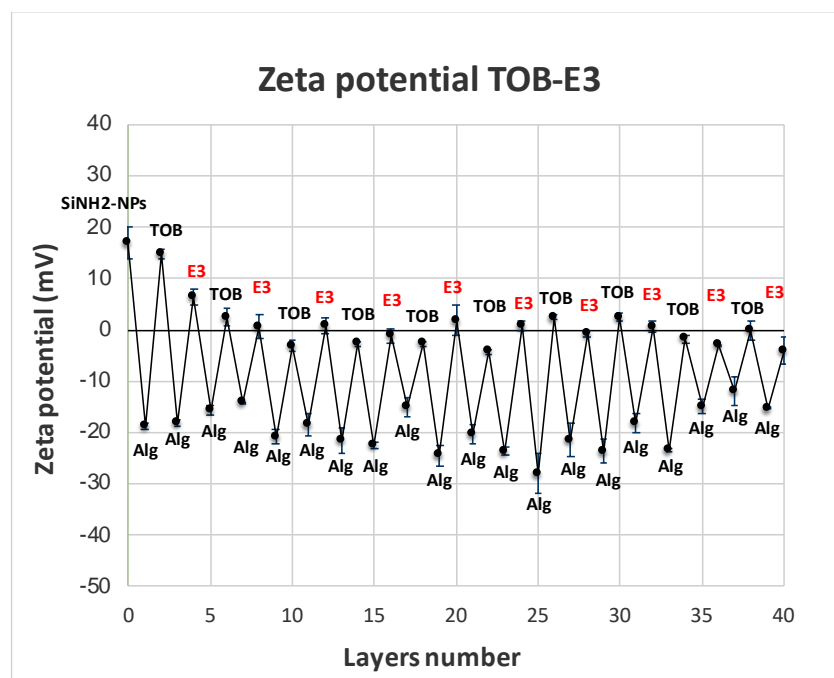


Figure 5.13: ζ potential for the coating system SI-NH₂NPs-Alg-TOB-Alg-E3. Mean \pm SD (N=1, n=3).

The positive charge of the aminoglycoside was easily turned into negative on Q3, -3.15 ± 0.36 mV, but no further increase of the negativity was observed until Q10. This was probably caused by the hydrolysis of the polycation which showed its positivity until Q6, where the value was close to 0, 0.64 ± 3.63 mV. However, from Q7 the potential of the polymer was inverted, -0.86 ± 0.84 mV, followed by a gradual rise of the negativity heading to -4.10 ± 1.15 mV on Q10.

Comparing the zig-zag pathways of the polymers of the group D, it was observed a good ability from the polymers of this group to control the negativity of the sodium alginate. This attitude was especially observed for E2 and E3, that, although were weak polycations, protected the drug coated in their own systems. Additionally, as previously described, the matrices TOB-E1, TOB-E2, and TOB-E3 confirmed that the development of coatings composed by quadruple layers instead of bilayers and including PBAEs, enhanced the stability of both drug and system.

F1

The polymers of the group F were employed as polycations for the development of 3 further nano delivery systems: TOB-F1, TOB, F2 and TOB-F3. The profiles gained by zeta potential measurements were representative of the success of the LbL deposition for PBAEs and tobramycin onto the surface of the matrices. Regarding TOB-F1, the initial positive charge resulting from the amino-functionalisation of the silica nanoparticles, dropped once the alginate was layered onto the system, -32.07 ± 0.64 mV, and it returned positive by adding the tobramycin, $+14.1 \pm 0.17$ mV. Additionally, the potential was negative again after depositing on the surface of the nanocarriers the alginate for the second time, -28.57 ± 0.23 mV, whereas it changed once again due to the coating of the PBAE F1, $+13.3 \pm 1.11$ mV (1-5 layers of figure 5.14).

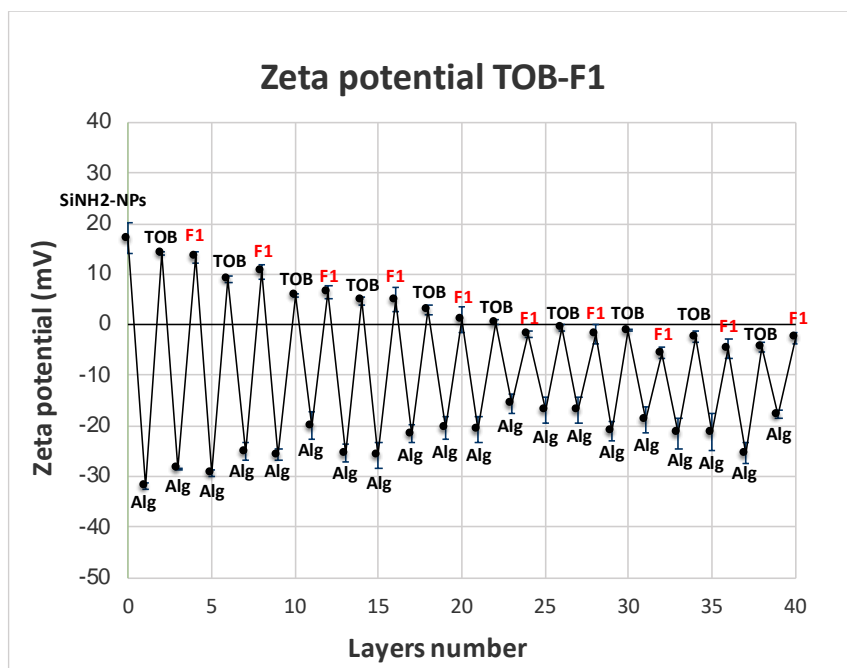


Figure 5.14: ζ potential for the coating system SI-NH₂NPs-Alg-TOB-Alg-F1. Mean \pm SD (N=1, n=3).

The positivity of the drug moderately decreased among the quadruple layers, showing value equal to $+9.0 \pm 0.52$ mV on Q2, which was half-reduced on Q4, $+4.67 \pm 0.95$ mV, and it decreased to 0.43 ± 0.42 mV on Q6. From Q7 a reversed charge was observed, -0.7 ± 0.62 mV, which led up to -4.52 ± 0.93 mV on Q10. Moreover, the degradation of the polymer was quite similar to the modulation of the charge measured for the drug. In particular, also in this case, the hydrolysis slowly occurred, providing a potential of $+10.53 \pm 1.46$ mV on Q2, with a gradual decline of the positivity until Q5, $+1.03 \pm 2.59$ mV. From Q6 there was an inversion of the polymeric charge, -1.86 ± 0.55 mV, which ended up to -2.53 ± 1.12 mV on Q10.

F2

The zeta potential was pursued also for the matrix where tobramycin and the PBAE F2 were coated onto the nanoparticles surface. As heretofore described, the initial detected potential was positive and equal to $+17.07 \pm 3.12$ mV, followed by a drastic drop into negative value, -26.4 ± 1.14 mV, due to the presence in the system of sodium alginate. Then, the charge was alternatively modulated by the coating of tobramycin, alginate for the second time and the PBAE F2 and respectively correspondent to $+24.6 \pm 1.4$ mV, -28.4 ± 0.53 mV and $+20.77 \pm 1.67$ mV. The zig-zag pathway reported in the figure 5.15 represents the success of the layer by layer deposition for the system TOB-F2.

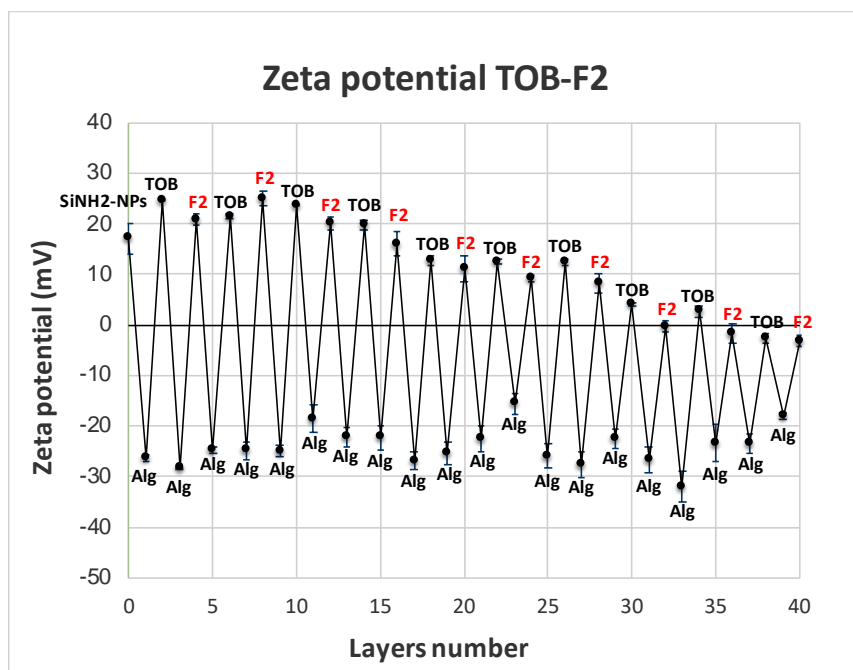


Figure 5.15: ζ potential for the coating system SI-NH₂NPs-Alg-TOB-Alg-F2. Mean \pm SD (N=1, n=3).

The polymer F2 properly controlled the positivity of the drug which was detected until Q9. Indeed, there was a slow decrease of the positivity showing a value of $+21.47 \pm 1.89$ mV on Q2, which kept falling on Q4, $+19.87 \pm 1.76$ mV, on Q6 $+12.53 \pm 1.21$ mV and on Q9, $+2.67 \pm 0.06$ mV. In this case the charge was reverted into negative only on Q10 with a potential of -2.63 ± 0.87 mV. On the other, the charge of the polymer was gradually reduced among the layers until Q8, reporting values such as: $+25.0 \pm 1.39$ mV on Q2, $+15.87 \pm 1.75$ mV on Q4, $+9.13 \pm 0.57$ mV on Q6 and it changed becoming negative on Q9, -1.73 ± 3.07 mV, reaching -3.17 ± 0.85 mV on Q10.

F3

To complete the PBAEs belonging to the group F, the polycation F3 was applied for the development of the nano delivery system TOB-F3, and the zeta potential was measured for all the layers embedded onto the nanoparticles surface. Starting from $+17.07 \pm 3.12$ mV before starting the LbL, the potential plummeted to -23.63 ± 1.42 mV after the deposition of the alginate, and it turned back into positive by coating the aminoglycoside to the system, $+25.6 \pm 0.87$ mV. Besides, the charge became negative again due to an additional layer of sodium alginate, and it returned positive by coating the PBAE F3 onto the surface of the nanoparticles (figure 5.16).

In this case, F3 was able to manage the positivity of the drug until Q6. Therefore, after a considerable reduction occurring between Q1 and Q2, where the charge of tobramycin was correspondent to $+7.2 \pm 0.07$ mV, the potential slowly decreased. For instance, the degradation was gradual up to Q6, showing values equal to $+3.85 \pm 0.71$ mV on Q4, and close to 0 on Q6, 0.61 ± 0.16 mV. However, the potential was negative on Q7, -0.60 ± 0.2 mV heading to -3.27 ± 0.11 mV on Q10. As contrary the positivity of the polymer remained stable up to Q5, $+1.95 \pm 0.24$, and the charge was inverted into negative on Q6, -1.20 ± 0.07 mV, with no further increase of the negativity observed until Q10, where the potential was correspondent to -0.40 ± 0.49 mV.

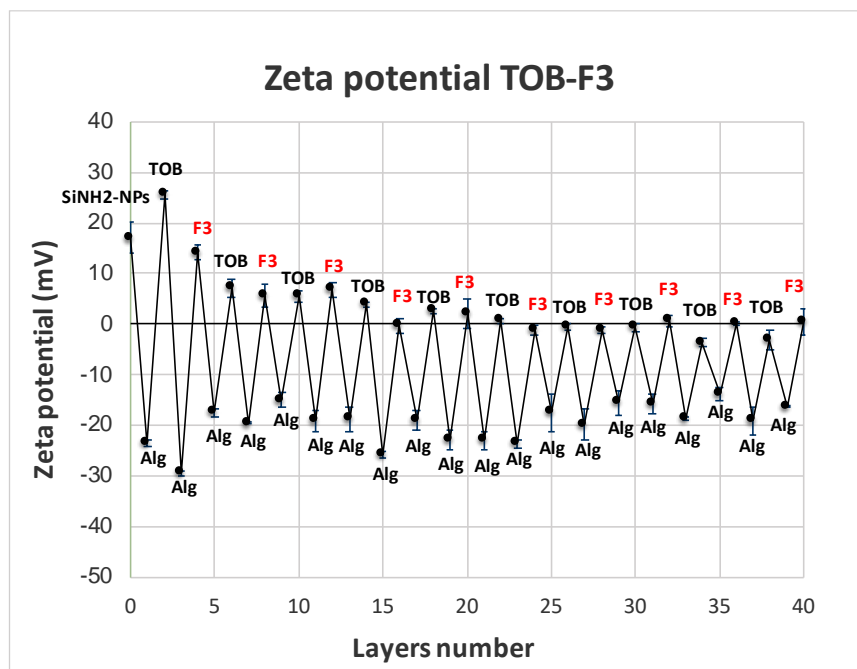


Figure 5.16: ζ potential for the coating system SI-NH₂NPs-Alg-TOB-Alg-F3. Mean \pm SD (N=1, n=3).

The controlled degradation the PBAEs of the group F greatly influenced the drug stability within the nanoconstructs. In particular, among the polymers heretofore analysed, F2 and F3 contributed to maintain positive the charge of the tobramycin until Q8 or Q9, whereas F1 until Q5, showing an attitude which was comparable to the previous polycations. As contrary, observing the zig-zag pathway of Alg-TOB, the charge of the drug was easily reversed into negative already from the second bilayer B2, followed by an increasing negativity caused by the presence of only alginate and drug into the matrix. Therefore, this confirmed that the application of PBAE and the choice of building up systems composed by quadruple layers

rather than bilayers, provided higher stability and a better management of drug and polyelectrolytes included into the nanoconstructs.

G1

The PBAEs of the group G are the last polymers applied for the development of delivery systems composed by quadruple layers were the tobramycin and PBAEs were entrapped onto silica nanocarriers. Regarding TOB-G1, the first quadruple layer was involving as follows: alginate, tobramycin, alginate and G1. Therefore, starting from the positive charge provided by the amino functionalisation of the particles, $+17.07 \pm 3.12$ mV, the potential dropped to -30.3 ± 0.4 mV after the deposition of the alginate onto the surface of the vectors. Additionally, the charge returned positive by coating the antibiotic, $+10.67 \pm 0.72$ mV, and it plummeted to -21.07 ± 0.90 mV, due to a new layer of sodium alginate. Finally, to complete the first quadruple layer, the 4th layer was represented by the polycation G1, which provided a positive charge equal to $+21.60 \pm 0.90$ mV (figure 5.17).

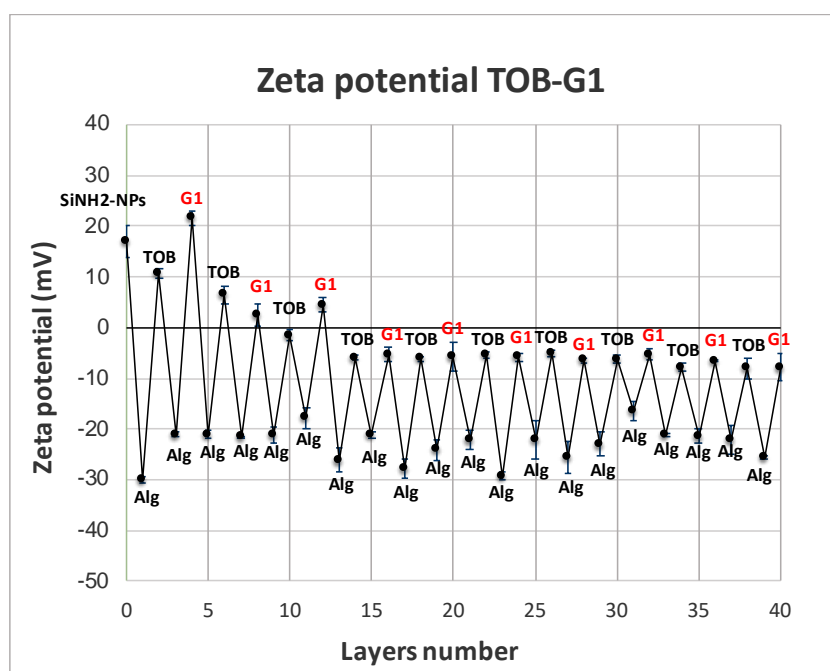


Figure 5.17: ζ potential for the coating system SI-NH₂NPs-Alg-TOB-Alg-G1. Mean \pm SD (N=1, n=3).

The positive charge of the drug was easily turned into negative after a reduction detected on Q2, $+6.48 \pm 0.32$ mV. From Q3, it became negative, -1.53 ± 0.66 mV, showing an increasing negativity on Q4, -5.99 ± 0.67 mV, which ended up to -8.05 ± 0.61 mV on Q10. As contrary G1

remained positive until Q3, $+4.49 \pm 1.53$ mV, providing a reversed potential from Q4, -5.24 ± 0.53 mV. However, the negative charge was quite stable up to Q6, -5.85 ± 0.7 mV, rising to -7.85 ± 0.7 mV on Q10.

G2

The zeta potential measurements were carried out also for the nanoconstruct TOB-G2 producing a typical zig-zag pathway which proved the success of tobramycin and PBAE deposition. As previously observed, the initial positive charge resulting from the measurement of the nanoparticles alone, changed into negative by adding the sodium alginate onto the system, -21.23 ± 3.52 mV. Then, the potential became positive again by layering the tobramycin, $+33.07 \pm 0.38$ mV, going back to negative with one further layer of sodium alginate, -28.03 ± 1.39 mV. Besides, the addition of the PBAE G2 contributed to form the first quadruple plus inverting into positive the charge, $+15.7 \pm 1.15$ mV (figure 5.18).

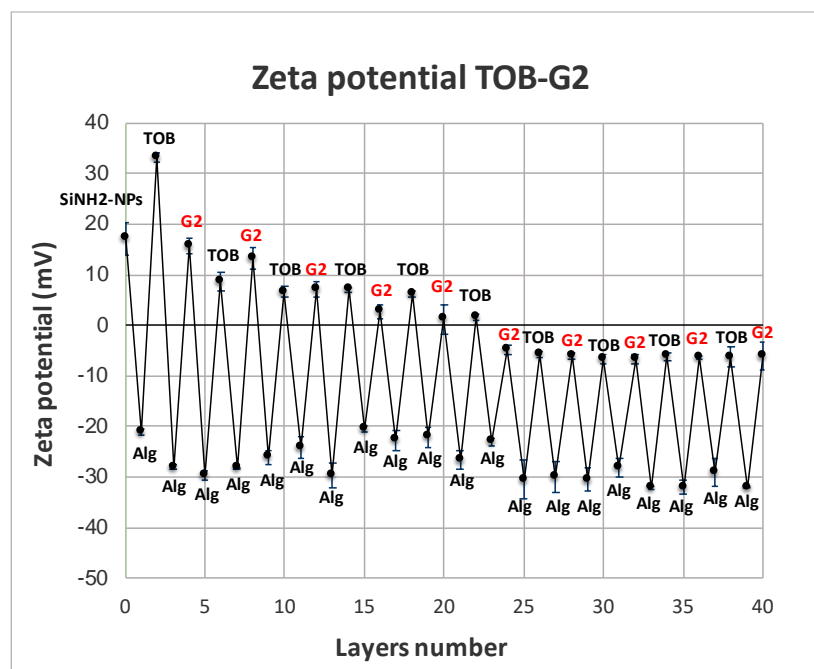


Figure 5.18: ζ potential for the coating system SI-NH₂NPs-Alg-TOB-Alg-G2. Mean \pm SD (N=1, n=3).

The charge of the drug remained positive until Q6, showing a decrease from the initial potential detected on Q1. Indeed, there was a drastic degradation between Q1 and Q2, where the potential was $+8.62 \pm 0.16$ mV, which slowly continued on Q4, $+7.01 \pm 1.51$ mV, and ending to $+1.57 \pm 0.98$ mV on Q6. Then, the charge dropped to -5.7 ± 0.68 mV, on Q7, with a

slight increase of the negativity heading to -6.33 ± 0.25 mV on Q10. However, the hydrolysis of the polymer gradually occurred, showing a potential of $+13.16 \pm 0.67$ mV on Q2, which was half-reduced on Q3, $+7.16 \pm 2.86$ mV. As contrary, the positivity then dropped to $+1.2 \pm 3.33$ mV on Q5, and an inversion of the charge was observed from Q6, -4.80 ± 0.65 mV, reaching -6.02 ± 0.24 mV on Q10.

G3

To complete the PBAEs belonging to the group G, a zig-zag pathway was also developed for the matrix TOB-G3. As heretofore described, all the quadruple layers were providing alternative charge due to the different polyelectrolytes embedded onto the system. For instance, also in this case, the positivity of the nanoparticles alone was reverted into negative by the sodium alginate, -21.7 ± 1.57 mV, with a return to a positive charge resulting from the coating of the aminoglycoside, $+14.87 \pm 0.85$ mV. Furthermore, a negative potential was detected after the deposition for the second time of the alginate, -26.37 ± 0.99 mV, followed by a further change of the charge by layering the polycation G3, $+16.6 \pm 1.54$ mV (figure 5.19).

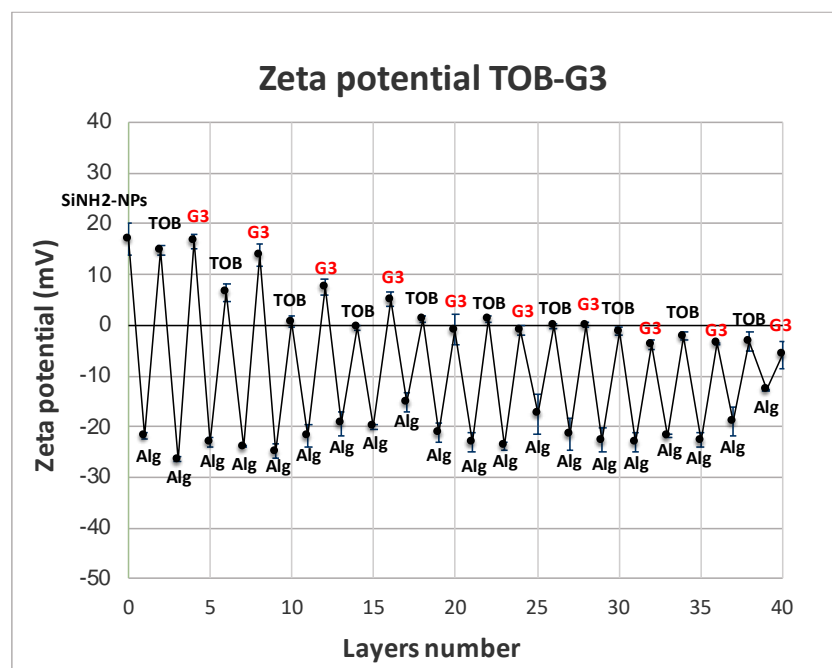


Figure 5.19: ζ potential for the coating system SI-NH₂NPs-Alg-TOB-Alg-G3. Mean \pm SD (N=1, n=3).

Overall, the reduction of the positivity for the drug mainly occurred among the first 3 quadruple layer. In particular, the initial positive charge of Q1, was $+6.48 \pm 0.32$ mV on Q2

and it dropped to 0.65 ± 0.18 mV on Q3. Then, the charge was stable to 0 until Q7, and it was turned into negative on Q8, -1.14 ± 3.54 mV, leading up to -5.7 ± 0.68 mV on Q10. On the other hand, a gradual degradation of the polymer was observed, until Q4, $+5.12 \pm 1.01$ mV, followed by a significant drop of its positivity on Q5, -0.28 ± 0.48 mV. Besides, from Q6 the charge became negative, -1.07 ± 1.08 mV, showing an increase of the negativity reaching -5.74 ± 0.5 mV on Q10.

Comparing the profiles of the group G, it was observed that G2 and G3 were able to manage the negativity of the sodium alginate, controlling the hydrolysis of the drug which in both cases after 10 quadruple layers showed a weak negative charge. However, the polymer G1 similarly degraded to the previous PBAEs with a reversion of the charge after the deposition of 3 quadruple layers. Despite that, considering the zig-zag profile of Alg-TOB, also in this case, there was an improvement of the stability of the drug, which highlight the importance of employing the PBAEs into the matrices plus the impact that the choice of the monomers could have on the hydrolysis of both polymer and drug.

Considering the zeta potential profiles of all the nanosystems TOB-PBAEs and the hydrolysis of the PBAEs detailed described in chapter 3, consistency was observed for the matrices including A2, A3, B2, B3, D3, E3, F1, F2, F3, G2 and G3. For instance, among the nanoconstructs involving polymers possessing piperazine (amine 1) as amine, a positive potential up to Q5 was detected only for the nano-system TOB-F1. As contrary most of the matrices possessing the amine 2, 4,4 trimethyldipiperidine, and 3, N-N bis [3-(methylamino) propyl] methylamine, showed a positive charge of both PBAE and drug for at least 5 quadruple layers. In particular, a positive potential until Q6 and Q7 was observed for the constructs TOB-B2 and TOB-F2, highlighting the ability of the PBAEs B2 and F2 to contrast the strong negativity of the sodium alginate.

Thermogravimetric analysis (TGA)

Thermogravimetric analysis (TGA) was performed to evaluate the weight loss distribution along the layers embedded onto the nanoparticles surface. Firstly, the experiment was carried out for the nanoconstruct Alg-TOB, then for the 18 delivery systems possessing

different PBAEs. The layers considered as object of analysis were as follows: B1, B3, B5, B7 and B10 for Alg-TOB, whereas Q1, Q3, Q5, Q7 and Q10 for TOB-PBAEs.

Bilayer: Alg-TOB

First of all, the TGA was pursued for the bilayer system Alg-TOB and the weight loss percentage is represented by the figures 5.20a and 5.20b below.

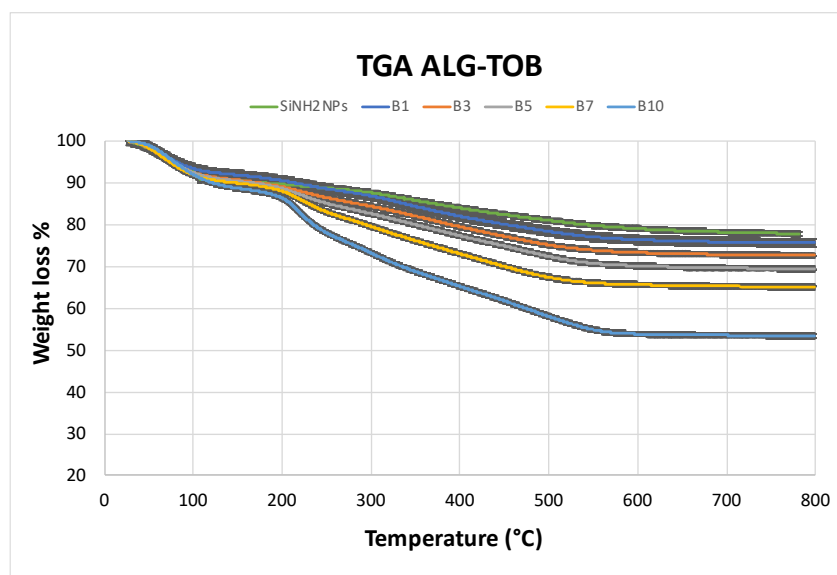


Figure 5.20a: Weight loss vs temperature for Si-NH₂NPs-Alg-TOB. Mean ± SD (N=1, n=2).

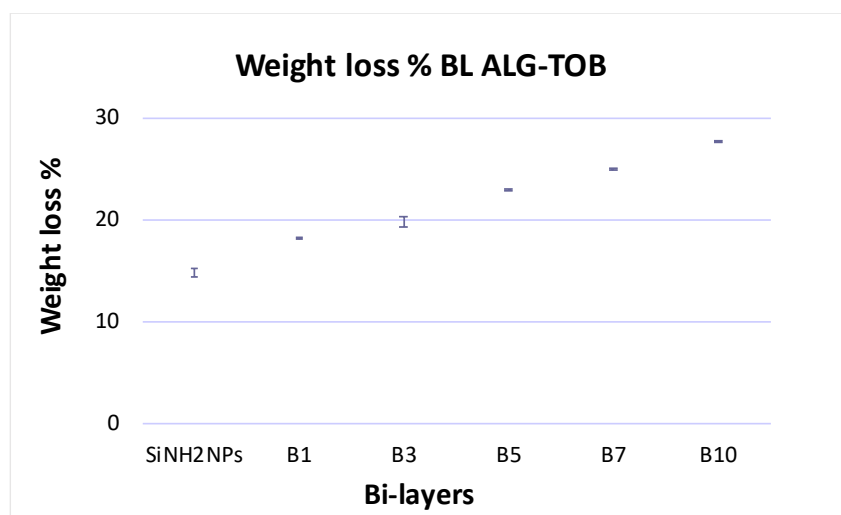


Figure 5.20b: Weight loss % for each B layer in the matrix Si-NH₂ NPs-Alg-TOB. Mean ± SD (N=1, n=2).

Initially, the weight loss percentage correspondent to the nanocarriers alone was equal to 14.80% ± 0.39, showing an increase of 3.02% after the first quadruple layer was coated onto

the matrix. In the average, it was observed that the weight loss rose up to $19.84\% \pm 0.03$ on B3, $22.97\% \pm 0.01$ on B5, $26.83\% \pm 0.01$ on B7 and $38.60\% \pm 0.22$ on B10. These results were compared to those of the nano delivery systems built up by quadruple layers with PBAE coated as polycations.

A1

Regarding TOB-A1, the initial value of weight loss of $14.86\% \pm 0.15$, typically representative of the silica amino functionalised nanoparticles, changed to $27.67\% \pm 1.10$ after the deposition of the first quadruple layer. Additionally, similarly to what described for Alg-TOB, it kept increasing once a new quadruple layer was embedded onto the system. Therefore, the percentage on Q3 was higher of 8% if compared to Q1, $35.79\% \pm 0.19$, reaching $41.63\% \pm 0.71$ on Q5. Finally, a further increment was detected with values of weight loss percentage equal to $53.10\% \pm 0.67$ on Q7 and $60.57\% \pm 0.62$ on Q10 (figures 5.21a-5.21b).

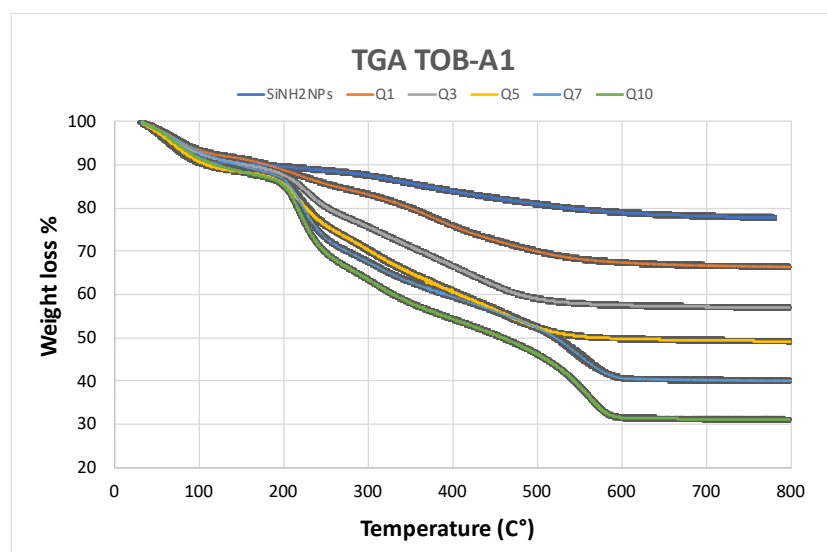


Figure 5.21a: Weight loss vs temperature for Si-NH₂NPs-Alg-TOB-Alg-A1. Mean \pm SD (N=1, n=2).

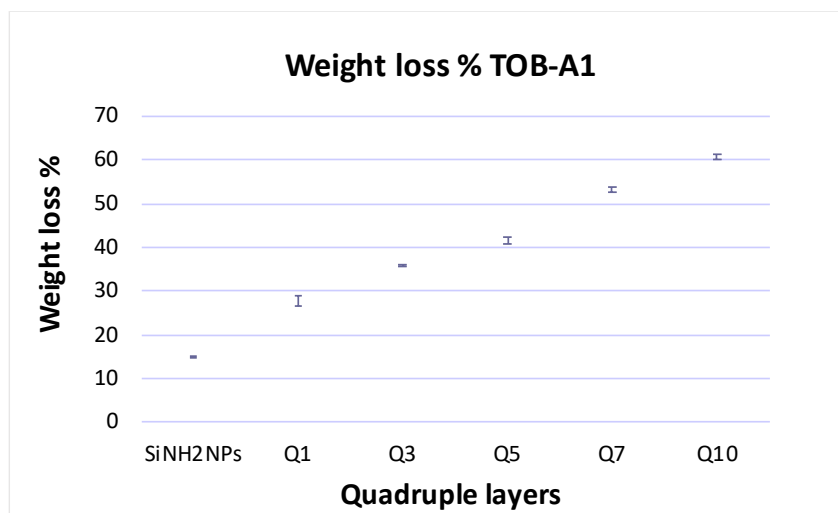


Figure 5.21b: Weight loss % among the QL for the matrix including TOB-A1. Mean \pm SD (N=1, n=2).

A2

The weight loss percentage was determined also for the nanoconstruct TOB-A2 showing an increase of the weight loss as previously observed (figure 5.22a).

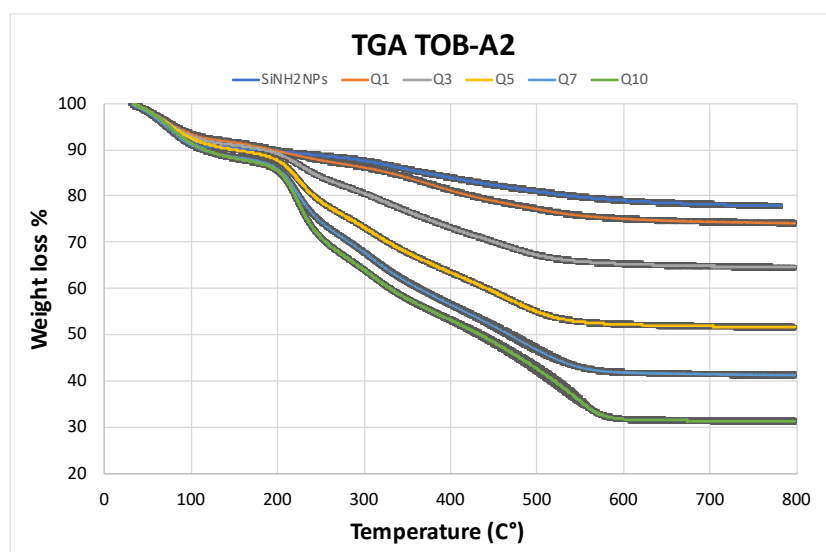


Figure 5.22a: Weight loss vs temperature for Si-NH₂NPs-Alg-TOB-Alg-A2. Mean \pm SD (N=1, n=2).

Starting from $14.86\% \pm 0.15$, the weight rose up to $19.32\% \pm 0.06$ on Q1, with an additional growth of 9% detected on Q3 and equal to $28.05\% \pm 0.37$. However, in this case, the weight loss % was higher than TOB-A1 (p-value < 0.05), with further increase of the percentage once more layers were coated onto the system. Thus, it was $40.85\% \pm 0.33$ on Q5, $49.71\% \pm 0.06$ on Q7 and $60.09\% \pm 0.83$ on Q10 (figure 5.22b).

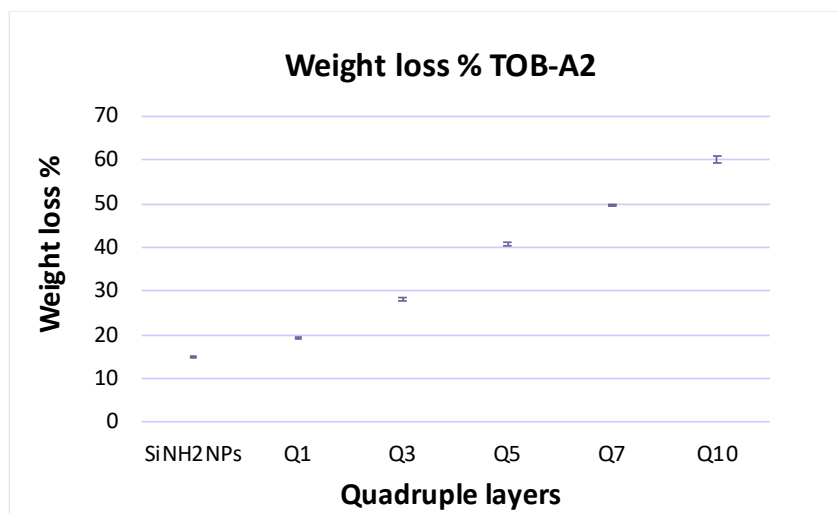


Figure 5.22b: Weight loss % among the QL for the matrix including TOB-A2. Mean \pm SD (N=1, n=2).

A3

The nano delivery system TOB-A3 was including the last polymer belonging to the group A and the weight loss distribution among the 10 quadruple layers is illustrated in the figure 5.23a.

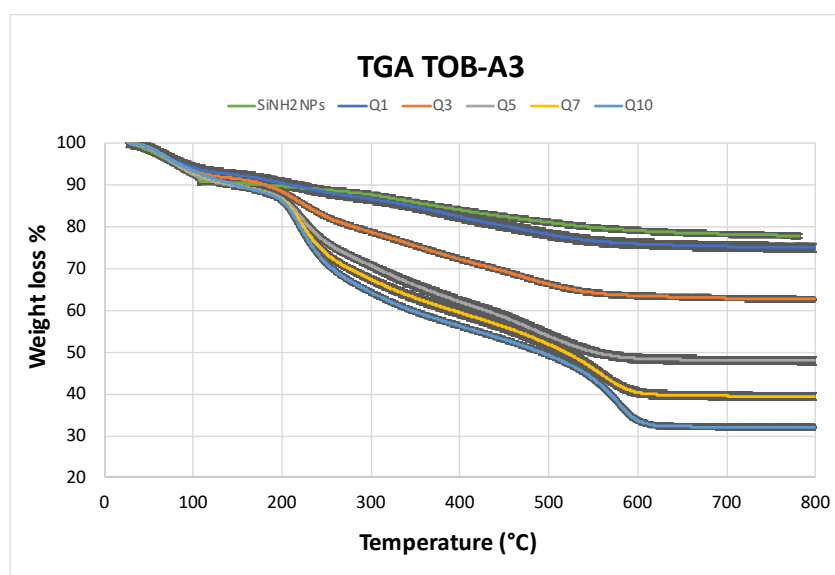


Figure 5.23a: Weight loss vs temperature for Si-NH₂NPs-Alg-TOB-Alg-A2. Mean \pm SD (N=1, n=2).

The weight loss % for the nanoparticles alone before starting the LbL was $14.80\% \pm 0.39$ and it rose on Q1 with a value equal to $19.09\% \pm 0.28$. Besides, the it kept increasing up to the last quadruple layer and in particular it was noticed that the profile of this system was similar to the ones of TOB-A1 and TOB-A2 (p-value > 0.05). Indeed, the weight loss was as follows:

30.73% \pm 0.1 on Q3, 44.62% \pm 0.99 on Q5, 53.64 \pm 0.57 on Q7 and 61.27% \pm 0.14 on Q10 (figure 5.23b).

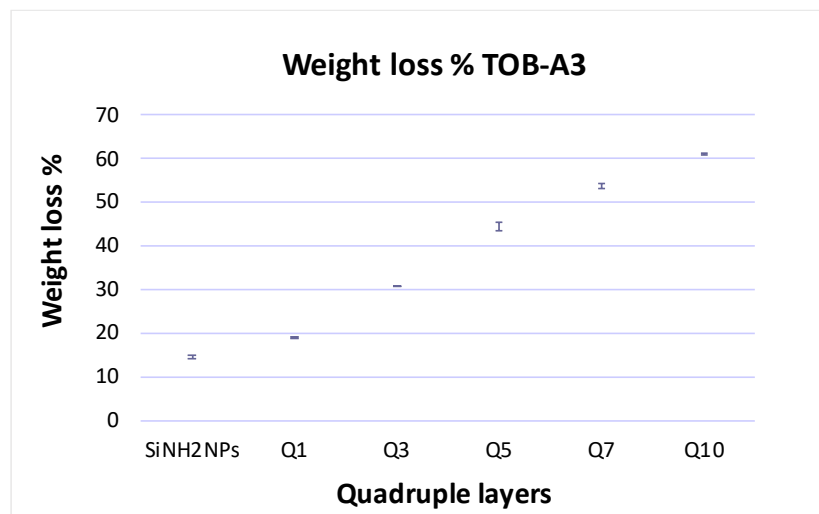


Figure 5.23b: Weight loss % among the QL for the matrix including TOB-A3. Mean \pm SD (N=1, n=2).

Overall, comparing the matrices formed by quadruple layers to Alg-TOB coating, a higher distribution of the weight loss % was observed among the layers which included the PBAEs rather than into the system possessing only alginate and the cargo. However, considering the nanoconstructs composed by the PBAEs of the group A no significant difference in the weight loss was noticed among the layers of the 3 nanocoatings (p -value $>$ 0.05). Therefore, the final quadruple layer Q10 was as follows: 60.57% \pm 0.62 for TOB-A1, 60.09% \pm 0.83 for TOB-A2 and 61.27% \pm 0.14 for TOB-A3.

B1

The thermogravimetric analysis was carried out also for the matrices having the PBAEs of the group B as polycations. Regarding B1, the weight loss percentage increased once a quadruple layer was coated onto the system, similarly to what previously observed for the nanocoatings TOB-A1, TOB-A2 and TOB-A3 (figure 5.24a).

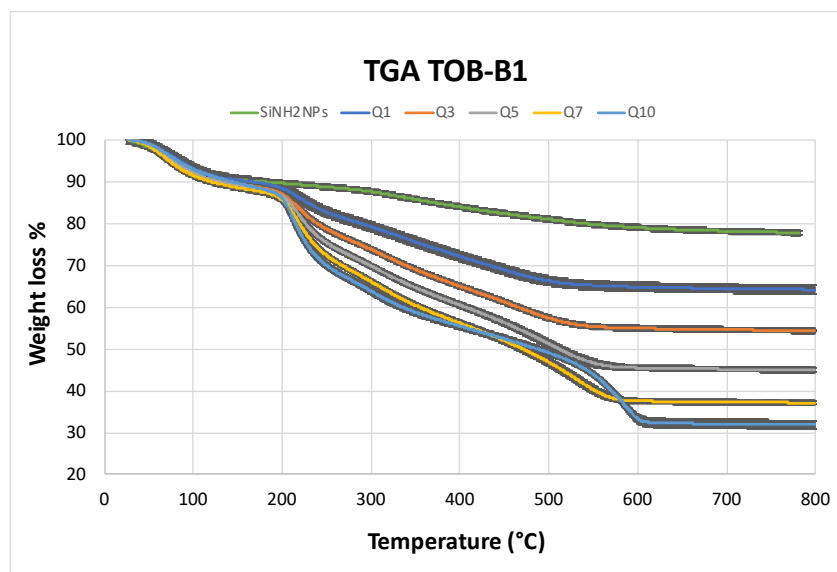


Figure 5.24a: Weight loss vs temperature for Si-NH₂NPs-Alg-TOB-Alg-B1. Mean \pm SD (N=1, n=2).

Starting from $14.80\% \pm 0.39$, the percentage was doubled after the deposition of the first quadruple layer, $28.98\% \pm 0.10$. Additionally, a further increase of 9% was detected on Q3, showing a value of $37.50\% \pm 0.28$, followed by an extra on Q5, $47.07\% \pm 0.01$. Then, the percentage steadily changed on Q7 and Q10, which was respectively correspondent to $54.33\% \pm 0.23$ and $61.06\% \pm 1.35$ (figure 5.24b).

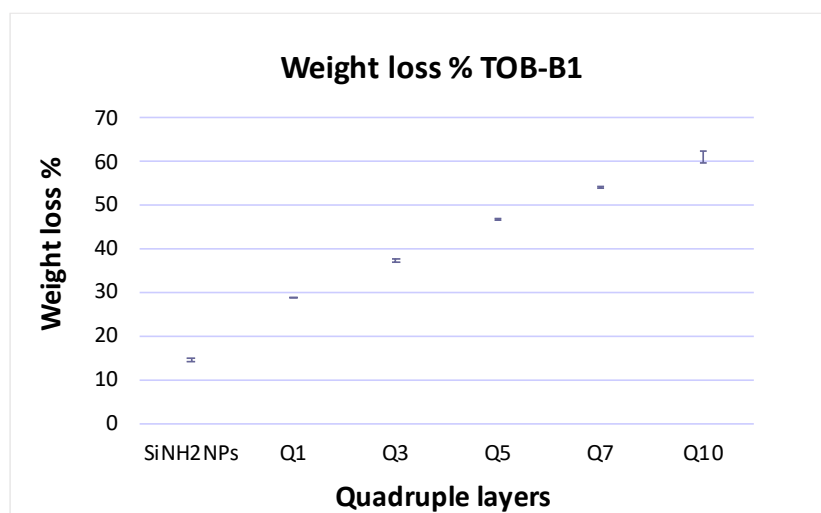


Figure 5.24b: Weight loss % among the QL for the matrix including TOB-B1. Mean \pm SD (N=1, n=2).

B2

The organic content distribution among the 10 quadruple layers was evaluated also for the nano delivery system TOB-B2 (figure 5.25a).

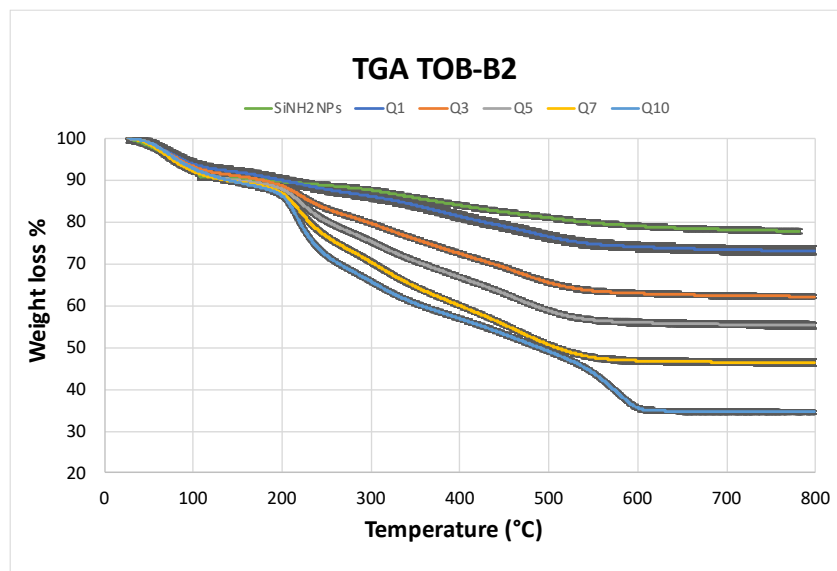


Figure 5.25a: Weight loss vs temperature for Si-NH₂NPs-Alg-TOB-Alg-B2. Mean \pm SD (N=1, n=2).

In this case, the major increase occurred between Q1 and Q3 with a constant increase of 8% of the weight loss on Q5 and Q3 followed by a rise of 13% on the last quadruple layer. Therefore, the weight loss percentage detected for this nanoconstruct was as follows: 20.79% \pm 0.13 on Q1, 31.09% \pm 0.18 on Q3, 37.23% \pm 0.16 on Q5, 45.76% \pm 0.98 on Q7 and 58.25% \pm 0.55 on Q10 (figure 5.25b).

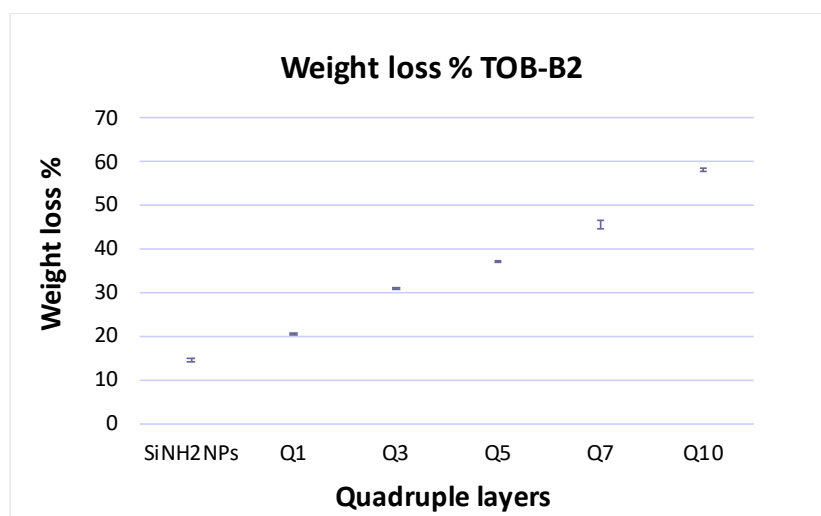


Figure 5.25b: Weight loss % among the QL for the matrix including TOB-B2. Mean \pm SD (N=1, n=2).

B3

To complete the analysis of the matrices including the PBAEs of the group B, the TGA was pursued also for the nanoconstruct TOB-B3 (figure 5.26a).

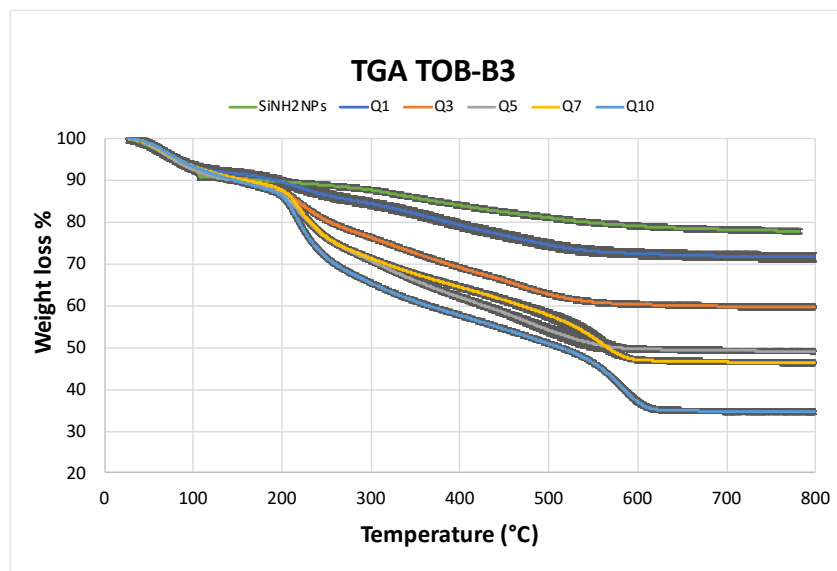


Figure 5.26a: Weight loss vs temperature for Si-NH₂NPs-Alg-TOB-Alg-B3. Mean \pm SD (N=1, n=2).

Initially, the weight loss percentage was low due to the amino functionalisation of the silica nanoparticles. Then, as previously observed, the increase was dependent on the number of layers embedded onto the system. Thus, it rose up to 21.67% \pm 0.50 on Q1, followed by a further increment which was equal to 32.96% \pm 0.18 on Q3. Besides, there was an additional rise of 9% on Q5 showing a value of 43.36% \pm 0.58 plus a steady improvement on Q7 and Q10 with respectively a percentage of 46.93% \pm 0.65 and 58.63% \pm 0.48 (figure 5.26b).

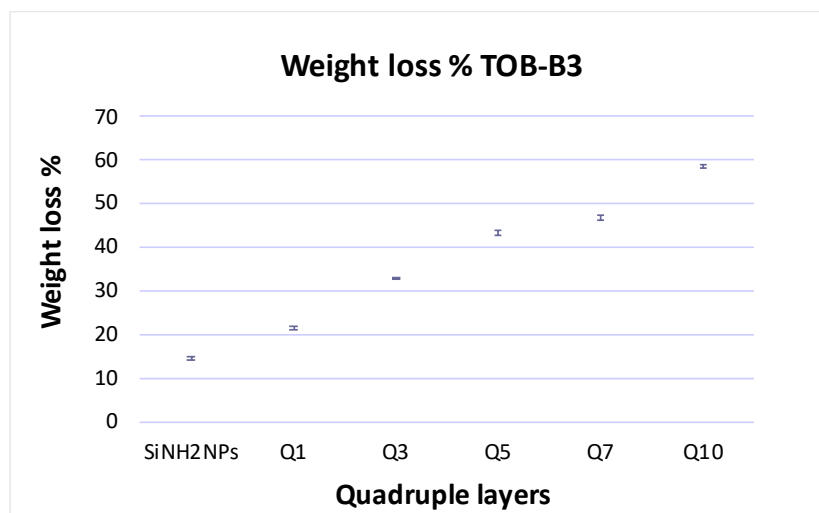


Figure 5.26b: Weight loss % among the QL for the matrix including TOB-B3. Mean \pm SD (N=1, n=2).

Overall, similarly to what previously described, the presence of PBAEs and the choice of building up matrices composed by quadruple layers rather than bilayers influenced the amount of organic content which was definitely lower in the Alg-TOB system when compared to the nanocoatings TOB-PBAEs (p -value < 0.05). However, among the coatings the group B, TOB-B1 showed the highest percentage of weight loss on Q10, $61.06\% \pm 1.35$ (p -value < 0.05), followed by TOB-B3, $58.63\% \pm 0.48$, and TOB-B2, $58.25\% \pm 0.55$ which instead presented similar profiles (p -value > 0.05). Furthermore, no substantial difference was observed among the nanoconstructs possessing the polycations of both groups A and B (p -value > 0.05).

D1

The organic matter determination was defined also for the matrices composed by the polymers of the group D (figure 5.27a).

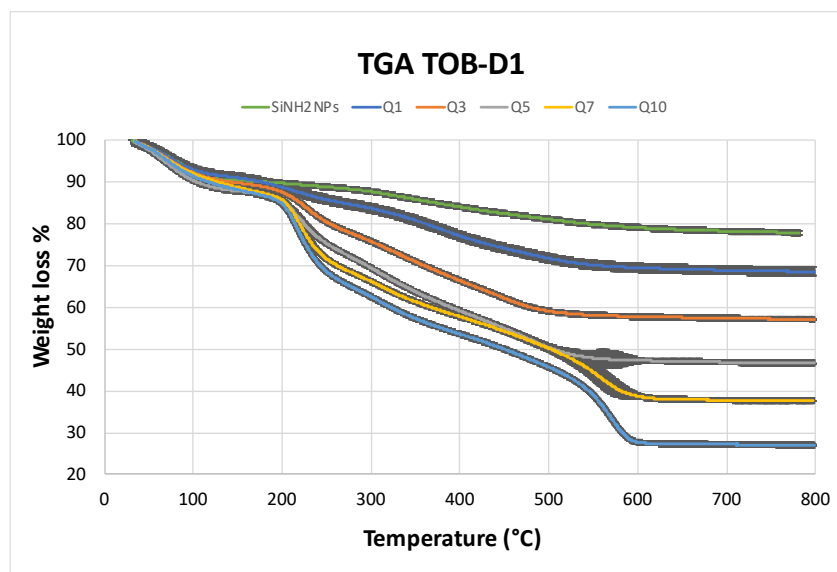


Figure 5.27a: Weight loss vs temperature for Si-NH₂NPs-Alg-TOB-Alg-D1. Mean \pm SD (N=1, n=2).

The initial weight loss percentage changed into 24.40% \pm 0.26 on Q1 with a growth of 10% on Q3, 34.97% \pm 0.08. Additionally, the amount kept increasing until Q10 showing an increment of the percentage as follows: 43.66% \pm 0.74 on Q5, 54.33% \pm 0.02 on Q7 and 64.26% \pm 0.33 representative of the last quadruple layer Q10 (figure 5.27b).

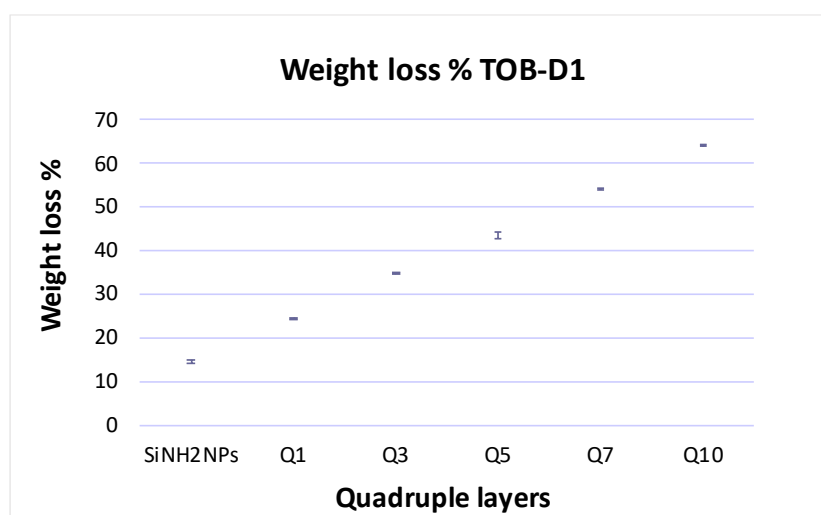


Figure 5.27b: Weight loss % among the QL for the matrix including TOB-D1. Mean \pm SD (N=1, n=2).

D2

The figures 5.28a and 5.28b illustrate the mass of Q1, Q3, Q5, Q7 and Q10 for the sample TOB-D2 after being heated up to 800°C.

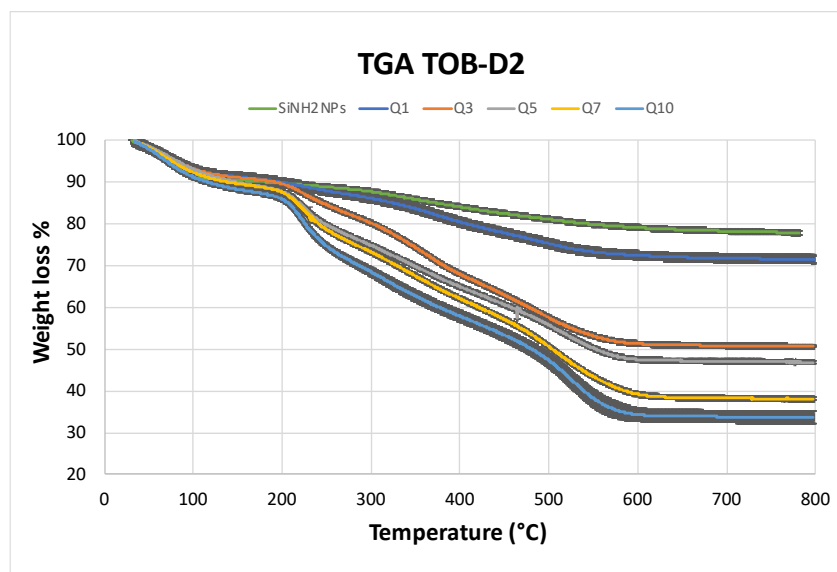


Figure 5.28a: Weight loss vs temperature for Si-NH₂NPs-Alg-TOB-Alg-D2. Mean ± SD (N=1, n=2).

The profile was similar to the one of TOB-D1 showing a slightly decrease of the weight loss distribution among the quadruple layers (p-value > 0.05). In particular, an increase of 7% was detected once the first quadruple layer was coated onto the silica amino-functionalised nanoparticles, 21.53% ± 0.13. This amount was doubled on Q3, 42.53% ± 0.24, and moderately changed on Q5 with a rise of only 4%, 46.16% ± 0.09. Finally, the rate of weight loss varied to 54.16% ± 0.17 on Q7 with a small increment of only 3% on Q10, showing a percentage equal to 57.47% ± 1.29 (figure 5.28b).

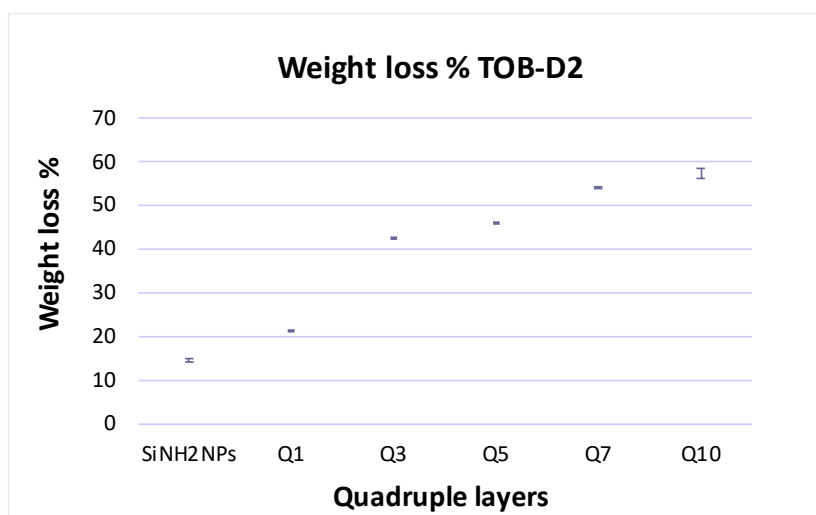


Figure 5.28b: Weight loss % among the QL for the matrix including TOB-D2. Mean ± SD (N=1, n=2).

D3

The nano-delivery system the PBAE D3 was also analysed to observe the modulation of its mass after the layer by layer deposition (figure 5.29a).

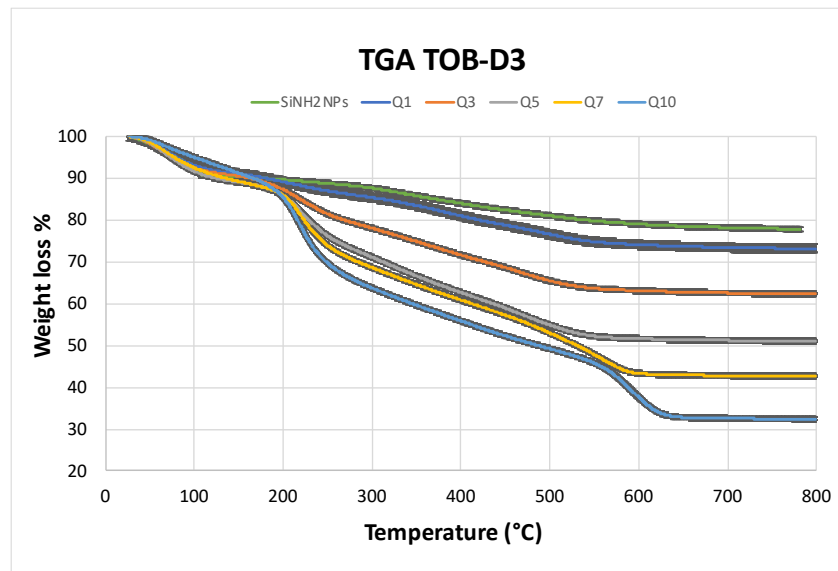


Figure 5.29a: Weight loss vs temperature for Si-NH₂NPs-Alg-TOB-Alg-D3. Mean ± SD (N=1, n=2).

Starting from 14.80% ± 0.39, there was a growth of the weight loss % of 5% by measuring Q1, 19.92% ± 0.35, followed by a considerable increase of 11% on Q3, 30.08% ± 0.30. Furthermore, an additional rise was observed on Q5, 40.60% ± 0.10, on Q7, 49.95% ± 0.14, followed by a further increment of 13% for the weight loss of Q10, 62.59% ± 0.49 (figure 5.29b).

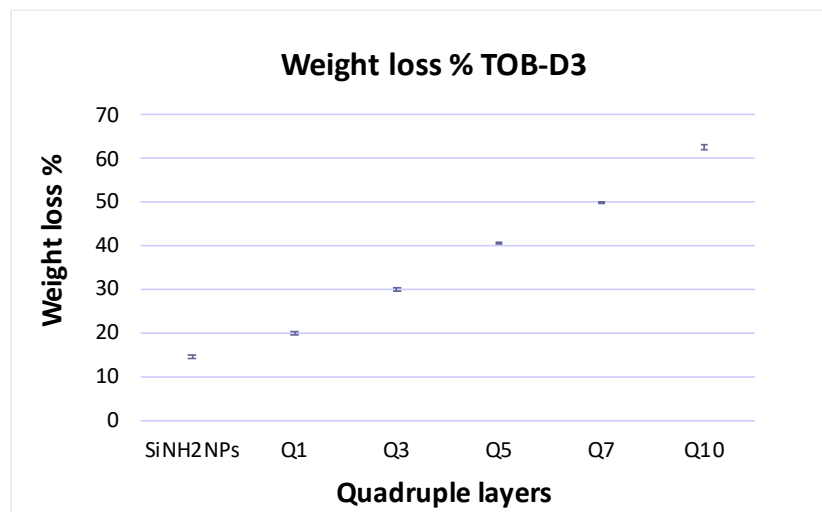


Figure 5.29: Weight loss % among the QL for the matrix including TOB-D3. Mean ± SD (N=1, n=2).

In this case, the TGA highlighted the difference among the 3 matrices of the group D (p-value < 0.05). For instance, the profile of TOB-D1 provided the highest amount of organic content for Q10, $64.26\% \pm 0.33$, if compared to TOB-D2 and TOB-D3 but also considering the previous nanoconstructs of the groups A and B. Besides, this value was followed by the measured weight loss of Q10 for TOB-D3, $62.59\% \pm 0.49$, and TOB-D2, $57.47\% \pm 1.29$, which instead was the lowest percentage detected among all the nanocoatings previously described (p-value < 0.05).

E1

Regarding TOB-E1, the weight loss for the nanocarriers alone was $14.86\% \pm 0.15$, and it increased of 11% after the deposition of the first quadruple layer, $25.86\% \pm 0.03$. Afterwards, the rate kept rising up to Q10. In particular, a growth of 12% was observed on Q3, $37.25\% \pm 0.43$, followed by a constant increment of 6-7% on both Q5 and Q7 showing values respectively equal to $44.03\% \pm 1.99$ and $50.28\% \pm 0.22$. Finally, a small increase of 4% was observed on Q10, where the percentage of weight loss was correspondent to $54.37\% \pm 0.97$ (figures 5.30a and 5.30b).

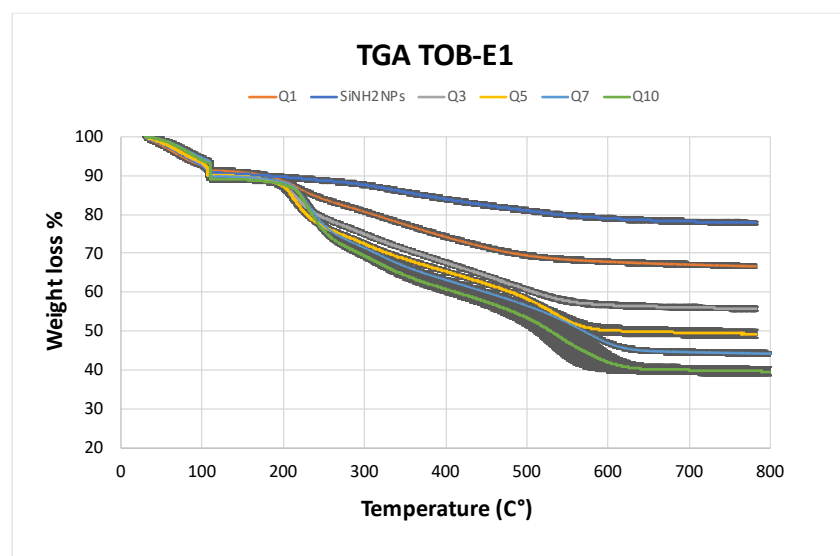


Figure 5.30a: Weight loss vs temperature for Si-NH₂NPs-Alg-TOB-Alg-E1. Mean ± SD (N=1, n=2).

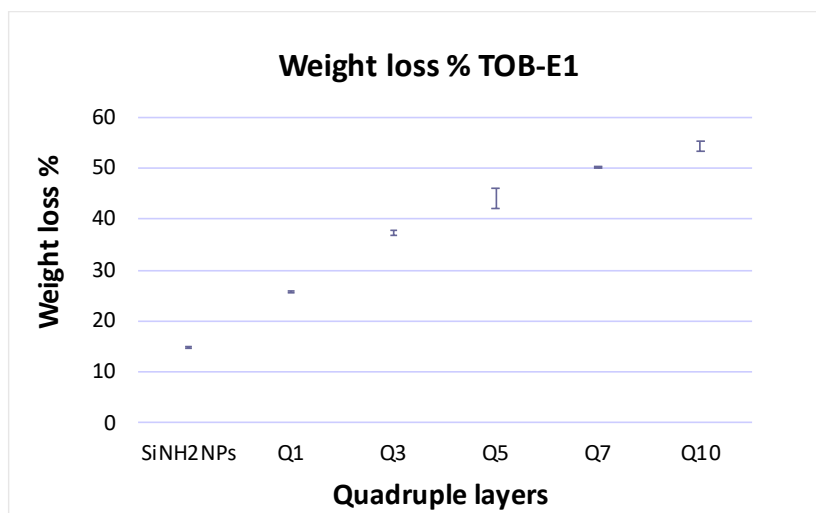


Figure 5.30b: Weight loss % among the QL for the matrix including TOB-E1. Mean \pm SD (N=1, n=2).

E2

The evaluation of the weight loss for the matrix TOB-E2 was determined by heating up to 800°C the sample considering the quadruple layers Q1, Q3, Q5, Q7 and Q10 (figure 5.31a). The weight loss % was initially 14.86% \pm 0.15 for the nanoparticles alone and it doubled to 23.98% \pm 0.10 on Q1. The amount kept increasing of 11% on Q3 and Q5, reporting values respectively equal to 34.74% \pm 0.88, and 45.43% \pm 0.10. Then, there was an increment of 8% on Q7, 53.12% \pm 0.39, followed by a rise of 6% on Q10 where the percentage was correspondent to 59.36% \pm 0.09 (figure 5.31b).

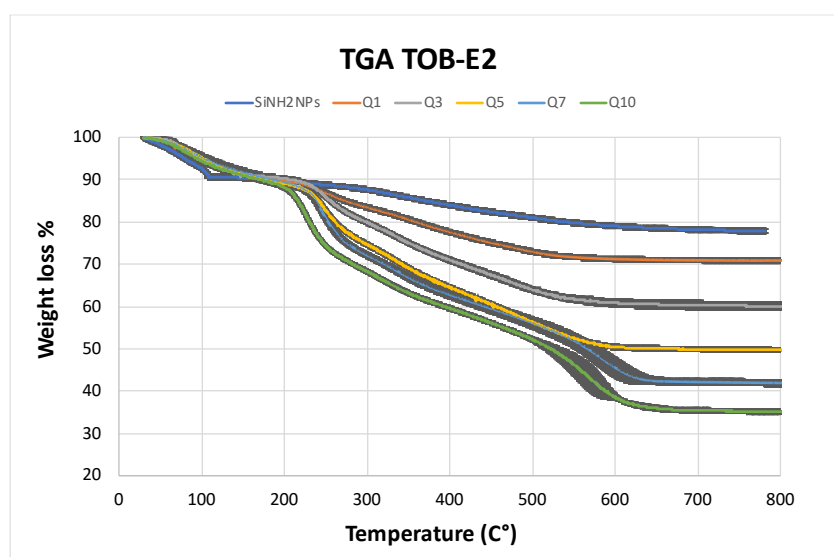


Figure 5.31a: Weight loss vs temperature for Si-NH₂NPs-Alg-TOB-Alg-E2. Mean \pm SD (N=1, n=2).

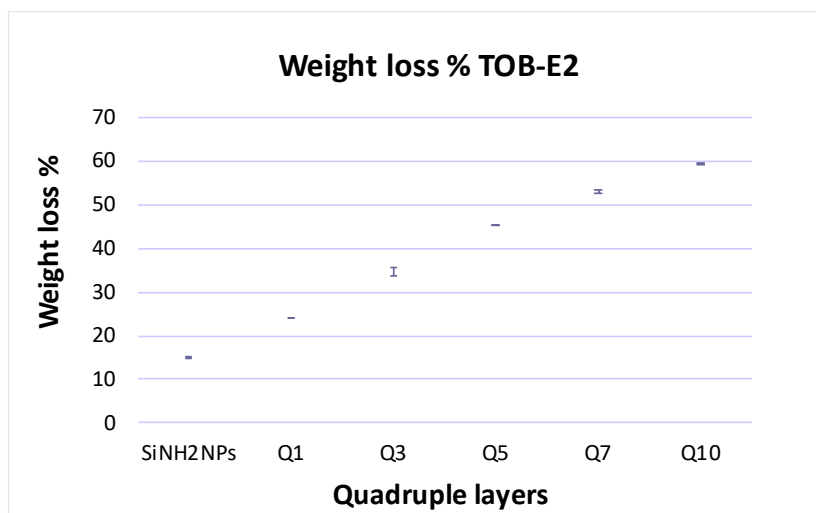


Figure 5.31b: Weight loss % among the QL for the matrix including TOB-E2. Mean \pm SD (N=1, n=2).

E3

The coating including the polycation E3 ended the matrices formed by PBAEs of the group E. (figure 5.32a).

Starting from $14.80\% \pm 0.39$, an increment of 9% was detected on Q1, $23.07\% \pm 0.27$. In this case there was a slower growth of the weight loss % among the all quadruple layers if compared to the previous matrix TOB-E2. For instance, the amount of mass loss was $36.09\% \pm 1.41$ on Q3, $43.03\% \pm 1.09$ on Q5, $47.55\% \pm 0.47$ on Q7 and finally $56.86\% \pm 0.13$ on Q10 (figure 5.32b).

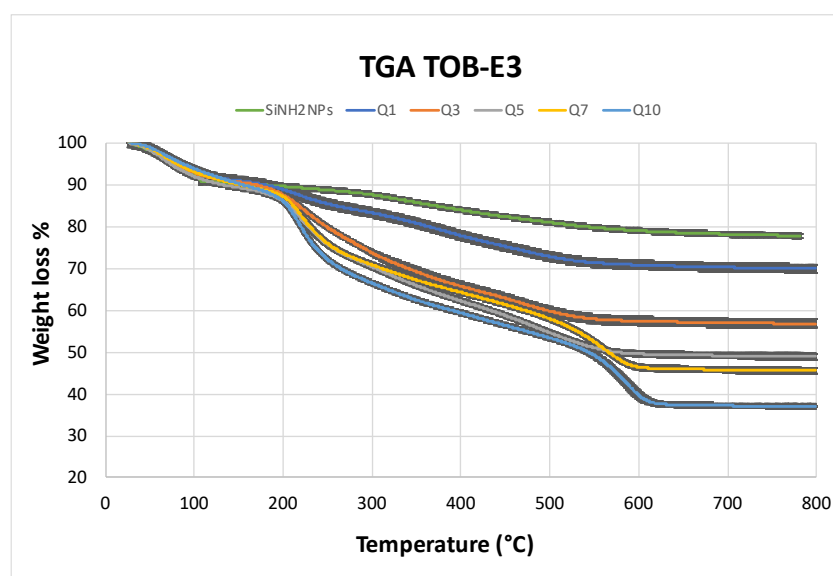


Figure 5.32a: Weight loss vs temperature for Si-NH₂NPs-Alg-TOB-Alg-E3. Mean \pm SD (N=1, n=2).

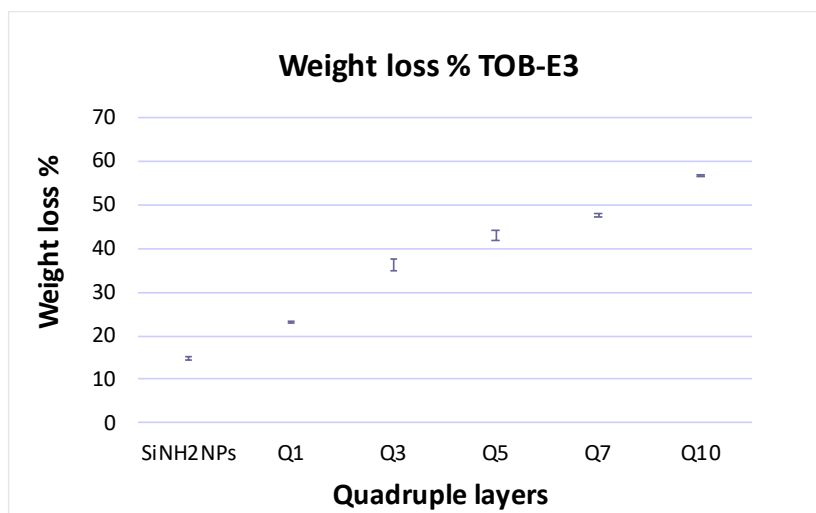


Figure 5.32b: Weight loss % among the QL for the matrix including TOB-E3. Mean \pm SD (N=1, n=2).

To sum up, the matrices having the PBAEs of the group E as polycations showed a gradual increase of the organic content percentage distributed among the 10 quadruple layers. For instance, the values gained from these nanoconstructs presented the lowest sample mass observed in all the systems described before. Therefore, in this case, considering Q10, it was observed that TOB-E2, $59.36\% \pm 0.09$, had the greatest rate among the nano delivery systems of the group E (p -value < 0.05), followed by TOB-E3, $56.86\% \pm 0.13$, and TOB-E1, $54.37\% \pm 0.97$, which was the smallest value so far detected (p -value > 0.05).

F1

The weight loss distribution was evaluated also for the coatings including the polymers F1, F2 and F3 as PBAEs. Regarding F1, the weight loss percentage was higher than those of the matrices previously analysed (figure 5.33a).

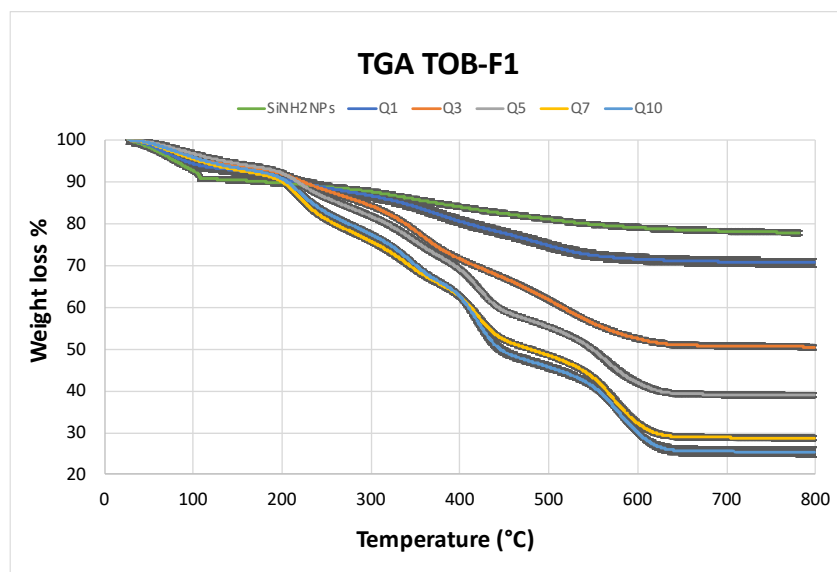


Figure 5.33a: Weight loss vs temperature for Si-NH₂NPs-Alg-TOB-Alg-F1. Mean ± SD (N=1, n=2).

Initially the mass loss before the LbL process was correspondent to $14.80\% \pm 0.39$ and it shifted to $23.73\% \pm 0.10$ once the first 4 layers, alginate, tobramycin, alginate, and F1, were embedded onto the surface of the silica amino-functionalised nanoparticles. Then, the rate of Q3, $45.25\% \pm 0.63$, was doubled if compared to the value of Q1 and it kept increasing up to Q10. The weight loss detected for the other quadruple layers was as follows: $57.82\% \pm 0.61$ on Q5, $66.70\% \pm 0.45$ on Q7 and lastly $70.43\% \pm 1.19$ on Q10 (figure 5.33b).

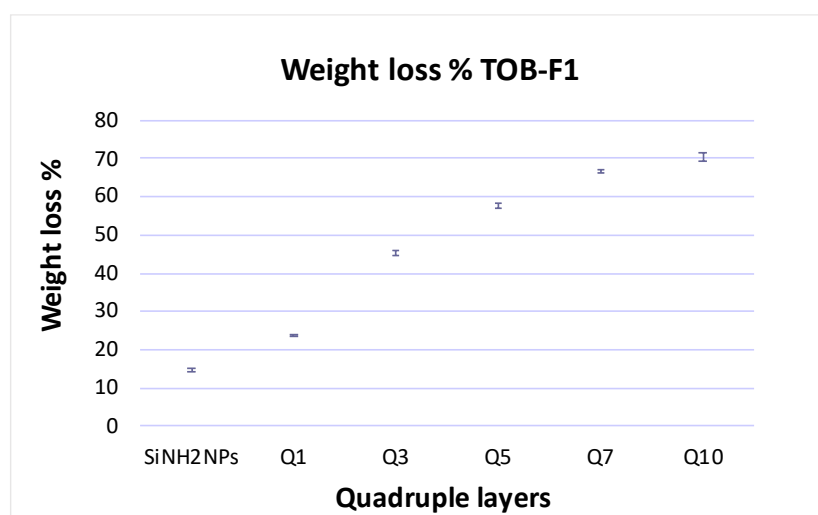


Figure 5.33b: Weight loss % among the QL for the matrix including TOB-F1. Mean ± SD (N=1, n=2).

F2

The TGA was carried out also for the nanoconstruct TOB-F2 and the weight mass distribution its variation among the layers are reported by the figures 5.34a and 5.34b below.

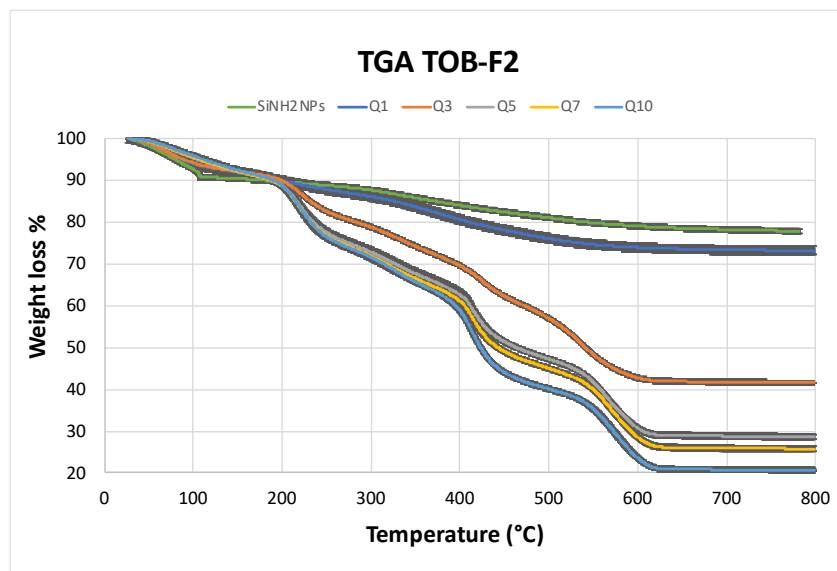


Figure 5.34a: Weight loss vs temperature for Si-NH₂NPs-Alg-TOB-Alg-F2. Mean \pm SD (N=1, n=2).

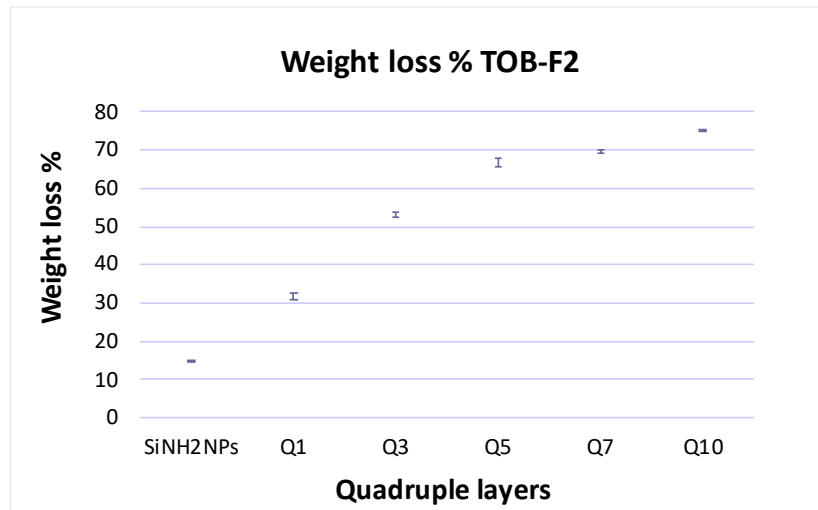


Figure 5.34b: Weight loss % among the QL for the matrix including TOB-F2. Mean \pm SD (N=1, n=2).

Starting from a value of $14.80\% \pm 0.39$, the weight loss percentage changed to $31.72\% \pm 0.76$ on Q1, and it considerably rose up to $53.00\% \pm 0.58$ on Q3. Then, there was a growth of over 13% between Q3 and Q5, showing an amount equal to $66.65\% \pm 1.11$ on Q5, with a tiny increase of 3% on Q7, $69.68\% \pm 0.61$. Finally, a rise of 6% was observed between Q7 and Q10, and the amount of Q10 was correspondent to $75.12\% \pm 0.09$.

F3

To complete the nanoconstruct belonging to the group F, the TGA was finally carried out for the matrix TOB-F3 following the same conditions adopted for the analysis of the previous systems (figure 5.35a).

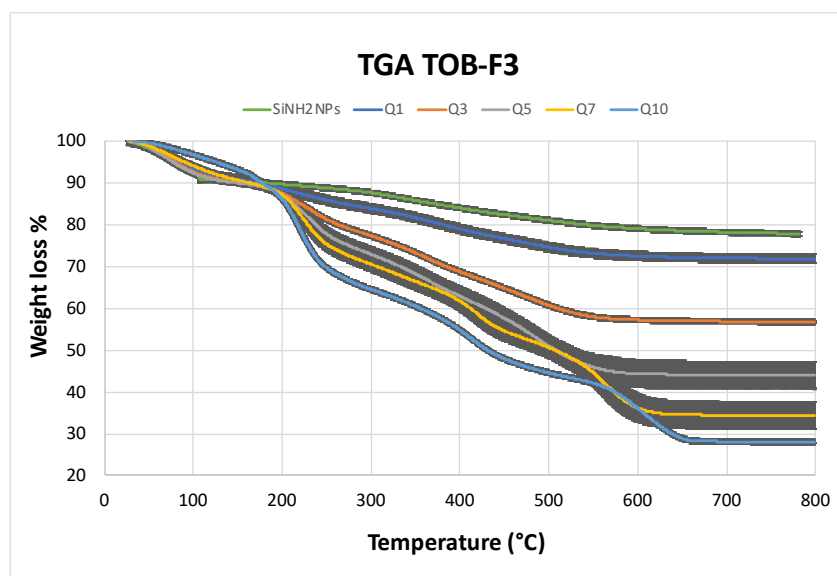


Figure 5.35a: Weight loss vs temperature for Si-NH₂NPs-Alg-TOB-Alg-F3. Mean \pm SD (N=1, n=2).

The weight loss % for the nanoparticles alone was equal to $14.80\% \pm 0.39$, and it increased of 7% on Q3 showing an amount of $21.34\% \pm 0.15$. Furthermore, the weight loss kept increasing with an increment of 14% on Q5, $35.72\% \pm 0.10$, shifting to $59.03\% \pm 3.92$ on Q7. Finally, a growth of 9% was detected for Q10, showing a value of $68.94\% \pm 0.28$ (figure 5.35b).

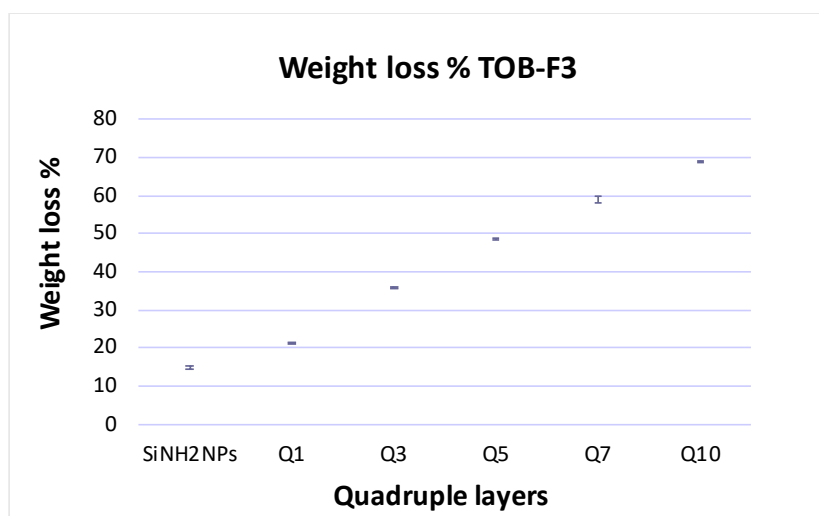


Figure 5.35b: Weight loss % among the QL for the matrix including TOB-F3. Mean \pm SD (N=1, n=2).

Differently to what previously observed, the matrices TOB-F1, TOB-F2 and TOB-F3 represented the nanoconstructs with highest amount of organic content detected for the last quadruple layer Q10. For instance, TOB-F2 showed the greatest value, $75.12\% \pm 0.09$, followed by TOB-F1, $70.43\% \pm 1.19$, and TOB-F3, $68.94\% \pm 0.28$ (p -value < 0.05). Therefore, these values highlighted a higher stability denoted between drug and polymers and the importance in choosing the monomers composing the PBAEs whose structure could influence the success of the building up system via electrostatic interactions.

G1

The last group of polymers was composed by G1, G2 and G3. Concerning the matrix TOB-G1, the modulation of the sample weigh loss is reproduced by the figure 5.36a below.

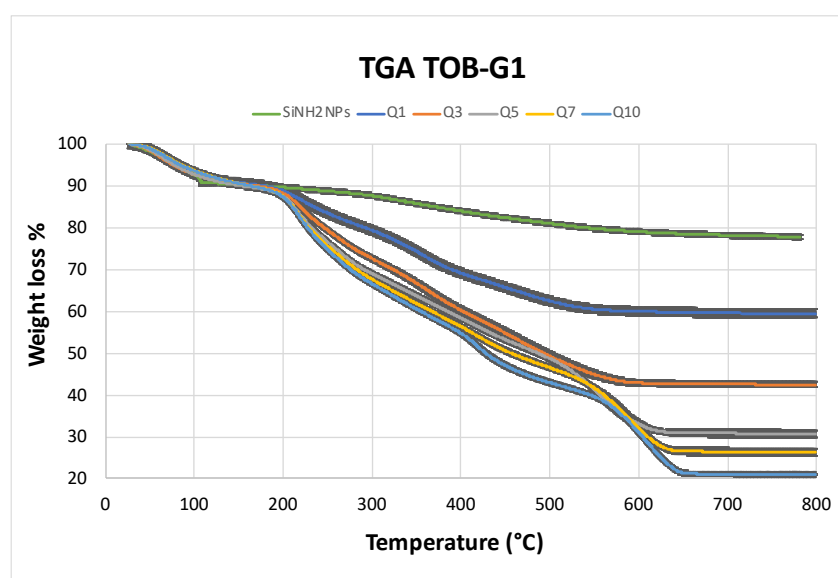


Figure 5.36a: Weight loss vs temperature for Si-NH₂NPs-Alg-TOB-Alg-G1. Mean \pm SD (N=1, n=2).

Starting from $14.80\% \pm 0.39$, the amount of weight loss increased of 19% on Q1, showing a value of $33.53\% \pm 0.30$. Then, the sample mass loss continued rising on Q3 with a further 17% on the amount detected for Q1, which ended to $50.29\% \pm 0.47$. Moreover, a growth of 12% added to the rate of Q3 was detected on Q5, $62.00\% \pm 0.96$, followed by a reduced increment of the percentage for both Q7 and Q10 which showed values correspondent to respectively, $67.36\% \pm 1.09$, and $72.61\% \pm 0.48$. The number measured for the last quadruple layer represented the second highest amount of organic content for Q10 detected among all the

other systems following the one of Q10 for TOB-F2 which instead was equal to $75.12\% \pm 0.09$ (figure 5.36b) (p -value < 0.05).

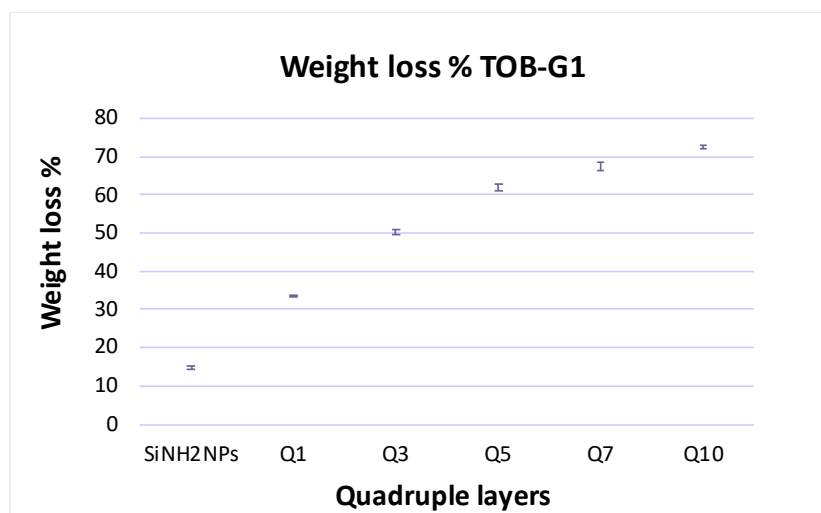


Figure 5.36b: Weight loss % among the QL for the matrix including TOB-G1. Mean \pm SD (N=1, n=2).

G2

The modulation of the mass loss depending on the change of the temperature was investigated also for the G2 layered nanoparticles and the results are shown in both figures 5.37a and 5.37b.

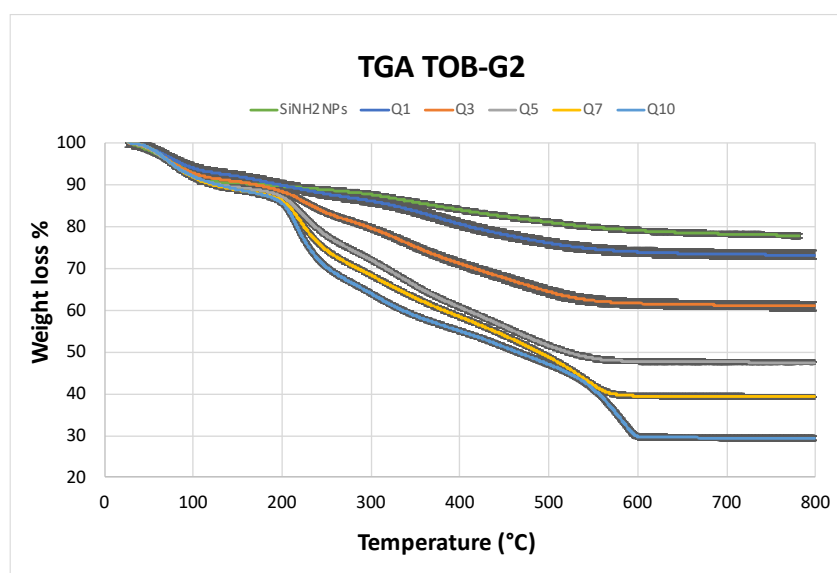


Figure 5.37a: Weight loss vs temperature for Si-NH₂NPs-Alg-TOB-Alg-G2. Mean \pm SD (N=1, n=2).

The initial weight loss percentage, $14.80\% \pm 0.39$, was object of an increase of 6% after the first quadruple layer was coated onto the vector surface, reporting a rate of $20.81\% \pm 0.08$. Then, the major increment was observed between Q3 and Q7, where in the first case there was a growth of 11% of the amount correspondent to $31.72\% \pm 0.76$, followed by an additional rise of 13% on Q5, $44.41\% \pm 0.45$, and 8% on Q7, $52.51\% \pm 0.01$. Lastly, after an improvement of extra 10%, the weight loss percentage of Q10 was equal to $62.62\% \pm 0.43$ (figure 5.37b).

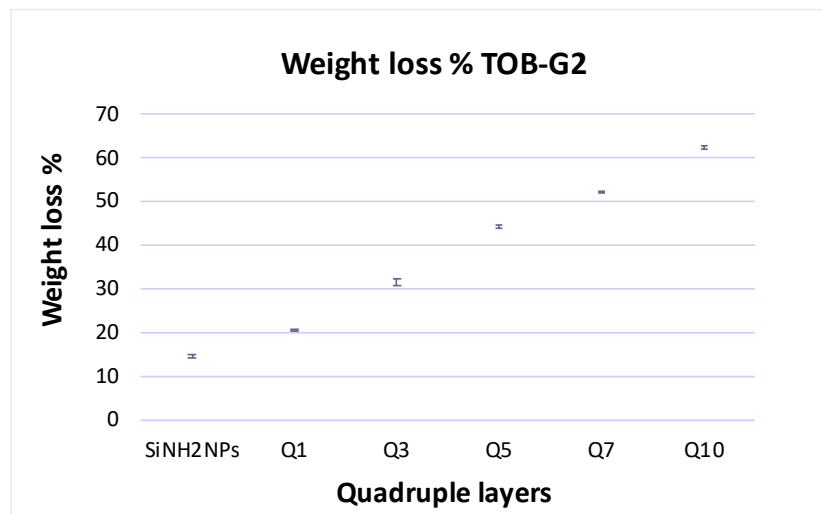


Figure 5.37b: Weight loss % among the QL for the matrix including TOB-G2. Mean \pm SD (N=1, n=2).

G3

To conclude the TGA was finally performed for the nanoconstruct TOB-G3 (figure 5.38a).

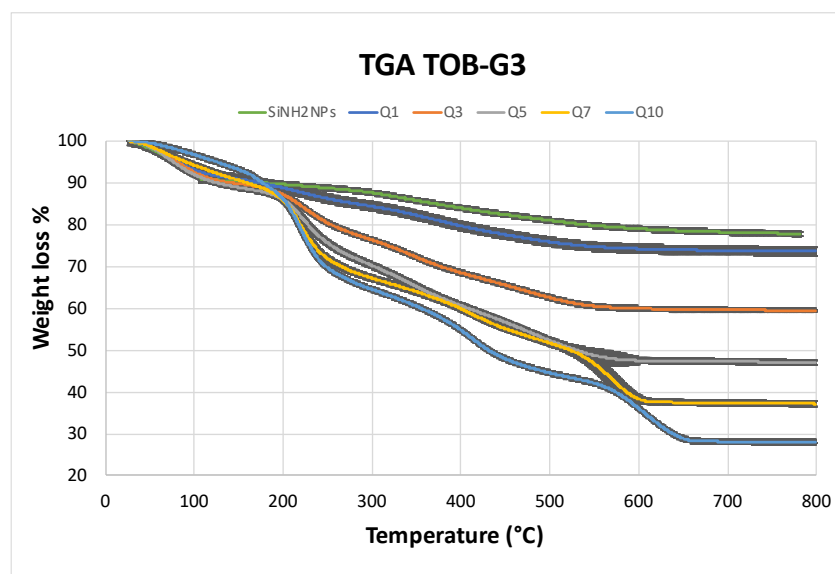


Figure 5.38a: Weight loss vs temperature for Si-NH₂NPs-Alg-TOB-Alg-G3. Mean \pm SD (N=1, n=2).

Starting from $14.80\% \pm 0.39$, the weight loss shifted to $19.50\% \pm 0.01$ on Q1, with an increase of 14% added to the amount of Q1 resulting to $33.06\% \pm 0.18$ on Q3. Then, there was an increment of 11% of the weight loss percentage which reached $44.85\% \pm 0.18$ on Q5 and kept rising up to 57.04 ± 0.16 on Q7. Finally, in this case, there was an improvement of 13% from Q7 to Q10 which ended to $68.75\% \pm 0.1$ for Q10 (figure 5.38b).

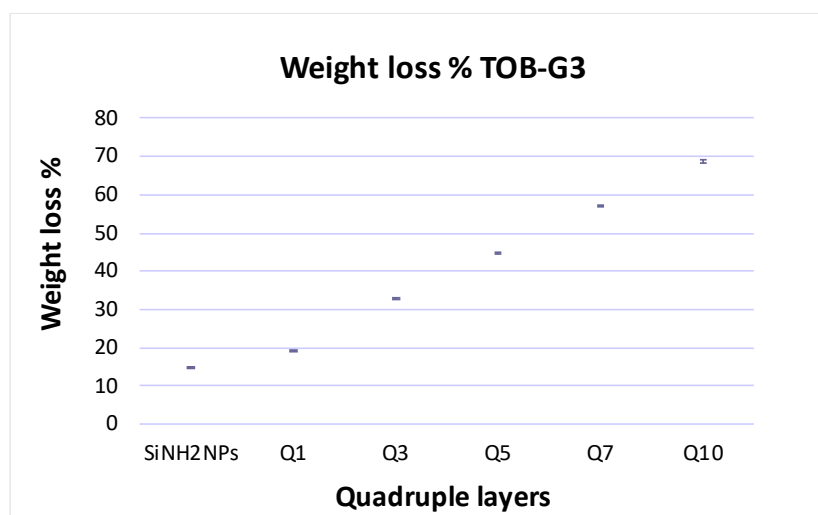


Figure 5.38b: Weight loss % among the QL for the matrix including TOB-G3. Mean \pm SD (N=1, n=2).

Considering the profiles of the group G, a difference was observed in the rate of weight loss detected for Q10 of the 3 nanoconstructs (p -value < 0.05). For instance, it was evident that TOB-G1 provided the highest value, $72.61\% \pm 0.48$, followed by TOB-G2, $62.62\% \pm 0.43$, and TOB-G3, $68.75\% \pm 0.1$. Thus, for this group of matrices, as previously described for those of the group F, the choice of the polymer employed into the coating was greatly influencing the stability of the nano delivery system as well as the interaction between the polymer and the drug during the LbL deposition.

Overall, the weight loss percentage detected for all the 18 TOB-PBAEs matrices ranged between 55% and 75% evidencing the success of the encapsulation of drug and PBAEs into the multilayers systems (Ng *et al.*, 2018b), (Perni and Prokopovich, 2014). Additionally, consistency for the nanoconstructs TOB-A2, TOB-A3, TOB-D2, TOB-D3, and TOB-G2 was observed between zeta potential pathways and organic content percentage. In particular, for the matrices possessing the group F and G as polycations the weight loss was the highest

detected showing values over 70% for the last quadruple Q10 and supported by the zeta potential measurements (p -value < 0.05).

Tobramycin release determination

Once the antibiotic was coated onto the systems via electrostatic interactions, 10 mg of Q10 for every nanoconstructs were suspended in 1mL of each medium, pH5 and pH7.4 and incubated at 37°C after being mixed under vortex for 2 minutes. After 24 hours, the surfactant was withdrawn and replaced with fresh buffers. This process was repeated every 24 hours for the whole period in which the drug was released from the nanoparticles. The drug release was evaluated by treating the surfactant of each medium with o-phthaldialdehyde reagent (OPA) which reacting with the amino moieties of the drug provided a fluorescent conjugate. The analysis occurred by adding in a black 96 well plate as follows: 70 μ L of PBS, 70 μ L of surfactant representing tobramycin released at pH5 or at pH7.4, 70 μ L of isopropanol and 70 μ L of OPA reagent. This procedure was applied for 3 replicates per sample withdrawn every 24 hours from the incubator with 1 independent experiment carried out per medium. Then, once prepared, the plate was read adopting λ excitation=340 nm and λ emission=455 nm as key parameters by using a fluoroscan (FLUOROstar Optima, BMG labtech).

Bilayer: Alg-TOB

Following the parameters described before, the first sample object of analysis was B10 resulting from the alternative deposition of sodium alginate and tobramycin up to 10 times to form the bilayer coating Alg-TOB (figure 5.39).

The profile below shows a pH-dependent tobramycin release which lasted 21 days for both media pH5 and pH7.4. Despite that, differences in the kinetics of release were detected between the two media: as already observed in chapter 4 for the chlorhexidine release, also in this case the drug was faster released at pH7.4 than at pH5 (p -value < 0.05). The main reason could be related to electrostatic interactions among the layers which are low at physiological environment and strong under acid conditions. For instance, the final cumulative release was correspondent to 1134.99 μ g/mL at pH5 whereas it was 3596.30 μ g/mL at pH7.4.

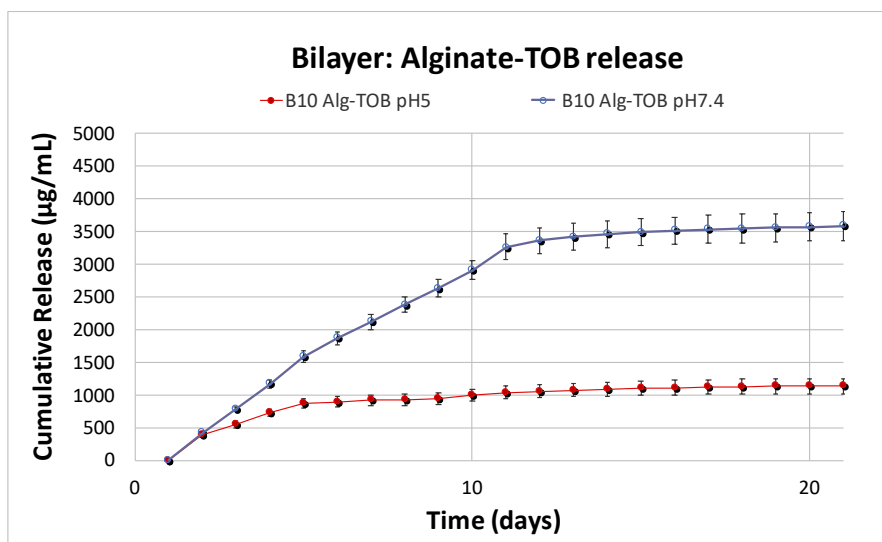


Figure 5.39: TOB release profile at pH5 and at pH7.4 for B10 of the construct Alg-TOB. For each curve: Mean \pm SD (N=1, n=3).

Additionally, at pH5, the drug was faster released in the first 4 days, reaching an average between 405.26-134.01 $\mu\text{g/mL}$ of daily drug release. The amount then significantly dropped, ranging from 49.33 to 22.26 $\mu\text{g/mL}$ up to day 10 (p-value < 0.05). The concentration of the drug release became minimal on day 11, 18.82 $\mu\text{g/mL}$ ending to 5.51 $\mu\text{g/mL}$ from day 18 to day 21 (p-value > 0.05). On the other hand, at pH7.4, the rate of daily drug release was 432.56-239.75 $\mu\text{g/mL}$ for the first 10 days and it drastically decreased from day 11, 92.77 $\mu\text{g/mL}$, reaching the plateau from day 21 with a small concentration equal to 7.74 $\mu\text{g/mL}$ (p-value < 0.05). The profiles of the bilayer Alg-TOB will be considered the control for following drug release pathways provided by the systems where PBAEs were employed as polycations.

A1

The first system including PBAEs as positive polyelectrolyte was TOB-A1 which provided a drug release of 30 days at both media (figure 5.40). Under acidic conditions, the initial daily release was 127.09 $\mu\text{g/mL}$, with a reduction between 75.65-29.45 $\mu\text{g/mL}$ from day 2 to day 12. Then, the amount changed starting from day 13 to day 29 with a gradual decrease of the drug released, 31.33-8.69 $\mu\text{g/mL}$ (p-value > 0.05), reaching a cumulative release equal to 1112.177 $\mu\text{g/mL}$ on day 30.

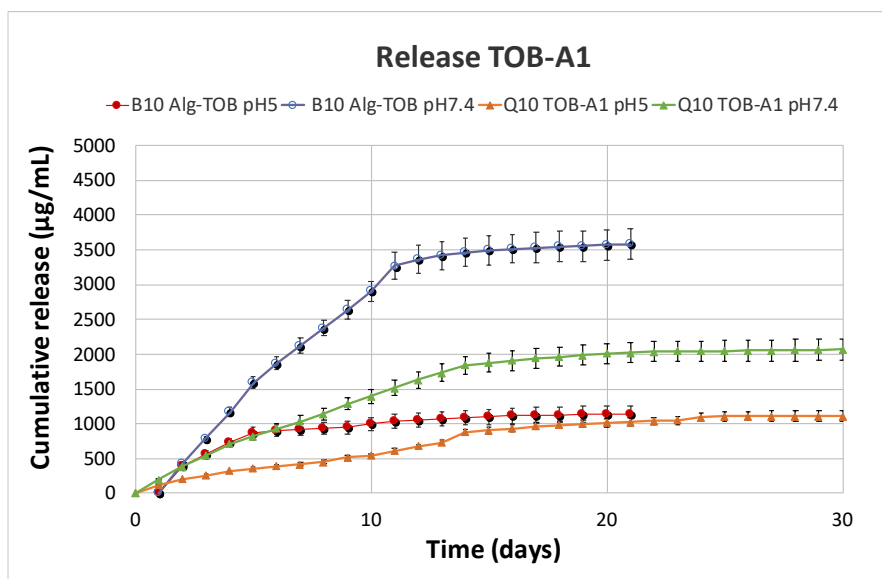


Figure 5.40: TOB release profile at pH5 and at pH7.4 for Q10 of the construct TOB-A1.

For each curve: Mean \pm SD (N=1, n=3).

At pH7.4, the rate of drug released within the first 4 days was 206.07-159.09 $\mu\text{g}/\text{mL}$ and it decreased up to 93.82 $\mu\text{g}/\text{mL}$ from day 5 to day 14. Additionally, the amount plummeted ranging between 40.46-20.79 $\mu\text{g}/\text{mL}$ in the next 6 days, reaching a concentration between 14.80 on day 21 (p-value < 0.05). The drug release was then minimal from day 22 up to day 30 (p-value > 0.05) ending to a cumulative release of 2067.35 $\mu\text{g}/\text{mL}$ which as expected was almost the double quantity of the drug release at pH5.

A2

The drug release was determined also for the nanocoating TOB-A2 over a period of 50 days. The cumulative release at pH5 was equal to 1113.26 $\mu\text{g}/\text{mL}$ and the amount was similar to the one at pH5 detected for TOB-A1 (p-value > 0.05). However, at pH7.4 the cumulative release for this nanoconstruct was doubled the rate of TOB-A1 and correspondent to 4288.60 $\mu\text{g}/\text{mL}$ (figure 5.41). Under acid conditions, the quantity of drug release per day was between 206.67-106.09 $\mu\text{g}/\text{mL}$ for the first 6 days changing to 28.68-16.61 $\mu\text{g}/\text{mL}$ from day 7 to day 27 (p-value < 0.05). Finally, the concentration gradually decreased to 11.78 $\mu\text{g}/\text{mL}$ on day 28 highlighting a long plateau until day 50 with a low daily release of 6.01 $\mu\text{g}/\text{mL}$ (p-value > 0.05). As contrary, the quantity of antibiotic released per day within the first 6 days was ranging between 500.14-410.08 $\mu\text{g}/\text{mL}$ and the amount dropped to 263.80 $\mu\text{g}/\text{mL}$ on day 7 reaching 186.20 $\mu\text{g}/\text{mL}$ on day 10. The amount then was half reduced from day 11, 102.25 $\mu\text{g}/\text{mL}$,

ending to 20.28 $\mu\text{g}/\text{mL}$ on day 20 (p -value < 0.05) and showing a minimal concentration of daily drug released between 9.98-3.32 $\mu\text{g}/\text{mL}$ starting from day 28 up to day 50 (p -value > 0.05).

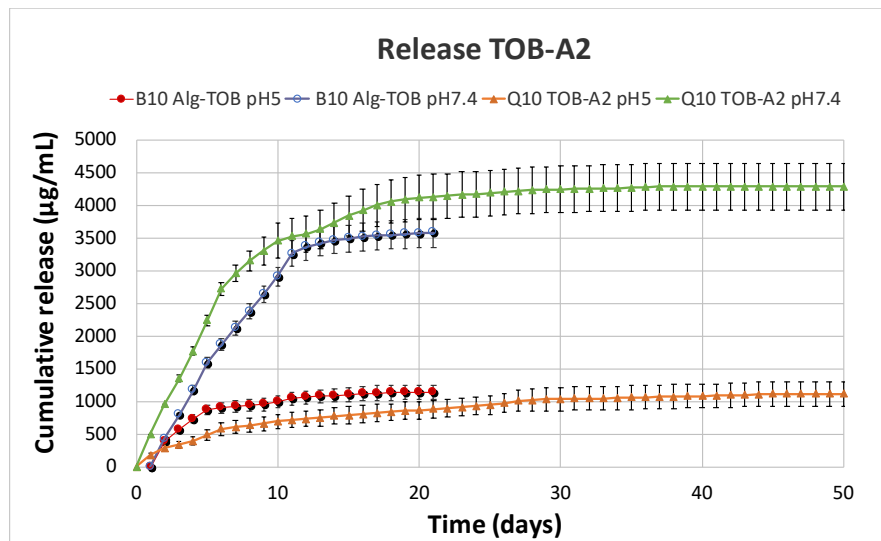


Figure 5.41: TOB release profile at pH5 and at pH7.4 for Q10 of the construct TOB-A2.

For each curve: Mean \pm SD (N=1, n=3).

A3

The drug release was evaluated also for the matrix TOB-A3. At both media the drug was released for 30 days and at pH5 after the high amount detected for day 1 845.88 $\mu\text{g}/\text{mL}$, there was a significant reduction in the daily concentration from day 2 to day 4 showing values between 332.09-106.26 $\mu\text{g}/\text{mL}$ (figure 5.42) (p -value < 0.05).

However, as previously observed, the daily release on day 5 until day 17 was equal to 30.22-28.31 $\mu\text{g}/\text{mL}$, and it slowly decreased up to 8.36 $\mu\text{g}/\text{mL}$ on day 18 with a cumulative release on day 30 correspondent to 1471.82 $\mu\text{g}/\text{mL}$. On the other hand, the cumulative release at pH7.4 was equal to 4104.61 $\mu\text{g}/\text{mL}$ and the drug was mainly released within the first 15 days. For instance, the quantity was ranging between 790.37-650-83 $\mu\text{g}/\text{mL}$ for the first 3 days and it plummeted to 252.82-82.88 $\mu\text{g}/\text{mL}$ from day 4 to day 15 (p -value < 0.05). Then, a plateau was reached starting from day 16 until day 30, with a daily drug release ranging between 26.82-6.46 $\mu\text{g}/\text{mL}$ (p -value > 0.05).

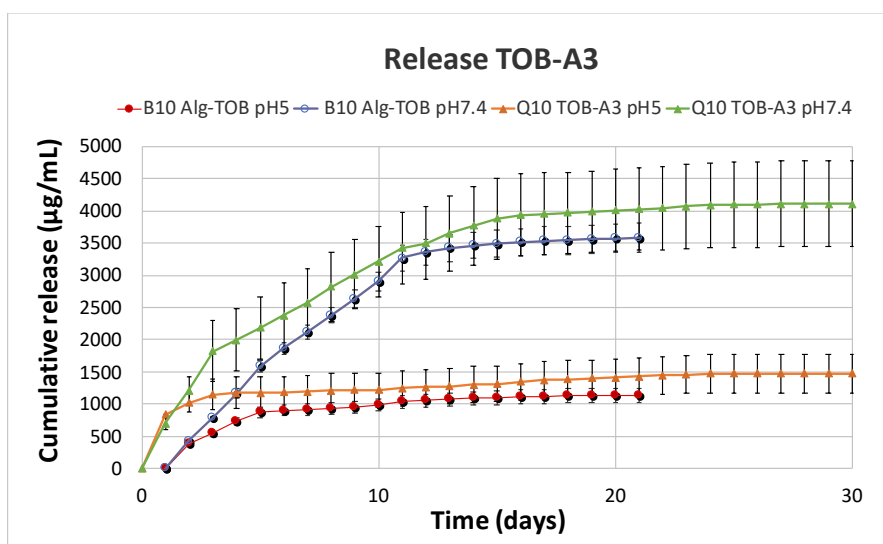


Figure 5.42: TOB release profile at pH5 and at pH7.4 for Q10 of the construct TOB-A3.

For each curve: Mean \pm SD (N=1, n=3).

Comparing the nanoconstructs of the group A to the profile of the bilayer Alg-TOB, it was observed that the presence of PBAEs into the systems improved the drug release properties. For example, at pH5, 1134.99 $\mu\text{g}/\text{mL}$ of antibiotic was released from the bilayer system after only 21 days; instead a similar value was detected for the TOB-A1 and TOB-A2 after respectively 30 and 50 days. However, the cumulative release for Alg-TOB was 3596.99 $\mu\text{g}/\text{mL}$ which was higher than TOB-A1, 2067.35 $\mu\text{g}/\text{mL}$, but lower than TOB-A3, 4104.61 $\mu\text{g}/\text{mL}$, and TOB-A2, 4288.60 $\mu\text{g}/\text{mL}$ (p-value < 0.05).

B1

The drug release determination was carried out for the nano delivery systems of the group B. Regarding TOB-B1 the antibiotic was released over a period of 40 days and the cumulative release was equal to 1640.88 $\mu\text{g}/\text{mL}$ at pH5 and 4179.52 $\mu\text{g}/\text{mL}$ at pH7.4 (figure 5.43).

Under acid conditions, the daily release for the first 15 days was ranging between 153.62-66.36 $\mu\text{g}/\text{mL}$ followed by a moderate decrease of the quantity released from day 16 which was correspondent to 59.47 $\mu\text{g}/\text{mL}$ (p-value < 0.05) which ended to 19.13 $\mu\text{g}/\text{mL}$ on day 26. Finally, a plateau was observed starting from day 27 to day 30 with a minimal release of the antibiotic between 8.14-3.36 $\mu\text{g}/\text{mL}$ (p-value > 0.05).

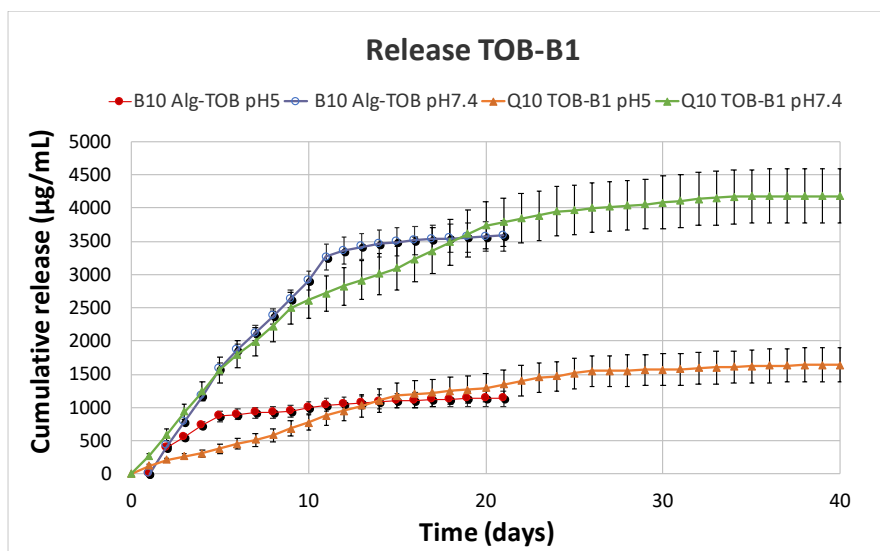


Figure 5.43: TOB release profile at pH5 and at pH7.4 for Q10 of the construct TOB-B1.

For each curve: Mean \pm SD (N=1, n=3).

As contrary, the quantity of drug release per day for the first 9 days at pH7.4 was 360.51-224.41 $\mu\text{g}/\text{mL}$ and it changed from day 10 to day 20 ranging between 141.36-78.66 $\mu\text{g}/\text{mL}$ (p -value < 0.05). Moreover, after a slow decrease on day 21, 67.44 $\mu\text{g}/\text{mL}$, the daily release dropped to 22.24 $\mu\text{g}/\text{mL}$ on day 32 followed by a plateau lasting 7 extra days where the concentration was between 6.45-3.42 $\mu\text{g}/\text{mL}$ (p -value > 0.05).

B2

The drug release was determined also for the nanoconstruct TOB-B2 and the cumulative release after 30 days was equal to 1269.80 $\mu\text{g}/\text{mL}$ at pH5 and 3004.80 $\mu\text{g}/\text{mL}$ at pH7.4 (figure 5.44).

At pH5, for the first 5 days the daily release was ranging between 220.65-117.58 $\mu\text{g}/\text{mL}$ per day and the daily amount dropped to 66.01 $\mu\text{g}/\text{mL}$ from day 6 reaching 28.46 $\mu\text{g}/\text{mL}$ on day 14 (p -value < 0.05). Furthermore, a long plateau of 16 more days was observed with a rate of drug between 10.21-2.07 $\mu\text{g}/\text{mL}$ released per day. On the other hand, the quantity of drug released per day for the first week at pH7.4 was doubled the amount detected at pH5, 459.10-195.56 $\mu\text{g}/\text{mL}$, and it plummeted to 139.03-107.67 $\mu\text{g}/\text{mL}$ from day 8 up to day 13 (p -value < 0.05). Finally, also in this case, a long plateau correspondent to 17 days was observed where the daily concentration of drug released was minimal, ranging between 8.89-2.63 $\mu\text{g}/\text{mL}$.

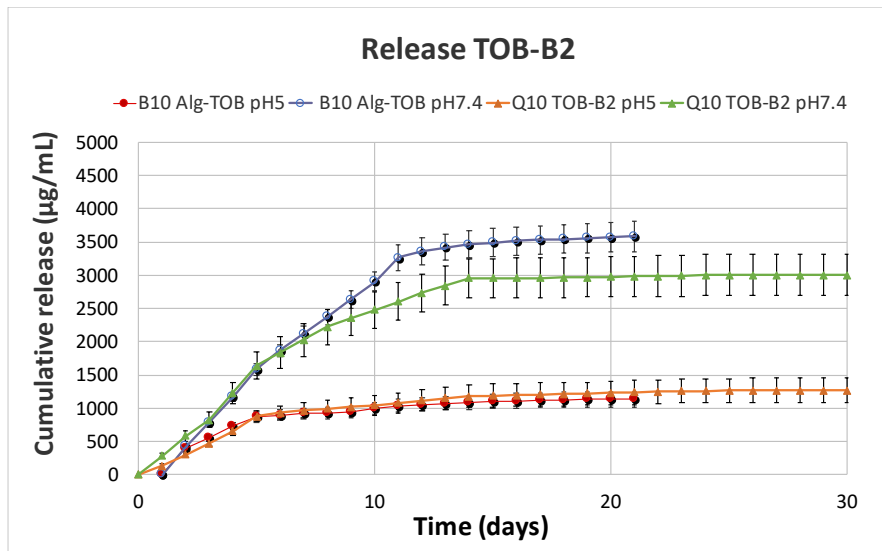


Figure 5.44: TOB release profile at pH5 and at pH7.4 for Q10 of the construct TOB-B2.

For each curve: Mean \pm SD (N=1, n=3).

B3

The last nano delivery system, including a PBAE of the group B as polycation, that was object of drug release evaluation was TOB-B3. Under acid conditions, the daily release was equal to 736.25 $\mu\text{g}/\text{mL}$ on day 1, and the detected quantity of drug released per day drastically decreased to 43.52 $\mu\text{g}/\text{mL}$ heading to 29.27 $\mu\text{g}/\text{mL}$ on day 16 (p-value < 0.05). The final part of the curve reported in the figure 5.45 evidences a plateau which lasted 14 days with a daily concentration ranging between 17.08-8.80 $\mu\text{g}/\text{mL}$ (p-value > 0.05).

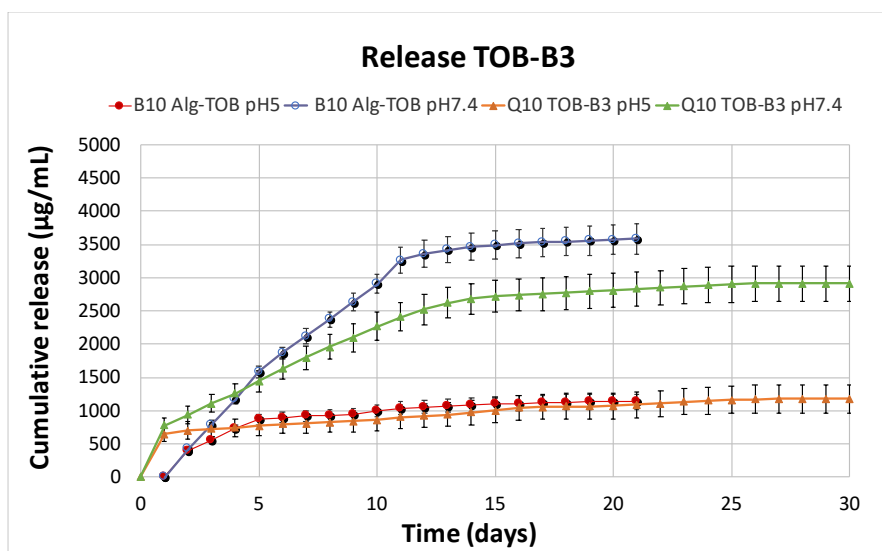


Figure 5.45: TOB release profile at pH5 and at pH7.4 for Q10 of the construct TOB-B3.

For each curve: Mean \pm SD (N=1, n=3).

As contrary, under physiological environment, the rate of drug release on day 1 was slightly higher, 845.89 $\mu\text{g}/\text{mL}$, if compared to the value detected on the same day at pH5, but it dropped to 199.97 $\mu\text{g}/\text{mL}$ on day 2 showing values up to 90.88 $\mu\text{g}/\text{mL}$ until day 13. Starting from day 14 the amount was then half reduced, 47.20 $\mu\text{g}/\text{mL}$, followed by a further decrease of the daily drug release, with ranged between 25.96-15.84 $\mu\text{g}/\text{mL}$ up to day 22 (p -value < 0.05). Finally, also in this case, the last part of the curve was represented by a plateau of 7 days where the concentration was minimal and between 11.25-5.37 $\mu\text{g}/\text{mL}$ per day.

Overall, it was observed that the antibiotic was highly released when B1 was employed into the system as polycation showing a greater value at both media, 1640.88 $\mu\text{g}/\text{mL}$ at pH5 and 4179.52 $\mu\text{g}/\text{mL}$ at pH7.4. However, the cargo was less released by coating B3 or B2, showing respectively a cumulative release of 1176.82 $\mu\text{g}/\text{mL}$ and 1269.80 $\mu\text{g}/\text{mL}$ at pH5, whereas 2911.16 $\mu\text{g}/\text{mL}$ and 3004.8 $\mu\text{g}/\text{mL}$ at pH7.4 (p -value > 0.05). Additionally, comparing the nanoconstructs of the group B to the bilayer system Alg-TOB, it was noticed that the profile of TOB-B2 and TOB-B3 were quite similar than Alg-TOB (p -value > 0.05), whereas the one of TOB-B1 was significantly higher at both media than the release detected from the matrix Alg-TOB (p -value < 0.05).

D1

The drug release profiles were developed also for the systems including the PBAEs D1, D2 and D3 as polycations. Regarding TOB-D1, the drug release lasted 60 days and the cumulative release was 1084.04 $\mu\text{g}/\text{mL}$ at pH5 whereas it was 4048.48 $\mu\text{g}/\text{mL}$ at pH7.4 (figure 5.46).

Starting from day 1 to day 6, at pH5, the daily release was equal to 97.74-51.43 $\mu\text{g}/\text{mL}$ and it decreased on day 7 with a value of 38.21 $\mu\text{g}/\text{mL}$ which reached 21.76 $\mu\text{g}/\text{mL}$ on day 13 (p -value < 0.05). Then, there was a gradual reduction of the amount of drug released from day 14 to day 45 that was ranging between 20.07-15.30 $\mu\text{g}/\text{mL}$, followed by a plateau of extra 15 days, where the concentration was between 3.67-1.99 $\mu\text{g}/\text{mL}$ (p -value > 0.05).

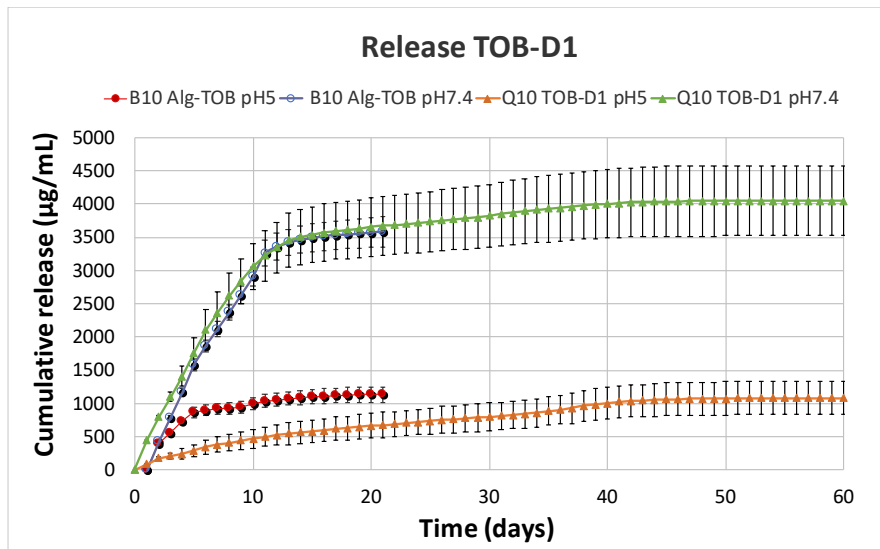


Figure 5.46: TOB release profile at pH5 and at pH7.4 for Q10 of the construct TOB-D1.

For each curve: Mean \pm SD (N=1, n=3).

On the other hand, the rate of drug release for the first 6 days at pH7.4 was 2-4 times higher than at pH5, 454.6-277.77 $\mu\text{g}/\text{mL}$, with a moderate decline of the quantity from day 7, 266.08 $\mu\text{g}/\text{mL}$, to day 33, 21.47 $\mu\text{g}/\text{mL}$ (p-value < 0.05). Moreover, a further decrease of the rate of drug release was detected for the following 10 days ending to 12.92 $\mu\text{g}/\text{mL}$ on day 44, followed by a plateau of 15 more days where the amount changed between 6.94-1.33 $\mu\text{g}/\text{mL}$ per day (p-value > 0.05).

D2

The figure 5.47 illustrates the drug release at both media for the system TOB-D2 which lasted 50 days and a cumulative release of 1491.78 $\mu\text{g}/\text{mL}$ at pH5 and 4634.72 $\mu\text{g}/\text{mL}$ at pH7.4. Considering the profile of the drug released under acid conditions, the daily amount was initially correspondent to 188.83-80.95 $\mu\text{g}/\text{mL}$ per day within the first 6 days, and it slowly decreased ranging between 64.67-24.98 $\mu\text{g}/\text{mL}$ up to day 19 (p-value < 0.05). Then, the quantity of drug released was gradually reduced from day 20 to day 38, 22.10-10.19 $\mu\text{g}/\text{mL}$, followed by a plateau of further 12 days with a low concentration equal to 9.75-2.04 $\mu\text{g}/\text{mL}$ (p-value > 0.05). On the hand, at physiological environment the drug was highly released in the first 6 days providing values between 500.15-378.03 $\mu\text{g}/\text{mL}$ per day. The rate of drug release was then half reduced on day 7, 266.61 $\mu\text{g}/\text{mL}$, and it plummeted to 34.7 $\mu\text{g}/\text{mL}$ on day 17 (p-value < 0.05). Furthermore, from day 18 the amount of drug release slowly

decreased reporting a concentration ranging between 21.10-7.26 $\mu\text{g}/\text{mL}$ until day 30, plus 20 extra days of plateau where the values ranged between 6.54-1.33 $\mu\text{g}/\text{mL}$ per day (p -value > 0.05).

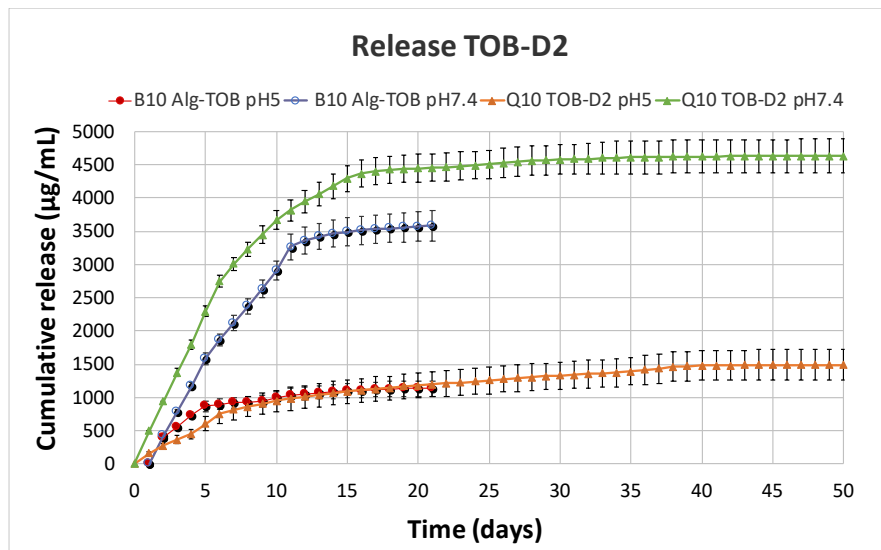


Figure 5.47: TOB release profile at pH5 and at pH7.4 for Q10 of the construct TOB-D2.

For each curve: Mean \pm SD (N=1, n=3).

D3

The drug release was determined for the nano delivery system TOB-D3 completing the matrices composed by PBAEs of the group D. In this case, the drug was released from the nanoparticles over a period of 30 days presenting a cumulative release equal to 1158.20 $\mu\text{g}/\text{mL}$ at pH5 and 2807.46 $\mu\text{g}/\text{mL}$ at pH7.4 (figure 5.48).

The amount of drug release on day 1 at pH5 was 736.25 $\mu\text{g}/\text{mL}$, and it dropped to 75.44 $\mu\text{g}/\text{mL}$ on day 2 (p -value < 0.05). Then, for the next 14 days the quantity was ranging between 70.43-30.62 $\mu\text{g}/\text{mL}$, with a further reduction of the daily rate from day 17 to day 30 with a concentration correspondent to 17.36-5.55 $\mu\text{g}/\text{mL}$. However, the drug was slightly higher released at pH7.4, showing a value of 845.88 $\mu\text{g}/\text{mL}$, which drastically changed on day 2, 199.57 $\mu\text{g}/\text{mL}$. From day 3 to day 13 the quantity of drug release oscillated between 178.55-90.38 $\mu\text{g}/\text{mL}$ per day (p -value < 0.05), dropping to 57.20 $\mu\text{g}/\text{mL}$ on day 18 and reaching 12.27 $\mu\text{g}/\text{mL}$ on da 17. Finally, as previously observed at pH5, a plateau was also detected at pH7.4 over a period of 13 days and with a tiny daily concentration ranging between 6.77-2.12 $\mu\text{g}/\text{mL}$.

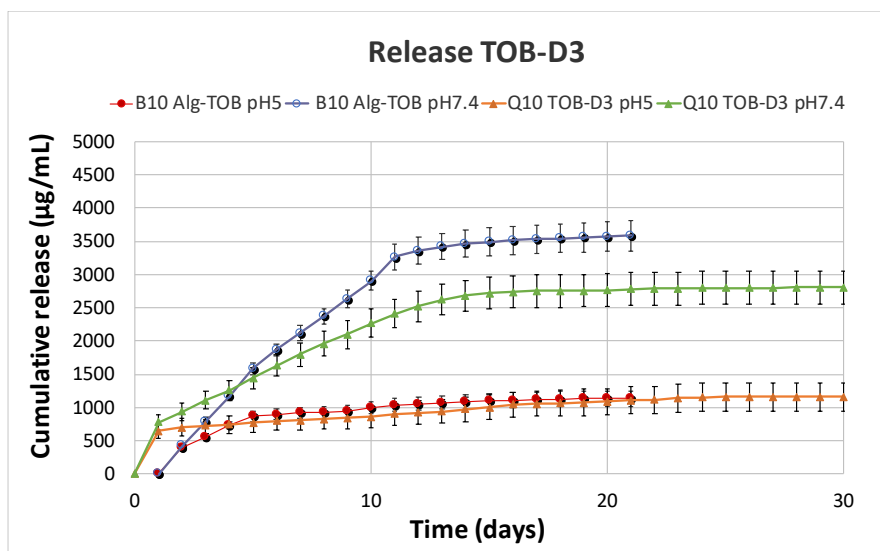


Figure 5.48: TOB release profile at pH5 and at pH7.4 for Q10 of the construct TOB-D3.

For each curve: Mean \pm SD (N=1, n=3).

Comparing the profiles of the group D, the antibiotic release was pH-dependent as previously discussed, and it was greatly influenced the choice of amine adopted in the synthesis of PBAEs. In particular, although tobramycin was longer released from TOB-D1 (60 days), the highest cumulative release at both media was provided by TOB-D2, 1491.78 $\mu\text{g/mL}$ at pH5 and 4634.72 $\mu\text{g/mL}$ at pH7.4, which instead lasted 50 days. As contrary, TOB-D3 provided the lowest amount of drug release especially at pH7.4, with a cumulative release of 2807.46 $\mu\text{g/mL}$ after 30 days ($p\text{-value} < 0.05$).

E1

Concerning the nanoconstruct TOB-E1, the drug was released from the nanocarrier for 40 days but showing the lowest cumulative release among the systems analysed before ($p\text{-value} < 0.05$). Thus, at pH5 it was equal to 550.92 $\mu\text{g/mL}$, whereas 1157.52 $\mu\text{g/mL}$ at pH7.4 (figure 5.49). The quantity of cargo released at pH5 for the first 3 days was ranging between 51.23-35.59 $\mu\text{g/mL}$ and it steadily decreased from day 4, 32.48 $\mu\text{g/mL}$, ending to 10.21 $\mu\text{g/mL}$ on day 27. Additionally, for the next 13 days, a long plateau was detected where the concentration was minimal with values between 9.81-2.46 $\mu\text{g/mL}$ per day ($p\text{-value} > 0.05$).

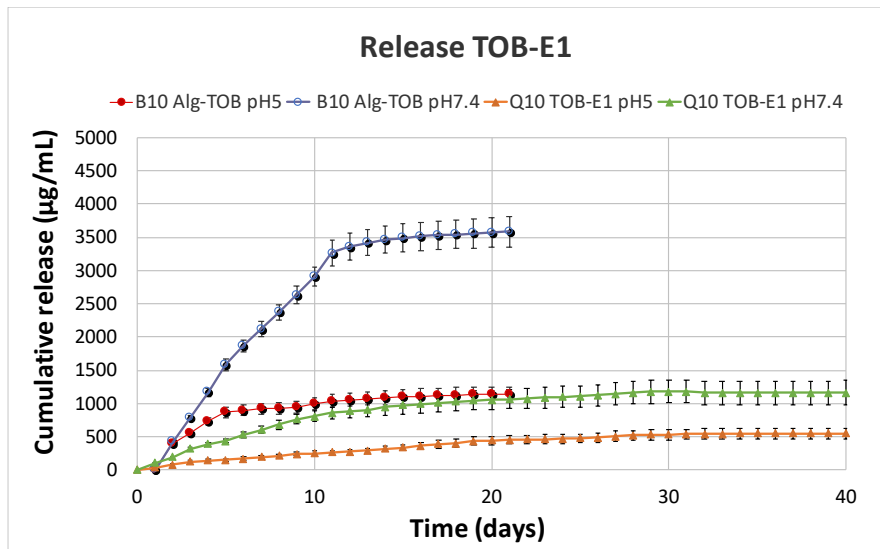


Figure 5.49: TOB release profile at pH5 and at pH7.4 for Q10 of the construct TOB-E1.

For each curve: Mean \pm SD (N=1, n=3).

On the other hand, the amount of drug released reported for the first 3 days at pH7.4 was doubled if compared to the curve of pH5 (p-value < 0.05). For instance, the rate was initially 133.67-87.31 $\mu\text{g}/\text{mL}$, and it plummeted from day 4, 84.99 $\mu\text{g}/\text{mL}$, heading to 26.13 $\mu\text{g}/\text{mL}$ on day 14. Then the daily value gradually kept decreasing for further 14 days, reaching 10.95 $\mu\text{g}/\text{mL}$ on day 29, plus a plateau of 11 more days with a low concentration ranging between 5.39-2.71 $\mu\text{g}/\text{mL}$ (p-value < 0.05).

E2

The figure 5.50 represents the tobramycin release profiles at both media for the nano delivery network TOB-E2. In this case, the cumulative release was higher than the one gained for TOB-E1 (p-value < 0.05): at pH5 after 30 days it was correspondent to 818.34 $\mu\text{g}/\text{mL}$, and 1438.45 $\mu\text{g}/\text{mL}$ at pH7.4.

Starting from day 1, the daily release under acid conditions was equal to 182.36 $\mu\text{g}/\text{mL}$, providing a greater value than the one observed at the same pH and day for TOB-E1, 51.23 $\mu\text{g}/\text{mL}$ (p-value < 0.05). There was a considerable reduction in the amount released from day 2, which ended up to 85.71 $\mu\text{g}/\text{mL}$ on day 3. The quantity then ranged between 64.45-43.32 $\mu\text{g}/\text{mL}$ until day 6 and it was half reduced from day 7, 21.69 $\mu\text{g}/\text{mL}$, with a gradual decline of

the rate up to day 21, 10.99 $\mu\text{g}/\text{mL}$. Finally, the plateau lasted 9 extra days with a minimal daily concentration between 8.52-2.65 $\mu\text{g}/\text{mL}$.

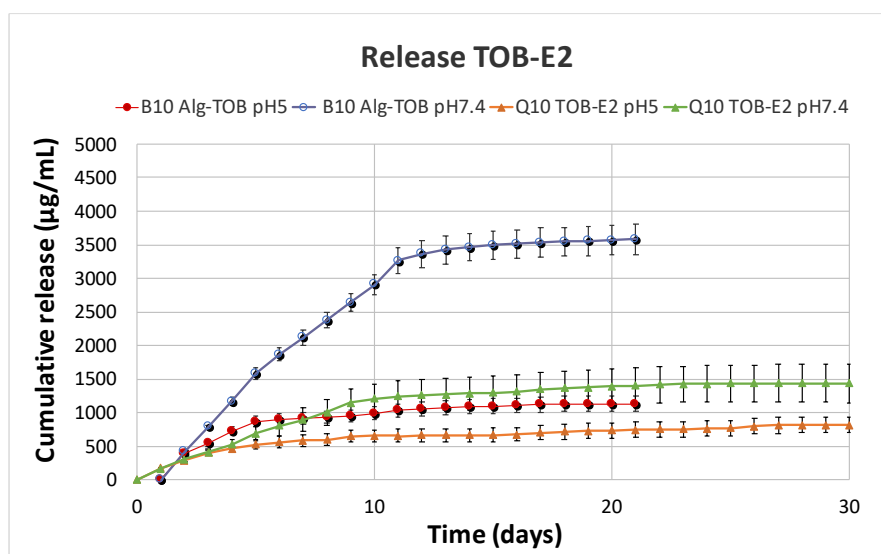


Figure 5.50: TOB release profile at pH5 and at pH7.4 for Q10 of the construct TOB-E2.

For each curve: Mean \pm SD (N=1, n=3).

However, at pH7.4, the drug was similarly released, for the first day. showing the same amount on day 1, 182.36 $\mu\text{g}/\text{mL}$, reported also at pH5. Differently, at this medium, the cargo was highly released until day 8, 96.06 $\mu\text{g}/\text{mL}$, with a moderate decrease from day 9, 71.85 $\mu\text{g}/\text{mL}$, to day 18, 21.42 $\mu\text{g}/\text{mL}$. Furthermore, the amount was slightly reduced from day 19, 16.24 $\mu\text{g}/\text{mL}$, to day 22, 11.82 $\mu\text{g}/\text{mL}$, followed by a plateau of 8 more days with a range of concentration between 8.28-5.09 $\mu\text{g}/\text{mL}$ detected per day.

E3

To complete the nanoconstructs including the PBAEs of the group E, the drug release was determined for the nanosystem TOB-E3. Overall, the antibiotic was released at both media over a period of 30 days reporting values such as 1285.86 $\mu\text{g}/\text{mL}$ at pH5 and 2824.13 $\mu\text{g}/\text{mL}$ at pH7.4. Regarding the profile developed at pH5, the drug was mainly released in the first day showing a rate of 839.76 $\mu\text{g}/\text{mL}$, which significantly decreased to 106.43 $\mu\text{g}/\text{mL}$ on day 2 and ending to 37.41 $\mu\text{g}/\text{mL}$ on day 13 (p-value < 0.05). Then, the amount released minimally changed from day 14 to day 24, ranging between 24.60-20.67 $\mu\text{g}/\text{mL}$ per day, followed by a

plateau of only 6 days with a quantity release between 12.35-4.22 $\mu\text{g}/\text{mL}$ (figure 5.51) (p -value > 0.05).

Analysing the curve representative of the tobramycin release from TOB-E3 at pH7.4, it was observed that as noticed for the profile at pH5 before, the drug was highly release on day 1, showing a concentration of 845.88 $\mu\text{g}/\text{mL}$. In the same way, the quantity released shifted from day 2, 242.33 $\mu\text{g}/\text{mL}$, reaching 152.77 $\mu\text{g}/\text{mL}$ on day 10, with a further decrease up to day 16, 39.52 $\mu\text{g}/\text{mL}$ (p -value < 0.05). Finally, the rate of drug released slightly varied from day 17 to day 23, 19.16-13.32 $\mu\text{g}/\text{mL}$, followed by a plateau of 7 days with a tiny concentration ranging between 6.48-4.27 $\mu\text{g}/\text{mL}$ per day.

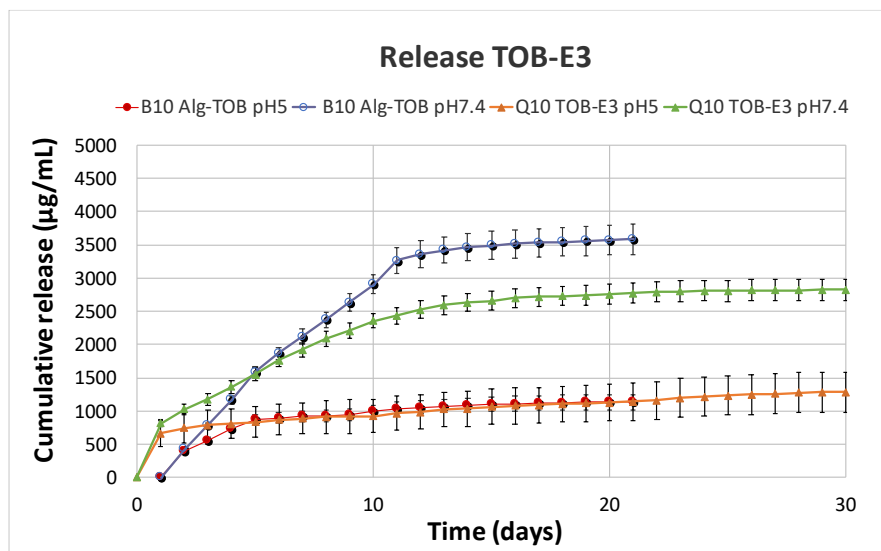


Figure 5.51: TOB release profile at pH5 and at pH7.4 for Q10 of the construct TOB-E3.

For each curve: Mean \pm SD (N=1, n=3).

Comparing the profiles developed for the 3 matrices TOB-E1, TOB-E2 and TOB-E3, it was observed that, although TOB-E1 provided a longer drug release, lasting 40 days, the greater cumulative release detected among the 3 system was gained by TOB-E3 which lasted only 30 days (TOB-E3>TOB-E2>TOB-E1) (p -value < 0.05). Moreover, it was evident that the addition of the PBAEs into the systems improved the stability of the nanoconstructs, controlling the kinetics of the drug release which instead were significantly high in the bilayer system Alg-TOB. For instance, even if the antibiotic release was pH-dependent, the cumulative release amount was definitely bigger at pH7.4 when the cargo was released from the bilayer matrix

showing a value of 3596.88 $\mu\text{g}/\text{mL}$, against 2824.13 $\mu\text{g}/\text{mL}$ of TOB-E3, that was the highest quantity detected among TOB-E1, TOB-E2 and TOB-E3 (p -value < 0.05).

F1

The drug release was evaluated for the system including the PBAEs of the group following the same parameters previously described. Hence, the cumulative release counted for TOB-F1 after 30 days was correspondent to 971.23 $\mu\text{g}/\text{mL}$ at pH5 and 1764.40 $\mu\text{g}/\text{mL}$ at pH7.4 (figure 5.52).

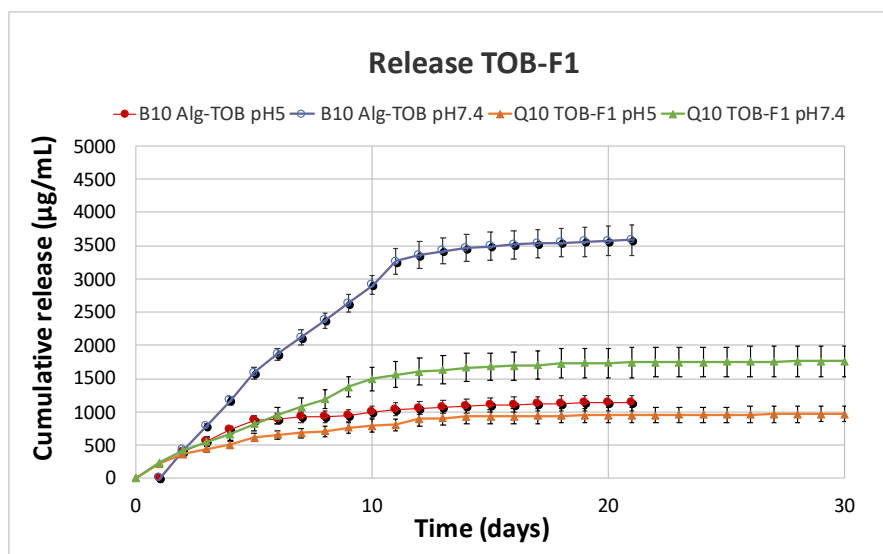


Figure 5.52: TOB release profile at pH5 and at pH7.4 for Q10 of the construct TOB-F1.

For each curve: Mean \pm SD (N=1, n=3).

The antibiotic was mainly released within the first 2 days showing an amount of 237.42 $\mu\text{g}/\text{mL}$ on day 1 which changed to 151.51 $\mu\text{g}/\text{mL}$ on day 2. Furthermore, the quantity dropped to 99.20 $\mu\text{g}/\text{mL}$ on day 3 and it was almost reduced up to day 9, 50.47 $\mu\text{g}/\text{mL}$. An additional reduction was also observed between day 10 and 15 where the rate of drug released plummeted from 26.44 $\mu\text{g}/\text{mL}$ to 10.16 (p -value < 0.05), followed by a long plateau of 15 days with a tiny concentration between 7.63-2.07 $\mu\text{g}/\text{mL}$ detected per day. Although the rate of tobramycin released on day 1 at pH7.4 was 244.20 $\mu\text{g}/\text{mL}$, reporting a value similar to what detected for the same day at pH5, the drug was highly released under physiological conditions with an amount ranging between 196.82-99.25 $\mu\text{g}/\text{mL}$ per day until day 10. Then, the quantity started slowly decreasing from day 11, 82.09 $\mu\text{g}/\text{mL}$, to day 20, 20.42 $\mu\text{g}/\text{mL}$, providing a

plateau of 10 more days where the rate ranged between 6.56-2.94 $\mu\text{g}/\text{mL}$ per day (p -value > 0.05).

F2

The determination of tobramycin release was carried out also for the matrix TOB-F2 and the curves at both media are reported in the figure 5.53. Starting from pH5, for the first 6 days the daily drug release showed values ranging between 167.97-88.82 $\mu\text{g}/\text{mL}$, shifting to 61.37 $\mu\text{g}/\text{mL}$ up to day 7 with a further decline of the amount on day 9, 40.08 $\mu\text{g}/\text{mL}$ (p -value < 0.05). Moreover, the quantity was half reduced from day 10, 20.57 $\mu\text{g}/\text{mL}$, reaching 10.71 $\mu\text{g}/\text{mL}$ on day 23, followed by a plateau of only 7 more days up to day 30 with a low concentration between 4.96-2.16 $\mu\text{g}/\text{mL}$ released per day.

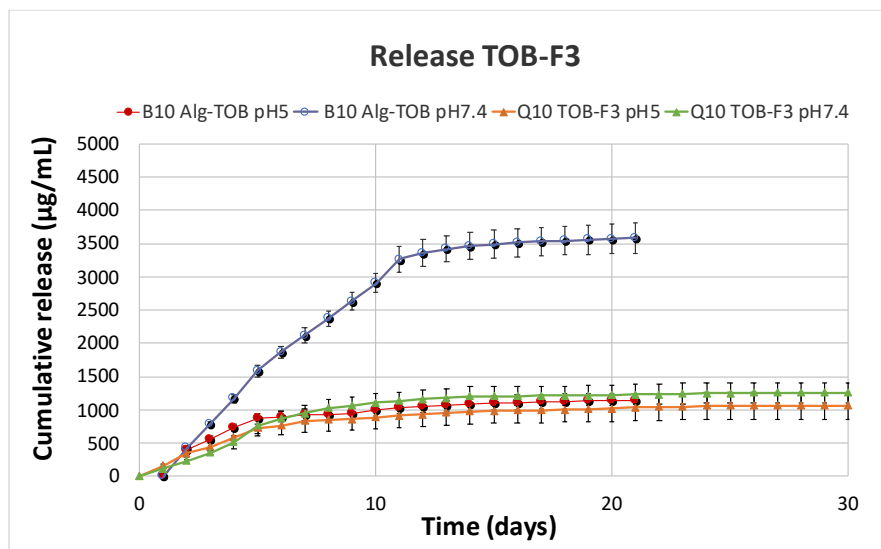


Figure 5.53: TOB release profile at pH5 and at pH7.4 for Q10 of the construct TOB-F2.

For each curve: Mean \pm SD (N=1, n=3).

On the other hand, the quantity of drug released at pH7.4 was between 220.53-172.06 $\mu\text{g}/\text{mL}$ for the first 2 days and it gradually decreased on day 4 164.86 $\mu\text{g}/\text{mL}$, with a considerable decline of the daily amount which ended to 119.10 $\mu\text{g}/\text{mL}$ on day 8. However, the main reduction occurred with 2 more days, where firstly, the concentration detected was equal to 47.11 $\mu\text{g}/\text{mL}$ on day 9 which then dropped to 21.71 $\mu\text{g}/\text{mL}$ on day 10. Furthermore, the rate of daily release kept falling showing a range between 16.01-10.35 $\mu\text{g}/\text{mL}$ up to day 18, plus a plateau of 12 more days where it was between 9.59-3.43 $\mu\text{g}/\text{mL}$ per day. Hence, the

cumulative release for this nanoconstruct after 30 days was 975.09 $\mu\text{g}/\text{mL}$ at pH5 and 1457.34 $\mu\text{g}/\text{mL}$ at pH7.4 (p-value > 0.05).

F3

To complete the nanoconstruct possessing the polymers of the group F, the tobramycin release was evaluated for TOB-F3. In this case, similarly to what analysed before for TOB-F1 and TOB-F2, the drug was released over a period of 30 days and the cumulative release was correspondent to 1062.75 $\mu\text{g}/\text{mL}$ under acid conditions and to 1255.45 $\mu\text{g}/\text{mL}$ at physiological environment. At pH5, the daily release was equal to 191.93-153.08 $\mu\text{g}/\text{mL}$ for the first 5 days and it plummeted to 55.65 $\mu\text{g}/\text{mL}$ on day 6, heading to 23.24 $\mu\text{g}/\text{mL}$ on day 8 (p-value < 0.05). Additionally, the amount of cargo released was ranging between 15.74-6.57 $\mu\text{g}/\text{mL}$ for the next 15 days with a plateau observed from day 25 to day 30 with a low concentration of 2.51-2.06 $\mu\text{g}/\text{mL}$ per day (figure 5.54).

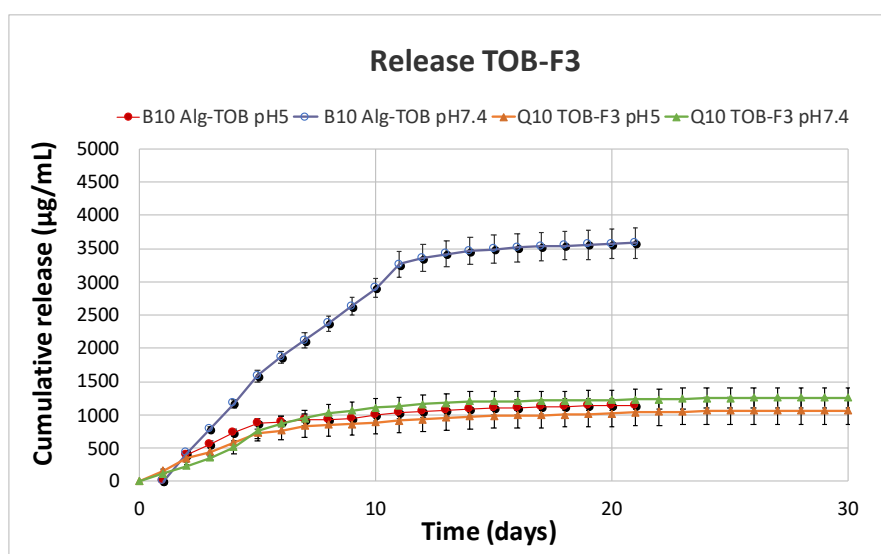


Figure 5.54: TOB release profile at pH5 and at pH7.4 for Q10 of the construct TOB-F3

As contrary, the drug release for the first 6 days at pH7.4 was equal to 271.62-100.21 $\mu\text{g}/\text{mL}$ detected per day, and this amount was moderately reduced in a period of extra 8 days, showing values between 89.98-80.51 $\mu\text{g}/\text{mL}$ on day 7 and 8 which dropped to 44.56-18.63 $\mu\text{g}/\text{mL}$ from day 9 to day 14. Finally, also at this medium a plateau characterised the last part of the drug release profile at pH7.4 lasting 16 more days and with a daily drug release ranging between 8.88-2.30 $\mu\text{g}/\text{mL}$.

Comparing the 3 nanoconstructs of the group F to the bilayer system release profile, it was observed a considerable difference in the quantity of tobramycin released (p -value < 0.05). For instance, the antibiotic was highly released from Alg-TOB, but the profiles at both media of TOB-F1, TOB-F2, and TOB-F3 were instead quite low. This was probably correlated to the complex molecular structure of the diacrylate F, which due to the strong hydrophobicity, was influencing the layer by layer self-assembly with a strong impact on the kinetics of drug release. Additionally, no difference was observed among the matrices of the group F, which all provided a drug release of 30 days. Therefore, the highest cumulative release was detected from TOB-F1, followed by TOB-F2 and TOB-F3 (p -value > 0.05).

G1

The drug release determination occurred also for the matrices of the group G. Regarding TOB-G1, the tobramycin was released for 40 days, showing a cumulative release of 1034.66 $\mu\text{g/mL}$ at pH5 and 3569.76 $\mu\text{g/mL}$ at pH7.4. Under acid conditions, for the first 14 days the range of concentration of drug release was between 74.28-54.84 $\mu\text{g/mL}$ and it was half reduced from day 15, 29.85 $\mu\text{g/mL}$, reaching 15.75 $\mu\text{g/mL}$ on day 25. Finally, there was a long plateau of 15 days where the drug released was correspondent to 11.87-3.21 $\mu\text{g/mL}$ per day (figure 5.55) (p -value > 0.05).

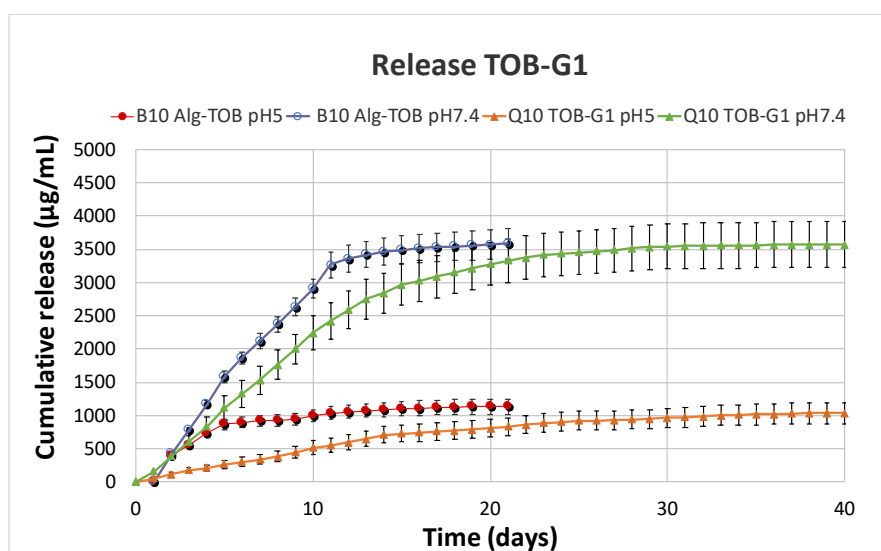


Figure 5.55: TOB release profile at pH5 and at pH7.4 for Q10 of the construct TOB-G1.

For each curve: Mean \pm SD (N=1, n=3).

At physiological environment, the drug was mainly released within the first 13 days, showing a range of values fluctuating between 261.14-155.13 $\mu\text{g}/\text{mL}$, which changed to 99.18 $\mu\text{g}/\text{mL}$ on day 14, plummeting to 18.86 $\mu\text{g}/\text{mL}$, on day 25 ($p\text{-value} < 0.05$). Then, the amount slightly varied from day 26, 11.58 $\mu\text{g}/\text{mL}$, to day 30, 10.82 $\mu\text{g}/\text{mL}$, followed a plateau of 10 more days in this case with a small daily release between 7.02-2.13 $\mu\text{g}/\text{mL}$ per day.

G2

The antibiotic was released for 45 days from the nano delivery system TOB-G2. At pH5, for the first 3 days the daily release was between 236.08 $\mu\text{g}/\text{mL}$ and 99.78 $\mu\text{g}/\text{mL}$, which gradually decreased on day 4, 94.72 $\mu\text{g}/\text{mL}$, dropping to 21.66 $\mu\text{g}/\text{mL}$ until day 12. Then, there was a slow reduction of the daily amount which ranged between 17.88-9.69 from day 13 to day 40, with a plateau of only 5 more days, ending up to a cumulative release equal to 1442.63 $\mu\text{g}/\text{mL}$ on day 45 ($p\text{-value} > 0.05$).

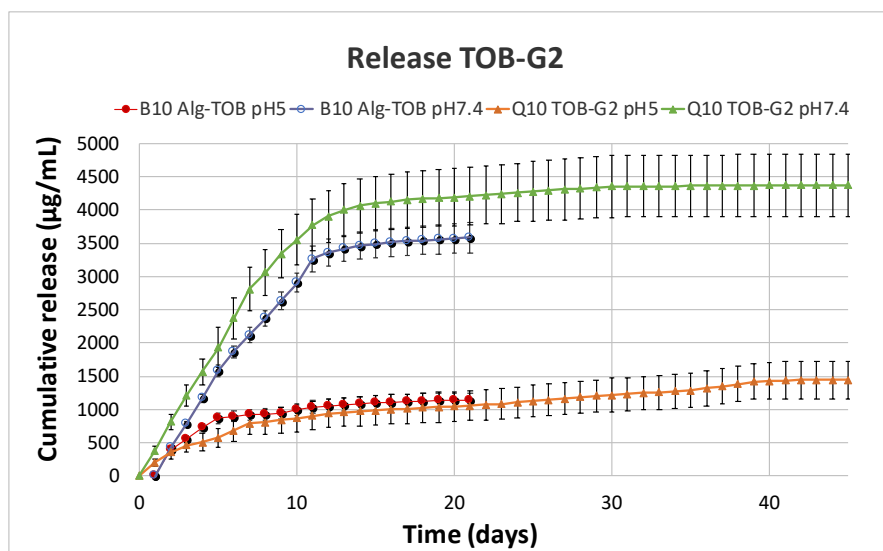


Figure 5.56: TOB release profile at pH5 and at pH7.4 for Q10 of the construct TOB-G2.

For each curve: Mean \pm SD (N=1, n=3).

As contrary, the daily quantity of drug released at pH7.4 was significantly high for the first 11 days showing a range of values between 454.62-316.72 $\mu\text{g}/\text{mL}$ from day 1 to day 7 which shifted to 274.82-201.72 $\mu\text{g}/\text{mL}$ up to day 11 ($p\text{-value} < 0.05$). Additionally, the daily rate reported on day 12, 138.41 $\mu\text{g}/\text{mL}$, decreased to 26.95 $\mu\text{g}/\text{mL}$ within the next 5 days, with a slow decrease from day 18, 17.75 $\mu\text{g}/\text{mL}$, to day 30, 12.09 $\mu\text{g}/\text{mL}$. Finally, similarly to what

observed at pH7.4 for the nanoconstruct TOB-G1, the final part of the curve was characterised by a long plateau of 15 days with a cumulative drug release of 4373.38 $\mu\text{g}/\text{mL}$ detected up to day 45 (figure 5.56).

G3

The last matrix analysed among the 18 nano delivery systems was TOB-G3, which provided at both media a drug release of 30 days, with a cumulative release of 796.20 $\mu\text{g}/\text{mL}$ at pH5 and 1163.44 $\mu\text{g}/\text{mL}$ at pH7.4. Under acid conditions, the daily release was between 132.12 $\mu\text{g}/\text{mL}$ and 99.46 $\mu\text{g}/\text{mL}$ for the first 5 days and it dropped to 24.27 $\mu\text{g}/\text{mL}$ on day 6 with a considerable reduction in the daily amount which ended up to 11.99 $\mu\text{g}/\text{mL}$ on day 21. In this case, the plateau lasted only 9 more days where the concentration oscillated between 8.44-5.21 $\mu\text{g}/\text{mL}$ detected per day (figure 5.57) ($p\text{-value} > 0.05$).

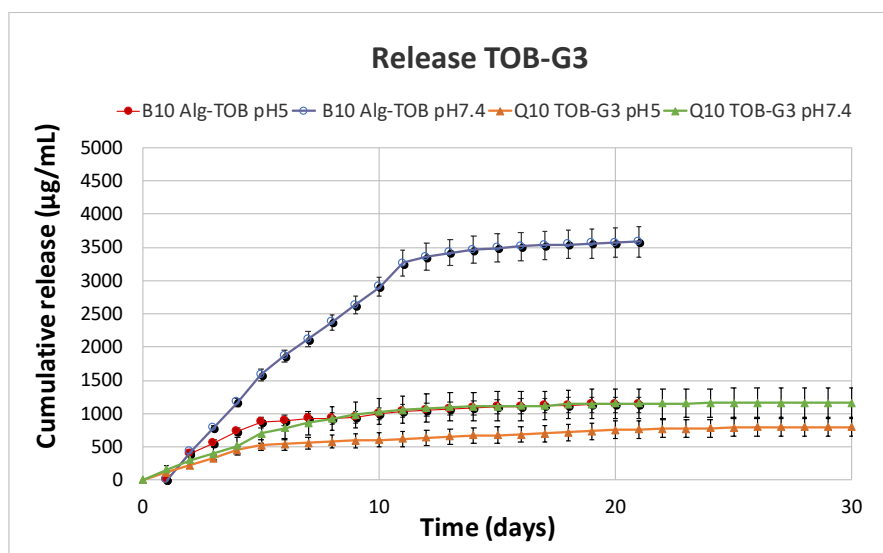


Figure 5.57: TOB release profile at pH5 and at pH7.4 for Q10 of the construct TOB-G3.

For each curve: Mean \pm SD (N=1, n=3).

At pH7.4, the drug release was ranging between 210.94-175.61 $\mu\text{g}/\text{mL}$ for the first 5 days and the quantity shifted to 94.75 $\mu\text{g}/\text{mL}$ on day 6 plummeting to 25.74 $\mu\text{g}/\text{mL}$ after 6 days. There was then a steady decrease of the rate within 2 days heading to 9.85 $\mu\text{g}/\text{mL}$ on day 14, followed by a long plateau of 16 extra days where the concentration ranged between 6.77-2.13 $\mu\text{g}/\text{mL}$ per day ($p\text{-value} > 0.05$).

Comparing the profiles of the group G there was a difference in the cumulative release achieved at the end of each drug release study. For example, the highest amount was gained by TOB-G2, followed by TOB-G1 and TOB-G3 which instead provided the lowest quantity among the 3 matrices (p-value < 0.05). Additionally, analysing these profiles plus the one of Alg-TOB, it was observed that the cumulative release of TOB-G1 was quite similar to the one of the bilayers with the difference that the employment of PBAE into the system helped in containing the drug release which reached the same cumulative release but only after 40 days rather than 21 (p-value > 0.05). As expected, TOB-G2 was higher than Alg-TOB, whereas for TOB-G3 the cumulative release was lower than the one of the bilayers system, even if it lasted longer (30 days) (p-value < 0.05).

Comparing the release of the aminoglycoside from the TOB-PBAEs nano-delivery systems to the results obtained from TGA and zeta potential profiles, it was observed consistency for the matrices including the PBAEs A2, A3, D3 and G2. For instance, the cargo was highly release from the nanoconstructs possessing the PBAEs A2, D2 and G2, proving a sustained release between 40-50 days and ranging between 1110-1490 µg/mL at pH5 (p-value < 0.05). Moreover, the drug was released from TOB-A3 and TOB-D3 systems for only 30 days and it was respectively equal to 1471.82 µg/mL and 1158.19 µg/mL under acid conditions (p-value > 0.05). The release profiles of these matrices were supported by the TGA, zeta potential and the PBAE hydrolysis.

Discussion

Zeta potential measurements

Zeta potential is a straightforward method applied in this project for monitoring the Layer by Layer self-assembly of the 18PBAEs-Tobramycin coatings. Tobramycin is an amphiphilic aminoglycoside composed by both hydroxylic and amino groups, but the presence of 5 amino groups in its chemical structure highlights its polycationic character which is the main responsible for its antibacterial activity (Lee *et al.*, 2015). Therefore, the LbL process for all the developed systems was carried out at pH5 to exploit the ability of the amino groups to be protonated under acid conditions and provide a positive charge to contrast the strong negativity of the alginate. Therefore, the LbL process was carried out in sodium acetate buffer pH5 and zeta potential measurements were pursued for each layer embedded onto the nanoparticles surface, producing a zig-zag pathway as proof of the success of the build-up systems.

Firstly, the profile provided by the matrix Alg-TOB showed that after an initial positivity of the drug in the first bilayer, $+13.37 \pm 0.55$ mV, the potential was close to 0 mV on B2 and it became negative on B3. Additionally, once a new layer of alginate was coated onto the system, the negativity of the drug increased as well (figure 5.1). This could be explained by the molecular structure of both the polymer alginate (Ma *et al.*, 2019) and the aminoglycoside (Dhondikubeer *et al.*, 2012): tobramycin is a small molecule, with a molecular weight of 467.52 g/mol and a lower number of ionisable groups than those present in the polyelectrolyte alginate (Kruizinga *et al.*, 2020). Hence, although the deposition of the drug was successful due to the electrostatic interactions occurring between the amino groups of the cargo and carboxyl groups of the alginate, the encapsulation of the tobramycin needed to be improved. For this reason, in this project, it was designed an alternative approach to entrap the drug onto the nanocarrier surface by employing poly(beta) amino esters (PBAEs) as polycations into matrices composed by quadruple layers rather than bilayers as follows: Alg-TOB-Alg-PBAE. Analysing the 18 TOB-PBAEs systems it was observed that for the first quadruple layer the results were quite similar for all of them. For example, the positive charge of the amino functionalised nanoparticles, $+17.07 \pm 3.12$ mV, was reversed once the alginate was embedded onto the system, -28.63 ± 1.20 mV. Then, the potential returned positive by

coating the drug, $+16.9 \pm 1.55$ mV; it was inverted again by a further layer of alginate, -29.06 ± 3.6 mV, changing into positive by coating a PBAE, which was different in each nanosystem and provided a weak positive charge as reported in the table 5.3 below:

LbL-assembly coatings	PBAE positive charge on Q1
TOB-A1	$+2.5 \pm 2.41$ mV
TOB-A2	$+12.9 \pm 1.2$ mV
TOB-A3	$+15.5 \pm 0.71$ mV
TOB-B1	$+4.4 \pm 0.68$ mV
TOB-B2	$+4.8 \pm 0.17$ mV
TOB-B3	$+8.8 \pm 0.33$ mV
TOB-D1	$+11.8 \pm 3.72$ mV
TOB-D2	$+15.5 \pm 4.50$ mV
TOB-D3	$+16.6 \pm 0.87$ mV
TOB-E1	$+13.4 \pm 0.23$ mV
TOB-E2	$+9.0 \pm 0.34$ mV
TOB-E3	$+6.4 \pm 0.74$ mV
TOB-F1	$+13.3 \pm 1.11$ mV
TOB-F2	$+20.8 \pm 1.67$ mV
TOB-F3	$+14.1 \pm 0.1$ mV
TOB-G1	$+21.6 \pm 0.90$ mV
TOB-G2	$+15.7 \pm 1.15$ mV
TOB-G3	$+16.6 \pm 1.54$ mV

Table 5.3: Positivity of PBAEs for Q1 of TOB-PBAEs coatings

Generally speaking, as reported from the figure 5.2 to 5.19, the profiles of TOB-PBAEs provided an alternative zig-zag pathway as previously observed for the system Alg-TOB. However, the presence of PBAEs as polycations in the matrices allowed to improve the deposition of the drug through the 10 quadruple layers: the potential of the cargo remained

positive for more layers whereas in the Alg-TOB layered nanoparticles it was easily reversed with the first two bilayers. Despite that, a remarkable difference was detected among the PBAEs layered nanoparticles: the choice of the amine as monomer for the PBAEs synthesis influenced the number of amino groups available for the interaction with the carboxyl groups of the alginate and thus, the success of the deposition of both cargo and PBAE on the nanocarrier surface. For instance, for the TOB-PBAEs nanoconstructs including the piperazine (1) as amine, the tobramycin positivity was converted into a negative value within the first 3 quadruple layers, except for TOB-F1, where tobramycin charge remained positive until Q5. As contrary, for the TOB-PBAEs matrices possessing 4-4 trimethyldipiperidine (2) and N,N-Bis[3-(methylamino)propyl]methylamine (3) as amines, a positive charge for tobramycin was detected for at least the first 5 quadruple layers. More specifically, for TOB-A2, TOB-B2, TOB-E3, TOB-F2, TOB-F3 and TOB-G3, the zeta potential of the drug was stable until Q8 with no influence from the strong negativity of the alginate. The strong negative zeta potential of sodium alginate reported in all the profiles corresponds to the value gained by Feng *et al.*, 2014 as well as the positivity of the pH-responsive polymers PBAEs was widely explained by Hammond, 2012, Li *et al.*, 2020. More specifically, (Little *et al.*, 2005) described the characterisation of different PBAEs containing microparticles, observing that the addition of these polymers reversed the zeta potential into positive and increased the efficiency and the loading of plasmid DNA. This could justify the difference in the zeta potential profiles developed in this project and the impact that the structure of PBAEs could have on the multilayer deposition.

Thermogravimetric analysis (TGA)

Thermogravimetric analysis (TGA) is a valid method applied for evaluating the thermal decomposition of polymers as well as for defining their thermal stabilities (Langtry, 1972), via determination of the weight loss as function of time and temperature in a controlled atmosphere (Ng *et al.*, 2018b).

TGA profiles reported from the figure 5.20 to 5.39 show similar curves that could be divided into two main parts. The first weigh loss occurs below 110°C corresponding to the evaporation of water and ethanol absorbed during the break of the microemulsion to form the amino-functionalised silica nanoparticles (AFSi-NPs). Additionally, the weight loss observed between

110°C and 500°C was instead attributed to the decomposition of the organic phase. This, in the TGA curve of AFSNPs before the LbL self-assembly, was representative of dehydroxylation for the remaining silanol groups, whereas for the bilayer and quadruple layers systems it was related to the decomposition of the amino groups of tobramycin and PBAEs (Lu, 2013). Comparing the weight losses gained from all the matrices developed in this project (table 5.4), a considerable difference was observed between the bilayer and the quadruple layer systems. For instance, in the Alg-TOB coating, the final weight loss on B10 was mainly attributed to the organic content resulting from the carboxyl and the amino groups of alginate and drug, instead in the all quadruple layers nanoconstructs the increased weight loss confirmed the presence of the PBAEs into the systems (Talavera-Pech *et al.*, 2018).

LbL-assembly coatings	Organic content % on B10/Q10
Alg-TOB	38.60% ± 0.22
TOB-A1	60.57% ± 0.62
TOB-A2	60.09% ± 0.83
TOB-A3	61.27% ± 0.14
TOB-B1	61.06% ± 1.35
TOB-B2	58.25% ± 0.55
TOB-B3	58.63% ± 0.48
TOB-D1	64.26% ± 0.33
TOB-D2	57.47% ± 1.29
TOB-D3	62.59% ± 0.49
TOB-E1	54.37% ± 0.97
TOB-E2	59.36% ± 0.09
TOB-E3	56.86% ± 0.13
TOB-F1	70.43% ± 1.19
TOB-F2	75.12% ± 0.09
TOB-F3	68.94% ± 0.28
TOB-G1	75.12% ± 0.09

TOB-G2	62.62% ± 0.43
TOB-G3	68.75% ± 0.1

Table 5.4: Organic content % for TOB-PBAEs for B10 or Q10

The difference in the organic content percentage among the nanosystems including PBAEs as polycations was caused by the variety of molecular structures of the monomers composing the polymers. In particular, TOB-F1, TOB-F2, TOB-F3, TOB-G1 and TOB-G2 provided the highest values of weight losses correspondent to the decomposition of an increased number of amino groups. Furthermore, the choice of the acrylate in this case influenced the weight loss: increased hydrophobicity lead to an higher mass losses (Akyol *et al.*, 2018). These results confirmed what observed with zeta potential measurements: the hydrophobicity of the diacrylates F, G and of the amine 2 and 3 had a great impact on the multilayer deposition of drug and PBAEs.

Tobramycin release quantification

In this project the antibiotic tobramycin (TOB) was entrapped onto two different type of matrices. Firstly, it was alternately encapsulated via LbL into a bilayer system composed by only the drug and the non-hydrolysable polymer alginate coated onto amino-functionalised silica nanoparticles surface. Then, it was embedded into quadruple layers systems including as follows: alginate-TOB-alginate-PBAE, employing 18 different PBAEs to form 18 TOB-PBAEs nanodelivery systems. In both cases, bilayer and quadruple layer matrices, the aminoglycoside was coated up to 10 times to provide systems composed in total by 10 bilayers or 10 quadruple layers. The drug release studies were carried out in two different buffers, sodium acetate pH5 and phosphate buffer pH7.4, to reproduce respectively acidic conditions typical of joint infections and physiological environment (Ribeiro, Monteiro and Ferraz, 2012). Analysing the profiles reported in the figures 5.39-5.57, the drug release was pH-dependent and based on the electrostatic interactions used to stack the polymer and the antibiotic in the multilayer coatings. Therefore, at pH7.4, weak electrostatic interactions had an impact on the drug release which was higher than at pH5, due to, instead, strong electrostatic interactions. For instance, in an acid environment, the increased number of protonated amino groups strengthened the electrostatic connection to the carboxyl groups of the sodium alginate heading to a stable state and thus controlling the drug release. As

contrary, the partial number of protonated amino groups under physiological environment loosened the electrostatic interactions and therefore provided a rapid antibiotic release (Zhou *et al.*, 2018), (Al Thaher *et al.*, 2018b). However, the release studies were pursued only for B10 or Q10 as representative layers with the highest amount of tobramycin released. The drug release was evaluated considering the cumulative release as function of time (days) and it is summarised in the table 5.5 below for all the matrices developed in this project.

LbL-assembly coatings	Cumulative release n° Days (pH5)	Cumulative release n° Days (pH7.4)	*Final Cumulative release at pH5	*Final Cumulative release at pH7.4
Alg-TOB	21	21	1134.99 µg/mL	3596.30 µg/mL
TOB-A1	30	30	1112.18 µg/mL	2067.35 µg/mL
TOB-A2	50	50	1113.26 µg/mL	4288.60 µg/mL
TOB-A3	30	30	1471.82 µg/mL	4104.61 µg/mL
TOB-B1	40	40	1640.88 µg/mL	4179.52 µg/mL
TOB-B2	30	30	1269.80 µg/mL	3004.83 µg/mL
TOB-B3	30	30	1176.82 µg/mL	2911.16 µg/mL
TOB-D1	60	60	1084.04 µg/mL	4048.48 µg/mL
TOB-D2	50	50	1491.78 µg/mL	4634.72 µg/mL
TOB-D3	30	30	1158.19 µg/mL	2807.46 µg/mL
TOB-E1	40	40	550.93 µg/mL	1157.52 µg/mL
TOB-E2	30	30	818.34 µg/mL	1438.45 µg/mL
TOB-E3	30	30	1285.86 µg/mL	2824.13 µg/mL
TOB-F1	30	30	971.27 µg/mL	1764.40 µg/mL
TOB-F2	30	30	975.10 µg/mL	1457.34 µg/mL
TOB-F3	30	30	1062.75 µg/mL	1255.45 µg/mL
TOB-G1	40	40	1034.66 µg/mL	3569.76 µg/mL
TOB-G2	45	45	1442.63 µg/mL	4373.38 µg/mL

TOB-G3	30	30	796.19 µg/mL	1163.44 µg/mL
---------------	----	----	--------------	---------------

***Daily release:** 20-30 µg/mL. **TOB-MIC:** 6.25 µg/mL against *Pseudomonas aeruginosa*, *Escherichia coli*, *Enterobacter species*, and *Klebsiella* (Krause *et al.*, 2016). **Table 5.5:** TOB cumulative release at pH5 and pH7.4.

Generally, the drug release from coatings designed via LbL occurs via diffusion through the multilayers, surface erosion or a combination of these two mechanisms (Smith *et al.*, 2009). Aminoglycosides, such as tobramycin, gentamycin and the glycopeptide vancomycin, encapsulated in LbL degradable systems possessing PBAEs provided antibiotic release which was dependent on several factors such as: the number of multilayers, the polymeric degradation, pH of the medium (Paula T. Hammond, 2012), (Wood *et al.*, 2005). The 18 TOB-PBAEs and the Alg-TOB bilayer coatings built up in this project showed drug release profiles which were consistent to previous studies. For example, from all the nanoconstructs, the antibiotic released through the layers via diffusion mechanism as Hammond *et al.* observed by incorporating gentamycin deposited via LbL into a system including a PBAE and hyaluronic acid (Hammond, Supervisor and Deen, 2008). Additionally, for all TOB-PBAEs layered nanoparticles the hydrolytic degradation and thus the drug release occurred more rapidly at pH7.4 than at pH5 as reported by Zhou *et al.* This research group achieved controlled tobramycin release for only 320 h by entrapping the antibiotic with chitosan via LbL on heparin micelles (Zhou *et al.*, 2018). As contrary, in this work, the cargo released from Alg-TOB matrix continued for 21 days, whereas it ranged between 30 and 60 days considering TOB-PBAEs coatings. This was a considerable improvement from the current nanocomposite formulations (Hill *et al.*, 2019), (Lee *et al.*, 2015), (Scott and Higham, 2003). However, differences in the amount of drug released were observed among the nano delivery systems which were dependent on the hydrolysis and the structure of the PBAEs. For example, considering the PBAEs A1 and B1 the presence of 2 more methylene groups (-CH₂) in the chemical structure of 1,6 hexanediol diacrylate (B) had a positive impact on the tobramycin release lasting 40 days from TOB-B1 against only 30 days from TOB-A1. Moreover, a hydrophobic diacrylate provided a more rapid drug release in a basic environment which was doubled than from TOB-A1 (table 5.3), but a controlled antibiotic release was detected at pH5 showing 1112.18 µg/mL for TOB-A1 and 1640.88 µg/mL for TOB-B1. Additionally, the choice of diacrylates with higher hydrophobicity such as D (neopentyl glycol diacrylate) or G (tricyclo [5.2.1.0²⁻⁶] decanodimethanol diacrylate) and a hydrophilic amine as piperazine (1) greatly

influenced the cargo release that occurred over a period of 40 days from TOB-G1 and 60 days from TOB-D1 with respectively 1034.66 $\mu\text{g}/\text{mL}$ and 1084.04 $\mu\text{g}/\text{mL}$ as cumulative release at pH5 and 3569.76 $\mu\text{g}/\text{mL}$ and 4048.48 $\mu\text{g}/\text{mL}$ at pH7.4. The difference in the length of drug release could be attributed to the polymeric solubility and the molecular structures, showing a straight chain for D1 instead ring chains for G1. However, although the PBAEs of the group F included a hydrophobic diacrylate, no prolonged release was observed for the matrices TOB-F1, TOB-F2 and TOB-F3. Indeed, the drug released through the thin multilayers for a period of only 30 days, with a low cumulative release especially at physiological environment ranging between 1255.45 $\mu\text{g}/\text{mL}$ to 1764.40 $\mu\text{g}/\text{mL}$. On the other hand, the employment as polycations of PBAEs possessing the amine 4,4 trimethyldipiperidine (2), which is more hydrophobic than amine 1 and 3, provided a longer drug release. For instance, considering TOB-A2, TOB-D2, TOB-G2, tobramycin release occurred for respectively 50 and 45 days showing a low cumulative release at pH5 for TOB-A2, 1113.26 $\mu\text{g}/\text{mL}$, rising up to 1442.63 $\mu\text{g}/\text{mL}$ for TOB-G2 and 1491.78 $\mu\text{g}/\text{mL}$ for TOB-D2. In this case, for these 3 matrices, at pH7.4, the drug release was more rapid than the profiles described before with the amine 1. These results were consistent to the zeta potential and TGA pathways representative of the nanoconstructs TOB-A2, TOB-G2 and TOB-D2. In particular, the choice of these polymers provided a sustained positive charge of PBAEs and antibiotic for a least 5 quadruple layers, and a weight loss percentage of Q10 over 60% confirming the success of the thin multilayer deposition. Overall, from all the matrices presented in this chapter, the aminoglycoside mainly released within the first 10-15 days overcoming the achievements of the current formulations (Lee *et al.*, 2015), with an initial daily release ranging between 30-50 $\mu\text{g}/\text{mL}$ at pH5 and 70-100 $\mu\text{g}/\text{mL}$ at pH7.4, followed by a reduction ranging between 6.25-2.49 $\mu\text{g}/\text{mL}$ released per day at both media characterising the plateau of each profile. The great amount detected in the first days indicated a concentration relatively high to kill pathogens causing orthopaedic implant infections (Krause *et al.*, 2016). Despite that, the high concentration could be promising for potential impregnation of the nanoparticles into poly(methyl methacrylate) (PMMA) bone cement.

Conclusions

In this chapter, the PBAEs were applied for the development of stimuli-responsive antibiotic release from bilayer or quadruple layers to prevent bacterial infections affecting biomaterials. In this case, the antimicrobial chosen was tobramycin, an aminoglycoside which mainly acts against Gram negative pathogens and especially possesses excellent bactericidal activity against *Pseudomonas aeruginosa* infections. In this work, tobramycin was entrapped into 18 PBAEs multilayers systems onto amino-functionalised silica nanoparticles surface, with the aim of minimising bacterial resistance and controlling the drug release. Firstly, the drug was alternately deposited into a bilayer system via Layer by Layer (LbL) self-assembly up to 10 bilayers. Then, it was encapsulated onto PBAEs-nanoparticles composed by 10 quadruple layers and each quadruple layer was composed as follows: alginate-TOB-alginate-PBAE. Therefore, 18 PBAEs were employed as polycations to form 18 TOB-PBAEs based nanoparticles. All the systems were characterised by zeta potential and TGA measurements and the drug release was evaluated by dispersing the nanoparticles after the LbL deposition in buffers at pH5 and pH7.4, to respectively reproduce acid conditions typical of the joint infections and physiological environment. The profiles gained for zeta potential, TGA and drug release studies contributed to explain that the pH-responsiveness of the multilayers, the number of layers composing the coatings and the choice of monomers for the synthesis of PBAEs are essential properties that can be adjusted to exploit the antibiotic release. For the first time, this work provided evidence that hydrophobic or hydrophilic monomers composing the PBAEs can greatly impact the drug release. In this case, PBAEs such as A2, D2, G2, B1, A3, D3 or A1 provided a prolonged antibiotic release lasting between 30 and 60 days, suggesting an early stage promising alternative for the treatment of early and late onset joint infections.

Chapter 6: General conclusion and future perspective

Total joint arthroplasty (TJA) is a life-enhancing procedure applied for the end-stage joint diseases to provide pain relief, to restore the bone function and to improve the quality of life for patients. However, one of its undesirable events is the prosthetic joint infection (PJI) which occurs between 0.5% and 3% of the cases. To avoid that the patient undergoes multiple revision surgeries to solve this problem, one of the treatments of PJI is the employment of antibiotic bone cement (ALBC) during the primary operation. Despite ALBC presents advantages such as the reduction of risk of PJI by delivering high concentration of antibiotic directly at the site of infection, on the other hand, there are concerns on its role in infection prevention and on its use in clinical practice. In particular, antibiotics could provide a short-term burst release followed by a decrease below the inhibitory concentration levels which lead to a continuous increase of bacterial resistance. Therefore, to improve the performance of ALBC, the development of new approaches is required.

The aims of this research project were: to develop silica nanocarriers releasing antimicrobial agents using Layer-by-Layer (LbL) technique employing poly (β -amino esters) (PBAEs) as polycations and to establish the optimal nanocarrier construct to provide sustained drug release for future applications on PMMA bone cement.

To reach these goals, in the initial stage, as reported in chapter 3, 18 amino-terminated linear PBAEs were synthesised and characterised via NMR spectroscopy and Gel Permeation Chromatography. It was found that the PBAE hydrolysis is caused by the cleavage of the ester bonds and the formation of diol products. This phenomenon mainly occurs at pH7.4. Therefore, as general concept: PBAEs rapidly hydrolyse at pH7.4 whereas slowly at pH5. This was observed for all the PBAEs synthesized along this PhD project. Additionally, the hydrolysis studies allowed to better understand that the choice of the monomers as well as the MW, charge and pH greatly influenced the polymeric degradation. More specifically, the combination between hydrophilic amine and diacrylates with short alkyl chain in their backbone promoted a rapid PBAEs hydrolysis (e.g. acrylates A, D, E and amine 1 and 3), instead hydrophobic amine and longer alkyl chain or the presence of aromatic units in the diacrylate backbone provided a gradual PBAE degradation (e.g. acrylates B, F, G and amine 2). Based on that, it was interesting to observe if the application of all the PBAEs synthesised along this project could have an impact on the drug encapsulation and its kinetics of release.

In this context, as discussed in chapter 4, the 18 PBAEs were employed as polycations to encapsulate chlorhexidine onto silica nanoparticles. In this project, mesoporous silica nanoparticles were chosen as nanocarrier due to their biocompatibility, high loading capability, easy synthesis and scale up with reasonable costs. However, unbonded silanol groups can cause membrane disruption leading to cell lysis. This side effect can reduce the application of these nanoconjugates as drug delivery system. Along this project, it was possible to overcome this problem by synthesizing amorphous amino-functionalised silica nanoparticles via wet chemistry whose size was 55 nm. Indeed, this approach of synthesis allowed to reduce the availability of unbonded silanol groups, and thus their toxicity on cells. Additionally, the amino-functionalisation of the nanocarriers facilitated the deposition of antimicrobial agents and cationic or anionic polyelectrolytes to form multilayer systems.

The characterisation of the nanoconjugates through zeta potential and thermogravimetric analysis (TGA) determined the success of the antimicrobial agent incorporation onto the nanocarrier surface. Furthermore, the comparison between the drug release profiles of PBAEs-CHX loaded nanoparticles and the system including only alginate and chlorhexidine, which was designed as control, allowed to understand that the presence of PBAEs into the coatings played an essential role on drug release profiles. Indeed, the physicochemical properties of these polymers such as MW, charge, hydrophobicity/hydrophilicity, solubility and their chemical structures had a great impact on chlorhexidine release which lasted between 30-110 days when the PBAE was coated, against the 25 days of the Alg-CHX nanoparticles. The CHX release was mainly regulated by the hydrolysis of PBAEs and this was confirmed by consistency detected between PBAE-CHX release and PBAE hydrolysis (via MW and charge) profiles. However, the choice of the monomers employed in the polymerisation was also important. For instance, PBAEs with aliphatic or aromatic diacrylates in their backbone such as B, D, F and G provided a prolonged drug release (over 60 days) especially if combined with the hydrophobic amine 2.

The development of the 18 PBAE-tobramycin nanoparticles and the evaluation of the antibiotic release, widely described in chapter 5, evidenced that the employment of PBAEs improved the performance of nanoconjugates including tobramycin. Indeed, the agent was gradually released over 30 days when a PBAE was embedded onto the drug delivery systems against the period of only 21 days detected by the control system alginate-tobramycin. In particular, in this case, PBAEs synthesised by the diacrylates A, D and G and the amines 2 and

3 provided a prolonged and controlled drug release between 30 and 60 days, which represent an alternative solution to the problem of the antibiotics burst release.

To conclude, the results obtained from this project, allowed to understand that the application of Layer by Layer as self-assembly technique plus the employment of PBAEs into multilayer formation, can control the antimicrobial agents release suggesting a promising early-stage approach for the treatment of early and delayed onset PJI.

To conclude the main findings of this project, suggest that the synthesis, the characterisation and the screening of PBAEs combined to nanotechnology enhance the release of antimicrobials. Furthermore, the choice of the monomers is crucial and has a great impact on the hydrolysis of polymers and drugs entrapped in the multilayer systems. Additionally, LbL self-assembly combined to nanotechnology provided prolonged antimicrobial release which depends on: the number of multilayers, the polymeric degradation and pH medium. Considering the systems possessing CHX-PBAEs and TOB-PBAEs, CHX-F2 (CHX release for 70 days) and TOB-D2 (TOB released over 30 days) are promising matrices which provided a significant improvement from the current nanocomposite formulations (up to 15 days).

For the future, before proceeding with the incorporation of PBAE-TOB or PBAE-CHX loaded nanoparticles on bone cement, it would be worthy to investigate different sets-up such as the influence of PBAEs alone or PBAE-antimicrobial formulations on cell viability and computational studies based on the chemistry of PBAEs. For instance, in the first case it would be interesting to observe whether the low toxicity of PBAEs remain unaltered or not after being incorporated into the nanocoatings and if a hydrophobic polymer such as B2, D2 or F2 would increase or decrease the viability on SaOS-2 osteoblasts cells. On the hand, in the second case, it would be helpful to study the interaction between all the PBAE and the antimicrobial agents based on the electrostatic interactions which regulated the drug release of both chlorhexidine and tobramycin. This would be a fundamental step in the development of novel chemical routes to synthesise or to modify other PBAEs.

References

- Aboltins, C. A. *et al.* (2007) 'Treatment of staphylococcal prosthetic joint infections with debridement, prosthesis retention and oral rifampicin and fusidic acid', *Clinical Microbiology and Infection*. European Society of Clinical Infectious Diseases, 13(6), pp. 586–591. doi: 10.1111/j.1469-0691.2007.01691.x.
- Agarwal, A. *et al.* (2012) 'Polymeric multilayers that localize the release of chlorhexidine from biologic wound dressings', *Biomaterials*. Elsevier Ltd, 33(28), pp. 6783–6792. doi: 10.1016/j.biomaterials.2012.05.068.
- Ai, H. *et al.* (2003) 'Biocompatibility of layer-by-layer self-assembled nanofilm on silicone rubber for neurons', 128, pp. 1–8. doi: 10.1016/S0165-0270(03)00191-2.
- Akinc, A. *et al.* (2003) 'Synthesis of poly(β -amino ester)s optimized for highly effective gene delivery', *Bioconjugate Chemistry*, 14(5), pp. 979–988. doi: 10.1021/bc034067y.
- Akyol, E. *et al.* (2018) 'Phosphonate-functionalized poly(β -amino ester) macromers as potential biomaterials', *Journal of Biomedical Materials Research - Part A*, 106(5), pp. 1390–1399. doi: 10.1002/jbm.a.36339.
- Altuncu, S. *et al.* (2019) 'Structure-property relationships of novel phosphonate-functionalized networks and gels of poly(β -amino esters)', *European Polymer Journal*. Elsevier, 113(November 2018), pp. 155–164. doi: 10.1016/j.eurpolymj.2019.01.052.
- Amano, Y. *et al.* (2016) 'Development of vascularized iPSC derived 3D-cardiomyocyte tissues by filtration Layer-by-Layer technique and their application for pharmaceutical assays', *Acta Biomaterialia*. Acta Materialia Inc., 33, pp. 110–121. doi: 10.1016/j.actbio.2016.01.033.
- Anagnostakos, K. and Kelm, J. (2009) 'Enhancement of antibiotic elution from acrylic bone cement', *Journal of Biomedical Materials Research - Part B Applied Biomaterials*, 90 B(1), pp. 467–475. doi: 10.1002/jbm.b.31281.
- and, S. E. B. and Barrett*, C. J. (2003) 'pH-Responsive Properties of Multilayered Poly(L-lysine)/Hyaluronic Acid Surfaces', pp. 1773–1783. doi: 10.1021/BM034184W.
- Anderson, D. G. *et al.* (2005) 'Structure/property studies of polymeric gene delivery using a library of poly(β -amino esters)', *Molecular Therapy*. The American Society of Gene Therapy, 11(3), pp. 426–434. doi: 10.1016/j.ymthe.2004.11.015.
- Anderson, D. G. *et al.* (2006) 'A combinatorial library of photocrosslinkable and degradable materials', *Advanced Materials*, 18(19), pp. 2614–2618. doi: 10.1002/adma.200600529.
- Anderson, D. G., Lynn, D. M. and Langer, R. (2003) 'Semi-automated synthesis and screening of a large library of degradable cationic polymers for gene delivery', *Angewandte Chemie - International Edition*, 42(27), pp. 3153–3158. doi: 10.1002/anie.200351244.
- Andorko, J. I. and Jewell, C. M. (2017) 'Designing biomaterials with immunomodulatory properties for tissue engineering and regenerative medicine', *Bioengineering & Translational Medicine*, 2(2), pp. 139–155. doi: 10.1002/btm2.10063.
- Ariga, K. *et al.* (1997) 'Alternately assembled ultrathin film of silica nanoparticles and linear polycations', *Chemistry Letters*, pp. 125–126. doi: 10.1246/cl.1997.125.
- Atkinson, H. D. E. (2017) 'The negatives of knee replacement surgery: complications and the dissatisfied patient', *Orthopaedics and Trauma*. Elsevier Ltd, 31(1), pp. 25–33. doi: 10.1016/j.morth.2016.09.011.
- Aubert-Viard, F. *et al.* (2019) 'Evaluation of antibacterial textile covered by layer-by-layer coating and loaded

with chlorhexidine for wound dressing application', *Materials Science and Engineering C*. Elsevier B.V, 100, pp. 554–563. doi: 10.1016/j.msec.2019.03.044.

Ayoade, F. (2020) 'Prosthetic Joint Infection (PMID : 28846340)', (November).

Azarikia, F. *et al.* (2017) 'Emulsion stability enhancement against environmental stresses using whey protein–tragacanthin complex: Comparison of layer-by-layer and mixing methods', *International Journal of Food Properties*. Taylor & Francis, 20(2), pp. 2084–2095. doi: 10.1080/10942912.2017.1362651.

Bahrami, N. *et al.* (2020) 'Layer-by-layer self-assembly of collagen and chitosan biomolecules on polyurethane films', *Journal of Applied Polymer Science*, 137(45), pp. 1–13. doi: 10.1002/app.49417.

Barceló, A. M. *et al.* (2016) 'Climatología del Balneario de Villavieja', *Anales de la Real Academia Nacional de Farmacia*, 82(5), pp. 108–126.

Barrett, L. and Atkins, B. (2014) 'The clinical presentation of prosthetic joint infection', *Journal of Antimicrobial Chemotherapy*, 69(SUPPL1), pp. 25–28. doi: 10.1093/jac/dku250.

Bejon, P. *et al.* (2010) 'Two-stage revision for prosthetic joint infection: predictors of outcome and the role of reimplantation microbiology', *Journal of Antimicrobial Chemotherapy*, 65(3), pp. 569–575. doi: 10.1093/jac/dkp469.

Biring, G. S. *et al.* (2009) 'Two-stage revision arthroplasty of the hip for infection using an interim articulated Prostalac hip spacer: a 10- to 15-year follow-up study', *The Journal of bone and joint surgery Br.*, 91(11), pp. 1431–1437. doi: 10.1302/0301-620X.91B11.22026; 10.1302/0301-620X.91B11.22026.

Bishop, C. J. *et al.* (2013) 'Binding and Gene Delivery', *Journal of the American Chemical Society*.

Bishop, C. J. *et al.* (2016) 'Layer-by-layer inorganic/polymeric nanoparticles for kinetically controlled multigene delivery', *Journal of Biomedical Materials Research - Part A*, 104(3), pp. 707–713. doi: 10.1002/jbm.a.35610.

Bistolfi, A. *et al.* (2011) 'Antibiotic-loaded cement in orthopedic surgery: a review.', *ISRN orthopedics*, 2011, p. 290851. doi: 10.5402/2011/290851.

Blodgett, K. B. (1935) 'Films Built by Depositing Successive Monomolecular Layers on a Solid Surface', *Journal of the American Chemical Society*, 57(6), pp. 1007–1022. doi: 10.1021/ja01309a011.

Bodey, G. P. and Stewart, D. (1972) 'In vitro studies of tobramycin.', *Antimicrobial agents and chemotherapy*, 2(3), pp. 109–113. doi: 10.1128/aac.2.3.109.

Boulmedais, F. *et al.* (2003) 'Buildup of exponentially growing multilayer polypeptide films with internal secondary structure', *Langmuir*, 19(2), pp. 440–445. doi: 10.1021/la0264522.

Brandt, C. M. *et al.* (1999) 'Staphylococcus aureus prosthetic joint infection treated with prosthesis removal and delayed reimplantation arthroplasty', *Mayo Clinic Proceedings*, 74(6), pp. 553–558. doi: 10.4065/74.6.553.

Brey, D. M., Erickson, I. and Burdick, J. A. (2008) 'Influence of macromer molecular weight and chemistry on poly(β -amino ester) network properties and initial cell interactions', *Journal of Biomedical Materials Research - Part A*, 85(3), pp. 731–741. doi: 10.1002/jbm.a.31494.

Brunauer, S. and Emmett, P. H. (1937) 'The Use of Low Temperature van der Waals Adsorption Isotherms in Determining the Surface Areas of Various Adsorbents', *Journal of the American Chemical Society*, 59(12), pp. 2682–2689. doi: 10.1021/ja01291a060.

Cai, K. *et al.* (2005) 'Polysaccharide-protein surface modification of titanium via a layer-by-layer technique:

Characterization and cell behaviour aspects', *Biomaterials*, 26(30), pp. 5960–5971. doi: 10.1016/j.biomaterials.2005.03.020.

Campoli-Richards, D. M. and Todd, P. A. (1987) 'Cefmenoxime: A Review of its Antibacterial Activity, Pharmacokinetic Properties and Therapeutic Use', *Drugs*, 34(2), pp. 188–221. doi: 10.2165/00003495-198734020-00002.

Caruso, F. (1998) 'Nanoengineering of Inorganic and Hybrid Hollow Spheres by Colloidal Templating', *Science*, 282(5391), pp. 1111–1114. doi: 10.1126/science.282.5391.1111.

Caseli, L. *et al.* (2006) 'The effect of the layer structure on the activity of immobilized enzymes in ultrathin films', *Journal of Colloid and Interface Science*, 303(1), pp. 326–331. doi: 10.1016/j.jcis.2006.07.013.

Chen, J. L. *et al.* (2009) 'Improving blood-compatibility of titanium by coating collagen-heparin multilayers', *Applied Surface Science*, 255(15), pp. 6894–6900. doi: 10.1016/j.apsusc.2009.03.011.

Chen, M. C. *et al.* (2005) 'A novel drug-eluting stent spray-coated with multi-layers of collagen and sirolimus', *Journal of Controlled Release*, 108(1), pp. 178–189. doi: 10.1016/j.jconrel.2005.07.022.

Chevalier, M. T., Gonzalez, J. and Alvarez, V. (2015) 'Biodegradable polymeric microparticles as drug delivery devices', *IFMBE Proceedings*, 49, pp. 187–190. doi: 10.1007/978-3-319-13117-7_49.

Choi, D. and Hong, J. (2014) 'Layer-by-layer assembly of multilayer films for controlled drug release', *Archives of Pharmacal Research*, 37(1), pp. 79–87. doi: 10.1007/s12272-013-0289-x.

Choi, H. and Chen, I. W. (2003) 'Surface-modified silica colloid for diagnostic imaging', *Journal of Colloid and Interface Science*, 258(2), pp. 435–437. doi: 10.1016/S0021-9797(02)00130-3.

Choi, H. R. *et al.* (2014) 'The Fate of Unplanned Retention of Prosthetic Articulating Spacers for Infected Total Hip and Total Knee Arthroplasty', *Journal of Arthroplasty*. Elsevier Inc., 29(4), pp. 690–693. doi: 10.1016/j.arth.2013.07.013.

Chuang, H. F., Smith, R. C. and Hammond, P. T. (2008) 'Polyelectrolyte multilayers for tunable release of antibiotics', *Biomacromolecules*, 9(6), pp. 1660–1668. doi: 10.1021/bm800185h.

Cordeiro, R. A. *et al.* (2019) 'Poly(β -amino ester)-based gene delivery systems: From discovery to therapeutic applications', *Journal of Controlled Release*. Elsevier, 310(August), pp. 155–187. doi: 10.1016/j.jconrel.2019.08.024.

Costerton, J. W., Stewart, P. S. and Greenberg, E. P. (1999) 'Bacterial biofilms: A common cause of persistent infections', *Science*, 284(5418), pp. 1318–1322. doi: 10.1126/science.284.5418.1318.

Daina, A., Michielin, O. and Zoete, V. (2017) 'SwissADME: A free web tool to evaluate pharmacokinetics, drug-likeness and medicinal chemistry friendliness of small molecules', *Scientific Reports*. Nature Publishing Group, 7(January), pp. 1–13. doi: 10.1038/srep42717.

Davidson, D. J., Spratt, D. and Liddle, A. D. (2019) 'Implant materials and prosthetic joint infection: The battle with the biofilm', *EFORT Open Reviews*, 4(11), pp. 633–639. doi: 10.1302/2058-5241.4.180095.

Decher, G. and Hong, J. -D (1991) 'Buildup of ultrathin multilayer films by a self-assembly process, 1 consecutive adsorption of anionic and cationic bipolar amphiphiles on charged surfaces', *Makromolekulare Chemie. Macromolecular Symposia*, 46(1), pp. 321–327. doi: 10.1002/masy.19910460145.

Delcea, M., Möhwald, H. and Skirtach, A. G. (2011) 'Stimuli-responsive LbL capsules and nanoshells for drug

delivery', *Advanced Drug Delivery Reviews*, 63(9), pp. 730–747. doi: 10.1016/j.addr.2011.03.010.

Detzel, C. J., Larkin, A. L. and Rajagopalan, P. (2011) 'Polyelectrolyte multilayers in tissue engineering', *Tissue Engineering - Part B: Reviews*, 17(2), pp. 101–113. doi: 10.1089/ten.teb.2010.0548.

Devalapally, H. *et al.* (2007) 'Poly(ethylene oxide)-modified poly(beta-amino ester) nanoparticles as a pH-sensitive system for tumor-targeted delivery of hydrophobic drugs: Part 3. Therapeutic efficacy and safety studies in ovarian cancer xenograft model', *Cancer Chemotherapy and Pharmacology*, 59(4), pp. 477–484. doi: 10.1007/s00280-006-0287-5.

Dhondikubeer, R. *et al.* (2012) 'Antibacterial activity of amphiphilic tobramycin', *Journal of Antibiotics*. Nature Publishing Group, 65(10), pp. 495–498. doi: 10.1038/ja.2012.59.

Dienstag, J. and Neu, H. C. (1972) 'In vitro studies of tobramycin, an aminoglycoside antibiotic.', *Antimicrobial agents and chemotherapy*, 1(1), pp. 41–45. doi: 10.1128/AAC.1.1.41.

Donato, D. I., Lazzara, G. and Milioto, S. (2010) 'Thermogravimetric analysis : A tool to evaluate the ability of mixtures in consolidating waterlogged archaeological woods', *Journal of Thermal Analysis and Calorimetry*, 101(3), pp. 1085–1091. doi: 10.1007/s10973-010-0717-9.

Egashira, K., Goodman, S. and Yang, F. (2014) 'Orthopaedic Implants to Modulate Inflammatory Response', 34(38), pp. 10287–10295. doi: 10.1016/j.biomaterials.2013.09.028.Mutant.

Eltoukhy, A. A. *et al.* (2012) 'Effect of molecular weight of amine end-modified poly(β -amino ester)s on gene delivery efficiency and toxicity', *Biomaterials*, 33(13), pp. 3594–3603. doi: 10.1016/j.biomaterials.2012.01.046.

Eltoukhy, A. A. *et al.* (2013) 'Degradable terpolymers with alkyl side chains demonstrate enhanced gene delivery potency and nanoparticle stability', *Advanced Materials*, 25(10), pp. 1487–1493. doi: 10.1002/adma.201204346.

Est-Witte, S. E. *et al.* (2020) 'Non-viral gene delivery of HIF-1 α promotes angiogenesis in human adipose-derived stem cells', *Acta Biomaterialia*. Elsevier Ltd, 113, pp. 279–288. doi: 10.1016/j.actbio.2020.06.042.

Fahmy, H. M., Aly, A. A. and Abou-Okeil, A. (2018) 'A non-woven fabric wound dressing containing layer – by – layer deposited hyaluronic acid and chitosan', *International Journal of Biological Macromolecules*. Elsevier B.V, 114(2017), pp. 929–934. doi: 10.1016/j.ijbiomac.2018.03.149.

Faria, G. *et al.* (2013) 'The effect of chlorhexidine on plaque index and mutans streptococci in orthodontic patients: A pilot study', *Open Journal of Stomatology*, 03(06), pp. 323–328. doi: 10.4236/ojst.2013.36054.

Farrar, D., Benson, R. and Milner, R. (2009) 'Antibiotic-loaded bone cements', *Drug-Device Combination Products: Delivery Technologies and Applications*, pp. 190–218. doi: 10.1533/9781845697488.2.190.

Feng, B. Z. *et al.* (2007) 'Direct Covalent Assembly to Fabricate Microcapsules with Ultrathin Walls and High Mechanical Strength **', (20434030), pp. 3687–3691. doi: 10.1002/adma.200700541.

Feng, C. *et al.* (2014) 'Immobilization of coacervate microcapsules in multilayer sodium alginate beads for efficient oral anticancer drug delivery', *Biomacromolecules*, 15(3), pp. 985–996. doi: 10.1021/bm401890x.

Feng, W. *et al.* (2014) 'Effect of pH-responsive alginate/chitosan multilayers coating on delivery efficiency, cellular uptake and biodistribution of mesoporous silica nanoparticles based nanocarriers', *ACS Applied Materials and Interfaces*, 6(11), pp. 8447–8460. doi: 10.1021/am501337s.

Fields, R. J. *et al.* (2012) 'Surface modified poly(β amino ester)-containing nanoparticles for plasmid DNA delivery', *Journal of Controlled Release*, 164(1), pp. 41–48. doi: 10.1016/j.jconrel.2012.09.020.

- Filipović, V. V. *et al.* (2018) 'Biocompatible and degradable scaffolds based on 2-hydroxyethyl methacrylate, gelatin and poly(beta amino ester) crosslinkers', *Polymer Testing*. Elsevier Ltd, 68, pp. 270–278. doi: 10.1016/j.polymertesting.2018.04.024.
- Francolini, I. *et al.* (2017) 'Antifouling and antimicrobial biomaterials: an overview', *Apmis*, 125(4), pp. 392–417. doi: 10.1111/apm.12675.
- Friedman, R. J. *et al.* (2013) 'Complication rates after hip or knee arthroplasty in morbidly obese patients', *Clinical Orthopaedics and Related Research*, 471(10), pp. 3358–3366. doi: 10.1007/s11999-013-3049-9.
- Fullriede, H. *et al.* (2016) 'PH-responsive release of chlorhexidine from modified nanoporous silica nanoparticles for dental applications', *BioNanoMaterials*, 17(1–2), pp. 59–72. doi: 10.1515/bnm-2016-0003.
- Gao, P. *et al.* (2011) 'Recent advances in materials for extended-release antibiotic delivery system', *Journal of Antibiotics*. Nature Publishing Group, 64(9), pp. 625–634. doi: 10.1038/ja.2011.58.
- Gentile, P. *et al.* (2014) 'An overview of poly(lactic-co-glycolic) Acid (PLGA)-based biomaterials for bone tissue engineering', *International Journal of Molecular Sciences*, 15(3), pp. 3640–3659. doi: 10.3390/ijms15033640.
- Gentile, P. *et al.* (2015) 'Layer by layer in the last decade', *Nanotechnology*, 26(422001).
- George, J., Klika, A. K. and Higuera, C. A. (2017) 'Use of Chlorhexidine Preparations in Total Joint Arthroplasty', *Journal of Bone and Joint Infection*, 2(1), pp. 15–22. doi: 10.7150/jbji.16934.
- GOMES, L. (2019) 'Diagnóstico precoce da infecção articular periprotética do quadril – situação atual , avanços e perspectivas. A Early Diagnosis of Periprosthetic Joint Infection of the Hip – Current Status , Advances and Perspectives', *Revista Brasileira de Ortopedia*, 54(4), pp. 368–376.
- Gong, Y. *et al.* (2007) 'Layer-by-layer assembly of chondroitin sulfate and collagen on aminolyzed poly(l-lactic acid) porous scaffolds to enhance their chondrogenesis', *Acta Biomaterialia*, 3(5), pp. 677–685. doi: 10.1016/j.actbio.2007.04.007.
- Gorbet, M. B. and Sefton, M. V. (2004) 'Biomaterial-associated thrombosis: Roles of coagulation factors, complement, platelets and leukocytes', *Biomaterials*, 25(26), pp. 5681–5703. doi: 10.1016/j.biomaterials.2004.01.023.
- Greasley, S. L. *et al.* (2016) 'Controlling particle size in the Stöber process and incorporation of calcium', *Journal of Colloid and Interface Science*, 469, pp. 213–223. doi: 10.1016/j.jcis.2016.01.065.
- Green, J. J. *et al.* (2006) 'Biodegradable polymeric vectors for gene delivery to human endothelial cells', *Bioconjugate Chemistry*, 17(5), pp. 1162–1169. doi: 10.1021/bc0600968.
- Green, J. J. *et al.* (2009) 'Poly(β -amino esters): Procedures for Synthesis and Gene Delivery BT - Macromolecular Drug Delivery: Methods and Protocols', in Belting, M. (ed.). Totowa, NJ: Humana Press, pp. 53–63. doi: 10.1007/978-1-59745-429-2_4.
- Green, J. J., Langer, R. and Anderson, D. G. (2008) 'A combinatorial polymer library approach yields insight into nonviral gene delivery', *Accounts of Chemical Research*, 41(6), pp. 749–759. doi: 10.1021/ar7002336.
- Gröger, C., Lutz, K. and Brunner, E. (2008) 'Biomolecular self-assembly and its relevance in silica biomineralization', *Cell Biochemistry and Biophysics*, pp. 23–39. doi: 10.1007/s12013-007-9003-2.
- Großhaus, C. *et al.* (2020) 'Melt Electrospinning of Nanofibers from Medical-Grade Poly(ϵ -Caprolactone) with a Modified Nozzle', *Small*, 16(44). doi: 10.1002/smll.202003471.

Gupta, P. *et al.* (2015) 'Quercetin conjugated poly(β -amino esters) nanogels for the treatment of cellular oxidative stress', *Acta Biomaterialia*. Acta Materialia Inc., 27, pp. 194–204. doi: 10.1016/j.actbio.2015.08.039.

Hammond, Paula T (2012) 'Building biomedical materials layer-by-layer', *Materials Today*, pp. 196–206. doi: 10.1016/S1369-7021(12)70090-1.

Hammond, Paula T. (2012) 'Building biomedical materials layer-by-layer', *Materials Today*. Elsevier Ltd, 15(5), pp. 196–206. doi: 10.1016/S1369-7021(12)70090-1.

Hammond, P. T., Supervisor, T. and Deen, W. M. (2008) 'POLYELECTROLYTE MULTILAYERS FOR TUNABLE by', pp. 1660–1668.

Han, Y. *et al.* (2017) 'Unraveling the growth mechanism of silica particles in the stöber method: In situ seeded growth model', *Langmuir*, 33(23), pp. 5879–5890. doi: 10.1021/acs.langmuir.7b01140.

Harnet, J. C. *et al.* (2009) 'Antibacterial protection of suture material by chlorhexidine-functionalized polyelectrolyte multilayer films', *Journal of Materials Science: Materials in Medicine*, 20(1), pp. 185–193. doi: 10.1007/s10856-008-3559-2.

He, T. and Chan, V. (2010) 'Covalent layer-by-layer assembly of polyethyleneimine multilayer for antibacterial applications', *Journal of Biomedical Materials Research - Part A*, 95 A(2), pp. 454–464. doi: 10.1002/jbm.a.32872.

Health Protection Agency (2012) 'Surveillance of Surgical Site Infections in NHS Hospitals in England, 2011/2012', London: Health Protection Agency, (April 2018). Available at: www.hpa.org.uk.

Hendriks, J. G. E. *et al.* (2004) 'Backgrounds of antibiotic-loaded bone cement and prosthesis-related infection', *Biomaterials*, 25(3), pp. 545–556. doi: 10.1016/S0142-9612(03)00554-4.

Henini, M. (2000) 'Handbook of Thin-Film Deposition Processes and Techniques', *Microelectronics Journal*, 31(3), p. 219. doi: 10.1016/S0026-2692(99)00122-6.

Hill, M. *et al.* (2019) 'Formulation of antimicrobial tobramycin loaded PLGA nanoparticles via complexation with AOT', *Journal of Functional Biomaterials*, 10(2). doi: 10.3390/jfb10020026.

Honary, S. *et al.* (2009) 'Formulation and characterization of doxorubicin nanovesicles', *Journal of Vacuum Science & Technology B: Microelectronics and Nanometer Structures*, 27(3), p. 1573. doi: 10.1116/1.3127504.

Honary, S. and Zahir, F. (2013) 'Effect of zeta potential on the properties of nano-drug delivery systems - A review (Part 1)', *Tropical Journal of Pharmaceutical Research*, 12(2), pp. 255–264. doi: 10.4314/tjpr.v12i2.19.

Hong, J. *et al.* (1999) 'Titanium is a highly thrombogenic biomaterial: Possible implications for osteogenesis', *Thrombosis and Haemostasis*, 82(1), pp. 58–64. doi: 10.1055/s-0037-1614630.

Hong, J. *et al.* (2011) 'Inherent charge-shifting polyelectrolyte multilayer blends: A facile route for tunable protein release from surfaces', *Biomacromolecules*, 12(8), pp. 2975–2981. doi: 10.1021/bm200566k.

Huang, L. and Yang, M. (2008) 'Surface immobilization of chondroitin 6-sulfate / heparin multilayer on stainless steel for developing drug-eluting coronary stents', 61, pp. 43–52. doi: 10.1016/j.colsurfb.2007.07.004.

Hunter, D. J. and Bierma-Zeinstra, S. (2019) 'Osteoarthritis', *The Lancet*, 393(10182), pp. 1745–1759. doi: 10.1016/S0140-6736(19)30417-9.

HUNTER, R. J. (1981) 'The Calculation of Zeta Potential', *Zeta Potential in Colloid Science*, pp. 59–124. doi: 10.1016/b978-0-12-361961-7.50007-9.

Huynh, D. P. *et al.* (2008) 'Functionalized injectable hydrogels for controlled insulin delivery', *Biomaterials*,

29(16), pp. 2527–2534. doi: 10.1016/j.biomaterials.2008.02.016.

Hwang, S. J. *et al.* (2007) 'pH-Sensitivity control of PEG-poly(β -amino ester) block copolymer micelle', *Macromolecular Research*, 15(5), pp. 437–442. doi: 10.1007/BF03218811.

Isac-García, J. *et al.* (2016) 'Lab Notebook', *Experimental Organic Chemistry*, pp. 29–43. doi: 10.1016/b978-0-12-803893-2.50002-4.

Jaganathan, S. K. *et al.* (2014) 'Biomaterials in cardiovascular research: Applications and clinical implications', *BioMed Research International*, 2014. doi: 10.1155/2014/459465.

James, S. L. *et al.* (2018) 'Global, regional, and national incidence, prevalence, and years lived with disability for 354 Diseases and Injuries for 195 countries and territories, 1990-2017: A systematic analysis for the Global Burden of Disease Study 2017', *The Lancet*, 392(10159), pp. 1789–1858. doi: 10.1016/S0140-6736(18)32279-7.

Jasper, L. L. *et al.* (2016) 'Risk factors for revision of total knee arthroplasty: a scoping review', *BMC Musculoskeletal Disorders*, 17(1), p. 182. doi: 10.1186/s12891-016-1025-8.

Jeckson, T. A. *et al.* (2020) 'Delivery of Therapeutics from Layer-by-Layer Electrospun Nanofiber Matrix for Wound Healing: An Update', *Journal of Pharmaceutical Sciences*. American Pharmacists Association. doi: 10.1016/j.xphs.2020.10.003.

Jenjob, R., Phakkeeree, T. and Crespy, D. (2020) 'Core-shell particles for drug-delivery, bioimaging, sensing, and tissue engineering', *Biomaterials science*. Royal Society of Chemistry, 8(10), pp. 2756–2770. doi: 10.1039/c9bm01872g.

Jiranek, W. a, Hanssen, A. D. and Greenwald, a S. (2006) 'Antibiotic-loaded bone cement for infection prophylaxis in total joint replacement.', *The Journal of bone and joint surgery. American volume*, 88(11), pp. 2487–2500. doi: 10.2106/JBJS.E.01126.

Jones, C. G. (1997) 'Chlorhexidine: is it still the gold standard?', *Periodontology 2000*, 15, pp. 55–62. doi: 10.1111/j.1600-0757.1997.tb00105.x.

Jordan, C. T., Hilt, J. Z. and Dziubla, T. D. (2019) 'Modeling the oxidative consumption of curcumin from controlled released poly(beta-amino ester) microparticles in the presence of a free radical generating system', *Regenerative Biomaterials*, 6(4), pp. 201–210. doi: 10.1093/rb/rbz002.

Kaltsas, D. S. (2004) 'Infection after total hip arthroplasty', *Annals of the Royal College of Surgeons of England*, 86(4), pp. 267–271. doi: 10.1308/147870804579.

Kamat, C. D. *et al.* (2013) 'Poly(β -amino ester) nanoparticle delivery of TP53 has activity against small cell lung cancer in vitro and in vivo', *Molecular Cancer Therapeutics*, 12(4), pp. 405–415. doi: 10.1158/1535-7163.MCT-12-0956.

Karabasz, A., Bzowska, M. and Szczepanowicz, K. (2020) 'Biomedical Applications of Multifunctional Polymeric Nanocarriers: A Review of Current Literature', *International journal of nanomedicine*, 15, pp. 8673–8696. doi: 10.2147/IJN.S231477.

Kardys, A. Y., Bharali, D. J. and Mousa, S. a (2013) 'Amino-Functionalized Silica Nanoparticles : In Vitro Evaluation for Targeted Delivery and Therapy of Pancreatic Cancer', 2013.

Katagiri, K. *et al.* (2002) 'Layered paving of vesicular nanoparticles formed with cerasome as a bioinspired organic-inorganic hybrid', *Journal of the American Chemical Society*, 124(27), pp. 7892–7893. doi:

10.1021/ja0259281.

Keeney, M. *et al.* (2013) 'Mutant MCP-1 protein delivery from layer-by-layer coatings on orthopedic implants to modulate inflammatory response', *Biomaterials*. Elsevier Ltd, 34(38), pp. 10287–10295. doi: 10.1016/j.biomaterials.2013.09.028.

Keeney, M. *et al.* (2015) 'Nanocoating for biomolecule delivery using layer-by-layer self-assembly', *Journal of Materials Chemistry B*. Royal Society of Chemistry, 3(45), pp. 8757–8770. doi: 10.1039/c5tb00450k.

Kern, W. and Schuegraf, K. K. (2001) 'Deposition Technologies and Applications', *Handbook of Thin Film Deposition Processes and Techniques*, i, pp. 11–43. doi: 10.1016/b978-081551442-8.50006-7.

Khan, F. *et al.* (2016) 'Dye aggregation in layer-by-layer dyeing of cotton fabrics', *RSC Advances*. Royal Society of Chemistry, 6(24), pp. 20286–20293. doi: 10.1039/c5ra27019g.

Kim, B. S. *et al.* (2009) 'MAD (multiagent delivery) nanolayer: Delivering multiple therapeutics from hierarchically assembled surface coatings', *Langmuir*, 25(24), pp. 14086–14092. doi: 10.1021/la9017618.

Kim, J. *et al.* (2018) 'Verteporfin-Loaded Poly(ethylene glycol)-Poly(beta-amino ester)-Poly(ethylene glycol) Triblock Micelles for Cancer Therapy', *Biomacromolecules*, 19(8), pp. 3361–3370. doi: 10.1021/acs.biomac.8b00640.

Kim, J., Sunshine, J. C. and Green, J. J. (2014) 'Differential polymer structure tunes mechanism of cellular uptake and transfection routes of poly(beta-amino ester) polyplexes in human breast cancer cells', *Bioconjugate Chemistry*, 25(1), pp. 43–51. doi: 10.1021/bc4002322.

Kim, Y. *et al.* (2013) 'Poly (amino ester) s-Based Polymeric Gene Carriers in Cancer Gene Therapy', *Novel gene therapy approaches*, pp. 376–396.

Kinnari, T. J. *et al.* (2010) 'Effect of surface roughness and sterilization on bacterial adherence to ultra-high molecular weight polyethylene.', *Clinical microbiology and infection : the official publication of the European Society of Clinical Microbiology and Infectious Diseases*, 16(7), pp. 1036–1041. doi: 10.1111/j.1469-0691.2009.02995.x.

Kirkland, N. T. (2012) 'Magnesium biomaterials: Past, present and future', *Corrosion Engineering Science and Technology*, 47(5), pp. 322–328. doi: 10.1179/1743278212Y.0000000034.

Klouche, S. *et al.* (2012) 'Infected total hip arthroplasty revision: One- or two-stage procedure?', *Orthopaedics and Traumatology: Surgery and Research*, 98(2), pp. 144–150. doi: 10.1016/j.otsr.2011.08.018.

Kneuer, C. *et al.* (2000) 'Silica nanoparticles modified with aminosilanes as carriers for plasmid DNA', *International Journal of Pharmaceutics*, 196(2), pp. 257–261. doi: 10.1016/S0378-5173(99)00435-4.

Kolinsky, D. C. and Liang, S. Y. (2018) 'Musculoskeletal Infections in the Emergency Department', *Emergency Medicine Clinics of North America*, 36(4), pp. 751–766. doi: 10.1016/j.emc.2018.06.006.

Komatsu, T. *et al.* (2011) 'Albumin nanotube.pdf', 109, pp. 3246–3248.

Kotra, L. P., Haddad, J. and Mobashery, S. (2000) 'Aminoglycosides: Perspectives on mechanisms of action and resistance and strategies to counter resistance', *Antimicrobial Agents and Chemotherapy*, 44(12), pp. 3249–3256. doi: 10.1128/AAC.44.12.3249-3256.2000.

Krause, K. M. *et al.* (2016) 'Aminoglycosides : An Overview'.

Kruizinga, M. D. *et al.* (2020) 'Pharmacokinetics of intravenous and inhaled salbutamol and tobramycin: An

exploratory study to investigate the potential of exhaled breath condensate as a matrix for pharmacokinetic analysis', *British Journal of Clinical Pharmacology*, 86(1), pp. 175–181. doi: 10.1111/bcp.14156.

Kuijpers, A. J. *et al.* (2000) 'In vitro and in vivo evaluation of gelatin } chondroitin sulphate hydrogels for controlled release of antibacterial proteins', 21, pp. 1763–1772.

Kurtz, S. *et al.* (2007) 'Projections of primary and revision hip and knee arthroplasty in the United States from 2005 to 2030', *Journal of Bone and Joint Surgery - Series A*, 89(4), pp. 780–785. doi: 10.2106/JBJS.F.00222.

L, P. *et al.* (1999) 'A Self-Destroying Polycationic Polymer : Biodegradable', *Peptides*, 4(19), pp. 5633–5639.

Lamagni, T. (2014) 'Epidemiology and burden of prosthetic joint infections', *Journal of Antimicrobial Chemotherapy*, 69(SUPPL1), pp. 5–10. doi: 10.1093/jac/dku247.

Langtry, B. N. (1972) 'Identity And Spatio-Temporal Continuity', *Australasian Journal of Philosophy*, 50(2), pp. 184–189. doi: 10.1080/00048407212341221.

Lee, H. S. *et al.* (2015) 'Targeted release of tobramycin from a pH-responsive grafted bilayer challenged with *S. aureus*', *Biomacromolecules*, 16(2), pp. 650–659. doi: 10.1021/bm501751v.

Lee, I. C. and Wu, Y. C. (2014) 'Facilitating neural stem/progenitor cell niche calibration for neural lineage differentiation by polyelectrolyte multilayer films', *Colloids and Surfaces B: Biointerfaces*, 121, pp. 54–65. doi: 10.1016/j.colsurfb.2014.05.033.

Lehmann-horn, K. *et al.* (2014) 'This article has been accepted for publication and undergone full peer review but has not been through the copyediting, typesetting, pagination and proofreading process which may lead to differences between this version and the Version of Record. Please c', *The Laryngoscope*, (August), pp. 2–31. doi: 10.1002/acr.22212.

Lenarcik, B. and Kierzkowska, A. (2010) 'Separation Science and Technology The Influence of Alkyl Chain Length and Steric Effect on Stability Constants and Extractability of Zn (II) Complexes with 1 - Alkyl - 4 (5) - Methylimidazoles The Influence of Alkyl Chain Length and', (October 2014), pp. 37–41. doi: 10.1081/SS-200033148.

Lenguerrand, E. *et al.* (2017) 'Revision for prosthetic joint infection following hip arthroplasty', *Bone and Joint Research*, 6(6), pp. 391–398. doi: 10.1302/2046-3758.66.BJR-2017-0003.R1.

Lewis, G. (2009) 'Properties of antibiotic-loaded acrylic bone cements for use in cemented arthroplasties: A state-of-the-art review', *Journal of Biomedical Materials Research - Part B Applied Biomaterials*, 89(2), pp. 558–574. doi: 10.1002/jbm.b.31220.

Lewis, G., Janna, S. and Bhattaram, A. (2005) 'Influence of the method of blending an antibiotic powder with an acrylic bone cement powder on physical, mechanical, and thermal properties of the cured cement', *Biomaterials*, 26(20), pp. 4317–4325. doi: 10.1016/j.biomaterials.2004.11.003.

Li, H. *et al.* (2012) 'The effect of layer-by-layer chitosan-hyaluronic acid coating on graft-to-bone healing of a poly(Ethylene Terephthalate) artificial ligament', *Journal of Biomaterials Science, Polymer Edition*, 23(1–4), pp. 425–438. doi: 10.1163/092050610X551989.

Li, M. *et al.* (2006) 'Elastin Blends for Tissue Engineering Scaffolds', *Journal of Biomedical Materials Research Part A*, 79(4), pp. 963–73. doi: 10.1002/jbm.a.

Li, Wen *et al.* (2020) 'New sight for in-situ monitoring of silica growth process: The incorporation of Stöber

process and aggregation-induced emission (AIE) technique', *Dyes and Pigments*. Elsevier Ltd, 182, p. 108637. doi: 10.1016/j.dyepig.2020.108637.

Li, Weinan *et al.* (2020) 'Synthesis and characterization of pH-responsive PEG-poly(β -amino ester) block copolymer micelles as drug carriers to eliminate cancer stem cells', *Pharmaceutics*, 12(2), pp. 1–17. doi: 10.3390/pharmaceutics12020111.

Lim, K. S. and Kam, P. C. A. (2008) 'Chlorhexidine - Pharmacology and clinical applications', *Anaesthesia and Intensive Care*, 36(4), pp. 502–512. doi: 10.1177/0310057x0803600404.

Limited, M. I. (2011) 'Zeta potential: An Introduction in 30 minutes', *Zetasizer Nano Serles Technical Note. MRK654-01*, 2, pp. 1–6. Available at: <http://scholar.google.com/scholar?hl=en&btnG=Search&q=intitle:Zeta+Potential+An+Introduction+in+30+Minutes#0>.

Lin, Q. *et al.* (2010) 'Heparin / collagen multilayer as a thromboresistant and endothelial favorable coating for intravascular stent', pp. 132–141. doi: 10.1002/jbm.a.32820.

Lin, Y. X. *et al.* (2016) 'PH-Sensitive Polymeric Nanoparticles Modulate Autophagic Effect via Lysosome Impairment', *Small*, 12(21), pp. 2921–2931. doi: 10.1002/smll.201503709.

Little, S. R. *et al.* (2005) 'Formulation and characterization of poly (β amino ester) microparticles for genetic vaccine delivery', *Journal of Controlled Release*, 107(3), pp. 449–462. doi: 10.1016/j.jconrel.2005.04.022.

Liu, S. *et al.* (2017) 'Alkylated branched poly(β -amino esters) demonstrate strong DNA encapsulation, high nanoparticle stability and robust gene transfection efficacy', *Journal of Materials Chemistry B*, 5(27), pp. 5307–5310. doi: 10.1039/c7tb00996h.

Liu, S., Volkmer, D. and Kurth, D. G. (2003) 'Functional polyoxometalate thin films via electrostatic layer-by-layer self-assembly', *Journal of Cluster Science*, 14(3), pp. 405–419. doi: 10.1023/B:JOCL.0000005072.28928.96.

Liu, Y. *et al.* (2015) 'Synthesis and characterization of silica nanoparticles functionalized with multiple TEMPO groups and investigation on their oxidation activity', *Polymer Chemistry*, 6(43), pp. 7514–7523. doi: 10.1039/c5py01190f.

Liu, Y. *et al.* (2019) 'Poly(β -Amino Esters): Synthesis, Formulations, and Their Biomedical Applications', *Advanced Healthcare Materials*, 8(2), pp. 1–24. doi: 10.1002/adhm.201801359.

Lu, B. *et al.* (2018) 'Novel wound dressing with chitosan gold nanoparticles capped with a small molecule for effective treatment of multi-antibiotic-resistant bacterial infections', *Nanotechnology*. IOP Publishing, 29(42). doi: 10.1088/1361-6528/aad7a7.

Lu, H. T. (2013) 'Synthesis and characterization of amino-functionalized silica nanoparticles', *Colloid Journal*, 75(3), pp. 311–318. doi: 10.1134/S1061933X13030125.

Lu, M. M. *et al.* (2017) 'Synergistic bactericidal activity of chlorhexidine-loaded, silver-decorated mesoporous silica nanoparticles', *International Journal of Nanomedicine*, 12, pp. 3577–3589. doi: 10.2147/IJN.S133846.

Luo, D. *et al.* (2016) 'Novel Formulation of Chlorhexidine Spheres and Sustained Release with Multilayered Encapsulation', *ACS Applied Materials and Interfaces*, 8(20), pp. 12652–12660. doi: 10.1021/acsami.6b02997.

Lvov, Y. *et al.* (1994) 'Successive Deposition of Alternate Layers of Polyelectrolytes and a Charged Virus', *Langmuir*, 10(11), pp. 4232–4236. doi: 10.1021/la00023a052.

- Lynn, D. M. and Langer, R. (2000) 'Degradable Poly (beta-amino esters): Synthesis , Characterization , and Self-Assembly with Plasmid DNA', *J Am Chem Soc*, 122(10), pp. 10761–10768. doi: 10.1021/ja0015388.
- Ma, M. *et al.* (2019) 'Lignin-containing cellulose nanocrystals/sodium alginate beads as highly effective adsorbents for cationic organic dyes', *International Journal of Biological Macromolecules*. Elsevier B.V., 139, pp. 640–646. doi: 10.1016/j.ijbiomac.2019.08.022.
- MacLean, S. B. M. *et al.* (2019) 'Application of dermal chlorhexidine antiseptics is ineffective at reducing *Propionibacterium acnes* colonization in shoulder surgery', *Shoulder and Elbow*, 11(2), pp. 98–105. doi: 10.1177/1758573218755570.
- Mahmud, T. *et al.* (2012) 'Assessing the gold standard: A review of 253 two-stage revisions for infected TKA knee', *Clinical Orthopaedics and Related Research*, 470(10), pp. 2730–2736. doi: 10.1007/s11999-012-2358-8.
- Malinzak, R. A. *et al.* (2009) 'Morbidly Obese, Diabetic, Younger, and Unilateral Joint Arthroplasty Patients Have Elevated Total Joint Arthroplasty Infection Rates', *Journal of Arthroplasty*. Elsevier B.V., 24(6 SUPPL.), pp. 84–88. doi: 10.1016/j.arth.2009.05.016.
- Marambio-Jones, C. and Hoek, E. M. V. (2010) 'A review of the antibacterial effects of silver nanomaterials and potential implications for human health and the environment', *Journal of Nanoparticle Research*, 12(5), pp. 1531–1551. doi: 10.1007/s11051-010-9900-y.
- Martínez-Moreno, J. *et al.* (2017) 'Antibiotic-loaded Bone Cement as Prophylaxis in Total Joint Replacement', *Orthopaedic Surgery*, 9(4), pp. 331–341. doi: 10.1111/os.12351.
- Masalov, V. M. *et al.* (2011) 'Mechanism of formation and nanostructure of Stöber silica particles', *Nanotechnology*, 22(27). doi: 10.1088/0957-4484/22/27/275718.
- Masri, B. A. *et al.* (1998) 'Long-term Elution of Antibiotics from Bone-Cement An in vivo Study Using the Prosthesis of Antibiotic-loaded Acrylic Cement (PROSTALAC) System', 13(3).
- Massazza, G. *et al.* (2015) *Antibiotics and cements for the prevention of biofilm-associated infections, Biomaterials and Medical Device - Associated Infections*. Woodhead Publishing Limited. doi: 10.1533/9780857097224.2.185.
- Masterakos, P. *et al.* (2016) 'Biodegradable DNA Nanoparticles that Provide Widespread Gene Delivery in the Brain', *Small*, 12(5), pp. 678–685. doi: 10.1002/smll.201502554.
- Matsusaki, M. *et al.* (2012) 'Layer-by-Layer Assembly Through Weak Interactions and Their Biomedical Applications'. doi: 10.1002/adma.201103698.
- Maugeri, I. F. S. and Scientifico, I. (2016) 'C Er[®] a C Er', (April 2011).
- Mcpherson, E. J. *et al.* (2002) 'Outcomes Using a Staging System', *Clinical Orthopaedics and Related Research*, (403), pp. 8–15. doi: 10.1097/01.blo.0000030172.56585.c6.
- Men, W. *et al.* (2020) 'Layer-by-layer pH-sensitive nanoparticles for drug delivery and controlled release with improved therapeutic efficacy in vivo', *Drug Delivery*. Taylor & Francis, 27(1), pp. 180–190. doi: 10.1080/10717544.2019.1709922.
- Mendelsohn, J. D. *et al.* (2000) 'Fabrication of microporous thin films from polyelectrolyte multilayers', *Langmuir*, 16(11), pp. 5017–5023. doi: 10.1021/la000075g.
- Mendelsohn, J. D. *et al.* (2003) 'Rational design of cytophilic and cytophobic polyelectrolyte multilayer thin films',

- Biomacromolecules*, 4(1), pp. 96–106. doi: 10.1021/bm0256101.
- Metcalfe, A. D. and Ferguson, M. W. J. (2007) 'Tissue engineering of replacement skin : the crossroads of biomaterials , wound healing , embryonic development , stem cells and regeneration', (December 2006), pp. 413–437. doi: 10.1098/rsif.2006.0179.
- Michel, M. *et al.* (2004) 'Layer by layer self-assembled polyelectrolyte multilayers with embedded phospholipid vesicles', *Langmuir*, 20(12), pp. 4835–4839. doi: 10.1021/la049736q.
- Michel, M. *et al.* (2005) 'Layer by layer self-assembled polyelectrolyte multilayers with embedded phospholipid vesicles obtained by spraying: Integrity of the vesicles', *Langmuir*, 21(17), pp. 7854–7859. doi: 10.1021/la050497w.
- Miller, A. O., Henry, M. W. and Brause, B. D. (2017) *Prevention of joint infections, Management of Periprosthetic Joint Infections (PJIs)*. Elsevier Ltd. doi: 10.1016/B978-0-08-100205-6.00001-X.
- Milstone, A. M., Passaretti, C. L. and Perl, T. M. (2008) 'Chlorhexidine: Expanding the armamentarium for infection control and prevention', *Clinical Infectious Diseases*, 46(2), pp. 274–281. doi: 10.1086/524736.
- Min, J., Braatz, R. D. and Hammond, P. T. (2014) 'Tunable staged release of therapeutics from layer-by-layer coatings with clay interlayer barrier', *Biomaterials*. Elsevier Ltd, 35(8), pp. 2507–2517. doi: 10.1016/j.biomaterials.2013.12.009.
- Monnery, B. D. *et al.* (2017) 'Cytotoxicity of polycations: Relationship of molecular weight and the hydrolytic theory of the mechanism of toxicity', *International Journal of Pharmaceutics*. Elsevier B.V., 521(1–2), pp. 249–258. doi: 10.1016/j.ijpharm.2017.02.048.
- Monolayers, S. and Brushes, P. (2005) 'Self-Assembled Monolayers and Polymer Brushes in Biotechnology: Current Applications and Future Perspectives', pp. 2427–2448.
- Moureau, N. L., Deschneau, M. and Pyrek, J. (2009) 'Evaluation of the clinical performance of a chlorhexidine gluconate antimicrobial transparent dressing', *Journal of Infection Prevention*, 10(SUPPL. 1), pp. 13–17. doi: 10.1177/1757177409342144.
- Müller, M. (2001) 'Orientation of α -helical poly(L-lysine) in consecutively adsorbed polyelectrolyte multilayers on texturized silicon substrates', *Biomacromolecules*, 2(1), pp. 262–269. doi: 10.1021/bm005628g.
- Multilayers, S. *et al.* (2005) 'Delivery Platform for Hydrophobic Drugs : Prodrug Approach Combined with', pp. 1626–1627.
- Murata, H. *et al.* (2007) 'Permanent , non-leaching antibacterial surfaces — 2 : How high density cationic surfaces kill bacterial cells', 28, pp. 4870–4879. doi: 10.1016/j.biomaterials.2007.06.012.
- Nacken, M. *et al.* (2003) 'Modified silica particles for gene delivery', *Materials Science and Engineering C*, 23(1–2), pp. 93–97. doi: 10.1016/s0928-4931(02)00238-2.
- Namba, R. S., Inacio, M. C. S. and Paxton, E. W. (2013) 'Risk factors associated with deep surgical site infections after primary total knee arthroplasty: An analysis of 56,216 knees', *Journal of Bone and Joint Surgery - Series A*, 95(9), pp. 775–782. doi: 10.2106/JBJS.L.00211.
- National Joint Registry for England Wales Northern Ireland and the Isle of Man (2019) '16th Annual Report 2019:National Joint Registry for England, Wales, Northern Ireland and the Isle of Man', *NJR 16th Annual Report 2019*, (December 2018), pp. 1–248. Available at: <https://www.hqip.org.uk/wp-content/uploads/2018/11/NJR->

15th-Annual-Report-2018.pdf.

Nayanathara, U., Kermaniyan, S. S. and Such, G. K. (2020) 'Multicompartment Polymeric Nanocarriers for Biomedical Applications', *Macromolecular Rapid Communications*, 41(18), pp. 1–10. doi: 10.1002/marc.202000298.

Ng, H. M. *et al.* (2018a) 'Thermogravimetric Analysis of Polymers', *Encyclopedia of Polymer Science and Technology*, (13), pp. 1–29. doi: 10.1002/0471440264.pst667.

Ng, H. M. *et al.* (2018b) 'Thermogravimetric Analysis of Polymers', *Encyclopedia of Polymer Science and Technology*, (January 2019), pp. 1–29. doi: 10.1002/0471440264.pst667.

Nuzzo, R. G. and Allara, D. L. (1983) 'Surfaces', 12(1 1), pp. 4481–4483.

Onda, M., Ariga, K. and Kunitake, T. (1999) 'Activity and stability of glucose oxidase in molecular films assembled alternately with polyions', *Journal of Bioscience and Bioengineering*, 87(1), pp. 69–75. doi: 10.1016/S1389-1723(99)80010-3.

Osmon, D. R. *et al.* (2013) 'Diagnosis and management of prosthetic joint infection: Clinical practice guidelines by the infectious diseases Society of America', *Clinical Infectious Diseases*, 56(1), pp. 1–25. doi: 10.1093/cid/cis803.

Otto-Lambertz, C. *et al.* (2017) 'Periprosthetic infection in joint replacement - Diagnosis and treatment', *Deutsches Arzteblatt International*, 114(20), pp. 347–354. doi: 10.3238/arztebl.2017.0347.

Park, S. *et al.* (2018) 'Layer-by-layer assembled polymeric thin films as prospective drug delivery carriers: Design and applications', *Biomaterials Research*. *Biomaterials Research*, 22, pp. 1–13. doi: 10.1186/s40824-018-0139-5.

Peel, T. N. *et al.* (2012) 'Early onset prosthetic hip and knee joint infection: treatment and outcomes in Victoria, Australia', *J Hosp Infect*, 82(4), pp. 248–253. doi: 10.1016/j.jhin.2012.09.005.

Peng, M. *et al.* (2019) 'Polyelectrolytes fabrication on magnesium alloy surface by layer-by-layer assembly technique with antiplatelet adhesion and antibacterial activities', *Journal of Coatings Technology and Research*. Springer US, 16(3), pp. 857–868. doi: 10.1007/s11998-018-00162-6.

Pérez-Anes, A. *et al.* (2015) 'Bioinspired Titanium Drug Eluting Platforms Based on a Poly- β -cyclodextrin-Chitosan Layer-by-Layer Self-Assembly Targeting Infections', *ACS Applied Materials and Interfaces*, 7(23), pp. 12882–12893. doi: 10.1021/acsami.5b02402.

Perni, S. *et al.* (2015) 'Antimicrobial activity of bone cements embedded with organic nanoparticles', *International Journal of Nanomedicine*, 10, pp. 6317–6329. doi: 10.2147/IJN.S86440.

Perni, S., Martini-Gilching, K. and Prokopovich, P. (2018) 'Controlling release kinetics of gentamicin from silica nano-carriers', *Colloids and Surfaces A: Physicochemical and Engineering Aspects*. Elsevier B.V., 541, pp. 212–221. doi: 10.1016/j.colsurfa.2017.04.063.

Perni, S. and Prokopovich, P. (2014) 'Continuous release of gentamicin from gold nanocarriers', *RSC Advances*. Royal Society of Chemistry, 4(94), pp. 51904–51910. doi: 10.1039/c4ra10023a.

Perni, S. and Prokopovich, P. (2017a) 'Poly-beta-amino-esters nano-vehicles based drug delivery system for cartilage', *Nanomedicine: Nanotechnology, Biology, and Medicine*. The Authors, 13(2), pp. 539–548. doi: 10.1016/j.nano.2016.10.001.

- Perni, S. and Prokopovich, P. (2017b) 'Poly-beta-amino-esters nano-vehicles based drug delivery system for cartilage', *Nanomedicine: Nanotechnology, Biology, and Medicine*. The Authors, 13(2), pp. 539–548. doi: 10.1016/j.nano.2016.10.001.
- Perni, S. and Prokopovich, P. (2020a) *Nanostructured coatings for antimicrobial applications*, *Advances in Nanostructured Materials and Nanopatterning Technologies*. Elsevier Inc. doi: 10.1016/b978-0-12-816865-3.00005-6.
- Perni, S. and Prokopovich, P. (2020b) 'Optimisation and feature selection of poly-beta-amino-ester as a drug delivery system for cartilage', *Journal of Materials Chemistry B*. Royal Society of Chemistry, 8(23), pp. 5096–5108. doi: 10.1039/c9tb02778e.
- Pithankuakul, K. *et al.* (2015) 'The Effects of Different Mixing Speeds on the Elution and Strength of High-Dose Antibiotic-Loaded Bone Cement Created With the Hand-Mixed Technique', *Journal of Arthroplasty*. Elsevier Inc., 30(5), pp. 858–863. doi: 10.1016/j.arth.2014.12.003.
- Podsiadlo, P. *et al.* (2005) 'Layer-by-layer assembly of nacre-like nanostructured composites with antimicrobial properties', in *AIChE Annual Meeting, Conference Proceedings*, pp. 5198–5210.
- Porrino, J. *et al.* (2020) 'Prosthetic joint infections: diagnosis, management, and complications of the two-stage replacement arthroplasty', *Skeletal Radiology*. Skeletal Radiology, 49(6), pp. 847–859. doi: 10.1007/s00256-020-03389-w.
- Prokopovich, P. *et al.* (2015) 'Potent antimicrobial activity of bone cement encapsulating silver nanoparticles capped with oleic acid', *Journal of Biomedical Materials Research - Part B Applied Biomaterials*, 103(2), pp. 273–281. doi: 10.1002/jbm.b.33196.
- Punkka, E. and Rubner, M. F. (1992) 'Molecular heterostructure devices composed of langmuir-blodgett films of conducting polymers', *Journal of Electronic Materials*, 21(11), pp. 1057–1063. doi: 10.1007/BF02665884.
- Qi, A. *et al.* (2011) 'Template-free synthesis and encapsulation technique for layer-by-layer polymer nanocarrier fabrication', *ACS Nano*, 5(12), pp. 9583–9591. doi: 10.1021/nn202833n.
- Qu, M. *et al.* (2020) 'Biodegradable microneedle patch for transdermal gene delivery', *Nanoscale*. Royal Society of Chemistry, 12(32), pp. 16724–16729. doi: 10.1039/d0nr02759f.
- Rabea, E. I. *et al.* (2003) 'Chitosan as antimicrobial agent: Applications and mode of action', *Biomacromolecules*, 4(6), pp. 1457–1465. doi: 10.1021/bm034130m.
- Rahimi, M. *et al.* (2020) 'Carbohydrate polymer-based silver nanocomposites: Recent progress in the antimicrobial wound dressings', *Carbohydrate Polymers*. Elsevier Ltd., 231(November), p. 115696. doi: 10.1016/j.carbpol.2019.115696.
- Rahman, W. A., Kazi, H. A. and Gollish, J. D. (2017) 'Results of single stage exchange arthroplasty with retention of well fixed cement-less femoral component in management of infected total hip arthroplasty', *World Journal of Orthopedics*, 8(3), p. 264. doi: 10.5312/wjo.v8.i3.264.
- Ramalingam, K. *et al.* (2016) 'Gene delivery using dendrimer/pDNA complexes immobilized in electrospun fibers using the Layer-by-Layer technique', *RSC Advances*, 6(99), pp. 97116–97128. doi: 10.1039/c6ra22444j.
- Rao, K. S. *et al.* (2005) 'A novel method for synthesis of silica nanoparticles', *Journal of Colloid and Interface Science*, 289(1), pp. 125–131. doi: 10.1016/j.jcis.2005.02.019.

Redfern, J. P. and Coats, A. P. (1963) 'Thermogravimetric Analysis', *Analyst*, 88(906). doi: 10.1038/1731011b0.

Regis, D. *et al.* (2013) 'Release of gentamicin and vancomycin from preformed spacers in infected total hip arthroplasties: Measurement of concentrations and inhibitory activity in patients' drainage fluids and serum', *The Scientific World Journal*, 2013(V). doi: 10.1155/2013/752184.

Registry, N. J. (2020) '17Th Annual Report', *National Joint Registry*, (December 2019).

Ren, K. and Ji, J. (2015) 'Polyelectrolyte Multilayers as Robust Coating for Cardiovascular Biomaterials', *Layer-by-Layer Films for Biomedical Applications*, pp. 399–418. doi: 10.1002/9783527675869.ch19.

Ribeiro, M., Monteiro, F. J. and Ferraz, M. P. (2012) 'Infection of orthopedic implants with emphasis on bacterial adhesion process and techniques used in studying bacterial-material interactions.', *Biomatter*, 2(4), pp. 176–194. doi: 10.4161/biom.22905.

Ronca, D. *et al.* (2016) 'Bone Tissue Engineering: 3D PCL-based Nanocomposite Scaffolds with Tailored Properties', *Procedia CIRP*. Elsevier B.V., 49, pp. 51–54. doi: 10.1016/j.procir.2015.07.028.

Rudelli, S. *et al.* (2008) 'One-Stage Revision of Infected Total Hip Arthroplasty with Bone Graft', *Journal of Arthroplasty*. Elsevier B.V., 23(8), pp. 1165–1177. doi: 10.1016/j.arth.2007.08.010.

Safranski, D. L. *et al.* (2014) 'Semi-degradable poly(β -amino ester) networks with temporally controlled enhancement of mechanical properties', *Acta Biomaterialia*. Acta Materialia Inc., 10(8), pp. 3475–3483. doi: 10.1016/j.actbio.2014.04.022.

Saleh, K. J. *et al.* (2016) 'Acrylic bone cement in total joint arthroplasty: A review', *Journal of Orthopaedic Research*. doi: 10.1002/jor.23184.

Samal, S. K. *et al.* (2012) 'Cationic polymers and their therapeutic potential', *Chemical Society Reviews*, 41(21), pp. 7147–7194. doi: 10.1039/c2cs35094g.

San Juan, A. M. T. *et al.* (2020) 'Layer by layer surface engineering of poly(lactide-co-glycolide) nanoparticles for plasmid DNA delivery', *Journal of Applied Polymer Science*, 137(32), pp. 1–8. doi: 10.1002/app.49377.

Saurer, E. M. *et al.* (2010) 'Layer-by-layer assembly of DNA- and protein-containing films on microneedles for drug delivery to the skin', *Biomacromolecules*, 11(11), pp. 3136–3143. doi: 10.1021/bm1009443.

Schneider, G. and Decher, G. (2004) 'From functional core/shell nanoparticles prepared via layer-by-layer deposition to empty nanospheres', *Nano Letters*, 4(10), pp. 1833–1839. doi: 10.1021/nl0490826.

Schneider, G. and Decher, G. (2008) 'Functional core/shell nanoparticles via layer-by-layer assembly. Investigation of the experimental parameters for controlling particle aggregation and for enhancing dispersion stability', *Langmuir*, 24(5), pp. 1778–1789. doi: 10.1021/la7021837.

Schwartz, A. B. (2004) 'Cortical Neural Prosthetics', *Annual Review of Neuroscience*, 27(1), pp. 487–507. doi: 10.1146/annurev.neuro.27.070203.144233.

Scott, C. P. and Higham, P. A. (2003) 'Antibiotic Bone Cement for the Treatment of Pseudomonas Aeruginosa in Joint Arthroplasty: Comparison of Tobramycin and Gentamicin-Loaded Cements', *Journal of Biomedical Materials Research - Part B Applied Biomaterials*, 64(2), pp. 94–98. doi: 10.1002/jbm.b.10515.

Segovia, N. *et al.* (2014) 'Oligopeptide-terminated poly(β -amino ester)s for highly efficient gene delivery and intracellular localization', *Acta Biomaterialia*. Acta Materialia Inc., 10(5), pp. 2147–2158. doi: 10.1016/j.actbio.2013.12.054.

Serhan, M. *et al.* (2019) 'Total iron measurement in human serum with a smartphone', *AIChE Annual Meeting, Conference Proceedings*, 2019-Novem. doi: 10.1039/x0xx00000x.

Shah, N. J. *et al.* (2012) 'Osteophilic multilayer coatings for accelerated bone tissue growth', *Advanced Materials*, 24(11), pp. 1445–1450. doi: 10.1002/adma.201104475.

Shimazaki, Y. *et al.* (1997) 'Preparation of the layer-by-layer deposited ultrathin film based on the charge-transfer interaction', *Langmuir*, 13(6), pp. 1385–1387. doi: 10.1021/la9609579.

Shukla, A. *et al.* (2010) 'Controlling the release of peptide antimicrobial agents from surfaces', *Biomaterials*. Elsevier Ltd, 31(8), pp. 2348–2357. doi: 10.1016/j.biomaterials.2009.11.082.

Simmen, H.-P. *et al.* (1993) 'Effect of peritoneal fluid pH on outcome of aminoglycoside treatment of intraabdominal infections', *World Journal of Surgery*, 17(3), pp. 393–397. doi: 10.1007/BF01658708.

Singh, R. and Lillard, J. W. (2009) 'Nanoparticle-based targeted drug delivery', *Experimental and Molecular Pathology*. Elsevier Inc., 86(3), pp. 215–223. doi: 10.1016/j.yexmp.2008.12.004.

Siqueira, M. B. P. *et al.* (2015) 'Modes of failure of total knee arthroplasty: registries and realities', *The journal of knee surgery*, 28(2), pp. 127–138. doi: 10.1055/s-0034-1396014.

Slane, J., Gietman, B. and Squire, M. (2018) 'Antibiotic elution from acrylic bone cement loaded with high doses of tobramycin and vancomycin', *Journal of Orthopaedic Research*, 36(4), pp. 1078–1085. doi: 10.1002/jor.23722.

Smith, R. C. *et al.* (2009) 'Layer-by-layer platform technology for small-molecule delivery', *Angewandte Chemie - International Edition*, 48(47), pp. 8974–8977. doi: 10.1002/anie.200902782.

Smith, W. R. *et al.* (2018a) 'Nanotechnology in orthopedics: A clinically oriented review', *BMC Musculoskeletal Disorders*. BMC Musculoskeletal Disorders, 19(1), pp. 1–10. doi: 10.1186/s12891-018-1990-1.

Smith, W. R. *et al.* (2018b) 'Nanotechnology in orthopedics: A clinically oriented review', *BMC Musculoskeletal Disorders*. BMC Musculoskeletal Disorders, 19(1), pp. 1–10. doi: 10.1186/s12891-018-1990-1.

Sosnik, A. (2014) 'Alginate Particles as Platform for Drug Delivery by the Oral Route: State-of-the-Art', *ISRN Pharmaceutics*, 2014, pp. 1–17. doi: 10.1155/2014/926157.

Sperling, C. *et al.* (2005) 'In vitro hemocompatibility of albumin – heparin multilayer coatings on polyethersulfone prepared by the layer-by-layer technique', pp. 5–7. doi: 10.1002/jbm.a.30519.

Stathopoulos, P. *et al.* (2011) 'Effect of titanium maxillofacial implants and osteosynthesis materials on platelet function', *British Journal of Oral and Maxillofacial Surgery*, 49(7), pp. 538–541. doi: 10.1016/j.bjoms.2010.09.003.

Stober, W. E. R. N. E. R. (1968) 'Controlled Growth of Monodisperse Silica Spheres in the Micron Size Range 1', 69, pp. 62–69.

Vander Straeten, A. *et al.* (2017) 'Protein-polyelectrolyte complexes to improve the biological activity of proteins in layer-by-layer assemblies', *Nanoscale*, 9(44), pp. 17186–17192. doi: 10.1039/c7nr04345g.

Sukhishvili, S. A. S. and Granick, S. (2000) 'Layered, Erasable, Ultrathin Polymer Films', *Journal of the American Chemical Society*, 122(14), pp. 9550–9551. doi: 10.1021/ja002410t.

Sukhorukov, G. B. *et al.* (1996) 'Multilayer films containing immobilized nucleic acids. Their structure and possibilities in biosensor applications', *Biosensors and Bioelectronics*, 11(9), pp. 913–922. doi: 10.1016/0956-5663(96)89440-1.

Sun, D. *et al.* (2016) 'Effect of zeta potential and particle size on the stability of SiO₂ nanospheres as carrier for ultrasound imaging contrast agents', *International Journal of Electrochemical Science*, 11(10), pp. 8520–8529. doi: 10.20964/2016.10.30.

Sunshine, J. C. *et al.* (2012) 'Poly(β -amino ester)-nanoparticle mediated transfection of retinal pigment epithelial cells in vitro and in vivo', *PLoS ONE*, 7(5). doi: 10.1371/journal.pone.0037543.

Sunshine, J. C., Peng, D. Y. and Green, J. J. (2012) 'Uptake and transfection with polymeric nanoparticles are dependent on polymer end-group structure, but largely independent of nanoparticle physical and chemical properties', *Molecular Pharmaceutics*, 9(11), pp. 3375–3383. doi: 10.1021/mp3004176.

Swain, S. *et al.* (2020) 'Trends in incidence and prevalence of osteoarthritis in the United Kingdom: findings from the Clinical Practice Research Datalink (CPRD)', *Osteoarthritis and Cartilage*. Elsevier Ltd, 28(6), pp. 792–801. doi: 10.1016/j.joca.2020.03.004.

Swearingen, M. C. *et al.* (2018) 'Elution of antibiotics from poly(methyl methacrylate) bone cement after extended implantation does not necessarily clear the infection despite susceptibility of the clinical isolates', *Pathogens and Disease*, 74(1), pp. 1–4. doi: 10.1093/femspd/ftv103.

Takahashi, S., Sato, K. and Anzai, J. I. (2012) 'Layer-by-layer construction of protein architectures through avidin-biotin and lectin-sugar interactions for biosensor applications', *Analytical and Bioanalytical Chemistry*, 402(5), pp. 1749–1758. doi: 10.1007/s00216-011-5317-4.

Talavera-Pech, W. A. *et al.* (2018) 'Synthesis of pH-sensitive poly(β -amino ester)-coated mesoporous silica nanoparticles for the controlled release of drugs', *Applied Nanoscience (Switzerland)*. Springer International Publishing, 8(4), pp. 853–866. doi: 10.1007/s13204-018-0716-x.

Tamanna, T., Bulitta, J. B. and Yu, A. (2015) 'Controlling antibiotic release from mesoporous silica nano drug carriers via self-assembled polyelectrolyte coating', *Journal of Materials Science: Materials in Medicine*, 26(2), pp. 1–7. doi: 10.1007/s10856-015-5444-0.

Tambunlertchai, S., Srisang, S. and Nasongkla, N. (2017) 'Development of antimicrobial coating by later-by-layer dip coating of chlorhexidine-loaded micelles', *Journal of Materials Science: Materials in Medicine*. Springer US, 28(6). doi: 10.1007/s10856-017-5899-2.

Tande, A. J. and Patel, R. (2014) 'Prosthetic Joint Infection', 27(2), pp. 302–345. doi: 10.1128/CMR.00111-13.

Tang, Z., Wang, Y., Podsiadlo, P. and Kotov, Nicholas A. (2006) 'Biomedical applications of layer-by-layer assembly: From biomimetics to tissue engineering', *Advanced Materials*, pp. 3203–3224. doi: 10.1002/adma.200600113.

Tang, Z., Wang, Y., Podsiadlo, P. and Kotov, Nicholas A (2006) 'Biomedical applications of layer-by-layer assembly: From biomimetics to tissue engineering', *Advanced Materials*, pp. 3203–3224. doi: 10.1002/adma.200600113.

Tang, Z., Zhang, Z., *et al.* (2006) 'Self-assembly of CdTe nanocrystals into free-floating sheets', *Science*, 314(5797), pp. 274–278. doi: 10.1126/science.1128045.

Tang, Z., Jing, W. and Wang, E. (2000) 'Self-assembled monolayer growth of phospholipids on hydrophobic surface toward mimetic biomembranes: scanning probe microscopy study', *Langmuir*, 16(4), pp. 1696–1702. doi: 10.1021/la981491s.

- Al Thaher, Y. *et al.* (2018a) 'Role of poly-beta-amino-esters hydrolysis and electrostatic attraction in gentamicin release from layer-by-layer coatings', *Journal of Colloid and Interface Science*. Elsevier Inc., 526, pp. 35–42. doi: 10.1016/j.jcis.2018.04.042.
- Al Thaher, Y. *et al.* (2018b) 'Role of poly-beta-amino-esters hydrolysis and electrostatic attraction in gentamicin release from layer-by-layer coatings', *Journal of Colloid and Interface Science*. Elsevier Inc., 526, pp. 35–42. doi: 10.1016/j.jcis.2018.04.042.
- Thomas, T. J., Tajmir-Riahi, H. A. and Pillai, C. K. S. (2019) 'Biodegradable polymers for gene delivery', *Molecules*, 24(20). doi: 10.3390/molecules24203744.
- Tkachev, V. A. *et al.* (1995) 'Structuring of tricyanocyanine dye molecules in Langmuir-Blodgett films', *Russian Chemical Bulletin*, 44(7), pp. 1232–1236. doi: 10.1007/BF00700894.
- Trebše, R. and Mihelič, A. (2012) 'Classification of Prosthetic Joint Infections', in Trebše, R. (ed.) *Infected Total Joint Arthroplasty: The Algorithmic Approach*. London: Springer London, pp. 31–34. doi: 10.1007/978-1-4471-2482-5_5.
- Tsaras, G. *et al.* (2012) 'Prosthetic Joint Infection (PJI): a Population Based study, Olmsted County, Minnesota, 1969-2007', *Infect Control Hosp Epidemiol*, 33(12), pp. 1207–1212. doi: 10.1086/668421.INCIDENT.
- Tsuji, H. (2019) 'Quiescent Crystallization of Poly(Lactic Acid) and Its Copolymers-Based Materials', pp. 37–86. doi: 10.1007/12_2019_46.
- Valdes, A. and Stocks, J. (2018) 'Osteoarthritis and ageing', *European Medical Journal Rheumatology*, 3(1), pp. 116–123.
- Versus Arthritis (2019) 'The state of musculoskeletal health 2019', *Versus Arthritis*, 91(5), pp. 31–32. Available at: <https://www.versusarthritis.org/media/14594/state-of-musculoskeletal-health-2019.pdf>.
- De Villiers, M. M. *et al.* (2011) 'Introduction to nanocoatings produced by layer-by-layer (LbL) self-assembly', *Advanced Drug Delivery Reviews*. Elsevier B.V., 63(9), pp. 701–715. doi: 10.1016/j.addr.2011.05.011.
- Wang, J. *et al.* (2013) 'A systematic review and meta-analysis of antibiotic-impregnated bone cement use in primary total hip or knee arthroplasty', *PLoS ONE*, 8(12), pp. 4–11. doi: 10.1371/journal.pone.0082745.
- Wang, J., Hao, H. and Cai, J. H. (2019) 'Amphiphilic Drug Delivery Microcapsules via Layer-by-Layer Self-Assembly', *Journal of Macromolecular Science, Part B: Physics*. Taylor & Francis, 58(5), pp. 535–550. doi: 10.1080/00222348.2019.1593640.
- Wang, Q. *et al.* (2006) 'Incorporation of Silver Ions into Ultrathin Titanium Phosphate Films : In Situ Reduction to Prepare Silver Nanoparticles and Their Antibacterial Activity', (14), pp. 1988–1994.
- Wang, X. D. *et al.* (2010) 'Preparation of spherical silica particles by Stöber process with high concentration of tetra-ethyl-orthosilicate', *Journal of Colloid and Interface Science*. Elsevier Inc., 341(1), pp. 23–29. doi: 10.1016/j.jcis.2009.09.018.
- Wattamwar, P. P. *et al.* (2012) 'Synthesis and characterization of poly(antioxidant β -amino esters) for controlled release of polyphenolic antioxidants', *Acta Biomaterialia*. Acta Materialia Inc., 8(7), pp. 2529–2537. doi: 10.1016/j.actbio.2012.03.022.
- Webb, J. C. J. and Spencer, R. F. (2007) 'The role of polymethylmethacrylate bone cement in modern orthopaedic surgery.', *The Journal of bone and joint surgery. British volume*, 89(7), pp. 851–7. doi: 10.1302/0301-

620X.89B7.19148.

Williams, D. H., Garbuz, D. S. and Masri, B. A. (2010) 'Total knee arthroplasty: Techniques and results', *British Columbia Medical Journal*, 52(9), pp. 447–454.

Wohl, B. M. and Engbersen, J. F. J. (2012) 'Responsive layer-by-layer materials for drug delivery', *Journal of Controlled Release*. Elsevier B.V., 158(1), pp. 2–14. doi: 10.1016/j.jconrel.2011.08.035.

Wood, K. C. *et al.* (2005) 'Tunable Drug Release from Hydrolytically Degradable Layer-by-Layer Thin Films Tunable Drug Release from Hydrolytically Degradable Layer-by-Layer Thin Films', (10), pp. 1603–1609. doi: 10.1021/la0476480.

Wu, C., Zhao, L. and Zhang, Y. (2017) 'PH-Responsive nanofiltration membranes based on porphyrin supramolecular self-assembly by layer-by-layer technique', *RSC Advances*. Royal Society of Chemistry, 7(75), pp. 47397–47406. doi: 10.1039/c7ra08568k.

Wu, S. C. *et al.* (2008) 'Use of chlorhexidine-impregnated patch at pin site to reduce local morbidity: The ChIPPS Pilot Trial', *International Wound Journal*, 5(3), pp. 416–422. doi: 10.1111/j.1742-481X.2007.00368.x.

Wurster, E. C. *et al.* (2013) 'Layer-by-layer assembled gold nanoparticles for the delivery of nucleic acids', *Methods in Molecular Biology*, 948, pp. 171–182. doi: 10.1007/978-1-62703-140-0_12.

Wylde, V. *et al.* (2018) 'Chronic pain after total knee arthroplasty', *EFORT Open Reviews*, 3(8), pp. 461–470. doi: 10.1302/2058-5241.3.180004.

Xin, Y., Hu, T. and Chu, P. K. (2011) 'In vitro studies of biomedical magnesium alloys in a simulated physiological environment: A review', *Acta Biomaterialia*, 7(4), pp. 1452–1459. doi: 10.1016/j.actbio.2010.12.004.

Xing, J. *et al.* (2017) 'A nano-scaled and multi-layered recombinant fibronectin/cadherin chimera composite selectively concentrates osteogenesis-related cells and factors to aid bone repair', *Acta Biomaterialia*. Acta Materialia Inc., 53, pp. 470–482. doi: 10.1016/j.actbio.2017.02.016.

Xu, J. *et al.* (2014) 'Surface structures of poly(methyl methacrylate) films influenced by chain entanglement in the corresponding film-formation solution', *Soft Matter*. Royal Society of Chemistry, 10(44), pp. 8992–9002. doi: 10.1039/c4sm01743a.

Xu, L., Zhu, Z. and Sukhishvili, S. A. (2011) 'Polyelectrolyte Multilayers of Diblock Copolymer Micelles with Temperature-Responsive Cores', 27(17), pp. 409–415. doi: 10.1021/la1038014.

Xu, Y. M. *et al.* (2020) 'Progress of antibiotic-loaded bone cement in joint arthroplasty', *Chinese medical journal*, 133(20), pp. 2486–2494. doi: 10.1097/CM9.0000000000001093.

Yan, H. *et al.* (2017) 'Effects of Chlorhexidine-Encapsulated Mesoporous Silica Nanoparticles on the Anti-Biofilm and Mechanical Properties of Glass Ionomer Cement', *Molecules*, 22(7), p. 1225. doi: 10.3390/molecules22071225.

Yang, C. *et al.* (2018) 'Delivery of anticancer drug using pH-sensitive micelles from triblock copolymer MPEG-b-PBAE-b-PLA', *Materials Science and Engineering C*. Elsevier, 84(December 2017), pp. 254–262. doi: 10.1016/j.msec.2017.12.003.

Yang, K. *et al.* (2018) 'Antimicrobial hydrogels: Promising materials for medical application', *International Journal of Nanomedicine*, 13, pp. 2217–2263. doi: 10.2147/IJN.S154748.

Yang, T. *et al.* (2013) 'Facile fabrication of core-shell-structured ag@carbon and mesoporous yolk-shell-

structured ag@carbon@silica by an extended stöber method', *Chemistry - A European Journal*, 19(22), pp. 6942–6945. doi: 10.1002/chem.201300523.

Yang, X. *et al.* (2017) 'Pharmaceutical Intermediate-Modified Gold Nanoparticles: Against Multidrug-Resistant Bacteria and Wound-Healing Application via an Electrospun Scaffold', *ACS Nano*, 11(6), pp. 5737–5745. doi: 10.1021/acsnano.7b01240.

Ying, P. *et al.* (2001) 'Using Self-assembled monolayers to understand the interactions of surfaces with cells', *Shengwu Yixue Gongchengxue Zazhi/Journal of Biomedical Engineering*, 18(2), pp. 276–279.

Yu, D.-G., Lin, W.-C. and Yang, M.-C. (2007) 'Surface Modification of Poly(L-lactic acid) Membrane via Layer-by-Layer Assembly of Silver Nanoparticle-Embedded Polyelectrolyte Multilayer', *Bioconjugate Chemistry*, 18(5), pp. 1521–1529. doi: 10.1021/bc060098s.

Zan, X. and Su, Z. (2010) 'Polyelectrolyte multilayer films containing silver as antibacterial coatings', *Thin Solid Films*. Elsevier B.V., 518(19), pp. 5478–5482. doi: 10.1016/j.tsf.2010.04.022.

Zeng, M. *et al.* (2019) 'Manipulation of Transgene Expression in Fibroblast Cells by a Multifunctional Linear-Branched Hybrid Poly(β -Amino Ester) Synthesized through an Oligomer Combination Approach', *Nano Letters*, 19(1), pp. 381–391. doi: 10.1021/acs.nanolett.8b04098.

Zhang, J. *et al.* (2005) 'Natural polyelectrolyte films based on layer-by layer deposition of collagen and hyaluronic acid', *Biomaterials*, 26(16), pp. 3353–3361. doi: 10.1016/j.biomaterials.2004.08.019.

Zhang, J. *et al.* (2017) 'pH-sensitive polymeric nanoparticles for co-delivery of doxorubicin and curcumin to treat cancer via enhanced pro-apoptotic and anti-angiogenic activities', *Acta Biomaterialia*, 58, pp. 349–364. doi: 10.1016/j.actbio.2017.04.029.

Zhang, J. *et al.* (2019) 'Layer-by-layer assembly for immobilizing enzymes in enzymatic biofuel cells', *Sustainable Energy and Fuels*. Royal Society of Chemistry, 4(1), pp. 68–79. doi: 10.1039/c9se00643e.

Zhang, X. Bin *et al.* (2013) 'An improved Stöber method towards uniform and monodisperse Fe₃O₄@C nanospheres', *Journal of Materials Chemistry A*, 1(25), pp. 7488–7493. doi: 10.1039/c3ta11249g.

Zhao, M. Y. *et al.* (2014) 'LBL coating of type I collagen and hyaluronic acid on aminolyzed PLLA to enhance the cell-material interaction', *Express Polymer Letters*, 8(5), pp. 322–335. doi: 10.3144/expresspolymlett.2014.36.

Zheng, H. *et al.* (2004) 'Controlling cell attachment selectively onto biological polymer-colloid templates using polymer-on-polymer stamping', *Langmuir*, 20(17), pp. 7215–7222. doi: 10.1021/la049856y.

Zhou, B. *et al.* (2014) 'Antibacterial multilayer films fabricated by layer-by-layer immobilizing lysozyme and gold nanoparticles on nanofibers', *Colloids and Surfaces B: Biointerfaces*, 116, pp. 432–438. doi: 10.1016/j.colsurfb.2014.01.016.

Zhou, W. *et al.* (2018a) 'Novel pH-responsive tobramycin-embedded micelles in nanostructured multilayer-coatings of chitosan/heparin with efficient and sustained antibacterial properties', *Materials Science and Engineering C*. Elsevier B.V, 90, pp. 693–705. doi: 10.1016/j.msec.2018.04.069.

Zhou, W. *et al.* (2018b) 'Novel pH-responsive tobramycin-embedded micelles in nanostructured multilayer-coatings of chitosan/heparin with efficient and sustained antibacterial properties', *Materials Science and Engineering C*. Elsevier, 90(May 2017), pp. 693–705. doi: 10.1016/j.msec.2018.04.069.

Zhu, X. and Jun Loh, X. (2015) 'Layer-by-layer assemblies for antibacterial applications', *Biomaterials Science*.

Royal Society of Chemistry, 3(12), pp. 1505–1518. doi: 10.1039/c5bm00307e.

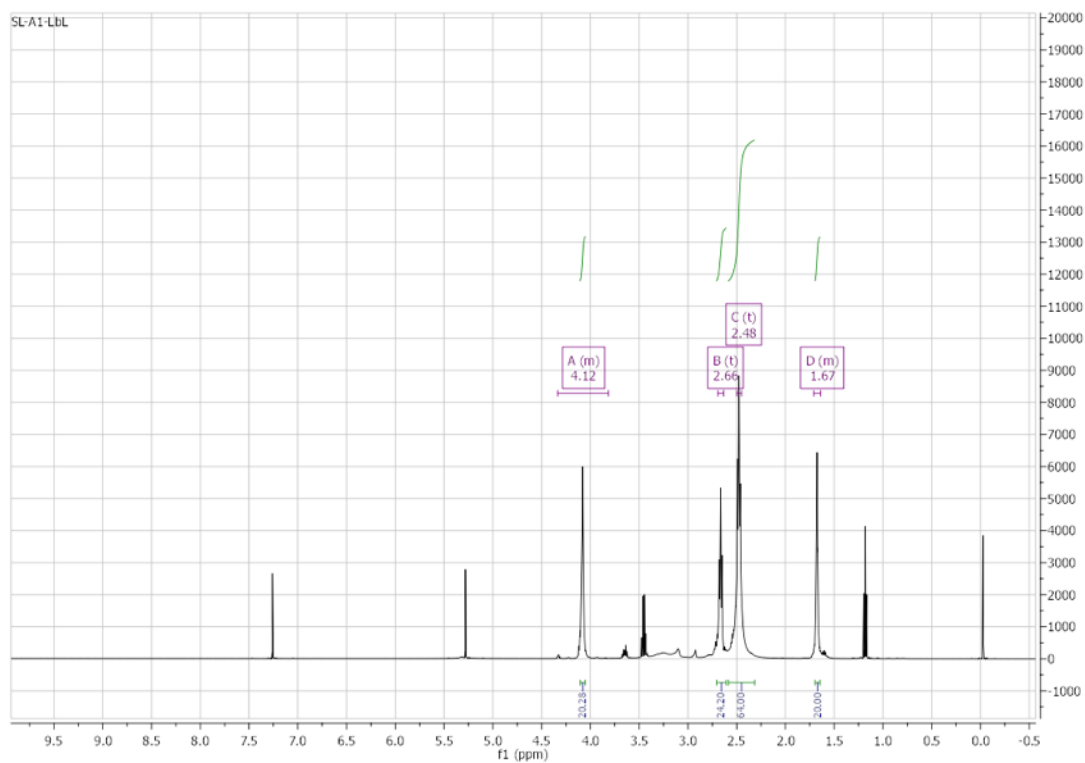
Zimmerli, W. (2006) 'Prosthetic-joint-associated infections', *Best Practice and Research: Clinical Rheumatology*, 20(6), pp. 1045–1063. doi: 10.1016/j.berh.2006.08.003.

Zou, Y. *et al.* (2020) 'Protein-reduced gold nanoparticles mixed with gentamicin sulfate and loaded into konjac/gelatin sponge heal wounds and kill drug-resistant bacteria', *International Journal of Biological Macromolecules*. Elsevier B.V, 148, pp. 921–931. doi: 10.1016/j.ijbiomac.2020.01.190.

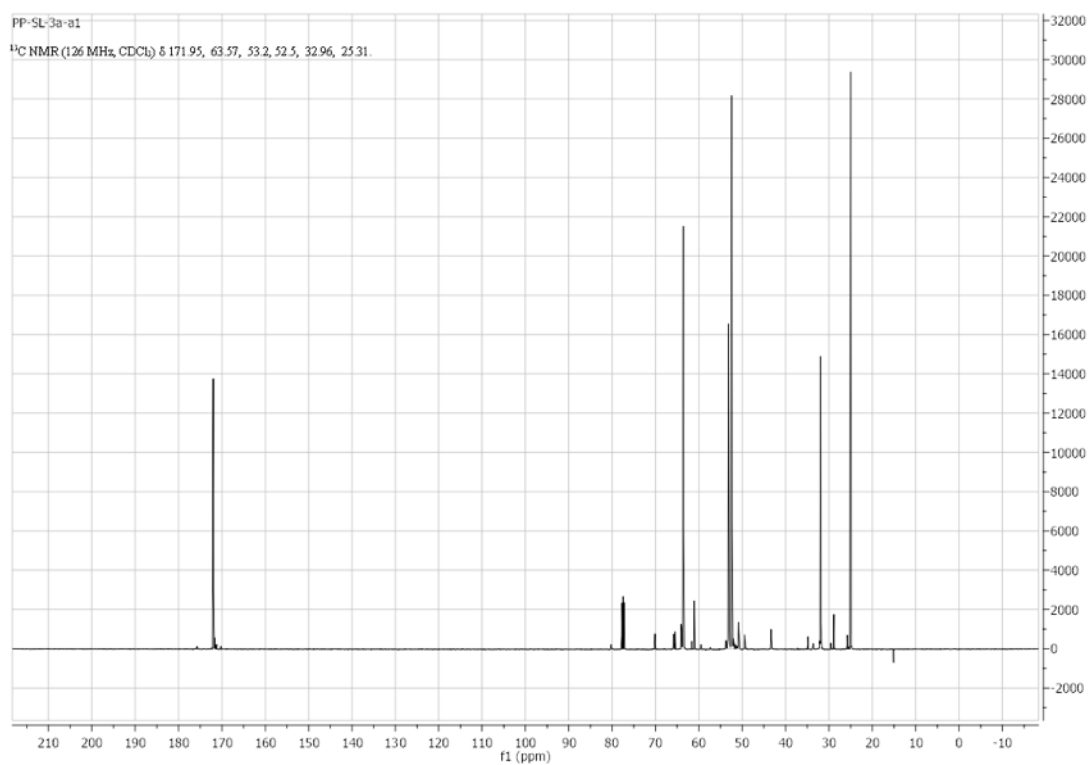
Zugates, G. T. *et al.* (2006) 'Synthesis of poly(β -amino ester)s with thiol-reactive side chains for DNA delivery', *Journal of the American Chemical Society*, 128(39), pp. 12726–12734. doi: 10.1021/ja061570n.

Appendix

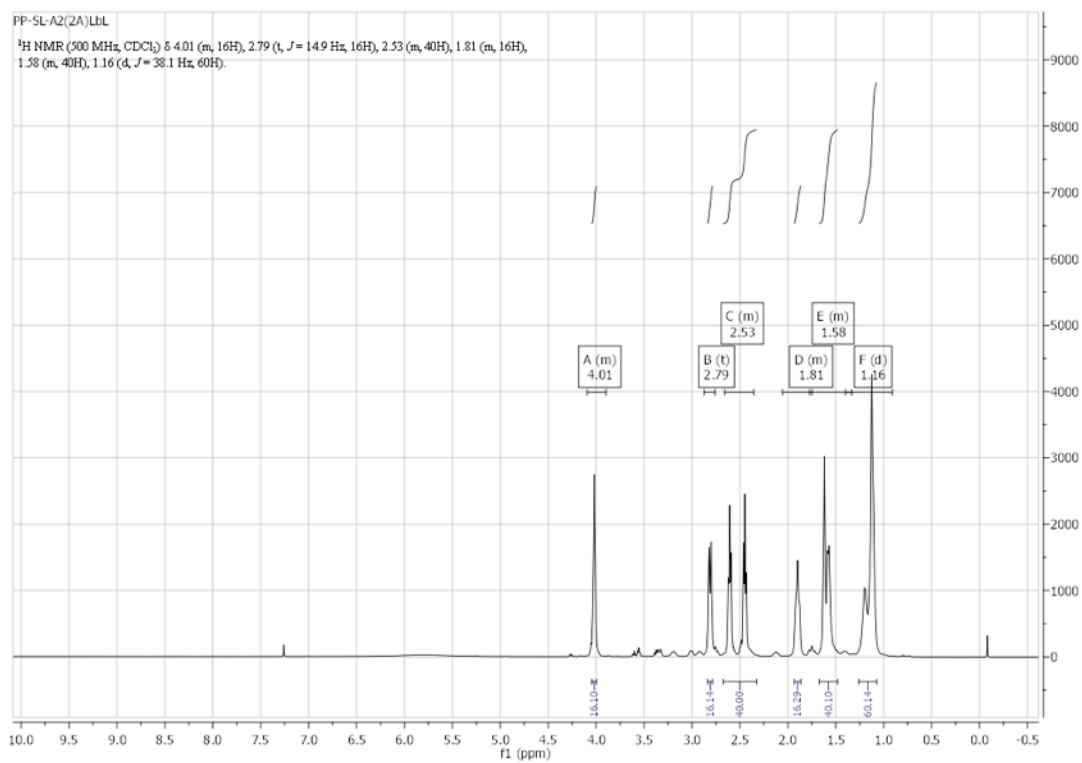
1a) ^1H NMR A1



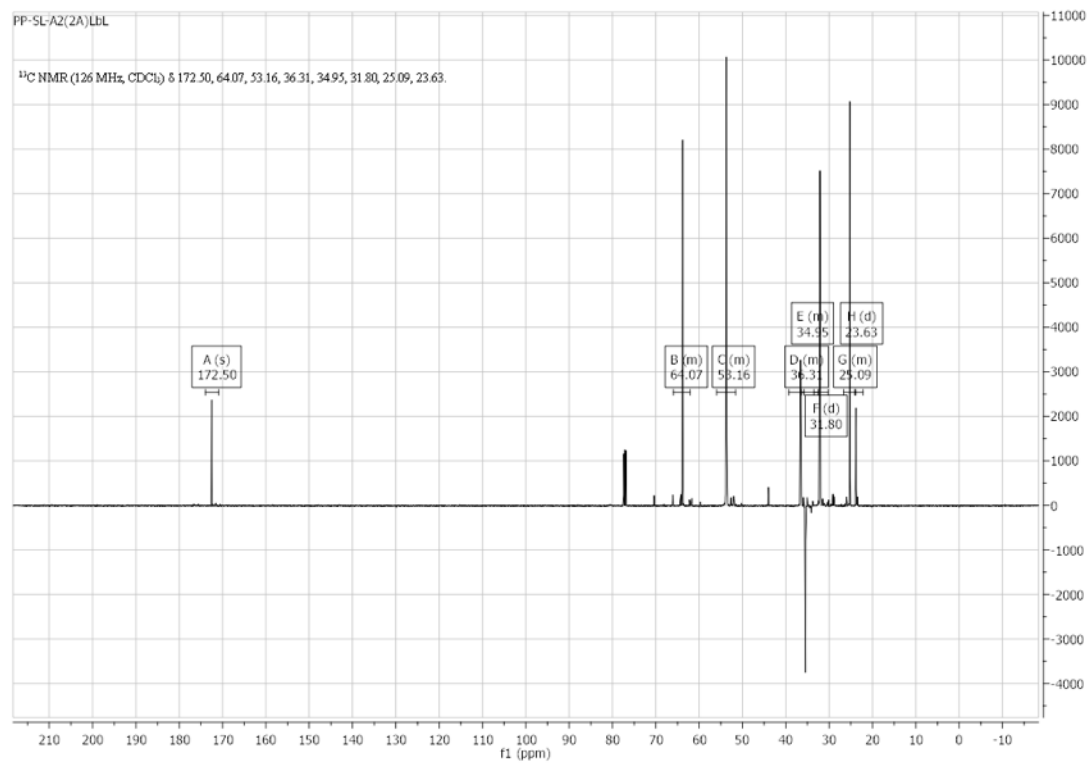
1b) ^{13}C NMR A1



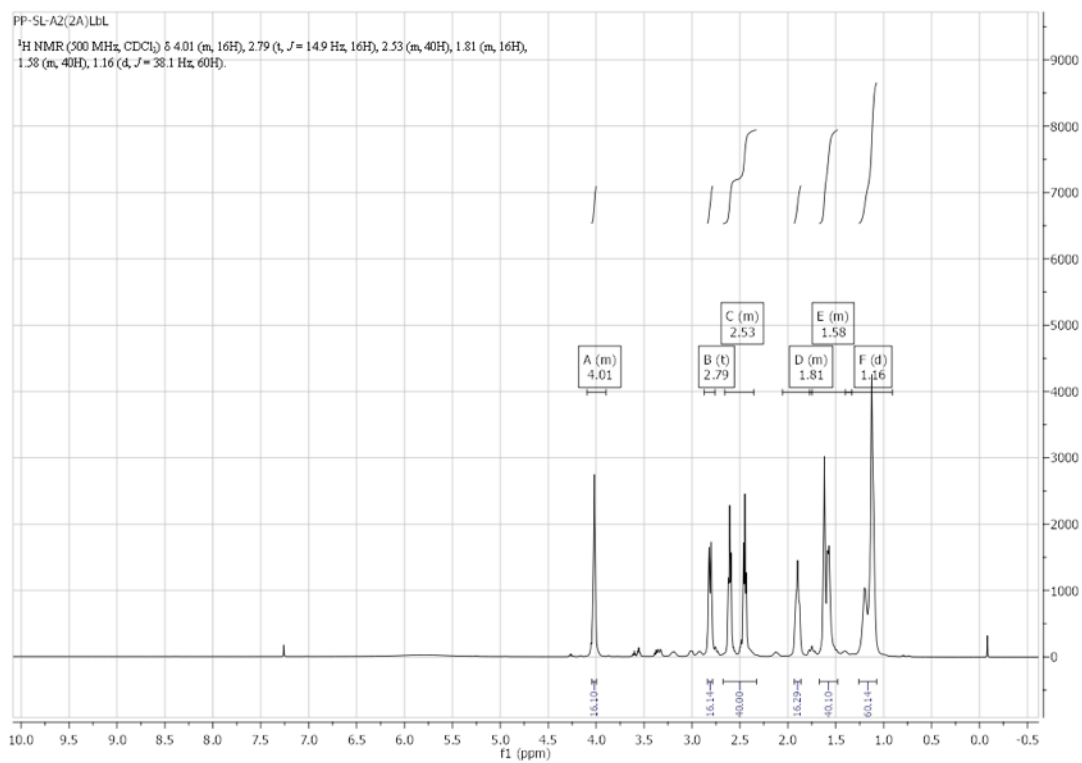
2a) ^1H NMR A2



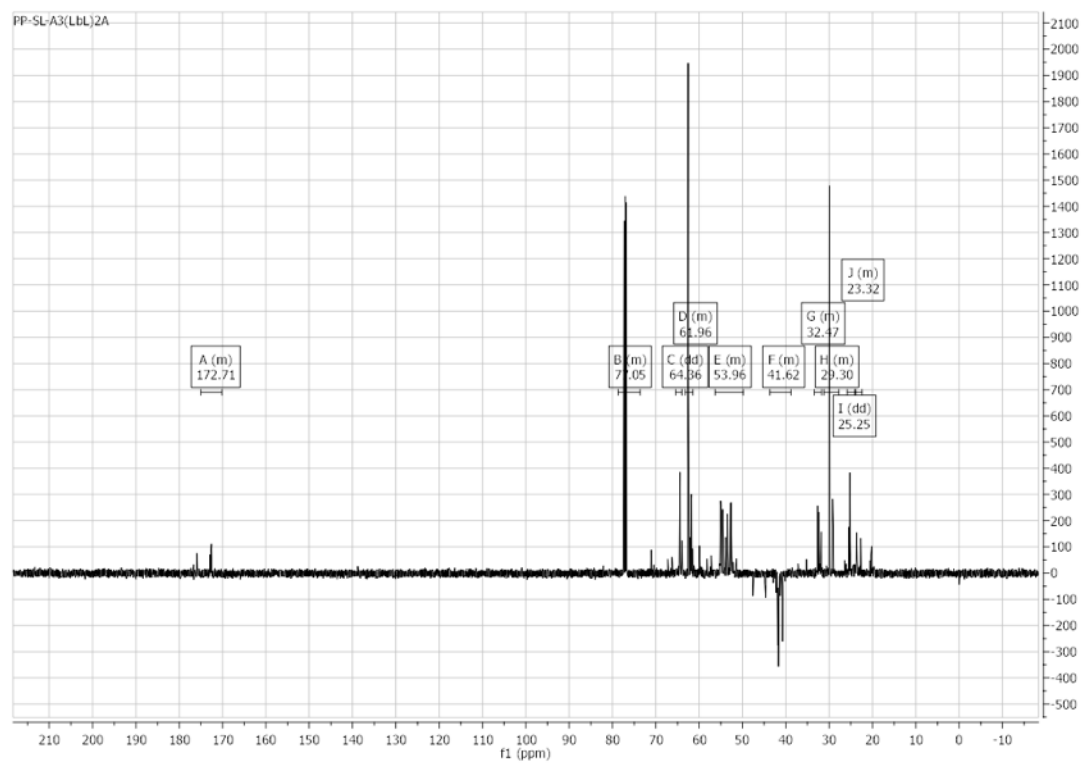
2b) ^{13}C NMR A2



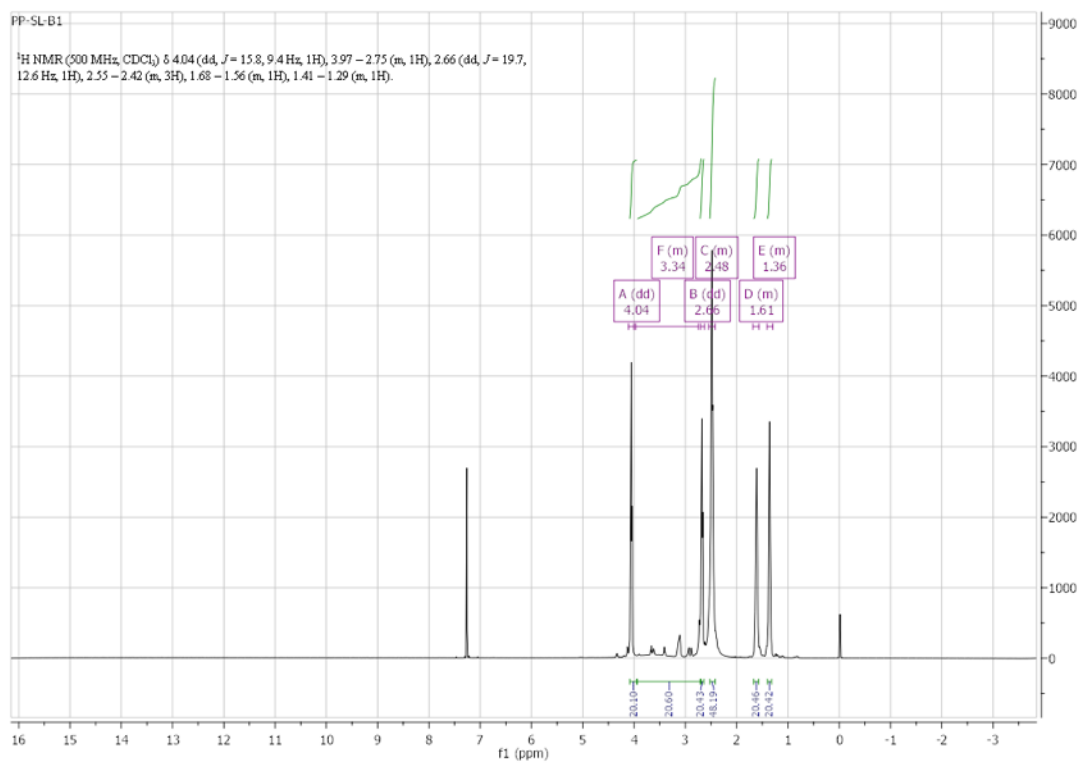
3a) ^1H NMR A3



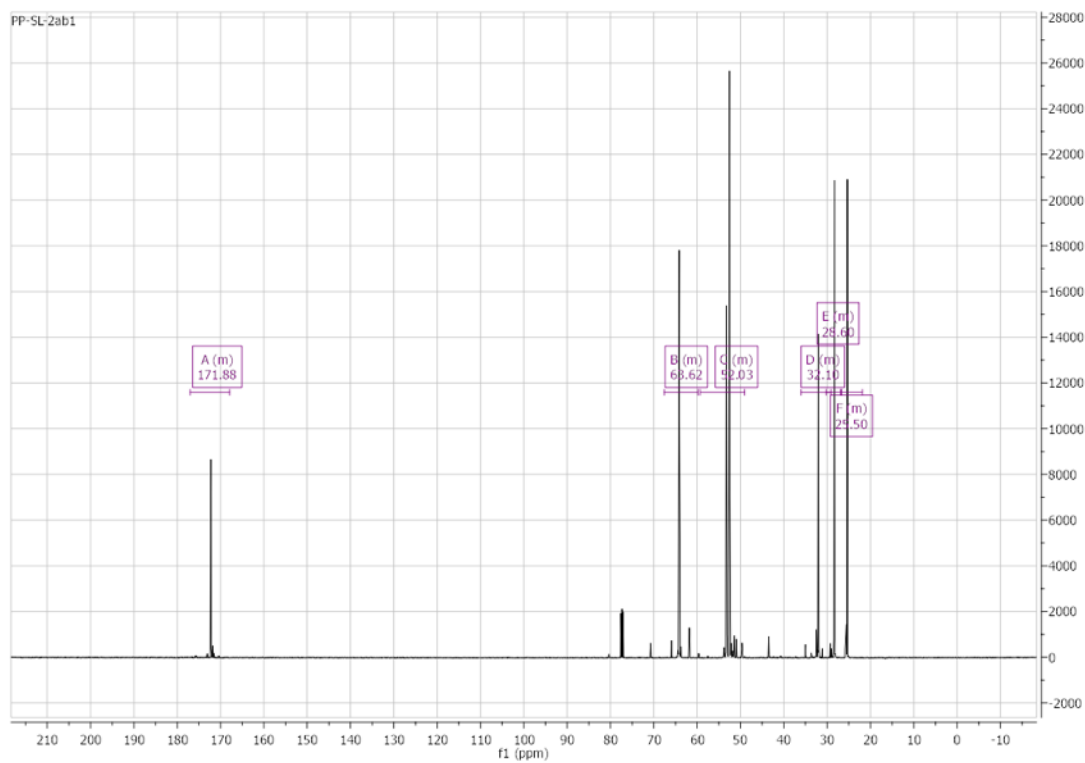
3b) ^{13}C NMR A3



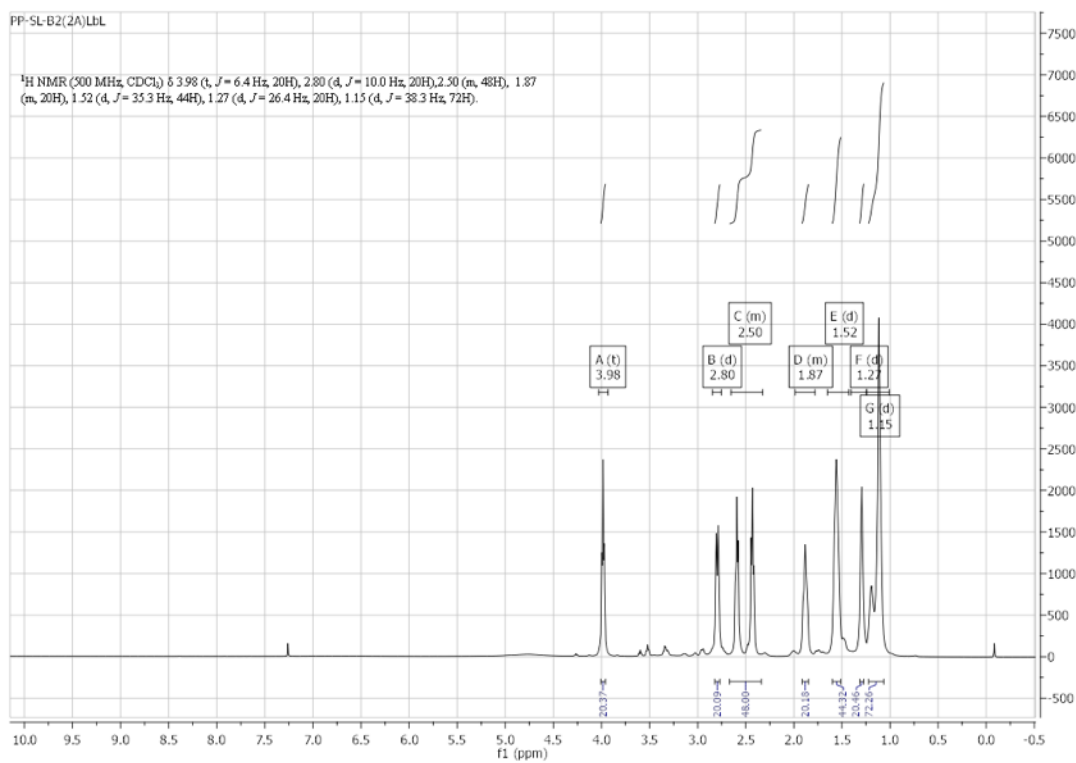
4a) ^1H NMR B1



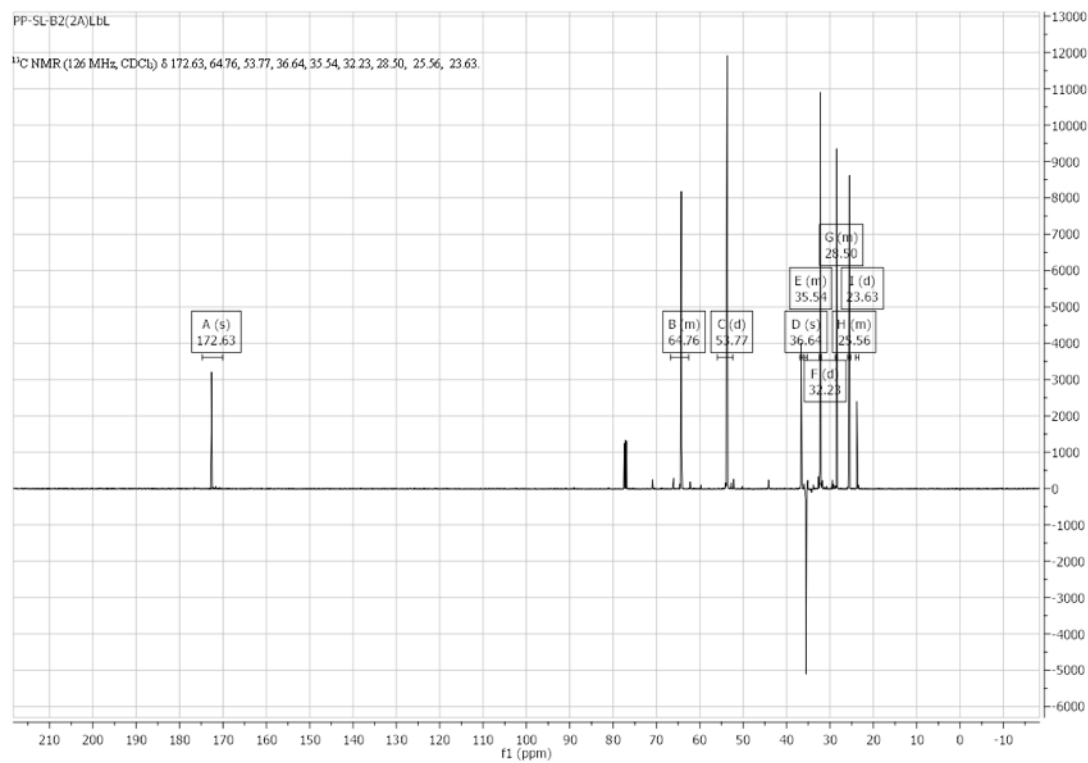
4b) ^{13}C NMR B1



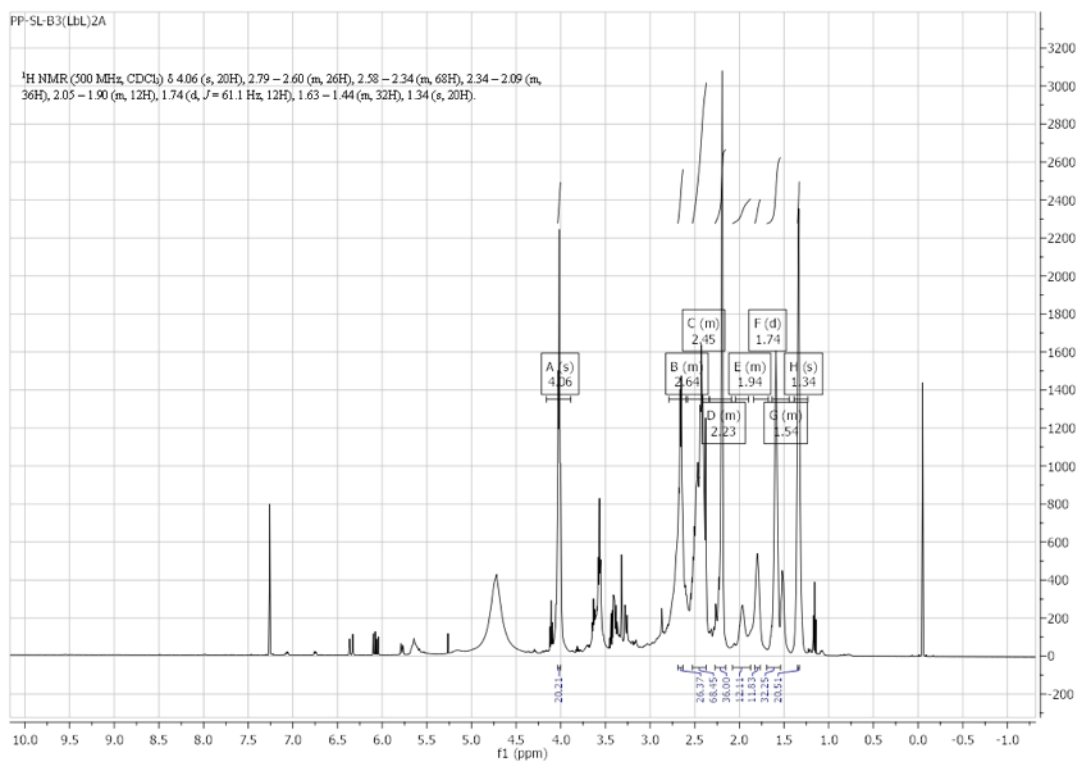
5a) ^1H NMR B2



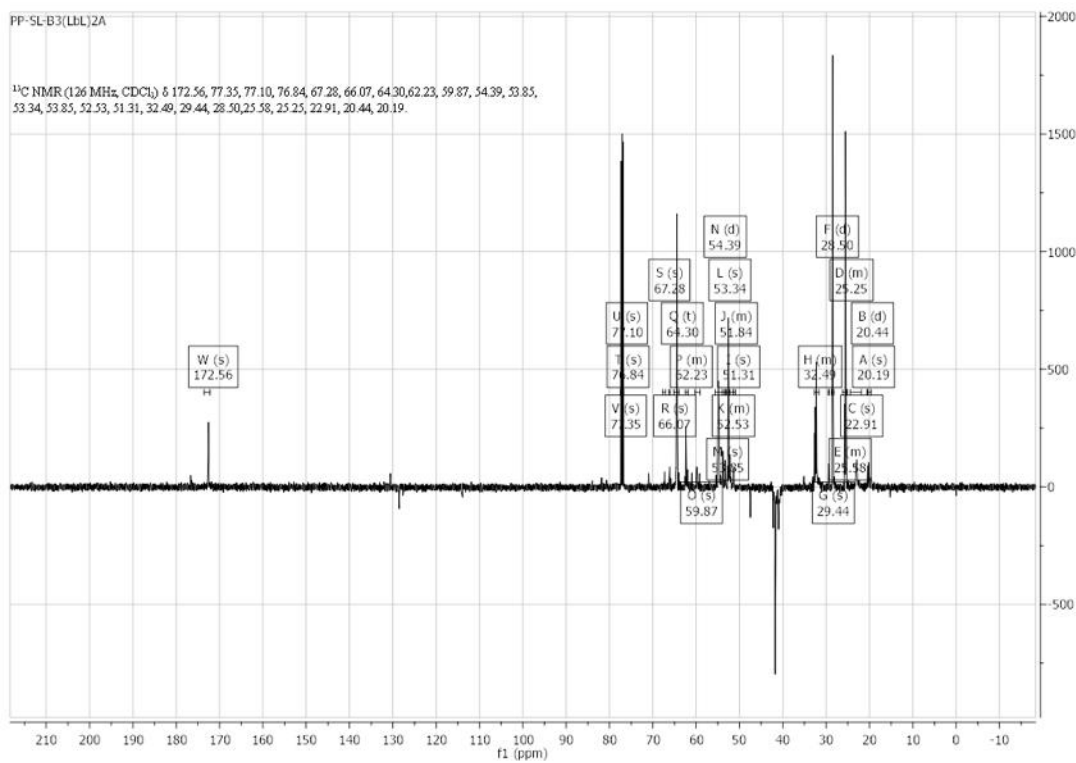
5b) ^{13}C NMR B2



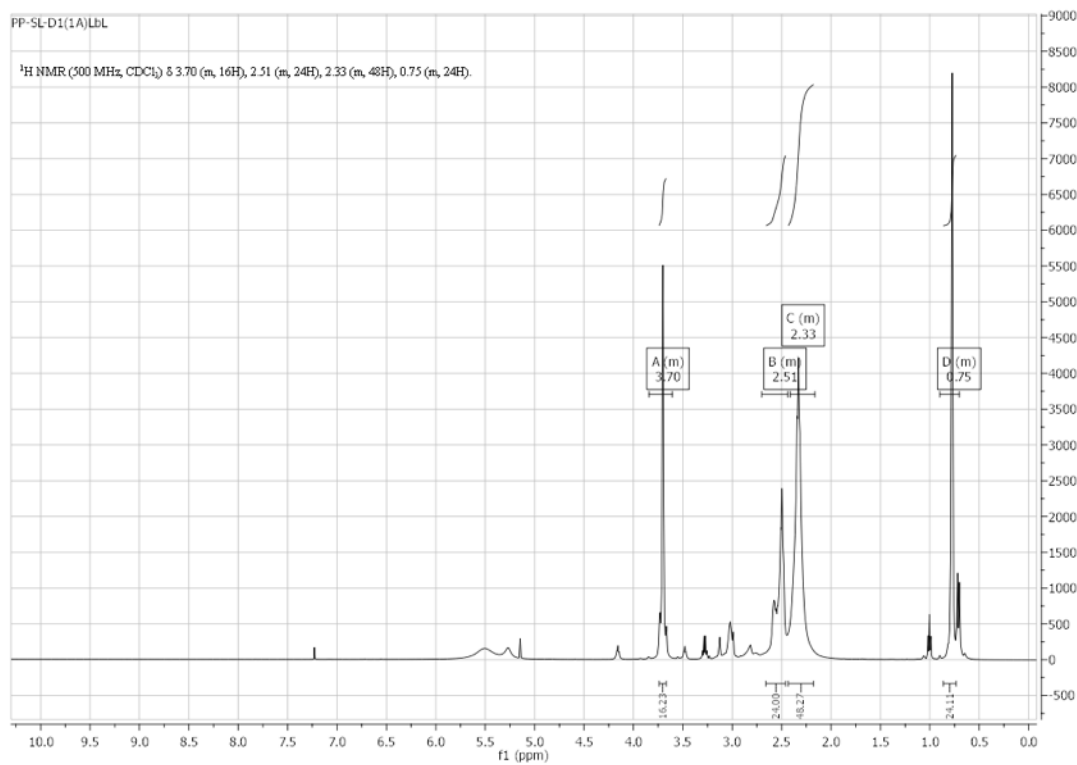
6a) ^1H NMR B3



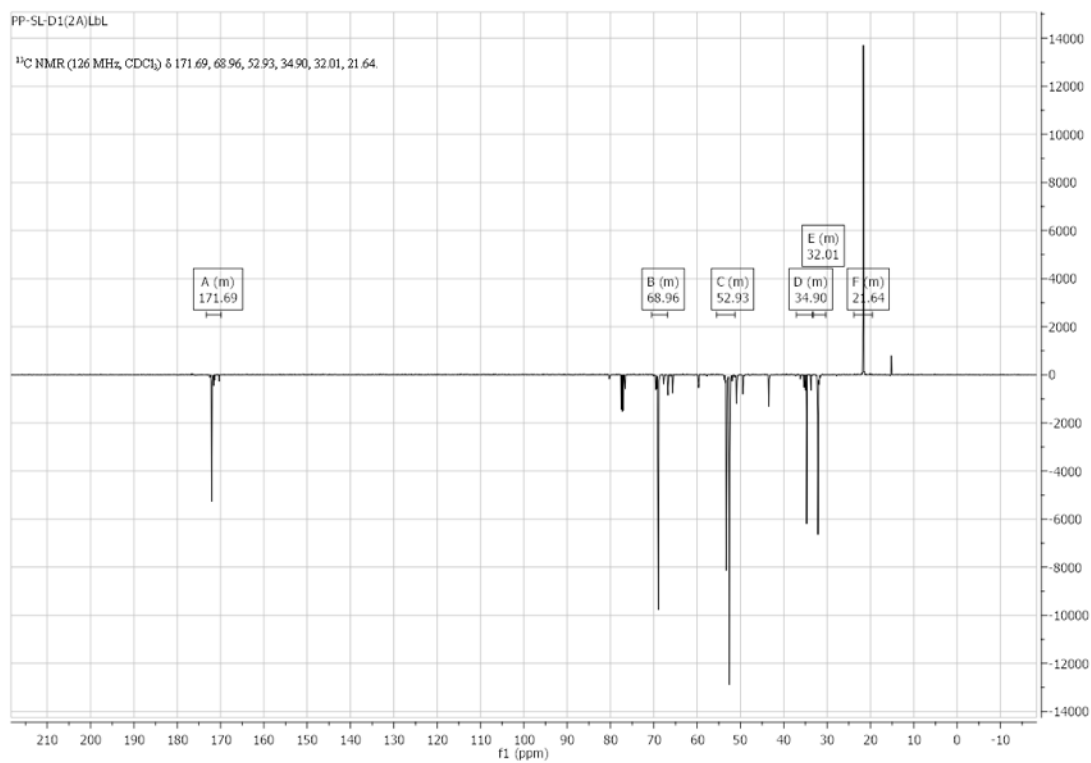
6b) ^{13}C NMR B3



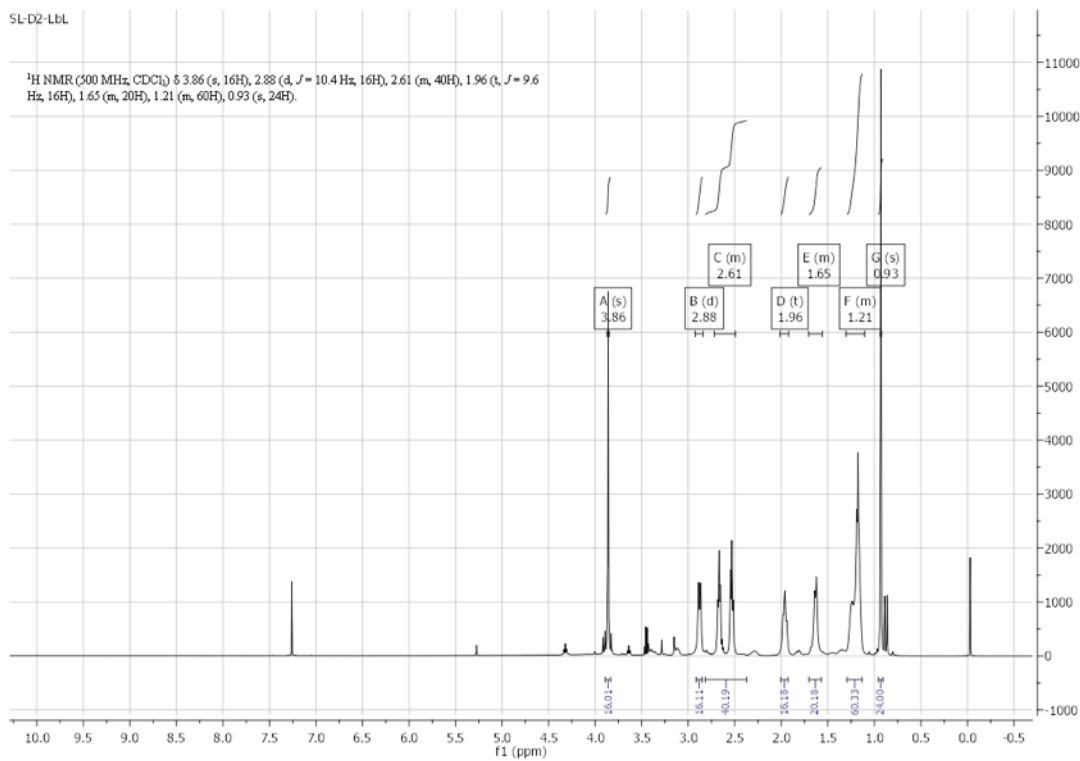
7a) ^1H NMR D1



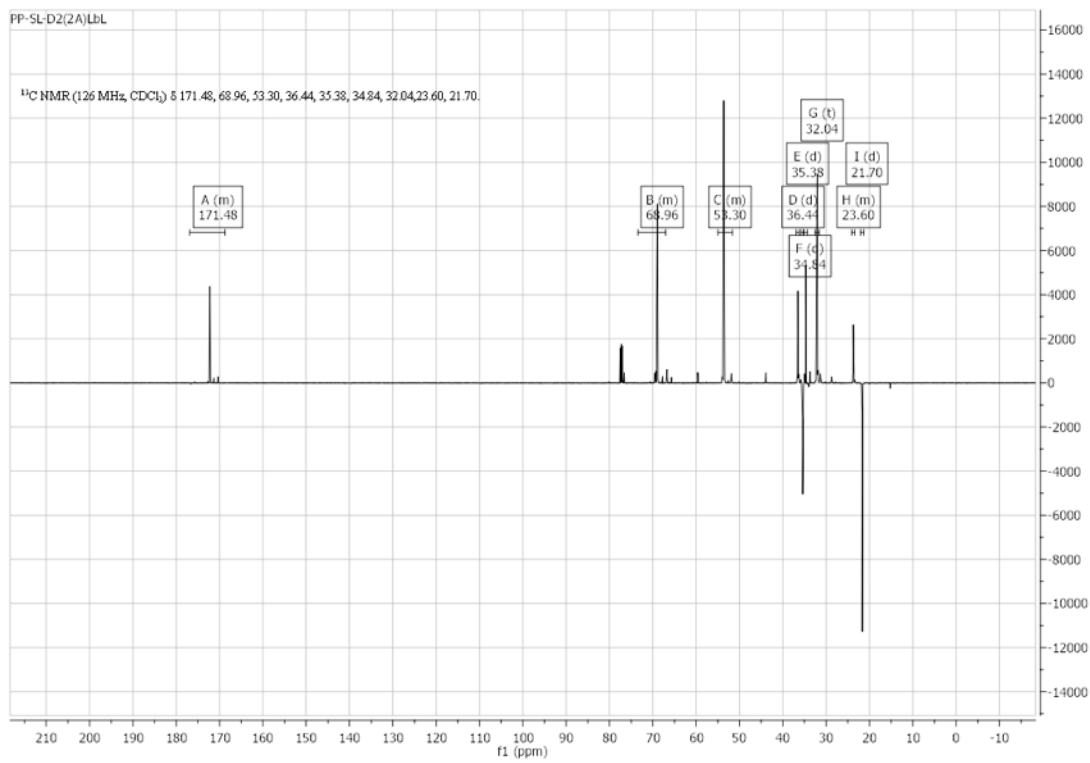
7b) ^{13}C NMR D1



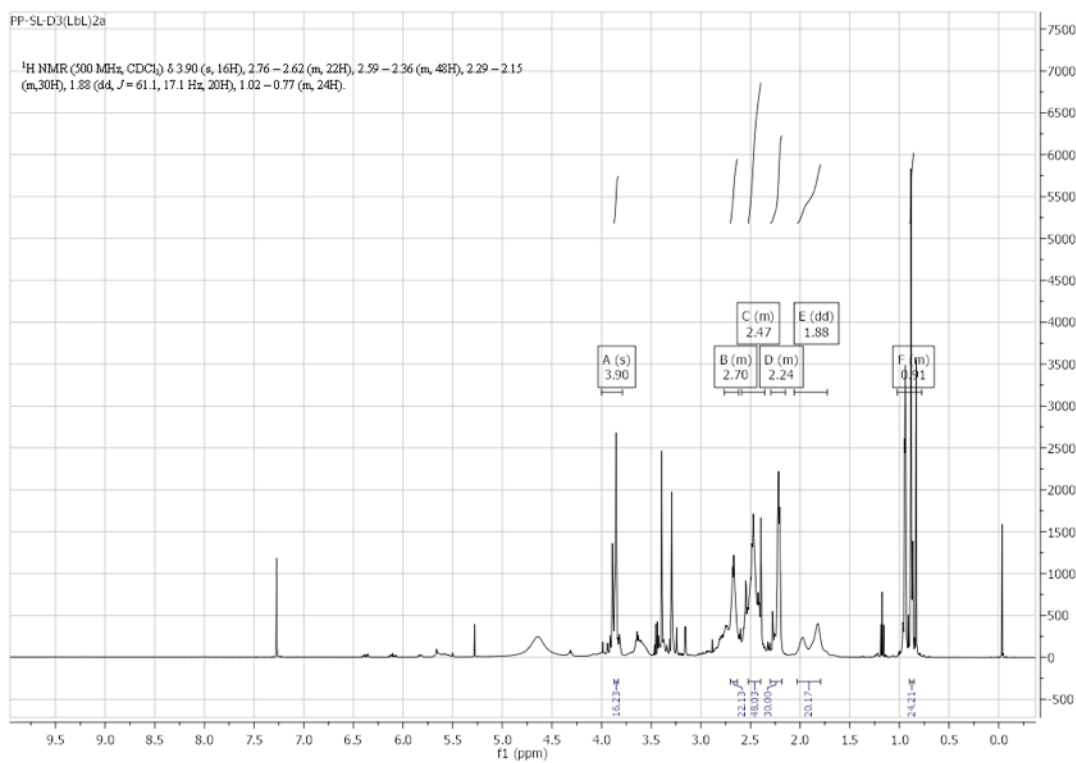
8a) ^1H NMR D2



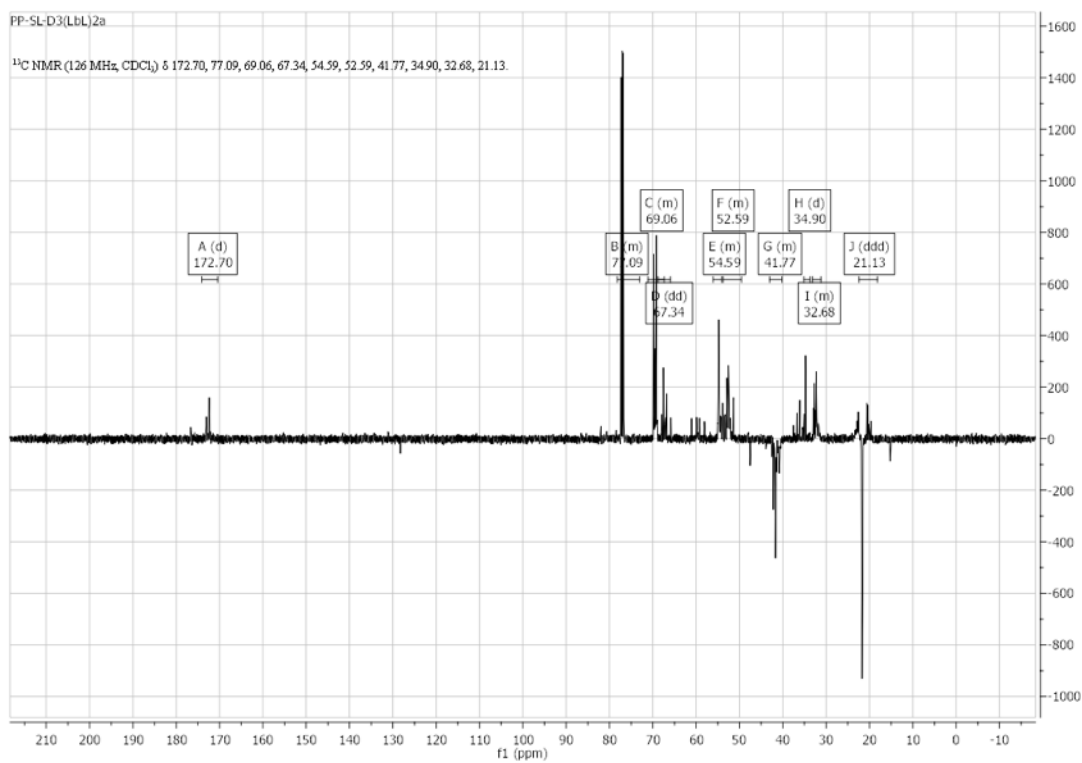
8b) ^{13}C NMR D2



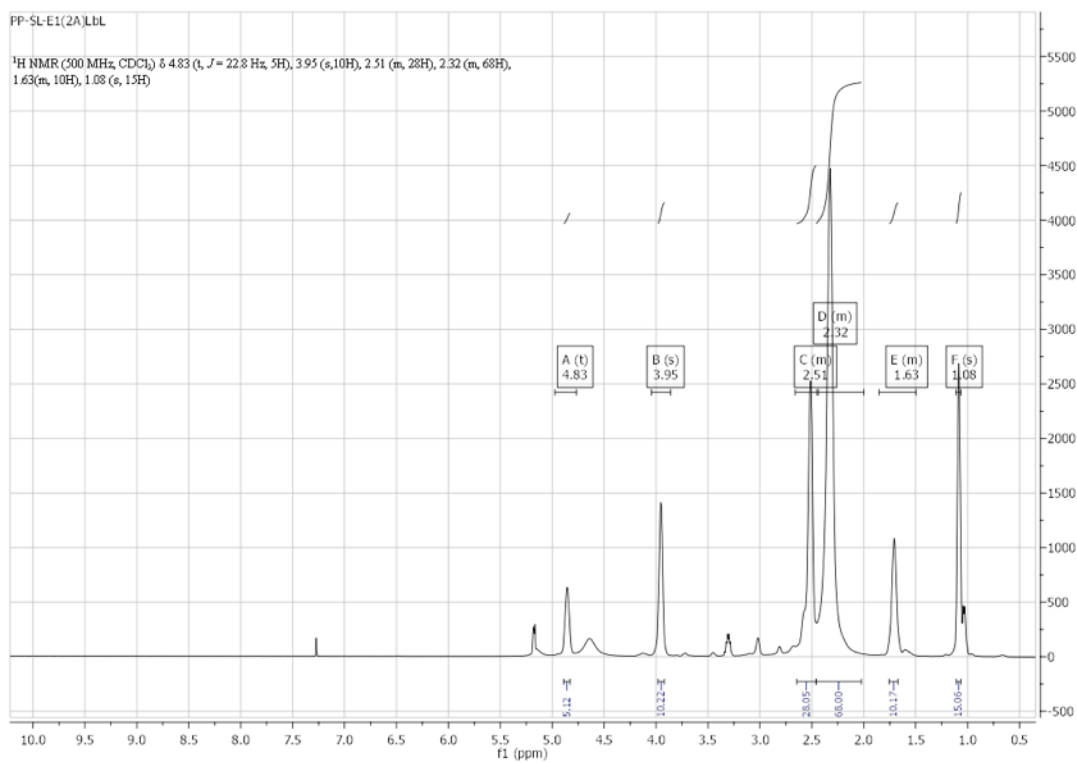
9a) ^1H NMR D3



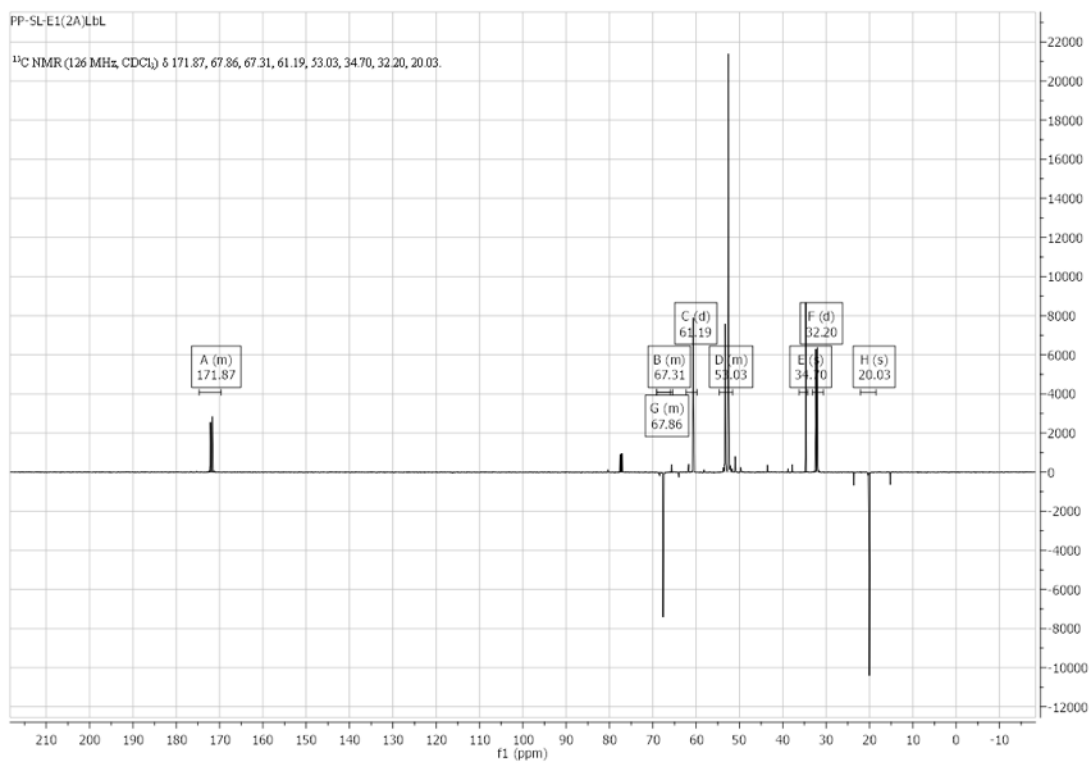
9b) ^{13}C NMR D3



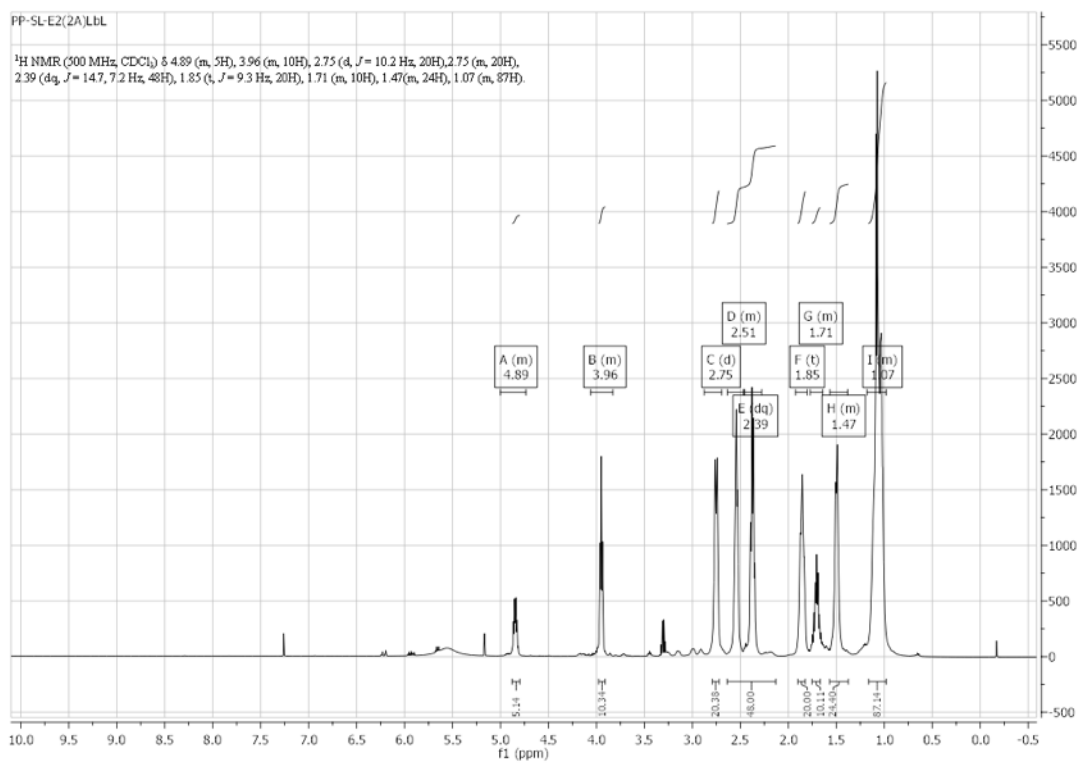
10a) ^1H NMR E1



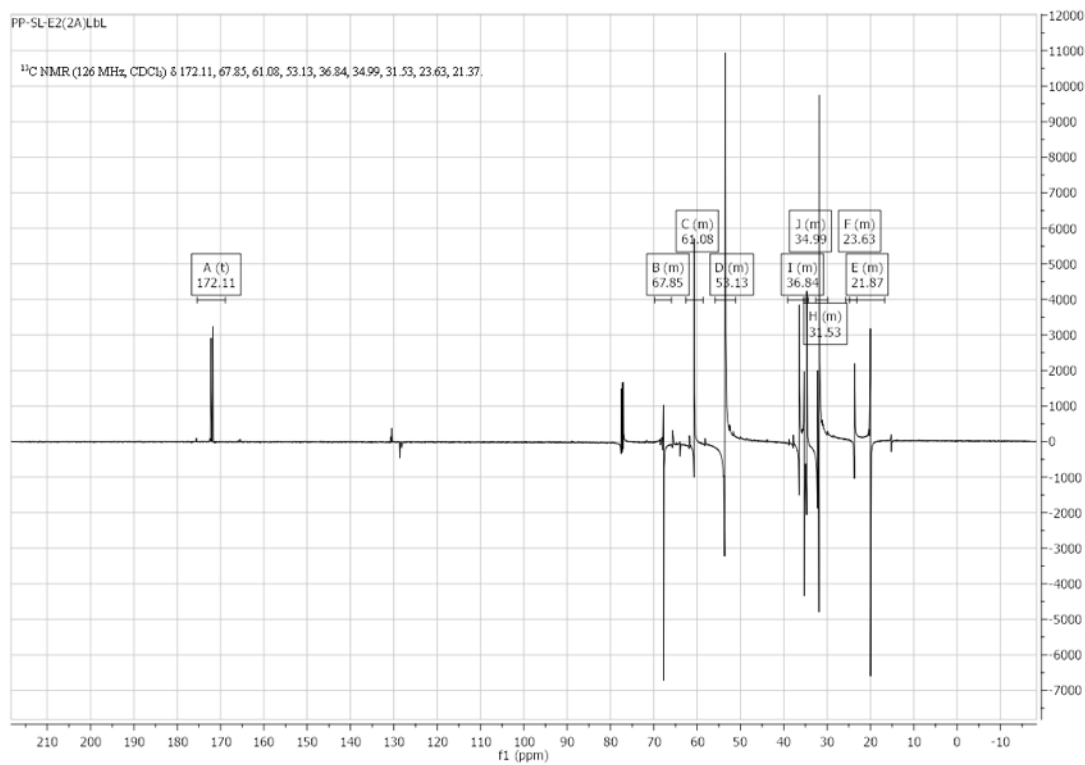
10b) ^{13}C NMR E1



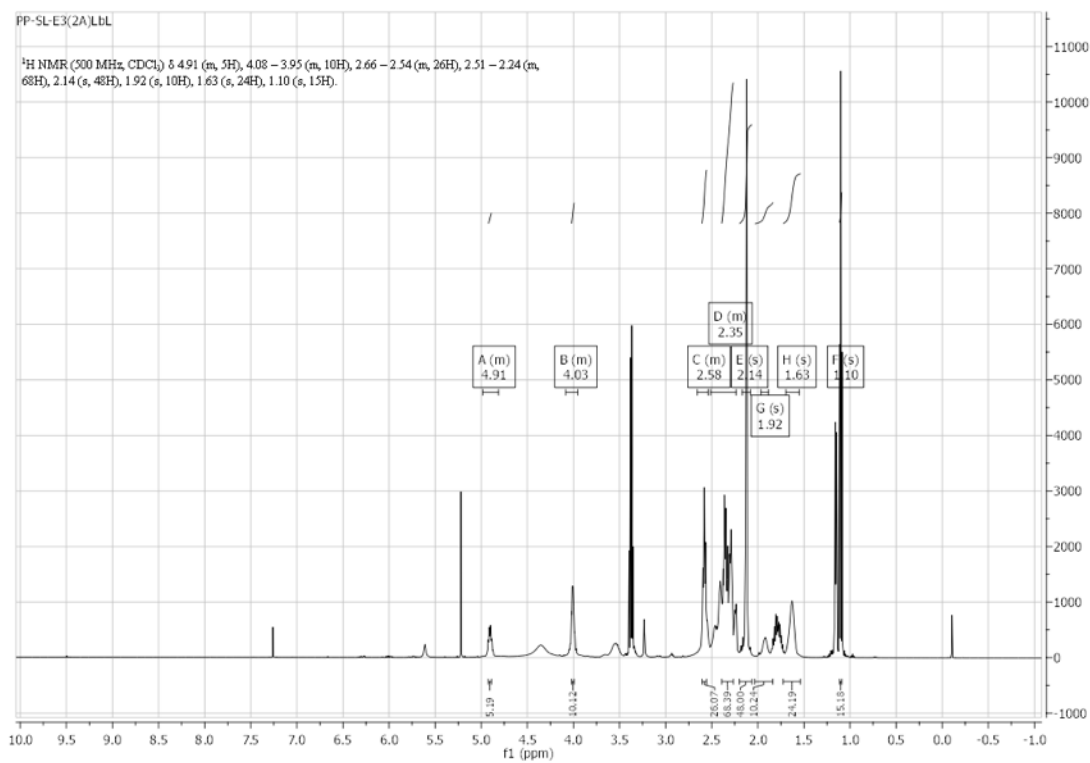
11a) ^1H NMR E2



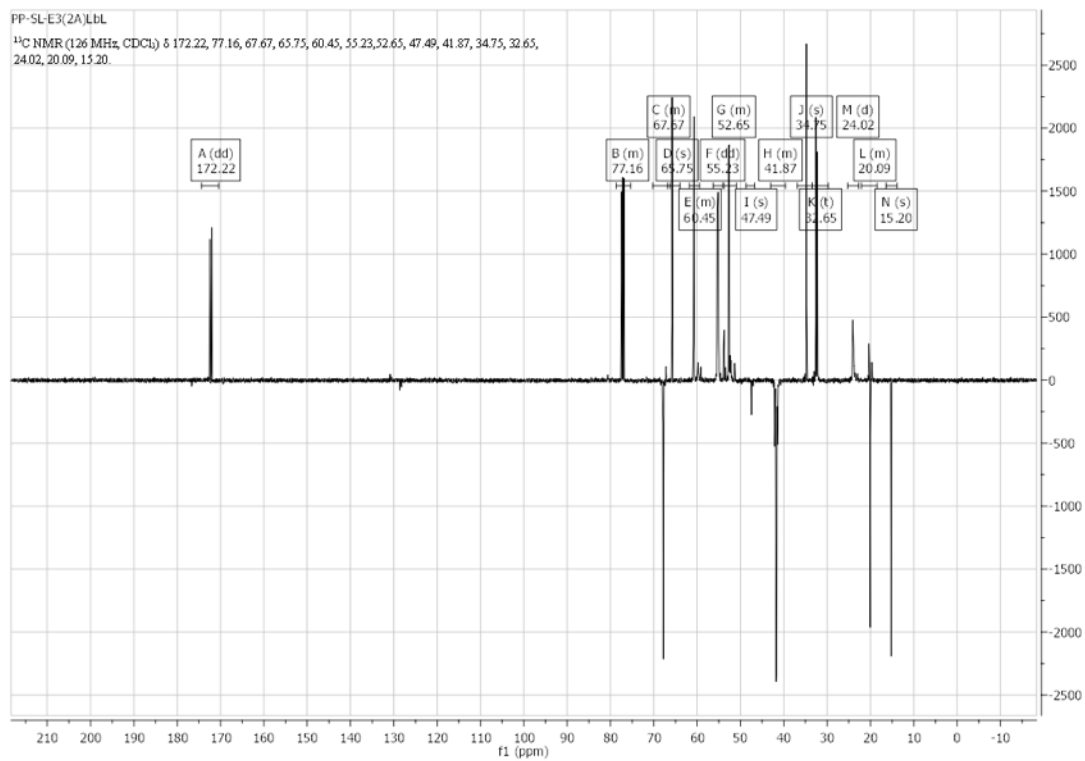
11b) ^{13}C NMR E2



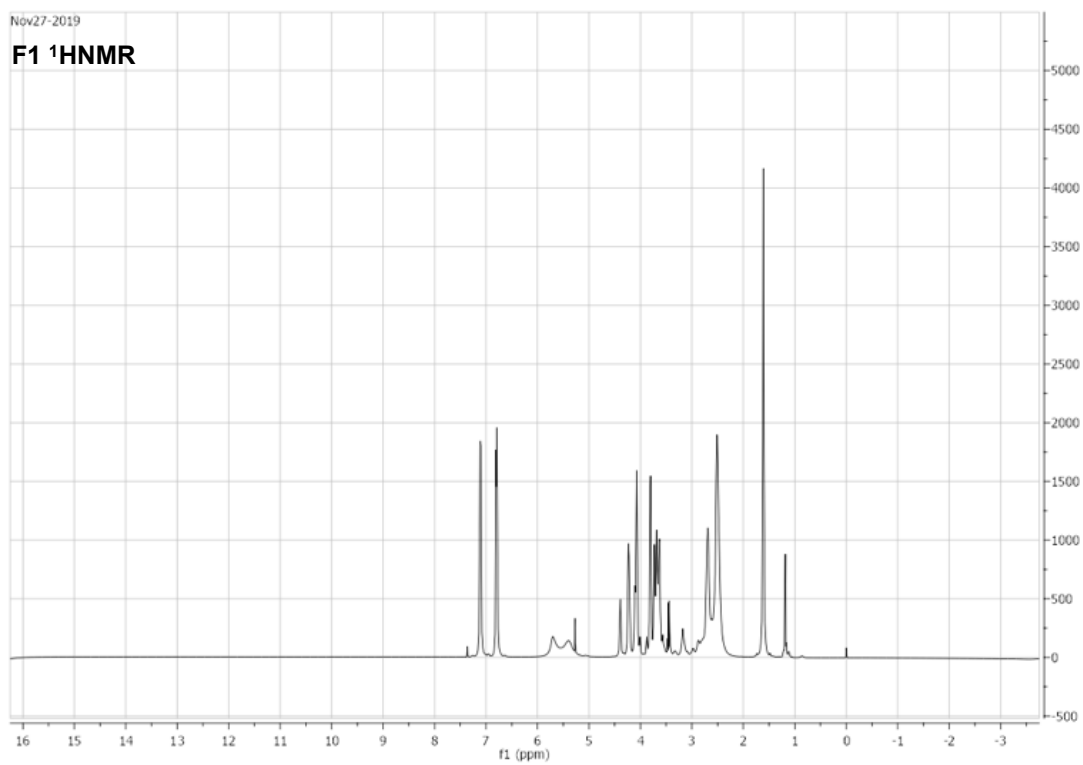
12a) ^1H NMR E3



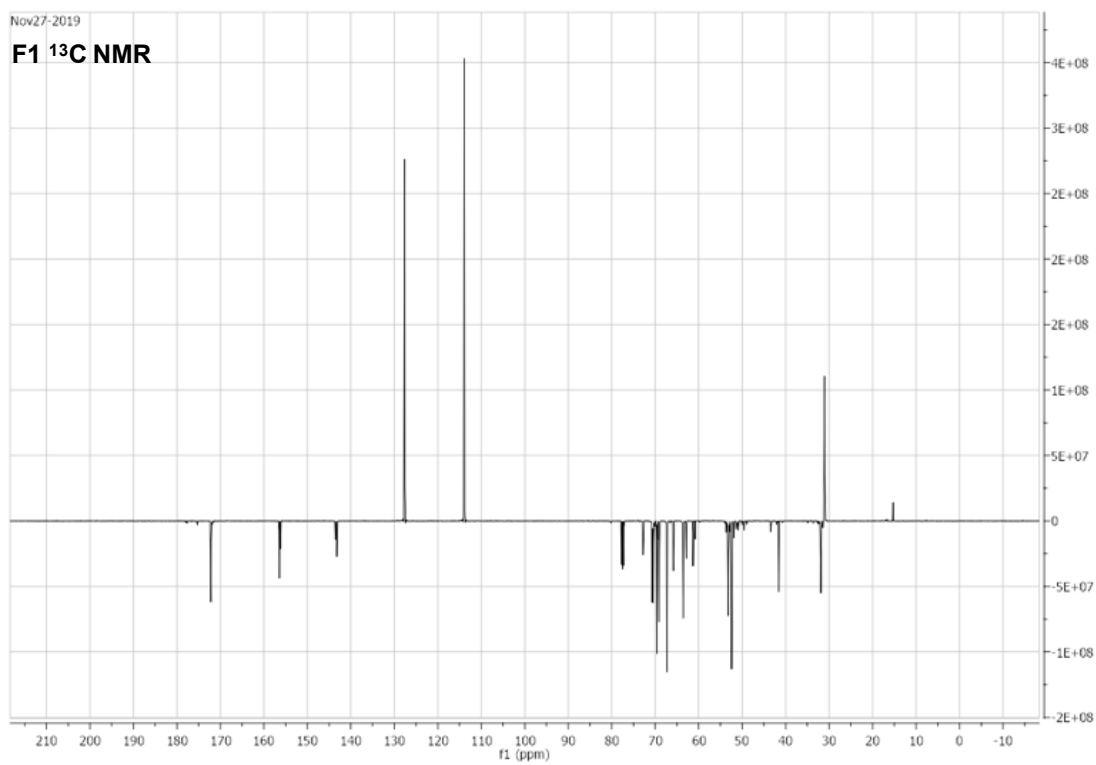
12b) ^{13}C NMR E3



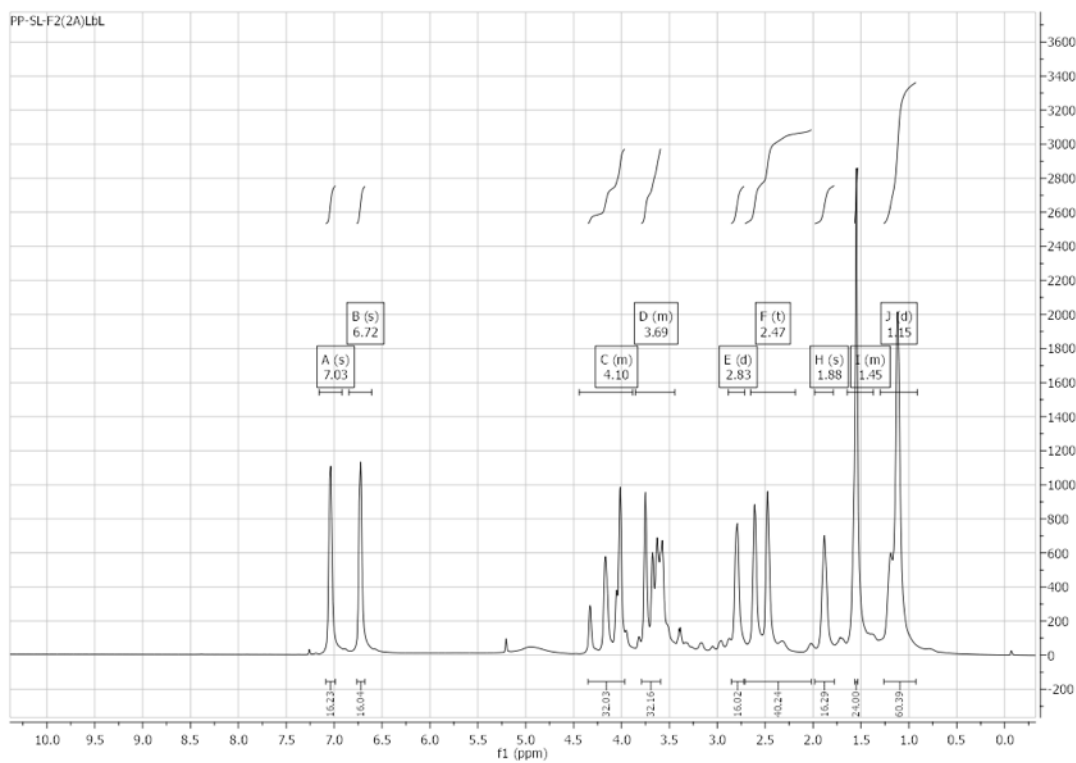
13a) H^1 NMR F1



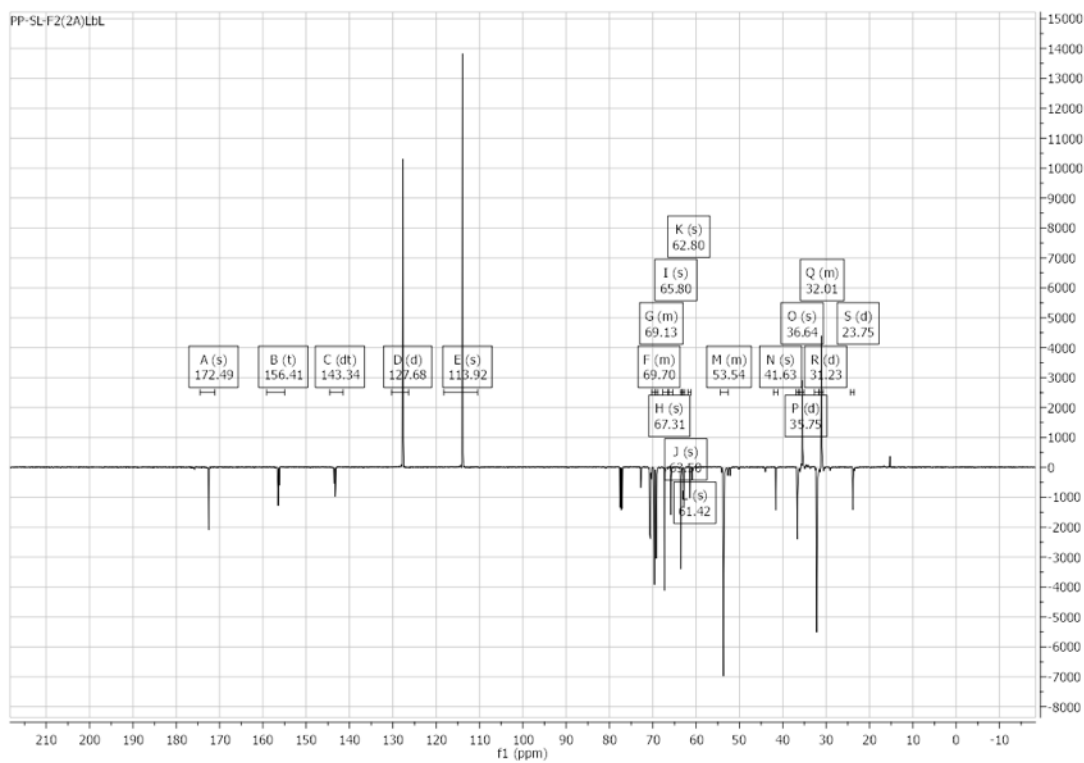
13b) C^{13} NMR F1



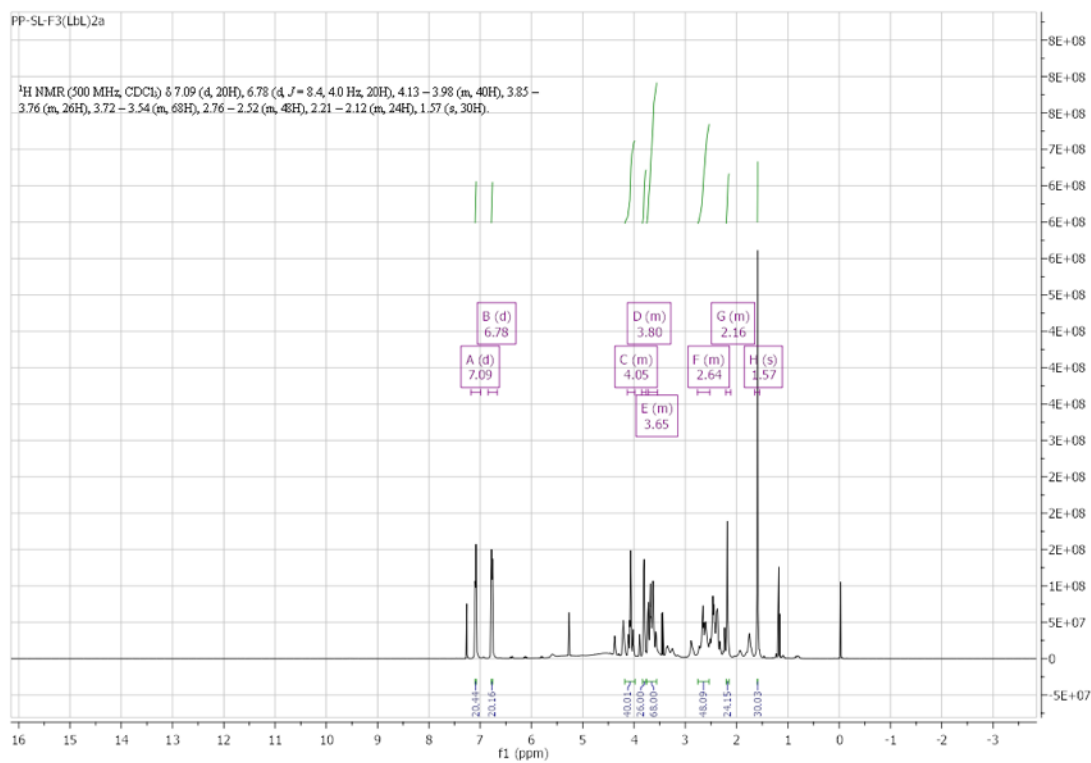
14a) ^1H NMR F2



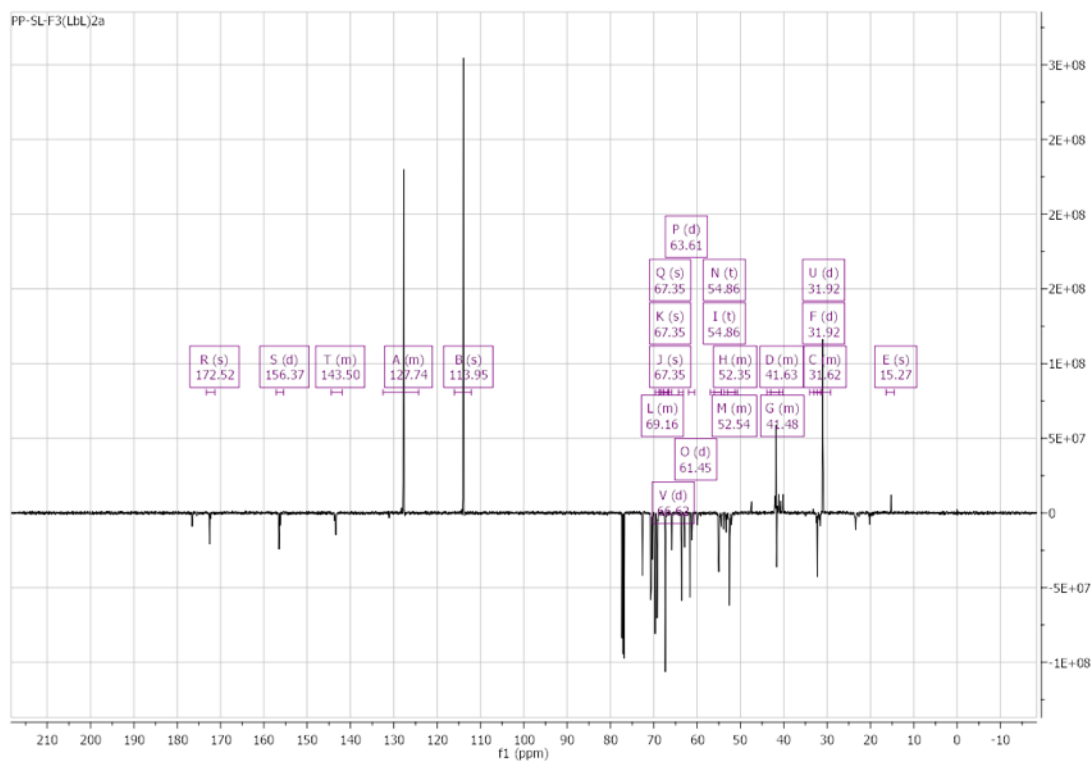
14b) ^{13}C NMR F2



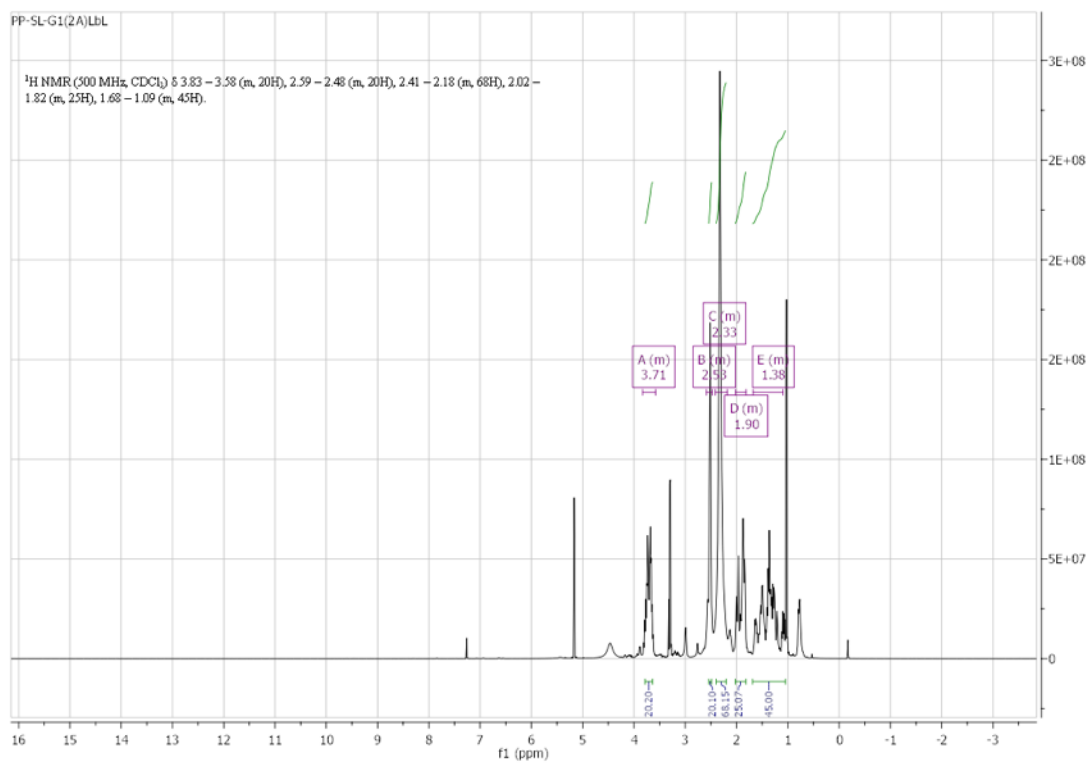
15a) ^1H NMR F3



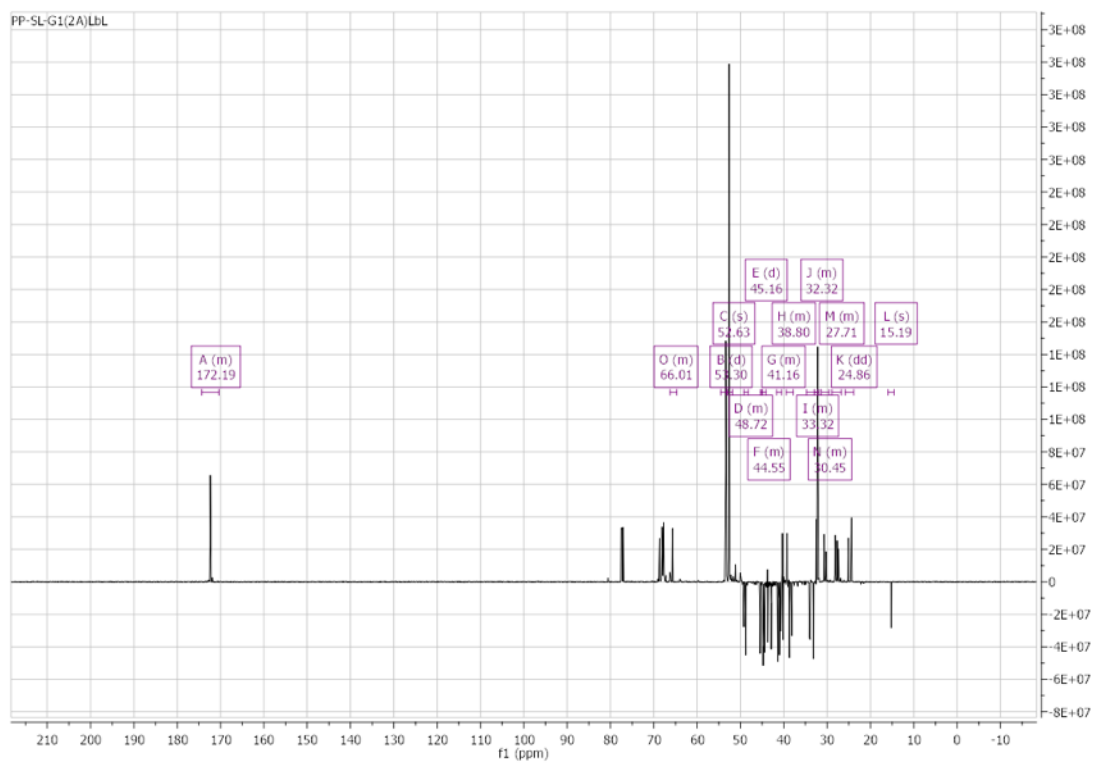
15b) ^{13}C NMR F3



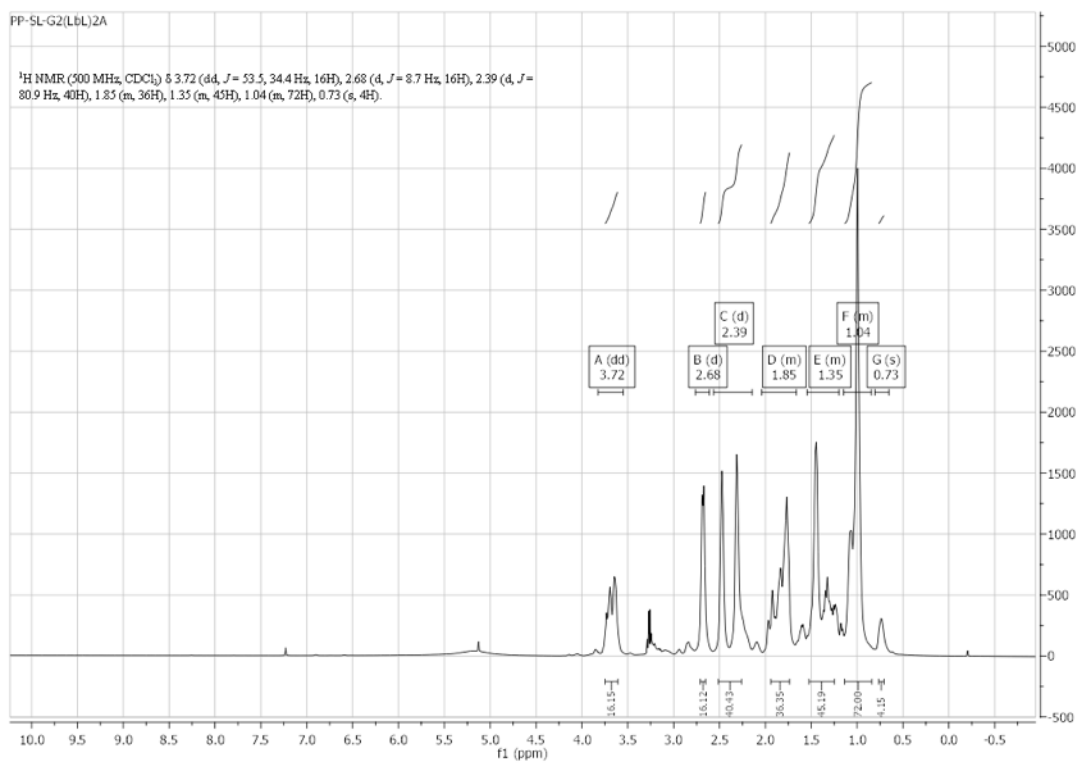
16a) ^1H NMR G1



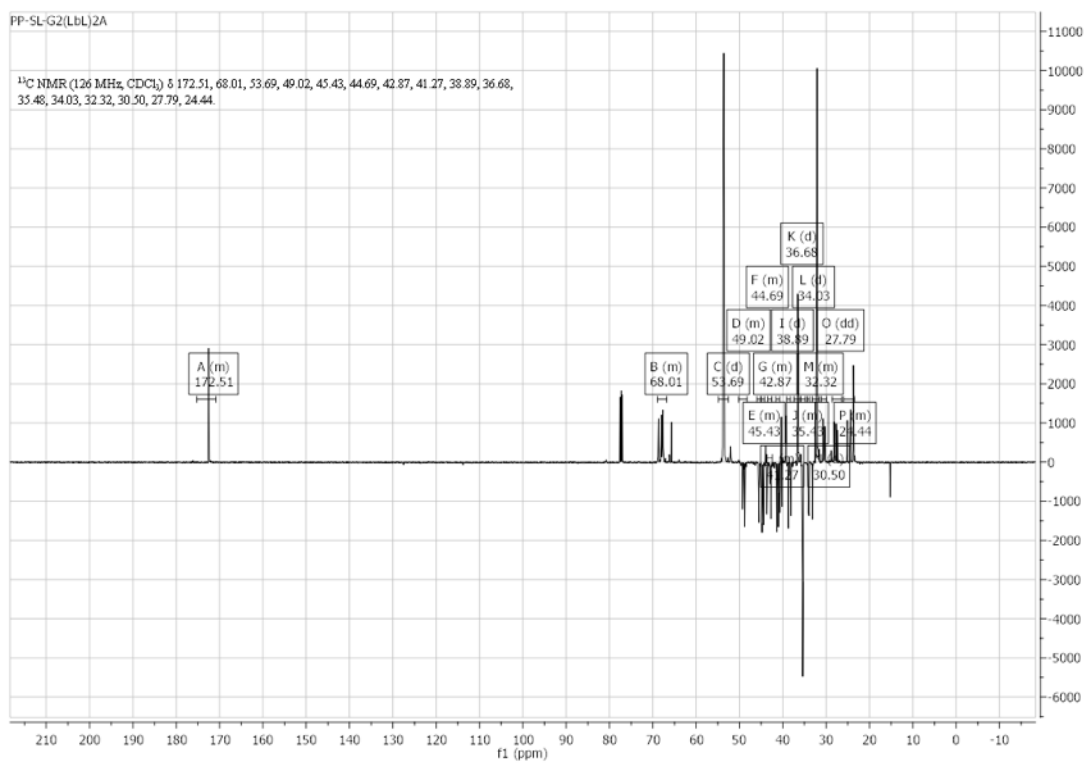
16b) ^{13}C NMR G1



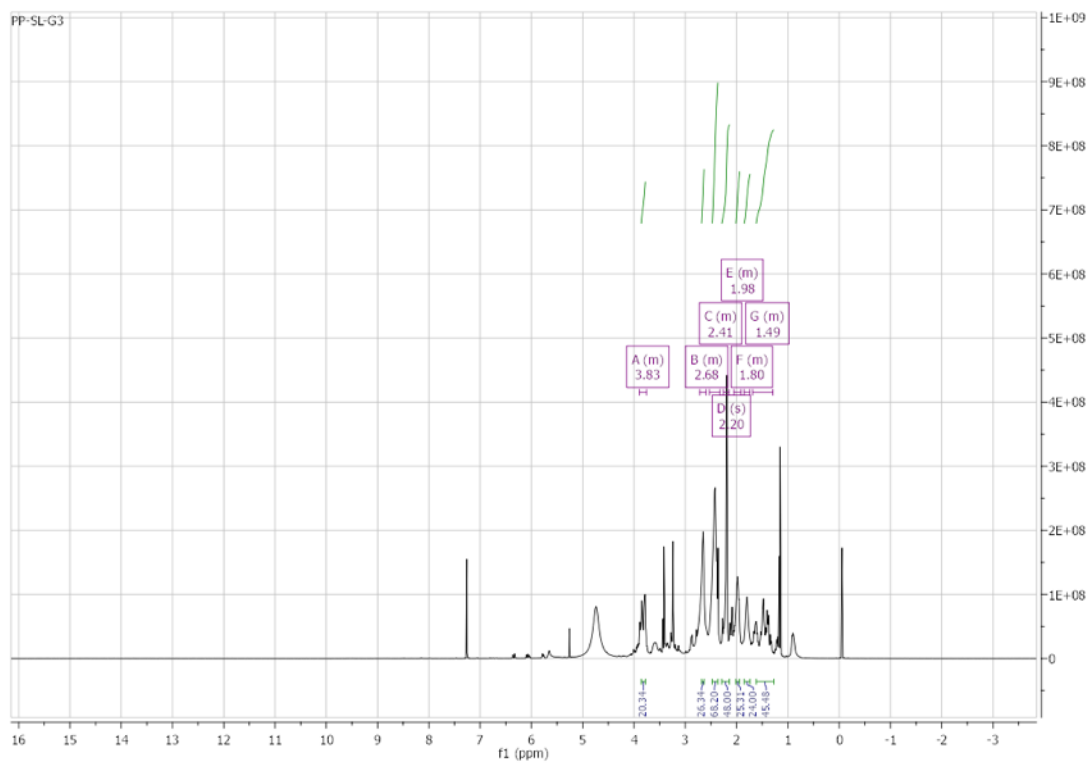
17a) ^1H NMR G2



17b) ^{13}C NMR G2



18a) ^1H NMR G3



18b) ^{13}C NMR G3

